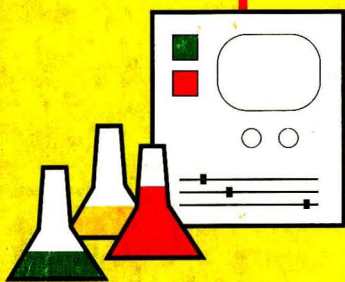
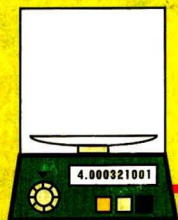
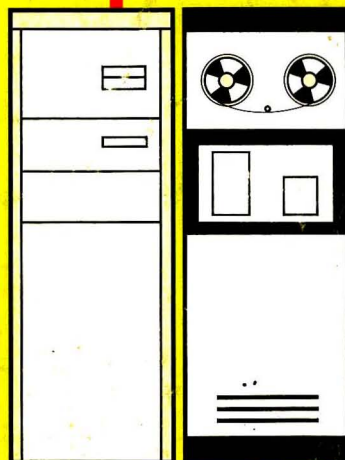
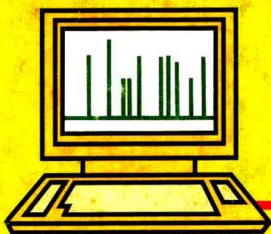


Analytical CHEMISTRY

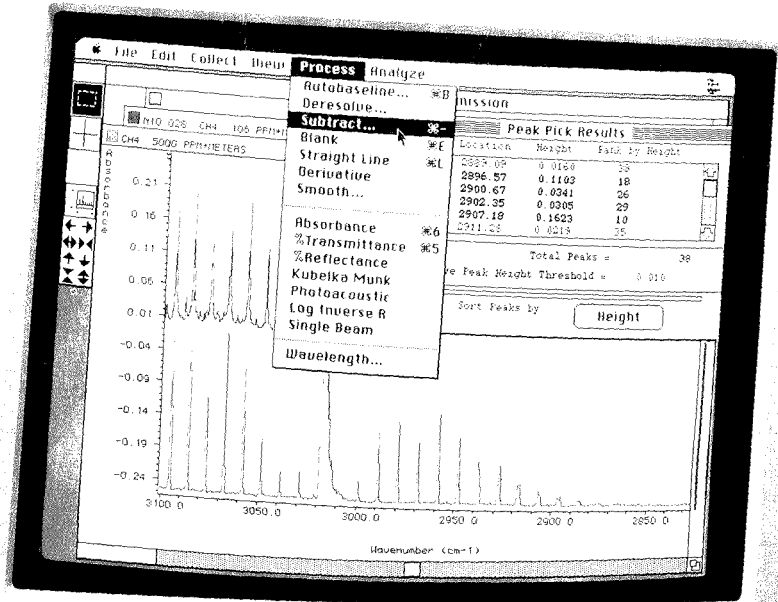


LOCAL AREA NETWORKS IN THE LABORATORY

94 A



Infrared Analysis just got easier.



Software for the Macintosh II

Nicolet

INSTRUMENTS OF DISCOVERY

Nicolet Analytical Instruments / 5225-1 Verona Rd. / Madison, WI 53711

CIRCLE 98 ON READER SERVICE CARD

(608) 271-3333

FAX: (608) 273-5046

If You're Shopping For A Sequential Plasma Spectrometer, Tear Out This Ad & Take It With You.

The spectrometer's galvanometer grating drive has no articulating surfaces and remains completely wear free.

Covers complete wavelength range from 160 to 850 nm.

Minimum interelement interferences with 0.008 nm resolution.

Built-in quality and reliability. Over 600 Jarrell Ash plasma spectrometers shipped to date.

Organics and other difficult samples are now analyzable with our directly coupled, autotuned 2KW RF generator.

Minimizes argon gas consumption on routine samples with low power/low flow operation; maximizes analytical results on difficult samples with high power/high flow operation.

Color graphics speeds peak selection, background and interelement correction, and other methods development tasks.

Full computer automated control of sample delivery, gas flows, RF power and observation height gives best possible accuracy and detection limits on every sample.

Fast, semiquantitative analysis of up to 72 elements with a three element standard.

Sophisticated command language provides decision making logic for complex analytical tasks—e.g. CLP protocol with autosampler operation.

Even novice technicians can get excellent results with minimal training. Menu-driven ThermoSPEC™ software gives frequent prompts and calls for easy 'fill in the blanks' responses and single key commands.

In the words of our chief engineer, our *AtomScan™ 25 Spectrometer* is "everything anyone ever wanted in a sequential ICP instrument."

It's the culmination of more than three decades of developmental work, incorporating the best features — RF generator, monochromator, sample delivery and excitation, data system and software — of all previous generations of Jarrell Ash plasma spectrometers.

And whether you are a research spectroscopist or an occasional user, that simply means you are going to get better accuracy and detection limits on every

element in any sample matrix with the *AtomScan 25* than with instruments costing twice as much.

Don't take our word for it.

Tear out this ad and take it with you on your trip to see brand X. See if they offer you anywhere near as much for so little.

We think we'll make you a believer.

For literature or a demonstration of the *AtomScan 25*, call (508) 520-1880. Or write Thermo Jarrell Ash Corp., 8 East Forge Parkway, Franklin, MA 02038-9101.

Thermo Jarrell Ash Corporation

A Division of Thermo Instrument Systems, Inc.

CIRCLE 137 ON READER SERVICE CARD

Clean solutions for troubled waters.

Environmental sample matrices can be hazardous to your productivity.

If you're struggling to detect water contaminants at the required levels, you'll be glad to know Dionex has an easier way.

Crash the ppb barrier in complex matrices.

Alkali and alkaline earth metals rob ICP spectroscopy of its sensitivity for measuring transition metals in sea water—unless you do a lot of sample prepping.

Couple Dionex Chelation Ion Chromatography to an ICP spectrometer and get those fractional ppb levels with a *direct introduction* of your sea water or acid digest sample.

Find a drop of chromium in a bucket of interferences.

Hexavalent chromium* in waste water is not unlike a needle in a haystack: so elusive, it devours your time.

With our new IC method, incorporating a very high-



Oxy-Halides Detection in Drinking Water†

Adequate separation between the chlorate and nitrate peaks could not be achieved with past anion columns. The new IonPac AS9 column provides the resolution needed for reliable detection of chlorite and chlorate.

Peaks	ppm
1. F ⁻	5.66
2. ClO ₂ ⁻	0.50
3. Cl ⁻	45.45
4. NO ₂ ⁻	0.06
5. Br ⁻	0.08
6. ClO ₃ ⁻	0.14
7. NO ₃ ⁻	42.11
8. HPO ₄ ²⁻	0.17
9. SO ₄ ²⁻	5.00

Column: IonPac AS9
Eluant: Na₂CO₃/NaHCO₃
Detection: Suppressed Conductivity

with chemically suppressed conductivity detection, does the job in one easy run.

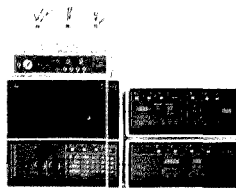
Series 4500i. The right solutions. Right now.

Determine chlorite and chlorate in a single run.

How do you measure oxy-halides in drinking water to the required 0.1 ppm? Until now, with great difficulty and not much reliability. Fortunately, the new, highly selective Dionex IonPac® AS9 column, combined

When you want solutions, you need Dionex. Find out how Dionex columns and the Series 4500i Systems can solve your environmental analysis problems—wet or dry. Contact your local Dionex representative or (in U.S.A.) call 1-800-227-1817, ext. 42 today.

Series 4500i Ion Chromatograph



DIONEX
A BETTER SOLUTION

Direct Metals Detection in Sea Water*

Metal	Detection Limit (ppb)	
	Direct Nebulization ¹	Chelation Concentration ²
Cd	10	0.1
Co	10	0.1
Cu	10	0.1
Fe	10	0.1
Mn	5	0.1
Ni	10	0.1
Pb	50	0.9
Zn	10	0.1

¹ With background correction
² 11 mL concentrated

*IC₁ ICP under EPA review

Dionex Chelation IC provides a 100-fold improvement in ICP detection limits.

capacity ion exchange column, non-metallic postcolumn chemistry, and photometric detection, you'll get 0.1 ppb sensitivity and no interferences in a 6-minute analysis.

*Method under EPA review

Dionex Corporation, P.O. Box 3603, Sunnyvale, CA 94088-3603, Canada Dionex Canada, Ltd., (416) 620-0077, England Dionex (UK) Ltd., (276) 69 722, West Germany Dionex GmbH, (612) 66036, France Dionex S.A., (1) 4621-6666, Italy Dionex S.r.l., (06) 3792979, Netherlands Dionex B.V. (76) 714800, © 1989 Dionex Corporation

CIRCLE 30 ON READER SERVICE CARD

Registered in U.S. Patent and Trademark Office; Copyright 1990 by the American Chemical Society

ANALYTICAL CHEMISTRY (ISSN 0003-2700) is published semimonthly by the American Chemical Society at 1155 16th St., N.W., Washington, DC 20036. Editorial offices are located at the same ACS address (202-872-4570; FAX 202-872-6325; TDD 202-872-8733). Second-class postage paid at Washington, DC, and additional mailing offices. Postmaster: Send address changes to ANALYTICAL CHEMISTRY Member & Subscriber Services, P.O. Box 3337, Columbus, OH 43210.

Claims for missing numbers will not be allowed if loss was due to failure of notice of change of address to be received in the time specified; if claim is dated (a) North America: more than 90 days beyond issue date, (b) all other foreign: more than one year beyond issue date, or if the reason given is "missing from files."

Copyright Permission: An individual may make a single reprographic copy of an article in this publication for personal use. Reprographic copying beyond that permitted by Section 107 or 108 of the U.S. Copyright Law is allowed, provided that the appropriate per-copy fee is paid through the Copyright Clearance Center, Inc., 27 Congress St., Salem, MA 01970. For reprint permission, write Copyright Administrator, Publications Division, ACS, 1155 16th St., N.W., Washington, DC 20036.

Registered names and trademarks, etc., used in this publication, even without specific indication thereof, are not to be considered unprotected by law.

Advertising Management: Centcom, Ltd., 500 Post Rd. East, Westport, CT 06880 (203-226-7131)

1990 subscription rates include air delivery outside the U.S., Canada, and Mexico

Members	1 yr	2 yr
Domestic	\$ 29	\$ 49
Canada and Mexico	64	119
Europe	96	183
All Other Countries	118	227
Nonmembers		
Domestic	59	100
Canada and Mexico	94	170
Europe	186	336
All Other Countries	206	380

Three-year and other rates contact: Member & Subscriber Services, ACS, P.O. Box 3337, Columbus, OH 43210 (614-447-3776 or 800-333-9511).

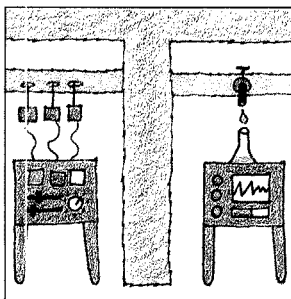
Subscription orders by phone may be charged to VISA, MasterCard, Barclay card, Access, or American Express. Call toll free 800-ACS-5558 in the continental United States; in the Washington, DC, metropolitan area and outside the continental United States, call 202-872-8065. Mail orders for new and renewal subscriptions should be sent with payment to the Business Management Division, ACS, P.O. Box 28597, Central Station, Washington, DC 20005.

Subscription service inquiries and changes of address (include both old and new addresses with ZIP code and *recent mailing label*) should be directed to the ACS Columbus address noted above. Please allow six weeks for changes to become effective.

ACS membership information: Lorraine Bowlin (202-872-4587)

Single issues, current year, \$8.00 except review issue, \$14.00, and LabGuide, \$49.00; **back issues and volumes and microform editions** available by single volume or back issue collection. For information or to order, call the number listed for subscription orders by phone; or write the Microform & Back Issues Office at the Washington address.

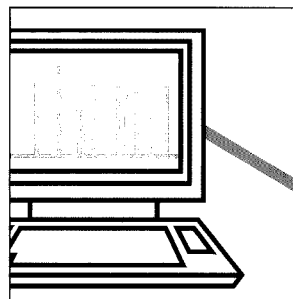
Nonmembers rates in Japan: Rates above do not apply to nonmember subscribers in Japan, who must enter subscription orders with Maruzen Company Ltd., 3-10 Nihonbashi 2-chome, Chuo-ku, Tokyo 103, Japan. Tel: (03) 272-7211.



REPORT

65 A

Process analytical chemistry is dedicated to improving manufacturing processes so that high-quality products are generated efficiently. Michael T. Riebe and Daniel J. Eustace of Polaroid Corporation describe PAC resources, technologies, and applications from an industrial perspective



A/C INTERFACE

94 A

On the cover. Local area networks in the laboratory. LANs are becoming more and more common in the laboratory. In the first of a two-part series, Steven A. Warner of Andrus Research Corporation explains what a LAN is and how data are communicated between various components

BRIEFS

54 A

NEWS

61 A

New Instrumentation Advisory Panel members. ▶ Subdivision calls for nominations. ▶ NATAS seeks nominations for Mettler Award. ▶ NIST standardizes MS/MS measurements. ▶ Hawaii in "vog". ▶ Warm weather produces more snow

MEETINGS

73 A

1990 conferences. ▶ Short courses and workshops. ▶ Call for papers

BOOKS

85 A

Critical reviews. Recently released books on inverse gas chromatography, microbore column chromatography, and LC troubleshooting are reviewed

FOCUS

89 A

Keeping aging planes healthy. With the average age of a commercial U.S. airplane hovering around 12 years, ensuring airworthiness has become a national issue. Nondestructive tests play an important role in identifying potential structural problems, and newer, more sophisticated tests are being developed for the future

NEW PRODUCTS & MANUFACTURERS' LITERATURE

92 A

AUTHOR INDEX

97

Articles

Voltammetry with Microvoltammetric Electrodes in Resistive Solvents under Linear Diffusion Conditions 98

Microelectrodes of 50- μm radius are used to characterize chemical reactions that accompany electron transfer in solvents with low dielectric constants.

David O. Wipf and R. Mark Wightman*, Department of Chemistry, Indiana University, Bloomington, IN 47405

Ionic Equilibria in Neutral Amphiprotic Solvents: Relationships between Electrolyte pK Values and Solvent Polarity and Composition for Several Binary Isopropyl Alcohol Mixtures 102

The effect of the addition of a second solvent to electrolyte solutions in isopropyl alcohol is studied. Equations that relate electrolyte pK values to solvent polarity, dielectric constant, and solvent composition are proposed and experimentally tested.

Elisabeth Bosch*, Clara Ràfols, and Martí Rosés, Departament de Química Analítica, Universitat de Barcelona, Barcelona, Spain

Mass Spectrometric Studies on the Response Mechanism of Surface Ionization Detectors for Gas Chromatography 107

Mass spectrometric studies at atmospheric pressure demonstrate that positive surface ionization is the response mechanism of surface ionization detectors for GC.

Toshihiro Fujii* and Hitoshi Jimba, National Institute for Environmental Studies, Tsukuba, Ibaraki 305, Japan and Hiromi Arimoto, Shimadzu Corporation, Nakagyo, Kyoto 604, Japan

Determination of Chromium in Urine by Stable Isotope Dilution Gas Chromatography/Mass Spectrometry Using Lithium Bis(trifluoroethyl)dithiocarbamate as a Chelating Agent 111

Chromium in the NIST freeze-dried urine SRM-2670 is quantitated at concentration values that are in good agreement with the NIST values of 13 $\mu\text{g/L}$ and 85 $\mu\text{g/L}$.

Suresh K. Aggarwal, Michael Kinter, Michael R. Wills, John Savory, and David A. Herold*, Departments of Pathology, Biochemistry, and Medicine, University of Virginia Health Sciences Center, Charlottesville, VA 22908

Study of Oil Field Chemicals by Combined Field Desorption/Collision-Activated Dissociation Mass Spectrometry via Linked Scan 116

FDMS is used for direct fingerprinting of oil field chemicals such as biocides, demulsifiers, and scale inhibitors. The gross composition of major ingredients is visualized in a FD spectrum. Molecular structural information is provided by FD/CAD MS via B/E linked scan.

J. Shen* and A. S. Al-Saeed, Saudi Arabian Oil Company, Box 8745, Dhahran 31311, Saudi Arabia

Protocol for Liquid Chromatography/Mass Spectrometry of Glutathione Conjugates Using Postcolumn Solvent Modification 121

Mixtures of glutathione conjugates are analyzed by thermospray ionization LC/MS when organic modifier is added to the mobile-phase postcolumn. The relative intensity of the molecular ions varies from 10 to 60%.

Mark F. Bean*, Sharon L. Pallante-Morell, Deanne M. Dulik, and Catherine Fenselau, Department of Pharmacology and Molecular Sciences, The Johns Hopkins University School of Medicine, Baltimore, MD 21205

Endothermic Ion-Molecule Reactions: Strategies for Tandem Mass Spectrometric Structural Analyses of Large Biomolecules 125

Reactive collisions with low endothermicity are proposed as a method for collisionally induced dissociation of peptides in tandem mass spectrometers.

Ron Orlando, Constance Murphy, and Catherine Fenselau, Structural Biochemistry Center, Department of Chemistry, University of Maryland Baltimore County, Baltimore, MD 21228, Gordon Hansen, Boehringer-Ingelheim Research and Development Center, Ridgefield, CT 06876, and Robert J. Cotter*, Middle Atlantic Mass Spectrometry Facility, Department of Pharmacology and Molecular Sciences, The Johns Hopkins University School of Medicine, Baltimore, MD 21205

Simultaneous Enhancement of Separation Selectivity and Solvent Strength in Reversed-Phase Liquid Chromatography Using Micelles in Hydro-Organic Solvents 130

Micelles and organic solvents are used as mobile-phase modifiers in reversed-phase LC to enhance the separation selectivity while reducing analysis time.

Morteza G. Khaledi*, Joost K. Strasters, Andrew H. Rodgers, and Emelita D. Breyer, Department of Chemistry, North Carolina State University, P.O. Box 8204, Raleigh, NC 27695-8204

Analytical and Micropreparative Ultrahigh Resolution of Oligonucleotides by Polyacrylamide Gel High-Performance Capillary Electrophoresis 137

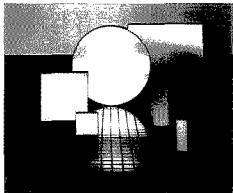
Separations of polydeoxyoligonucleotides on polyacrylamide gel capillary columns with plate counts in excess of 30×10^6 per meter are shown. The use of electric field programming for the isolation of purified fractions from high-resolution separations is presented.

A. Guttman, A. S. Cohen, D. N. Heiger, and B. L. Karger*, Barnett Institute and Department of Chemistry, Northeastern University, Boston, MA 02115

* Corresponding author

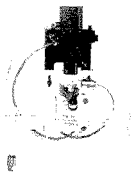
Ruled and Holographic Diffraction Gratings

Instruments SA provides a wide variety of high performance diffraction gratings. Among the many standard types available are aberration corrected blazed and ion etched concave monochromator gratings, flat field gratings for use with diode array detectors, toroidal gratings for use in the VUV and classically ruled as well as holographic plane gratings. Applications range from upper atmosphere ozone monitoring by satellite to bio testing and emission spectrometers. For further information contact Jobin Yvon, Instruments SA (201) 494-8660. CIRCLE 63



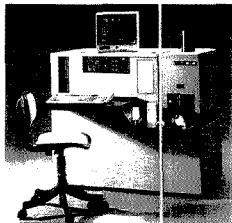
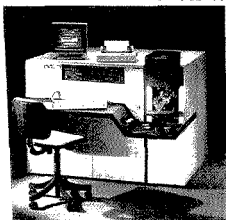
ICP Sample Introduction

JY has solved the problem of changing the nebulizer, spray chamber and torch for different applications by developing an exclusive system of "interchangeable cassettes". Various sample introduction systems are assembled into individual cartridges which, by use of electro-pneumatic devices for the gas flows, can be rapidly interchanged. For further information contact Jobin Yvon, Instruments SA (201) 494-8660. CIRCLE 64



Glow Discharge Spectroanalyzer

The GDL Excitation Source for direct solid sample analysis, uses the principle of cathodic sputtering. The conducting sample forms the cathode which is bombarded with positive argon ions to excite the sample atoms. The GDL is used for both elemental and surface analysis of metals including ferrous and non-ferrous alloys, noble metals and ceramics. For further information contact Jobin Yvon, Instruments SA (201) 494-8660. CIRCLE 65

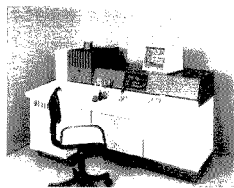
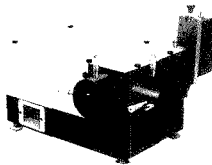


Compact Sequential ICP Spectrometer

The JY 24 has the advantages of a full featured ICP spectrometer in a single, compact, space-saving unit. By using a large surface area and high groove density holographic grating, the resolution and light gathering power of the JY 24 are unequalled for its size. For further information contact Jobin Yvon, Instruments SA (201) 494-8660. CIRCLE 66

Spectrometers

With a line of single and double spectrometers which spans from 100 to 1500 nm in focal length, Instruments SA/Jobin Yvon can furnish the ideal spectrometer for any UV, Visible or IR application. This broad range of instruments significantly reduces the need for compromise in coverage, stray light rejection or resolution when specifying a system. Each spectrometer can be automated for integration into a spectroanalytical system. For further information contact Instruments SA/Jobin Yvon (201) 494-8660. CIRCLE 67



Simultaneous and Sequential ICP Spectrometers

The JY 70 Plus consists of an integrated direct reading double polychromator — sequential spectrometer. This ICP system combines the speed of simultaneous, multi-element analysis with the versatility and flexibility of the sequential system. For further information on the JY 70 Plus or JY 38 Plus contact Jobin Yvon, Instruments SA (201) 494-8660. CIRCLE 68

INTRODUCING THE NEW JY 50 POLYSCAN FROM A WORLD LEADER IN ICP SYSTEMS

The JY 50 PolyScan not only provides all the advantages inherent in a simultaneous multi-element Spectroanalyzer but also offers spectral line selection flexibility which previously was found only in sequential ICP systems. Jobin Yvon has developed a new scanning entrance slit which furnishes 2.2 nm wavelength displacement from any of the preselected fixed analytical channels.

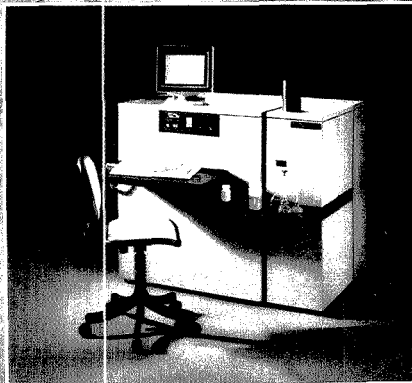
For more information on the JY 50 PolyScan and the complete spectrum of JY instruments, use the reader service card, or write or call today.

CIRCLE 69 ON READER SERVICE CARD

JOBIN YVON  **J-Y DIVISION**
Instruments SA, Inc.

6 Olsen Avenue, Edison, NJ 08820-2419
Tel. (201) 494-8660, Telex 844516
FAX (201) 494-8796

In Europe: Jobin Yvon, 16-18 Rue du
Canal 91163 Longjumeau, France
Tel. (33) 1 69 09 34 93
Telex JOBYVON 692882F
FAX 011-331-6909-0721



Sample Introduction Techniques for the Determination of Osmium Isotope Ratios by Inductively Coupled Plasma Mass Spectrometry 141

Osmium isotope ratios with precisions of 0.2%, 0.3%, and 0.5% can be determined by using solution nebulization, osmium tetroxide vapor generation, and electrothermal vaporization sample introduction techniques, respectively.

D. Conrad Gregoire, Geological Survey of Canada, 601 Booth Street, Ottawa, Ontario, Canada K1A 0E8

Effect of Wet Decomposition Methods on the Determination of Cobalt, Copper, Selenium, and Zinc in Biological Samples Using Electrophoresis 146

A method combining radiotracer techniques with paper electrophoresis is used to investigate the optimal decomposition conditions for cobalt, copper, selenium, and zinc in rat liver samples. The results indicate that Co- and Se-containing liver samples decompose more easily than Cu- and Zn-containing liver samples.

J. Y. Yang and M. H. Yang*, Institute of Nuclear Science, National Tsing Hua University, Hsinchu, Taiwan, Republic of China and **S. M. Lin**, School of Technology for Medical Sciences, Kaohsiung Medical College, Kaohsiung, Taiwan, Republic of China

Electrodeposition of Palladium, Iridium, Ruthenium, and Platinum in Poly(4-vinylpyridine) Films for Electrocatalysis 151

Characterization of the metal/polymer films by electrochemical techniques, energy-dispersive X-ray spectroscopy, and scanning electron microscopy reveals that the metal microparticles are nucleated at the carbon-polymer interface and that growth occurs through the polymer to the polymer-solution interface.

Kent M. Kost and Duane E. Bartak*, Department of Chemistry, University of North Dakota, Grand Forks, ND 58202 and **Beth Kazee and Theodore Kuwana**, University of Kansas, Center for Bioanalytical Research, 2095 Constant Avenue, Lawrence, KS 66046

Laser-Excited Atomic Fluorescence in a Pulsed Hollow-Cathode Glow Discharge 157

Solutions are deposited on disposable graphite electrodes that function as hollow cathodes in a pulsed discharge. Detection limits for Pb and Ir are 100 pg/mL (500 fg) and 6 ng/mL (20 pg), respectively.

Mark Glick, Benjamin W. Smith, and James D. Winefordner*, Department of Chemistry, University of Florida, Gainesville, FL 32611

Automated Instrumentation for Comprehensive Two-Dimensional High-Performance Liquid Chromatography of Proteins 161

Separation of a nine-component protein sample and serum samples is achieved with a comprehensive two-dimensional LC system. The use of an ion-exchange column followed by a size exclusion column provides resolution and peak capacities greater than either column used alone.

Michelle M. Bushey and James W. Jorgenson*, Department of Chemistry, University of North Carolina, Chapel Hill, NC 27599-3290

Near-Infrared Diffuse Reflectance Analysis of Athabasca Oil Sand 167

Bitumen in oil sand is determined at 1-cm sampling intervals within a length of core using a model based on the first derivative of absorbance spectra. The model provides a high-resolution profile of grade variability as a function of depth.

Robert C. Shaw, Research Department, Syncrude Canada Ltd., Edmonton, Alberta, Canada T6C 4G3 and **Byron Kratochvil***, Department of Chemistry, University of Alberta, Edmonton, Alberta, Canada T6G 2G2

Normalized Measure of Overlap between Non-Gaussian Chromatographic Peaks 174

A measure of overlap between two chromatographic peaks is defined. Its properties and application to Gaussian and non-Gaussian peaks (as found in preparative chromatography) are described.

Eric V. Dose and Georges Guiochon*, Department of Chemistry, University of Tennessee, Knoxville, TN 37996 and Analytical Chemistry Division, Oak Ridge National Laboratory, Oak Ridge, TN 37831

Gas Sensor and Permeation Apparatus for the Determination of Chlorinated Hydrocarbons in Water 182

A solid-state gas sensor is combined with a silicone rubber permeation apparatus for the on-line determination of hydrocarbons in water. The sensor response is linear for low concentrations of chloroform, trichloroethane, and chlorobenzene.

Joseph H. Stetter* and Zhuang Cao, Department of Chemistry, Illinois Institute of Technology, Chicago, IL 60616

On-Line Fluorescence Lifetime Detection for Chromatographic Peak Resolution 186

Highly overlapping chromatographic peaks are resolved by heterogeneity analysis of on-the-fly frequency-domain fluorescence lifetime measurements.

W. Tyler Cobb and Linda B. McGown*, Department of Chemistry, P. M. Gross Chemical Laboratory, Duke University, Durham, NC 27706

The Physical Sense of Simulation Models of Liquid Chromatography: Propagation through a Grid or Solution of the Mass Balance Equation? 189

The similarity and differences between commonly used simulation methods are demonstrated by two different concepts. Errors introduced by the calculation methods are related to chromatographic band broadening.

Martin Czok and Georges Guiochon*, Department of Chemistry, University of Tennessee, Knoxville, TN 37996-1600 and Division of Analytical Chemistry, Oak Ridge National Laboratory, Oak Ridge, TN 37831-6120

Bayesian versus Fourier Spectral Analysis of Ion Cyclotron Resonance Time-Domain Signals 20

Bayesian analysis can surpass FFT analysis for high accuracy determination of signal frequencies from a noisy time-domain signal, as in FT-ICR MS.

Joseph E. Meier and Alan G. Marshall*, Department of Chemistry, The Ohio State University, 120 West 18th Avenue, Columbus, OH 43210

Acrodisc: The Difference is Clear.

Clearly the Widest Selection.

Gelman Sciences Acrodiscs® are available in a wide variety of membrane types, with 0.2 μ m or 0.45 μ m pore sizes and 13mm or 25mm diameters.

Clearly Identified.

Acrodiscs are printed with identifying information, and are color-coded to the product packaging. Convenient tube containers allow you to see their contents at a glance.

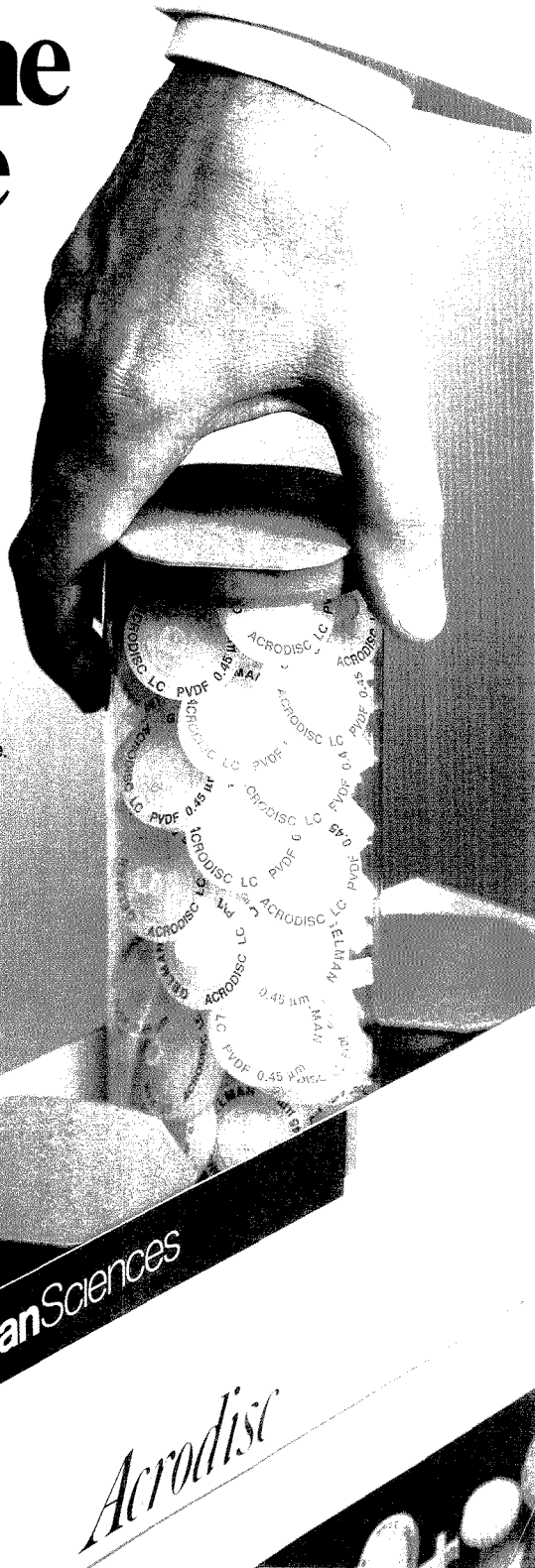
Clearly the Best Performance.

Gelman Sciences is so certain you'll be satisfied with the performance of its Acrodisc syringe filters, every package is covered by a free-replacement guarantee. So order Gelman Sciences Acrodiscs today through your local laboratory products distributor.

CIRCLE 52 ON READER SERVICE CARD

 **Gelman Sciences**

600 S. Wagner Rd. • Ann Arbor, MI 48106-1448 • 313-665-0657



Analytica 90

12th International Trade Fair for
Biochemical and
Instrumental
Analysis with
International
Conference



MESE MÜNCHEN INTERNATIONAL

**Innovative Analysis
Technology**

- ▶ Biology, biotechnology
- ▶ Biochemistry
- ▶ Genetics, genetic engineering
- ▶ Medical diagnostics
- ▶ Pharmacology
- ▶ Food analysis
- ▶ Environmental analysis
- ▶ Industrial analysis

Information:

Kallman Associates, 5 Maple Court, Ridgewood, NJ 07450,
Tel. (201) 652-7070, Tfax (201) 652-3898

Munich, May 8-11, 1990

BRIEFS

Resonance Ionization Mass Spectrometry of Sputtered Osmium and Rhenium Atoms 209

A useful yield of 1% and a detection limit of 8 ppb are demonstrated for in situ osmium concentration measurement, with an elemental selectivity of more than 1000 for osmium over rhenium.

Joel D. Blum*, M. J. Pellin, W. F. Calaway, C. E. Young, and D. M. Gruen, Materials Science, Chemistry, and Chemical Technology Divisions, Argonne National Laboratory, Argonne, IL 60439 and I. D. Hutcheon and G. J. Wasserburg, Lunatic Asylum of the Charles Arms Laboratory, Division of Geological and Planetary Sciences, California Institute of Technology, Pasadena, CA 91125

Correspondence

Reversing Enantioselectivity in Capillary Gas Chromatography with Polar and Nonpolar Cyclodextrin Derivative Phases 214

Daniel W. Armstrong* and Weiyong Li, Department of Chemistry, University of Missouri—Rolla, Rolla, MO 65401 and Josef Pitha, National Institutes of Health, NIA/GRC, Baltimore, MD 21224

Effect of a Difference of the Column Saturation Capacities for the Two Components of a Mixture on the Relative Intensities of the Displacement and Tag-Along Effects in Nonlinear Chromatography 217

Sadroddin Golshan-Shirazi and Georges Guiochon*, Department of Chemistry, University of Tennessee, Knoxville, TN 37996-1600 and Division of Analytical Chemistry, Building 4500-S, M.S. 120, Oak Ridge National Laboratory, Oak Ridge, TN 37831-6120

Technical Notes

Anion-Exchange Separation of Carbohydrates with Pulsed Amperometric Detection Using a pH-Selective Reference Electrode 220

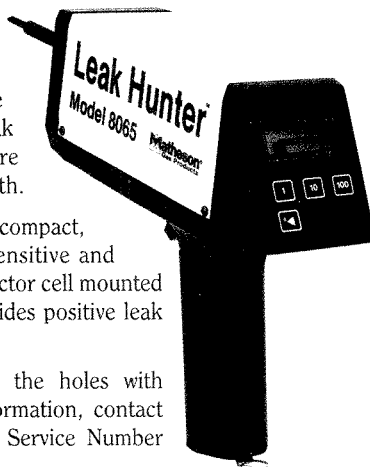
William R. LaCourse*, David A. Mead, Jr., and Dennis C. Johnson, Department of Chemistry, Iowa State University, Ames, IA 50011

If Your GC Has A Leak... Then Your Analysis May Be Full Of Holes, Too.

Leaks in your GC system can cause inaccurate results and shorten column life. Now, you can instantly determine if your instrument has a leak with the Matheson Model 8065 LEAK HUNTER™. This easy to use, hand-held gas leak detector is perfect for pinpointing leaks. It will detect a helium leak as small as 1×10^{-5} cc/sec, and is designed to get at even the hardest to reach places. Simply point the LEAK HUNTER and pull the trigger. Both audio and visual leak indicators are provided. No more messy soap solutions to deal with.

Solid state electronics make this compact, portable leak detector highly sensitive and reliable. An advanced design detector cell mounted in the front end of the unit provides positive leak location quickly and efficiently.

Improve your analysis . . . plug the holes with LEAK HUNTER. For more information, contact Matheson, or circle the Reader Service Number below.

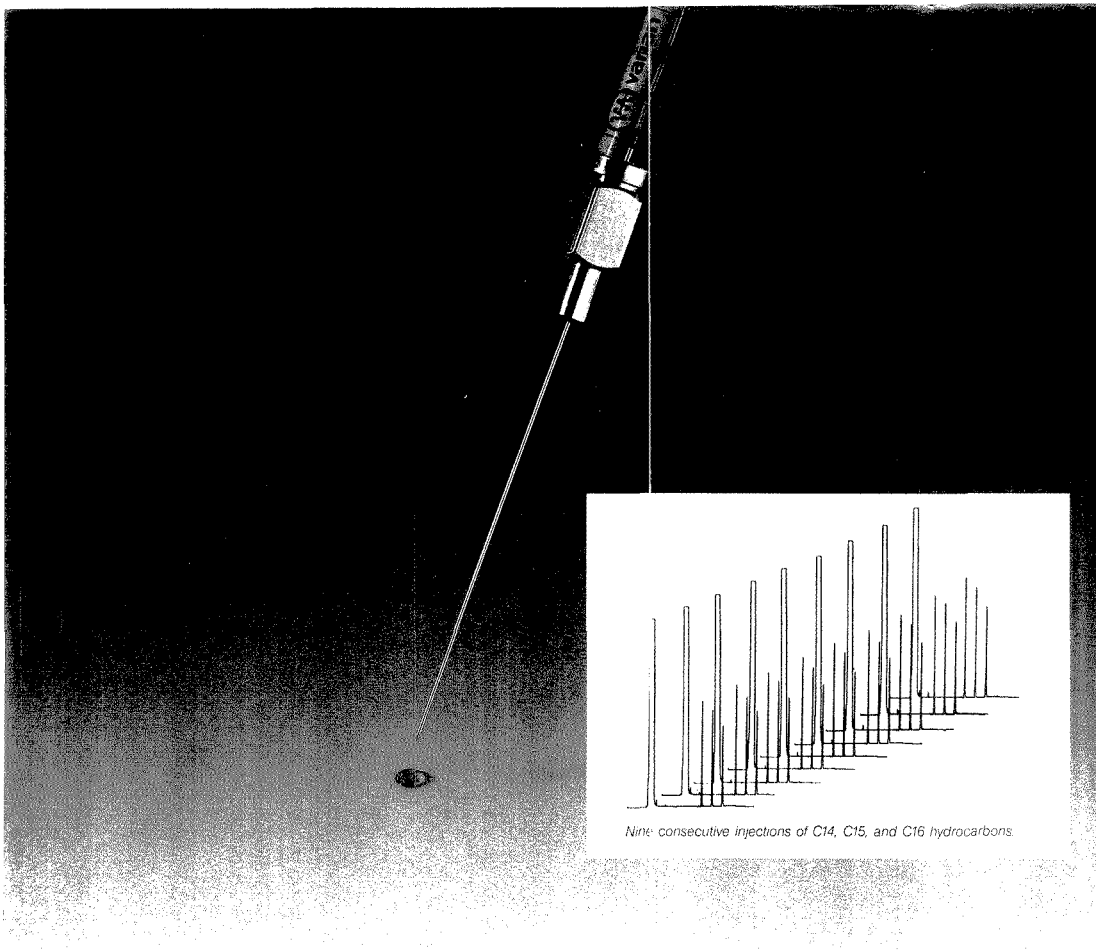


Matheson
Gas Products

World Leader in Specialty Gases & Equipment
30 Seaview Drive, Secaucus, NJ 07096-1587
FAX 201-867-4572

CIRCLE 88 ON READER SERVICE CARD

ANALYTICAL CHEMISTRY, VOL. 62, NO. 2, JANUARY 15, 1990 • 59 A



Nine consecutive injections of C14, C15, and C16 hydrocarbons.

NO LOSS IS YOUR GAIN.

Nine 1 μ L injections from only 10 μ L of sample.

Imagine being able to perform multiple injections with such a minute amount of sample! Varian does. With our new 8100 AutoSampler™, we have redefined low loss autosampling into virtually no loss.

Imagine the possibility of no sample carryover! None whatsoever. The 8100 AutoSampler is unique because of the dynamic purge design of the wash system. You inject the whole sample, and nothing but the sample.

The impossible becomes possible because of the superior capabilities of the 8100 achieved with the "sandwich" technique — a technique that not only improves precision and accuracy, but also ensures that what is measured is injected.

With an 8100 installed on your Varian Gas Chromatograph, you'll easily see the benefits to your lab in increased productivity. It's more than just a sample saver. It's easy to use because it's completely controlled via the keyboard on the GC.

AutoSampler methods are stored and battery protected, so for unattended operation, just load it and go.

Let us show you how the "no loss" 8100 AutoSampler can be your gain. For more information, call 800-231-8134. In Canada, call 416-457-4130.

CIRCLE 144 ON READER SERVICE CARD

GC WITH A FUTURE

New Instrumentation Panel Members

Daniel Armstrong, Thomas Chester, and Brenda Shaw have been appointed to three-year terms on ANALYTICAL CHEMISTRY's Instrumentation Advisory Panel. They replace departing panel members James Callis, University of Washington; Ronald Majors, Hewlett Packard; and Linda McGown, Duke University. Six other analytical chemists serve on the panel: D. Bruce Chase, Du Pont; R. Graham Cooks, Purdue University; L. J. Cline Love, Seton Hall University; Sanford Markey, National Institute of Mental Health; Gary Small, University of Iowa; and R. Mark Wightman, University of North Carolina.

Instrumentation Advisory Panel members propose appropriate topics and authors for INSTRUMENTATION and other A-page features. They also contribute to a dialogue on the overall aims and scope for INSTRUMENTATION articles, which introduce and promote interest in various chemical measurement systems (including instrument design and application). These features are written for the nonspecialist and need not be comprehensive reviews. In addition to the panel-generated invitations, ANALYTICAL CHEMISTRY considers unsolicited articles.

Brief biographical sketches of the new members follow.



Daniel Armstrong is professor of chemistry and head of the Bioanalytical Research Institute and the Division of Analytical Chemistry at the University of Missouri-Rolla. He received a B.S. degree (1972) from Washington & Lee University and an M.S. degree (1974) and Ph.D. (1977) from Texas A&M University.

Armstrong's research interests include the theory and use of secondary equilibria (i.e., micelles, colloids, and cyclodextrins) in chromatography and spectroscopy, field-flow fractionation, centrifugal counter-current chromatography, and membrane-mediated separations.

His current research focuses on methods for the specific detection of enantiomers, the role of computer modeling in molecular recognition, and the development of new analytical techniques. Armstrong introduced the three-phase model for separations as well as the concept of critical phenomena in the gradient chromatographic separation of polymeric materials.

Thomas Chester received a B.S. degree from Florida State University (1971) and then joined the Verona Division of the Baychem Corporation (now Mobay Corp.) in Charleston, SC. After receiving his Ph.D. from the University of Florida (1976), he joined Procter & Gamble's Miami Valley Laboratories, where he currently heads the Separations and Instrumentation Technology Section, Corporate Research Division.



Chester's research has centered on chromatography, particularly element-selective and other detectors; HPLC and GC processes; and, most recently, SFC. His SFC work includes injection processes, retention mechanisms, detector interfaces, molecular weight range extension, and the chemical derivatization of polar and ionic solutes.



Brenda Shaw, associate professor of chemistry at the University of Connecticut, received an A.B. degree (1977) from Earlham College and a Ph.D. (1983) from the University of Illinois, Urbana-Champaign.

She is interested in the development of electrochemical sensors and detectors that use bulk-modified composite working and reference electrodes. These sensors and detectors, which include micro-sensors based on ring-modified multimicroelectrodes, are being optimized for biomedical and environmental analysis.

Shaw's work also focuses on gas-phase electrochemistry and electrocatalysis that occurs in dry molecular sieves at temperatures where they are ionic conductors. These systems can serve in gas-phase synthesis and as gas sensors.

Subdivision Calls for Nominations

The Division of Analytical Chemistry's Chromatography and Separations Chemistry Subdivision is seeking nominations for chairman-elect, secretary, and two members-at-large of the Executive Committee. Terms of office begin October 1 and continue for two years, except for the chairman-elect, whose term runs for one year. Subdivision members must submit nominations by February 1 to Ronald Majors, Hewlett Packard, Avondale Division, Route 41, P.O. Box 900, Avondale, PA 19311-0900 (215-268-2281).

Mettler Award in Thermal Analysis

The North American Thermal Analysis Society (NATAS) requests nominations for the 1990 Mettler Award in Thermal Analysis. The award consists of a certificate, \$2000, and a travel allowance to the September 1990 meeting of NATAS in Boston. Nominations, which must include a description of the nominee's accomplishments, should be sent to Jack Knox, 1564 Swallow Street, Naperville, IL 60565. Deadline is January 31.

"Vog" Strikes Hawaii

Scientists with Sandia National Laboratories and the U.S. Geological Survey have proposed a new theory for a unique type of acid rain. The rain occurs naturally when molten lava encounters seawater.

The theory is based on studies at Hawaii's Kupapa'u Point, where lava from Kilauea Volcano flows into the Pa-

cific Ocean, creating spectacular steam explosions and plume clouds with pH levels as low as 1.75. The term "vog" has been coined for these acidic volcanic fogs. Respiratory problems and environmental damage are now being linked to the vog.

According to the researchers, the low pH arises primarily from the hydrolysis of steam by $MgCl_2$ in seawater brine. The chloride salts collect after seawater is flash dried by the hot lava. These salts then react with the steam to generate HCl. Acidic water rises into the atmosphere via the steam plumes. Previous speculation had attributed the acid rain to degassing of the lava.

Analysis of the steam plumes revealed that the concentration of salts was about 2.5 times greater than seawater with about the same relative proportions. However, the concentrations of several minor constituents—Al, Fe, Mn, and Si—were enriched in the fog to more than 10^3 times their normal levels in seawater.

The Hawaii data echoed results observed earlier at the Waste Isolation Pilot Plant near Carlsbad, NM. Experiments at the site that involved heating brine in boreholes drilled into rock salt had also generated HCl.

The acid rain poses a particular health hazard for Hawaiians. Continuous eruptions since 1986 along the east rift zone of Kilauea Volcano have created a lava tube system that allows hot lava to reach the ocean.

Warmer Planet, Deeper Snow

Contrary to popular fears that a greenhouse effect is presently melting polar ice, recent measurements suggest that the Antarctica ice cap may be getting bigger. According to polar researcher Charles Bentley of the University of Wisconsin-Madison, observations over the past 30 years indicate that the Antarctica ice sheet would not contribute to global rise in ocean levels. More likely, said Bentley, it is removing water from the sea.

Researchers have predicted that a greenhouse effect could lead to a catastrophic rise in ocean levels. However, recent surface elevation data indicate that snow accumulation in the Antarctic presently outpaces ice loss to the ocean. The difference could account for a drop in sea level of as much as 0.5 mm per year.

Nevertheless, ocean levels could rise because of thermal expansion of greenhouse-warmed waters. Furthermore, icebergs spawned by glaciers on other continents might also contribute to a rise in sea levels. On the other hand, a warmer climate would increase the amount of moisture in the atmosphere and should produce even more snowfall over the Antarctica ice sheet, Bentley pointed out.

Polar scientists now believe that the Antarctica ice sheet is a dynamic system that responds to climate changes over varying lengths of time, ranging from centuries to tens of thousands of years. "The bottom of the ice sheet," Bentley said, "is responding only now to changes that occurred at the end of the last Ice Age."

Standardized MS/MS Measurements

The National Institute of Standards and Technology (NIST) has published a kinetics-based protocol (*J. Res. NIST* 1989, 94, 281) for instrument-independent tandem mass spectrometry (MS/MS) measurements within XqQ type instruments. X denotes the first mass analyzer, which can be a quadrupole mass filter (denoted by a Q) or a sector analyzer (denoted by EB or BE); q denotes a rf-only quadrupole collision cell; and the second mass analyzer is a Q

(e.g., QqQ, BEqQ). The adoption of standardized operating conditions enables the interchange of reproducible MS/MS spectra and, more importantly, ensures that experiments can be replicated in these instruments. In addition, this protocol should prevent the dissemination of incorrect ion-molecule mechanisms caused by the instrumental distortions resulting from discrimination effects. The precepts of the protocol should also apply to other tandem mass spectrometer designs that have strong focusing properties (e.g., quadrupole-hexapole-quadrupole).

The protocol was validated by a recent NIST round robin study (sponsored by the Environmental Protection Agency) which indicated that at least half of the commercial QqQ type machines can provide instrument-independent measurements and that charge-transfer reactions can be employed as generic "transfer" standards, providing in situ calibration of effective target thickness within the collision regions of XqQ instruments. Consequently, a standardized CAD spectrum of a known species measured in one XqQ machine can be used to identify the same species in another XqQ instrument. A second NIST round robin will explore the feasibility of using the protocol for standardized MS/MS measurements under multiple-collision conditions.

The protocol should also aid in the development of a standardized, instrument-independent MS/MS database or library for XqQ instruments. NIST has proposed creating an MS/MS database for the identification of unknown compounds by using MS/MS "fingerprints" analogous to infrared group frequencies. For more information, or to contribute spectra to the database, contact Richard Martinez, Chemical Kinetics Division, A260-222, NIST, Gaithersburg, MD 20899 (301-975-2516).

For Your Information

The White House is soliciting nominations of outstanding science and mathematics teachers for its **1990 Presidential Awards for Excellence**. Nominees must have at least 5 years of experience teaching in public or private schools and work in any of the grades from 7 through 12. Winners earn a \$7500 NSF grant and other gifts for their school, plus a trip to Washington, DC, to receive the award. Nominations are due by March 1 and should be sent to: PAESMT; National Science Teachers Association; Special Projects; 5112 Berwyn Road, Third Floor; College Park, MD 20743.

Science magazine has initiated an annual "Molecule of the Year" award honoring what editor Daniel Koshland described as "a process rather than a personality." The first winner, announced last December 22, is the polymerase molecule used in the polymerase chain reaction (PCR).

Extrel Corporation has acquired Nicolet Instrument Corporation's FT/MS Business Unit. Extrel is presently the third largest manufacturer of mass spectrometers in the United States.

MIPROPS, a computer program for calculating thermo-physical properties of 12 important industrial fluids, is now available online worldwide. The program quickly calculates properties of He, Ar, O₂, N₂, H₂, NF₃, and the hydrocarbon series running from CH₄ to *n*- and *iso*-butane. For more information, contact the Office of Standard Reference Data, National Institute for Science and Technology, A323 Physics Bldg., Gaithersburg, MD 20899 (301-975-2208).

More choices.

The ITD™ works with the column of your choice. And you can add CI capabilities now or later.

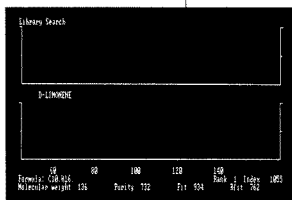
Easier to use.

You don't need a lot of experience to be up and running fast on the ITD. Just ask an ITD user.



Simple maintenance.

The ITD is designed so that you spend less time cleaning the ion source and more time running samples and producing results.



More information.

Get library-searchable, full-scan mass spectra for positive identification throughout the entire concentration range. To profit from the performance that only the ITD can deliver, contact your Finnigan MAT representative today.

The ITD just gained one more advantage over the MSD.

More value.

A complete GC/MS/DS for \$49,500. Place your order for the ITD 804A GC/MS with COMPAQ® PC by March 15, 1990 and receive a 23% discount off the U.S. list price.*



U.S. DISTRICT OFFICES
Southwest, Pleasanton, CA • (714) 961-0727
Northwest, San Jose, CA • (408) 433-4600
Atlanta, Marietta, GA • (404) 424-7880
Midwest, Schaumburg, IL • (708) 310-0140
Washington, D.C., Frederick, MD • (301) 698-9750
Boston, Andover, MA • (508) 975-5330
New Jersey, Livingston, NJ • (201) 740-9177
Central, Cincinnati, OH • (513) 891-1255
Houston, Houston, TX • (713) 449-0253

*For orders placed and delivered within the United States only.

ITD is a trademark of Finnigan Corporation. COMPAQ is a registered trademark of Compaq Computer Corporation.

Automation


in the titration laboratory


Metrohm sample changers handle your routine titrations even during breaks and after work. Rapidly, reliably and reproducibly. Models exist

- for 10, 32, 64 or 96 samples (from 10 ... 250 mL)
- with single or double titration stations for complex analyses
- in several versions, e.g. for Karl Fischer water determinations and for COD determinations

They naturally also take over the sample preparation steps such as stirring, dissolution, dilution, pipetting, evacuation, gassing, degassing, etc.

Metrohm automation systems can be accommodated in the modern analytical laboratory with ease. They communicate and cooperate with PC, laboratory robots and LIMS.



 **Metrohm**
Measurement in Chemistry
Worldwide with Metrohm

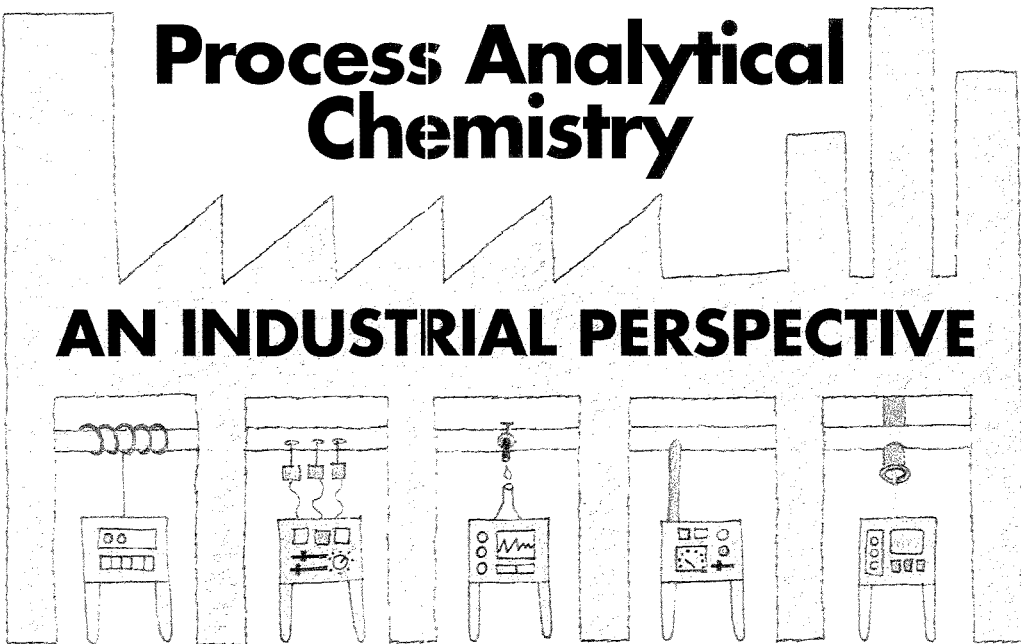
METROHM Ltd. /
CH-9101 Herisau Switzerland
Phone 071 / 53 11 33
Telefax 071 / 52 11 14
Telex 88 27 12 metr ch

Brinkmann
INSTRUMENTS, INC.
Cantiague Rd., Westbury, New York 11590
(516) 334-7500 (800) 645-3050

CIRCLE 90 ON READER SERVICE CARD

Process Analytical Chemistry

AN INDUSTRIAL PERSPECTIVE



Michael T. Riebe and Daniel J. Eustace

Polaroid Corporation
Cambridge, MA 02139

Competitiveness. Productivity. Quality. Waste reduction. These words are heard frequently in industrial circles. The pressure is growing to make higher quality goods at lower cost and with less waste.

In response to this clamor, a new subsdiscipline of analytical chemistry has emerged. Unlike traditional chemical analysis, which is performed in sophisticated laboratories by highly trained specialists who aim to identify and quantify small samples of material, process analytical chemistry (PAC) is performed on the front lines of the chemical process industry, where 10,000 gallons of sample at a time are analyzed under significant schedule and budget pressures. This new environment is typically far removed from the "comfort" of the traditional laboratory.

What is PAC?

The PAC approach is quite different from the traditional analytical philoso-

phy (Figure 1). The first and most obvious difference is *location*. In a traditional manufacturing environment, the analytical chemistry lab is centralized. Samples are taken from many process vessels or production lines and transported with a request for analysis to the central laboratory. Here, samples are logged in, stored and prioritized, and analyzed with state-of-the-art instruments in a climate-controlled laboratory. Results are then sent back to the requester or simply filed for future reference. In comparison, PAC analyzers are located in or right next to the process. They are physically and operationally a part of the process.

Laboratory instrumentation tends to be sophisticated, versatile, and sensitive. Process analyzers, however, must be *rugged and dependable*. Versatility is usually not important because the instrument is most often dedicated to a single process, but tolerance of fluctuations in temperature and humidity and environment-proof enclosures that can withstand the spray of fire hoses are required for the process environment.

The *time frame* for obtaining results is another distinguishing characteristic of PAC. In a centralized laboratory, results are obtained and recorded hours,

or sometimes days, after sampling. They are not typically used to adjust the process, but instead are used to identify products that must be scrapped or reworked. The major value of the traditional central QA/QC laboratory is in post-mortem system analysis. If the analytical results are critical to the continuation of a process, the process should be designed to accommodate the expected delay between sampling and results. These significantly longer process cycles lead to less

REPORT

efficient production schedules. PAC data, on the other hand, are used immediately for process control and optimization. Any deviation from the norm elicits an immediate response.

The difference between these two approaches is analogous to intelligence gathering in a military crisis. The traditional analytical approach corresponds to launching a reconnaissance satellite, retrieving it, and developing the pictures before deciding what to do next. The PAC approach puts scouts with

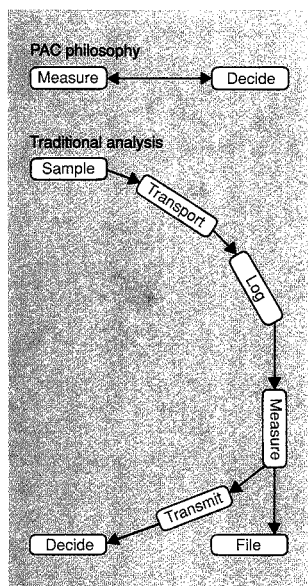


Figure 1. PAC strategy versus the traditional analytical chemistry strategy.

radios atop key hills and uses pilotless drones with video cameras to provide real-time information about the situation.

Whereas central laboratories have specialists with state-of-the-art instrumentation who are very good at solving unique and infrequent problems, the process analytical world demands generalists and problem solvers. *PAC* is

problem-driven, not technique-driven, although it has certainly benefited from recent rapid technological development in fields such as microelectronics and photonics. *PAC* requires a team approach to problem solving that involves the efforts of process chemical engineers, process and analytical chemists, and instrument and electronics technicians (1).

PAC is not a new idea; it has been the natural philosophy of the commodity chemical and petrochemical industries since the early 1950s. However, the level of recognition and activity has accelerated recently in response to the increased pressure for competitive advantage in price, availability, quality, and waste-free operations (2, 3). This growing interest in *PAC* may also reflect the maturation of manufacturing in the industrial world (4). As an industrial sector matures, the major source of competitive advantage shifts from product innovations to process innovations. Resources and activity shift from improving products to improving the manufacturing process so that higher quality products are generated more efficiently. This improvement in manufacturing processes is the primary goal of *PAC*.

PAC resources

The Center for Process Analytical Chemistry (CPAC) at the University of Washington in Seattle is a focal point for activity in this field. CPAC is one of the most successful of the National Science Foundation (NSF) centers for industry-university collaboration. Established in 1984 with the help of NSF and 21 corporate sponsors, CPAC currently boasts more than 45 industrial

sponsors representing the premier manufacturing and instrumentation companies in the United States. The benefits derived from CPAC extend beyond the results of the process analytical-oriented research performed there. The semiannual meetings provide an important venue for interaction among industrial practitioners of this technique.

Other forums such as the Pittsburgh Conference and the Instrument Society of America and FACSS annual meetings have also devoted attention to *PAC* symposia in recent years. A popular ACS short course on *PAC* has regularly been taught by Ken Clevett of Clevett Associates, Inc., most recently at the 1989 Pittcon in Atlanta. Some excellent texts are available on the subject of process analysis (5, 6). Finally, journals such as *ANALYTICAL CHEMISTRY* and magazines such as *American Laboratory* and *Trends in Analytical Chemistry* devote considerable space to research results in the field.

PAC perspective

The *PAC* team, being problem rather than technique driven, views the world from a different perspective than that of the traditional analyst. The viewpoint is not "What problems can my instrument solve?" but rather "What techniques can I use to solve my problem?" Figure 2 illustrates this new perspective in terms of a problem centered in a sphere of technologies that draws solutions from many directions. These solutions can range from simple physical measurements such as temperature, pressure, density, or refractive index, to the use of more complicated sensors such as pH or ion-selective electrodes and single-wavelength absorption spectrometers, with strong emphasis on analyzer ruggedness and simplicity. A growing number of very sophisticated instruments (e.g., plasma spectrometers, FT-IR spectrometers, and X-ray fluorescence spectrometers in rugged versions) are being used in the process environment. Some manufacturers tend to simply move laboratory instruments into the field inside a protective box, but this often fails. Novel and creative approaches are frequently required when you go to the factory floor.

Another piece of the *PAC* perspective is timing. A preconceived design of process analysis from a recipe for a process is not possible. Only after the critical process parameters are established in relation to product performance can final process analysis strategies be implemented. It is of little use to add instruments to a forgiving process, because none of the measurements will

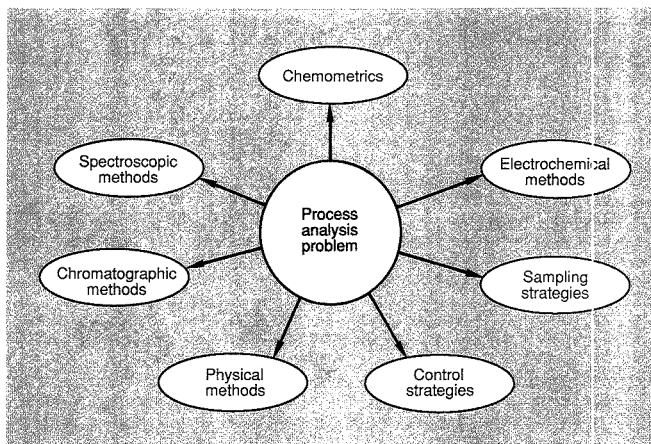


Figure 2. *PAC* perspective.

have an impact on product performance. In contrast, the return may be great if the measured parameter plays a critical role in the quality of the product or the efficiency of the process.

Deming and co-workers have presented an interesting paradigm of technological maturation (7). In this description, the "pie-in-the-sky" phase drives the initial development of an analytical technology. Exorbitant claims are often made at this point about the advantages that an instrument offers. Next comes the "disenchantment" phase, when reality rears its ugly head and limitations and barriers appear. Finally, a "mature" phase emerges, when realistic, albeit limited solutions to problems are found. PAC as a whole is currently in the euphoric stage, headed toward disillusionment. The problems and applications of PAC abound and the technology is moving forward in great strides, but many practitioners realize that a tremendous effort is required for implementation.

Some PAC technologies such as refractive index probes and pH electrodes have survived the first two phases and emerged as routine. Others, such as on-line FT-NMR and induc-

tively coupled plasma spectrometry, are still in the euphoric stage. Of course, the phase of any particular technology varies from industry to industry and even from company to company, so no sweeping generalizations can be made. The point is that the progression from idea to implementation is difficult for PAC, involving many more people and much more engineering than typical laboratory instrumentation.

Key PAC technologies

PAC is a multidisciplinary field, and no single technological development has made PAC possible. However, certain technologies have facilitated its rapid growth. Several aspects of the microelectronics revolution have fanned the PAC flames (8-10). Sensor systems based on incorporating gate electrodes that are sensitive to chemical or biological species in field-effect transistors are beginning to emerge from academic and industrial research labs (11). Silicon micromachining, or the formation of mechanical components by the etching or deposition of semiconductor materials, makes it possible to fabricate microdevices for measuring fluid flows,

pressure, density, and acceleration. Finally, novel spectroscopic sources, such as LEDs of various wavelengths and laser diodes and array detectors, have in many cases eliminated the need for scanning monochromators in spectroscopic sensing applications. Because large, precisely moving parts are often problematic in the harsh manufacturing environment, the availability of microelectronic alternatives provides a clear advantage.

Photonics, particularly fiber optics (12), is a second technology that is useful in PAC. Although the primary emphasis of most research in this field is communications, several innovations also serve the manufacturing environment. For example, intrinsic fiber-optic sensors (those that involve the direct interaction of the fiber with the measured parameter) have been demonstrated for monitoring electromagnetic fields, force/pressure, temperature, and chemical concentrations. Extrinsic fiber-optic sensors (those that use the fiber as a conduit for light to and from a spectroscopic instrument) have been applied in almost every type of optical spectroscopy including absorption, fluorescence, and Raman.



Lowest
price
\$6,850

Environmental Purge and Trap

for EPA analysis

HIGHEST PERFORMANCE

CCS
Model 1300

Optional Features

- Microprocessor controlled with 9 method storage
- Trap dry and bake standard
- Interfaces to carousel or discrete autosamplers

Cryogenic focuser with 1° increments

Thermal desorption of sampling cartridges without removing trap

☆ AIR ☆ SOLIDS ☆ SOILS

CCS INSTRUMENTS

A product line of Autoclave Engineers
7000 Limestone Road, Oxford, PA 19363
Phone: 215-932-3636 Fax: 215-932-4158
Telex: 83-5308

Call toll free today **800-541-6593**

CIRCLE 24 ON READER SERVICE CARD

The advantages of this approach are small size, rugged construction, and immunity to electromagnetic interference.

A third technology that has had an impact on PAC is chemometrics (13). Because manufacturing operations are not always completely understood and cannot be easily modeled, statistical methods that empirically determine correlations between process parameters and product performance are often essential. The inability to create a model is magnified by the multivariate nature of most processes. For example, measuring just the temperature of a reaction is insufficient when pressure, impurities, and feed rates are also important. Interactions and correlations among input variables make single-measurement control systems useless. Recently CPAC researchers developed a technique they call multivariate statistical process control (MSPC) that allows several process parameters to be consolidated, without loss of information, into a few variables that are then easier to monitor (14).

The expanding use of computers, allowing greater use of statistical methods, real-time analysis, and process feedback, is another important development. True control rather than simple monitoring and recording requires analytical information about the process in real time. It is frequently unacceptable and inefficient to follow a physical recipe of material additions, mixing, and termination of the process at a specified time. PAC makes it possible to ensure quality throughout a process, which is much more useful than performing QC checks on the resulting product.

Impact of PAC

PAC involves two critical steps: the measurement of process parameters and the conversion of the measurement data to process information. This information is then used to document, correct, and improve process performance. These steps of acquisition and interpretation of data are not unlike most other analytical methods. The difference is that the benefits of PAC seem to accumulate in many small steps rather than by single great leaps of change. In the short term, there typically is an immediate gain from improved knowledge of the analyzed process. Frequently, process analyzers are installed and process control features are implemented in response to customer demand, government regulation, or strong competition. These pressures force an operation to focus on a rigorous manufacturing discipline that determines critical process steps and

identifies variables that act to reduce quality, raise costs, and have an adverse impact on the environment. Such knowledge and discipline serve as the foundation for building PAC into the manufacturing process.

In the long term, companies benefit from continuous improvement of processes or products through statistical process control and greater under-

standing. The process development cycle can also be accelerated by implementing PAC in the process development environment rather than trying to retrofit an existing process. The chemical knowledge provided by PAC gives more rapid and higher quality information about what is going on in the process than reliance on traditional trial-and-error techniques.

Table I. Recently reported industrial applications of PAC

Industry	Technology	Analyte/matrix	Investigator/affiliation	Reference
Chemicals	Air ICP	Elemental analysis of process fluid	D. Nygaard, Baird	FACSS '88 #K47
	FIA	Fe(II) in scrubber solution	D. Olsen, Shell Development	FACSS '88 #K28
	MS	Ethylene manufacturing process	C. Weaver, Extrel Corp.	Pittcon '89 #895
	LC	Trace phenols in aqueous streams	R. Melcher, Dow Chemical USA	FACSS '87 #131
	UV-vis	Real-time reactant concentrations in vessel	H. Harris, Eastman Kodak	FACSS '87 #394
	Near-IR	Polymers and additives in polymers	S. Bush, Rohm & Haas	EAS '88 #282
	Near-IR	Chlropicrin raw material identification	R. Harner, Dow Chemical USA	FACSS '87 #512
	Near-IR	Ethanolamines in water	E. Baughman, Amoco	Pittcon '88 #312
	NMR	Moisture of Al ₂ O ₃ during drying	L. Ream, Auburn International	FACSS '87 #397
	Titration	On-line chemical composition	R. Puzic, Esso Chemicals	FACSS '88 #K66
Combustion	FT-IR	Emission/transmission of particles, gases in flames	R. Carangelo, Advanced Fuel Research	FACSS '87 #423
Environment	UV-vis	Fiber-optic system for chloroform in ground-water	S. Angel, Livermore National Lab	FACSS '87 #79
Food	Electrochemistry	Trimethylamine in fish for freshness monitoring	Y. Shimizu, Toray Industries	19
	Near-IR	Protein, oil, and moisture in grains	K. Norris, USDA	FACSS '87 #54
Petroleum	XRF	Lead and bromine in leaded gasoline	A. Harding, Tracor X-Ray	FACSS '87 #583
Pharmaceuticals	RI	Pharmaceutical formulation monitoring	J. Shabushnig, Upjohn	Pittcon '89 #892
Textiles	Near-IR	Barium activ. no., mercerization, cellulose conversion	S. Ghosh, Institute of Textile Technology	FACSS '87 #128

When well designed, installed, and executed, process analytical systems shift the quality perspective from detection to prevention. The economic perspective shifts from the cost of scrap, rework, and blending to the cost of fully integrated, well-maintained instrumentation. The environmental perspective is no longer fear of out-of-compliance operation, but knowledge that the process is running within the acceptable boundaries and that waste and byproducts are therefore minimized.

Providing process operators with

real-time, at-line analyzers can be a positive factor in efforts to improve quality and productivity. PAC enhances the workers' environment and provides them with instantaneous feedback and control.

The impact of the PAC philosophy can be compared with the effect of sequencing of traffic signals along a busy street. Manufacturing processes are complicated affairs, not unlike traffic on a major thoroughfare. Traditionally, a process must stop and wait at several points for analytical information while en route to completion. PAC provides

information in real time that allows processes to proceed without impediments. The result is more efficient and consistent production and less idling and waiting for the light to change.

PAC applications

A clear indication of the progress in this field is the record of application and achievement. A decade ago developments occurred primarily in application laboratories of instrument companies and universities. Adoption of PAC in the industrial sector is strongly dependent on a team approach because of the complexity of the process environment. Jacobs and Mehta (1) provide an excellent outline of their systematic approach to the development of process quality measurement systems, including time lines, key team participants, and system design criteria.

Industrial applications of simple physical sensors abound. Much more sophisticated analytical instruments are now being adapted to the process environment, as shown in Table I. These new analyzers are a response to the need for greater chemical selectivity than is possible with simple density, refractive index, or single-wavelength spectroscopic sensors. It is obvious that just because the application is in the manufacturing environment doesn't mean that state-of-the-art analytical technology cannot be used.

Most chemical manufacturing processes are quite complex. As one example of the PAC approach, we will review the manufacture of light-sensitive photographic emulsions. The basic chemical process is outlined in Figure 3; References 15 and 16 are other excellent sources for more complete information. In the first step, solutions of silver nitrate and some soluble halide salt are combined in the presence of gelatin, resulting in the precipitation of silver halide crystals. These crystals are then allowed to grow by conditions that encourage dissolution of small crystals and re-precipitation of the AgX material on the surfaces of larger crystals. Washing removes the excess salts from the emulsion so that no salt crystals are formed upon drying of the thinly coated films. Chemical sensitization puts small specks of a dissimilar material such as gold or sulfur onto the grains. These "sensitization specks" serve as loci for the clusters of photo-reduced silver atoms produced by exposure to light, making this exposure process more efficient and the "latent image" thus formed more stable. In the next step, dyes are added to provide sensitivity in the correct region of the spectrum, typically red, green, or blue. Several chemical additives are then included to

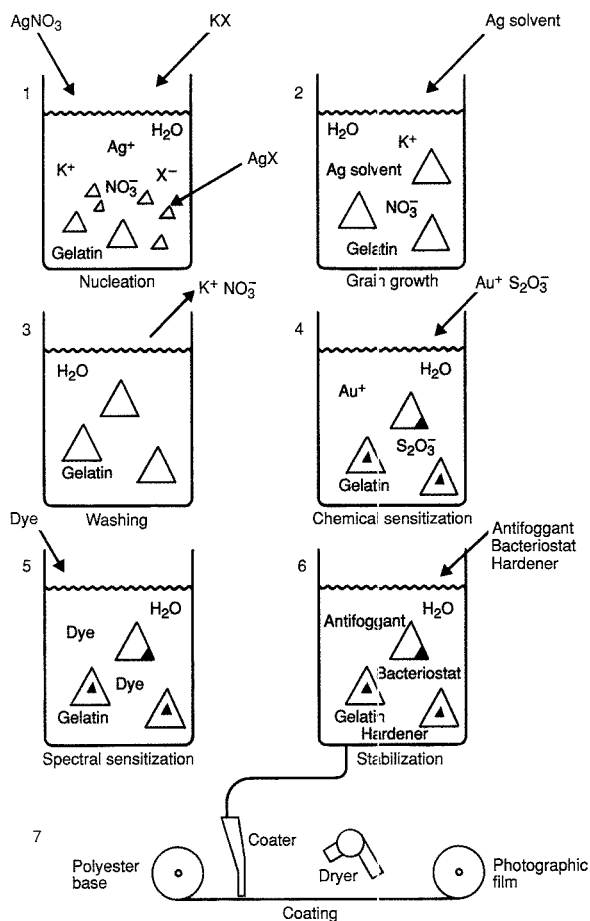


Figure 3. Essential steps in production of photographic emulsions.

improve stability, efficiency, and photographic performance of the emulsion. Finally, the material is coated in a thin layer on a plastic or paper base and dried, resulting in the familiar imaging products.

One way to graphically identify and present process stages and critical process steps within each stage is the Fishbone Diagram (also referred to as cause-effect or Ishikawa Diagrams). Figure 4 outlines a typical silver halide production process with such a diagram. The main branches identify important production phases, and sub-branches represent leading components and parameters that have an impact on product performance in photographic films.

Two examples of the application of PAC to this process involve monitoring of ammonia and silver concentrations in solution. Kumal reported that ammonium hydroxide concentration control is a major contributor to reproducibility in large-scale manufacture (17). Ammonia acts as a silver solvent, forming soluble complexes with silver, and is used in the nucleation and grain growth steps of the process. Specific gravity was chosen to assess ammonia concentration in the process stream. One might also consider other methods, including "at-line" acid-base titration, "on-line" refractive index, and "in-line" velocity of sound measurements. (For an explanation of these terms, see Reference 3.) Factors such as accuracy, reproducibility, ease of calibration, equipment, and maintenance requirements must all be weighed in choosing the best method.

Roberts has reviewed several factors affecting silver halide sensitivity to light (18). He points out that pH and pAg levels are important factors in a number of stages in the operation; this is reflected in the Fishbone Diagram. Electrode fouling and poisoning as well as difficulties in reliable calibration have led manufacturers to devise methods for pH and specific ion measurement that are quite different from traditional laboratory techniques.

Further advances in light-sensitive emulsions will come from the complementary application of new knowledge in both solid-state physics and process optimization. PAC plays a most important role in the process optimization theater.

Future of PAC

The future is bright for PAC, because many manufacturing operations can benefit from its application. The growing emphasis on competitive advantage through process rather than product innovation also implies strong growth

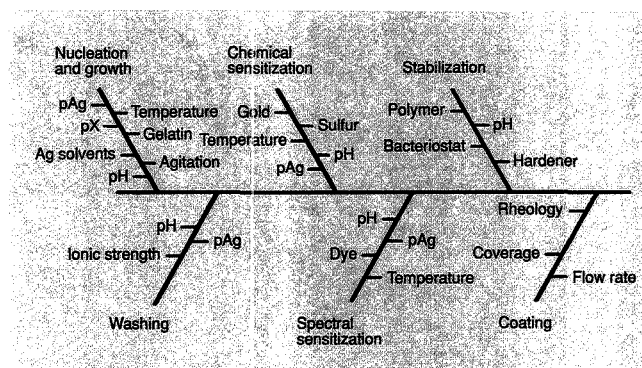


Figure 4. Fishbone Diagram showing process steps and critical parameters for the photographic emulsion manufacturing process.

in PAC. The hurdles that must be overcome include inertia and a need for more specific chemical sensors and more durable analytical systems.

Inertia is inherent in the manufacturing environment. There is a justifiable reluctance to modify products or processes that have been operating successfully for long periods of time. Retrofits of PAC technologies to these processes are difficult because process changes require significant testing and disrupt the operation, thereby creating downtime, reducing efficiency, and potentially producing a lot of inferior and unsalable material. Process operators may also be reluctant to use retrofitted analyzers after they have grown accustomed to previous patterns of operation. These are valid concerns in the manufacturing world and cannot be circumvented.

A more fruitful approach is to direct PAC resources toward products and processes that are currently in the development stage. Such processes are still flexible enough that the merit of PAC techniques can be proved through well-designed experimentation. It is also at this stage that information about the process is most needed. Only with an adequate supply of data can sifting be done to establish the relative significance of each of the parameters that might be measured in a full-scale manufacturing operation. Pressure for ever-faster development of products and processes means that the knowledge that can be obtained by PAC instrumentation must replace empirical information obtained by lengthy pilot-scale trials.

It would even be desirable to push the PAC philosophy all the way back into the process research labs. Instrumentation for real-time reaction moni-

toring and optimization could be beneficial to synthetic chemists. Imagine a system that uses artificial intelligence and PAC to investigate and optimize chemical syntheses.

A second trend that will grow in importance is the movement away from simple physical sensors of temperature and pressure (to name only two) to chemically specific analyzers. Developments in this area will parallel developments in the technologies of microelectronics, photonics, and chemometrics. The movement toward chemically specific analyzers can be accomplished either directly by using more sophisticated instrumentation or indirectly by using chemometric methods to develop correlations between the responses of arrays of nonspecific sensors and the chemical composition or product properties of interest.

The development of more rugged alternatives to traditional laboratory instruments will also continue to accelerate. Consider some recent advances in the field of optical spectroscopy. Development of compact and essentially monochromatic systems such as light-emitting diodes, laser diodes in the near-IR (and probably soon in the visible), and tunable solid-state lasers such as Ti:Sapphire and Alexandrite will eliminate the need for monochromators or filters with moving parts and low efficiency. Fiber optics promise to facilitate instrument and sensor design by eliminating the need for many lenses and mirrors. Monochromators with concave holographic gratings, coupled with planar multichannel sensors such as charge-coupled or charge-injection devices, can reduce both the size and the complexity of traditional detection systems. Acousto-optically tunable filters or piezoelectrically tun-

able Fabry-Perot interferometers also show promise as rugged devices for separating optical wavelengths. At the same time, the spectral capabilities of all of these components are being extended to include the deep ultraviolet and the infrared, making more chemical information available to the process analytical chemist.

Further development in several new areas called the pacing technologies will benefit PAC. The interface between operator and instrument is one such technology. Process information should not be used as an "idiot light" that says "check engine." At the other extreme, the information cannot be so complicated or voluminous that it is overwhelming. For example, it is often difficult to interpret the latent variables in a complicated partial least-squares statistical analysis. Imagine an operator noting that latent variable number 3 is unusually high, and then trying to figure out what to do about it when there are some 25 independent variables contributing to that latent variable.

Sampling remains a major concern. In-line sensors tend to foul quickly and are difficult to calibrate. Major advances have been made in sample conditioning systems that bring the analyte and calibration solutions to the sensor quickly and efficiently, but more effort must be expended in this area. Practitioners of PAC consistently remark that the sampling system consumes 90-95% of the effort in making an analyzer functional. Other alternatives that will reduce sensor fouling or provide for in situ cleaning and calibration must be developed. Flow injection analysis (FIA) is one alternative, allowing filtration, dilution, and calibration to be easily incorporated in a single instrument. FIA also doesn't subject the probe to continuous contact with the often harsh or corrosive sample.

Opportunities exist for incorporating other new technologies into the PAC world. For example, investigation of the spatial domain in spectroscopy may provide a chemical imaging system capable of showing images of chemical functional group distribution. This might be useful for locating material defects and monitoring coating operations. Another development will be the extension of useful spectroscopic analyzers into the microwave region on one end of the spectrum and into the X-ray region on the other. Ultrasound, the subject of much recent research, could be the basis for many new sensor systems, given its ability to discriminate among materials of different densities.

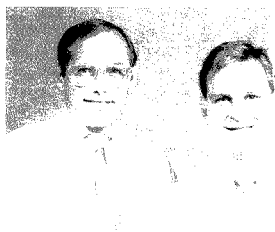
Future applications include medical

sensing, environmental monitoring, and resource recovery. Most of the effort to date has been expended on commercial chemical processes. Living systems and ecosystems are also chemical processes for which on-line, real-time analytical capabilities are desired. For example, real-time in vivo sensing of blood glucose could provide the feedback required for the implementation of an implantable insulin pump for diabetics. Development of local-sensing rather than remote-sensing capabilities for recovery of mineral and petroleum raw materials is another potential application of PAC.

From an industrial perspective, the field of process analytical chemistry is driven by the need for competitiveness, productivity, quality, and minimization of pollution. Time constraints, harsh environments, sampling, sensor calibration, and the need to demonstrate a correlation between chemical information and process or product performance are problems inherent in all PAC applications. PAC is like an adolescent child stemming from the marriage of analytical and process chemistry. It is growing and maturing rapidly, having left the analytical laboratory for the challenges, opportunities, and adventures of the front lines of manufacturing.

References

- Jacobs, S. M.; Mehta, S. M. *Am. Lab.* 1987, 20(11), 15.
- Hirschfeld, T.; Callis, J. B.; Kowalski, B. R. *Science* 1984, 226, 312.
- Calis, J. B.; Illman, D. L.; Kowalski, B. R. *Anal. Chem.* 1987, 59, 624 A.
- Utterback, J. M. In *Technology and Global Industry*; Guile, B.; Brooks, H., Eds.; National Academy of Engineering: Washington, DC, 1987.
- Clevett, K. J. *Process Analyzer Technology*; Wiley: New York, 1986.
- Mir, P. E. *The Design and Application of Process Analyzer Systems*; Wiley Interscience: New York, 1984.
- deMonchy, A. R.; Forster, A. R.; Arretweig, J. R.; Le, L.; Deming, S.N. *Anal. Chem.* 1988, 60, 1355 A.
- Chowdhury, J. *Chem. Eng.* 1989, 96, 30.
- Goldman, D. S. *Am. Lab.* 1988, 20(11), 102.
- Edmonds, T. E. *Chemical Sensors*; Chapman and Hall: New York, 1988.
- Morrison, S. *Sensors* 1988, 5, 39.
- Lieberman, R. A.; Wlodarczyk, M. T., Eds. *Chemical, Biochemical, and Environmental Applications of Fibers*; Proceedings of the SPIE, Vol. 990; SPIE: Bellingham, WA, 1989.
- Becbe, K. R.; Kowalski, B. R. *Anal. Chem.* 1987, 59, 1007 A.
- Wise, B. M.; Veltkamp, D. J.; Davis, B. R.; Zicker, N. L.; Kowalski, B. R. (*Am. Nucl. Soc.*) *Waste Management 88 Proceedings*, 1988, 2, 811.
- James, T. H. *The Theory of the Photographic Process*, 4th ed.; Macmillan: New York, 1977.
- Hamilton, J. F. *Adv. Phys.* 1988, 37, 359.
- Kumal, A. J. *Appl. Photographic Eng.* 1981, 7, 88.
- Roberts H. E. J. *Imaging Sci.* 1985, 29, 175.
- Shimizu, Y. J. *Electrochem. Soc.* 1988, 135, 2539.



Michael T. Riebe (right), a scientist in the Chemical Research Division of Polaroid, received a B.S. degree in chemistry from Kalamazoo College and a Ph.D. in analytical chemistry from the University of Wisconsin. His research interests include process analysis, optical spectroscopy, and artificial intelligence.

Daniel J. Eustace (left), project manager of chemical operations in the Negative Manufacturing Division of Polaroid, received a B.A. degree from the State University of New York at Buffalo and a Ph.D. from Brandeis University. He is interested in the use of process analysis in manufacturing systems.

CORRECTION

Laszlo Zechmeister: A Pioneer of Chromatography
Leslie S. Eitre (*Anal. Chem.* 1989, 61, 1315 A-1322 A)

The caption for Figure 2 should indicate that the figure was drawn by the author from the detailed description of the chromatogram and a photo of the column in Reference 25.

Reference 25 should indicate that two editions of the book, *Die chromatographische Adsorptionsmethode* by Zechmeister and Cholnoky were published, the first in 1937 and the second in 1938. About one-third of the greatly enlarged second edition dealt with fundamentals and methodology, while about two-thirds of it discussed applications.

The last paragraph of the acknowledgement was inadvertently omitted and appears below.

Very recently, after my lectures on Zechmeister at the meetings in Leipzig and Budapest, I received, via my brother, some of the newest material compiled in Hungary on the occasion of the centenary of Zechmeister's birth, originating from the Archives (Mrs. I. Sányi), the Library (Mrs. F. Jászberényi), and the Museum (Mr. J. Bana) of the county and city of Győr. This material permitted me to clear up some still unresolved points. Many thanks to all of them.

"Authoritative, well-written, and easy to assimilate."—CHEMTECH

CHEMTRACTS

ANALYTICAL, PHYSICAL, AND INORGANIC CHEMISTRY

Editors: **HARRY GRAY**,
California Institute of Technology,
and **ROYCE W. MURRAY**,
University of North Carolina

The second edition in the **CHEMTRACTS** series of review publications—Now incorporating the discipline of Inorganic Chemistry!

Special Reduced Rate Available to 1990 Subscribers!

CHEMTRACTS-Analytical, Physical and Inorganic Chemistry is a creative contribution to how analytical, physical, and inorganic chemists receive and digest important information. The journal provides rapid review of current research in a unique format intended to initiate and stimulate new research activity.

Every **CHEMTRACTS** issue includes up to thirty detailed research condensations, providing you with the most focused updates available. All reviews are written by internationally recognized authorities. You have the unique advantage of quick reporting on current studies and of information that has been carefully critiqued. And potentially useful work—that is seemingly outside of your own speciality—can be readily appraised, offering an invaluable added perspective with a minimum time investment.

In addition to literature screening, **CHEMTRACTS** features invited articles from today's most eminent scientists, providing insight to major new directions in chemical research.

CHEMTRACTS-Analytical, Physical, and Inorganic Chemistry ISSN: 0899-7810 Volume 2, 1990

6 issues \$48 U.S., or \$78 Outside of U.S.
"Individual" Subscriptions: * must be paid by personal check or charged to a personal credit card
\$175 U.S. Institution, \$226.00 Institution Outside of U.S.
Subscription Rates Outside of U.S. Include Air Service



CHEMTRACTS is a major advance over previous reference sources.

Every research study is accompanied by a full range of analysis, including:

- Purpose of the Study
- What the Researchers Accomplished
- Background Information on Methods
- Researcher's Approach
- Commentary on Research Implications
- References

PLUS Annual Cumulative Index makes any article, on any subject, in any published issue, easy to locate.

CHEMTRACTS-Analytical, Physical, and Inorganic Chemistry is just one edition in a series of review publications. Overall management of the project is in the hands of Fred Basolo of Northwestern University. The other **CHEMTRACTS** editions include:

- Organic Chemistry
- Biochemistry and Molecular Biology
- Macromolecular Chemistry



Co-Published by Data Trace, Inc.
and John Wiley & Sons, Inc.



**Send for a free specimen issue or
descriptive literature**

Contact T. Pekar, John Wiley & Sons, Inc.,
605 Third Avenue, New York, NY 10158

CIRCLE 152 ON READER SERVICE CARD

Conferences

■ **2nd International Symposium on High-Performance Capillary Electrophoresis.** Jan. 29–31. San Francisco, CA. Contact: Shirley Schlessinger, 400 East Randolph Dr., Suite 1015, Chicago, IL 60601 (312-527-2011)

■ **International Forum on Process Analytical Chemistry.** Jan. 30–31. Houston, TX. Contact: IFPAC Committee, c/o Infoscience Services, 3000 Dundee Rd., Suite 313, Northbrook, IL 60062 (312-291-9161)

■ **Meeting on Laser Applications to Chemical Analysis.** Feb. 5–8. Incline Village, NV. Contact: Optical Society of America, 1816 Jefferson Pl., N.W., Washington, DC 20036 (202-223-0920)

■ **4th International Symposium on Biological and Environmental Reference Materials.** Feb. 5–8. Orlando, FL. Contact: Wayne Wolf, B311 Chemistry Bldg., NIST, Gaithersburg, MD 20899 (301-975-2030)

■ **International Symposium on Free Radicals in Biotechnology and Medicine.** Feb. 7. London, U.K. Contact: P. E. Hutchinson, Analytical Division, Royal Society of Chemistry, Burlington House, London W1V 0BN, U.K.

■ **Meeting of the American Academy of Forensic Sciences.** Feb. 19–24. Cincinnati, OH. Contact: American Academy of Forensic Sciences, 225 South Academy Blvd., Colorado Springs, CO 80910

■ **Symposium on Hyphenated Techniques in Chromatography.** Feb. 22–23. Antwerp, Belgium. Contact: VCV, Section Analytical Chemistry, c/o R. Smits, BASF Antwerpen N.V., Scheldelaan, B-2040 Antwerp, Belgium

■ **41st Pittsburgh Conference on Analytical Chemistry and Applied Spectroscopy.** March 5–9. New York, NY. Contact: Pittsburgh Conference, 300 Penn Center Blvd., Suite 332, Pittsburgh, PA 15235 (800-825-3221)

■ **Gordon Research Conference on Bioanalytical Sensors.** March 12–16. Ventura, CA. Contact: Alexander M. Cruickshank, Gordon Research Center, University of Rhode Island, Kingston, RI 02881 (401-783-4011 or 3372)

■ **3rd Latin American Congress on Chromatography.** March 14–16. São Paulo, Brazil. Contact: Fernando Lanas, University of São Paulo, Institute of Physics and Chemistry of São Carlos, 13560, São Carlos, SP, Brazil

■ **Analytica '90.** March 18–23. Pretoria, South Africa. Contact: J. F. van Staden, Dept. of Chemistry, University of Pretoria, Pretoria 0002, South Africa

■ **International Conference on Tropospheric Ozone and the Environment.** March 19–22. Los Angeles, CA. Contact: Air and Waste Management Association, P.O. Box 2861, Pittsburgh, PA 15230 (412-232-3444)

■ **CHROMEXPO '90.** March 26. Washington, DC. Contact: Janet Cunningham, Barr Enterprises, P.O. Box 279, Walkersville, MD 21793 (301-898-3772)

■ **International Meeting on the Use of Thermal Methods for the Characterization of Pharmaceuticals.** March 26–28. London, U.K. Contact: G. Buchton, The School of Pharmacy, University of London, 29–39 Brunswick Square, London WC1N 1AX, U.K.

■ **12th International Conference on Cerent Microscopy.** April 2–5. Vancouver, Canada. Contact: Charles Buchanan, Jr., 409 Santee Dr., Santee, SC 29142

■ **2nd International Symposium on Applications of Analytical Techniques to Industrial Process Control (ANATECH '90).** April 3–5. Noordwijkerhout, The Netherlands. Contact: Willem van der Linden, Laboratory for Chemical Analysis—CT, University of Twente, P.O. Box 217, NL-7500 AE Enschede, The Netherlands

■ **Oak Ridge Conference on Advanced Analytical Concepts for the Clinical Laboratory.** April 5–6. Tampa, FL. Contact: AACC, 2029 K St., N.W., 7th Fl., Washington, DC 20006 (202-857-0717)

■ **7th International Symposium on Preparative Chromatography.** April 8–11. Ghent, Belgium. Contact: M. Verzele, RUG-LOS, Krijgslaan 281 (S4), B-9000 Ghent, Belgium

■ **Royal Society of Chemistry Annual Congress.** April 9–12. Belfast,

U.K. Contact: Royal Society of Chemistry, Burlington House, London W1V 0BN, U.K.

■ **1st International Congress on Electrophoresis, Supercomputers, and the Human Genome.** April 10–13. Tallahassee, FL. Contact: H. Lim or R. McMullen, Florida State University, Tallahassee, FL (904-644-1010)

■ **Symposium on Remote Sensing and Signal and Image Processing.** April 16–20. Orlando, FL. Contact: SPIE, P.O. Box 10, Bellingham, WA 98227 (206-676-3290)

■ **Meeting of the Materials Research Society.** April 16–21. San Francisco, CA. Contact: MRS, 9800 McKnight Rd., Suite 327, Pittsburgh, PA 15237 (412-367-3003)

■ **20th International Roland W. Frei Memorial Symposium on Environmental Analytical Chemistry.** April 17–20. Strasbourg, France. Contact: M. Frei-Häusler, Postfach 46, CH-4123 Allschwil 2, Switzerland

■ **4th Workshop on Chemistry and Analysis of Hydrocarbons.** April 19–21. Strasbourg, France. Contact: M. Frei-Häusler, Postfach 46, CH-4123 Allschwil 2, Switzerland

■ **Annual Meeting of the American Oil Chemists Society.** April 22–26. Baltimore, MD. Contact: American Oil Chemists Society, 1608 Broadmoor, P.O. Box 3489, Champaign, IL 61821

■ **199th National Meeting of the American Chemical Society.** April 22–27. Boston, MA. Contact: Meetings Dept., American Chemical Society, 1155 16th St., N.W., Washington, DC 20036 (202-872-4396)

■ **4th Symposium on the Analysis of Steroids.** April 24–26. Pécs, Hungary. Contact: S. Görög, c/o Chemical Works of Gedeon Richter Ltd., P.O.B. 27, H-1475 Budapest, Hungary

■ **2nd Annual National Forum on Laboratory Accreditation.** April 30–May 1. Baltimore, MD. Contact: Robin Gildersleeve, CEEM, P.O. Box 200, Fairfax Station, VA 22039 (703-250-5900)

■ **International Symposium on Measurement of Toxic and Related Air Pollutants.** April 30–May 3. Raleigh, NC. Contact: Bruce Gay, Atmospheric Research Exposure Assessment Laboratory, U.S. EPA, Research

Triangle Park, NC 27709

■ **20th Annual Symposium on Advances in Applied Analytical Chemistry.** May 2-3. Kenner, LA. Contact: Judy Timpa, SRRC, ARS, USDA, P.O. Box 19687, New Orleans, LA 70179 (504-286-4360)

■ **1st World Congress on Biosensors (Biosensors '90).** May 2-4. Singapore. Contact: Penny Moon, Elsevier Seminars, Mayfield House, 256 Banbury Rd., Oxford OX2 7DH, U.K.

■ **Meeting of the Electrochemical Society.** May 6-11. Montreal, Canada. Contact: Electrochemical Society, 10 South Main St., Pennington, NJ 08534

■ **Southeastern Safety and Health Conference and Exhibition.** May 8-10. Atlanta, GA. Contact: Education Extension Service, Georgia Institute of Technology, Atlanta, GA 30332 (404-894-2400)

■ **International Conference on Computer Networks (COMNET '90).** May 8-10. Budapest, Hungary. Contact: COMNET '90 Secretariat, P.O. Box 240, H-1368 Budapest, Hungary

■ **12th International Conference on Biochemical Analysis (Biochemische Analytik '90).** May 8-11. Munich, F.R.G. Contact: Biochemische Analytik '90, Nymphenburger Straße 70, D-8000 München 2, F.R.G.

■ **Symposium on Analysis of Paints and Related Materials.** May 14-15. Pittsburgh, PA. Contact: Dorothy Savini, ASTM, 1916 Race St., Philadelphia, PA 19103 (215-299-5413)

■ **11th International Symposium on Capillary Chromatography.** May 14-17. Monterey, CA. Contact: Pat Sandra, Laboratory of Organic Chemistry, University of Gent, Krijgslaan 281 (S4), B-9000 Gent, Belgium

■ **34th Annual Meeting of the American Association of Bioanalysts.** May 14-19. Virginia Beach, VA. Contact: Mark Birenbaum, 818 Olive St., Suite 918, St. Louis, MO 63101 (314-241-1445)

■ **14th International Symposium on Column Liquid Chromatography.** May 20-25. Boston MA. Contact: Shirley Schlessinger, 400 East Randolph Dr., Suite 1015, Chicago, IL 60601 (312-527-2011)

■ **43rd Annual Conference of the Society for Imaging Science and Technology.** May 20-25. Rochester, NY. Contact: SPSE, 7003 Kilworth Lane, Springfield, VA 22151

■ **7th Symposium on Radiation Measurements and Applications.** May 21-24. Ann Arbor, MI. Contact: Helen Lum, 3034 Phoenix Memorial Laboratory, University of Michigan, Ann Arbor, MI 48109 (313-764-6214)

■ **10th Annual Conference on La-**

sers and Electro-Optics (CLEO '90). May 21-25. Anaheim, CA. Contact: Optical Society of America, 1816 Jefferson Pl., N.W., Washington, DC 20036 (202-223-8130)

■ **2nd Scientific Computing and Automation Conference and Exhibition.** May 22-25. Maastricht, The Netherlands. Contact: Robi Va'khoff, Reunion International, Geldersekade 89, 1011 EL Amsterdam, The Netherlands

■ **38th ASMS Conference on Mass Spectrometry and Allied Topics.** June 3-8. Tucson, AZ. Contact: Judith Watson, ASMS, P.O. Box 1508, East Lansing, MI 48826 (517-337-2548)

■ **Symposium on Optical Spectroscopic Instrumentation and Techniques for the 1990s: Applications in Astronomy, Chemistry, and Physics.** June 4-6. Las Cruces, NM. Contact: SPIE, P.O. Box 10, Bellingham, WA 98227 (206-676-3290)

■ **4th International LIMS Conference.** June 4-7. Pittsburgh, PA. Contact: Gerst Gibbon, LIMS Institute, c/o U.S. DOE/PETC, P.O. Box 109400, Pittsburgh, PA 15236

■ **5th World Filtration Congress (Interfilt '90).** June 5-8. Nice, France. Contact: Interfilt '90, c/o IDEXPO, 21 Ave. de la Div. Leclerc, F-94230 Chachan, France

■ **3rd Symposium on Computer-Enhanced Analytical Spectroscopy.** June 6-8. Snowbird, UT. Contact: Peter Jurs, Dept. of Chemistry Penn State University, University Park, PA 16802

■ **International Conference on Chirality.** June 7-9. Cancun, Mexico. Contact: D. W. Armstrong or I. W. Wainer, Dept. of Chemistry, University of Missouri—Rolla, Rolla, MO 65401 (314-341-4429)

■ **4th Annual Seminar on Analytical Biotechnology.** June 11-14. Arlington, VA. Contact: Janet Cunningham, Barr Enterprises, P.O. Box 279, Walkersville, MD 21793 (301-898-3772)

■ **14th Annual Conference of the International Precious Metals Institute.** June 17-21. San Diego, CA. Contact: Precious Metals Institute, Government Building, ABE Airport, Allentown, PA 18103 (215-226-1570)

■ **3rd International Colloquium on Centrifugal Partition Chromatography.** June 21-22. San Mateo, CA. Contact: Eleanor Cazes, Sanni Laboratories, 106 Folcroft East Business Park, Sharon Hill, PA 19079 (215-583-2010)

■ **33rd IUPAC International Symposium on Macromolecules (Macro '90).** July 8-13. Montreal, Canada. Contact: Macro '90 Secretariat, Dept.

of Chemical Engineering, McGill University, 3480 University St., Montreal H3A 2A7, Canada

■ **5th European Congress of Biotechnology.** July 8-14. Copenhagen, Denmark. Contact: Edvard Falch, Novo Industri A/S, Novo Alle 1, DK-2880 Bagsvaerd, Denmark

■ **International Conference and Industrial Exhibition on Ion-Exchange Processes (Ion-Ex '90).** July 9-11. Wrexham, U.K. Contact: Hayden Hughes, Research Division, The North East Wales Institute, Connah's Quay, Deeside, Clwyd, CH5 4BR, U.K.

■ **Meeting on Electrochemical Techniques in Speciation Studies.** July 9-11. Liverpool, U.K. Contact: A. E. Bottom, Kent Industrial Measurements Ltd., Oldends Lane, Stonehouse, Glos. GL10 3TA, U.K.

■ **2nd International Meeting on Spectroscopy across the Spectrum—Techniques and Applications of Analytical Spectroscopy.** July 9-12. Hertford, U.K. Contact: P. R. Brawn, Unilever Research, Colworth Laboratory, Sharnbrook, Beds. MK44 1LQ, U.K.

■ **5th Biennial National Atomic Spectroscopy Symposium.** July 18-20. Loughborough, U.K. Contact: J. R. Dean, Dept. of Chemical and Life Sciences, Newcastle upon Tyne Polytechnic, Ellison Bldg., Newcastle upon Tyne NE1 8ST, U.K.

■ **Meeting of the American Association for Clinical Chemistry.** July 22-26. San Francisco, CA. Contact: AACC, 1725 K St., N.W., Washington, DC 20006

■ **3rd International Symposium on Polymer Analysis and Characterization.** July 23-25. Brno, Czechoslovakia. Contact: Howard Barth, Du Pont Co., Experimental Station, E228/238, P.O. Box 80228, Wilmington, DE 19880 (302-695-4354)

■ **43rd ACS Summer Symposium on Analytical Chemistry—Mass Spectrometry.** July 24-27. Oak Ridge, TN. Contact: David Donohue, ORNL, Analytical Chemistry Div., Bldg. 4500-S, Mail Stop 6142, Oak Ridge, TN 37831 (615-574-8955)

■ **13th International EPR Symposium.** July 29-Aug. 2. Denver, CO. Contact: Gareth Eaton, Dept. of Chemistry, University of Denver, Denver, CO 80208 (303-871-2980)

■ **7th International Congress of Pesticide Chemistry.** Aug. 5-10. Hamburg, F.R.G. Contact: Secretariat, Bank Court Chambers, 2-3 Pound Way, Cowley Centre, Oxford OX4 3YF, U.K.

■ **1st Changchun International Symposium on Analytical Chemistry.** Aug. 7-11. Changchun, People's

Republic of China. Contact: Qinhua Jin, Dept. of Chemistry, Jilin University, Changchun, Jilin 130021, People's Republic of China

■ **2nd International Symposium on Microcolumn Separation Methods.** Aug. 20-22. Upland, Sweden. Contact: Eva Mattsson, Swedish Chemical Society, Analytical Div., Wallingatan 26 B, S-111 24 Stockholm, Sweden

■ **J. Heyrovský Centennial Congress on Polarography and 41st Meeting of the International Society of Electrochemistry.** Aug. 20-25. Prague, Czechoslovakia. Contact: Secretariat, J. Heyrovský Centennial Congress, Czechoslovak Academy of Sciences, J. Heyrovský Institute of Physical Chemistry and Electrochemistry, Dolejškova 3, 182 23 Prague 8, Czechoslovakia

■ **6th International Symposium on Bioluminescence and Chemiluminescence.** Aug. 26-30. Cambridge, MA. Contact: L. J. Kricka, Dept. of Pathology and Laboratory Medicine, 3400 Spruce St., 784 Founders Pavilion, Philadelphia, PA 19104 (215-662-6575)

■ **Euroanalysis VII.** Aug. 26-31. Vienna, Austria. Contact: D. M. Grasserbauer, c/o Interconvention, Austria Center Vienna, A-1450 Vienna, Austria

■ **200th National Meeting of the American Chemical Society.** Aug. 26-31. Washington, DC. Contact: Meetings Dept., American Chemical Society, 1155 16th St., N.W., Washington, DC 20036 (202-872-4396)

■ **104th Annual AOAC International Meeting and Exposition.** Sept. 10-13. New Orleans, LA. Contact: Margaret Ridgell, AOAC, Suite 400, 2200 Wilson Blvd., Arlington, VA 22201 (703-522-3032)

■ **12th International Symposium on Capillary Chromatography.** Sept. 11-14. Kobe, Japan. Contact: Kiyokatsu Jinno, School of Materials Science, Toyohashi University of Technology, Toyohashi 440, Japan

■ **5th International Symposium on Resonance Ionization Spectroscopy and Its Applications.** Sept. 16-21. Varese, Italy. Contact: Shannon Bays, Institute of Resonance Ionization Spectroscopy, 10521 Research Dr., Suite 300, Knoxville, TN 37932 (615-675-9570)

■ **18th International Symposium on Chromatography.** Sept. 23-28. Amsterdam, The Netherlands. Contact: Symposium on Chromatography, c/o RAI Organisatie Bureau Amsterdam bv, Europaplein 12, 1078 GZ Amsterdam, The Netherlands

■ **3rd International Meeting on Chemical Sensors.** Sept. 24-26.

Cleveland, OH. Contact: Jean McNulty, Bingham Bldg., Electronics Design Center, Case Western Reserve University, Cleveland, OH 44106

■ **7th International Symposium on Capillary Electrophoresis and Isoelectrophoresis.** Oct. 2-4. High Tatras, Czechoslovakia. Contact: Dušan Kaniensky, Institute of Chemistry, Comenius University, Mlynská Dolina CH-2, CS-84215 Bratislava, Czechoslovakia

■ **17th Annual Meeting of the Federation of Analytical Chemistry and Spectroscopy Societies.** Oct. 7-12. Cleveland, OH. Contact: Charles J. Belle, Lucas Aerospace PEC, 4259 W. 192nd St., Fairview Park, OH 44126 (216-662-1001)

■ **3rd International Symposium on Analytical Methods and Problems in Biotechnology (Anabiotec '90).** Oct. 22-24. Burlingame, CA. Contact: Shirley Schlessinger, 400 East Randolph Dr., Suite 1015, Chicago, IL 60601 (312-527-2011)

■ **Symposium on Chemometrics with Environmental Applications.** Oct. 30-Nov. 1. Las Vegas, NV. Contact: M. Stapanian, Lockheed Engineering & Sciences Co., 1050 E. Flamingo Pk., Las Vegas, NV 89119 (702-734-3208)

■ **7th Montreux Symposium on Liquid Chromatography/Mass Spectrometry (LC/MS; SFC/MS; CZE/MS; MS/MS).** Oct. 31-Nov. 2. Montreux, Switzerland. Contact: M. Frei-Häusler, Postfach 46, CH-4123 Allschwil 2, Switzerland

■ **Eastern Analytical Symposium.** Nov. 11-16. Franklin Township, NJ. Contact: EAS, P.O. Box 633, Montchanin, DE 19710 (302-453-0785)

Short Courses and Workshops

For information on the following courses, contact University of North Carolina, OSHERC, 109 Conner Dr., Suite 101, Chapel Hill, NC 27514 (919-962-2101)

■ **Asbestos Identification by Polarized Light Microscopy.** Jan. 29-Feb. 2 and March 26-30. Chapel Hill, NC

■ **Sampling and Evaluating Airborne Asbestos Dust.** Feb. 12-16, March 19-23, April 16-20, and June 25-29. Chapel Hill, NC

■ **10th Annual Occupational Safety and Health Winter Institute.** Feb. 12-16. St. Petersburg, FL

For information on the following courses, contact Barbara Nowicki,

Me? Enroll in the ACS Employment Service?



I'm head of a major research department!

Even for the successful chemist or scientist in an allied field, sometimes the best way to get ahead is to make a change.

The ACS Employment Service offers the opportunity to investigate the possibilities discreetly—and at very low cost. Our Employment Service is free to all ACS members. If you request confidentiality from current employers or other designated organizations there is a nominal charge.

For more information write,
use coupon, or
**CALL TOLL FREE
800-227-5558**

Employment Services Office,
American Chemical Society
1155 Sixteenth Street, NW,
Washington, DC 20036

Yes. I am a member of ACS and I would like to learn how the ACS Employment Service can help me advance my career.

Name (please print) _____

Membership # _____

Address _____

City _____

State _____

ZIP _____

The American Chemical Society is interested in new software products!

Have you written a new program or a program to use with existing software for the IBM-PC or Macintosh that you think might have broad appeal in the scientific community?

If so, why not discuss it with the ACS? Call Susan Robinson at (202)872-4378 or write to her at the following address:

American Chemical Society,
1155 Sixteenth Street, NW,
Washington, DC 20036

 **ACS**
Software

MEETINGS

Professional Analytical and Consulting Services, 409 Meade Dr., Coraopolis, PA 15108 (412-262-4222)

■ **Courses on Quality Assurance of Chemical Measurements and Quality Assurance of Environmental Measurements.** Jan. 29–31. Pittsburgh, PA

■ **Courses on Spectroscopy Data Interpretation: Mass, Infrared, Near-Infrared, NMR, and 2D NMR.** Feb. 21–25. Pittsburgh, PA

■ **Course on Sampling and Evaluating Airborne Asbestos Dust.** Feb. 5–9. Los Angeles, CA. Contact: University of Southern California, Institute of Safety and Systems Management, Professional Programs, 3500 South Figueroa St., Suite 202, Los Angeles, CA 90007 (213-743-6523)

■ **Course on Indoor Air Quality.** Feb. 6–8. Atlanta, GA. Contact: Education Extension—R, Georgia Institute of Technology, Atlanta, GA 30332 (404-894-2400)

■ **Course on Experimental Design for Productivity and Quality in Research, Development, and Manufacturing.** Feb. 19–23. Houston, TX. Contact: Statistical Designs, 9941 Rowlett, Suite 6, Houston, TX 77075 (713-947-1551)

■ **Bioseparations: Scale-Up and Design Workshop.** Feb. 27–March 2 and June 5–8. University Park, PA. Contact: Jim Shillenn, 519 Vartik Laboratory, Pennsylvania State University, University Park, PA 16802 (800-833-5533)

■ **Design and Operation of Clean Rooms.** March 12–13. San Francisco, CA; March 15–16. Los Angeles, CA; March 20–21. Dallas, TX; March 22–23. Orlando, FL; April 2–3. Boston, MA; April 4–5. Newark, NJ; April 9–10. Chicago, IL. Contact: Contamination Control Seminars, 11844 Brookfield Ave., Livonia, MI 48150 (313-427-8450)

■ **Quality in the Test Laboratory.** March 13–14 and June 5–6. Warren, MI. Contact: Macomb Community College, Advanced Center for Manufacturing Technology, 14500 Twelve Mile Rd., Warren, MI 48093 (313-445-7880)

■ **Short Course on Aerosol Measurement.** April 18–20. Cincinnati, OH. Contact: Susan Millman, University of Cincinnati Medical Center, Institute of Environmental Health, Kettering Laboratory, 3223 Eden Ave., Cincinnati, OH 45267 (513-558-1732)

■ **Survey of Industrial Hygiene.** April 24–27. Cincinnati, OH. Contact: Susan Millman, University of Cincinnati Medical Center, Institute of En-

vironmental Health, Kettering Laboratory, 3223 Eden Ave., Cincinnati, OH 45267 (513-558-1732)

■ **Quantitative Capillary GC Workshop.** May 7–9. Blacksburg, VA. Contact: Harold McNair, Chemistry Dept., Virginia Tech, Blacksburg, VA 24061 (703-231-6579)

■ **Principles of Industrial Hygiene.** June 4–8. Piscataway, NJ. Contact: Environmental and Occupational Safety and Health Education and Training Center, UMDNJ—Robert Wood Johnson Medical School, Brookwood Plaza II, 45 Knightsbridge Rd., Piscataway, NJ 08854 (201-463-5062)

For information on the following courses, contact Joseph Goldstein, Dept. of Materials Science and Engineering, Bldg. 5, Lehigh University, Bethlehem, PA 18015 (215-758-5133)

■ **Basic Course on Scanning Electron Microscopy and X-ray Microanalysis.** June 11–15. Bethlehem, PA

■ **Advanced Topics in Scanning Electron Microscopy and X-ray Microanalysis.** June 18–21. Bethlehem, PA

■ **Course on Analytical Electron Microscopy.** June 18–21. Bethlehem, PA

■ **Course on Thin Specimen Preparation.** June 21–22. Bethlehem, PA

■ **Workshop on Molecular Microspectroscopy.** June 17–20. Oxford, OH. Contact: Molecular Microspectroscopy Laboratory, Miami University, Oxford, OH 45056 (513-529-2873)

■ **Advanced HPLC Workshop.** June 26–28. Blacksburg, VA. Contact: Harold McNair, Chemistry Dept., Virginia Tech, Blacksburg, VA 24061 (703-231-6579)

■ **Techniques, Instrumentation, Data Handling: UV Spectroscopy for the '90s.** July 1–6. Yorkshire, U.K. Contact: T. Frost, The Wellcome Foundation Ltd., Temple Hill, Dartford, Kent DA1 5AH, U.K.

■ **Short Course on LC/MS, SFC/MS, and CZE/MS.** Oct. 29–30. Montreux, Switzerland. Contact: M. Freihäusler, Postfach 46, CH-4123 Allschwil 2, Switzerland

ACS Courses

■ **Gas Chromatography: Packed and Capillary Columns.** Feb. 12–16 and Aug. 27–31. Blacksburg, VA. Harold McNair

■ **The Computer-Integrated Laboratory: A Hands-On Experience in**

Laboratory Automation. April 22-27 and Dec. 9-14. Blacksburg, VA. Raymond Dessy

■ **High-Performance Liquid Chromatography.** April 23-26 and Dec. 3-6. Blacksburg, VA. Harold McNair

The following courses are offered in conjunction with the Pittsburgh Conference and Exposition to be held March 5-9 in New York City.

■ **Electronics for Laboratory Instrumentation.** March 1-3. Howard Malmstadt, Christie Enke, and Stanley Crouch

■ **Applied Optical Microscopy.** March 2-4. Barbara Foster and Robert Hoffman

■ **Experimental Design for Productivity and Quality in R & D.** March 2-4. Stanley Deming and Stephen Morgan

■ **On-Line Process Analyzers: The Key To Maximizing Industrial Process Efficiency.** March 2-4. Kenneth Clevert

■ **X-ray Fluorescence Spectrometry.** March 2-4. Ronald Jenkins and John Croke

■ **Analytical Chemistry of Contaminants in Surface and Groundwater.** March 3-4. E. Michael Thurman and Michael Reddy

■ **Analytical Infrared Spectroscopy: Techniques, Applications, Computer Methods.** March 3-4. Howard Sloane and John Coates

■ **Capillary Gas Chromatography: Techniques and Problem Solving.** March 3-4. Milos Novotny and Stuart Cram

■ **The Computer-Integrated Laboratory: Tutorials and Case Histories in Laboratory Automation.** March 3-4. Raymond Dessy

■ **Diagnostic Immunology.** March 3-4. David Normansell

■ **Effective Management of Chemical Analysis Laboratories.** March 3-4. John H. Taylor, Jr., and Mary Routson

■ **Effective Supervision of Scientists and the Technical Staff.** March 3-4. David Gootnick

■ **Environmental Analytical Chemistry: Air Toxics.** March 3-4. Marcus Cooke and William Winberry

■ **Environmental Analytical Chemistry: Water and Waste.** March 3-4.

Marcus Cooke

■ **Environmental Laboratory QA/QC Validation.** March 3-4. Henry Nowicki and William Purves

■ **Environmental Law and Regulations.** March 3-4. J. Herbert O'Toole, Jean Hoff, and Marcus Cooke

■ **Gas Chromatography/Mass Spectrometry.** March 3-4. J. Throck Watson and O. David Sparkman

■ **How To Manage Complex Laboratory Data Systems.** March 3-4. Walter Shackelford and Marcus Cooke

■ **Laboratory Applications of Lotus 1-2-3 and Other Software: Beyond the Basics.** March 3-4. Glenn Ouchi

■ **Quality Assurance of Chemical Measurements.** March 3-4. John K. Taylor


■ **Size-Exclusion Chromatography.** March 3-4. Alfred Rudin

■ **Spectroscopic Characterization of Polymers.** March 3-4. Jack Koenig and Bruce Chase

■ **Spectroscopy for Chemical Analysis: Basics, Advanced Methods, and Rapid Screening.** March 3-4. Tuan Vo-Dinh and Marcus Cooke

■ **Supercritical Fluid Extraction/**

WONDERS SCIENCE



Fun Physical Science Activities for Children and Adults to Do Together

- colorful comic book format
- useful at home or in classrooms
- reinforces language and math skills
- relates science concepts to technology
- aimed at 4th through 6th graders

Price per subscription (one-year, four-issues)	
To continental U.S. addresses	1-4 \$4.00 each 5-19 \$3.00 each 20 or more \$2.00 each
To addresses outside the continental U.S.	50 or more \$3.00 each (minimum)

For subscription information write or call:
American Chemical Society
Prehigh School Science Program
1155 Sixteenth St., N.W.
Washington, DC 20036
(202) 452-2113

THE PITTSBURGH CONFERENCE
is turning



UPSIDE DOWN!

MARCH 5-9, 1990

Jacob K. Javits Convention Center
New York, New York

Contact us at our new location:
THE PITTSBURGH CONFERENCE
300 Penn Center Boulevard, Suite 332, Pittsburgh, PA 15235 U.S.A.
1-800-825-3221, (412) 825-3220, FAX (412) 825-3224

CIRCLE 115 ON READER SERVICE CARD

MEETINGS

Chromatography. March 3-4. Larry Taylor

■ **Laboratory Information Management Systems: From Problem Definition to System Evaluation.** March 3-4. Gerst Gibbon, Joseph Golden, and Ann Cibulas

■ **Maintaining and Troubleshooting Chromatographic Systems.** March 3-4. M.P.T. Bradley

■ **Modern NMR Spectrometry.** March 3-4. Joseph Lambert

■ **Modern Techniques in Gas Chromatography.** March 3-4. Harold McNair, Patrick Sandra, and Jacques Rijks

■ **Particle Size Distribution: Assessment and Characterization.** March 3-4. Theodore Provder, J. Calvin Giddings, Brian Kaye, Bruce Weiner, David Fairhurst, and Richard Karuhn

■ **Practical Analytical Atomic Spectroscopy: AAS, ICP-AES, ICP/MS.** March 3-4. Theodore Rains and Howard Taylor

■ **Practical HPLC Method Development.** March 3-4. J. J. Kirkland and Lloyd Snyder

■ **Practical LC/MS, SFC/MS, and**

CZE/MS. March 3-4. Jack Fenion and David Games

■ **Practical Near-IR Analysis.** March 3-4. Donald Burns

■ **Surface Analysis Techniques.** March 3-4. John Grant

■ **Technical Writing Workshop.** March 3-4. Anne Eisenberg

■ **Thermal Analysis in Materials Characterization.** March 3-4. Edith Turi, Patrick Gallagher, and James Seferis

■ **Expert Systems for Chemists.** March 4. Frank Settle, Jr., and Michael Pleva

■ **Microwave Sample Preparation: Theory and Practice.** March 4. H. M. Kingston and Lois Jassie

■ **Advanced Analytical Laboratory Management Workshop.** March 10-11. John H. Taylor, Jr., and Mary Routson

■ **Chromatography Data Handling.** March 10-11. Glenn Ouchi

For information on these and other ACS courses, contact the Department of Continuing Education, American Chemical Society, 1155 16th St., N.W.,

Washington, DC 20036 (202-872-4508).

Call for Papers

■ **5th International Symposium on Resonance Ionization Spectroscopy and Its Applications.** Varese, Italy. Sept. 16-21. The symposium will feature invited lectures and contributed papers and posters on the following topics: new laser sources and techniques; atomic and molecular sources; RIS instrumentation; laser ionization mechanisms; collisional and field ionization of laser-prepared states; resonance ionization mass spectrometry; ultra high resolution and isotopic selectivity; molecular RIS; physics applications; surface analysis; environmental and trace analysis; biological and medical applications; and state-selective chemistry. Prospective authors should submit 200-400-word abstracts by April 16 to James Parks, University of Tennessee, Institute of Resonance Ionization Spectroscopy, 10521 Research Dr., Suite 300, Knoxville, TN 37932 (615-675-9570).

**Choosing a graduate school?
Need to know who's doing
research critical to yours?**

**New
edition!**

**All the information you need on chemical research and
researchers at universities in the U.S. and Canada . . .
in a single source.**

The ACS Directory of Graduate Research 1989

- Contains a wealth of facts on 683 academic departments, 11,938 faculty members, and 68,276 publication citations.
- Includes listings for chemistry, chemical engineering, pharmaceutical/medical chemistry, clinical chemistry, and polymer science.
- Lists universities with names and biographical information for all faculty members, their areas of specialization, titles of papers published in the last two years, and telephone numbers, FAX numbers, and computer addresses.

1436 pages (1989) Clothbound
Price: US & Canada \$55.00 Export \$66.00

Call toll free (800) 227-5558 and charge your credit card. In Washington, D.C., call 872-4363.

Please send me _____ copy(ies) of the ACS Directory of Graduate Research 1989.

Price: US & Canada \$55.00, Export \$66.00.

Payment enclosed (make checks payable to American Chemical Society)

Purchase order enclosed. P.O. # _____

Charge my: Master/Card American Express Diners Club/Carte Blanche

Account # _____ Expires _____

Signature _____ Phone _____

Ship books to:

Name _____

Address _____

City, State, ZIP _____

Orders from individuals must be prepaid. Please allow 4-6 weeks for delivery. Prices are quoted in U.S. dollars.

Mail this order form with your payment to: American Chemical Society, Distribution Office Dept. 705,
P.O. Box 57136, West End Station, Washington, D.C. 20037.

705

Here's Why Two Esteemed, Technical Societies Want *Your* Expertise...

The American Chemical Society & American Institute of Chemical Engineers
Announce their 1990 co-publication of

BIOTECHNOLOGY PROGRESS

Editor, Jerome S. Schultz, *University of Pittsburgh*

SUBMIT YOUR PAPERS NOW TO THIS IMPORTANT "NEW" PUBLISHING MEDIUM

Beginning January 1990 BIOTECHNOLOGY PROGRESS, a well-established journal of the American Institute of Chemical Engineers, will become a joint publication of the American Chemical Society and AIChE. As a collaborative effort, several significant changes will occur, *providing enhanced editorial coverage and expanded readership*. These include:

- **Accelerated frequency** — from quarterly to bimonthly issues!
- **A redesigned format** which will better meet the needs of both new and current subscribers.
- **A redefined editorial focus** guaranteed to attract:
 - 1) additional topical papers and primary research findings
 - 2) an audience comprising the very experts *you* want to reach!

ATTENTION CHEMISTS, LIFE SCIENTISTS, AND ENGINEERS!

In bimonthly issues, BIOTECHNOLOGY PROGRESS will provide the latest concepts — in genetics...microbiology and biochemistry...molecular and cellular biology...chemistry and chemical engineering — as they apply to the development of processes, products, and devices. Emphasis will be placed on the *application of fundamental engineering principles* to the *analysis* of biological phenomena involved.

BIOTECHNOLOGY PROGRESS will be of particular interest to *practitioners of R&D in process development, product development, and equipment/instrumentation design for the biotechnology/bioprocess industry*. Its coverage will encompass food, pharmaceutical, and biomedical arenas.

LOOK FOR HIGHLY TARGETED TOPICS LIKE THESE

- **Applied Biochemistry:** Equilibrium data, protein conformations in solution, mapping of molecular surfaces.
- **Applied Molecular Biology:** Cell physiology, gene expression, protein transport, metabolic engineering.
- **Bioreactor Technology:** Reactor engineering, mechanical engineering, materials science, process control, biosensors.
- **Biocatalytic Processes:** Site specific mutagenesis, enzyme mimetics, cofactor regeneration, applied pharmaceutical mimetics.
- **Formulation and Product Delivery.**
- **Bioanalysis:** Online monitoring, containment, containment monitoring, offline analysis, statistical analysis (nonlinear regression, multifactor analysis).
- **Bioseparations.**

ADDRESS YOUR MANUSCRIPT SUBMISSIONS & AUTHOR INQUIRIES TO:

Jerome S. Schultz
Editor, BIOTECHNOLOGY PROGRESS
Center for Biotechnology and Bioengineering
University of Pittsburgh
911 William Pitt Union
Pittsburgh, PA 15260
Telephone: 412/648-7956 Fax: 412/624-7145

To receive editorial updates please write:
American Chemical Society, Marketing,
BIOTECHNOLOGY PROGRESS, Room 609,
1155 Sixteenth St., N.W., Washington, D.C. 20036
FAX: 202/872-6005
Telex: 440159 ACSP UI or 89 2582 ACSPUBS

Analytical chemists . . . prepare
of the 1990s. Register today to

SHORT

to be held in conjunction with
the premier analytical science
exposition

ANALYTICAL CHEMISTRY 1990

40 COURSES TO CHOOSE FROM:

Advanced Laboratory Management Workshop

Saturday-Sunday, March 10-11, 1990

Learn how to deal more effectively with lab management problems

Analytical Chemistry of Contaminants in Surface and Ground Water

Saturday-Sunday, March 3-4, 1990

Understand the latest sampling and analytical techniques

Analytical Infrared Spectroscopy: Techniques, Applications, Computer Methods

Saturday-Sunday, March 3-4, 1990

Master a versatile method for analyzing solids, liquids, and gases

Applied Optical Microscopy

Friday-Sunday, March 2-4, 1990

Gain hands-on experience to apply to problems of contrast enhancement and measurement

Capillary Gas Chromatography: Techniques and Problem Solving

Saturday-Sunday, March 3-4, 1990

Learn how to facilitate the transitions from packed to capillary columns

Chromatography Data Handling: From Detector to Decision

Saturday-Sunday, March 10-11, 1990

Learn how to use computer systems to efficiently organize and report chromatography data

The Computer-Integrated Laboratory

Saturday-Sunday, March 3-4, 1990

Meet the demands of laboratory automation with a sound understanding of this rapidly developing field

Diagnostic Immunology

Saturday-Sunday, March 3-4, 1990

Understand how new procedures and discoveries of immunology are applied to the diagnostic lab

Effective Management of Chemical Analysis Laboratories

Saturday-Sunday, March 3-4, 1990

A course that will show you how to increase productivity and decrease costs—the twin goals of a well-run laboratory

Effective Supervision of Scientists and Technical Staff

Saturday-Sunday, March 3-4, 1990

Improve your management skills with this acclaimed course

Electronics for Laboratory Instrumentation

Thursday-Saturday, March 1-3, 1990

Receive valuable hands-on training that will help you understand and benefit from modern instrumentation

Environmental Analytical Chemistry: Air Toxics

Saturday-Sunday, March 3-4, 1990

Hear the latest word on advanced sampling and analysis techniques for air toxics measurement

Environmental Analytical Chemistry: Water and Waste

Saturday-Sunday, March 3-4, 1990

Master the fundamentals of applied environmental measurements of pollutants in liquid and solid samples

Environmental Laboratory (QA/QC Data Validation

Saturday-Sunday, March 3-4, 1990

Increase laboratory data quality and meet user needs—present and future laboratory goals

Environmental Law and Regulations

Saturday-Sunday, March 3-4, 1990

Gain a better understanding of how environmental law was formulated and how it's currently administered

Experimental Design for Productivity and Quality in R&D

Friday-Sunday, March 2-4, 1990

Learn the proper way to design experiments for improved research quality

Expert System Tools for Chemists

Sunday, March 4, 1990

Gain an understanding of current expert system development tools and their application to current problems

Gas Chromatography—Mass Spectrometry

Saturday-Sunday, March 3-4, 1990

Learn how GC-MS can solve your sample separation and identification problems

How to Manage Complex Laboratory Data Systems

Saturday-Sunday, March 3-4, 1990

Learn a complete systems approach to handling laboratory data

Laboratory Information Management Systems: From Problem Definition to System Evaluation

Saturday-Sunday, March 3-4, 1990

Examine the impact a LIMS would have on your laboratory

Lotus in the Laboratory: Putting Spreadsheets, Graphics and Database Management Software to Work

Saturday-Sunday, March 3-4, 1990

Improve your data analysis and manage your data more effectively

Maintaining and Troubleshooting Chromatographic Systems

Saturday-Sunday, March 3-4, 1990

Focus on LC and GC separation problems in this up-to-date course

Microwave Sample Preparation: Theory and Methods

Sunday, March 4, 1990

Receive an introduction to state-of-the-art equipment, control, and practical methods involved in microwave sample preparation

Modern Methods of Particle Size Distribution: Assessment and Characterization

Saturday-Sunday, March 3-4, 1990

Learn the advantages and limitations of specific particle size analysis methods

...to meet the challenges
of the American Chemical Society

COURSES

at the Pittsburgh Conference
on Analytical Chemistry and Instrumentation
this year!

NEW YORK, NY

Modern NMR Spectroscopy

Saturday-Sunday, March 3-4, 1990

Keep up-to-date on current techniques for this vital analytical method

Modern Techniques in Gas Chromatography

Saturday-Sunday, March 3-4, 1990

Learn about the latest developments in gas chromatography, including a wide variety of practical applications

Online Process Analyzers: The Key to

Maximizing Industrial Process Efficiency

Friday-Sunday, March 2-4, 1990

Achieve a sound working knowledge of process analyzer technology in the shortest time possible

Practical Analytical Atomic Spectroscopy:

AS, ICP-AES, and ICP/MS

Saturday-Sunday, March 3-4, 1990

Learn practical analytical applications of AAS, ICP, and ICP/MS

Practical HPLC Method Development

Saturday-Sunday, March 3-4, 1990

Investigate strategies, techniques, and methods guaranteed to minimize your time and effort spent without compromising the goals of method development

Practical LC/MS, SFC/MS, and CZE/MS

Saturday-Sunday, March 3-4, 1990

Learn effective techniques for analyzing and characterizing organic compounds

Practical Near-IR Analysis

Saturday-Sunday, March 3-4, 1990

Learn state-of-the-art industrial applications of this rapid, accurate, non-destructive method of analysis

Quality Assurance of Chemical Measurements

Saturday-Sunday, March 3-4, 1990

Master techniques used in quality control and assessment of chemical measurement

Size Exclusion Chromatography

Saturday-Sunday, March 3-4, 1990

Gain an understanding of the advantages and limitations of SEC

Spectroscopic Characterization of Polymers

Saturday-Sunday, March 3-4, 1990

Learn techniques to help solve your polymer structural problems

Spectroscopy for Chemical Analysis: Basics, Advanced Methods, and Rapid Screening

Saturday-Sunday, March 3-4, 1990

Receive an overview of a modern spectroscopic methods for chemical analysis

Supercritical Fluid Extraction/Chromatography

Saturday-Sunday, March 3-4, 1990

Find out if SFC/SFE technology can provide a solution to your separation problems

Surface Analysis Techniques

Saturday-Sunday, March 3-4, 1990

Gain an understanding of physical concepts, capabilities, and applications of surface analysis techniques

Technical Writing Workshop

Saturday-Sunday, March 3-4, 1990

Learn from a master teacher how to improve your professional writing skills

Thermal Analysis in Materials Characterization

Saturday-Sunday, March 3-4, 1990

Apply down-to-earth systematic applications of thermal analysis to a very broad range of materials

X-Ray Fluorescence Spectrometry

Friday-Sunday, March 2-4, 1990

Learn about the latest theory and practice of this important technique



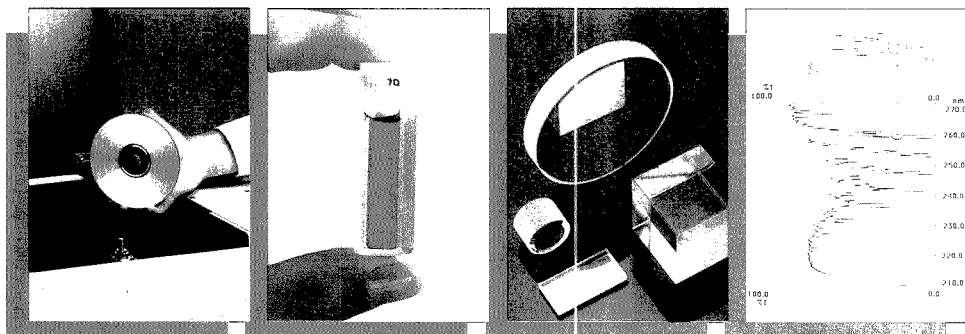
For a free brochure describing all of the ACS Short Courses to be held at the 1990 Pittsburgh Conference & Exposition, mail in the coupon below. Or call TOLL FREE (800) 227-5558, press 3, and ask for ext. 3340.

Yes! Please send me a FREE brochure describing the ACS Short Courses to be held at the Pittsburgh Conference & Exposition, March 1990, in New York, NY.

Name _____
Title _____
Organization _____
Address _____
City, State, Zip _____

Mail to: American Chemical Society, Dept. of Continuing Education, Meeting Code PCE90030, 1155 Sixteenth Street, N.W., Washington, DC 20036.

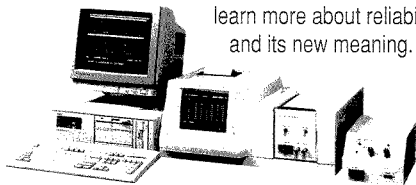
Compare Our 99%[†] Guaranteed Up-Time Before Your Next UV/Visible Purchase!



Solve your application problems with the UV/Visible or UV/Vis/NIR spectrophotometer designed for reliability and performance. Software for scanning, kinetics, quantitative analysis, thin film measurements and advanced spectral processing is available with six different instruments to provide the right choice for your next UV/Vis purchase decision.

Reliability... New Meaning for an Overused Term.

In survey after survey, UV/Visible users have indicated that reliability is the most important factor considered in a new purchase decision. Our service records confirm such outstanding dependability that we can now offer a guaranteed 99% up-time policy on all our analytical instruments. Call us now, and learn more about reliability... and its new meaning.



With each instrument you receive a certificate of "Our Pledge of Quality to You". This guarantees you a 99% up-time, or we pay the bill.



For Details...

Call us Toll-Free (800)548-9001
or write: Hitachi Instruments, Inc.
15 Miry Brook Road, Danbury, Ct 06810

Hitachi Instruments, Inc.

CIRCLE 60 ON READER SERVICE CARD

LC, GC, and Column Chromatography

Microbore Column Chromatography: A Unified Approach to Chromatography. Frank J. Yang, Ed. 424 pp. Marcel Dekker, 270 Madison Ave., New York, NY 10016. 1989. \$120

Reviewed by James Jorgenson, Department of Chemistry, University of North Carolina, Chapel Hill, NC 27514

This 405-page book is intended to provide an overview of microcolumn techniques in gas, liquid, and supercritical fluid chromatography. From the title, one might expect a balanced treatment of microcolumn GC, LC, and SFC. This is, however, not the case. The only discussion devoted to capillary GC is contained within seven pages of the introductory chapter and consists mostly of a qualitative description of the capabilities of capillary GC. Such brief treatment of GC is perhaps understandable, as this is a mature technique, and there are many books available that cover this topic in detail.

The next set of six chapters deals with the topic of microcolumn LC. It begins with a chapter entitled Packing Materials and Packing Techniques for Micro-HPLC Columns. This is a remarkable title, as the chapter contains essentially no information about micro-HPLC columns. The chapter is, in reality, mostly a review of packing materials, with the bulk of the column performance data taken from columns of conventional (4.6 mm) diameter. There is nothing said about peculiarities of packing and performance of microcolumns. The next chapter (50 pages) deals with gradient elution and reviews methods for forming gradients at microliter-per-minute flow rates used in microcolumn LC. This chapter is extremely thorough. The next three chapters (94 pages) are devoted to various optical methods of detection in micro-LC. This section begins with a chapter on FT-IR, fluorescence, optical rotation, thermal lens, and refractive index. This is followed by a chapter on fluorescence detection with diode arrays and a chapter on inductively cou-

pled plasma atomic emission detection. These three chapters give good coverage to these detection techniques. What is surprising, however, is that there are no chapters devoted to UV absorption detection, electrochemical detection, and LC/MS. Equally surprising is that microsample handling and microinjection, topics of special significance for microcolumn LC, are not covered in this book. A special chapter on two-dimensional separations via micro LC/capillary GC is included. This chapter contains a nice

“A special chapter on two-dimensional separations via micro LC/capillary GC . . . contains a nice balance of practical detail and applications . . .”

balance of practical detail and applications illustrating the technique.

The final four chapters of the book cover SFC. This section is well balanced, with the following topics discussed: an overview of capillary SFC, detection in capillary SFC, SFC/MS, and applications to samples of industrial origin.

In summary, most of the chapters are useful and well written. The biggest flaw of the book is that it does not cover many topics of obvious importance in the area of microcolumn LC, and for this reason it is poorly balanced. By not including any serious discussion of capillary GC, the book also fails to live up to its title. As for the book being “A Unified Approach to Chromatography,” the balance of the book never justifies this statement. Although a unified theory may underlie GC, LC,

and SFC they are still, in a practical sense, quite different techniques, which this book amply demonstrates.

Inverse Gas Chromatography: Characterization of Polymers and Other Materials. Douglas R. Lloyd, Thomas Carl Ward, and Henry P. Schreiber, Eds. 231 pp. American Chemical Society Distribution Office, 1155 16th St., N.W., Washington, DC 20036. 1989. \$70

Reviewed by Karin Caldwell, Center for Biopolymers at Interfaces, Department of Bioengineering, University of Utah, Salt Lake City, UT 84112

More than 20 years have passed since the publication of the first articles by Kiselev (*Advances in Chromatography*, 1967) and Smidsrød and Guillet (*Macromolecules*, 1969), suggesting that gas chromatography, which by that time had matured into an eminently useful high-resolution technique for purification and characterization of volatile substances, could also be profitably used in the analysis of such nonvolatiles as high molecular weight polymers and other solids. As long as the analyte could be packed in a column long enough to show measurable retention of well-characterized volatile probe molecules, the retention would be a measure of the probe's tendency to partition itself between the mobile and stationary phases. By varying the amount of injected probe, one could conveniently establish adsorption isotherms for the various probes on the solid substrate. Subsequent studies would show that measurements of retention were direct reflections of the work of adhesion between probe and surface, and would therefore give valuable information on the surface free energy of the solid analyte; for rough or porous surfaces, such data would often be impossible to collect by other means.

This new way of utilizing the well-established gas chromatographic technique became known as inverse gas

chromatography (IGC) because of its focus on the stationary phase, as opposed to the volatile solute. From constituting a modest 3% of all GC publications in the decade prior to 1977, the technique is at present discussed in nearly one-third of all articles on GC. Reflecting this significant growth in interest, the Division of Polymeric Materials Science and Engineering of the American Chemical Society and the Macromolecular Science and Engineering Division of the Chemical Institute of Canada jointly sponsored a symposium on IGC at the 195th ACS meeting in Toronto in June of 1988. Given that no comprehensive text on the subject of IGC exists, the decision to collect the various contributions to this symposium in one volume should be welcomed by everybody with a current or anticipated interest in the technique.

In addition to an introductory chapter by two of the three editors, the book

“... review of the many ways IGC can be used to characterize both surface and bulk properties of nonvolatile materials.”

contains 21 chapters organized in six sections: Methodology and Instrumentation, Sorption and Diffusion in Polymers, Polymer Blend Characterization, Surface and Interface Characterization, Analytical Applications, and a small section entitled Special Applications. Reflecting the editors' research interests, a strong focus is given to the characterization of synthetic polymers and their interactions with fibrous reinforcement materials, while other active areas such as the application of IGC to the study of textile fibers are not covered. As with any collection of research papers, much of the necessary background and theoretical foundations are assumed to be known to the reader and are not treated in great detail. However, the large number of listed references will be helpful to the uninitiated reader.

The methodology section begins with an informative description by Bolvari et al. of procedures and pitfalls in coating particulates or capillaries to be used as stationary phases in the IGC analysis. These authors point to a common source of error, later elaborated on by Munk et al. and Su and Fried, namely, the often incomplete coating of the substrate surface and the resulting ef-

fect on probe retention and the thermodynamic parameters derived from these data (e.g., solubility parameters or the Flory-Huggins interaction parameter χ for blended polymers). Guillet et al. review a number of applications pioneered by their group, notably the determination of polymer transition temperatures and percent crystallinity, rates of isothermal crystallization of polymeric melts, and the determination of adsorption isotherms and surface areas. The methodology section concludes with a simulation of the retention behavior developed by Hattam, Du, and Munk, which demonstrates how to distinguish between the different modes of interaction (i.e., surface or bulk) that may develop between probe and stationary phase.

In the section on sorption and diffusion, Price describes the determination of polymer solubility parameters δ from the retention of numerous volatile probes. The range of measured δ -values

for different mixing ratios, and extrapolating to the value of zero indicative of phase separation, a set of critical temperatures is obtained that establishes a phase diagram for the polystyrene/poly(vinyl methyl ether) system that is in good agreement with data in the literature.

The section entitled Surface and Interface Characterization devotes much attention to determinations of the various components of the surface free energy of fibrous materials to be embedded in polymeric matrices for structural reinforcement. From IGC measurements of the London component of the surface free energy, Vukov and Gray demonstrate the existence of specific high-energy adsorption sites on certain carbon fibers and stress the need to discriminate between values for the surface free energy obtained at finite, as compared with zero, coverage by the probe. Whereas the "finite coverage" value represents an average surface energy, the "zero coverage" value specifically characterizes the high-energy sites that are competing more effectively for the small amount of probe. In addition to the London component of surface tension, both Schultz and Lavielle and Bolvari and Ward measure the acid/base characteristics of a variety of surface-treated carbon fibers and demonstrate strong correlations between the strength of the fiber-matrix adhesion on the one hand and the complementarity of the acid/base properties of fiber and matrix on the other. An elegant study by Wesson and Allred shows agreement between surface energies determined by wetting and by IGC for a number of plasma- and heat-treated carbon fibers. The acid/base characteristics are assessed by titration as well as by the IGC retention of acidic and basic probes, and X-ray photoelectron spectroscopy shows the existence of surface carboxyl groups in proportion to the acidity determined by IGC. Similar studies are made on glass fibers by Osmont and Schreiber, and on surface modified silica particles by Papirer et al.

Two short sections on analytical and special applications illustrate the use of IGC in the analysis of siloxane polymers (Laub and Tyagi) and polyimides (Raymer et al.) as well as coal samples (Neill and Winans) and starch (Gilbert).

All in all, this volume gives a thorough and critical review of the many ways IGC can be used to characterize both surface and bulk properties of nonvolatile materials. The editors should be congratulated on having assembled a valuable collection of representative articles by authors who have

is limited, and some unexplained departures from expected behavior are reasons for caution in using this approach. Gaseous adsorption and diffusion are both important characteristics of polymeric membranes, and Shiyao et al. report on the differential adsorption to various polymeric materials suitable for use in gas separation. In articles by Demertzis and Kononimas and Arnould and Laurence, plate height studies are used to gain information on probe diffusivity through the polymeric stationary phase.

Since IGC is extensively used to determine Flory-Huggins parameters for polymer blends, it is most gratifying to read the four chapters included in the section on polymer blend characterization, which all voice some caution regarding the application of IGC to measurements of χ . A certain probe-to-probe variation is seen by all contributors to this section, although DiPaola-Baranyi and El-Hibri et al. both find convincing trends in such parameters determined for several blends. Klotz et al. find Flory-Huggins parameters determined by IGC to be at variance with data from small angle neutron scattering. However, when following the temperature variation of χ

contributed significantly to the field of IGC analysis during the past two decades. This being said, however, one wishes to express some concern over the many misprints and errors that have crept into both text and equations, making the reading at times somewhat less enjoyable.

Troubleshooting LC Systems: A Practical Approach to Troubleshooting LC Equipment and Separations. John W. Dolan and Lloyd R. Snyder. 515 pp. Humana Press, Inc., Crescent Manor, P.O. Box 2148, Clifton, NJ 07015. 1989. \$65

Reviewed by John G. Dorsey, Department of Chemistry, University of Cincinnati, Cincinnati, OH 45221-0172

This book is not designed for the office, nor to be taken home and read. Rather, it is an extremely valuable aid for the practicing chromatographer, and a copy should be near the bench of everyone using liquid chromatography.

This book represents a compilation or "hard copy" of a successful short course taught by the authors, augmented by much additional useful information. Dolan and Snyder take the approach that there are two central themes for successful LC troubleshooting. First, there must be an understanding of *how* the instrument operates; second, they believe strongly in preventive maintenance. The book is divided roughly along these themes. Chapter 1 is an introduction, and begins with a section titled *If You Can't Wait*, which tells the reader immediately how to use the troubleshooting sections of the book. Section I, *General Considerations*, comprises four chapters—*Logical Approaches to Troubleshooting*, *Separation Basics*, *Principles of Troubleshooting*, and *Prevention of Problems*. Section II, *Individual LC Modules*, has eight chapters dealing with the individual LC components and includes separate chapters on *Fittings and Tubing*, things too often taken for granted by casual users of LC. Section III, *Troubleshooting the Separation plus Other Problems*, has four chapters dealing more with chemical than with instrumental problems, such as *band tailing*, *sample reactivity*, *problems with quantitation*, and a chapter on *gradient elution and sample pretreatment*.

The sections of the book that will be most heavily used are two tables that, in flow-chart fashion, work the reader through the most likely causes of problems. Table 2.2, *Overview of Likely Problems*, arbitrarily divides problems

into five classifications: pressure, leaks, quantitation or data quality, hardware, and chromatogram. This table is six pages and is recommended for experienced users who need a quick overview of what is the likely cause of a particular problem. It can also be used as a guide to find the proper entry point into the more detailed table. Table 2.3, *Detailed Problem Isolation Flowchart*, is 54 pages, and from a symptom, works the reader through the most likely causes. For instance, there are almost nine pages dealing with baseline noise. The problem is first divided into noise spikes, short-term noise, random noise, rhythmic noise, baseline drift, or a cycling baseline. For each decision in the flowchart there is a suggested action, and then a question as to whether this improved the symptom. The suggested actions are logically chosen to work from the most likely cause of a problem to less likely causes. This table alone will make the book invaluable for many users of LC.

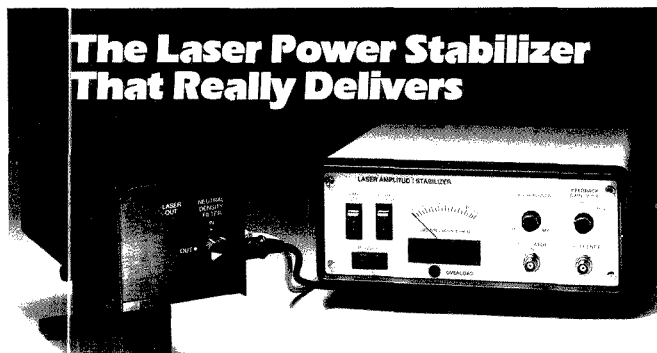
The section on instrumentation is extremely well done, with detailed discussions of the principles of operation of each piece of equipment, and here there are other tables that work the

reader from the known cause of a problem to its solution. For instance, in the chapter dealing with pumps, a cause would be listed as seal wear, the symptom would be leakage behind the pump head, and the solution would be to replace the pump seal. Less experienced users will find highly valuable suggestions for spare parts that should be routinely stocked. The authors are thorough almost to a fault; on page 377 they twice tell users of strip charts to stock spare pens!

It's hard to find fault with this book; the authors accomplish their goals in a fashion that will be easily used by many routine users of LC. The only minor annoyance was in Chapter 3, *Separation Basics*, where seven times (!) the authors suggested the use of DryLab, marketed by the authors' company, for help and guidance in method development.

This book is a wealth of practical information. If it were used only once to save time in troubleshooting, it would be worth the price. It will likely be used, however, over and over by technicians, students, and users of LC, and will be a great bargain for the savings it will provide.

The Laser Power Stabilizer That Really Delivers



If you've spent any time trying to remove laser power noise and drift, you've probably been disappointed by Power Stabilizers that don't deliver; that can only be used with single power and wavelength settings; that 'latch-up'; that have poor long-term stability and are unwieldy to use.

Now consider the Power Stabilizer that is the choice of major standards labs — the LS-100, from CRI. The LS-100 reduces laser noise and drift by a factor of 400 over a wide range of wavelengths (400-950nm) and power levels (5½ decades), both user-adjustable. This versatile, simple-to-use device stabilizes CW and mode-locked laser power to within 0.05% rms, has a transmittance of over 70%, and can be easily interfaced for external control.

So remove your laser noise with the LS-100 — the Power Stabilizer that really delivers.

Cambridge Research & Instrumentation, Inc.

2 Erie Street, Cambridge, MA 02139 • (617) 491-2627 • FAX (617) 864-3730

CRI

Wastewater TOC

Dirty, salty or particulate laden water... The Dohrmann® DC-190 High-Temperature TOC Analyzer does them all.



The world's largest community of TOC users and Dohrmann's three decades of experience have led to the creation of an advanced system that satisfies the most demanding requirements. Here are some of the features of this compact, modern TOC analyzer:

- **Flexibility:** The DC-190 operates at 680°C for industrial wastewater or seawater monitoring. The system is variable to 900°C for environmental analyses in compliance with Standard Method 505A as referred to by EPA methods 415.1 and 9060.
- **Manual or automated.** The DC-190 handles your toughest, real-world samples. From sample container to combustion tube, the DC-190's operation provides true TOC not just DOC.
- **Minimum downtime, high throughput.** All key components of the DC-190 system are readily accessible, making service a simple matter.

There's a lot more to know about the DC-190. Contact Dohrmann today at 1-800-538-7708.

See us at Booth #3643, Pittsburgh Conference

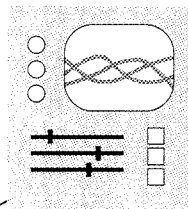
Rosemount Analytical Inc.
Dohrmann Division
3240 Scott Boulevard
Santa Clara, CA 95054
(800) 538-7708 (408) 727-6000
FAX: (408) 727-1601 Telex: 346395

ROSEMOUNT

Measurement
Control
Analytical
Valves

CIRCLE 28 ON READER SERVICE CARD

Keeping Aging Planes Healthy



Few industries dwell more in the public eye than the airlines. Thus, when Aloha Flight 243 made an emergency landing at Maui's Kahului Airport on April 28, 1988, missing an 18-ft section of upper fuselage, the world took notice. The lost section, which formed the roof of the passenger compartment, had suddenly and violently ripped free while the 19-year-old Boeing 737 was traveling 330 mph at 24,000 ft. The rapid decompression threw a stewardess out of the plane and injured 61 passengers (1).

The publicity surrounding the dramatic accident alerted the public to the fact that U.S. carriers are flying large numbers of older planes. The incident also warned federal agencies and Congress that it was time to reevaluate inspection and maintenance procedures. One immediate result of this heightened national concern has been greater support for developing new inspection procedures, especially those classified as nondestructive.

The entire U.S. plane contingent now averages around 12 years in age. However, that value varies with individual carriers. Eastern's fleet, for instance, averages about 14 years, whereas Delta's aircraft average 8.4 years (2). Twenty-year-old planes such as Alo-

ha's Boeing 737 are not uncommon. Given the rising cost of new planes and the fact that more people are flying, U.S. carriers will probably continue to fly older planes. In contrast, many European carriers fly newer planes. West Germany's Lufthansa rolls out Boeing 747s that average 5.1 years in age, and British Airways fields a fleet averaging about 8 years of use (2).

However, old planes are not the problem; it is the job of inspecting and maintaining their airworthiness that is difficult. In their review of the Aloha accident, the National Transportation Safety Board attributed the incident to metal fatigue and weakened adhesive bonding between fuselage sections. According to the board, Aloha and Boeing failed to properly maintain and correct problems on the 737.

"Things break and cracks appear," says Stephen Bobo, a mechanical engineer with the Department of Transportation's Research and Special Programs Administration in Cambridge, MA. Airlines are responsible for careful inspections for three constant enemies: corrosion, cracking, and loss of adhesive bonding. (A significant amount of adhesive is used to glue down overlapping sections of aircraft). Visual inspection by trained technicians has al-

ways been essential in spotting damage, but nondestructive tests now also assume an important role.

To understand the process of inspecting planes and the techniques being developed, it is important to understand the maintenance procedures airlines now follow. As regulated by the Federal Aviation Administration (FAA), airplanes now undergo a clearly defined and hierarchical series of inspections. The timing of these checks varies with each air carrier, the differ-

FOCUS

ent types of planes it flies, the availability of maintenance facilities, and the numbers of technical personnel working. FAA enforces inspection schedules by random and unannounced checks on airline inspection facilities.

"Basically, there are four categories of scheduled maintenance, commonly referred to as A through D checks," explains Fred Duvall, manager of FAA's Flight Standards Division Aging Fleet Office in Seattle. "An A check is a primary inspection looking at the general condition of the aircraft." Mainte-

nance personnel visually check the plane for obvious signs of damage.

On the venerable Boeing 727, A checks or their equivalent are performed, on a worldwide average, about every 149 h of flight time. Because most planes are in use approximately 8 h per day, an A check occurs almost every 20 days.

"The B check," continues Duvall, "is an intermediate check, an operational check for airworthiness." Switches and warning lights are tested, and oil filters might be changed. For 727s, this inspection occurs on average about every 612 h. At the same time the A check is repeated, just as the A and B checks will be repeated during the C check. "You are constantly duplicating the lower checks," says Duvall.

During the C inspection, access doors and panels are removed so that pumps, systems, and electronics can be tested against specified standards. For example, fuel pump low-pressure systems are tested, the autopilot is evaluated, and the VHF radio is checked. On 727s, C checks average every 3000 h of flight time, or roughly once a year.

"The D check is the most extensive, an intensified structural inspection," says Duvall. The airplane is partially dismantled and internal structures are carefully examined for structural integrity. Some interior cabin equipment is removed and most panels are opened. Depending on the size of the staff, D checks can last from 30 days to up to 3 months. Costs to the company can run well over half a million dollars.

Engine inspections are carried out by another procedure, usually at the same time as the airframe inspections. The important parameter for jet engines is cycles that correspond to each round of start up through shutdown.

Finally, FAA issues airworthiness directives whenever significant concerns arise about the continued airworthiness of an airplane fleet. One such directive after the Aloha incident mandated the immediate inspection of 737s.

Most of the testing, which takes place during the D check or its equivalent, is nondestructive. Three nondestructive methods are now widely used: eddy currents, ultrasonics, and X-ray analysis. These techniques can examine only small areas at a time and therefore are applied to points especially vulnerable to cracking and corrosion. For instance, X-rays in the 200-300-kV range probe for cracks in the frame surrounding the pilot's sliding window, and the eddy current technique regularly checks tire rims.

Eddy current testing uses a pencil-shaped probe to search for cracks, es-

pecially subsurface defects. The probe contains a coil through which a high-frequency alternating current runs. Associated with the current is a magnetic field, which in turn induces a current in the test material. Therefore the probe never touches the test surface. Defects in the test section perturb the induced current, leading to a reduction in conductivity. This affects the sample's impedance, which is detected by a second coil in the probe.

"The depth of penetration depends on the frequency," explains Stephen Bobo. Examination of the 0.039-in. (0.99 mm) thick metal skin of a Boeing aircraft or the 0.050-in. (1.3 mm) deep sections of a McDonnell Douglas DC-9 requires frequencies in the range of 20-

“What seems to be needed are automated techniques that examine wide areas and detect various problems.”

500 kHz. Practical considerations limit eddy current testing to a maximum depth of about 0.25 in. (6.4 mm).

"Ultrasound," says Bobo, "is more useful since it is not limited by depth. It detects corrosion and, in some cases, adhesive dis-bonding." High-frequency pulses of sound are sent into the test site, and the rate of signal return is measured. Defects or thinning from corrosion send the signal back sooner.

Following the Aloha incident, the U.S. government began reevaluating its inspection procedures. In 1988 Congress passed the Aviation Safety Research Act, which led to the establishment of a National Aging Aircraft Research Program by FAA. Congress specifically mandated that FAA use 15% of its research budget on long-term projects (3).

The airline industry has responded with its own initiative, the Airworthiness Assurance Task Force. This forum, which examines issues related to aging aircraft, is a who's who of the flight business. The task force includes representatives from American and foreign airlines, manufacturers, FAA and similar agencies in other countries, NASA, and the military. The group has already recommended an \$800 million maintenance program for aging Boeing planes (4).

NASA is also taking a more active

role in the national overhaul of inspecting older aircraft. Under the leadership of FAA, NASA is developing new testing methods. "What seems to be needed are automated techniques that examine wide areas and detect various problems," says NASA's Thomas Crooker, program manager for materials in the Office of Aeronautics and Space Technology in Washington, DC. Airlines also want tests that are economical and fast. Toward that end NASA plans to investigate a number of new nondestructive tests. One of the most promising is thermal analysis.

There are several versions of this procedure. Essentially, a large section of the airframe is heated while an IR video camera sensitive to 0.1 °C temperature differences images the test section. Anomalous heat flow indicates problems. Thermal analysis is particularly useful for checking laminated surfaces for dis-bonding. Furthermore, as a "stand-off" technique, it need not physically contact the plane. NASA already uses this technique to examine the solid rocket motors and carbon-carbon brakes on its Space Shuttle.

At NASA-Langley, researchers are refining this technique by what Joseph Heyman, head of the Nondestructive Measurement Science Branch, calls "inversion of the thermal data. Instead of just looking, we are telling it how to heat."

Heyman's group models thermal diffusion in large surfaces and determines which properties provide the highest contrast for defects. What they learn is how to collect and analyze the data. "No one cares if the plane is painted uniformly," he says. Instead, their approach provides a more quantitative assessment of the data, which in turn offers a clearer picture. Heyman also has some preliminary data suggesting that thermal analysis could detect corrosion.

Laser holography, another promising method under investigation, also looks at large sections for dis-bonding. A large-area laser scanner is used to measure displacements of a test section under stress. Uneven expansion could indicate structural problems.

For example, by pressurizing the aircraft's cabin, as if in flight, the fuselage can be forced to expand approximately 0.10 in. (2.5 mm). (This normal bulging of the hull is a major contributor to metal fatigue.) The laser technique now being developed can detect in- and out-of-plane displacements as small as 0.1 μm in a surface with vibrations up to 50 kHz. This method could resolve tiny strains in the metal before they became a major problem, and early detection would lower repair costs.

Other, more long-term approaches are also being pursued. Acoustic emission is a well-established technique for detecting cracks in simple devices such as pressure bottles or storage tanks. Changes in the internal pressure can cause cracks to form or grow. As the crack expands, it emits sounds that can be picked up by transducers for analysis. However, this type of analysis becomes difficult on an object as complicated as a jet plane.

"We are looking at the next generation, which we feel will work on complex structures," says Heyman. Instead of using transducers that measure a very narrow acoustic range, NASA researchers are employing broad-band transducers to avoid missing important information. In addition, they have distributed the transducers across or have incorporated them into the test surface. They then collect sound waves before they propagate a great distance, aiding in the interpretation of the data.

Finally, NASA is studying ways to obtain more information from data. An algorithm for ultrasound analysis, called minimum error deconvolution, works in real time and provides sharper resolution. The program not only examines the sound data being collected, but also factors in information about the transducer recording the signal. With this program ultrasound could examine laminated surfaces.

NASA is also looking at fatigue testing. The agency has been evaluating proof testing, a controversial technique that deliberately overloads the plane to look for multisite problems. Planes that fail a test such as overpressurizing the fuselage are taken out of service. However, many workers worry that proof testing could actually introduce damage in planes certified as flight-worthy. NASA plans to publicly release the results of its evaluation of proof testing in the near future.

With Congress, federal agencies, and the public now keenly interested in proper maintenance of aging aircraft, it is apparent that the accident on Aloha Airlines marks a turning point for the airline industry. The changes instituted by the United States as a result of this accident will have worldwide ramifications. As Duvall summarized it, "[The U.S.] sets the marching order."

Alan R. Newman

References

- (1) *Time* May 16, 1988, pp. 62-65.
- (2) *Aviation Week & Space Technology* July 24, 1989, p. 69.
- (3) *Aviation Week & Space Technology* July 24, 1989, p. 60.
- (4) *Aviation Week & Space Technology* March 6, 1989, p. 64.

NUPRO Valves and Filters for Analytical Applications

NUPRO Valves and Filters offer these design and performance choices:

■ **End Connections:** SWAGelok® Tube Fittings, NPT, Tube Stub, Weld, CAJON VCO® & VCR®

■ **Service Ratings:** vacuum to 6000 psi; temperatures to 900°F

STOCKED FOR IMMEDIATE DELIVERY
BY AUTHORIZED SALES AND SERVICE
REPRESENTATIVES.

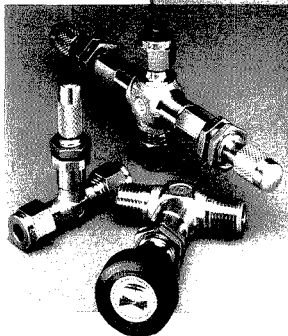
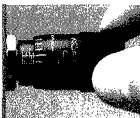


NUPRO COMPANY
4800 East 345th Street
Willoughby, OH 44094

METERING

Valves for precise flow control in laboratory and instrument systems

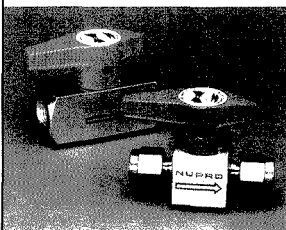
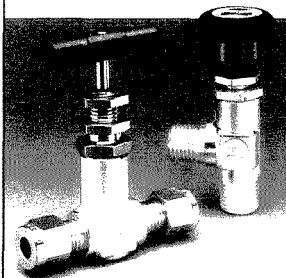
- accurate, repeatable flow adjustment with no initial surge
- compact, low dead space
- stem threads removed from system



SHUT OFF

Compact valves for reliable flow regulation and shut off

- stem threads removed from system fluid
- compact designs
- ball tip or regulating stems



- quick-acting, 1/4 turn
- full flow
- easy maintenance



FILTRATION

In-line and tee type filters to protect instruments by removing hard particle contamination from fluid lines

- choice of sintered and wire mesh elements from 0.5 to 440 microns
- compact designs
- all metal construction

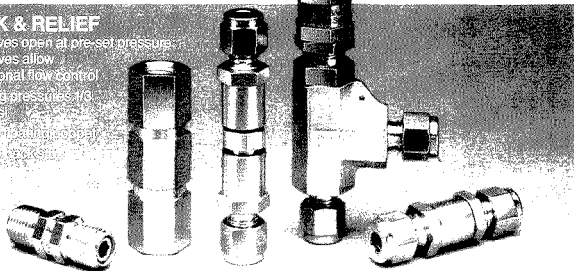
SWAGelok — TM Crawford Fitting Company
CAJON, VCO & VCR — TM Cajon Company
© 1986 SWAGelok Co., all rights reserved N-56a

CHECK & RELIEF

Relief valves open at pre-set pressure; check valves allow unidirectional flow control

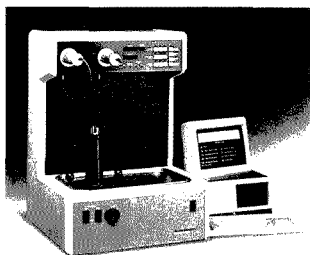
- cracking pressures: 1/3 to 6000 psi
- service ratings: vacuum to 6000 psi
- stem threads removed from system

Check valves: 1/2, 3/8, 1/4, 1/8, 1/16 inch



CIRCLE 125 ON READER SERVICE CARD

NEW PRODUCTS



PoreSizer 9320 mercury porosimeter collects up to 250 data points using pressures from 0 to 30,000 psia. A digital status display allows observation of the intrusion in real time. Micromeritics 401

Ion chromatography. Wescan ICM-300 ion chromatography module includes a conductivity detector, column heater, injection valve, and metal-free flow path. The detector features one-touch background correction and remote-operation capabilities. Alltech Associates 404

Fluorescence. Model F-4010 fluorescence spectrophotometer allows 3D and contour plotting of excitation and emission spectra. The software is available on disk and is designed to acquire, display, and plot spectra as a function of intensity, excitation, and emission wavelengths. Hitachi Instruments 405

Oxygen. Model TMO2 oxygen analyzer is unaffected by normal changes in ambient temperature or by variations in sample flow rate. Use of glass-coated thermistors rather than a hot wire filament eliminates errors resulting from reaction of hydrocarbon vapors. Panametrics 406

Electrophoresis. Model 1600 capillary electrophoresis system incorporates automatic buffer/electrolyte replenishment and programmable buffer/electrolyte cycling. The system, which has a 96-vial capacity, allows one to nine injections per vial using either electromigration or controlled vacuum injection. Microphoretic Systems 407

LC. Janitor II automatically flushes buffers and corrosive solvents from isocratic HPLC systems at the end of unattended operation. The unit then shuts down power to the HPLC system, improving pump and lamp lifetimes and reducing solvent consumption. Jones Chromatography 408

AA. ARL/GBC 908 is a multielement atomic absorption spectrophotometer that incorporates a four-lamp turret and automatic wavelength and slit settings. Software features include storage of signal graphics, temperature profiles, overlays, and wavelength scans. Applied Research Laboratories/Fisons Instruments 409

IR. Miran 1FF fixed-filter IR spectrometer is designed to quantify petroleum hydrocarbons in soil by gauging the intensity of infrared absorption of the C-H stretch band in a contaminated sample. Measurements are displayed on the unit's analog readout. Foxboro 410

Hydrogen sulfide. ISA-86H₂S monitor measures hydrogen sulfide concentrations in the range 0 to 50 ppm. Features include explosion-proof sensor design, low/high alarm modes, battery backup capability, and service relay contacts for auxiliary alarm or other functions. Ennet 411

Microanalysis. IR_{MS} is a molecular microanalysis system for pharmaceutical laboratories that integrates visible microscopy with molecular spectroscopy. Applications include the study of drug metabolism and uptake in thin tissue sections, analysis of transport mechanisms in cell membranes, and the evaluation of drug efficacy. Spectra-Tech 412

Particle size. Fritsch particle size analyzer provides automatic particle size analysis of suspensions or dry powders using a multielement detector to record angle distribution of diffracted, low-power laser light. Results are displayed as frequency distributions, cumulative distribution curves, or 31-channel tabular data. Gilson 413

Clinical analysis. Alpha 4 analyzer, which performs a variety of immuno-

logical and enzyme analyses, can carry out up to 384 tests simultaneously using as many as 16 different protocols at a time. Any technique based on microdots or reactant strips can be used. SFRI 414

Surface analysis. PHI 7000 SALI system combines laser ionization with time-of-flight analysis of post-ionized neutrals. Applications include chemical analysis of synthetic polymer blends, analysis of semiconductor and metallurgical samples, and surface analysis of biomedical devices. Perkin-Elmer 415

Software

Information management. LIMS/DM version 1.8 features bar code label printing; user-extendable database; automatic review and notification; printed worksheets at log-in; and on-line database backup, archive, and retrieval. Varian Associates 417

AA. DP1000 version 4.00 is designed for flame and graphite furnace atomic absorption spectrometry. The software, which includes a built-in spreadsheet, supports manual and automatic sampling as well as incorporation of dilution and weight corrections. Labtronics 418

Manufacturers' Literature

Spectrometry. Brochure highlights the SpectraSpan 7 direct current plasma spectrometer. Fully integrated software that provides system control, graphics, and data storage is described. Applied Research Laboratories/Fisons Instruments 420

Application notes. Series of notes discuss applications of pyrochemiluminescent nitrogen systems, pyrofluorescent sulfur systems, and gas chromatographs. Titles include insulin

For more information on listed items, circle the appropriate numbers on one of our Readers' Service Cards

production monitoring and analysis of additives in polyolefins. Antek Instruments 421

Newsletter. *The Supelco Reporter*, Vol. VIII, No. 5, includes information on simultaneous analytical and confirmational analyses of EPA method 608 pesticides, separation and purification of biopolymers, and determination of sodium content in foods. 12 pp. Supelco 422

Electrophoresis. Application notes describe the separation of proteins, peptides, small organics, and pharmaceuticals using capillary electrophoresis. Analysis conditions, electrophoretic data, and comparisons with existing separation techniques are discussed. Applied Biosystems 423

IR. *Bruker Report* features articles on high-temperature superconductivity, high-resolution FT-IR spectroscopy with a PC, and application of FT-IR spectroscopy to the study of reactions in liquids. 52 pp. Bruker Instruments 424

Carbon. Brochure highlights the 1500 series total organic carbon and total carbon analyzer. Features, applications, and principles of operation are discussed. 6 pp. Ionics 425

Newsletter. Information on products and applications in areas including electron and ion microscopy, surface analysis, E-beam microlithography, and microcircuit failure analysis and repair is featured in the newsletter *fei focus*. FEI 426

Catalogs

GC. Catalog lists capillary columns and accessories; packings; septa; traps; fittings; valves; syringes; analytical standards; and autosampler vials, caps, and seals. 196 pp. Chemical Research Supplies 428

Chemicals. Catalog includes research chemicals, high-purity acids, distilled-in-glass solvents, and desiccants. Tables of oxidation-reduction indicators and colorimetric reagents for iron and copper are included. 474 pp. GFS Chemicals 429

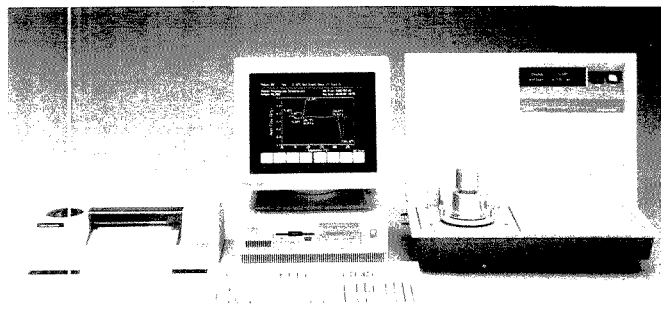
Reagents/chromatography. Catalog includes laboratory reagents; high-purity acids and solvents; columns and packings for HPLC; and products for solid-phase extraction, biochromatography, and chiral chromatography. J. T. Baker 432

Life sciences. Catalog features products for molecular biology, immunology, protein synthesis, electrophoresis, biomedical research assays, and autoradiography. Amersham 430

ICP. Catalog describes sample introduction accessories, software, and training and support services for ICP spectrometry. Also included are single-

element and multielement standards. 20 pp. Leeman Labs 433

Chromatography. Catalog lists products for biochromatography, column chromatography, GC, HPLC, and TLC. Included are columns, pumps, detectors, autosampler supplies, fraction collectors, glassware, and syringes. 256 pp. Fisher Scientific 434



DSC 2910 differential scanning calorimeter features electronic controls, five-point temperature calibration, programmed heating and cooling from 0.01 to 200 °C/min, step heating and cooling, and isothermal operation. Du Pont 402

The National Institute of Standards and Technology has developed a series of SRM's to serve as calibrants, test mixtures, and standardization materials for Quality Control of analytical instrumentation and methodology.

MEASUREMENTS and STANDARDS are important to everyone who needs quality. NIST has over 1,000 Standard Reference Materials that can help you calibrate instruments and check on measurement accuracy. For more information phone or write for a free catalog.

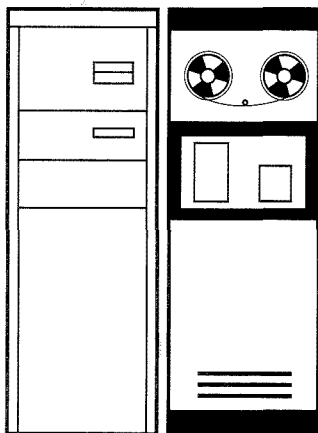
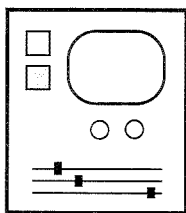
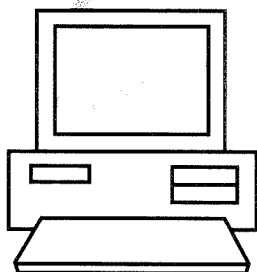
**Telephone (301) 975-0SRM (6776)
FAX (301) 948-3730**

STANDARD REFERENCE MATERIAL PROGRAM

**Building 202, Room 204
National Institute of Standards and Technology
Gaithersburg, MD. 20899**

CIRCLE 94 ON READER SERVICE CARD

Local Area Networks in the Laboratory



Steven A. Warner

Andrulis Research Corporation
4600 East-West Highway, Suite 901
Bethesda, MD 20814

Local area networks (LANs) are becoming more and more common in the laboratory. In the first of a two-part series, Steve Warner explains what a LAN is and how data are communicated between the various components. The second part of the series, to be published in the March 15 issue, will describe how to set up a LAN in the laboratory and how various vendor solutions have been used for specific laboratory needs.

What is a local area network? There are several cumbersome and technical definitions that can create confusion for the novice (and the expert!). A LAN can best be described as a data communications (hardware and software) system that connects a collection of host computers and client computers, terminals, or peripheral devices (e.g., printers or instruments) over a "local area." What is a local area? It can range from a single room to an entire city.

LANs enable isolated computer systems to share data at high speeds without physically transporting magnetic storage media. Instruments may pass data to host computer systems via a LAN for further analysis and for collation with other information into management reports. LANs also support the effective use of shared applications (databases and electronic mail) and resources (time-sharing computer systems and expensive printers).

A wide area network (WAN) on the other hand, supplies similar connectivity, but over a "wide area." WANs use a different blend of hardware and soft-

ware technologies, typically with lower transmission speeds. As LAN technologies have improved, it has actually become possible for a LAN to be larger than a very small WAN. To add further confusion, many large organizations connect geographically distant LANs through a WAN, creating an "enterprise-wide network."

Data communications

Data communications is the transmission of data between two sources through a medium (copper cable, fiber optics, air, outer space, etc.) according to a protocol. Data within a computer are represented by electromagnetic patterns arranged in space or time (Figure 1). The basic building block of these patterns is a bit. Electrically, a bit is either off (no or low voltage) or on (high voltage). We abstractly view bits that are off as a "0" and bits that are on as a "1." A group of eight bits is called a byte, which is the most common higher level arrangement of bits used for encoding data. Bytes can be viewed as electrical patterns, bit patterns (0's and 1's—their binary representation), or hexadecimal (base 16—0...9, A...F) representation.

All data that a computer works with are based on some convention of encoding something that is meaningful to hu-

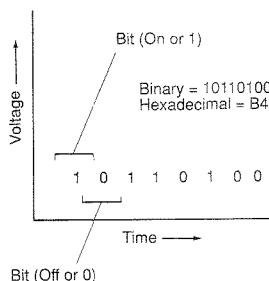


Figure 1. Electrical representation of a byte (8 bits) in time.

A/C INTERFACE

mans (such as text, images, or numbers) into something that is meaningful to the machine (bits and bytes). Examples of encoding conventions include the American Standard Code for Information Interchange (ASCII), binary-coded decimal numbers, and floating-point numbers. Figure 2a shows the bits that make up the letter "H" in ASCII code. This H will be used in examples that follow as user data.

The user data must be encapsulated before they can be transferred. Encapsulation involves the addition of control elements such as file structure, formatting, and error-checking information. Figure 2b shows the data that are added to the letter H when it is put into a Wordstar word processor file. Figure 2c shows the formatting information added to the contents of our Wordstar file after we underline the letter H.

Layered communications protocol standards

Communications protocols define how data are reliably transferred from a transmitter to a receiver, including where and when the data should be sent and how to verify whether errors in data transmission have occurred. The International Standards Organization Open Systems Interconnect (ISO-OSI) Model, shown in the box, standardizes how these protocols may be mixed and matched. Older LANs that predate the establishment of this or other standards may still be understood in ISO-OSI terms.

The ISO-OSI model defines seven layers (a stack) of protocols between the end-user and the physical network cable. The upper three layers correspond to a computer's programs and operating system with network-aware extensions. The transport and network layers provide communications management and addressing, whereas the

lowest layers define the network cable and hardware along with the software that manages the hardware.

The ISO-OSI model enables a hardware or software developer to depend on standard interfaces between network functions. The user or network designer is thus assured of being able to mix and match components from different vendors. It is important to realize that each of the upper six layers of the model can add control data to our data in a manner analogous to that shown in Figures 2b and 2c.

Physical layer features

A variety of physical layer interfaces are found in networks. There are many standards such as RS 232-C that describe these interfaces.

LANs typically use copper cable, either coaxial (a single central conductor surrounded by a braided shield) or twisted pair (one or more pairs of conductors that are twisted around each other), as transmission media. Glass

Layer	Function
Application	Supplies screen and menu service to the user (programs)
Presentation	Converts data format (operating system with network-aware extensions)
Session	Coordinates dialogue and controls access between user applications and network services
Transport	Controls selection of network service quality
Network	Controls routing and flow
Data link	Provides error detection and correction and access control to the physical layer
Physical	Connects electrical devices

and plastic fiber-optic cables are becoming more common in LAN systems as their cost and fragility decrease.

A LAN either has its own cable or shares cable with other communications systems (voice, video, or other LANs). Cable may be assembled in a variety of "topologies," the characteristic physical structure for a particular

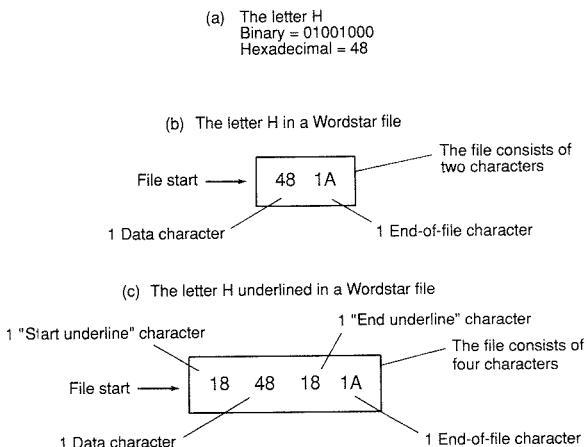


Figure 2. Structure of data in simple files.

network. Figure 3 shows some of the more common cable schemes.

Data link layer features

A second standards scheme has also emerged. The Institute of Electrical and Electronic Engineers (IEEE) has established the IEEE 802 LAN Standards Committees, four of which are relevant to this discussion: 802.2 (Logical Link Control), 802.3 (CSMA/CD), 802.4 (Token Bus), and 802.5 (Token Ring).

These 802 standards deal with different approaches to implementation of the data link layer of the ISO-OSI model. The IEEE committees split the data link layer into an upper logical link control (LLC) layer and a lower media access control (MAC) layer. The LLC layer establishes the link between two devices that wish to exchange data. The MAC layer controls access to the network cable; it determines when data can be sent. The two most common MAC layer protocols are CSMA/CD (carrier sense multiple access with collision detection) and token ring.

CSMA/CD and 802.3. CSMA/CD was first used in a networking scheme called Ethernet, which predates the IEEE 802 committees. The 802.3 committee later adopted and modified

CSMA/CD to develop the IEEE 802.3 specification. The 802.3 networks are *not* Ethernets, although the terms are frequently (and incorrectly) used interchangeably.

CSMA/CD is best explained through an analogy. Imagine that you are in a room full of people. You wish to speak to someone in the group. Before speaking, you wait for a moment of silence (carrier sense). Of course, anyone (or everyone) could be waiting for that same moment of silence to speak (multiple access). If you can speak more than a few words, then no one else will interrupt you until the room is silent again. However, if someone starts speaking at about the same time that you do, you will both become aware of this mutual interruption (collision detection). You both become silent. During this moment of silence, anyone could again begin to speak. The most common implementations of CSMA/CD are Ethernet and 802.3.

Token ring and 802.5. Token rings evolved from earlier token passing schemes developed in the 1970s, such as Datapoint Corporation's ARCNet. The most common implementation is the IBM Token Ring Network.

Let us go back to our room full of people to see how a token ring operates.

Sit everyone in a circle and assume that you can only communicate by passing a written message. Circulate a single piece of paper and pen. If you have nothing to say, pass the paper on. If you wish to say something to someone, write it down and pass the paper on. Eventually, the message will traverse the circle and reach the individual for whom it was intended.

Network and higher layer features

A variety of standards exist for the network and higher protocol layers. A common group of standards called the Transmission Control Protocol/Internet Protocol (TCP/IP) suite is commonly used in both LANs and WANs within academia and the federal government. TCP/IP predates the ISO-OSI Model and corresponds approximately to its Network and Transport layers.

TCP/IP is both the name for a group of protocols and two of the protocols in the group. Other protocols that usually accompany it provide for file transfer (file transfer protocol, FTP), a standard terminal interface (Telnet), and transfer of electronic mail (simple mail transfer protocol, SMTP). These other protocols are usually implemented as programs with the same name.

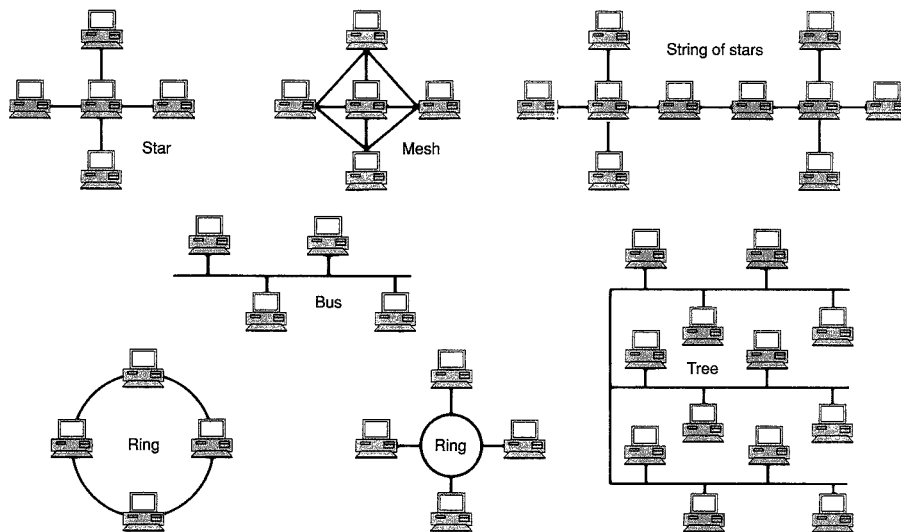


Figure 3. Common network cable schemes.

NEW

THE MERCK INDEX Eleventh Edition



Keeping pace with chemistry and biochemistry...
for over 100 years

Since 1889, *The Merck Index* has provided pertinent, authoritative information of interest to scientists the world over. Now we are pleased to present the newly published Eleventh/Centennial Edition. This special leather-bound edition provides expanded coverage of therapeutically important biotechnology products, agriculturals and compounds of environmental impact, and features an entirely new therapeutic category/bioactivity index as well as CAS Registry Number indices. And you'll find information on more than 10,000 significant drugs, chemicals, and natural substances.

To order, call toll-free 1-800-999-3633, extension 750 (VISA or MasterCard only) or complete the coupon.

NEW

THE
CENTENNIAL
EDITION



Merck & Co., Inc., a research-intensive company, publishes *The Merck Index* as a non-profit service to the scientific and medical communities.

CIRCLE 92 ON READER SERVICE CARD

Enclosed is my payment for \$35.00 for the Eleventh/Centennial Edition of THE MERCK INDEX. I will not be charged for shipping.

Check enclosed. Make check payable to Merck & Co., Inc. VISA MasterCard

Card No. _____ Exp. Date _____

Signature _____

Name _____

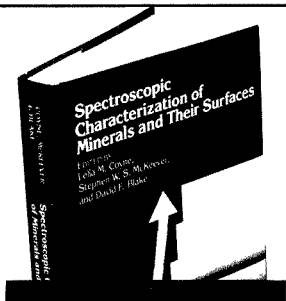
Address _____

City _____

State _____ Zip _____

Merck & Co., Inc.
Professional Handbooks
Department 750
P.O. Box 2000
Rahway, NJ 07065-0901

Please allow four to six weeks for delivery.



Spectroscopic Characterization of Minerals and Their Surfaces

Here is an overview of the powerful spectroscopic methods in use today for characterizing crystal structure, chemistry, morphology, and excited states of minerals. With a triple focus, this new summary of the latest techniques emphasizes:

- the structural and physical properties of minerals that have been associated with promotion of chemical reactions on their surfaces
- the fact that most naturally occurring minerals store electronic energy in quantities sufficient to significantly alter some of their properties, and
- the spectroscopic means by which biologically deposited minerals can be distinguished from geologically deposited ones

Twenty-three chapters describe a variety of new applications of mineral spectroscopy to determine composition, purity, interaction with energy, characterization of active centers, and adsorbate interactions. A discussion of nonoptical methods includes instruction on how to describe a mineral and its surface before studying it. Other chapters focus on energy storage within minerals. A section on active centers uses clays as a model, because in spite of its complexity, it is one of the most important classes of natural reactive minerals.

If you are a physicist, chemist, geologist, or fuel, soil, agricultural, and environmental scientist interested in interfacial chemistry of geological surfaces, this book will stimulate your thinking and inspire you to try these new characterization methods.

Lelia M. Coyne, *Editor*, San Jose State University

Stephen W.S. McKeever, *Editor*, Oklahoma State University

David F. Blake, *Editor*, NASA-Ames Research Center

Developed from a symposium sponsored by the Division of Geochemistry of the American Chemical Society

ACS Symposium Series No. 415

492 pages (1989) Clothbound

ISBN 0-8412-1716-5 LC 89-27755

\$94.95

O R D E R F R O M

American Chemical Society
Distribution Office, Dept. 56
1155 Sixteenth St., N.W.
Washington, DC 20036

or CALL TOLL FREE

800-227-5558

(in Washington, D.C. 872-4363) and use your credit card!

A/C INTERFACE

Understanding LAN component operation via the ISO-OSI Model

Figure 4 shows the LAN hardware of a simple peer-to-peer network consisting of two IBM-compatible microcomputers equipped with a fixed (hard) disk, an Excelan Ethernet network interface card with tee adapter in each microcomputer, a 1-m RG-58 coaxial cable segment connecting the tee adapters, and 50-ohm terminators on the open ends of the tee adapters. The network software consists of MS-DOS version 3.2 and Excelan TCP/IP network software on both microcomputers. This hardware and software together are referred to as a TCP/IP Ethernet.

Every network device (i.e., each microcomputer) has equivalent capabilities on this type of network. The transmitting system must package the data to be transmitted to the other network device and then transmit the data package; the receiving system must receive the data package, unpack the data, and verify its accuracy, requesting retransmission if errors were observed.

LAN protocols and standards define the rules by which these operations occur. Vendors that adhere to standards allow components to be mixed and matched as a LAN is designed and built.

The operation of this LAN can be

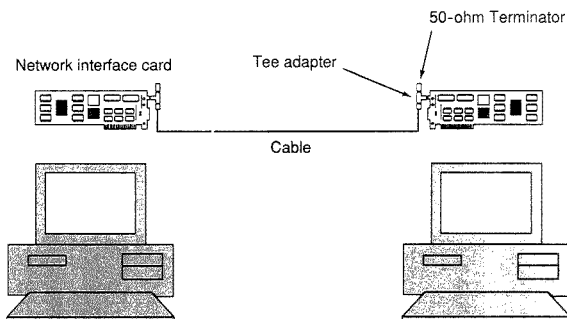


Figure 4. Typical LAN hardware.

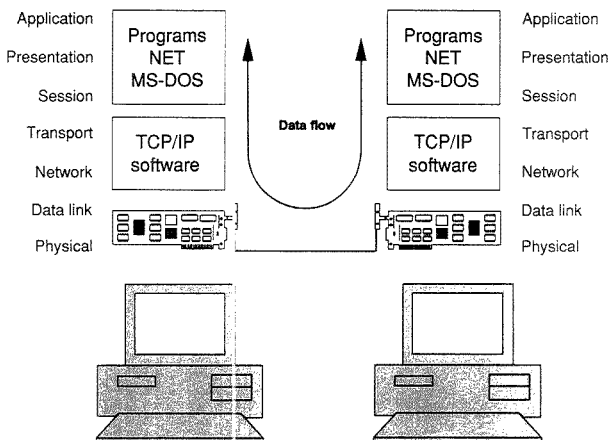


Figure 5. LAN components and the ISO-OSI model.

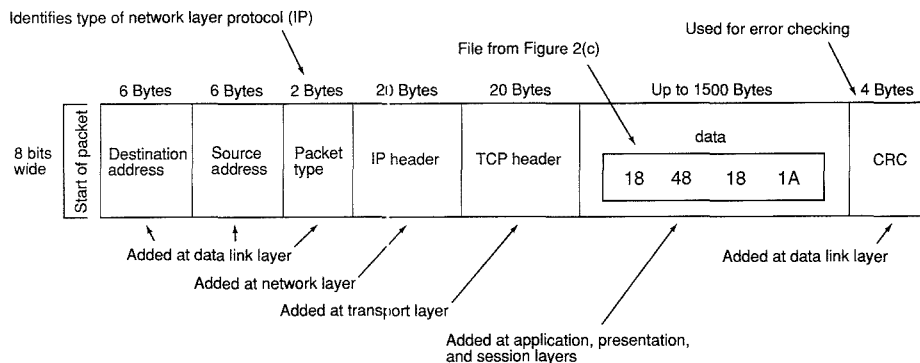


Figure 6. Anatomy of a TCP/IP-Ethernet data packet. "CRC" indicates cyclic redundancy check.

understood in terms of the ISO-OSI model, even though it is based on standards that predate it. To copy a Wordstar file (named FILE) from one microcomputer to the other across the LAN, the MS-DOS COPY command is used. But before the file can be COPYed, the TCP/IP network software, which establishes a connection at the transport and network layers between the two microcomputers, must be loaded on each microcomputer. The NET USE command on each computer is then used to access the other computer's fixed disk drive as drive D:. The NET program executes and then stays resident in memory, where it continuously scans for MS-DOS commands that must be redirected across the network. A connection between the two microcomputers at the presentation and session layers (Figure 5) is thus made. The user's computer now has a second disk drive, named D:, which can be accessed across the network while still accessible as C: from its own microcomputer. Each microcomputer can reciprocally access the other's fixed disk and perform other tasks; in other words, each can function as a nondedicated file server for the other.

Figure 6 shows the transmission of our file within a single TCP/IP-Ethernet data packet. This is a parallel transmission, because it is bit-wide and byte-long. The packet contains both user data and protocol information.

When the MS-DOS command (application layer) COPY FILE D: is executed, NET (presentation and session layers) redirects the contents of our file through the TCP/IP software (transport and network layers) to the network interface card (data link and

physical layers). The network interface card sends the file contents, now within a data packet, across the network cable (physical layer) to the other microcomputer's network interface card. The packet is then passed to the TCP/IP software and NET, where the communication protocol data characters are stripped from it. The file is now located on the remote microcomputer's hard disk.

Programs can also be stored on the D: hard disk (Figure 7). These programs, or programs on our local hard disk, may access data files on either the

remote or local hard disk. Large programs or files, however, do not load entirely in a computer's memory but are instead continuously swapped back and forth between the remote disk and the local microcomputer. This swapping across the network cable can have a profound effect on the performance of large LANs.

Programs such as FTP work the same way as the MS-DOS COPY command, but they also replace the NET program. In addition, they provide the capability to limit or deny user access to the remote hard disk. However, FTP

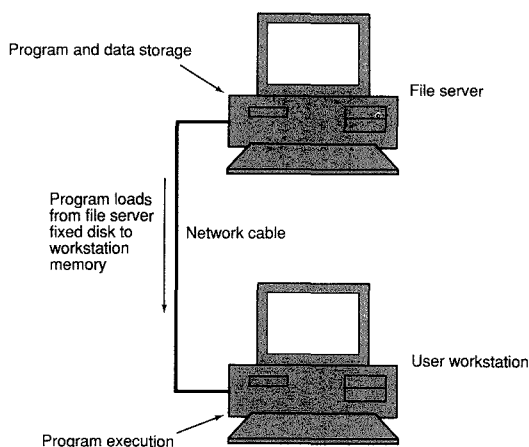


Figure 7. Execution of programs from network storage.

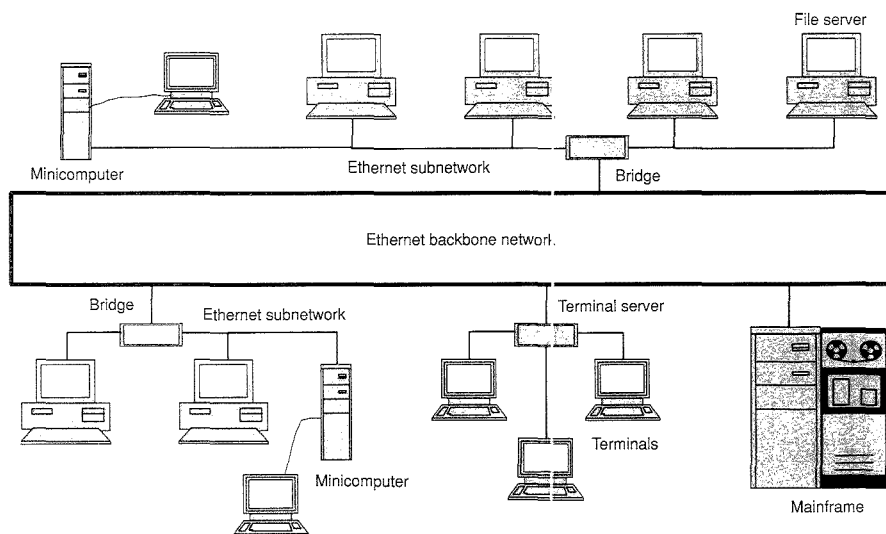


Figure 8. Hybrid LAN.

may only be used for file transfer—program execution is not possible.

Dedicated file server-based networks. Dedicated file servers cannot function as user workstations; for example, word processing programs cannot be run on them. Because these file servers perform no other function, they frequently exhibit higher performance than do nondedicated file servers, but are otherwise identical to the example shown in Figure 4.

Bridges, routers, and access servers. No LAN should be an island. What do we do when our LANs become very large? What if we need to connect two very different types of LANs? What if we want to connect two LANs that are miles apart? In these cases, we need some additional hardware. We can use repeaters, bridges, routers, and access servers to tie all the pieces together. A hybrid network that uses bridges to tie multiple subnetwork segments together is shown in Figure 8.

A repeater is a signal booster (a physical layer device) that is positioned between two cable segments. It retransmits at a greater strength anything that it receives. It may also connect two different types of cable. Repeaters can be used for LANs that are geographically large but have relatively few workstations on them. If there are a large num-

ber of workstations, however, repeaters can cause more problems than they solve. For example, a CSMA/CD network with a large number of workstations will have a large number of collisions, and thus the valid traffic across the network will slow down.

Bridges are the solution to the traffic problems that can arise in large networks. They are MAC and physical layer devices that only look at addresses within the MAC layer (i.e., they do not look at higher layer protocols). Bridges can connect two LANs so that they appear as one, just as repeaters do. However, they keep traffic that is local to a particular LAN on that LAN only. All traffic stays within its own LAN unless a message is specifically directed to a particular member of the LAN. Bridges are powerful tools for the LAN designer. Dividing a LAN into two segments connected by a bridge is an inexpensive means of increasing network performance. In addition, because bridges permit the network administrator to keep certain workstations from accessing devices on the other side of the bridge, they offer a measure of network security.

Routers are network layer devices, and any networks that they connect must use the same network layer protocols (or different network layer proto-

cols that are otherwise translated by a particular vendor's router). Routers use the addresses that exist within the network layer and are independent of the other layers. Routers are used to connect multiple cable segments into large LANs. Like bridges, routers perform traffic management functions. They also manage the path by which data can move; this path management capability enables a network administrator to balance the loads moving across multiple paths.

Routers offer more value than bridges. However, they are usually slower than bridges and are also more expensive. The selection of one or the other in a network design is a function of the specific organization's requirements and projected traffic flow. A variety of hybrid bridge-routers are also becoming available; no two are alike (a potential headache for the network designer).

Access servers are a catchall for anything that is not a router or a bridge. A terminal server enables one or more nonintelligent terminals to connect with the LAN to access minicomputer or mainframe computer hosts. Nonintelligent terminals are designed to use data that are serially transmitted one bit at a time through an RS 232 connection. The terminal server usually has a



High-quality software programs for the personal computer that meet the standards you expect from the ACS

For information about ACS SOFTWARE, call TOLL FREE (800) 227-5558 or write to:

American Chemical Society,
Marketing Communications Dept.,
1155 Sixteenth Street, N.W.,
Washington, D.C. 20036

**There are
224 reasons why...**

*most chemists
in the U.S. belong to the
American Chemical Society.*

The fact is, there are more than 137,000 chemists in this vital, career-enhancing society — *the largest scientific organization in the world dedicated to chemistry-related sciences!*

To learn those reasons, CALL TOLL FREE 1-800-ACS-5558 or mail this card to:

American Chemical Society, Membership Division
1155 Sixteenth St., NW, Washington, DC 20036

Yes!

I would like to know 224 reasons to join the American Chemical Society. Please send free brochures to:

Name _____

Address _____

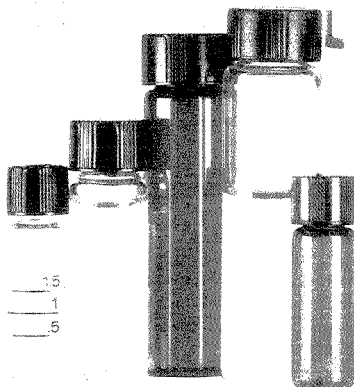
City, State, ZIP _____

SPECIFY WHEATON-33TM SAMPLE VIALS

...for Safekeeping

- Wheaton-33 low extractable borosilicate glass is the best protection you can provide for sensitive samples
- Wheaton-33 low extractable borosilicate glass maintains sample purity and pH
- Wheaton-33 low extractable borosilicate glass can be heat sterilized and stored at low temperature
- Wheaton-33 low extractable borosilicate glass is manufactured exclusively by Wheaton

Not all sample vials are alike. Not all sample vials provide the protection required to maintain the integrity of your valuable samples. Only Wheaton-33 sample vials are manufactured from Wheaton-33 low extractable borosilicate glass — the best protection you can provide for sensitive samples.



WHEATON

1501 North Tenth Street
Millville, NJ 08332 USA

Call Toll-Free: 1-800-225-1437, Ext. 2768

TLX: 55-1295 (WHEATON US)

FAX: 1-609-825-1368

CIRCLE 150 ON READER SERVICE CARD

single network connection and multiple RS-232 connections, which are used to interface with the terminals. Microcomputers may also access a minicomputer or mainframe computer host through the LAN. This usually requires the use of terminal emulation software that is network aware.

Modem pools are like terminal servers, but instead of terminals they have modems connected to them. They are accessible as a network device from any workstation. Gateways connect LANs with other LANs or WANs that use different protocols. For example, X.25 gateways are used to connect LANs with WANs such as Tymnet. A router that translates protocols is really a gateway.

Instrumentation and the LAN

A variety of instrument interfaces transmit either serial or parallel data. Serial data are transmitted through either an RS-232 connection or a current loop connection. Such data streams from an instrument can be captured through a connection to a microcomputer and then forwarded across a LAN connection. The instrument can

also be connected to a terminal server through an RS-232 connection.

A number of methods are available for parallel data capture, but all of them normally end up with the data stored on a microcomputer. A device, usually a microcomputer, will sit between the LAN and the instrumentation.

Where do we go from here?

We have defined a LAN and the industry standards. We have also seen that a LAN can be the door to a variety of automated resources. However, a LAN is nothing more than a tool like a typewriter, a telephone, or a gas chromatograph. How we use a LAN will determine how we find solutions that provide new capabilities within the laboratory. This will be the topic of the second article in this series.

Recommended reading

- Hancock, W. *Designing and Implementing Ethernet Networks*, 2nd ed.; QED Information Sciences: Wellesley, MA, 1988.
- Black, U. *Computer Networks: Protocols, Standards, and Interfaces*; Prentice-Hall: Englewood Cliffs, NJ, 1987.

The author wishes to thank Dave Pfeifer of Novell for technical information and review of the draft article.



Steven A. Warner is a senior engineer at Andrus Research Corp. He received a B.S. degree in biology/chemistry (1977) from Eckerd College (St. Petersburg, FL) and a Ph.D. in botany/biochemistry (1982) from the University of North Carolina at Chapel Hill. After two years of postdoctoral work, he began working exclusively in the data processing field, and now provides office and laboratory information systems planning, implementation, and support for various government agencies.

LABORATORY SERVICE CENTER

Acetylthiourea • 3-Aminophthalhydrazide • p-Anisic Acid • L-Arabinose
 p-Chloranil • 3,3'-Diaminobenzidine 4HCl • 1,2-Dibenzoyl ethylene
 2,6-Dichloroindophenol, Sodium • 2,2-Dichloropropane • Diethylformamic e
 Diiodomethane • p-Dimethoxybenzene • Dithione • Furfuryl Methyl Sulfide
 Furoic Acid & Methyl Ester • m-Hydroxybenzoic Acid • Janus Green B
 Levulinic Acid • 2-Methylcyclohexanol • Methyl Green • Neocuproine & HCl
 Oxamide • Sebacic Acid • Sodium Diethyldithiocarbamate • Suberic Acid
 L-Thyroxine, Na Salt • Toluidine Blue O • Tripalmitin • Vanillic Acid

Write for our Products List of over 3,000 chemicals

Tel: 516-273-0900 • TOLL FREE: 800-645-5566 Telefax: 516-273-0858 • Telex: 4974275

EASTERN CHEMICAL
 A Division of UNITED-GUARDIAN, INC.

P.O. Box 2500
 DEPT. AC
 SMITHTOWN, N.Y. 11787

Laboratory Service Center (Equipment, Materials, Services, Instruments for Leasing), Maximum space — 4 inches per advertisement. Column width, 2-3/16"; two column width, 4-9/16". Artwork accepted. No combination of directory rates with ROP advertising. Rates based on number of inches used within 12 months from first date of first insertion. Per inch: 1" — \$165; 12" — \$160; 24" — \$155; 36" — \$150; 48" — \$145.

CALL OR WRITE JANE GATENBY

ANALYTICAL CHEMISTRY
 500 Post Road East
 P.O. Box 231
 Westport, CT 06880
 203-226-7131/FAX: 203-454-9939

HELP WANTED ADS

ROP display at ROP rates. Rate based on number of insertions within contract year. Cannot be combined for frequency.

Unit	1-TI	6-TI	12-TI
1" (25 mm)	\$190	\$170	\$160
	24-TI	48-TI	72-TI
	\$150	\$140	\$130

CALL OR WRITE JANE GATENBY

ANALYTICAL CHEMISTRY

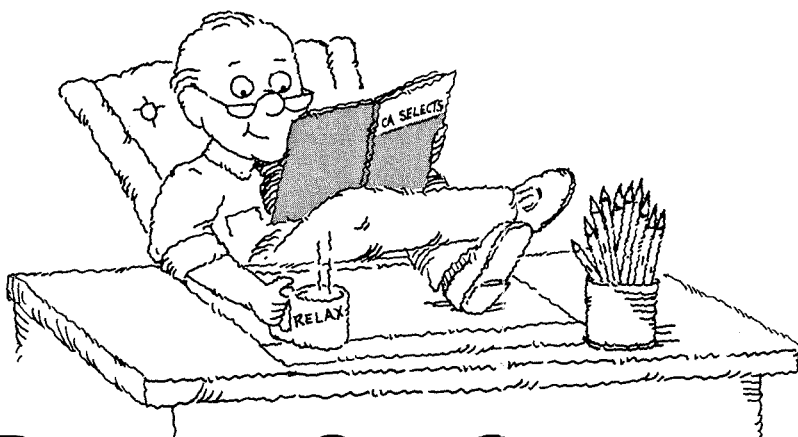
500 Post Road East
 P.O. Box 231
 Westport, CT 06880
 203-226-7131
 FAX: 203-454-9939

FREE DATA, FAST

To quickly amass data on all of the products you need, consult the Lab Data Service Section on our Analytical Chemistry reader reply card insert.

INDEX TO ADVERTISERS IN THIS ISSUE

CIRCLE INQUIRY NO.	ADVERTISERS	PAGE NO.	CIRCLE INQUIRY NO.	ADVERTISERS	PAGE NO.
1	Analytica 90 Kallman Associates	58A	144	*Varian Lanig Associates	60A
22	Cambridge Research & Instrumentation Inc.	87A	150	*Wheaton The Wheaton Agency	101A
24	*CDS Insituments Altman-Hall Associates	67A	152	John Wiley & Sons, Inc.	72A
30	*Dionex Corporation Rainoldi, Kerzner & Radcliffe	52A	<i>Directory section, see page 102A.</i> <i>* See ad in ACS Laboratory Guide.</i> <i>Advertising Management for the American Chemical Society Publications</i>		
28	Dohrmann Division/Rosemount Analytical Inc. Pan & Associates	88A	CENTCOM, LTD <i>President</i> James A. Byrne <i>Executive Vice President</i> Benjamin W. Jones Clay S. Holden, Vice President Robert L. Voepel, Vice President Joseph P. Stenza, Production Director 500 Post Road East P.O. Box 231 Westport, Connecticut 06880 (Area Code 203) 226-7131 Telex No.643310 FAX: 203-454-9939		
40	Finnigan MAT Corporation Lena Chow, Inc.	63A	ADVERTISING SALES MANAGER Bruce E. Poorman ADVERTISING PRODUCTION MANAGER Jane F. Gatenby		
52	Gelman Sciences	57A	SALES REPRESENTATIVES		
58	*Hewlett-Packard Company Brooks Communications	OBC	Philadelphia, PA ... Patricia O'Donnell, CENTCOM, LTD., GSB Building, Suite 405, 1 Belmont Avenue, Bala Cynwyd, Pa. 19004. Telephone: 215-667-9666, FAX: 215-667-9353 New York, NY ... John F. Raftery, CENTCOM, LTD., 60 East 42nd St., New York, N.Y. 10165. Telephone: 212-972-9660 Westport, CT ... Edward M. Black, CENTCOM, LTD., 500 Post Road East, P.O. Box 231, Westport, Ct. 06880. Telephone: 203-226-7131, Telex 643310, FAX: 203-454-9939 Cleveland, OH ... Bruce E. Poorman, John C. Guyot, CENTCOM, LTD., 325 Front St., Suite 2, Berea, Ohio 44017. Telephone: 216-234-1333, FAX: 216-234-3425 Chicago, IL ... Michael J. Pak, CENTCOM, LTD., 540 Frontage Rd., Northfield, Ill. 60093. Telephone: 708-441-6383, FAX: 708-441-6382 Houston, TX ... Michael J. Pak, CENTCOM, LTD. Telephone: 708-441-6383 San Francisco, CA ... Paul M. Butts, CENTCOM, LTD., Suite 1070, 2672 Bayshore Frontage Road, Mountain View, CA 94043. Telephone: 415-969-4604 Los Angeles, CA ... Clay S. Holden, CENTCOM, LTD., Newton Pacific Center, 3142 Pacific Coast Highway, Suite 200, Torrance, CA 90505. Telephone: 213-325-1903 Boston, MA ... Edward M. Black, CENTCOM, LTD. Telephone: 203-226-7131 Atlanta, GA ... John F. Raftery, CENTCOM, LTD. Telephone: 212-972-9660 Denver, CO ... Paul M. Butts, CENTCOM, LTD. Telephone: 415-969-4604 United Kingdom Reading, England ... Malcolm Thiele, Technomedia Ltd., Wood Cottage, Shurlock Row, Reading RG10 0QE, Berkshire, England. Telephone: 073-434-3302, Telex #848800, FAX: 073-434-3848 Lancashire, England ... Technomedia Ltd., c/o Meconomics Ltd., Meconomics House, 31 Old Street, Ashton Under Lyne, Lancashire, England. Telephone: 061-308-3025 Continental Europe ... Andre Jamar, International Communications, Inc., Rue Mallat 1, 4800 Verviers, Belgium. Telephone: (087) 22-53-85, FAX: (087) 23-03-29 Tokyo, Japan ... Sumio Oka, International Media Representatives Ltd., 2-29 Toranomon, 1-Chome Minato-ku Tokyo 105 Japan. Telephone: 502-0656, Telex #22633, FAX: 591-2530		
60	*Hitachi Instruments, Inc.	84A			
63-69	*Instruments SA, Inc./J-Y Division Kathy Wyatt & Associates	55A			
88	*Matheson Gas Products Kenyon Hoag Associates	59A			
92	Merck & Company, Inc. William Douglas McAdams, Inc.	97A			
90	*Metrohm, Ltd. Ecknauer + Schoch Werbeagentur ASW	64A			
94	*National Institute of Standards & Technology	93A			
96	*Nicolet Analytical Instruments	IFC			
125	*Nupro Company/A Swagelok Company Falls Advertising Company	91A			
115	The Pittsburgh Conference	77A			
137	*Thermo Jarrell Ash Corporation Noon, Inc.	51A			



RELAX AND STAY CURRENT WITH CHEMICAL LITERATURE

CA SELECTS is a series of current awareness publications that are produced from the Chemical Abstracts (CA) database. *You can relax*, knowing that a profile will be run every other week to search all relevant current literature covered by CA for your area of interest. From our computer to you, a review of chemical literature in just 10–12 pages (on the average).

All this for just \$170.00—\$6.54 an issue, about 5 cents per abstract! Find out if CA SELECTS covers your research interests by sending for your FREE copy of all 215 topic descriptions.

Mail coupon to:
Chemical Abstracts Service
Marketing Dept. 31390
2540 Olentangy River Road
P.O. Box 3012
Columbus, Ohio 43210, U.S.A.

Or call us at: (614) 447-3731;
or 1-800-848-6538 (ask for Customer Service).

CA SELECTS Catalog Coupon

.....
YES! Please send me the descriptions of all 215 topics.

Name _____

Job Title _____

Organization _____

Address _____

City _____

State/Zip _____

Country _____

Phone Number _____

Chemical Abstracts Service is a division of the American Chemical Society.

EDITOR: GEORGE H. MORRISON

ASSOCIATE EDITORS: Catherine C. Fenselau,
Georges Guiochon, Walter C. Herlihy, Robert
A. Osteryoung, Edward S. Yeung

Editorial Headquarters

1155 Sixteenth St., N.W.
Washington, DC 20036
Phone: 202-872-4570
Telefax: 202-872-6325

Managing Editor: Sharon G. Boots

Associate Editors: Louise Voress,
Mary Warner

Assistant Editors: Grace K. Lee,
Alan R. Newman

Editorial Assistant: Felicia Wach

Contributing Editor: Marcia Vogel

Director, Operational Support: C. Michael
Phillippe

Head, Production Department: Leroy L.
Corcoran

Art Director: Alan Kahan

Designers: Amy Meyer Phifer, Robert Sargent

Production Editor: Elizabeth E. Wood

Circulation: Claud Robinson

Editorial Assistant, LabGuide: Joanne Mullican

Journals Dept., Columbus, Ohio

Associate Head: Marianne Brogan

Journals Editing Manager: Joseph E. Yurvati

Associate Editor: Rodney L. Temos

Advisory Board: Bernard J. Bulkin, Michael S.
Epstein, Renaat Gijbels, William S. Hancock,
Thomas L. Isenhour, James W. Jorgenson,
Peter C. Jurs, Alan G. Marshall, Lawrence A.
Pachla, John F. Rabolt, Debra R. Rolison, Ralph
E. Sturgeon, Shigeru Terabe, George S. Wil-
son, Mary J. Wirth, Richard N. Zare
Ex Officio: Sam P. Perone

Instrumentation Advisory Panel: Daniel W.
Armstrong, Bruce Chase, Thomas L. Chester,
R. Graham Cooks, L. J. Cline Love, Sanford P.
Markey, Brenda R. Shaw, Gary W. Small, R.
Mark Wightman

Published by the
AMERICAN CHEMICAL SOCIETY
1155 16th Street, N.W.
Washington, DC 20036

Publications Division

Director: Robert H. Marks

Journals: Charles R. Bertsch

Special Publications: Randall E. Wedin

Manuscript requirements are published in the
January 1, 1990 issue, page 89. Manuscripts
for publication (4 copies) should be submitted
to ANALYTICAL CHEMISTRY at the ACS Washing-
ton address.

The American Chemical Society and its editors
assume no responsibility for the statements
and opinions advanced by contributors. Views
expressed in the editorials are those of the
editors and do not necessarily represent the
official position of the American Chemical
Society.

- Aggarwal, S. K., 111
Al-Saeed, A. S., 116
Arimoto, H., 107
Armstrong, D. W., 214
- Bartak, D. E., 151
Bean, M. F., 121
Blum, J. D., 209
Bosch, E., 102
Breyer, E. D., 130
Bushey, M. M., 161
- Calaway, W. F., 209
Cao, Z., 182
Cobb, W. T., 186
Cohen, A. S., 137
Cotter, R. J., 125
Czok, M., 189
- Dose, E. V., 174
Dulik, D. M., 121
- Fenselau, C., 121, 125
Fujii, T., 107
- Glick, M., 157
Golshan-Shirazi, S., 217
Gregoire, D. C., 141
Gruen, D. M., 209
Guiochon, G., 174, 189, 217
Guttman, A., 137
- Hansen, G., 125
Heiger, D. N., 137
Herold, D. A., 111
Hutcheon, I. D., 209
- Jimba, H., 107
Johnson, D. C., 220
Jorgenson, J. W., 161
- Karger, B. L., 137
- Kazee, B., 151
Khaledi, M. G., 130
Kinter, M., 111
Kost, K. M., 151
Kratochvil, B., 167
Kuwana, T., 151
- LaCourse, W. R., 220
Li, W., 214
Lin, S. M., 146
- Marshall, A. G., 201
McGown, L. B., 186
Mead, D. A., Jr., 220
Meier, J. E., 201
Murphy, C., 125
- Orlando, R., 125
- Pallante-Morell, S. L., 121
Pellin, M. J., 209
Pitha, J., 214
- Râfols, C., 102
Rodgers, A. H., 130
Rosés, M., 102
- Savory, J., 111
Shaw, R. C., 167
Shen, J., 116
Smith, B. W., 157
Stetter, J. R., 182
Strasters, J. K., 130
- Wasserburg, G. J., 209
Wightman, R. M., 98
Wills, M. R., 111
Winefordner, J. D., 157
Wipf, D. O., 98
- Yang, J. Y., 146
Yang, M. H., 146
Young, C. E., 209

Voltammetry with Microvoltammetric Electrodes in Resistive Solvents under Linear Diffusion Conditions

David O. Wipf and R. Mark Wightman*¹

Department of Chemistry, Indiana University, Bloomington, Indiana 47405

Cyclic voltammetry has been investigated with gold electrodes of 50- μm radius. These electrodes are advantageous for use under conditions of linear diffusion at moderate sweep rates in solvents with low dielectric constants. The solvents investigated include tetrahydrofuran, methylene chloride, 1,2-dimethoxyethane, and chlorobenzene, all containing 0.5 M tetraalkylammonium salts. The oxidation of ferrocene has been used to probe the amount of ohmic drop in these solutions at scan rates from 5 to 250 V s⁻¹. Modest ohmic drop is found in the voltammograms, but it is much less than previously reported at electrodes of conventional size. Cyclic voltammetry with these electrodes is well suited to characterize chemical reactions that accompany electron transfer. As an example, the rate constant for the cleavage of the radical anion of chloroanthracene has been examined in these four solvents and compared with results in more polar, aprotic solvents. The results show a strong correlation of the logarithm of the rate constant with the ability to solvate the anionic transition state, rather than with the dielectric constant of the solvent.

INTRODUCTION

Voltammetric electrodes with dimensions in the micrometer range provide electrochemical cells with submicrosecond time constants (1). This has enabled the use of cyclic voltammetry at scan rates exceeding 1 MV s⁻¹ at microdisks (2-9). Thus, the time scale of cyclic voltammetry extends over greater than 8 orders of magnitude when the use of microdisks is combined with that of electrodes of conventional size. This makes cyclic voltammetry a powerful technique for the investigation of heterogeneous electron-transfer rates and the investigation of chemical reactions associated with electron transfer. Electrodes of very small size are also advantageous, because they are less susceptible to the effects of ohmic drop than are electrodes of conventional size (1). Thus, they can be used in solvents that were previously intractable for voltammetric measurements.

At a small-radius electrode or at low scan rates, cyclic voltammograms can have a significant steady-state appearance as a result of mass transport by convergent diffusion. Such voltammograms have been used to measure heterogeneous electron-transfer rates (10-12); however, they are less useful for the measurement of chemical processes associated with electron transfer, because the product of the electrochemical reaction is rapidly transported away from the electrode (13). The diffusion process for a reversible system investigated by cyclic voltammetry can be predicted as a function of the dimensionless parameter, p , given by

$$p = [nfv(r^2v/D)]^{1/2}$$

where r is the disk radius, v is the scan rate, D is the diffusion

coefficient, n is the number of electrons transferred per mole, and $f = F/RT$ (14). At large values of p ($p > 17$), linear diffusion predominates, and conventional, peak-shaped voltammograms are obtained. To achieve linear diffusion conditions, we have restricted our lower scan rate for use with 5- μm -radius electrodes to 200 V s⁻¹ in aqueous solutions.

In this paper, we describe the use of microdisk electrodes of $\sim 50\text{-}\mu\text{m}$ radius. The larger size of these microelectrodes extends the lower limit of scan rates that can be employed with a predominance of linear diffusion and, thus, where chemical kinetics can be investigated. At the same time, a considerable advantage over electrodes of conventional size is obtained with respect to ohmic drop. Although the upper scan-rate limit is lower than with smaller electrodes, the limit is compatible with some commercial potentiostats. Thus, these electrodes are ideal for use at intermediate potential scan rates and for use in resistive solvents. This will be demonstrated by a study of the reduction of chloroanthracene in several solvents with low dielectric constants.

EXPERIMENTAL SECTION

Reagents. All solvents were of reagent grade and were used as received. Ferrocene (Johnson Matthey, Inc., Seabrook, NH) was purified by sublimation. Tetra-*n*-butylammonium perchlorate (TBAP) and tetra-*n*-hexylammonium perchlorate (THAP) (both from G. F. Smith Chemical Co., Columbus, OH) and 9-chloroanthracene (Alfa Products, Danvers, MA) were used as received.

Electrodes. Gold disk electrodes with nominal radii of 50 μm were constructed by sealing gold wire (Aesar, Seabrook, NH) into soft glass tubes and then polishing to expose a disk-shaped electrode. This method has been described for the construction of electrodes of smaller dimensions (1). Electrochemical and scanning electron micrographic measurements of the electrode area indicated an electrode area of $8.61 \times 10^{-6} \text{ cm}^2$. If the electrode is assumed to be a perfect disk, then a radius of 52 μm is obtained. This value was used for all calculations.

The gold wire and the soft glass appear by electron microscopy to have formed a good seal. The absence of large charging currents in cyclic voltammetry also indicates that a good electrode seal was obtained. In contrast, good seals for large gold disk electrodes in glass are difficult to obtain (15).

For experiments requiring a three-electrode configuration, a coil of platinum wire served as the auxiliary electrode while a silver wire was used as a quasi-reference electrode (16). For two-electrode configurations, a coil of silver wire served as a counter electrode.

Instrumentation. Some of the experiments described were performed on the BAS 100A electrochemical analyzer and low-current module on loan from Bioanalytical Systems, Inc. (West Lafayette, IN). Other experiments were done with the use of an EI-400 potentiostat (Ensmann Instrumentation, Bloomington, IN). Cyclic voltammetric data acquired with the BAS 100A was analyzed with the use of the built-in data analysis routines. Cyclic voltammograms generated with the EI-400 instrument were digitized with the use of a digital oscilloscope (Nicolet Model 320, Madison, WI) and were transferred to an IBM PC compatible computer for storage and analysis.

Electrochemical Procedures. Solutions for voltammetry contained 0.5 M TBAP or THAP supporting electrolyte plus depolarizer and were sparged with argon to remove dissolved oxygen. The electrochemical cell was a 25-mL vial. Electrodes were repolished briefly (~ 10 s) on an aqueous suspension of

* Author to whom correspondence should be addressed.

¹ Present address: Department of Chemistry, University of North Carolina, Chapel Hill, NC 27599-3290.

Table I. Electrochemical Data for Ferrocene Oxidation in Various Solvents

solvent/electrolyte	$D, \text{cm}^2 \text{s}^{-1}$	$R_s, \text{k}\Omega$	$\rho, \Omega \text{cm}$
1. DME/0.5 M TBAP	1.3×10^{-5}	27	570
2. THF/0.5 M TBAP	1.3×10^{-5}	30	630
3. CH_2Cl_2 /0.5 M TBAP	1.4×10^{-5}	10	210
4. Cl-benzene/0.5 M THAP	6.1×10^{-6}	145	3040

^a Determined with 3- or 5- μm -radii electrodes under steady-state conditions. ^b Determined at a 52- μm -radius electrode.

0.05- μm alumina after about every sixth cyclic voltammogram to prevent passivation of the electrode response by products of the electrode reaction. The electrodes were rinsed with methanol and pure solvent after polishing to prevent the introduction of water into the electrochemical cell.

Diffusion coefficients of ferrocene in different solvents were measured on the basis of the limiting current at gold-disk ultramicroelectrodes (3.0- and 5.0- μm radius) under steady-state conditions (1). Interference by chemical reactions that followed electron transfer prevented the measurement of the diffusion coefficient for 9-chloroanthracene by steady-state measurements. Instead, diffusion coefficients were estimated from peak-current ratios of ferrocene and chloroanthracene taken under linear diffusion conditions. All potentials are reported versus the ferrocene/ferrocinium couple. Measurements were made at room temperature.

Digital Simulations. Finite difference digital simulations for linear diffusion were after Feldberg and have been described (3). The simulations also provided for calculation of the effect of ohmic drop and cell time constant on the simulated cyclic voltammograms based on the electrode/solution resistance and double-layer capacitance. To determine the rate constant for the cleavage of the 9-chloroanthracene radical anion, the data was fit to an ECE-DISP1 mechanism (3). The simulation requires values for the formal reduction potential for 9-chloroanthracene and the anthryl radical, E°_1 and E°_2 ; the diffusion coefficient, D ; the heterogeneous rate parameters for the initial reduction step, k°_1 and α ; the disproportionation equilibrium constant, K_1 ; and the cleavage rate constant, k_1 . Also, the uncompensated solution resistance and double-layer capacitance must be known.

Values for E°_1 were obtained from the midpoint between the forward and reverse peaks under conditions of chemical reversibility, and D was estimated from the peak height. The equilibrium constant, K_1 , and E°_2 are related by

$$K_1 = \exp(nf(E^{\circ}_2 - E^{\circ}_1))$$

The value of E°_2 was set at 1.0 V positive of E°_1 ; its value does not greatly affect the simulation result (2). The heterogeneous kinetic parameters, k°_1 and α , were assumed to be the same as found for the reduction of chloroanthracene in CH_3CN , 3 $\text{cm}^2 \text{s}^{-1}$ and 0.5 (2). The double-layer capacitance was determined from the charging current magnitude at fast scan rates, and the resistance was obtained from the voltammograms of ferrocene. Thus, only the value of k_1 needed to be adjusted to fit the cyclic voltammograms. (Slight changes (<10%) were made from the initial estimates of $D^{1/2}$ to optimize the fit.) A visual comparison of the experimental and simulated data was used to determine a best fit to the data and, hence, the reported rate constant.

RESULTS AND DISCUSSION

Diffusional Behavior of Ferrocene at 52- μm -Radius Disk Electrode. The cyclic voltammetric response at the 52- μm -radius gold disk electrode was examined for compliance with the expected behavior of a change from steady-state to linear diffusion. The oxidation of ferrocene was chosen as a test system, because the couple is stable and has a large heterogeneous rate constant ($k^{\circ} = 3.1 \text{ cm}^2 \text{ s}^{-1}$ at a gold electrode in 0.6 M tetraethylammonium perchlorate/acetonitrile (4)). Cyclic voltammograms were obtained in the following solvents: 1,2-dimethoxyethane (DME), tetrahydrofuran (THF), methylene chloride, and chlorobenzene, all containing 0.5 M supporting electrolyte. Under steady-state conditions, the volt-

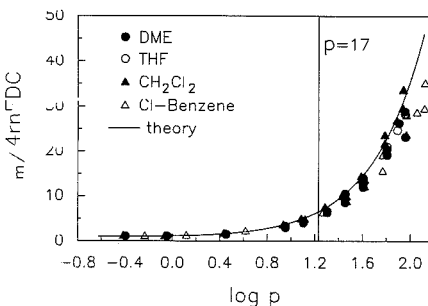


Figure 1. Normalized maximum current for the oxidation of ferrocene ($C = 1-2 \text{ mM}$) in solvents containing 0.5 M supporting electrolyte as a function of the dimensionless parameter, p . Voltammograms were obtained with a 52- μm -radius gold disk electrode. Scan rates were from 2 mV s^{-1} to 250 V s^{-1} .

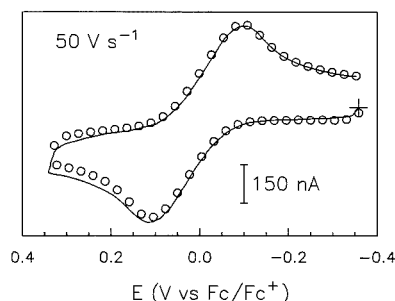


Figure 2. Cyclic voltammogram for the oxidation of 1.1 mM ferrocene in 0.5 M THAP/Cl-benzene solution at 52- μm -radius gold disk electrode at a scan rate of 50 V s^{-1} , showing (—) experimental data and (O) simulation for the following conditions: $D = 6.1 \times 10^{-6} \text{ cm}^2 \text{ s}^{-1}$; $R_s = 145 \text{ k}\Omega$; $C_d = 1 \text{ nF}$; $k^{\circ} = 3.1 \text{ cm}^2 \text{ s}^{-1}$; $\alpha = 0.5$; nominal concentration and electrode area.

ammograms obtained with 3- or 5- μm electrodes are not distorted by ohmic drop (16) and can be used to obtain the diffusion coefficient of ferrocene (Table I).

A summary of the voltammetric data at the 52- μm -radius electrode is given in Figure 1 for scan rates from 0.002 to 250 V s^{-1} . The maximum observed current for the oxidation wave, I_m , normalized by the current expected at totally steady-state conditions, $4\pi rFDc$, is shown as a function of the dimensionless parameter, p . Also shown in Figure 1 is the theoretical behavior for an electrochemically reversible system in the absence of ohmic drop or cell time constant effects (14). Reasonable agreement with theory exists, although deviations occur at large values of p because of these effects. This is especially notable for the chlorobenzene data.

Aoki et al. have shown that at p values of 0.6 or less the response of a reversible voltammogram will be within 10% of the steady-state value (14). For the conditions of this work, steady-state voltammograms will only be observed with a 52- μm -radius electrode at a scan rate of 0.005 V s^{-1} or less. The cyclic voltammetric response is predicted to be within 10% of the value for linear diffusion at p values of 17 and greater, which, in this work, corresponds to scan rates greater than 5 V s^{-1} . Therefore, 5 V s^{-1} is the lower limit for acquiring data that is to be analyzed assuming semiinfinite linear diffusion. Simulations of the entire voltammogram, accounting for ohmic drop and cell time constant, fit well to the experimental data (Figure 2), except in the most positive part of the scan where the background current behaves in a nonideal manner.

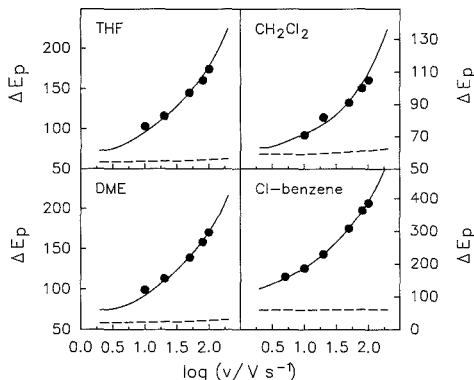


Figure 3. Plots of experimental and simulated peak separation for the oxidation of 2 mM ferrocene at 52- μm -radius gold disk electrode: (●) experimental data; (---) simulation for no ohmic drop; (—) simulation with ohmic drop. Resistance values are given in Table I.

Resistance Effects. The solvents examined all have a low dielectric constant value and are expected to have a large solution resistance and, thus, exhibit ohmic drop. The separation of the anodic and cathodic waves (Figure 2) at scan rates sufficient for linear diffusion to predominate is considerably greater than the maximum value expected for a compound with the rapid heterogeneous rate expected for ferrocene ($\Delta E_p \leq 62$ mV). If the electron-transfer kinetics were predominant, the separation of peak potentials would be independent of electrode size. In contrast to this prediction, the peak separation is less under linear diffusion conditions (at higher scan rates) at 6.5- μm -radius electrodes (16). Therefore, we attribute the increased peak separation to ohmic drop. Simulations of the voltammetric data accounting for ohmic drop (3) agree with the shift in anodic peak potential over a wide scan-rate range (Figure 3). The resistance values used for the simulations are summarized in Table I. From the resistance (R_s) values, a value for the specific resistance, ρ (Ω cm), can be estimated by

$$\rho = 4rR_s$$

which is valid for the case of an embedded disk electrode placed at infinite distance (i.e. $>10r$) from a counter electrode (1). The values of ρ obtained in this way are within 15% of those obtained by more traditional impedance measurements (17, 18). Part of the error may arise because exact temperature control was not used in these experiments. Nevertheless, the specific resistance in these solutions was up to 100 times greater than found in the more traditional electrochemical solvent, acetonitrile (4).

Thus, voltammograms in these solvents follow linear diffusion and are distorted to some degree by the solution impedance. The upper scan-rate limit for distortion-free cyclic voltammograms can be evaluated by consideration of two dimensionless parameters (19). The dimensionless ohmic drop, ρ' , is given by

$$\rho' = (nF)^{3/2}(Dv)^{1/2}R_s nFAc$$

where F is the Faraday constant, A is the electrode area, D is the diffusion coefficient, and c is the concentration. The dimensionless time constant, θ , is given by

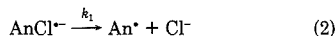
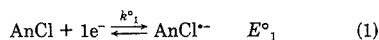
$$\theta = nFR_s C_d v$$

where C_d is the double-layer capacitance. If $\theta < 0.1$ and $\rho' < 1$, distortion will be minimal. For chlorobenzene, $\theta = 0.1$ at 17 V s^{-1} , whereas this condition is encountered at 85 V s^{-1}

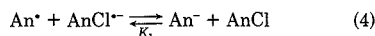
in tetrahydrofuran. Therefore, the effects of these sources of distortion must be included in the simulation of the majority of the voltammograms. It is important to note that the ohmic drop problem is considerably less than found with electrodes of conventional size. For example, ohmic drops of over 1 V have been reported at scan rates greater than 1 V s^{-1} in DME (20).

Decomposition of 9-Chloroanthracene Radical Anion. Most electrochemical reactions are not fully characterized with respect to solvent effects due to the distortion of voltammetric data in resistive solvents. The use of the 52- μm disk electrode should alleviate this restriction because faster rates of scan can be used to outrun chemical reactions that accompany electron transfer. To demonstrate this, the first-order cleavage rate constant for the 9-chloroanthracene radical anion has been determined in four highly resistive solutions—DME, THF, methylene chloride, and chlorobenzene.

The reduction of 9-chloroanthracene in polar aprotic solvents, CH_3CN and $(\text{CH}_3)_2\text{SO}_2$, has been previously described (2, 21). The cyclic voltammetric response at slow scan rates consists of an irreversible, two-electron wave that corresponds to the chloroanthracene reduction. A second, chemically reversible, one-electron wave follows at more negative potentials and corresponds to anthracene reduction (2, 21). At faster scan rates, the first wave changes to a one-electron, reversible process as the second wave disappears. The overall reduction process is adequately modeled as a mixed ECE-DISP1 mechanism where an initial one-electron process results in the formation of a radical anion (reaction 1) (21). The



anthryl radical is thought to have a much more positive reduction potential than the parent by analogy to other aromatic radicals (22) and will undergo further reduction either at the electrode surface (reaction 3) or by a homogeneous disproportionation reaction (reaction 4). Protonation of the an-



thracene anion results in anthracene. In addition to these reactions, hydrogen-atom abstraction by the anthryl radical from the solvent may occur. However, this possibility is indistinguishable by cyclic voltammetry from the scheme described here (23).

The reduction of 9-chloroanthracene in the four solvents has been examined by cyclic voltammetry at scan rates from 2 to 250 V s^{-1} . The voltammograms obtained are qualitatively similar to those reported in CH_3CN and $(\text{CH}_3)_2\text{SO}_2$. Results in each of the solvents are summarized below.

DME. Cyclic voltammograms for the reduction of 9-chloroanthracene at scan rates less than 6 V s^{-1} result in an irreversible wave followed by a reversible wave. At scan rates larger than 6 V s^{-1} , the first reduction wave exhibits a reverse wave which increases in size with increased scan rate. The growth of this wave occurs simultaneously with a decrease in the second reduction wave. The separation of the forward and reverse peak current for the first wave increases with increasing scan rate, indicating the presence of ohmic drop. Examples of the experimental voltammograms are given in Figure 4 along with simulations of the measured response.

THF. Cyclic voltammograms for the 9-chloroanthracene reduction are similar to those in DME with the exception that the reverse wave for the first reduction is seen at a slightly lower scan rate. The voltammetric data exhibited the most variability in this solvent. This was particularly true with

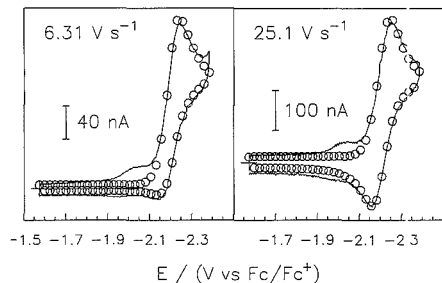


Figure 4. Reduction of 1.1 mM 9-chloroanthracene at a 52- μm -radius gold disk electrode in 0.5 M TBAP/DME at scan rates of 6.31 and 25.1 V s^{-1} : (—) experimental data; (O) simulation with ohmic drop for conditions in text and Table II. The prewave at -2.0 V was present in all voltammograms and was not accounted for in the simulation. It is likely an impurity.

Table II. Electrochemical Data for 9-Chloroanthracene Reduction in Various Solvents

solvent/ electrolyte	D , $\text{cm}^2 \text{s}^{-1}$	E°_1 , V ^c	E°_2 , V ^c	k_1 , s^{-1}	ΔN^d	A^e
1. DME/0.5 M TBAP	6.0×10^{-6}	-2.20	-2.42	50	10.2	0.21
2. THF/0.5 M TBAP	1.0×10^{-5}	-2.20	-2.42	40	8.0	0.17
3. CH_2Cl_2 /0.5 M TBAP	9.0×10^{-6}	-2.21	-	220	10.4	0.33
4. Cl-benzene 0.5 M THAP	4.0×10^{-6}	-2.25	-2.47	60	-	0.20
5. CH_3CN /0.6 M TEAP ^{a,g}	1.1×10^{-5}	-1.78 ^f	-2.00 ^f	200	18.9	0.37
6. $(\text{CH}_3)_2\text{SO}_2$ /0.1 M TEAP ^{b,g}	-	-1.67 ^f	-1.86 ^f	150	19.3	-

^a Reference 2. ^b Reference 21. ^c Volts versus Fc/Fc^+ . ^d Acceptor number, ref 25. ^e Anion solvating tendency, ref 24. ^f Volts versus SCE(aq). ^g TEAP is tetraethylammonium perchlorate.

respect to the measured peak height which may be a result of evaporation of the solvent during the measurement interval.

Methylene Chloride. Cyclic voltammograms in methylene chloride for the 9-chloroanthracene reduction show an irreversible voltammogram for all scan rates less than 25 V s^{-1} . A reverse wave appears for scan rates larger than 25 V s^{-1} . The second reduction wave cannot be observed due to the presence of large currents, presumably due to the solvent, at more negative potentials.

Chlorobenzene. Cyclic voltammograms for 9-chloroanthracene show a reverse wave at scan rates of 10 V s^{-1} and larger. The response is similar to that seen in DME except that ohmic drop effects are more evident.

Effect of Solvent on Rate Constant. The complete set of data are summarized in Table II. Shown in Figure 5 is a plot of the apparent number of electrons, n_{app} (i.e. the ratio of the experimental peak current divided by the peak current for a voltammogram in the absence of chemical kinetics), versus the dimensionless chemical kinetic parameter, $\lambda = k_1/(unf)$. The experimental values of n_{app} show good agreement for the values of n_{app} calculated by the simulations, except in tetrahydrofuran. The simulated curve given in Figure 5 for this solvent comes from the set of cyclic voltammograms that gave the best fit with respect to the scan-rate dependence of the reverse wave.

The rate constants for 9-chloroanthracene show that the solvent can affect the cleavage rate by a factor of 5. Thus, a pronounced solvation effect is apparent for this first-order reaction which does not correlate with the dielectric constants

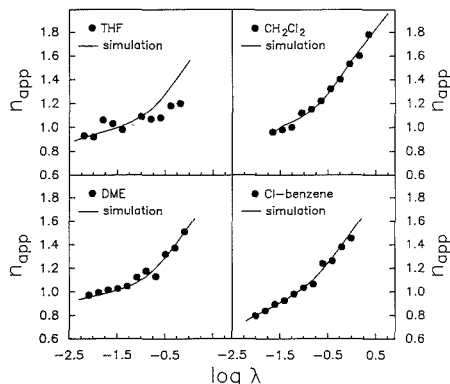


Figure 5. Plot for n_{app} versus $\log \lambda$ for the mixed ECE/ DISP1 kinetics model: (—) from simulation with conditions in text and Table II; (●) experimental data.

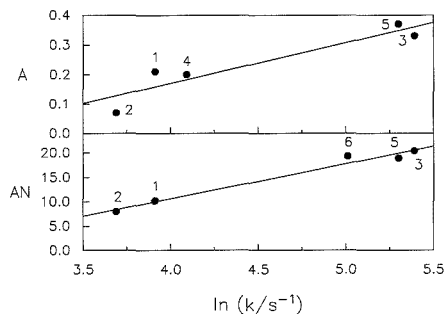


Figure 6. Plot of Gutmann's acceptor number (AN) and Swain's A parameter versus the natural logarithm of the experimental and literature rate constants (Table II) for the 9-chloroanthracene radical anion cleavage. The numbers refer to the solvents in Table II.

of the solvents. The transition state for the cleavage reaction involves a transfer of the negative charge of the chloroanthracene radical anion to the chlorine atom. The solvent can affect this by stabilizing the localized negative charge and lowering the energy of the transition state, resulting in more rapid cleavage. Therefore, the rate of cleavage should be related to the electrophilic properties of the solvents.

A useful solvent scale for anion solvating ability is Swain's A parameter (24). A plot of the experimental and literature values for the natural logarithm of the cleavage rate constant and A is linear with a correlation coefficient of 0.97 (Figure 6). The Gutmann acceptor number (AN) scale also has been shown to be an excellent predictor of anion solvating ability (25). A linear relationship has been shown to exist between the AN and free energies of solvation of the chloride ion. A similar plot of the cleavage rate constants and the AN values is linear with a correlation coefficient of 0.99 (Figure 6). These correlations support the hypothesis that a causal relationship exists between the anion solvating ability of the solvent and the cleavage rate constant.

CONCLUSIONS

Electrodes of intermediate size (50 μm) can be used to complement the electrochemical data collected at conventional and microdisk electrodes. Their small size, as compared to that of conventional electrodes, results in less ohmic drop and allows shorter time-scale measurements. Their large size, as compared to that of microdisk electrodes, makes them less susceptible to convergent diffusion effects and allows longer

time scales to be explored. In addition, these electrodes are easier to construct than either conventional or microdisk electrodes. Finally, the instrumentation required to generate and record voltammetric signals is commercially available. This is in contrast to electrochemistry at smaller electrodes at high speeds that require custom equipment and high-speed data recorders.

ACKNOWLEDGMENT

The loan of a potentiostat from Bioanalytical Systems is greatly appreciated.

LITERATURE CITED

- (1) Wightman, R. M.; Wipf, D. O. *Electroanalytical Chemistry*; Bard, A. J., Ed.; Dekker: New York, 1989; Vol. 15.
- (2) Wipf, D. O.; Wightman, R. M. *J. Phys. Chem.* **1989**, *93*, 4286-4291.
- (3) Wipf, D. O.; Wightman, R. M. *Anal. Chem.* **1988**, *60*, 2460-2464.
- (4) Wipf, D. O.; Kristensen, E. W.; Deakin, M. R.; Wightman, R. M. *Anal. Chem.* **1988**, *60*, 306-310.
- (5) Andrieux, C. P.; Hapiot, P.; Saveant, J.-M. *J. Phys. Chem.* **1988**, *92*, 5987-5992.
- (6) Wightman, R. M. *Science* **1988**, *240*, 415-420.
- (7) Andrieux, C. P.; Garreau, D.; Hapiot, P.; Pinson, J.; Saveant, J.-M. *J. Electroanal. Chem. Interfacial Electrochem.* **1988**, *243*, 321-335.
- (8) Amatore, C. A.; Jutand, A.; Pfluger, F. J. *J. Electroanal. Chem. Interfacial Electrochem.* **1987**, *218*, 361-365.
- (9) Fitch, A.; Evans, D. H. *J. Electroanal. Chem. Interfacial Electrochem.* **1986**, *202*, 89-92.
- (10) Oldham, K. B.; Zoski, C. G.; Bond, A. M.; Sweigart, D. A. *J. Electroanal. Chem. Interfacial Electrochem.* **1988**, *248*, 467-473.

- (11) Russell, A.; Repka, K.; Dibble, T.; Ghoroghchian, J.; Smith, J. J.; Fleischmann, M.; Pitt, C. H.; Pons, S. *Anal. Chem.* **1986**, *58*, 296-2964.
- (12) Fleischmann, M.; Lasserre, F.; Robinson, J. *J. Electroanal. Chem. Interfacial Electrochem.* **1984**, *177*, 115-127.
- (13) Wipf, D. O.; Michael, A. C.; Wightman, R. M. *J. Electroanal. Chem. Interfacial Electrochem.* **1989**, *269*, 15-25.
- (14) Aoki, K.; Akimato, K.; Tokuda, K.; Matsuda, H.; Osteryoung, J. J. *Electroanal. Chem. Interfacial Electrochem.* **1984**, *171*, 219-230.
- (15) Sawyer, D. T.; Roberts, J. L. *Experimental Electrochemistry for Chemists*; Wiley: New York, 1974.
- (16) Howall, J. O.; Wightman, R. M. *J. Phys. Chem.* **1984**, *88*, 3915-3918.
- (17) House, H. O.; Feng, E.; Peet, N. P. *J. Org. Chem.* **1971**, *36*, 2371-2375.
- (18) Kadish, K. M.; Ding, J. Q.; Malinski, T. *Anal. Chem.* **1984**, *56*, 1741-1744.
- (19) Imbiaux, J. C.; Saveant, J.-M. *J. Electroanal. Chem. Interfacial Electrochem.* **1970**, *28*, 325-338.
- (20) Vandjen Born, H. W.; Evans, D. H. *Anal. Chem.* **1974**, *46*, 643-646.
- (21) Andrieux, C. P.; Bloccman, C.; Durmas-Bouchiat, J. M.; M'Halla, F.; Saveant, J.-M. *J. Am. Chem. Soc.* **1980**, *102*, 3806-3813.
- (22) Juar, B.; Schwarz, J.; Breslow, R. *J. Am. Chem. Soc.* **1980**, *102*, 5741-5748.
- (23) Amatore, C.; Pinson, J.; Saveant, J.-M.; Thiebault, A. *J. Am. Chem. Soc.* **1982**, *104*, 817-826.
- (24) Swain, C. G.; Swain, M. S.; Powell, A. L.; Alunni, A. *J. Am. Chem. Soc.* **1983**, *105*, 502-513.
- (25) Gutmann, V. *Coord. Chem. Rev.* **1976**, *18*, 225-255.

RECEIVED for review May 1, 1989. Accepted October 23, 1989. This research was supported by the National Science Foundation (CHE-8808102).

Ionic Equilibria in Neutral Amphiprotic Solvents: Relationships between Electrolyte pK Values and Solvent Polarity and Composition for Several Binary Isopropyl Alcohol Mixtures

Elisabeth Bosch,* Clara Ràfols, and Martí Rosés

Departament de Química Analítica, Universitat de Barcelona, Barcelona, Spain

The progressive addition of cosolvent into any particular solution of an electrolyte causes a gradual change in the dissociation constant (pK) of the electrolyte. The changes in pK values of picric acid and tetrabutylammonium picrate in isopropyl alcohol-cosolvent mixtures have been related with the dielectric constant (ϵ) and the polarity of the mixed solvent, the latter measured by means of E_T^{30} Dimroth-Reichardt's parameter. Theoretical equations, which show linear relationships between these magnitudes and also with the solvent composition, have been developed and checked experimentally for solutions up to about 20% (v/v) of cosolvent. A variety of cosolvents of different polarity have been used.

In an earlier paper (1), the addition of different solvents to solutions of electrolytes in *tert*-butyl alcohol was studied. Theoretical equations to predict the dissociation constant of the electrolyte in the mixed medium were developed and experimentally tested. *tert*-Butyl and isopropyl alcohols are the neutral amphiprotic solvents most commonly used in nonaqueous titrations (2-9). Since the addition of a cosolvent can significantly change the properties of the reaction medium, we have studied the effect of this addition on the dissociation constants of picric acid and tetrabutylammonium picrate in

isopropyl alcohol medium. The dissociation constants have been determined for several solvent compositions (approximately up to an addition of 20% of cosolvent) and related with the composition by means of the theoretical equations previously derived (1). Also, theoretical equations that relate the dissociation constants with one of the most widely used polarity parameters for the characterization of solvents, the E_T^{30} parameter proposed by Dimroth and Reichardt (10), have been derived.

The E_T^{30} parameter has been measured for solvent mixtures and the experimental results agree with the developed equations which show that the pK value of an electrolyte can be correlated, in a simple way, with the composition and polarity of the mixed solvent.

THEORY

The dissociation constant of a substance in different solvents with similar acid-base character is related with the dielectric constant of the medium by means of the equation

$$pK = A + B/\epsilon \quad (1)$$

where A and B are constants. In fact, this equation applies only for changes in the polarity of solvents without specific solute-solvent interactions. If any solvent shows specific interactions with any species of the electrolyte (ion, ionic pair, or molecular form), eq 1 would not apply. However, if all solvents show similar specific solute-solvent interactions, the

change in pK values can be attributed mainly to the change in dielectric constant.

In a series of mixed binary solvents this is valid for a limited range of composition, where the specific solute-cosolvent interactions are negligible as compared with the specific solute-main solvent interactions. In this range the pK value of the electrolyte can be computed if the dielectric constant of the mixed medium is known.

Winkelmann and Quitzsch (11) have related the dielectric constant, ϵ , and the average internal refractive index, n , of the mixed media with the dielectric constant of the pure solvents, ϵ_i , and the volume fraction of each solvent component, v_i

$$\frac{(\epsilon - 1)(2\epsilon + n^2)}{\epsilon} = \sum v_i \frac{(\epsilon_i - 1)(2\epsilon_i + n^2)}{\epsilon_i} \quad (2)$$

In a previous work (1), it has been demonstrated that for binary mixtures with $n^2 \approx 2$ (a valid assumption in most solvents), eq 2 can be simplified to

$$\epsilon/\epsilon_1 = 1 + Cv_2 \quad (3)$$

or

$$\epsilon_1/\epsilon = 1 + Cv_2 \quad (4)$$

where

$$C = (\epsilon_2 - \epsilon_1 + 1/\epsilon_1 - 1/\epsilon_2)/\epsilon_1 \approx -C' \quad (5)$$

In these equations subscript 1 denotes the main solvent and subscript 2 the cosolvent.

With expression 1 in eq 3 or 4 the pK value of an electrolyte in a mixed medium can be related to the medium composition by the equations

$$1/(pK - A) = (1 + Cv_2)/D \quad (6)$$

or

$$pK = A + D(1 + Cv_2) \quad (7)$$

where

$$D = B/\epsilon_1 \quad (8)$$

Equation 7 is very useful, it shows that the variation in pK values can be directly related with the volume of cosolvent added. This was experimentally tested for mixtures of *tert*-butyl alcohol with water or alcoholic or aprotic solvents up to 15–20% (1).

In all the previous equations, it has been assumed that the change in dissociation pK values is caused only by the variation in ϵ . This assumption is not always valid, since in many cases there are specific interactions between the electrolytes and the cosolvent that are not considered in the computed ϵ value. These interactions can affect the dissociation constants to a different degree than the change in ϵ would, though the linearity with the addition of cosolvent may stay. So, it would be interesting to relate the pK values with an experimental measure of nonspecific solute-solvent interactions such as the polarity of the medium. Many substances have been suggested as indicators of the polarity of the medium. One of the most useful is 4-(2,4,6-triphenylpyridinium) 2,6-diphenylphenoxide, proposed by Dimroth and Reichardt (10). The shift in the maximum of the absorption of this compound is used to define the $E_T(30)$ polarity scale, and more than 270 pure solvents and many solvent mixtures have been characterized in this way (10). A normalized scale, $E_T^N(30)$, is at present strongly recommended, according to the expression

$$E_T^N(30) = (E_T(30) - 30.7)/32.4 \quad (9)$$

In general, the $E_T(30)$ values of binary solvent mixtures are not related with their composition in a simple way (10), but

for low concentrations of the more polar solvent Langhals showed that the $E_T(30)$ values of the mixtures increase linearly with the molar concentration of the more polar solvent (10, 12).

Since the $E_T(30)$ value of a solvent is related with the dipolarity-polarizability of the medium, and the latter with the dielectric constant, it seems possible to relate $E_T(30)$ values with ϵ and v_2 , through either eq 3 or 4.

For ten aprotic aliphatic solvents with nonspecific solute-solvent interactions, Bekárek and Jurina (13) have related $E_T(30)$ with the dielectric constant and the refractive index of the medium through the equation

$$E_T(30) = 29.83 + 81.99 \left[\frac{\epsilon - 1}{2\epsilon + 1} \right]^2 - 40.14 \frac{(\epsilon - 1)(n^2 - 1)}{(2\epsilon + 1)(2n^2 + 1)} \quad (10)$$

$$R = 0.994 \quad \text{SD} = 0.49$$

By use of the approximation $n^2 = 2$, eq 10 becomes

$$E_T(30) = 29.83 + 81.99 \left[\frac{\epsilon - 1}{2\epsilon + 1} \right]^2 - 8.03 \left[\frac{\epsilon - 1}{2\epsilon + 1} \right] \quad (11)$$

or

$$E_T(30) = 29.83 + \frac{65.93\epsilon^2 - 155.95\epsilon + 90.02}{4\epsilon^2 + 4\epsilon + 1} \quad (12)$$

Dividing the numerator by the denominator, we get the series

$$E_T(30) = 46.3125 - \frac{55.47}{\epsilon} + \frac{73.855}{\epsilon^2} - \frac{59.9875}{\epsilon^3} + \dots \quad (13)$$

If $\epsilon \geq 10$, eq 13 can be simplified to the following

$$E_T(30) = 46.3 - \frac{55.5}{\epsilon} \quad (14)$$

or

$$E_T^N(30) = 0.481 - \frac{1.71}{\epsilon} \quad (15)$$

with negative errors less than 2%.

These equations show that $E_T(30)$ values can be directly correlated with $1/\epsilon$.

Placing eq 4 in eq 15

$$E_T^N(30) = F - Gv_2 \quad (16)$$

where $F = 0.481 - 1.71/\epsilon_1$ and $G = 1.71C'/\epsilon_1$.

Equation 16 shows that the $E_T(30)$ value changes proportionally with the addition of cosolvent.

$E_T^N(30)$ values can be also related with pK values by putting eq 1 in eq 15

$$pK = H - IE_T^N(30) \quad (17)$$

where $H = A + 0.28B$ and $I = 0.58B$.

Since the purpose of this paper is the study of the effect of the medium polarity (measured by $E_T(30)$ values) on the dissociation constants of electrolytes in mixed solvents, it would be interesting to relate the change in pK values (ΔpK) with the change in $E_T^N(30)$ values ($\Delta E_T^N(30)$) when a cosolvent is added to a pure solvent. According to eq 17 this relation is

$$\Delta pK = -I\Delta E_T^N(30) \quad (18)$$

Equation 18 shows that the addition of a cosolvent causes a variation in the pK value of the electrolyte proportional to the variation of the $E_T(30)$ value.

In fact, eq 16 only works for solvents with refractive index values close to $2^{1/2}$, with a relatively high dielectric constant, and with nonspecific interactions with the solute only. The

Table I. Variation of pK of Picric Acid in Isopropyl Alcohol with the Addition of Cosolvents

volume fraction	equivalent concn	cosolvent									
		hexane		benzene		ethyl alcohol		methyl alcohol		water	
		Λ	pK	Λ	pK	Λ	pK	Λ	pK	Λ	pK
0	2.42×10^{-4}	14.83	4.20	14.83	4.20	14.83	4.20	14.79	4.20	14.83	4.20
2.00×10^{-3}	2.42×10^{-4}	14.86	4.20	14.91	4.19	15.03	4.18	15.03	4.18	15.49	4.15
3.98×10^{-3}	2.41×10^{-4}	14.81	4.20	14.89	4.20	15.10	4.18	15.14	4.18	16.60	4.07
7.94×10^{-3}	2.40×10^{-4}	14.75	4.21	14.79	4.21	15.16	4.18	15.37	4.16	17.83	3.98
1.96×10^{-2}	2.37×10^{-4}	14.50	4.23	14.54	4.23	15.43	4.16	15.89	4.13	19.81	3.85
3.85×10^{-2}	2.33×10^{-4}	14.14	4.27	14.10	4.27	15.81	4.14	16.80	4.07	22.05	3.71
5.66×10^{-2}	2.29×10^{-4}	13.75	4.31	13.62	4.32	16.21	4.12	17.65	4.01	24.00	3.58
9.09×10^{-2}	2.22×10^{-4}	13.09	4.38	12.73	4.41	17.00	4.08	19.45	3.90	27.41	3.34
1.67×10^{-1}	2.07×10^{-4}	11.21	4.58	10.41	4.65	18.79	3.98	24.00	3.62	35.50	-
C'_{exptl}		1.2		1.5		-0.7		-1.9		-15.1	-3.9
C'_{theoret}		0.9		0.9		-0.2		-0.6		-2.9	

Table II. Variation of pK of Tetrabutylammonium Picrate in Isopropyl Alcohol with the Addition of Cosolvents

volume fraction	equivalent concn	cosolvent									
		hexane		benzene		ethyl alcohol		methyl alcohol		water	
		Λ	pK	Λ	pK	Λ	pK	Λ	pK	Λ	pK
0	4.83×10^{-3}	12.18	2.70	12.11	2.70	12.11	2.70	12.11	2.70	12.11	2.70
2.00×10^{-3}	4.82×10^{-3}	12.18	2.69	12.16	2.70	12.20	2.69	12.26	2.69	12.32	2.68
3.98×10^{-3}	4.81×10^{-3}	12.18	2.69	12.18	2.69	12.26	2.69	12.39	2.67	12.53	2.66
7.94×10^{-3}	4.79×10^{-3}	12.19	2.70	12.21	2.69	12.38	2.67	12.63	2.65	12.92	2.61
1.96×10^{-2}	4.74×10^{-3}	12.19	2.70	12.25	2.69	12.67	2.65	13.33	2.58	13.87	2.51
3.85×10^{-2}	4.65×10^{-3}	12.19	2.70	12.32	2.69	13.11	2.60	14.49	2.44	15.27	2.34
5.66×10^{-2}	4.57×10^{-3}	12.14	2.72	12.33	2.69	13.56	2.56	15.63	2.30	16.20	2.22
9.09×10^{-2}	4.43×10^{-3}	12.05	2.74	12.28	2.71	14.42	2.46	17.76	1.91	17.42	2.06
1.67×10^{-1}	4.14×10^{-3}	11.43	2.84	11.70	2.81	16.37	2.21	22.88	-	18.83	1.87
C'_{exptl}		0.4		0.3		-1.5		-3.8		-4.7	
C'_{theoret}		0.9		0.9		-0.2		-0.6		-2.9	

latter condition is the most restrictive. When Bekárek and Jurina (13) extended eq 11 to 40 aprotic aliphatic solvents (some capable of specific solute-solvent interactions) they obtained

$$E_T(30) = 29.87 + 72.02 \left[\frac{\epsilon - 1}{2\epsilon + 1} \right]^2 - 29.16 \frac{(\epsilon - 1)(n^2 - 1)}{(2\epsilon + 1)(2n^2 + 1)} \quad (19)$$

$$R = 0.957 \quad \text{SD} = 1.332$$

This relationship leads to equations of the same kind as eq 11-18, but with different parameters, especially parameter I, which moves from 0.58B to 0.65B, while parameter H practically does not change ($H = A + 0.29B$).

So, the specific solute-solvent interactions preserve the linearity of the plots of $E_T^N(30)$ vs v_2 and ΔpK vs $\Delta E_T^N(30)$, but they have a strong influence on the slope of this last plot.

EXPERIMENTAL SECTION

Apparatus. A Radiometer CDM 83 conductometer and a Radiometer CDC 304 cell were used. The cell constant (1.003 cm^{-2}) was determined from the conductance of a 0.0100 M KCl at $25 \pm 0.2^\circ \text{C}$. A Beckman DU-7 spectrophotometer with 10-mm cells and an IBM-PC computer were used for acquisition and numerical treatment of absorbance data.

Chemicals. Substances. The following substances were used: picric acid, Doesder RA > 99.8% ACS (vacuum dried); tetrabutylammonium hydroxide 0.1 M in isopropyl alcohol, Carlo-Erba RPE, with a content of 8% of methyl alcohol determined by gas chromatography analysis; tetrabutylammonium picrate, prepared by neutralization of picric acid with tetrabutylammonium hydroxide solution; Dimroth-Reichardt's betaine dye, >95%, provided by Professor C. Reichardt.

Solvents. The following solvents were used: isopropyl alcohol, Merck GR > 99.7%, with a water content of 0.035%; ethyl alcohol, Merck GR > 99.8%, with a water content of 0.075%; methyl

alcohol, Merck GR > 99.5%, with a water content of 0.069%; hexane, Merck GR > 99.0%, with a water content lower than 0.02%; benzene, Merck GR > 99.7%, with a water content of 0.039%; tridistilled water. The water content in every solvent was determined by the Karl-Fischer method.

Procedure. In the conductivity measurements, the volumes 0.1, 0.2, 0.4, 1.0, 2.0, 3.0, 5.0, and 10.0 mL of each cosolvent were added to 50 mL of a 2×10^{-4} M solution of picric acid or a 5×10^{-3} M solution of tetrabutylammonium picrate in isopropyl alcohol. The conductivity of the solution was measured for each addition.

The equivalent conductivities (Λ) for each substance and cosolvent are presented in Tables I and II.

In the spectrophotometric measurements the amounts above mentioned of each cosolvent were added to 50 mL of a 10^{-4} M solution of the betaine dye in pure isopropyl alcohol. The solution was continuously circulated between the vessel and the spectrophotometer cell by means of a peristaltic pump. The spectrum of the solution was recorded for each addition from 450 to 710 nm at 0.5-nm intervals.

Special care was taken in the addition of benzene to avoid accidental inhalation of this toxic compound. All the measurements were taken in a closed vessel outwardly thermostated at $25 \pm 0.2^\circ \text{C}$ with a water flow.

Calculation of pK Values. The dissociation constant (K) of each electrolyte was computed for each addition of each cosolvent from the expression

$$K = c\alpha^2\gamma^2/(1 - \alpha) \quad (20)$$

where c is the analytical concentration and α the degree of dissociation computed from conductometric measurements by the method of Shedlovsky (14) according to the equations

$$\alpha = (z/2 + (1 + (z/2)^2)^{1/2})^2 \Lambda_0 \quad (21)$$

$$z = S(c\Lambda)^{1/2} / \Lambda_0^{3/2} \quad (22)$$

$$S = ((8.18 \times 10^5) \Lambda_0) / (\epsilon T)^{3/2} + 82 / \eta (\epsilon T)^{1/2} \quad (23)$$

Table III. Variation of $E_T(30)$ Values in Isopropyl Alcohol with the Addition of Cosolvent

volume fraction	hexane			benzene			ethyl alcohol			methyl alcohol			water		
	λ_{\max}	E_T	E_T^N	λ_{\max}	E_T	E_T^N	λ_{\max}	E_T	E_T^N	λ_{\max}	E_T	E_T^N	λ_{\max}	E_T	E_T^N
0	591.5	48.3	0.544	592.0	48.3	0.543	592.5	48.2	0.542	592.0	48.3	0.543	592.5	48.2	0.542
2.00×10^{-3}	591.5	48.3	0.544	592.0	48.3	0.543	592.0	48.3	0.543	592.0	48.3	0.543	591.0	48.4	0.545
3.98×10^{-3}	591.5	48.3	0.544	592.0	48.3	0.543	591.5	48.3	0.544	591.5	48.3	0.544	590.5	48.4	0.547
7.94×10^{-3}	592.0	48.3	0.543	592.5	48.2	0.542	591.5	48.3	0.544	590.5	48.4	0.547	589.5	48.5	0.549
1.96×10^{-2}	592.5	48.2	0.542	593.0	48.2	0.540	590.5	48.4	0.547	588.5	48.6	0.552	587.0	48.7	0.556
3.85×10^{-2}	593.0	48.2	0.541	594.5	48.1	0.537	589.5	48.5	0.549	585.5	48.8	0.560	582.0	49.1	0.568
5.66×10^{-2}	593.5	48.2	0.539	595.5	48.0	0.534	588.5	48.6	0.552	582.5	49.1	0.567	577.5	49.5	0.581
9.09×10^{-2}	594.5	48.1	0.537	597.5	47.8	0.529	586.5	48.7	0.557	577.0	49.5	0.582	571.0	50.1	0.598
1.67×10^{-1}	597.5	47.8	0.529	603.0	47.4	0.516	583.0	49.0	0.566	567.0	50.4	0.609	561.5	50.9	0.624
G_{exptl}	0.09			0.16			-0.14			-0.40			-0.61		

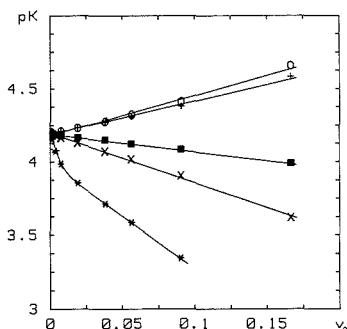


Figure 1. Variation of the dissociation constant of picric acid in isopropyl alcohol with the addition of cosolvents: +, hexane; O, benzene; ■, ethyl alcohol; X, methyl alcohol; *, water.

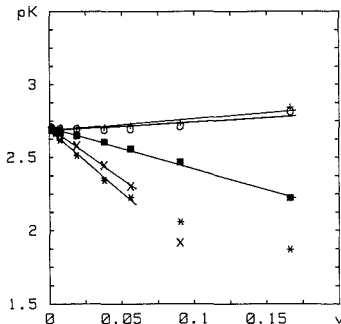


Figure 2. Variation of the dissociation constant of tetrabutylammonium picrate in isopropyl alcohol with the addition of cosolvent. Cosolvents are the same as given in Figure 1.

where $T = 298.16$ K and $\eta = 0.0213$ P (15).

The Debye-Hückel equation was used for computing activity coefficients, γ ($A = 4.00$ and $B = 6.02 \times 10^7$). " a " was computed from the limiting equivalent conductivity Λ_0 by means of the Stokes-Einstein relation. Λ_0 was calculated for solutions of pure isopropyl alcohol solvent ($\Lambda_0 = 36.1$ for picric acid and $\Lambda_0 = 23.5$ for tetrabutylammonium picrate) and it was assumed that Λ_0 did not change with the addition of other solvents. This assumption is generally reliable for not very large volumes of added solvents for which the developed equations are accurate. The dielectric constant of the medium, ϵ , was taken as 19.9 corresponding to pure isopropyl alcohol.

Calculation of $E_T(30)$ Values. The maximum of the betaine dye spectrum in each solvent mixture was obtained after numerical smooth of the absorbance data. A $E_T(30)$ value was calculated from each maximum λ value by using the equation (10)

$$E_T(\text{kcal/mol}) = h\nu N_A = (2.859 \times 10^{-8})/\lambda \text{ (cm)} \quad (24)$$

E_T^N was computed from eq 9. All these data are presented in Table III.

RESULTS AND DISCUSSION

The dissociation constant, pK values, of picric acid and tetrabutylammonium picrate in isopropyl alcohol solutions after addition of some cosolvents are presented in Tables I and II. Figures 1 and 2 show the plots of pK vs v_2 for the addition of some cosolvents (chosen among those most used for solving titrants) to solutions of picric acid and tetrabutylammonium picrate in isopropyl alcohol up to an addition of 15–20%. A straight line in all the studied range of v_2 is obtained except for the addition of solvents of high dielectric constant, such as methyl alcohol and water, to the solution of tetrabutylammonium picrate which are linear up to 5%. Similar lines are obtained when $1/(pK - A)$ is plotted vs v_2 .

The slopes of these plots are presented in Tables I and II, and they agree with the computed ones from eq 5 for aprotic

cosolvents such as hexane and benzene. The absolute values of the slopes obtained for the addition of alcohols and water are markedly higher than the theoretical ones, showing that these kinds of mixtures present higher dielectric constants than those predicted by the theory. This can be explained in terms of the formation of hydrogen bonds between the solvent and cosolvent, which increase the electric moment of the hydrogen bond donor group and, thus, the dielectric constant of the medium (1, 16). As in *tert*-butyl alcohol (1), the addition of water to the solution of picric acid shows a special behavior: the experimental points can be fitted into two straight lines, one for an addition up to 1%, with a very negative slope, and another for additions higher than 1%, with a less negative slope. The latter one is similar to the slope of the addition of water to the solution of tetrabutylammonium picrate.

In other words, the addition of small quantities of water causes a high decrease in the dissociation pK values of picric acid in isopropyl alcohol, as well as in the case of *tert*-butyl alcohol (1). According to Chantooni and Kolthoff (6) water acts as proton acceptor in *tert*-butyl alcohol favoring the dissociation of acids. The results in this medium have been explained in this way, and the same explanation can be applied to isopropyl alcohol medium. For higher additions of water, the proton is almost completely solvated. Further addition of water causes variation of pK values mainly due to the variation in dielectric constant. So, a second straight line is observed in Figure 1 with a slope similar to the one obtained for the addition of water to solutions of tetrabutylammonium picrate (Figure 2).

For all the studied cosolvents and electrolytes, the theoretical equations 6 and 7 apply for a higher linearity range in isopropyl than in *tert*-butyl alcohol because of its higher dielectric constant. This linearity range is in most cases about 15–20% of cosolvent, which is approximately the percentage

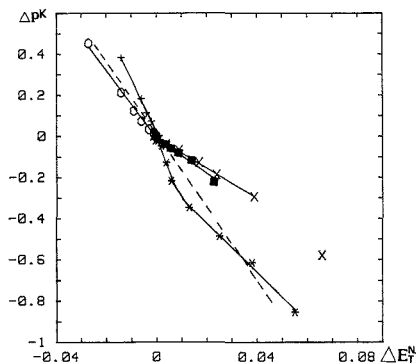


Figure 3. Variation of pK values of picric acid with the $E_T^N(30)$ values of isopropyl alcohol-cosolvent mixtures. Cosolvents are given in Figure 1. Slope of dashed line is according to eq 18.

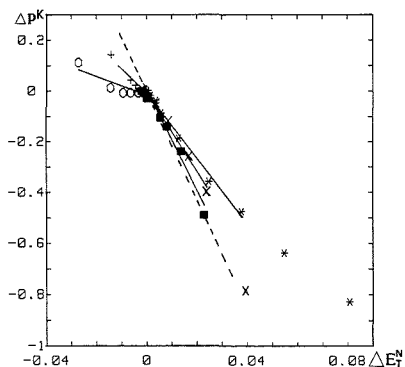


Figure 4. Variation of pK values of tetrabutylammonium picrate with the $E_T^N(30)$ values of isopropyl alcohol-cosolvent mixtures. Cosolvents are given in Figure 1. Slope of dashed line is according to eq 18.

of cosolvent added with the titrant in everyday nonaqueous titrations.

$E_T(30)$ and $E_T^N(30)$ values for the studied isopropyl alcohol-cosolvent mixtures are presented in Table III. $E_T^N(30)$ values change linearly with the addition of cosolvent up to 15–20%, except for the addition of the most polar cosolvent, i.e. water, which is only up to 10%. As expected, $E_T^N(30)$ values increase with the addition of ethyl alcohol, methyl alcohol, or water, which are more polar than isopropyl alcohol, and decrease with the addition of nonpolar cosolvents (hexane, benzene). The slope of the straight lines obtained is presented in Table III. The intercept of these lines is the experimental $E_T^N(30)$ value of pure isopropyl alcohol (0.543), which agrees with the literature values (10).

Figures 3 and 4 show the variation of pK values with the variation of E_T^N values for picric acid and tetrabutylammonium picrate. In these figures the theoretical line predicted by eq 18, computed from the B values previously reported (30.8 and 36.4 for picric acid and tetrabutylammonium picrate respectively) (1), has been also plotted. The theoretical I values are 17.9 for Figure 3 and 21.1 for Figure 4.

Since isopropyl alcohol is a protic solvent, eq 10–18 should not apply for its solutions, because of specific interactions solute-isopropyl alcohol. But, if the change in polarity predominates over the specific interactions, the linearity of the plot ΔpK vs $\Delta E_T^N(30)$ should be kept, as is demonstrated in

the last paragraph of the theoretical part (eq 19).

Since isopropyl alcohol is always the main solvent, the specific solute-isopropyl alcohol interactions predominate over the specific solute-cosolvent interactions in the whole range of composition. Thus, the change in $E_T(30)$ values can be attributed mainly to the change in dielectric constant, and a linear relation between pK and $E_T^N(30)$ is obtained, as Figures 3 and 4 show.

However, experimental deviations of the slope value in eq 18 are expected when the specific solute-cosolvent interactions are stronger than the specific solute-isopropyl alcohol interactions, though the linearity should remain for a certain range of composition.

So, the theoretical lines are expected to agree with the experimental ones for aprotic cosolvents like hexane and benzene. These cosolvents do not have or have very small specific interactions with the $E_T(30)$ indicator. This can be observed in Figure 3 for the addition of these cosolvents to the solution of picric acid but not in Figure 4 for the solution of tetrabutylammonium picrate. In fact, the pK values obtained for the addition of hexane or benzene are markedly lower than the expected ones from the change in polarity (theoretical line). This can be also observed in Figure 2 and Table II, where C' values for hexane and benzene are lower than the theoretical ones or than those obtained for picric acid. So, this decrease should be attributed to specific interactions of the tetrabutylammonium picrate with hexane and benzene. These interactions, which picric acid does not show, can be explained by preferential solvation of tetrabutylammonium cation in these cosolvents.

Cations of low charge density, such as Bu_4N^+ , tend to avoid protic solvents and prefer to be solvated by aprotic ones (17). Thus, the partial solvation of Bu_4N^+ by the cosolvent would decrease the concentration of cation solvated by the main solvent and therefore this would favor the dissociation of the salt. On the contrary, H^+ , cation of high charge density would be solvated by the main solvent, more basic than hexane or benzene, and the variation of pK can be attributed only to the variation in polarity. This same effect can be observed in the plots of pK vs v_2 in *tert*-butyl alcohol-hexane or benzene mixtures (1) but in less degree because hexane and benzene are more similar in properties to *tert*-butyl alcohol than to isopropyl alcohol.

In Figures 3 and 4 the theoretical lines agree quite well with the experimental ones of ethyl alcohol, methyl alcohol, and water in tetrabutylammonium picrate solution and ethyl alcohol and methyl alcohol in the picric acid solution. The high deviation of water in this last solution can be explained because of its large basicity toward H^+ , which favors the dissociation of the acid as has been explained. The small deviations seen with the other protic cosolvents can be attributed to specific interactions between the cosolvent and $E_T(30)$ indicator, which change the slope of the plot as has been explained in the theoretical section. As well as to polarity, $E_T(30)$ is sensitive to the acidity of the solvent, since its phenoxide oxygen can interact with hydrogen bond donor solvents lowering the ground state (10, 18). Because water ($\alpha = 1.09$) is more hydrogen bond donor than methyl alcohol ($\alpha = 0.60$) and this one more than ethyl alcohol ($\alpha = 0.54$) (10), the deviation is expected to be the highest for water and the lowest for ethyl alcohol, as Figures 3 and 4 show.

In summary, the pK values for binary mixtures of solvents show linear correlation with v_2 , $1/\epsilon$, and $E_T(30)$ parameters, which agree with the developed equations, and therefore provide a reasonable estimate of any parameter if others are known.

ACKNOWLEDGMENT

We thank Professor C. Reichardt of Philipps-Universität

Marburg for his helpful comments and for his kind providing of indicator betaine.

LITERATURE CITED

- (1) Bosch, E.; Rosés, M. *Anal. Chem.* **1988**, *60*, 2008-2013.
- (2) Fritz, J. S. *Acid-Base Titrations in Nonaqueous Solvents*; Allyn and Bacon: Boston, MA, 1973.
- (3) Fritz, J. S.; Marple, L. W. *Anal. Chem.* **1962**, *34*, 921-924.
- (4) Marple, L. W.; Fritz, S. J. *Anal. Chem.* **1963**, *35*, 1223-1227.
- (5) Marple, L. W.; Fritz, S. J. *Anal. Chem.* **1963**, *35*, 1431-1434.
- (6) Chantooni, M. K.; Kolthoff, I. M. *J. Phys. Chem.* **1978**, *82*, 994-1000.
- (7) Safarik, L.; Stransky, Z. In *Comprehensive Analytical Chemistry*; Elsevier: Amsterdam, 1986; Vol. XXII.
- (8) Kolthoff, I. M.; Chantooni, M. K. *Anal. Chem.* **1978**, *50*, 1440-1446.
- (9) Kolthoff, I. M.; Chantooni, M. K. *J. Phys. Chem.* **1979**, *83*, 468-474.
- (10) Reichardt, C. *Solvents and Solvent Effects in Organic Chemistry*, 2nd

- ed.; VCH Verlagsgesellschaft: Weinheim, 1988.
- (11) Winkelmann, J.; Quitzsch, K. *Phys. Chem. (Leipzig)* **1972**, *250*, 355-366.
 - (12) Langhals, H. *Angew. Chem., Int. Ed. Engl.* **1982**, *21*, 724-733.
 - (13) Bekárek, V.; Jurina, J. *Collect. Czech. Chem. Commun.* **1982**, *47*, 1060-1068.
 - (14) Fuoss, R.; Shedlovsky, T. *J. Am. Chem. Soc.* **1949**, *71*, 96-1498.
 - (15) *Handbook of Chemistry and Physics*, 59th ed.; CRC: Boca Raton, FL, 1979.
 - (16) Onsager, L. *J. Am. Chem. Soc.* **1936**, *58*, 1486-1493.
 - (17) Marcus, Y. *Ion Solvation*; J. Wiley: New York, 1985.
 - (18) Kamlet, M. J.; Abboud, J. L. M.; Abraham, M. H.; Taft, R. W. *J. Org. Chem.* **1983**, *48*, 2877-2887.

RECEIVED for review June 28, 1989. Accepted October 11, 1989.

Mass Spectrometric Studies on the Response Mechanism of Surface Ionization Detectors for Gas Chromatography

Toshihiro Fujii* and Hitoshi Jimba

National Institute for Environmental Studies, Tsukuba, Ibaraki 305, Japan

Hiromi Arimoto

Shimadzu Corporation, Nakagyo, Kyoto 604, Japan

Mass spectrometric techniques at atmospheric pressure are used to measure the ionic species generated when organic compounds from a gas chromatograph come into contact with a hot Pt emitter. The intensities and types of ions formed against surface temperature, gas environments around the emitter, and emitter material were investigated. In almost every sample studied, the observed ion species in the mass spectrum are the same as those obtained with SIOMS (surface ionization organic mass spectrometry in vacuum condition) with only the intensity distribution showing differences. The results confirm that positive surface ionization is the mechanism of the production of charge carriers in the surface ionization detector.

INTRODUCTION

In previous papers (1, 2), the surface ionization detector (SID) has been described for gas chromatography. The SID utilizes a platinum filament emitter which is heated electrically. The emitter is connected to the power supply and is positioned 2 mm above the nozzle of the carrier gas exit. The emitter is maintained at a positive potential with respect to the ion collector. This detector is extremely sensitive to organic compounds such as tri-*n*-butylamine which dissociates to species having low ionization potentials. It can be operated in any kind of carrier gas and the addition of air (oxygen) to the detector environment improves the performance.

Previous work indicated that the ionization mechanism involves positive ionization of organic species generated on the hot surface. The molecules being detected decompose on the hot surface into radicals which have lower ionization energy (IE) than the molecules and are ionized efficiently. The ion current of the secondary species (s) is dependent (3) on the surface temperature, T

$$j_s(T) = \frac{n Y_s(T)}{1 + (g_0/g_+) \exp[(IE - \varphi)/kT]}$$

where n is the number of molecules impinging on the surface, $Y_s(T)$ is the yield of chemical reactions on the surface, φ is the work function of the surface, and g_0/g_+ is the ratio of the statistical weights of the ions and neutral species. The total ion current is $J(T) = \sum j_s(T)$.

The positive surface ionization mechanism seems to be preferred so far. However, the exact identification of the charged species being formed in the SID has not been made. The produced ion should be identified, which directly reveals the response mechanism. In addition, the study furthers the understanding of the detector characteristics as well as improves its operation technique.

Atmospheric pressure ionization mass spectrometry (AP-IMS) is a novel type of mass spectrometry (4) in which ionization is carried out in a reaction chamber (at atmospheric pressure) external to the low-pressure region of a mass analyzer. Ions present in the source enter the mass analyzer region through a small aperture. By use of this technique, the details of various ion processes in atmospheric conditions have been determined by the direct mass spectrometric analysis with a 1 atm plasma.

In studies by Horning et al. (5) and by Grimsrud et al. (6) in APIMS ion source was modified to be an actual electron capture detector (ECD), complete with a cell electrode, so that the ECD function of this ion source could be obtained simultaneously with negative ion measurements. This combination not only provides an ideal means of studying electron capture reactions but also appears to constitute a promising technique in itself for the analysis of trace amounts of organic substances.

Because of the demonstrated success of APIMS for the sensitive measurement of ions formed within its ECD-like source, a similar approach was used for the mechanism study of SID. The instrument used is a specialized atmospheric pressure surface ionization mass spectrometer. Its ion source is an actual SID.

* To whom correspondence should be directed.

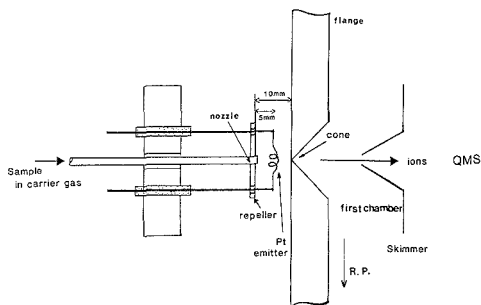


Figure 1. Experimental setup of APIMS(SID); a SID ion source attached to the front flange of the vacuum envelope of a mass spectrometer.

The authors began to explore the areas of application of the SID about 3 years ago by choosing various compounds. Recently the authors reported on several types of environmentally and biologically important compounds (7) to provide a broader understanding of the potential application of the SID in chemical analysis. Polyaromatic hydrocarbons, antidepressant compounds, and α -pinene were chosen for the present study, because the SID is clearly sensitive, being suitable for the qualitative and quantitative analysis of these compounds. Triethylamine (TEA), 1,3,5-cycloheptatriene, *N,N*-dimethylaniline, and piperidine were also used. These compounds were chosen because they were studied in detail by SIOMS (surface ionization organic mass spectrometry in vacuum conditions) (8, 9). The present reports include (1) the exact mass spectrometric identification of positive ions formed in the SID, (2) the effect of surface temperature, gas environments, and emitter material on the intensity and types of ions formed, and (3) the comparison of the SID ions with those obtained by SIOMS.

EXPERIMENTAL SECTION

The main instrument used for the mass spectrometric studies on the response mechanism of the SID, is the modification of the apparatus specifically prepared by the Shimadzu Corp. for an atmospheric pressure ionization mass spectrometry. This is essentially a combination of mass spectrometry and SID for gas chromatography, which is referred to as APIMS(SID) hereafter. With this instrument, the SID response can be monitored along with mass spectral measurement of the ions formed in the SID.

The atmospheric pressure ionization mass spectrometer for sampling the ions under atmospheric pressure has been described in detail elsewhere (10). Briefly, the components are a sampling interface, a three-stage differential vacuum system, an electrostatic ion lens system, and an ion detection system with the channeltron electron multiplier detector operated both in the pulse mode and in the analog mode.

A detailed view of the SID atmospheric pressure ion source is shown in Figure 1. The SID ion source is an open-type modification (without any envelope) of a standard SID for gas chromatography. Therefore, we assume that the pressure at which the ions are formed is nearly 1 atm. It is noted that a precise pressure measurement was not made because of experimental difficulty. The coiled Pt emitter is positioned at the midpoint between the stainless steel nozzle and entrance cone of the atmospheric pressure ionization mass spectrometer. The repeller electrode around the nozzle is made of a 30 mm diameter stainless steel disk which is 5 mm behind the emitter. All the SID ionic measurements reported were obtained by applying 300 V to both the repeller and the emitter.

The open-type SID ion source is fixed on the front flange of the vacuum envelope of the atmospheric pressure ionization mass spectrometer, where a 0.5 mm diameter orifice was drilled. This entrance cone, along with the skimmer (1 mm diameter), provides a controlled leak of the ion source contents into the vacuum region.

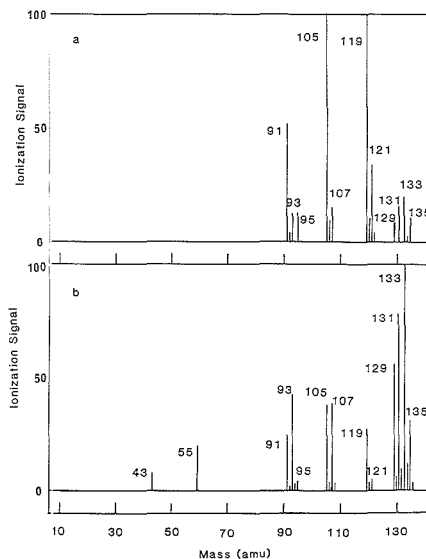


Figure 2. Mass spectra of α -pinene obtained with unit resolution where the ions are produced by either (a) surface ionization with the Pt emitter at atmospheric pressure, APIMS(SID), or (b) the Re oxide emitter surface ionization at vacuum condition, SIOMS. The relative abundance is reported. Peaks having less than 2% base peak intensity were omitted. APIMS(SID) is operated in the pulse mode of the multichannel scaling (ref 10), while SIOMS is operated in the analog mode. Note the difference in relative intensity of the mass spectrum.

It is observed that the 500 L/min first-stage rotary pump is loaded to give a first chamber pressure of 2.6 Torr (see Figure 1). Thus, the magnitude of the total gas flow into the mass spectrometer is calculated as 1700 mL/min, most of which would be the air stream from the atmosphere. The grounded flange in Figure 1 serves as the cathode to which a positively charged species will migrate.

Samples are introduced to the carrier gas stream via a temperature-controlled diffusion cell in which either a diffusion tube or a permeation tube is placed. A heated stainless steel transfer tube connects this cell with the nozzle.

The SIOMS was performed with a Finnigan 3300 gas chromatograph-quadrupole mass spectrometer equipped with a home-made thermionic ion source. The oxidized Re ribbon was prepared and used as a surface ionization emitter. The sample substances were admitted to the mass spectrometer from a reservoir via a variable leak valve or gas chromatograph. Full experimental details have been reported previously (11).

A Shimadzu gas chromatograph equipped with the SID (now commercially available) was used for the gas chromatography of the SID response, GC(SID).

All the test materials (10 compounds) were purchased from the Eeda Chemical, Tsukuba, and used without further purification.

RESULTS AND DISCUSSION

Mass Spectra. Numerous experiments were conducted for each of the 10 tested compounds listed in Table I along with the formulas, molecular weights, and ionization energies. Table I also includes the following experimental results: (1) the GC(SID) responses, expressed in terms of sensitivity (C/g), under the optimum conditions (1) for the detection limit; (2) the APIMS(SID) mass spectrum by the Pt emitter (composed of an intense peak) with the ion current (A) referenced to the sample amount of 1 g/s (determined from the height of the lines in the mass spectrum) for five volatile compounds, data taken at the optimum emitter temperature give the maximum total ion signal to each of the sample; (3) the SIOMS mass

Table I. Response Comparison of APIMS(SID), SIOMS in Vacuum Condition, and GC(SID)

compounds (<i>m/e</i> , IE)	GC(SID), C/g	APIMS(SID)		SIOMS	
		A _i /(g/s)	mass spectrum ^a (<i>m/z</i> , %)	A _i /Torr	mass spectrum ^a (<i>m/z</i> , %)
triethylamine (101, 7.50) C ₆ H ₁₅ N	1.6	1.2 × 10 ⁻³	86, 100 (M - H), 63.6	22.8	(M - H), 100 86, 10
<i>N,N</i> -dimethylaniline (121, ?) C ₈ H ₁₁ N	8.6 × 10 ⁻¹	1.1 × 10 ⁻³	(M - H), 100	17.9	(M - H), 100
piperidine (85, 8.7) C ₅ H ₁₁ N	3.3	3.3 × 10 ⁻³	(M - H), 100 (M - 3H), 11.9	45.8	(M - H), 100 (M - 3H), 16 (M - 5H), 14 (M - H), 100
1,3,5-cycloheptatriene (92, 8.28) C ₇ H ₈	2.6 × 10 ⁻²	6.4 × 10 ⁻⁴	(M - H), 100	3.3	(M - H), 100
α -pinene (136, 8.07) C ₁₀ H ₁₆	4.6 × 10 ⁻³	1.2 × 10 ⁻⁵	119, 100 105, 100 91, 51.4 121, 34.3 (M - 3H), 20.0 (M - 5H), 15.1 107, 15.1 95, 12 93, 12 (M - H), 11.1 120, 11 M, 100 (M + 1), 17.2	9 × 10 ⁻²	(M - 3H), 100 (M - 5H), 77.8 (M - 7H), 55.6 93, 42.2 107, 38.9 105, 37.8 (M - H), 32.2 119, 26.7 91, 24.4 55, 20 134, 12.2 M, 100 (M + 1), 17
anthracene (178, 7.41) C ₁₄ H ₁₀	2.7 × 10 ⁻¹				
pyrene (202, 7.48) C ₁₆ H ₁₀	6.5 × 10 ⁻¹		M, 100 (M + 1), 19.8		M, 100 (M + 1), 19.3
fluorene (166, 7.93) C ₁₂ H ₁₀	4.3 × 10 ⁻²		(M - H), 100 166, 16.0		(M - H), 100 166, 15.3
imipramine (HCl) (280, ?) C ₁₅ H ₂₄ N ₂	8.3 × 10 ⁻¹		58, 100 84, 22.5		58, 100 84, 14
lidocaine (234, ?) C ₁₄ H ₂₂ N ₂ O	2.0		86, 100 120, 23.3		86, 100

^aSpectrum is composed of an intense peak having more than 10% base peak intensity.

spectrum for Re-oxide emitter with the ion current (A) referenced to a pressure of 1 Torr. Ion current expressed in amperes is output of the ion multiplier with the gain at 5 × 10³ in both APIMS(SID) and SIOMS experiments.

Table I demonstrates parallels between sensitivity of GC(SID) and that obtained on APIMS(SID). The order of sensitivity magnitudes observed by APIMS(SID) is the same as that observed with the present SID for GC. This correlation provides support for the assumption inherent in this study that mass spectrometric study explains the responses observed in an actual SID of GC.

In comparison of positive charge carriers produced from APIMS(SID) with ion species obtained on conventional SIOMS using the oxide Re emitter, it was found that the observed ion species are exactly the same in both cases for all the compounds. The exact agreement of ion species confirms that the mechanism, which was initially considered in the previous study, need not be modified in order to account for the present results. The mechanism for the response of SID which detects positive-charge carriers is positive surface ionization.

However, the relative intensity of the observed ion species is changed, except for some substances which yield a single ion peak. The example of this change is shown for α -pinene in Figure 2a, where molecular ions of (M - nH)⁺ are dominant in the spectrum obtained by the SIOMS. In Figure 2b where the APIMS(SID) is done, ionic species having lower *m/z* values are produced more efficiently. The point is that the ionization observed by the APIMS(SID) is more prone to

produce the extensively dissociated ion species than the SIOMS.

This result was expected. In the vacuum environment of the SIOMS, sample molecules interact directly with the hot emitter surface, and the ions formed are the result of thermal pyrolysis. In the APIMS(SID), the hot emitter is placed in an atmospheric pressure "plasma" which contains substantial concentrations of chemically active species such as H atoms and O atoms, as well as substantial amounts of water vapor. This is a thermal and combustion environment as opposed to the thermal pyrolysis prevailing in the vacuum. It is certain that the differences are partly due to the difference in the emitter material which causes a different work function and different pyrolytic properties and hence a shift in the response.

The mass spectrometric study on imipramine and lidocaine is especially interesting. These compounds were successfully examined in the previous study as a good example of drug analysis. The authors believe the SID technique can play a very important role in the analytical chemistry of many drugs in the near future. These compounds are also interesting from the view of surface ionization mass spectrometry, because they are nonvolatile compounds with a rather complex structure.

The APIMS(SID) spectra of these compounds are characterized by the dissociative surface ionization (DSI) ions, which are produced through the formation process of dissociative surface reaction product with a low ionization energy followed by the surface ionization. These DSI ions are the charge carrier causing the response in the SID.

No indication is given that the molecular ions are formed

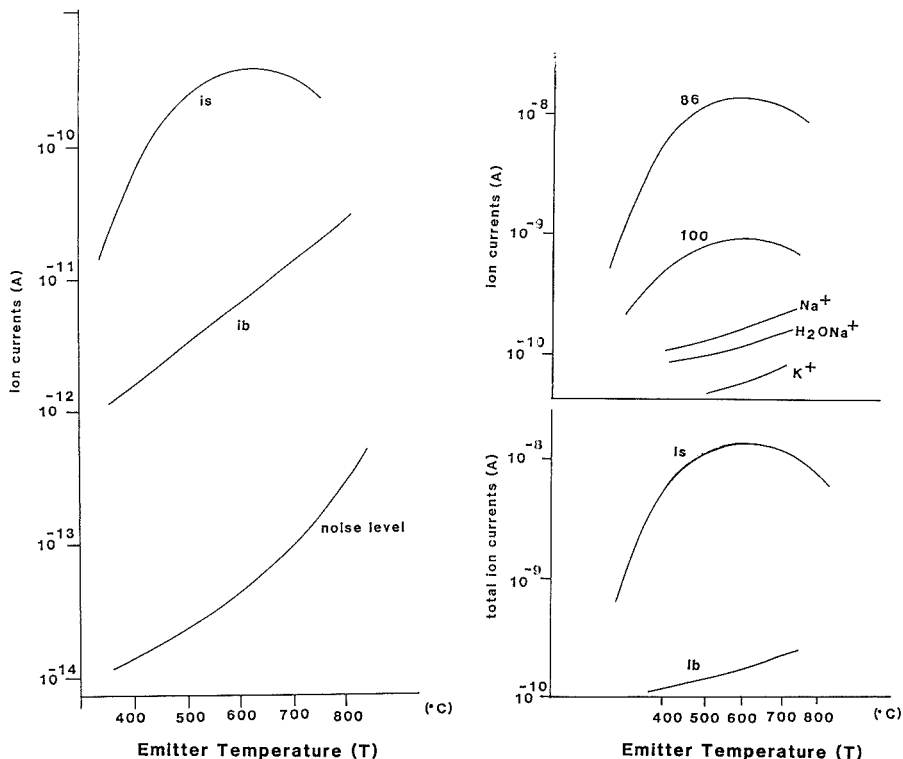


Figure 3. Emitter temperature dependence of triethylamine (TEA) response and background current for (left) GC(SID) and (right) APIMS(SID). For GC(SID) the results are taken under a 30 mL/min helium carrier gas mixed with additional gas of the dried air at 50 mL/min. Sample size was 2.6 ng of TEA in dichloromethane. For APIMS(SID), at the upper level, the resulting ion currents at m/z 86, 100, 23, 39, and 41 were shown under the conditions that the TEA was introduced at the rate of 7.2×10^{-4} g/min and was carried by the 50 mL/min air carrier gas. At the lower level, two curves of total ion currents either from the TEA sample or from alkali-atom impurities are drawn.

for both compounds in contrast to other substances. But the difference in relative intensity of the mass spectrum between APIMS(SID) and SIOMS was observed again just like other compounds.

The APIMS(SID) spectrum of imipramine exhibits three intense peaks, m/z 58, 84, and 72, whose structures are probably $(\text{CH}_3)_2\text{NCH}_2^+$, $(\text{CH}_3)_2\text{NCH}_2\text{CH}_2^+$, and $(\text{CH}_3)_2\text{NCH}_2\text{CH}_2\text{CH}_2^+$, respectively, via the dissociative reaction of a direct cleavage. The SIOMS spectrum has peaks at m/z 232, 186, and 70, whose composition has not been postulated thus far.

The mass spectra of lidocaine comprise only two peaks at m/z 86 and 120. The most intense in the spectrum is the m/z 86 ion presumably with the structure of $(\text{C}_2\text{H}_5)_2\text{NCH}_2^+$.

Responses to Change. Emitter Temperature Effect. Figure 3 illustrates the response signal change caused by varying the emitter surface temperature (T) of the GC(SID) and APIMS(SID). Emitter temperature is varied by changing the emitter heating current. The detailed operating conditions are described in the caption. On the left side, the temperature dependence of both signal (i_s) and background currents (i_b) for the GC(SID) is shown. The results of APIMS(SID) are given on the right side. At the upper level, the temperature dependence of the respective sample ion species at m/z 86 and 100 as well as ions of alkali atoms at m/z 23, 39, and 41 from the impurity in the Pt emitter material are shown. At the lower level, the temperature dependence of the total ion currents results either from the sample substance or from the

alkali atom impurity, $I_s(T)$ or $I_b(T)$.

No difference was observed in the shape of the $i_s(T)$ curve for the GC(SID) and the $I_s(T)$ curve for the APIMS(SID). Both curves were increased with emitter temperature, and reached the maximum at an emitter temperature around 600 °C with a slight decrease at the higher temperature. Again, this agreement provides additional support for the assumption that the SID mechanism is the positive surface ionization.

In a previous study, the background current of SID was initially considered to be the appearance of Na^+ and K^+ ions from Na and K impurity atoms in the Pt material of emitter. This assumption is essentially consistent with the present observation of ionic species Na^+ , K^+ , H_2OK^+ , and H_2ONa^+ , which presumably are the adduct ions associated with the water vapor in the atmospheric environment.

Effect of Field on APIMS(SID) Response. To demonstrate the effects of field, which is generated by applying the same voltage to the emitter and the repeller, the test sample of TEA was introduced through the diffusion tube. The response increased with the applied voltage and leveled off at about 150 V as expected. The applied voltage affects the desorption of the ion species from the surface as well as the ion transportation to the inlet of the mass spectrometer.

Emitter Material. The effect on the response caused by varying the emitter surface was studied. Pt and Ir metals were examined because both provide excellent performance as an emitter material. Both emitters were formed into six-turn loops from wire of 0.25 mm diameter and then assembled into

the ion source housing so as to give the same length (area) and position. Since these emitter conditions were carefully controlled, it is certain that the observed large difference in $i_s(T)$ behavior is due to the differences in the properties of the emitter materials.

It was found that the Ir emitter gave comparable results. The i vs T characteristics were essentially the same. The ion signal increased with heating current and leveled off at saturation values.

Gaseous Environment around the Emitter. It could be concluded from the previous study that an oxidized emitter should be used in order to improve sensitivity and stability. Such an oxidized emitter can be obtained if air (oxygen) is added to the emitter surface from another gas line. The addition of 10 mL of air to helium as a carrier gas had effects on the signals observed by the APIMS(SID). This effect was an increase in total ion intensity with a slight corresponding change in product ion distribution. This suggests that air serves the purpose of modifying the surface leading to a change in the work function as well as the chemical property of the surface, which is responsible for the difference in response.

CONCLUSION

This study demonstrated the existence and theoretical basis of the SID mechanism; positive surface ionization is the mechanism of ion formation in SID. Thus, the probability of ion formation is related to the IE of the adsorbed species. On the hot surface, some of the compounds decompose through a series of unimolecular reactions. At each step of the decomposition newly formed species may be ionized. If the species has a low IE, its positive ion is formed.

The charge carriers collected at the conventional SID collector may not be those originally formed. The ion of GC(SID) moving through a gas in a longer electric field than the present experimental setup of the API(SID)MS may ex-

perience charge stripping, charge transfer, ion/molecule reaction, etc. However, the SID response depends only on the total intensity of ion species initially formed.

The incorporation of the SID into the ion source of an APIMS is very easily done. Since a heat Pt emitter reacts under atmospheric pressure condition as SID does to ionize compounds, the APIMS(SID) may provide a powerful combination of functions which should be useful for trace organic analysis of specific substances. This is particularly the case in the parallel use of an ion counting system.

ACKNOWLEDGMENT

The authors are grateful to M. L. Messersmith at Yokota Air Base for manuscript preparation. H.J. is a graduate student from Meisei University.

Registry No. Pt, 7440-06-4; Ir, 7439-88-5.

LITERATURE CITED

- (1) Fujii, T.; Arimoto, H. *Anal. Chem.* **1985**, *57*, 2625.
- (2) Fujii, T.; Arimoto, H. *J. Chromatogr.* **1986**, *355*, 365.
- (3) Zandberg, E. Ya.; Ionov, N. I. *Surface Ionization*; Israel Program for Scientific Translations: Jerusalem, 1971.
- (4) McKeown, M.; Siegel, M. W. *Am. Lab.* **1975**, *89*.
- (5) Horning, E. C.; Carroll, D. I.; Dzidic, I.; Lin, S. N.; Stillwell, R. N.; The not, J. P. *J. Chromatogr.* **1977**, *142*, 481.
- (6) Grimsrud, E. P.; Kim, S. H.; Gobby, P. L. *Anal. Chem.* **1979**, *51*, 223.
- (7) Fujii, T.; Jimba, H.; Ogura, M.; Arimoto, H.; Ozaki, K. *Analyst* **1988**, *1134*, 789.
- (8) Fujii, T.; Kitai, T. *Int. J. Mass Spectrom. Ion Processes* **1986**, *71*, 129.
- (9) Fujii, T.; Suzuki, H.; Obuchi, M. *J. Phys. Chem.* **1985**, *89*, 4687.
- (10) Fujii, T.; Ogura, M.; Jimba, H. *Anal. Chem.* **1989**, *61*, 1026.
- (11) Fujii, T. *Int. J. Mass Spectrom. Ion Processes* **1984**, *57*, 63.

RECEIVED for review May 16, 1989. Revised manuscript received October 6, 1989. Accepted October 18, 1989. Work was supported in part by the Ministry of Education, Science, and Culture of Japan; Grand-in-Aid for General Scientific Research (No. 63540452).

Determination of Chromium in Urine by Stable Isotope Dilution Gas Chromatography/Mass Spectrometry Using Lithium Bis(trifluoroethyl)dithiocarbamate as a Chelating Agent

Suresh K. Aggarwal, Michael Kinter, Michael R. Wills, John Savory, and David A. Herold*

Departments of Pathology, Biochemistry, and Medicine, University of Virginia Health Sciences Center, Charlottesville, Virginia 22908

An isotope dilution gas chromatography/mass spectrometry method using lithium bis(trifluoroethyl)dithiocarbamate as a chelating agent is described for the determination of chromium in urine. A wet digestion procedure with $\text{HNO}_3\text{-H}_2\text{O}_2$ is used for oxidizing the organic matter associated with urine samples. The isotope ratios are measured by selected ion monitoring in a general-purpose mass spectrometer using a 10-m fused silica capillary column. Memory effect, in sequential analyses of samples with different isotope ratios, was evaluated by preparing a series of synthetic mixtures and was found to be negligible. The accuracy of the method was verified by quantitation of chromium in the NIST freeze-dried urine reference material, SRM-2670, with a recommended chromium concentration of 13 $\mu\text{g/L}$ in the normal level and certified chromium concentration of $85 \pm 6 \mu\text{g/L}$ in the elevated level.

INTRODUCTION

Chromium (Cr) has been recognized as an essential micronutrient for humans that is involved in important biochemical processes such as glucose metabolism and the action of insulin (1). Current knowledge about the role of Cr in human nutrition has been reviewed in a recent article by Offenbacher and Pi-Sunyer (2). Nutrient Cr, Cr(III), is present in food in the trivalent form, while hexavalent chromium, Cr(VI), is considered to be an occupational hazard because of its allergenic and carcinogenic activities. Since the major pathway of elimination of absorbed Cr is excretion in urine, urinary Cr levels have been suggested as an indicator of total body burden and recent uptake (3). Blood Cr levels have been suggested to reflect long-term exposure to Cr (4).

As with most other metals, Cr in biological materials is generally determined by electrothermal atomic absorption

spectrometry (EAAS) because of the speed, minimum need for sample preparation, possibility of automation, and good sensitivity of this technique (5). However, EAAS measurement of Cr is very susceptible to matrix effects and, therefore, requires standards similar to the samples. Urinary Cr concentrations in normal subjects have been found to be below 1 $\mu\text{g/L}$ with a range of 0.2–1 $\mu\text{g/L}$ (6–9). In serum, Cr values ranging from <0.05 to 0.29 $\mu\text{g/L}$ (mean = $0.11 \pm 0.07 \mu\text{g/L}$; $n = 15$) have been reported recently by EAAS (10).

In a recent report on the determination of Cr in biological materials by members of the International Union of Pure and Applied Chemistry (IUPAC), it has been emphasized that analytical chemists should provide methods that are sufficiently sensitive to give accurate results at levels of less than 10 $\mu\text{g/L}$ Cr (11). Stable isotope dilution mass spectrometry, which has long been used by nuclear and geological scientists, is a well recognized technique for trace metal determinations in complex matrices. This technique offers the advantage of freedom from matrix effects and the constraints of quantitative sample preparation. Since the method employs an ideal internal standard, i.e. an enriched isotope of the same element, a high degree of accuracy can be readily achieved in concentration determinations. Stable isotope dilution mass spectrometry would supplement EAAS methods, providing an alternative physicochemical principle for the quantitation of chromium.

The use of general-purpose mass spectrometers for trace metal determinations is attractive because these instruments are widely available, which would allow many clinical laboratories to carry out trace metal determinations without additional specialized and expensive instrumentation. Further, combined gas chromatography/mass spectrometry (GC/MS) also offers the advantage of shorter analysis times and the ability to separate different metal chelates. The potential of general-purpose mass spectrometers for trace metal determinations has been demonstrated in a few published studies (12–15). However, one of the fundamental problems preventing the widespread application of GC/MS methods has been the observation of carryover, or memory, in the sequential analysis of samples with different isotope ratios (13). This can be a serious problem and must be evaluated for the metal and the chelating agent under investigation.

We have recently developed an isotope dilution GC/MS method using lithium bis(trifluoroethyl)dithiocarbamate, Li(FDEDTC), as a chelating agent for the quantitation of nickel (16, 17). In this paper, we continue this line of research by demonstrating the suitability of Li(FDEDTC) as a chelating agent for the determination of Cr in biological materials by isotope dilution GC/MS; we validate the method by using NIST reference materials.

The method offers high sensitivity with detection limits down to the sub-part-per-billion level ($\mu\text{g/L}$) with the inherent advantages of stable isotope dilution, most notably that the accuracy and precision of the analyses are not affected by incomplete recovery.

EXPERIMENTAL SECTION

Instrumentation. The GC/MS system consisted of a double-focusing, reverse geometry mass spectrometer (Model 8230, Finnigan MAT, San Jose, CA) coupled to a gas chromatograph (Varian 3700). The mass spectrometer, equipped with a SpectroSystem 300 data system for on-line data acquisition and processing, was operated as previously described (17).

Reagents. The ^{50}Cr -enriched Cr_2O_3 (>96 atom % ^{50}Cr) used as a spike for isotope dilution was obtained from Oak Ridge National Laboratory (Oak Ridge, TN). Certified Atomic Absorption Standard (potassium dichromate) was purchased from Fisher Scientific (Fairlawn, NJ) and used as the primary standard for spike calibration. Double sub-boiling quartz distilled HNO_3

and H_2SO_4 in Teflon bottles were obtained from the National Institute of Standards and Technology (NIST, Gaithersburg, MD). Ultrex grade ammonium hydroxide solution (30%) was purchased from J. T. Baker Chemical Co. (Phillipsburg, NJ), and stabilized hydrogen peroxide (50%) was obtained from Fisher Scientific. Potassium permanganate was obtained from Mallinckrodt, Inc. (Paris, KY). The standard reference material, freeze-dried urine SRM 2670 (normal and elevated levels of toxic metals), was purchased from the NIST and prepared according to their directions. Lithium bis(trifluoroethyl)dithiocarbamate, Li(FDEDTC), was synthesized by using bis(trifluoroethyl)amine from PCR Research Chemicals (Gainesville, FL), and *n*-butyllithium and carbon disulfide from Aldrich Chemical Co. (Milwaukee, WI) in an inert atmosphere at -70°C (18).

Several precautions were necessary to minimize the potential for Cr contamination from the apparatus, reagents, personnel, and the laboratory environment, as previously reported (17). Since the overall blank defines the detection limit of the method and limits the applicability of this technique at extremely low levels, it was necessary to identify a lot of H_2O_2 (Lot No. 791310) containing minimum amounts of Cr. The levels of Cr, determined by EAAS, present in various reagents used were as follows: chelating agent Li(FDEDTC), 0.06 $\mu\text{g/L}$; 4% solution of ammonium hydroxide, 0.016 $\mu\text{g/L}$; hydrogen peroxide, 0.4 $\mu\text{g/L}$; 0.5% (w/v) solution of KMnO_4 , 1.5 $\mu\text{g/L}$; pH 3 acetate buffer, 0.8 $\mu\text{g/L}$. An overall blank of less than 1 ng was present due to the volumes of these different reagents used in the procedure for digestion and chelate formation.

Preparation and Standardization of Spike Solution. A ^{50}Cr spike solution was prepared by dissolving the $^{50}\text{Cr}_2\text{O}_3$ in a minimum amount of Ultrex HClO_4 with heating in a Teflon beaker. The solution was brought to volume with 0.5 M HNO_3 . Diluted spike solutions were prepared from this stock solution, on a weight basis, for isotope dilution experiments. The isotopic composition of Cr in the spike was determined experimentally by preparing $\text{Cr}(\text{FDEDTC})_3$ chelate. The spike solution was calibrated as previously reported by reverse-isotope dilution GC/MS using the natural Cr primary standard (17, 19).

Digestion and Chelate Formation. A known volume (1 mL) of the reconstituted urine reference material was mixed with a weighed amount of ^{50}Cr spike solution in a Teflon beaker. The amount of Cr in the spike solution added to the urine sample was optimized to obtain an isotope ratio in the mixture, corresponding to the geometric mean of isotope ratio m/z 562/564 in the sample and the spike. This is not an essential requirement of the method, but it is advisable for obtaining the best results. The spiked mixture was treated with 1 mL of concentrated HNO_3 and was allowed to stand overnight to allow the partial digestion of the organic matter and reduce foaming during subsequent heating. The partially digested solution was heated gently on a hot plate at 50°C to reduce the volume to about 100 μL , and then 100 μL of 50% H_2O_2 was added. The solution was again heated gently and inspected periodically. The contents were mixed and the beaker was tapped gently to disperse frothing. The digestion with H_2O_2 was performed four or five times until a white residue remained on complete evaporation of the solution. The procedure required about 1 mL of H_2O_2 and took 3–4 h. The dried residue was dissolved in 1 mL of deionized water (DW), and the solution was again heated until completely dry. The residue was redissolved in 2 mL of DW, and the solution was transferred to a polypropylene (PP) tube. To the solution in the PP tube, 50 μL of 0.5% (w/v) KMnO_4 solution followed by 100 μL of 1 M H_2SO_4 was added to oxidize Cr(III) to Cr(VI). The solution in the PP tube was heated in a boiling water bath for about 30 min to complete the oxidation of Cr. The solution was allowed to cool to room temperature and adjusted to pH 3 by using 50–100 μL of a 4% solution of ammonium hydroxide. Subsequently, 500 μL of pH 3 acetate buffer was added and the Cr chelate formed by adding 200 μL of 20 mM solution of the chelating agent Li(FDEDTC). The Cr chelate was extracted with two 500- μL aliquots of CH_2Cl_2 . The organic extract containing the Cr chelate was allowed to evaporate to dryness at room temperature in the laminar flow hood and reconstituted in 20 μL of CH_2Cl_2 prior to GC/MS analysis. Samples containing 10 μg of Cr(VI) were used for optimizing the conditions of chelate formation. The chelate formation, at this high concentration, was immediately evident

Table I. Theoretically Expected and Measured Abundances of Different Ion Peaks in Natural Chromium

atomic mass	atom % abund ^a	molecular ion peak (M ⁺)			fragment ion peak (M - L) ⁺		
		ion <i>m/z</i>	calcd %	measd ^b %	ion <i>m/z</i>	calcd %	measd ^b %
⁵⁰ Cr	4.345	818	2.95	3.08	562	3.32	3.36
⁵² Cr	83.789	820	57.69	57.66	564	64.58	64.11
⁵³ Cr	9.501	821	19.62	19.38	565	17.09	17.18
⁵⁴ Cr	2.365	822	19.75	19.88	566	15.01	15.35

^a Taken from ref 20. ^b Injecting 5 ng of Cr on column.

Table II. Theoretically Expected and Measured Abundances of Different Ion Peaks in Chromium Spike

atomic mass	atom % abund ^a	molecular ion peak (M ⁺)			fragment ion peak (M - L) ⁺		
		ion <i>m/z</i>	calcd %	measd ^b %	ion <i>m/z</i>	calcd %	measd ^b %
⁵⁰ Cr	96.40	818	39.27	68.44	562	78.28	78.04
⁵² Cr	3.33	820	22.59	22.92	564	17.46	17.68
⁵³ Cr	0.22	821	4.89	5.11	565	2.62	2.61
⁵⁴ Cr	0.05	822	3.25	3.53	566	1.64	1.67

^a Values given by the supplier (Oak Ridge National Laboratory) of enriched isotope. ^b Injecting 5 ng of Cr on column.

from a change in the color of the solution as soon as chelating agent was added.

Gas Chromatography/Mass Spectrometry. Prior to Cr isotope ratio measurements, the focusing conditions of the mass spectrometer were optimized and mass calibration was established by using perfluorokerosene. The Cr isotope ratios were measured in duplicate by injecting 1 μ L of the chelate solution and monitoring the group of peaks corresponding to the fragment ion (M - L)⁺, formed by the loss of one ligand molecule. Data were obtained in a selected ion monitoring (SIM) experiment by integrating the chromatographic peak areas as previously described (17).

RESULTS AND DISCUSSION

Precision and Accuracy in Isotope Ratio Measurements. The mass spectrum exhibits several isotopic groups of peaks corresponding to Cr(FDEDTC)₃⁺, Cr(FDEDTC)₂⁺, and Cr(FDEDTC)⁺ designated by M⁺, (M - L)⁺, and (M - 2L)⁺, respectively (16). Among the various ion peaks containing the metal atom, the fragment ion Cr(FDEDTC)₂⁺ formed by the loss of one ligand is of maximum intensity. The most abundant isotopic group of Cr(FDEDTC)₂⁺ ions nominally at *m/z* 562 was used throughout the experiments to achieve high sensitivity. This ion group consists of four peaks at *m/z* 561.88, 563.88, 564.88, and 565.88, corresponding respectively to ⁵⁰Cr, ⁵²Cr, ⁵³Cr, and ⁵⁴Cr isotopes in Cr(FDEDTC)₂⁺. Further, the presence of a molecular ion as well as the observation of symmetrical and sharp chromatographic peaks indicates the thermal stability of the Cr chelate at nanogram levels under the experimental conditions used.

Tables I and II present the results obtained for isotope ratio measurements of natural Cr and ⁵⁰Cr-enriched spike, respectively. For these measurements, 1 μ L of the chelate solution containing 5 ng of Cr was injected. The atom percent abundances of different isotopes in natural Cr (Table I) are the recommended values based on the values measured experimentally by various laboratories (20). The atom percent abundances of different Cr isotopes in ⁵⁰Cr spike (Table II) are the values provided by the supplier of the enriched isotope (Oak Ridge National Laboratory). The theoretically calculated values are also given in these tables for the abundances of various Cr-containing peaks in the molecular ion, Cr(FDEDTC)₃⁺, and in the fragment ion, Cr(FDEDTC)₂⁺. These values have been obtained by calculating the contributions of the isotopes of chromium, carbon, nitrogen, and sulfur in these ions (21, 22). As can be seen from the data in Tables I and II, there is excellent agreement among the calculated and measured abundances of the various ions in the natural Cr as well as in the ⁵⁰Cr spike. This shows that,

Table III. Precision in Determining Isotope Ratios of Natural Cr by Using Cr(FDEDTC)₃

	isotope ratio ^a		
	562/564	565/564	566/564
mean of means	0.0543	0.2728	0.2432
within-run precision, %	1.9	1.2	1.3
between-run precision, %	6.1	3.6	3.0
overall precision, ^b %	6.4	3.8	3.2

^a Injecting 5 ng of Cr on column. ^b Overall precision *S_t* was calculated by combining the within-run precision (*S_i*) and between-run precision (*S_j*), using the formula *S_t* = (*S_i*² + *S_j*²)^{1/2}.

within the experimental uncertainties, there was no mass discrimination due to the use of different accelerating voltages when isotope ratios were determined by voltage peak switching. This lack of bias is likely due to the small relative mass difference at the high *m/z* values of the ions. In the presence of mass discrimination, a general trend toward decreasing abundances with increasing mass of Cr isotope would have been observed. Since this was not observed, no correction was applied to the experimentally determined isotope ratios over the 4-amu mass range measured at either the molecular ion (*m/z* 818–822) or the fragment ion (*m/z* 562–566). Moreover, any mass discrimination factor that might be observed is canceled in isotope dilution experiments as the spike calibration is performed by reverse-isotope dilution using a primary standard in the same experiment (19).

Precision in the determination of various isotope ratios was evaluated by performing measurements of chelated natural Cr on three different days. Five to 10 replicate injections of 5 ng of Cr were made on each of the three days. Mean values and standard deviations were calculated from the data obtained on each day. These mean values were used to calculate the mean of means and its standard deviation, referred to as between-run precision and given in Table III. The within-run precision was calculated by considering the standard deviation values obtained on different days. Overall precision was calculated by combining the within-run precision and between-run precision values. This was done to evaluate the effects of any variations in the mass spectrometer operating parameters that may occur from one day to another. Overall precision values of 3–6% were obtained at the 5-ng level. As expected, the precision is better when the ratios to be measured are closer to unity (for example, *m/z* 565/564 and 566/564 versus 562/564 in Table III), and this can be achieved by optimum spiking in the isotope dilution step.

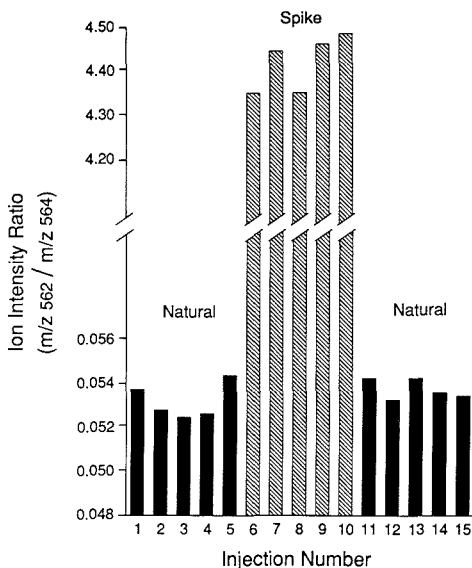


Figure 1. Evaluation of cross-contamination between samples of very different isotopic compositions, in consecutive analyses. Injections 1–5 and 11–15 are from a natural Cr sample and injections 6–10 are from a ^{50}Cr spike.

Memory Effect. One problem with the GC/MS analyses of metal chelates for isotope ratio measurements is the cross-contamination in the GC/MS system between sequential analyses of samples with widely different isotope ratios. This can be the limiting factor for some metals and chelating agents. This phenomenon, referred to as the memory effect, can adversely affect the accuracy of the measurement of altered (nonnatural) isotope ratios. Memory effect has been an analytical problem due, in part, to the nonavailability of a suitable chelating agent. The Li(FDEDTC) chelating agent used in this work offers advantages in comparison to trifluoroacetylacetone (TFA) used earlier for Cr determination in biological materials (12), geological materials (23), and seawater (24). The advantages include the quick preparation of chelates at room temperature, negligible memory effect, and the measurement of isotope ratios over a limited range (2–4 amu) at high mass (m/z 560 or 830), thereby reducing the mass discrimination effects and chemical interferences in the mass spectrometer. Also, the use of Li(FDEDTC) as a chelating agent is promising because of its applicability to several elements which can be readily separated on a capillary GC column (25). In the present studies of Li(FDEDTC) as a chelating agent, the memory effect was evaluated by using two different approaches. The first method involved the sequential analysis of a solution of natural Cr and a solution of the ^{50}Cr spike measuring the m/z 562/564 isotope ratio. The analyses were carried out in the following sequence: five injections of natural Cr, five injections of ^{50}Cr spike, five injections of natural Cr. The results obtained are shown in Figure 1. For these data, no appreciable memory or carryover is observed when these samples with isotope ratios differing by a factor of about 90 are analyzed sequentially.

The second approach used to investigate the suitability of GC/MS using Cr(FDEDTC)₃ chelate was an evaluation of the accuracy of determining isotope ratios different from those of natural samples. For this experiment, five synthetic mixtures differing in the m/z 562/564 ratio by a factor of 10 (range

Table IV. Determination of Chromium in Spike Solution Using Five Synthetic Mixtures with Altered Isotope Ratios Ranging from 0.2 to 2

ion used	isotope ratio	mean concn, ^a μg of Cr/g of soln	std dev, $\mu\text{g}/\text{g}$	range, $\mu\text{g}/\text{g}$
Cr(FDEDTC) ₃ ⁺⁺	818/820	2.31	0.04	2.26–2.34
	818/821	2.29	0.03	2.24–2.33
	818/822	2.33	0.04	2.28–2.34
Cr(FDEDTC) ₂ ⁺	562/564	2.22	0.06	2.15–2.29
	562/565	2.31	0.06	2.20–2.37
	562/566	2.35	0.05	2.27–2.41

^a Injecting 5 ng of Cr on column, mean from five synthetic mixtures.

Table V. Standardization of ^{50}Cr Spike Solution by Reverse Isotope Dilution

ion used	isotope ratio	mean concn, ^a μg of Cr/g of soln	std dev, $\mu\text{g}/\text{g}$	range, $\mu\text{g}/\text{g}$
Cr(FDEDTC) ₃ ⁺⁺	818/820	2.31	0.02	2.30–2.36
	818/821	2.31	0.03	2.28–2.35
	818/822	2.31	0.05	2.27–2.38
Cr(FDEDTC) ₂ ⁺	562/564	2.26	0.04	2.21–2.32
	562/565	2.31	0.02	2.28–2.33
	562/566	2.30	0.02	2.28–2.33

^a Injecting 5 ng of Cr on column, mean from five independent samples.

0.2–2) were prepared by mixing weighed aliquots of the primary standard solution and the ^{50}Cr spike solution. The mixtures were prepared to contain almost equal amounts of total Cr. Three injections, each with 5 ng of Cr, were made from each of the mixtures, and the isotope ratios m/z 562/564, 562/565, and 562/566, corresponding to the different Cr isotopes in the fragment ion Cr(FDEDTC)₂⁺, were determined. On another day, the isotope ratios m/z 818/820, 818/821, and 818/822, corresponding to different Cr isotopes in the molecular ion Cr(FDEDTC)₃⁺⁺, were also determined by using these synthetic mixtures. The mixtures were analyzed in the sequence of increasing isotope ratios. The isotope ratios determined from these mixtures were used to calculate the Cr concentration in the spike solution by using reverse-isotope dilution methodology, and the results are given in Table IV. The consistency in the concentration of Cr in the spike solution, shown by low standard deviations and narrow ranges of the calculated concentration, shows that the isotope ratios were measured accurately. Further, the constancy in the isotope ratios determined by replicate injections from each of the synthetic mixtures also demonstrated no appreciable memory effect.

Isotope Dilution Results. The ^{50}Cr spike solution was calibrated by reverse isotope dilution using a primary standard of natural Cr. For this standardization, five samples were prepared by mixing weighed amounts of primary standard and ^{50}Cr spike solutions to achieve an optimum isotope ratio m/z 562/564 in the spiked mixtures. The results obtained for Cr concentration in the spike solution are given in Table V. The concentration values calculated from the different isotope ratios are all in good agreement. The concentration values are given in units of $\mu\text{g}/\text{g}$ since the aliquots were taken on a weight basis to eliminate pipetting errors. The standard deviation observed for the concentration values in Table V is better compared to that in Table IV. This is because the concentration values in Table V were derived from samples with optimum isotope ratios (i.e. m/z 562/564 ~ 0.5) whereas

Table VI. Determination of Cr in SRM-2670 Urine by Isotope Dilution GC/MS

NIST value, $\mu\text{g/L}$	isotope ratio	mean concn, ^a μg of Cr/L of soln	std dev, $\mu\text{g/L}$	range, $\mu\text{g/L}$
85 ± 6	562/564	89 ($n = 11$)	6	75-99
	562/565	94 ($n = 11$)	5	89-101
	562/566	92 ($n = 11$)	9	73-101
$13 \pm ?$	562/564	13 ($n = 5$)	2	11-15
	562/565	13 ($n = 5$)	3	11-17
	562/566	12 ($n = 5$)	3	9-17

^a Injecting 2 ng of Cr on column.

the values in Table IV were from samples with a range of isotope ratios (i.e. m/z 562/564 from 0.2 to 2).

The calibrated ^{50}Cr spike solution was then used to quantitate Cr in the NIST freeze-dried urine reference material SRM 2670. This reference material consists of two different urine samples containing 13 μg of Cr/L (recommended value) and 85 ± 6 μg of Cr/L (certified value). The signal-to-noise ratio (>100 to 1 for 13 μg of Cr/L) observed in the GC peak indicates potential limits of detection down to sub-parts-per-billion levels. In principle, the detection limit of the method (2-3 ng/L) limits the quantitative measurement of Cr; however, contamination from reagents, laboratory, and analyst makes the practical limit 0.1-1 $\mu\text{g/L}$ with reasonable precautions. All the isotope ratios corresponding to different Cr isotopes in the fragment ion $\text{Cr}(\text{FDEDTC})_2^+$ were recorded and used for calculating the Cr concentration in the urine samples. The results obtained are shown in Table VI and have been corrected for Cr blank. Since the Cr concentration values in the urine reference material are provided in units of $\mu\text{g/L}$ by NIST, the urine sample aliquots were taken on a volume basis instead of weight basis so that the Cr concentration values in urine are given in $\mu\text{g/L}$. The concentration values calculated by using the different isotope ratios are in good agreement with one another as well as with the NIST values in the reference material SRM 2670.

CONCLUSION

The results of this work demonstrate that isotope dilution GC/MS using Li(FDEDTC) as a chelating agent can be used for determining Cr in urine. Results obtained are shown to be accurate and precise. No significant memory effect is seen in the determination of altered isotope ratios. This absence of memory effect not only allows accurate quantitation but also shows that the technique can be used for isotope ratio measurements in metabolic and bioavailability studies (26).

ACKNOWLEDGMENT

The authors thank James Nicholson for providing the electrothermal atomic absorption spectrometric results and

Patrick K. Anonick for assistance in synthesis.

Registry No. Li(FDEDTC), 74613-66-4; Cr, 7440-47-3.

LITERATURE CITED

- Jeejeebhoy, K. N.; Chu, R. C.; Marlliss, E. B.; Greenberg, G. R.; Bruce-Robertson, A. *Am. J. Clin. Nutr.* **1977**, *30*, 531-538.
- Offenbacher, E. G.; Pi-Sunyer, F. X. *Ann. Rev. Nutr.* **1988**, *8*, 543-563.
- Rinehart, W. E.; Gad, S. C. *Am. Ind. Hyg. Assoc. J.* **1986**, *47*, 696-699.
- McAughey, J. J.; Smith, N. J. *Anal. Chim. Acta* **1987**, *193*, 137-146.
- Veillon, C. In *Methods in Enzymology*; Riordan, J. F., Vallee, B. L., Eds.; Academic Press, Inc.: San Diego, CA, 1988; Vol. 158, Part A, Chapter 24.
- Routh, M. W. *Anal. Chem.* **1980**, *52*, 182-185.
- Veillon, C.; Patterson, K. Y.; Bryden, N. A. *Anal. Chim. Acta* **1982**, *136*, 233-241.
- Veillon, C.; Patterson, K. Y.; Bryden, N. A. *Clin. Chem.* **1982**, *28*, 2309-2311.
- Dube, P. *Analyst* **1988**, *113*, 917-921.
- Veillon, C.; Patterson, K. Y.; Bryden, N. A. *Anal. Chim. Acta* **1984**, *164*, 67-76.
- Ottaway, J. M.; Fell, G. S. *Pure Appl. Chem.* **1986**, *58*, 1707-1720.
- Veillon, C.; Wolf, W. R.; Guthrie, B. E. *Anal. Chem.* **1979**, *51*, 1022-1024.
- Hachey, D. L.; Blais, J. C.; Klein, P. D. *Anal. Chem.* **1980**, *52*, 1131-1135.
- Buckley, W. T.; Hucklin, S. N.; Budac, J. J.; Elgendorf, G. K. *Anal. Chem.* **1982**, *54*, 504-510.
- Reamer, D. C.; Veillon, C. *Anal. Chem.* **1981**, *53*, 2166-2169.
- Aggarwal, S. K.; Kinter, M.; Willis, M. R.; Savory, J.; Herold, D. A. *Anal. Chim. Acta* **1989**, *224*, 83-95.
- Aggarwal, S. K.; Kinter, M.; Willis, M. R.; Savory, J.; Herold, D. A. *Anal. Chem.* **1989**, *61*, 1099-1103.
- Sucre, L.; Jennings, W. *Anal. Lett.* **1980**, *13*, 497-501.
- Aggarwal, S. K.; Duggal, R. K.; Rao, R.; Jain, H. C. *Int. J. Mass Spectrom. Ion Processes* **1986**, *71*, 221-231.
- DeBievre, P.; Gallet, M.; Holden, N. E.; Barnes, I. L. *J. Phys. Chem. Ref. Data* **1984**, *13*, 809-891.
- Beynon, J. H. *Mass Spectrometry and Its Application to Organic Chemistry*; Elsevier: Amsterdam, 1960.
- Beynon, J. H.; Williams, A. E. *Mass and Abundance Tables for Use in Mass Spectrometry*; Elsevier: Amsterdam, 1963.
- Frew, N. M.; Leary, J. J.; Isehour, T. L. *Anal. Chem.* **1972**, *44*, 665-671.
- Siu, K. W. M.; Bednas, M. E.; Berman, S. S. *Anal. Chem.* **1983**, *55*, 473-476.
- Schaller, H.; Neeb, R. *Fresenius' Z. Anal. Chem.* **1986**, *323*, 473-476.
- Turnlund, J. R. *J. Nutr.* **1989**, *119*, 7-14.

RECEIVED for review March 27, 1989. Revised manuscript received October 10, 1989. Accepted October 18, 1989. Funding for the purchase of the high-resolution mass spectrometer was obtained from the National Institutes of Health, Division of Research Resources Shared Instrumentation Grant Program, Grant Number 1-S10-RR0-2418-01. Additional funding support from the John Lee Pratt Fund of the University of Virginia and Grant ESO 4464 of the National Institute of Environmental Health Sciences is also gratefully acknowledged. S.K.A. Thanks the Division of Experimental Pathology, Department of Pathology, University of Virginia Health Sciences Center, for a postdoctoral fellowship and the authorities at Bhabha Atomic Research Center, Trombay, Bombay 400 085, India, for granting leave.

Study of Oil Field Chemicals by Combined Field Desorption/Collision-Activated Dissociation Mass Spectrometry via Linked Scan

J. Shen* and A. S. Al-Saeed

Saudi Arabian Oil Company, Box 8745, Dhahran 31311, Saudi Arabia

Field desorption mass spectrometry (FDMS) is used as a convenient technique for direct fingerprinting of oil field chemicals such as biocides, demulsifiers, scale inhibitors, etc. The composition of individual ingredients in these chemicals, which is often difficult to monitor otherwise, may be visualized easily in a FD spectrum. When it is necessary to study the molecular structure of an individual component, combined field desorption/collision-activated dissociation (FD/CAD) mass spectrometry via linked scan can often provide the information needed. In the study of quaternary ammonium salts in biocides, dissociation at bond locations remote from the charge center was observed.

Mass spectrometry has been one of the most useful techniques for studying molecular structures. Samples can be in gas, liquid, or solid forms. The mass spectrometric study of oil field chemicals such as biocides, corrosion inhibitors, and scale inhibitors, however, is often limited by their low vapor pressures and requires special sampling and/or ionization techniques. In recent years, a number of desorption ionization techniques have been found useful for nonvolatile and thermally labile materials.

The more commonly used desorption ionization methods include plasma desorption (1, 2), particle desorption (3-6), field desorption (7-9), desorption chemical ionization (10, 11), and laser desorption mass spectrometry (12-14). These desorption techniques often reduce ion fragmentation and enhance the yield of molecular ions. In addition, these techniques in general require little sample preparation and are capable of generating ions directly from sample matrices that are either nonvolatile or thermally labile. These soft ionization techniques provide a convenient means for direct mixture analysis without prior chromatographic separations.

Among these desorption ionization techniques, field desorption mass spectrometry (FDMS) gives the least amount of ion fragmentation (15). As a result, one can often visualize easily the gross composition of a sample mixture directly from a FD spectrum. FDMS therefore can be a convenient tool for fingerprinting of chemical mixtures.

For the purpose of elucidating molecular structures, however, it is useful to have fragment ions characteristic of the molecular ion structure. This requires (1) generating molecular ions, (2) inducing the fragmentation of the molecular ions, and (3) establishing the relationship between the fragment and the molecular ions by tandem mass spectrometry (MS/MS). The dissociation of a molecular ion could take place either naturally as a unimolecular process or via collision-activated dissociation (CAD) processes. MS/MS is best carried out in a tandem mass spectrometer. However, when a tandem mass spectrometer is not available, linked scan using double-focusing equipment is a convenient alternative.

This paper discusses the application of FDMS as a fingerprinting technique for quality assurance of oil field chem-

icals such as biocides and the use of combined FD/CAD MS via B/E linked scan for studying molecular structures of selected components in these chemicals.

EXPERIMENTAL SECTION

A Jeol DX-300 double-focusing mass spectrometer equipped with a combined field desorption/field ionization/electron impact (FD/FI/EI) source was used for this study. The instrument was controlled by a Jeol DA-5000 data system with linked scan softwares. Typically, samples were applied directly to an activated carbon emitter via a microsyringe. The cathodic voltage applied was 5.5 kV. The emitter temperature can be programmed by passing through a current ranging from 0 to 60 mA at a selected rate. The combined FD/CAD mass spectrometry was accomplished by colliding the selected ions with helium molecules in a collision chamber immediately after the ion source and monitoring via B/E linked scan. It is important to set the emitter temperature at the best anode temperature (BAT). Under the experimental conditions used, BAT for quaternary ammonium salts in biocides, for example, was about 20 mA.

RESULTS AND DISCUSSION

Fingerprinting of Biocides. Biocides are commonly used in oil field operations to help ensure water qualities. Our previous in-house work has used nuclear magnetic resonance (NMR) spectroscopy as a convenient means of fingerprinting purchased biocides for quality assurance purposes (16). NMR fingerprints have been able to verify the presence and reveal the unexpected variations of the major ingredients in biocides such as various types of quaternary ammonium salts. Specific identities of these salts, however, are difficult to determine. As a result, when compositional variations of biocides do occur, their significance is difficult to ascertain. A complementary technique that can help monitor individual components is therefore highly desirable.

Quaternary ammonium salts in general are highly polar and nonvolatile and are difficult to separate by chromatographic means without extensive sample preparation steps. While spectrophotometric and titrimetric methods can be used to quantitate these surfactants (17), they are limited in probing the chemical structure of individual components in a mixture.

FDMS has been previously applied to study cationic surfactants (18). Figure 1 shows a typical FD fingerprint of biocide A that contains quaternary ammonium salts. As reported before, the cationic portion of the quaternary ammonium salt molecules, C^+ , was observed intact in the FD spectrum. In addition, $(C_2A)^+$ cations were observed (19).

The major C^+ ion (m/z 326) observed in Figure 1 suggests the main salt component has a general molecular formula of $C_{22}H_{48}N^+Cl^-$, yielding $C_{22}H_{48}N^+$ and $[C_{22}H_{48}N]_2Cl^+$ ions at m/z 326 and 688, respectively. Additional C^+ ions observed at m/z 200, 228, 270, and 298 indicate the presence of the homologues $C_9H_{22}N^+Cl^-$, $C_{11}H_{26}N^+Cl^-$, $C_{18}H_{40}N^+Cl^-$, and $C_{20}H_{44}N^+Cl^-$, respectively. The $(C_2A)^+$ ions from the minor homologues were not observed. However, hybrid $(C_1C_2A)^+$ ions were observed at m/z 562 and 660, consisting of a minor

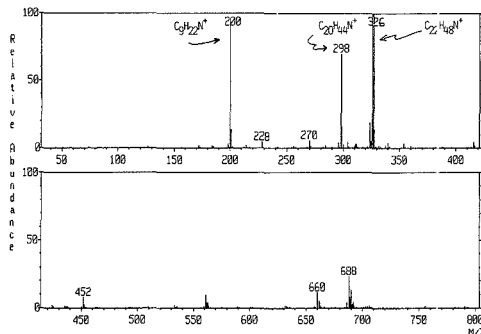


Figure 1. FD spectrum of biocide A with tetraalkylammonium salts as major ingredients.

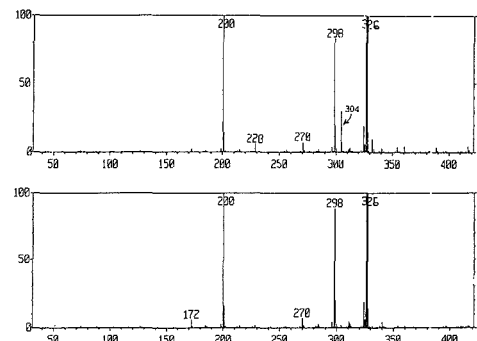


Figure 2. FD fingerprints of two different batches of biocide A.

salt molecule ($C_9H_{22}N^+Cl^-$ or $C_{20}H_{44}N^+Cl^-$) and C^+ from the major salt (i.e. $C_{22}H_{48}N^+$, m/z 326).

The tetraalkylammonium ions observed in Figure 1, which are the cationic portion of the quaternary ammonium salts in biocide A, have a general formula of



Figure 2 shows FD fingerprints of two separate batches of biocide A received several months apart. There is apparently no significant variation in the relative concentrations of major tetraalkylammonium salts. A minor cation observed at m/z 304, however, does show variance in the two batches of biocide A. As will be discussed later, the m/z 304 ion is the cation from a benzylated quaternary ammonium salt. In this instance, the compositional variance observed in the two batches of biocide A has had no significant effects on their performances in the oil field.

Figure 3 shows the FD fingerprint of biocide B. When compared with Figure 1, the differences are obvious. Tetraalkylammonium chlorides are no longer the major components. The C^+ ions observed at m/z 304 and 356 indicate that different types of quaternary ammonium salts have become the major ingredients in biocide B.

In addition to quaternary ammonium salts, certain aldehydes such as glutaraldehyde have been known as major ingredients in biocides. Glutaraldehyde, being a volatile component, however, is not observed in the FD spectra. Most of the volatile components were lost when the FD sampling probe was introduced into the ion source via a differentially

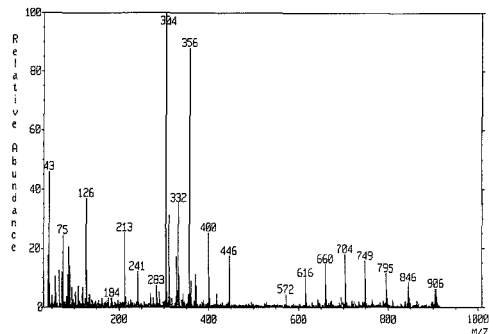


Figure 3. FD spectrum of biocide B with benzylated and ethoxylated quaternary ammonium salts.

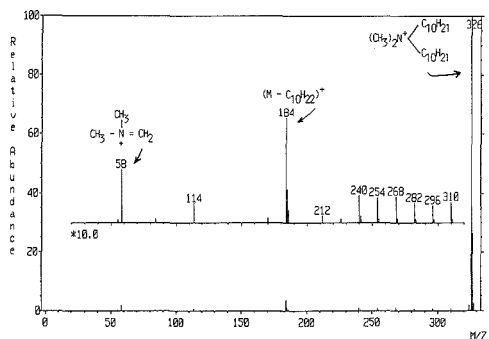
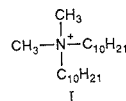


Figure 4. FD/CAD spectrum of $C_{22}H_{48}N^+$ (m/z 326).

pumped vacuum lock. FD spectra of biocides as shown in Figures 1 and 3 therefore display mainly quaternary ammonium salts. For quality assurance purposes, glutaraldehyde can be monitored separately by NMR spectroscopy.

Identification of Quaternary Ammonium Salts. Detailed structural information about quaternary ammonium salts in biocides can be provided by combined FD/CAD mass spectrometry via B/E linked scan. With a tandem mass spectrometer, FD/CAD MS has been used previously for structural elucidation of surfactants in mixtures (20–22). The instrument, however, did not provide adequate resolution within one full scan, and each CAD spectrum was recorded in three separate but overlapped mass ranges. With the use of a double-focusing instrument, good quality FD/CAD mass spectra have been obtained via linked scan (22, 23).

Figure 4 shows a FD/CAD spectrum of the major C^+ ion (m/z 326) observed in the FD spectrum of biocide A (Figure 1). The daughter ions of the m/z 326 ion suggest it has a dimethyldeacylammonium ion structure (I).



The presence of a decyl group in I is suggested by the daughter ion observed at m/z 184 formed via the loss of $C_{10}H_{22}$ from I. The loss of C_nH_{2n+2} from tetraalkylammonium ions is a mass spectrometric process that has been observed before and has been verified by isotope labeling experiments (24). The dominant dissociation path of a quaternary ammonium

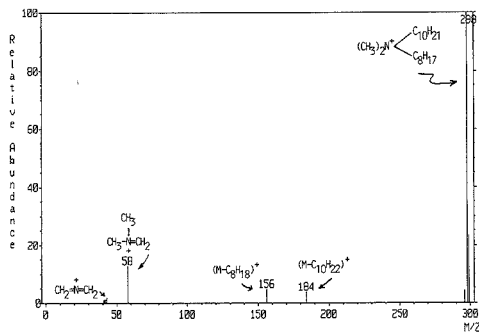
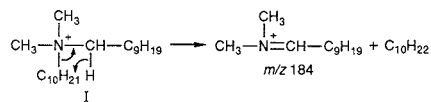
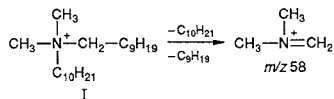


Figure 5. FD/CAD spectrum of $C_{20}H_{44}N^+$ (m/z 298).

cation is frequently the loss of the largest substituent group followed by hydrogen transfer. Thus, the m/z 184 fragment ion can be formed via the following path:



A second major dissociation path of a quaternary ammonium cation also involves the loss of the largest substituent group, but is followed by α cleavage in a neighboring alkyl group, leading to the formation of a stable iminium ion at m/z 58, which indicates the presence of a dimethyl structure in I.



Other minor daughter ions observed in Figure 4 include a series of ions from m/z 212 to 310 at regular 14-amu intervals, resulting from C-C bond cleavages of the long chain alkyl group followed by hydrogen transfer. This further confirms the presence of long chain alkyl groups in the precursor ion I. This particular dissociation path, however, is unique in that it takes place at bond locations remote from the charge center.

Bond Dissociation Remote from the Charge Center.

Dissociation at bond locations remote from the charge center has been previously recognized from FAB/CAD spectra of fatty carboxylate anions (25) and long-chained amine and phosphonium cations (26) resulting from high-energy collisions in magnetic sector instruments. A six-electron reaction mechanism has been proposed based on isotope labeling experiments, and its application to anions was supported by recent molecular orbital study results (27). (A reviewer has pointed out that calculations for anions may not be applicable to cations.)

If one applies the six-electron mechanism, the m/z 240 ion in Figure 4, for example, could be formed via the following path:

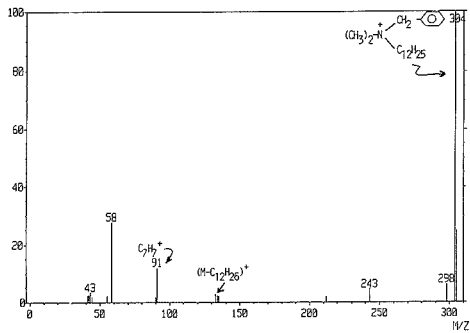
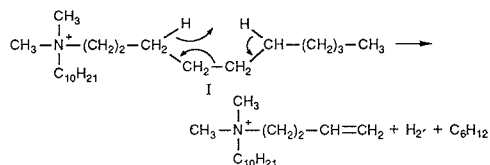


Figure 6. FD/CAD spectrum of benzylated cation (m/z 304).

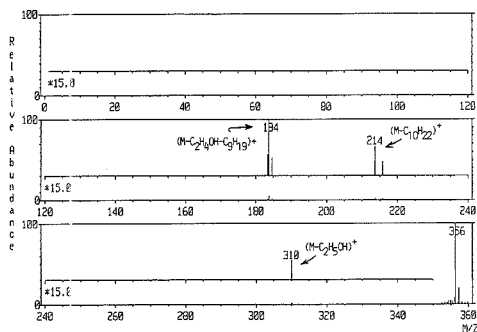
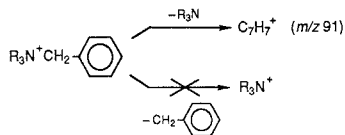


Figure 7. FD/CAP spectrum of ethoxylated cation (m/z 356).

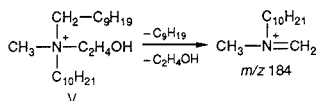
In support of this mechanism, under our FD/CAD conditions, similar dissociation did not take place at the C-C bond next to the charge center. As a result, the m/z 198 ion was not observed in Figure 4. As discussed above, the formation of iminium ions typically would involve two neighboring substituent groups.

Similar FD/CAD data suggest the presence of dimethyloctyldecylammonium chloride (II) and trimethylhexylammonium chloride (III) in biocide A. Presumably they are present as byproducts of the major salt component. Under FD conditions, II yields C^+ at m/z 298 and III yields C^+ at m/z 200 (see Figure 1). Figure 5 shows, as another example, the FD/CAD spectrum of the C^+ ion at m/z 298, which yields iminium daughter ions at m/z 58, 156, and 184, respectively, indicating the presence of dimethyl, octyl, and decyl groups in II.

Benzylated Quaternary Ammonium Salt. The C^+ ion at m/z 304 observed in Figure 1 is not part of the homologues of the tetraalkylammonium ions. The daughter ions of the m/z 304 ion (see Figure 6) indicate the presence of a benzyl group in addition to a dodecyl and two methyl groups. This suggests a molecular structure of dimethyl-dodecylbenzylammonium chloride (IV) for the precursor salt. The presence of a benzyl group is suggested by the $C_7H_7^+$ (m/z 91) daughter ion, which frequently has both benzyl and propyl ion structures under electron impact ionization conditions (28). Unlike in the tetraalkylammonium ions, which retain the charge on the nitrogen after losing an alkyl substituent group, cleavage of the benzylic bond in a trialkylbenzylammonium ion leaves the charge with the aromatic moiety ($C_7H_7^+$) instead of the trialkylammonium moiety.



In addition to dimethyldodecylbenzylammonium salt, the C^+ ion observed at m/z 356 in Figure 3 indicated the presence of an ethoxylated salt in biocide B. The daughter ions of this m/z 356 ion were observed at m/z 310 and 214 (see Figure 7), indicating the presence of ethoxy and dodecyl groups, respectively. The m/z 356 cation, however, does not have a dimethyl structure, and as a result, the m/z 58 ion was not observed in the FD/CAD spectrum of the m/z 356 ion. The most likely structure of the m/z 356 ion is therefore that of a methyl dodecylethoxyammonium ion (V). This structure is further supported by the daughter ion observed at m/z 184 formed from the following dissociation path:



The molecular structure of V is similar to that of choline, a family of N-ethoxylated N-alkyl quaternary ammonium salts.

Table I lists the major quaternary ammonium salts found in the two biocides studied. The presence of aromatic and ethoxylated components has also been confirmed by NMR spectroscopy.

Field Applications. FDMS was applied to determine the presence of residual biocides in the solids deposited in an internally coated water pipeline. The solids were recovered during scraping operations. The presence of residual biocides in these scraping solids was suspected because some of the biocides used in the field appear to have good film-forming ability, which may help cause the accumulation of solid deposits on the pipe wall.

Figure 8 shows the FD spectrum of a water extract of a solid deposit sample. In addition to Na^+ (m/z 23) and K^+ (m/z 39) ions, whose salts are commonly present in seawater and oil field brines, the ions observed at m/z 298 and 326 confirmed the presence of tetraalkylammonium salts (compare with Figure 1), and the ions observed at m/z 304 and 356 confirmed the presence of benzylated and ethoxylated quaternary ammonium salts (compare with Figure 2).

Fingerprinting of Demulsifiers. Demulsifiers are commonly used in the wet crude handling facilities for separating brines from crude oils. The performance of a demulsifier is important to the operating efficiency of a wet crude handling plant. Figures 9 and 10 show the FD fingerprints of two different types of demulsifiers. Figure 9 shows a demulsifier consisting mainly of alkyl amides, $RCONH_2$. Figure 10 shows one blended mainly with ethoxylated materials, indicated by a group of major ions that are 44 amu apart from each other.

Figure 11 shows the FD spectrum of an unknown surfactant sample suspected of mixing with amide type demulsifiers. The presence of amide type demulsifiers in the suspected sample is clearly indicated by a group of ions similar to those observed in Figure 9.

Scale Inhibitors. Scaling occurs frequently in the oil fields associated with wet production. Scale inhibitors are commonly used for scaling control. Typically, these scale inhibitors function as a threshold inhibitor that retards the growth of scaling crystals at the nucleation stage. Threshold inhibition usually needs only a very small amount of scale inhibitors, but their continuous presence in the scaling fluid is required.

Table I. Comparison of Major Quaternary Ammonium Salts in Biocides

	major salts	biocide A	biocide B
I	$\begin{array}{c} \text{CH}_3 \\ \\ [\text{CH}_3-\text{N}-\text{C}_{10}\text{H}_{21}]^+\text{Cl}^- \\ \\ \text{C}_{10}\text{H}_{21} \end{array}$ and homologues	major	not obsd
II	$\begin{array}{c} \text{CH}_3 \\ \\ [\text{CH}_3-\text{N}-\text{CH}_2-\text{C}_6\text{H}_5]^+\text{Cl}^- \\ \\ \text{C}_{10}\text{H}_{21} \end{array}$ and homologues	minor	major
III	$\begin{array}{c} \text{CH}_2-\text{CH}_2-\text{OH} \\ \\ [\text{CH}_3-\text{N}-\text{C}_{10}\text{H}_{21}]^+\text{Cl}^- \\ \\ \text{C}_{10}\text{H}_{21} \end{array}$ and homologues	not obsd	major

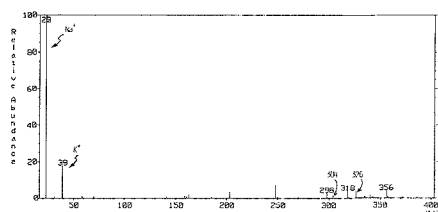


Figure 8. FD spectrum of a water extract of a solid deposit sample recovered from oil field water pipeline during scraping operation.

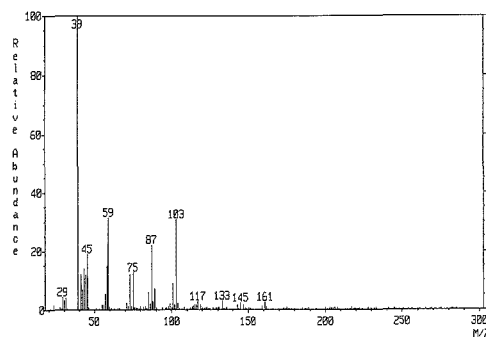


Figure 9. FD spectrum of an amide type demulsifier.

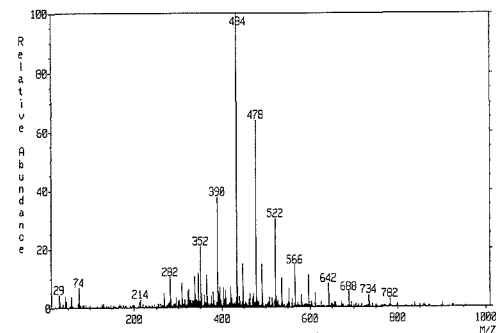


Figure 10. FD spectrum of an ethoxylated type demulsifier.

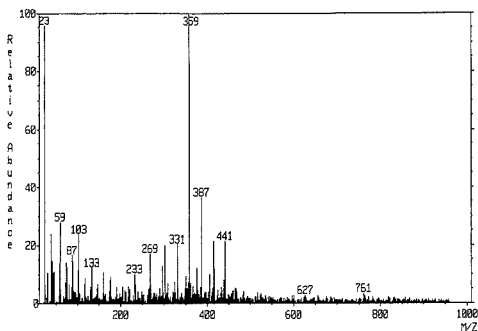


Figure 11. FD spectrum of an unknown surfactant suspected of mixing with amide demulsifiers.

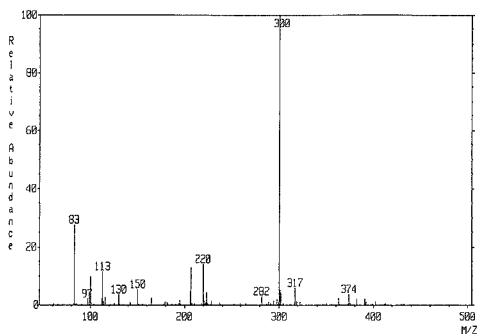


Figure 12. FD spectrum of an aminotrimethylenephosphonic acid blend.

Table II. Daughter Ions in the FD/CAD Spectrum of the Protonated ATMP Ion, m/z 300

m/z	daughter ion	m/z	daughter ion
300	$(M + H)^+$, $N[(CH_2PO_3H_2)_3]H^+$	96	$(CH_2PO_3H_3)^+$
218	$(M + H)^+ - H_3PO_3$	81	$H_2PO_3^+$
135	$(M + H)^+ - H_4PO_3 - H_3PO_3$	65	$H_2PO_2^+$
124	$(M + H)^+ - H_4PO_3 - CH_2PO_3H_2$	47	PO^+
105	$(M + H)^+ - H_3PO_3 - CH_2PO_3H_2 - H_2O$	42	$CH_2=N^+=CH_2$

One of the methods of applying scale inhibitors is to squeeze an inhibitor downhole into the near wellbore region of a wet producer. The small amount of the inhibitor that returns subsequently with the well fluid then protects the producing facilities against scaling. The cost effectiveness of such a procedure depends on the time interval required for resqueeze, which in turn depends on the specific chemicals in use.

Figure 12 shows the FD spectrum of a phosphonic acid, which, in our experience, when applied appropriately to limestone reservoirs, can extend the squeeze interval from less than 3 to over 18 months. The presence of the scale inhibitor in free acid form as aminotrimethylenephosphonic acid (ATMP) may be verified by the $(M + H)^+$ ion (m/z 300) observed in the FD spectrum of the inhibitor solution. Figure 13 shows the FD/CAD spectrum of the m/z 300 ion, which

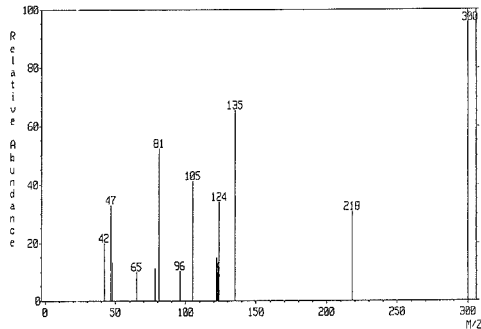


Figure 13. FD/CAD spectrum of m/z 300, protonated molecular ion of aminotrimethylenephosphonic acid.

provides information that further supports the molecular structure of ATMP. The dissociation paths leading to the daughter ions observed in Figure 13 are summarized in Table II.

Registry No. I, 7173-51-5; II, 965-32-2; III, 96837-00-2.

LITERATURE CITED

- (1) Cotter, R. J. *Anal. Chem.* **1988**, *60*, 781A.
- (2) MacFarlane, R. D.; Skowronski, R. P.; Torgerson, D. F. *Biochem. Biophys. Res. Commun.* **1974**, *60*, 616.
- (3) Day, R. J.; Unger, S. E.; Cooks, R. G. *Anal. Chem.* **1980**, *52*, 557A.
- (4) Garcella, J. A., Jr.; Hercules, D. M. *Anal. Chem.* **1980**, *52*, 226.
- (5) Benninghoven, A.; Muller, K. H.; Schemmer, M. *Surf. Sci.* **1978**, *78*, 565.
- (6) Barber, M.; Bordoli, R. S.; Elliott, G. J.; Sedgwick, R. D.; Tyler, A. N. *Anal. Chem.* **1982**, *54*, 645A.
- (7) Reynolds, W. D. *Anal. Chem.* **1979**, *51*, 283A.
- (8) Beckey, H. D. *Principles of Field Ionization and Field Desorption Mass Spectrometry*; Pergamon: London, 1977.
- (9) Beckey, H. D.; Schulten, H. R. *Angew. Chem., Int. Ed. Engl.* **1975**, *14*, 403.
- (10) Cotter, R. J. *Anal. Chem.* **1980**, *52*, 1589A.
- (11) Baldwin, M. A.; McLafferty, F. W. *Org. Mass. Spectrom.* **1973**, *7*, 135.
- (12) Posthumus, M. A.; Kistemaker, P. G.; Meuzelaar, H. L. C.; Ten Noever de Erauw, M. C. *Anal. Chem.* **1978**, *50*, 985.
- (13) Huang, S. Q.; Kolařik, L.; Lubman, D. M. *Appl. Spectrosc.* **1987**, *41*, 1371.
- (14) Cotter, R. J. *Anal. Chem.* **1984**, *56*, 485A.
- (15) Lattimer, R. P.; Harris, R. E.; Rhee, C. K.; Schulten, H. R. *Anal. Chem.* **1986**, *58*, 3188-3195.
- (16) Rosser, H. R.; Engen, R. J.; Saudi Arabian American Oil Company, Saudi Arabia, unpublished results, 1986.
- (17) Lienado, R. A.; Nuebecker, T. A. *Anal. Chem.* **1983**, *55*, 93R-102R.
- (18) Brert, D. A.; Rouse, D. J.; Sammons, M. C.; Burse, M. M. *Tetrahedron Lett.* **1973**, *No. 42*, 4127.
- (19) Schulten, H. R.; Roligen, F. W. *Org. Mass Spectrom.* **1975**, *10*, 649-659.
- (20) Louter, G. J.; Boerboom, A. J. H.; Stalmeier, P. F. M.; Tuithof, H. H.; Kistemaker, J. *Int. J. Mass Spectrom. Ion Phys.* **1980**, *33*, 335.
- (21) Weter, R.; Levsen, K.; Louter, G. J.; Boerboom, A. J. H.; Haverkamp, J. *Anal. Chem.* **1982**, *54*, 1458-1466.
- (22) Schneider, E.; Levsen, K.; Boerboom, A. J. H.; Kistemaker, P.; McLuckey, S. A.; Przybylski, M. *Anal. Chem.* **1984**, *56*, 1987-1988.
- (23) Fischer, M.; Veith, H. J. *Helv. Chim. Acta* **1978**, *61*, 3038.
- (24) Veith, H. J. *Org. Mass Spectrom.* **1983**, *18*, 154.
- (25) Tomer, K. B.; Crow, F. W.; Gross, M. L. *J. Am. Chem. Soc.* **1983**, *105*, 5487.
- (26) Jensen, J. J.; Tomer, K. B.; Gross, M. L. *J. Am. Chem. Soc.* **1985**, *107*, 1863-1868.
- (27) Siegel, M. M.; Colthup, N. B. *Appl. Spectrosc.* **1988**, *42*, 1214.
- (28) Sheri, J.; Dunbar, R. C.; Olah, G. A. *J. Am. Chem. Soc.* **1974**, *96*, 6227.

RECEIVED for review July 14, 1989. Accepted October 12, 1989. Thanks are given to Saudi Arabian American Oil Company for support and permission to publish this work.

Protocol for Liquid Chromatography/Mass Spectrometry of Glutathione Conjugates Using Postcolumn Solvent Modification

Mark F. Bean,^{*1} Sharon L. Pallante-Morell,² Deanne M. Dulik,³ and Catherine Fenselau²

Department of Pharmacology and Molecular Sciences, The Johns Hopkins University School of Medicine, Baltimore, Maryland 21205

A novel protocol for thermospray liquid chromatography/mass spectrometry (LC/MS) analysis of mixtures of glutathione conjugates is reported. Solvent conditions for optimal high-performance liquid chromatography are not always the same as for optimal thermospray ionization mass spectrometry. Labile glutathione conjugates that give poor spectra in aqueous ammonium acetate yield more intense molecular ion signals with increased percentages of acetonitrile. Direct injection thermospray ionization using 30–60% acetonitrile in aqueous ammonium acetate produced protonated molecular ions for glutathione conjugates of menadione, styrene oxide, pentachlorophenyl methyl sulfone, chlorodinitrobenzene, and chlorambucil. Since, the high percentages of organic modifier needed for good molecular ion intensity preclude chromatographic separation of these polar compounds, successful LC/MS was facilitated by postcolumn addition of organic modifiers to the mobile phase. This new methodology allowed excellent chromatographic separations and thermospray ionization mass spectra to be obtained for a mixture of haloalkane glutathione conjugates. Moreover, cleavage of the γ -glutamyl-cysteine amide bond of glutathione results in class-characteristic fragment ions. Changes in the fragmentation pathways in spectra acquired with and without organic modifiers shed light on the importance of the desolvation process in obtaining good molecular ion sensitivity in thermospray.

Reduced glutathione or (γ -glutamylcysteinyl)glycine (GSH), the major non-protein thiol constituent of cells, plays a key role in detoxification of electrophilic xenobiotics (1). However, conversion of these conjugates to free thiols via the cysteine- β -lyase pathway may result in greater toxicity of compounds such as some halogenated alkanes (2). Also, recent reports (3) implicate glutathione conjugates in the development of resistance to antineoplastic agents. These chemically and thermally unstable polar metabolites require extensive derivatization for gas chromatography-mass spectrometric analysis (4) and do not produce molecular ions in direct chemical ionization (DCI) mass spectrometry (5). Characterization by fast atom bombardment (FAB) (6) or plasma desorption mass spectrometry (7) gives reliable molecular weight information but few diagnostic fragments and may be hampered by the presence of sample contaminants and salts. Low-energy collisionally induced dissociation analyses of glutathione conjugates ionized by FAB have also recently been presented (8–10). Enzymatic and chromatographic determinations of glutathione in biological samples have been reviewed (11).

Thermospray liquid chromatography/mass spectrometry (LC/MS) (12, 13) is an attractive technique for the analysis of glutathione conjugates for several reasons: (1) detection is independent of UV chromophoric moieties, (2) the analysis of complex mixtures of nonvolatile, structurally similar compounds is possible with minimal sample manipulation, and (3) it not only provides molecular weight information but also yields a number of fragment ions diagnostic of the presence of glutathione conjugates.

Although isolated reports of thermospray mass spectrometry of glutathione conjugates have appeared in the literature (14–18), these studies failed to produce good data for the molecular ions (0–1% of the sample base peak intensity), and some did not involve the chromatographic potential of thermospray. The objective of this study was to develop a reliable and general protocol for the liquid chromatographic separation and mass spectrometric detection of glutathione conjugates in a mixture by the simplest possible means.

EXPERIMENTAL SECTION

Reagents. HPLC grade acetonitrile, methanol, ethyl acetate, trifluoroacetic acid, and ammonium acetate were obtained from J. T. Baker Chemical Co. (Phillipsburg, NJ). Water was doubly distilled, deionized, filtered, and stored in high-density polypropylene plastic bottles. Reduced and oxidized glutathione (γ -glutamylcysteinyl)glycine, L-glutamine, L-glutamic acid, ethacrynic acid (2,3-dichloro-4-(2-methylene-1-oxobutyl)phenoxy)acetic acid, and 1-chloro-2,4-dinitrobenzene were obtained from Sigma Chemical Co. (St. Louis, MO). (S)-(-)-2-Pyrrolidone-5-carboxylic acid was purchased from Aldrich Chemical Co. (Milwaukee, WI). Styrene oxide (racemic mixture) was purchased from MC/B (Gibbstown, NJ). The glutathione conjugates of trichloroethylene, hexafluoropropene, and 2-chloro-1,1,2-trifluoroethylene were prepared by James Stevens, W. Alton Jones Cell Science Center, Lake Placid, NY. The glutathione conjugate of menadione (2-methyl-1,4-naphthalenedione) was provided by Thomas Jones, University of Maryland School of Medicine, Baltimore, MD. Pentachlorophenyl methyl sulfone was provided by Vernon Feil, USDA-MRLL, Fargo, ND, and chlorambucil (4-[bis(2-chloroethyl)amino]benzenebutanoic acid) was provided by John Hilton, The Johns Hopkins University Oncology Center, Baltimore, MD.

Preparation of Glutathione Conjugates. Glutathione conjugates of pentachlorophenyl methyl sulfone and chlorambucil were prepared enzymatically by using immobilized microsomal glutathione S-transferases as previously described (19). The conjugates of 1-chloro-2,4-dinitrobenzene, ethacrynic acid, styrene oxide, and halogenated alkanes were synthesized under basic conditions (pH 10–12) according to a published procedure (20) and purified by solvent washes of the sample retained on octadecylsilyl silica (C₁₈) cartridges.

Mass Spectrometry. Mass spectra were recorded on a MS-80RF double-focusing mass spectrometer (Kratos Analytical, Manchester, UK). Three-seconds-per-decade scans were taken from m/z 900 to m/z 100 at a resolution of 1500. Data acquisition and processing were managed by the Kratos DS55 software on a Data General Nova 3 minicomputer with a Kratos fast preprocessor. Our version of the thermospray LC/MS interface, also from Kratos, did not have a probe temperature gradient controller, although the probe temperature was made to track mobile phase gradients manually without difficulty. Similarly, there was no

¹Present address: Department of Physical and Structural Chemistry, Smith Kline and French Research Laboratories, King of Prussia, PA 19406-0939.

²Present address: Department of Chemistry, University of Maryland, Baltimore County, Baltimore, MD 21228.

³Present address: Department of Drug Metabolism, Smith Kline and French Research Laboratories, King of Prussia, PA 19406-0939.

filament power supply, repeller, or glow discharge electrode. The instrument was modified as follows: the low-voltage first beam-centering plate was moved 3 mm further away from the high-voltage source block; a heating tape around the vacuum manifold near the focus assembly maintained the ion optics at about 60 °C; a -90 °C refrigerated vacuum vapor trap (model RT409A, Savant Instruments, Hicksville, NY) was inserted in the solvent take-off line between the mass spectrometer and the liquid nitrogen cold finger. These alterations were effective in completely eliminating any high-voltage arcing in the source housing. Heating the focus assembly reduced the slight beam defocusing observable in solvent gradient runs.

The extra vapor trap reduced liquid nitrogen consumption by two-thirds, prevented clogging of the glass cold finger inlet, protected the mechanical pump from corrosive vapors, and resulted in sublimation of all frozen solvents from the cold finger over to the refrigerated trap at the end of the day as the cold finger warmed to room temperature. Pumping efficiency was not reduced by the extra trap and related plumbing.

Calibration of the magnet scan was effected with 100- μ L injections of dilute mixtures of poly(ethylene glycol) polymers in ammonium acetate and observation of the MNH_4^+ ions.

Liquid Chromatography. The principal solvent delivery system consisted of two Beckman 114M pumps and a Model 420 gradient controller (Beckman Instruments, Inc., Berkeley, CA). Precolumn hardware included a Rheodyne Model 7125 injector with 250- μ L loop and Rheodyne three-way column switching valve (Rainin Instrument Co., Woburn, MA) and a 5- μ m filter (Alltech Associates, Deerfield, IL). The following columns were used with appropriate 3-cm guard columns: Brownlee RP-8 Spheri-10 (25 cm \times 0.46 cm i.d., 10 μ m), Brownlee RP-18 (10 cm \times 0.46 cm i.d., 5 μ m), a 10 μ m aminopropyl Shandon Hypersil APS (25 cm \times 0.46 cm, 5 μ m). A Brownlee C₁₈ guard column was used in line in all cases. It served to dampen the probe temperature fluctuations observed in columnless direct injections caused by introduction of the sample in a solvent different from the operational mobile phase. The postcolumn solvent delivery system consisted of a Spectroflow 400 pump with special pulse dampener (Kratos Analytical, Manchester, UK) and a MCVT/100 micrometering T-valve (Scientific Glass Engineering Inc., Austin, TX) or a 10- μ L Lee Micro Mixer (The Lee Co., Westbrook, CT).

RESULTS AND DISCUSSION

Glutathione. Reduced glutathione was selected for preliminary optimization of experimental parameters for the thermospray LC/MS interface as well as the mass spectrometer. Initial results from direct HPLC injection via a C₁₈ guard column using an aqueous ammonium acetate mobile phase (0.1 M) were disappointing in that no quasi-molecular ions were observed (Figure 1a). Manipulating the probe and source temperatures or the buffer concentrations resulted in spectra that at best had weak protonated molecular ions. Substitution of the buffer by 0.1 M trifluoroacetic acid or ammonium trifluoroacetate likewise resulted in no improvement. However, as the percentage of acetonitrile in the HPLC mobile phase was increased, and the probe temperature was decreased to compensate for the lower vaporization temperature of the mobile phase, we obtained excellent spectra of the reduced tripeptide (Figure 1b).

In addition to an intense protonated molecular ion peak, the spectrum obtained in 30% acetonitrile (Figure 1b) differs from the one obtained without organic modifier (Figure 1a) in the mass of the base peak: m/z 129 vs m/z 130. This difference is also observed in spectra of glutathione conjugates obtained with and without organic modifier. As has been noted previously (21), the most obvious path for formation of ions of mass 130 from glutathione involves temperature-dependent intramolecular cyclization of the γ -glutamyl residue to yield protonated (m/z 130) and ammoniated (m/z 147) pyrrolidone carboxylic acid (pyroglutamic acid) and displacement of cysteinylglycine (protonated mass of 179).

The prominent peak at m/z 129 in the spectrum acquired in the presence of acetonitrile differs from the pyrrolidone

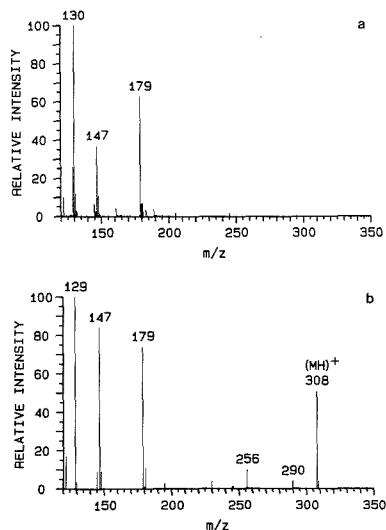


Figure 1. Thermospray ionization mass spectrum of glutathione, direct injection: (a) aqueous NH_4OAc ; (b) 30% acetonitrile in aqueous NH_4OAc .

carboxylic acid peak at m/z 130 by 1 dalton, requiring a difference in the number of nitrogens and suggesting that the peak is glutamine related rather than glutamic acid related. Although this probably arises from ammonolysis of the unusual, unhindered γ -Glu-Cys bond followed by dehydration, the possibility of concurrent contributions from fragmentation of the molecular ion ($\text{C}_1 + 2\text{H}$ like cleavages from the molecular ion and the dehydrated molecular ion) should not be excluded. Concurrent contributions to the peak at m/z 147 are also probable since protonated glutamine, ammoniated pyrrolidone carboxylic acid, and a fragment derived from cleavage of the N-C bond of the cysteinyl residue with retention of two additional hydrogens on the glutamyl portion are isobaric and since the observed peak has almost double the intensity in relation to m/z 179 when compared to the spectrum acquired without organic modifier.

It seems apparent that organic solvents such as acetonitrile, methanol, or 2-propanol stabilize the glutathione conjugates against cleavage of the glutamic acid residue, resulting in intense molecular ions; the precise cause is not known. Increased concentrations of organic modifier have similarly been shown to minimize certain solvolytic reactions (22).

Direct Injection of Glutathione Conjugates. The same mobile phase (30% acetonitrile in 0.1 M aqueous NH_4OAc) that had been successful for the analysis of glutathione produced variable results for direct injections of glutathione conjugates through a guard column. The glutathione conjugate of a toxic metabolite of polystyrene monomer, styrene oxide, yielded good spectra showing MH^+ (16% of sample base peak intensity) and, due to NaOH contamination from the synthetic conjugation reaction, a smaller MNA^+ (m/z 450), Figure 2. The same protocol applied to the GSH conjugate of the diuretic drug ethacrynic acid yielded protonated molecular ions of low intensity and variable chlorine isotope peak distributions. Increasing the concentration of acetonitrile to 70% and the consequent decrease of the vaporizer tip temperature resulted in more consistent, more intense molecular ion patterns, and decreased the summed ion currents over the fragment ion region (Figure 3). High concentrations of acetonitrile also produced good spectra of the GSH conjugates

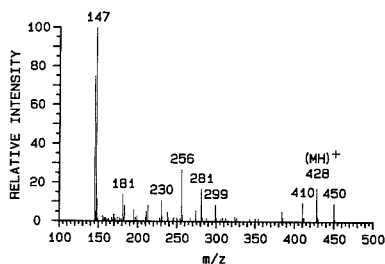


Figure 2. Thermospray ionization mass spectrum of glutathionylstyrene oxide, direct injection (50% acetonitrile in aqueous NH_4OAc).

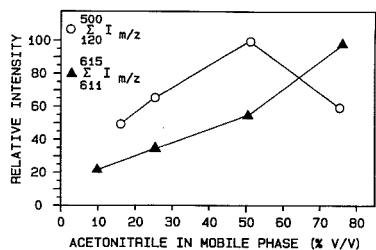


Figure 3. Plot of ion intensities in the thermospray spectrum of glutathionylethacrynic acid as a function of the percentage of acetonitrile in the mobile phase.

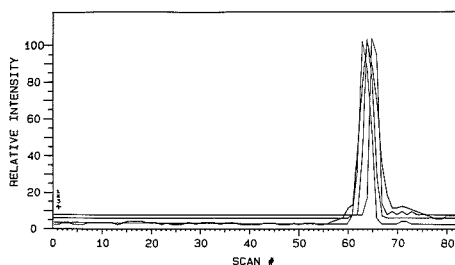


Figure 4. Total ion and selected ion chromatogram of a mixture of achromophoric glutathione conjugates of halogenated alkanes (40% acetonitrile in 0.2 M NH_4OAc , 0.8 mL/min, C_8 column): (1) m/z 402, (2) m/z 424, (3) m/z 458, (4) total ion current.

of menadione, and chlorambucil; the spectra of pentachlorophenyl methyl sulfone and ethacrynic acid showed good relative intensity of the molecular ions (15–60% of sample base peak) but isotopic ratios that varied from scan to scan indicating poor ion statistics. The conjugates of ethylene dichloride, chlorotrifluoroethane, and hexafluoropropane were less exigent, and produced intense molecular ions (15–100% of the sample base peak intensity) in 25–75% acetonitrile.

LC/MS of Glutathione Conjugates. Although LC/MS provides much more structural information than HPLC with UV detection, it is especially useful for the analysis of compounds that absorb only below 215 nm where solvent gradients can produce sharply sloping UV absorption base-line traces. In this vein, attempts to separate and identify the components of a mixture of haloalkane glutathione conjugates using 30–70% acetonitrile in aqueous ammonium acetate and an octadecylsilyl silica column met with immediate frustration. Glutathione conjugates of even these highly nonpolar compounds were still too polar to be adequately retained on the column. Figure 4 illustrates the poor resolution of the three main components of the mixture as represented by the total

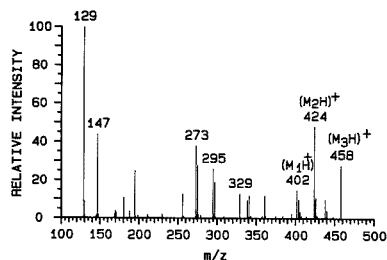


Figure 5. Thermospray ionization mass spectrum of scan 64 of the chromatogram in Figure 4. LC/MS, postcolumn combined solvent was 27% acetonitrile in 1.5 M aqueous NH_4OAc .

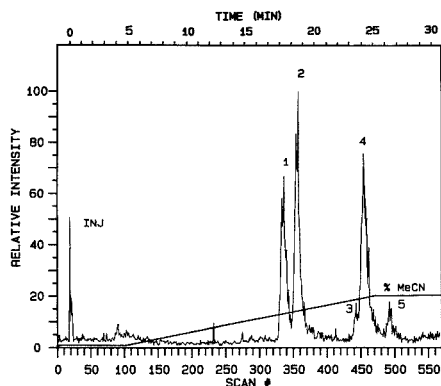


Figure 6. Total ion LC/MS chromatogram of a mixture of achromophoric glutathione conjugates of halogenated alkanes (LC pumps, 0–20% MeCN in 0.2 M NH_4OAc during 20 min, 0.8 mL/min, C_8 column; postcolumn pump, 100% MeCN, 0.4 mL/min): (1) glutathionyl-dichloroethylene, (2) glutathionylchlorotrifluoroethane, (3) unknown = glutathionylpentafluoropropene, (4) glutathionylhexafluoropropane, (5) unknown = glutathionylhexafluorobutene.

ion current and selected ion chromatograms of the protonated molecular ions expected for glutathionyl-dichloroethylene (402), glutathionylchlorotrifluoroethane (424), and glutathionylhexafluoropropane (458). In Figure 5 the three protonated molecular ion species are observed in the same scan. It is possible to recognize the three main components of the mixture even with negligible separation by following the changing ion intensities in the successive scans. Nevertheless, we were also interested in identifying minor contaminants in the mixture which were not discernible without better chromatographic separation.

The use of a bonded octylsilyl silica or propylamino stationary phase instead of C_{18} did not result in sufficient column retention. It was evident that the constrictions on the mobile phase necessary to produce consistent and intense quasi-molecular ions negated the possibility of HPLC separations. Optimal mobile phase conditions for thermospray ionization were not the optimal conditions for chromatography.

In order to free the chromatography from the constrictions of the mass spectrometer, it was necessary to insert a third, pulse-dampened, postcolumn pump, joined by a micrometering T valve to the probe inlet. It was now possible to perform the chromatography with a low percentage acetonitrile gradient and low flow rates in order to effect separation while adding acetonitrile postcolumn to achieve optimal spectra. The resulting ion chromatogram is illustrated for the separation of the mixture of haloalkane glutathione conjugates on a C_8 column in Figure 6. In addition to achieving base-line

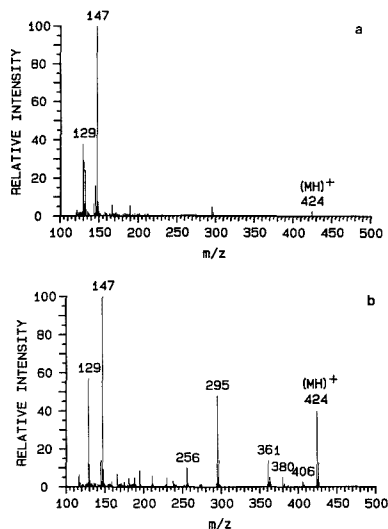


Figure 7. Therospray ionization mass spectrum of glutathionyl-dichloroethylene: (a) direct injection, 0.2 M aqueous NH_4OAc ; (b) LC/MS, postcolumn combined solvent was 27% acetonitrile in 1.5 M aqueous NH_4OAc .

separation of the principal components and excellent spectra, it was possible to identify two unknown fluorinated contaminants in the mixture. Peak 3 in Figure 6 can be assigned to a glutathionylpentafluoropropene (m/z 438) while peak 5 must be a glutathionylhexafluorobutene (m/z 470). The improvement in quasi-molecular ion intensity using the new protocol over direct injection in aqueous NH_4OAc is illustrated for glutathionyl-dichloroethylene in Figure 7.

The spectral pattern in therospray LC/MS of glutathione conjugates provides a series of three class-characteristic peaks: m/z 129, 147, and $(\text{MH} - 129)^+$, which together indicate an N-terminal glutamic acid. Thus the two impurities in the haloalkane mixture were readily identifiable as glutathione conjugates using the combined LC/MS system.

ACKNOWLEDGMENT

We thank Tom Jones, University of Maryland School of Medicine, and James Stevens, W. Alton Jones Cell Biology Center, Lake Placid, NY, for their contribution of several glutathione conjugates used in this study.

LITERATURE CITED

- Moldeus, P. In *Drug Metabolism, Molecular Approaches and Pharmaceutical Implications*; Siest, G., Ed.; Pergamon: Oxford, 1985; pp 69-73.
- Monks, T. J.; Lau, S. S. *Drug Metab. Dispos.* **1987**, *15*, 437-441.
- Arrick, B. A.; Nathan, C. F. *Cancer Res.* **1984**, *44*, 4224-4232.
- Wolfe, D. E.; VandenHeuvel, W. J. A.; Tyler, T. R.; Walker, R. W.; Koniuszy, F. R.; Gruber, V.; Arison, B. H.; Rosegay, A.; Jacob, T. A.; Wolf, F. J. *Drug Metab. Dispos.* **1980**, *8*, 131-136.
- Nelson, S. D.; Yaishnav, Y.; Kambora, H.; Baillie, T. A. *Biomed. Mass Spectrom.* **1981**, *8*, 244-251.
- Dulik, D. M.; Fenselau, C.; Hilton, J. *Biochem. Pharmacol.* **1986**, *35*, 3405-3409.
- Alai, M.; Dulik, D.; Pallante-Morell, S. Presented at the 34th Annual Conference on Mass Spectrometry and Allied Topics, Cincinnati, OH, 1986; pp 1005-1006.
- Straub, K. M. In *Mass Spectrometry in Biomedical Research*; Gaskell, S. J., Ed.; J. Wiley and Sons: Chichester, 1986; pp 115-134.
- Heeremans, C. E. M.; te Koppel, J. M.; Niessen, W. M. A.; van der Greef, J.; Brussee, J.; La Vos, G. F.; ten Noever de Brauw, M. C.; van der Greef, J. *Biomed. Environ. Mass Spectrom.* **1988**, *17*, 181-186.
- Haroldsen, D. E.; Reilly, M. H.; Hughes, H.; Gaskell, S. J.; Porter, C. J. *Biomed. Environ. Mass Spectrom.* **1988**, 615-621.
- Anderson, M. E. *Methods Enzymol.* **1985**, *113*, 548-555.
- Blakley, C. R.; Vestal, M. L. *Anal. Chem.* **1983**, *55*, 750-754.
- Vestal, M. L. In *Ion Formation from Organic Solids*; Benninghoven, A., Ed.; Springer-Verlag: Berlin, 1983; pp 246-263.
- Nocerini, M. R.; Yost, G. S.; Carlson, J. R.; Liberato, D. T.; Breeze, R. G. *Drug Metab. Dispos.* **1985**, *13*, 690-694.
- Betowski, L. D.; Korfmacher, W. A.; Lay, J. O., Jr.; Potter, D. W.; Hinson, J. A. *Biomed. Environ. Mass Spectrom.* **1987**, *14*, 705-709.
- Sasame, H. A.; Liberato, D. J.; Gillette, J. R. *Drug Metab. Dispos.* **1987**, *15*, 349-355.
- Parker, C. E.; DeWitt, J. S.; Smith, R. W.; Gopinathan, M. B.; Hernandez, O.; Tomer, K. B.; Vestal, C. H.; Sanders, J. M.; Bend, J. R. *Biomed. Environ. Mass Spectrom.* **1988**, 623-634.
- Conchillo, A.; Casas, J.; Messguer, A.; Abian, J. *Biomed. Environ. Mass Spectrom.* **1988**, *16*, 339-344.
- Pallante, S. L.; Lisek, C. A.; Dulik, D. M.; Fenselau, C. *Drug Metab. Dispos.* **1986**, *14*, 313-318.
- Ryan, A. J.; Bend, J. R. *Drug Metab. Dispos.* **1977**, *5*, 363-367.
- Lagna, W. M.; Callery, P. S. *Biomed. Environ. Mass Spectrom.* **1985**, *12*, 699-703.
- Bean, M. F.; Pallante-Morell, S. L.; Fenselau, C. *Biomed. Environ. Mass Spectrom.* **1989**, *18*, 219-223.

RECEIVED for review May 15, 1989. Revised manuscript received October 2, 1989. Accepted October 12, 1989. The research described in this article was funded by grants from the National Institutes of Health (GM 21248 and RR02241) and from the National Science Foundation (DCB 85-09638).

Endothermic Ion-Molecule Reactions: Strategies for Tandem Mass Spectrometric Structural Analyses of Large Biomolecules

Ron Orlando, Constance Murphy, and Catherine Fenselau

Structural Biochemistry Center, Department of Chemistry, University of Maryland Baltimore County, Baltimore, Maryland 21228

Gordon Hansen

Boehringer-Ingelheim Research and Development Center, Ridgefield, Connecticut 06876

Robert J. Cotter*

Middle Atlantic Mass Spectrometry Facility, Department of Pharmacology and Molecular Sciences, The Johns Hopkins University School of Medicine, Baltimore, Maryland 21205

Very low energy collisions between the protonated peptide leucine-enkephalin and ammonia on a tandem mass spectrometer lead to the formation of a proton-bound collision complex, which dissociates to form fragment ions of the peptide or by transferring a proton to ammonia (neutralization). The endothermicity of the proton transfer reaction suggests that the proton was initially located on the amide bonds of the peptide. From these studies we conclude that endothermic ion-molecule reactions may be effective for the fragmentation of large peptides and/or as the first step in a neutralization/chemical reionization scheme in which the reverse (exothermic) reaction is used for reprotonation.

INTRODUCTION

Over the past several years there has been an increasing interest in the use of tandem mass spectrometry (or MS/MS) for the structural analysis of complex biomolecules (1-3). In the most common experiment the first mass analyzer (MS1) is used to select ions (generally molecular ions) of a particular mass. These are then fragmented in a field-free region between the analyzers and enter the second mass analyzer (MS2) which is scanned to produce a *product ion* spectrum.

The advantages of MS/MS analysis for sequencing peptides (4) and carbohydrates (5) and for other structural problems have been described. The major advantage is, of course, the ability to select the molecular ion of a single analyte from a mixture and obtain its mass spectrum, for example a specific tryptic fragment in the presence of other peptides coeluting from a reversed-phase high-performance liquid chromatography separation. When *fast atom bombardment*, FAB (6), is used as the ionization technique, the normal mass spectra are characterized by an abundance of peaks arising from the liquid matrix, adduct ions, and a general *peak-at-every-mass* background (7). In many cases, several molecular ion species (e.g. MH⁺ and MNa⁺) are produced. Selection of a single molecular ion species in an MS/MS experiment produces a mass spectrum whose peaks are unambiguously attributable to the analyte and for which the signal/noise relative to background ions may be considerably improved.

A second advantage is that the fragmentation induced in the field-free region between the analyzers may be more extensive than and/or different from the occurring during ionization. Reinhold et al. (5) have noted that FAB mass spectra of carbohydrates generally produce little sequence information. Although chemical derivatization has been proposed to improve fragmentation (8), the problem can also be alleviated

by *collisionally induced dissociation* (CID). Biemann et al. (9) have described a number of side-chain fragmentation pathways for peptides, which occur in addition to the normal N- and C-terminal sequence ions (10). Fragment ions arising from side-chain cleavages can be used to distinguish residues, i.e. leucine and isoleucine, whose normal sequence ions would fall at the same mass. The relative abundances of such cleavages can be controlled somewhat by the beam energy in a collisionally induced dissociation analysis (9). Gross et al. (11) have reported an increase in *charge site remote fragmentation* in collisionally induced dissociation spectra and have demonstrated its usefulness in determining the location of double bonds in unsaturated fatty acyl moieties.

While electrons (12), photons (13), and solid targets (14) have all been used to induce fragmentation, collision of molecular ions with neutral atoms or molecules has been the most common approach (15). The energy required for dissociation of the ions may be derived from the electronic, vibrational, and relative translational energies (in the center of mass frame) of the colliding particles (16). The latter is related to the ion kinetic energy in the laboratory frame (E_{lab}) by

$$E_{cm} = (E_{lab}M_n)/(M_{ion} + M_n) \quad (1)$$

where M_n is the mass of the (target) neutral and M_{ion} is the mass of the (projectile) ion, assuming that the target atoms or molecules are at rest. When translational energies are very low, ion-molecule (or ion-atom) reactions occur leading to charge transfer, dissociation, and other chemical reactions. For reactions that are endothermic, there is a threshold for the appearance of ionic products on the kinetic energy scale from which information on the heats of reaction, heats of formation, proton affinities, and electronic states of reactants and products may be determined (17, 18). Many of these reactions occur via a long-lived collision complex between the projectile ion and the target molecule (17, 18). As the translational energy of the projectile ion is increased, the internal energy of the collision complex is also increased, and fragment ions are formed as several dissociation channels are opened up. The important aspect of ion-molecule reactions in this energy regime is that the relative translational energy is almost completely utilized in the formation of the collision complex and subsequent dissociative products and is the reason that the relative energy scale can be used to determine endothermicity. While such reactions have been studied extensively by physical chemists for determining heats of formation and proton affinities, they have not been utilized for the dissociation of large biomolecules.

At slightly higher translational energies, product ion formation follows more *direct* processes, where direct vibrational

coupling leads to fragmentation with very high (10–100 Å²) cross section (19). In the laboratory frame this generally corresponds to energies $E_{lab} = 10\text{--}100$ eV, the low energy regime for collisionally induced dissociation reactions common on triple quadrupole (3) and hybrid (e.g. BEQQ) (20) instruments.

Collisionally induced dissociation of high energy ions is generally carried out in the several kiloelectronvolt region (21). In this case, the interaction between the ion and the neutral target occurs in less than a vibrational period. The energy transferred to the ion is only a small fraction of the relative energy available and results in electronic excitation, energy equilibration according to the quasi-equilibrium theory (QET) and fragmentation patterns similar to those observed from (unimolecular) decomposition of ions formed by electron impact (22). High energy collisionally induced decomposition is most conveniently carried out on four sector instruments, i.e. two mass analyzers each composed of a double focusing electrostatic energy analyzer (E) and magnetic field (B) combination.

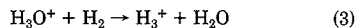
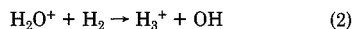
For both high- and low-energy CID, eq 1 presents a distinct problem for heavy ions. For example, the molecular ion (MH⁺) of bovine insulin of mass 5775 daltons, when accelerated from the ion source to an energy of 8 keV, collides with a helium atom with a relative energy of only 5.5 eV. Only a portion of this energy is imparted to the molecular ion, and must be distributed over a very large number of degrees of freedom. The situation would appear to be improved by the use of heavier targets such as neon or xenon. However, scattering losses in these cases would greatly reduce the transmission of the product ions formed (23). Thus, while Biemann has reported the sequencing by MS/MS of a tryptic peptide of 3 kDa mass (4), there are few, if any, examples of fragmentation of larger species.

Laser induced photodissociation (13), and solid targets (14) for which M_p would effectively be infinite and $E_{cm} = E_{lab}$, would seem to be solutions to the relative energy problem for high mass ions, and indeed they are currently under development. Alternatively, McLafferty et al. (24) have noted that structural information may also be obtained by reionizing the neutral products formed from unimolecular or collisionally induced dissociation. They have introduced a technique known as neutralization/reionization mass spectrometry (NRMS), in which a mass selected high-energy ion beam from MS1 is neutralized by collision with a metal vapor and then reionized and mass analyzed by MS2 (25). The collision chamber consists of two regions (26). Vaporized metals in the first chamber favor charge exchange over collisionally activated dissociation. Reionization by collision with O₂ is the most efficient (27, 28) of the target gases tested and occurs in the second collision chamber, producing fragment ions as well for structural information. Both charge transfer processes (neutralization and reionization) take place at high kinetic energy and involve electron transfer. In McLafferty's experiments, mass analyses in MS2 were performed with an electric sector only.

We suggest that ion-molecule reactions of low endothermicity between a protonated molecular ion and a suitable reactive target molecule would also offer a solution to the relative energy problem for high mass ions. The low relative energy required would place such reactions within range of the laboratory energy scale for even large molecular ions. The long-lived collision complexes between the projectile ion and the target molecule would lead to efficient fragmentation as well as neutralization, which could be utilized for reionization studies.

We have noted that the neutralization/reionization scheme of McLafferty et al. (25) involves electron transfer reactions

to neutralize and re-form radical ion species, while the molecular ions of complex biomolecules produced by desorption techniques are generally protonated, even electron species. Thus, endothermic reactions, such as the proton transfer reactions



which have been used previously by one of us to determine proton affinities (17, 18), have been of interest to us for some time as a possible means for neutralizing protonated molecular ions, which would then be followed by reionization. Both reactions proceed via a collision complex near threshold and by direct (stripping) mechanism at higher energies. The abrupt decay in H₃⁺ intensity in reaction 3 indicated that the proton-bound complex between H₂O and H₂ leads to a number of other fragmentation pathways. Thus we became interested in whether the formation of proton-bound complexes between protonated molecular ions and target molecules of slightly lower proton affinity would, in addition to neutralization, lead to an increase in ion fragmentation. The reaction



has been studied by Yamdagni and Kebarle (29) and is slightly exothermic

$$PA(NH_3) - PA(CH_3CONH_3^+) = \\ 207 \text{ kcal/mol} - 210.4 \text{ kcal/mol} = -3.4 \text{ kcal/mol}$$

Assuming that protons are attached to the amide bonds in a peptide and that the proton affinity for attachment at that site is similar to that of acetamide, the (reverse) reaction between a protonated peptide and ammonia should be barely endothermic.

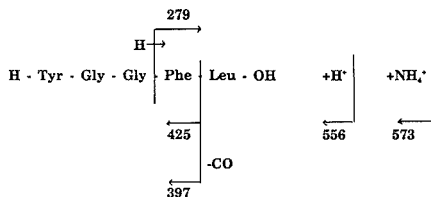
Thus, in this study, we followed the formation of the proton-bound collision complex, fragmentation, and neutralization that takes place in the reaction between protonated leucine-enkephalin and ammonia near threshold and at higher translational energies where direct processes occur. We increased the target gas pressure to promote multiple collisions and compared the results with the reaction of starchose with ammonia (for which proton transfer is exothermic). From these preliminary studies, we draw some conclusions on the value of endothermic and reactive collisions for inducing fragmentation and propose a scheme, known as neutralization/chemical reionization mass spectrometry (NCRMS) which can be carried out in a single collision cell which is also a high-pressure chemical ionization (CI) source.

EXPERIMENTAL SECTION

Product ion mass spectra were obtained for protonated leucine-enkephalin and starchose using ammonia as the collision gas. Our initial experiments were carried out on a Kratos (Ramsey, NJ) MS80RFQQ mass spectrometer, a hybrid instrument with an EBQQ configuration. Protonated molecular ions were formed by fast atom bombardment and mass selected by MS1 (EB). The quadrupole mass analyzer (Q2) was tuned to the molecular ion at a collision energy of 20 eV and the ammonia gas pressure in the collision chamber (Q1) was adjusted until the beam was attenuated by about 50%. Product ion spectra were then obtained at 20, 40, 60, 20, and 10 eV, scanning a mass range which would also include adduct ions formed between the protonated molecular ion and ammonia. The instrument was then returned to 20 eV and product ion spectra was obtained at 20, 10, 6, and 4 eV. The relative intensities in the spectra obtained at the overlapping points at 10 and 20 eV agreed to within 2%.

Our most recent experiments employed a JEOL (Tokyo, Japan) Model HX110/HX110 four-sector (EBEB configuration) tandem mass spectrometer. Protonated molecular ions were produced by fast atom bombardment, accelerated to 10 keV and mass selected by MS1. The collision cell voltage was placed at 10 kV - V_{lab} , where V_{lab} is the collision voltage which was varied from

Chart I



0 to 80 V, measured as the potential difference between the collision cell and the ion source. Since the product ions of different masses are reaccelerated to (approximately) the same kinetic energy, the product ion spectra were obtained by scanning only the magnetic field, over a range which included the mass of the major fragment ions and the collision complex. (Strictly speaking, the electric field sector should be scanned as well. However, when the collision cell voltage is nearly equal to the ion source voltage, scanning the magnetic field alone has no appreciable adverse effects on the transmission of fragment ions of nearly equal energy and is operationally simpler.) A major advantage of this instrument is the much higher ion transmission at very low energies. This enabled the use of higher collision gas pressures to attenuate the protonated molecular ion beam by 80 and 99.5% in order to promote multiple collisions.

RESULTS AND DISCUSSION

Chart I shows the ions appearing in the product ion spectra of protonated leucine-enkephalin and ammonia gas that were followed in this study. These include the protonated molecular ion (556), the $M + NH_4^+$ ion (573), the C-terminal sequence ions (425 and 397), and the N-terminal sequence ion (279).

Collisions at 50% Attenuation. The results for the product ion spectra obtained on the hybrid instrument are plotted as a function of laboratory energy in Figure 1. At all collision energies, the molecular ion (MH^+) was the most abundant species in the mass range examined. In Figure 1a, the fragment ions (279, 397, and 425) resulting from direct, low-energy collisionally induced decomposition are observed in the region from 10 to 60 eV. Below 10 eV, however, there is a large increase in the relative abundances of these fragment ions, which reaches a maximum around 8 eV (0.24 eV in the CM frame). At the same time, the proton bound complex ($M + NH_4^+$) shows a similar maximum at 6 eV (0.18 eV in the CM frame). Thus, the results exhibit a behavior typical of endothermic ion-molecule reactions which proceed via a collision complex. In this case the collision complex itself can be recorded. It is stable at low energies but is not formed at energies where direct processes occur. The ion-molecule reaction products, in this case fragment ions of leucine enkephalin, reach their maximum intensities at slightly higher energies than the collision complex as the internal energy of the complex is increased. Figure 1b shows the strong attenuation of the MH^+ ion in the region for which ion-molecule reactions occur.

In contrast, the reaction between protonated stachyose and ammonia (Figure 2) is clearly exothermic. The $M + NH_4^+$ ion and an ammoniated fragment ion ($505 + NH_4^+$) are the most abundant species at the lowest beam energies studied. As they decrease at higher beam energies, the relative abundance of the MH^+ ion increases, as do two fragment ions (505 and 487) formed by direct processes.

Ion transmission and signal/noise is poor at the lowest beam energies, so that it was not possible to accurately determine thresholds for the reactions between leucine-enkephalin and ammonia. Alexander and Boyd (30) have noted that for reactions occurring in an rf-only quadrupole cell, the variations in intensity vs E_{lab} must be interpreted with some caution in view of the strong spatial focusing effects on ion transmission,

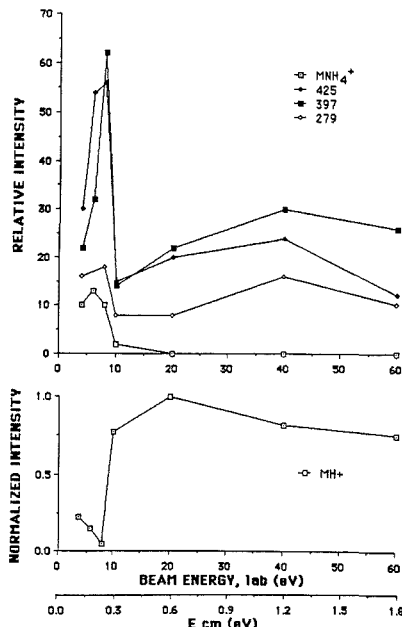


Figure 1. Reaction of protonated leucine-enkephalin with ammonia in the collision chamber of an EBQQ tandem hybrid mass spectrometer: (A) intensity of fragment ions of masses 279, 397, and 425 amu and the ammonium adduct ion relative to the molecular ion as a function of the ion kinetic energy, E_{lab} ; (B) intensity of the molecular ion normalized to its intensity observed at 20 eV as a function of ion kinetic energy. For convenience, the relative energy scale, E_{cm} , is also included.

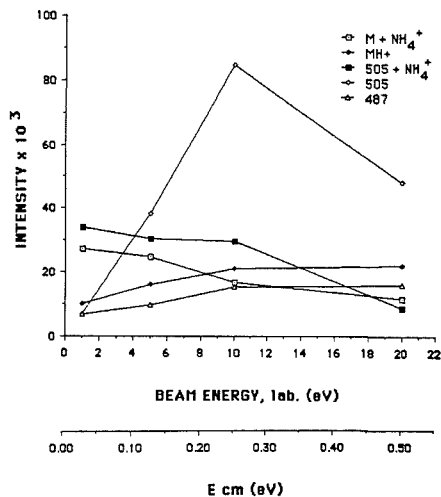


Figure 2. Intensities of the product ions from the reaction of protonated stachyose with ammonia in the collision chamber of an EBQQ tandem hybrid mass spectrometer as a function of the ion kinetic energy, E_{lab} , and relative energy, E_{cm} , in the center of mass frame.

particularly for a configuration in which a sector mass analyzer (B, BE or EB) is coupled to a quadrupole collision chamber. In addition, ions entering a quadrupole collision chamber undergo an oscillatory motion induced by the rf-field, so that

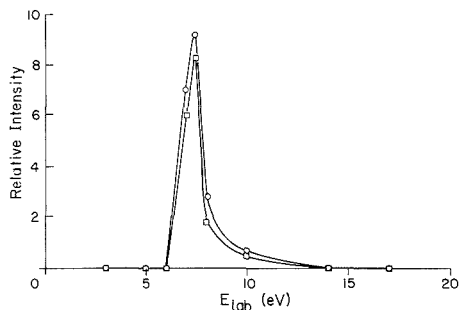


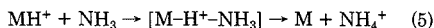
Figure 3. Relative intensities of the proton bound complex (O) and ammonium ion (□) vs ion kinetic energy for the reaction of protonated leucine-enkephalin with ammonia carried out at 80% attenuation of the molecular ion in the collision chamber of a four sector mass spectrometer.

their transverse velocities become significant as one approaches zero beam energy and ion-molecule reactions can be observed below the expected threshold. Errors in threshold may also be brought about by *Doppler broadening*, i.e. an increase in the low energy tail near the reaction threshold due to the thermal velocity distributions of reactant ions and neutrals (31). This effect, in fact, becomes more pronounced (in the laboratory frame) in cases in which a heavy projectile collides with a relatively light target (18). Product ions may also be observed below the expected threshold for reactions in which the projectile ion contains appreciable *precollision* internal energy (30). In reaction 3, for example, a distribution of H_3O^+ ions formed in the ground and first excited (triplet) states resulted in product ion intensities vs beam energy which reflected both endothermic and exothermic processes (18).

Thus, in this study, it is encouraging that endothermic behavior is observed for the reaction between Leu-enkephalin and ammonia, that it occurs at relative energies consistent with the 0.15 eV endothermicity predicted from the results of Kebarle (29), and that there is a dramatic qualitative difference between that reaction and that of stachyose with ammonia.

Collisions at Higher Attenuations. The four-sector tandem mass spectrometer enables us to overcome some of the problems encountered in studying these reactions at very low beam energies. The high ion transmission permitted measurements with good signal/noise down to beam energies of 1 eV, which could be maintained at collision chamber pressures for which the precursor ion was attenuated up to 99.5%.

Figure 3 shows the results for the proton transfer ion-molecule reaction



when the collision gas pressure has been adjusted to attenuate the MH^+ ion by 80% at 20 eV. The collision complex and the NH_4^+ product ion show very similar behavior, suggesting that redissociation of the complex with the proton attached to ammonia occurs with little excess energy. The threshold for the proton transfer reaction is observed at 6 eV, or about 0.18 eV in the CM frame. At higher energies, other dissociation channels are available as shown in Figure 4. The picture is more detailed than that obtained on the hybrid instrument and suggests that the fragment ion at 279 is formed with less excess internal energy than the ions at 425 and 397 (which differ by the loss of a neutral CO). At higher energies, direct, collisionally induced decomposition is observed.

When the pressure of the collision gas is increased so as to attenuate the protonated molecular ion by 99.5%, several

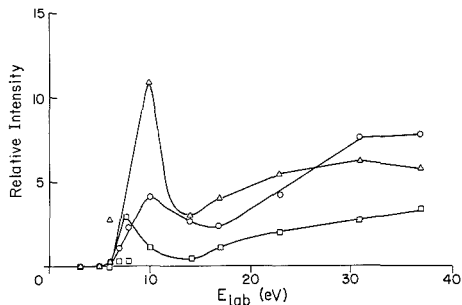


Figure 4. Relative intensities of fragment product ions vs ion kinetic energy for the reaction of protonated leucine-enkephalin with ammonia carried out at 80% attenuation of the molecular ion in the collision chamber of a four sector mass spectrometer (Δ , 425; O, 397; \square , 279 m/z).

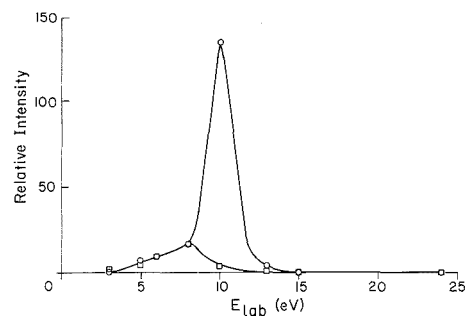


Figure 5. Relative intensities of the proton bound complex (O) and ammonium ion (□) vs ion kinetic energy for the reaction of protonated leucine-enkephalin with ammonia carried out at 99.5% attenuation of the molecular ion in the collision chamber of a four sector mass spectrometer.

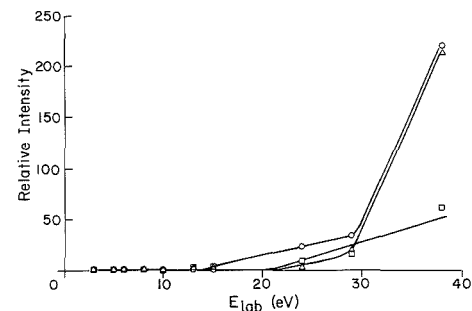


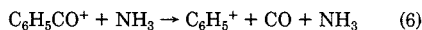
Figure 6. Relative intensities of fragment product ions vs ion kinetic energy for the reaction of protonated leucine-enkephalin with ammonia carried out at 99.5% attenuation of the molecular ion in the collision chamber of a four sector mass spectrometer (\square , 425; O, 397; Δ , 279 m/z).

interesting things happen, which can most likely be attributed to an increase in multiple collisions. Figure 5 shows that the $M + NH_4^+$ ion continues to increase in relative intensity reaching a value at 10 eV which exceeds that of the MH^+ ion. This may result from collisions of the protonated molecular ion, which reduce its energy prior to the formation of the collision complex, or collisions occurring after formation of the complex, which stabilize it and reduce the possibilities for fragmentation. The proton transfer to ammonia is also con-

siderably increased, as reflected in the relative intensity of the NH_4^+ ion. For both ions, the energy range for which they can be observed has been broadened. In Figure 6, the formation of fragments from the collision complex has been eliminated, and only those formed by direct processes at higher energies are observed. Thus, it would appear that multiple collisions at low energies favor neutralization (proton transfer) and stable complex formation over fragmentation.

CONCLUSIONS

MS/MS experiments in which ammonia was used as the target gas have been reported by a number of other laboratories (32, 33). White et al. (32) investigated the products formed from the reaction of benzoyl cation with NH_3 . They observed products for which the reaction is exothermic, e.g.



and may proceed via a collision complex; but they did not observe a reaction threshold or a dramatic decrease in molecular ion abundance indicative of extensive neutralization. (In this case, charge rather than proton transfer would be involved.) In contrast, Schmit et al. (33) observed neutralization of protonated molecular ions of several compounds by proton transfer to ammonia. Formation of this proton-bound collision complex was barely endothermic with a maximum around 0.02 eV (relative energy), while NH_4^+ ion formation showed a steep maximum at 0.05 eV and decreased at slightly higher beam energies. In some cases the NH_4^+ ion current rose again at still higher beam energies reflecting proton transfer (neutralization) reactions by more direct processes.

These experiments, as well as our own suggest at least two strategies for the MS/MS analysis of large molecules for which the low relative energy in direct (both low- and high-energy CID) processes is a problem.

The first strategy exploits the efficient fragmentation resulting from endothermic ion-molecule reactions between a protonated peptide and ammonia. In addition to selecting the molecular ion in MS1, one would also select a collision voltage. For leucine enkephalin, we have noted that the fragment ion signal is maximized at 10 eV. For insulin, it would occur at approximately 100 eV. Interestingly, the latter is an energy though not a mass range suitable for triple quadrupole instruments. Thus, it would seem that there is a need for more studies of low-energy (and reactive) collisions of large molecules on sector tandem instruments.

Our studies of low-energy collisions are based upon an assumption that the proton is attached to the amide bond and, in addition, that the endothermicity can be estimated from the exothermicity of the reverse reaction studied by Kebarle (29). It is likely that peptides containing more basic residues will exhibit greater endothermicity toward proton transfer, and our future studies will focus on peptides containing one or more arginine and/or lysine residues. At the same time, our threshold results appear to support these assumptions and suggest that similar studies could be used to locate the sites for proton attachment.

The second strategy involves development of conditions that promote neutralization by proton transfer. As a first step in a neutralization/reionization scheme, endothermic proton transfer reactions could provide several advantages over the scheme proposed by McLafferty (25). First, proton transfer reactions would be a more logical approach than charge (electron) transfer for the protonated, even electron molecular ions produced by desorption techniques. Secondly, an en-

dothermic reaction would permit neutralization and reionization to take place in the same collision cell. An ion entering the cell with high kinetic energy would undergo multiple collisions until its energy was reduced to permit transfer of a proton in an endothermic reaction. If the cell was also a CI source, it would then reionize after further collisions, by the reverse, exothermic reaction. We propose the name neutralization/chemical reionization mass spectrometry (NCRMS) for this technique. A suitable collision cell, known as CI2, has been constructed and is currently being tested in our laboratory.

LITERATURE CITED

- (1) Busch, K. L.; Cooks, R. G. *Anal. Chem.* **1983**, *55*, 38A.
- (2) McLafferty, F. W. *Science* **1981**, *241*, 260-267.
- (3) Yost, R. A.; Enke, C. G. *J. Am. Chem. Soc.* **1978**, *100*, 2274.
- (4) Blumann, K. *Anal. Chem.* **1986**, *58*, 1289A-1300A.
- (5) Carr, S. A.; Reinhold, V. N.; Green, B. N.; Hass, J. R. *Biomed. Environ. Mass Spectrom.* **1985**, *12*, 288.
- (6) Barber, M.; Bordoli, R. S.; Sedgwick, R. D.; Tyler, A. N., *J. Chem. Soc., Chem. Commun.* **1981**, 325-326.
- (7) Fenselau, C.; Cotter, R. J. *Chem. Rev.* **1987**, *87*, 501-512.
- (8) Dell, A.; Thomas-Oates, J. E. In *Analysis of Carbohydrates by GLC and MS*; Biermann, C. J., McGinnis, G. D., Eds.; CRC Press: Boca Raton, FL, **1988**; pp 217-236.
- (9) Johnson, R. S.; Martin, S. A.; Blumann, K. *Int. J. Mass Spectrom. Ion Processes* **1988**, *86*, 137-154.
- (10) Roepstorff, P.; Fohlman, J. *Biomed. Mass Spectrom.* **1984**, *11*, 601.
- (11) Adams, J.; Gross, M. L. *J. Am. Chem. Soc.* **1986**, *108*, 6915-6921.
- (12) Cody, R. B.; Freiser, B. S. *Anal. Chem.* **1979**, *51*, 547.
- (13) Baykut, G.; Watson, C. H.; Weller, R. R.; Eyley, J. R. *J. Am. Chem. Soc.* **1985**, *107*, 8036-8042.
- (14) Mabud, Md. A.; Dekrey, M. J.; Cooks, R. G. *Int. J. Mass Spectrom. Ion Processes* **1985**, *67*, 285-294.
- (15) *Collision Spectroscopy*; Cooks, R. G., Ed.; Plenum: New York, **1978**.
- (16) Futrell, J. H.; Tiernan, T. O. In *Ion-Molecule Reactions*; Franklin, J. L., Ed.; Plenum: New York, **1972**; Vol. 2, pp 520-534.
- (17) Cotter, R. J.; Rozett, R. W.; Koski, W. S. *J. Chem. Phys.* **1972**, *57*, 4100-4103.
- (18) Cotter, R. J.; Koski, W. S. *J. Chem. Phys.* **1973**, *59*, 784-787.
- (19) Dawson, P. H.; Douglas, D. J. In *Tandem Mass Spectrometry*; McLafferty, F. W., Ed.; John Wiley: New York, **1983**; pp 125-148.
- (20) Glish, G. L.; McLuckey, S. A.; Ridley, E. Y.; Cooks, R. G. *Int. J. Mass Spectrom. Ion Phys.* **1982**, *41*, 157-177.
- (21) Todd, P. J.; McLafferty, F. W. In *Tandem Mass Spectrometry*; McLafferty, F. W., Ed.; John Wiley: New York, **1983**; pp 149-174.
- (22) Levens, K.; Schwartz, H. *Mass Spectrom. Rev.* **1983**, *83*, 77-148.
- (23) Laramée, J. A.; Cameron, D.; Cooks, R. G. *J. Am. Chem. Soc.* **1981**, *103*, 12-17.
- (24) McLafferty, F. W.; Todd, P. J.; McGilvery, D. C.; Baldwin, M. A. *J. Am. Chem. Soc.* **1980**, *102*, 3360-3363.
- (25) Danis, P. O.; Wesdemiotis, C.; McLafferty, F. W. *J. Am. Chem. Soc.* **1983**, *105*, 7454-7456.
- (26) Danis, P. O.; Feng, R.; McLafferty, F. W. *Anal. Chem.* **1986**, *58*, 348-354.
- (27) Gellene, G. I.; Porter, R. F. *Int. J. Mass Spectrom. Ion Processes* **1985**, *64*, 55-66.
- (28) Danis, P. O.; Feng, R.; McLafferty, F. W. *Anal. Chem.* **1986**, *58*, 355-358.
- (29) Yamdagni, R.; Kebarle, P. *J. Am. Chem. Soc.* **1973**, *95*, 3504-3510.
- (30) Alexander, A. J.; Boyd, R. K. *Int. J. Mass Spectrom. Ion Processes* **1989**, *90*, 211-240.
- (31) Chantry, P. J. *J. Chem. Phys.* **1971**, *55*, 2746.
- (32) White, E. L.; Tabet, J.-C.; Bursley, M. M. *Org. Mass Spectrom.* **1987**, *22*, 132-139.
- (33) Schmit, J.-P.; Beaudet, S.; Brisson, A. *Org. Mass Spectrom.* **1986**, *21*, 493-498.

RECEIVED for review July 24, 1989. Accepted October 19, 1989. Mass spectral measurements were carried out at Boehringer-Ingelheim (MS80RFQQ) and the Structural Biochemistry Center at the University of Maryland Baltimore County (HX110/HX110), an NSF supported Biological Center. Research was supported in part by Grant DIR 8714238 from the National Science Foundation. The authors gratefully acknowledge the support of Dr. Frank Hatch for research carried out at Boehringer-Ingelheim. This work was presented in part at the Annual Meeting of the Federation of Analytical Chemists and Spectroscopy Societies (FACSS), October 1986.

Simultaneous Enhancement of Separation Selectivity and Solvent Strength in Reversed-Phase Liquid Chromatography Using Micelles in Hydro-Organic Solvents

Morteza G. Khaledi,* Joost K. Strasters, Andrew H. Rodgers,¹ and Emelita D. Breyer

Department of Chemistry, North Carolina State University, P.O. Box 8204, Raleigh, North Carolina 27695-8204

The role of micelles and organic solvents as the modifiers of the aqueous mobile phase in reversed-phase liquid chromatography (RPLC) in controlling retention and selectivity is discussed. Elution strength increases in RPLC with an increase in organic solvent or micelle concentration. Simultaneous enhancement of separation selectivity with elution strength in the hybrid eluents of water-organic solvent-micelles was observed. This selectivity enhancement occurs systematically, i.e. peak separation increases monotonically with volume fraction of organic solvent added to micellar eluent, and is observed for a large number of ionic and non-ionic compounds with different functional groups and for two surfactants (anionic and cationic). For two test mixtures, 13 amino acids/peptides and 15 phenols, it is shown that a better separation and shorter analysis time are observed at stronger hybrid eluents. This selectivity enhancement can be attributed to the competing partitioning equilibria in micellar LC systems and/or to the unique characteristics of micelles to compartmentalize solutes and organic solvents.

INTRODUCTION

The popularity of micellar liquid chromatography (MLC) has increased in the past few years due to several unique advantages such as capability of simultaneous separation of ionic and nonionic compounds, rapid gradient capability, possibility of direct injection of physiological fluids, gradient compatibility with electrochemical detectors, enhanced luminescence detection, etc. (1-6). These capabilities are particularly advantageous in bioanalytical applications (5).

One of the noticeable characteristics of MLC from the very early publications has been the unique separation selectivity of micellar mobile phases. Frequent elution reversals as a result of changes in micelle concentration or surfactant head group have been the indicators of this selectivity (7, 8).

Poor chromatographic efficiency is the most important disadvantage of MLC. Several workers have examined the reason(s) behind the poor efficiency and the methods for improving it, especially the influence of adding an organic solvent to micellar eluents (9-12). Dorsey et al. suggested the addition of a small concentration of propanol (about 3%) and operating at high temperatures to improve the chromatographic efficiency (9). Other workers, however, argued that the addition of an organic solvent might reduce the role of micelles and would create a system that is closer to hydro-organic eluents (10). Surprisingly, the effect of organic solvent on the chromatographic selectivity has largely been ignored.

An extensive investigation has been initiated in our laboratory in order to better understand the effect of adding organic solvents to micelles for controlling retention and selectivity in RPLC and how it compares with the hydro-organic

RPLC system. In previous publications, we reported that the retention behavior in MLC can be quite different from that in hydro-organic RPLC despite the fact that both systems are considered to be reversed-phase LC as hydrophobic interactions are the main driving force for retention in both systems (13, 14). It was shown that adding an organic solvent to micellar eluents would *not* create a hydro-organic system. In fact retention characteristics with a ternary mobile phase of organic solvent-water-micelles was similar to that in a purely aqueous micellar eluent. It was concluded that in these mobile phases, it is micelles that influence the role of an organic cosolvent in the mobile phase. The "anomalous" behavior in MLC was attributed to different factors such as the heterogeneous nature of micelles that provide different microenvironment polarity for different compounds in a given mobile phase composition, the organizing ability of micelles that can encompass compounds (solutes and organic cosolvent), and the existence of two competing equilibria that influence selectivity (13, 14).

It was observed that methylene selectivity did not change upon addition of propanol to micellar eluents, i.e. the solvent strength was increased without sacrificing selectivity. This is in contrast to normal behavior in a RPLC system as solvent strength and selectivity are generally inversely related. In fact an eluotropic solvent strength scale for RPLC solvents is based on the reciprocal relationship between solvent strength and methylene selectivity (14).

In this paper we report some preliminary results on the effect of adding organic solvents to micellar eluents on functional group selectivity as well as separation selectivity between any two adjacent peaks in a mixture. The term "hybrid" is used for the ternary eluents of water-organic solvent-micelles throughout the text. Surprisingly, we often observed an increase in selectivity with the addition of an organic solvent to a micellar eluent, i.e. with increasing eluent strength.

EXPERIMENTAL SECTION

Apparatus. The HPLC system was either a Rainin gradient chromatograph consisting of three Rainin Rabbit pumps and an ISCO UV-vis, 4V variable-wavelength detector for substituted benzenes or a Waters Associates (Milford, MA) liquid chromatograph comprised of a 6000A and M45 pumps, an M680 solvent programmer, and a Varian UV 50 variable wavelength detector set at 200 nm for peptide experiments. The analytical columns were Altex Octyl Ultrasphere (15 × 0.46 cm) for substituted benzenes and a C-18 LichroCART (12.5 × 0.46 cm, $V_M = 0.67$ ml) (EM Science) for peptides. The void volumes of the columns were measured from the injection point of water samples and the first deviation of the base line. A silica precolumn and a dry-packed C-18 column were employed to saturate the mobile phase with silicates and to protect the analytical column. The silica precolumn, the guard column, and the analytical column were water jacketed and thermostated at 38 °C with a Hauk (Karlsruhe, GFR) circulating bath.

Reagents. Stock solutions of sodium dodecyl sulfate, SDS (Polyscience), and myristyltrimethylammonium bromide, C_{14} TAB (Aldrich), were prepared in doubly distilled, deionized water and

¹ Present address: University of New Orleans, Department of Chemistry, New Orleans, LA 70148.

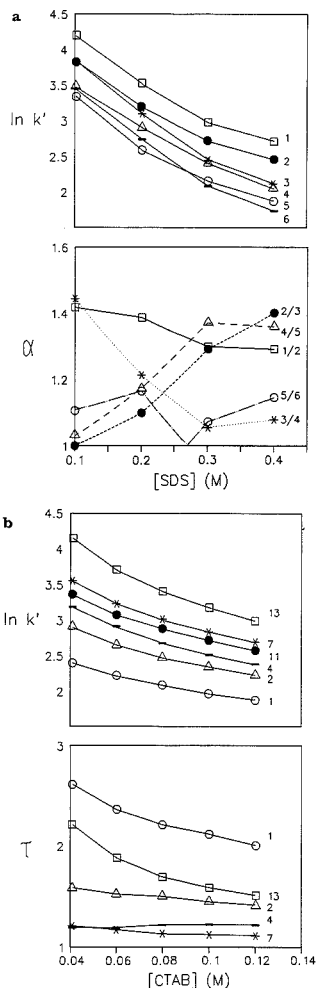


Figure 1. Retention and (group) selectivity as a function of the concentration of surfactant in the micellar mobile phase (experimental details in the text): (a) retention ($\ln k'$) and selectivity (α) of a set of peptides and amino acids with sodium dodecyl sulfate (SDS) as surfactant; identity of amino acids and peptides is by a single letter code (1, LW; 2, L; 3, R; 4, M; 5, LY; 6, GL); (b) retention ($\ln k'$) and group selectivity with respect to benzene (τ) of a set of alkyl benzenes with myristyltrimethylammonium bromide (CTAB) as surfactant; numbers refer to those used in Table I.

were filtered through a 0.45- μm Nylon-66 membrane filter (Rainin Instruments). Monosubstituted benzenes were mostly obtained from Aldrich, the peptides with 99% purity were supplied by Sigma.

RESULTS AND DISCUSSIONS

Micelle concentration and volume fraction of organic solvent in hybrid eluents can significantly influence retention and selectivity.

Effect of Micelle Concentration. Figure 1 illustrates the general behavior for zwitterionic compounds (amino acids and small peptides) and nonionic aromatic compounds. As shown in Figure 1a convergence, divergence, and reversal of the peaks can occur for the zwitterionic compounds as a result of an increase in micelle concentration, while for the aromatic

compounds mainly peak convergence is observed (Figure 1b).

In a micellar RPLC system, retention and selectivity are controlled by three competing equilibria, namely partitioning (or binding) from bulk solvent to micelles or alkyl-bonded stationary phase or a direct transfer from micelles to stationary phase. Retention in micellar systems can be described as

$$k' = (P_{sw}\Phi) / \{K_{mw}[M] + 1\} \quad (1)$$

where $[M]$ is micelle concentration, Φ is phase ratio, K_{mw} is the binding constant of solute to micelles, and P_{sw} is the partition coefficient of compound from mobile phase into stationary phase (1).

According to eq 1, eluent strength increases with increasing micelle concentration (as long as a solute interacts with micelles). It has been shown that for ionic compounds under certain mobile/stationary phase conditions, retention might increase with micelle concentration due to electrostatic repulsion into the stationary phase; however, this is rather an exception in MLC and not the rule (8).

Selectivity might increase or decrease with micelle concentration depending on the type of compounds and the type of surfactants. The related equation for selectivity can easily be derived from eq 1 (14)

$$\alpha = \frac{(\alpha_{sw})\{[M] + 1/K_{mw,1}\}}{(\alpha_{mw})\{[M] + 1/K_{mw,2}\}} \quad (2)$$

where α_{sw} is the stationary phase partitioning selectivity ($P_{sw,2}/P_{sw,1}$) and α_{mw} is the selectivity of binding to (or partitioning into) micelles ($K_{mw,2}/K_{mw,1}$).

Differentiation of eq 2 results in

$$\frac{d\alpha}{d[M]} = \frac{\alpha_{sw}}{\alpha_{mw}} \left(\frac{1}{K_{mw,2}} - \frac{1}{K_{mw,1}} \right) \left/ \left\{ [M] + \frac{1}{K_{mw,2}} \right\}^2 \right. \quad (3)$$

Selectivity enhancement will be observed when $d(\alpha)/d[M] > 0$. Since α_{sw} and α_{mw} are both positive, it follows from eq 3 that $K_{mw,2} < K_{mw,1}$ to observe an increase in selectivity. However, since α is by definition larger than 1, this must be combined with the requirement

$$\frac{P_{sw,2}}{K_{mw,2}[M] + 1} > \frac{P_{sw,1}}{K_{mw,1}[M] + 1}$$

For instance, this situation will occur when one of the two compounds selectively interacts with the ionic head group of surfactants in micelles and/or with those adsorbed on the stationary phase. This can be seen for zwitterionic compounds in Figure 1a. At pH 2.5 the amino acids and peptides are positively charged and therefore can have electrostatic attraction with the anionic SDS surfactant. Obviously, hydrophobic interactions can also play an important role in influencing retention. The contribution of electrostatic and hydrophobic interactions to retention would not be the same for different zwitterionic compounds and is a function of their structural properties. Due to different types of interactions and the competing equilibria in MLC, one can expect any form of the selectivity behavior (i.e. peak convergence, divergence, and crossover) with changes in micelle concentration. Retention behavior and selectivity of zwitterionic compounds in MLC will be published elsewhere (15).

However, for a large group of compounds (especially nonionics), partitioning into the micelles and into the alkyl-bonded phase, as expressed by K_{mw} and P_{sw} , is directly related. This is mainly because hydrophobic interactions play the upper role in both cases. In addition, the alkyl-bonded phase is modified with surfactant monomers which makes the environment of the micelles closely related to that of the stationary phase. In fact for a set of 16 monosubstituted benzenes, we observed a linear relationship between k_{mw} and P_{sw} ($P_{sw} =$

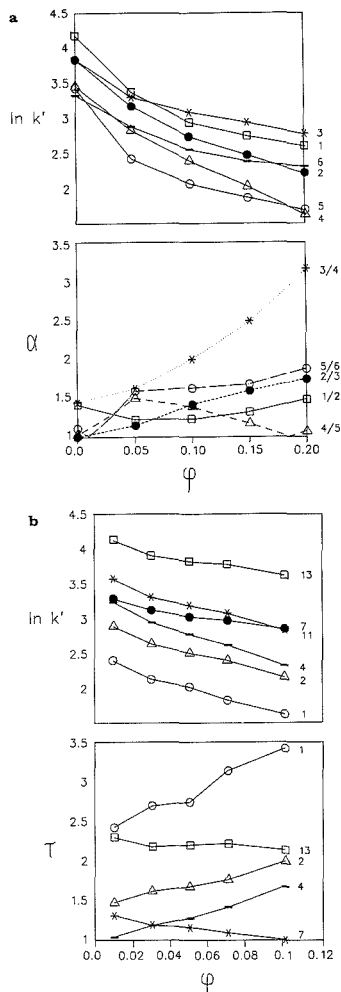


Figure 2. Retention and (group) selectivity as a function of the fraction of organic modifier (ϕ) in a hybrid mobile phase: (a) retention ($\ln k'$) and selectivity (α) of a set of peptides and amino acids in a mobile phase containing 0.1 M SDS and varying amounts of 2-propanol, identity of components is given in Figure 1; (b) retention ($\ln k'$) and group selectivity with respect to benzene (τ) of a set of alkyl benzenes in a mobile phase containing 0.04 M CTAB and varying amounts of 2-propanol; numbers refer to those used in Table I.

$-39.6 + 2.90K_{mw}$, $n = 16$, $R^2 = 0.997$). In such cases, a decrease in functional group selectivity τ will be observed with increasing micelle concentration (Figure 1b) where τ is defined as the ratio of capacity factors of a compound with a substituent to that of a parent compound, e.g. $k'(Bz-R)/k'(Bz)$ for substituted benzenes. Note that $\ln \tau$ represents the free energy of transfer of a functional group from mobile to stationary phase. Information about τ is valuable in structure-retention relationship and retention mechanism studies (16).

Figure 1a illustrates elution reversal due to a change in micelle concentration. It should be noted that the frequently observed phenomenon of elution order reversal in MLC as a result of a change in micelle concentration does not necessarily translate into a systematic enhancement. Although elution

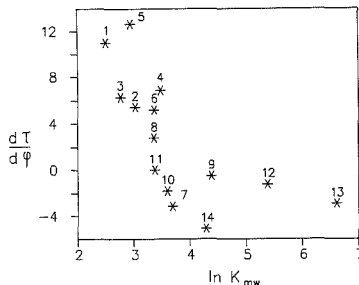


Figure 3. Average change in the group selectivity (with respect to benzene) with varying fraction of 2-propanol, $d(\tau)/d(\phi)$, as a function of the partition coefficient between micelles and bulk mobile phase, K_{mw} , of a set of alkyl benzenes. Components are identified according to Table I.

order reversal is indicative of a unique separation mechanism in MLC and its selectivity, peak crossing for a few compounds in a complex mixture does not necessarily mean an improvement in the overall separation. It is interesting to note that peak crossing is often (and mistakenly) considered as a proof of "enhanced selectivity of MLC" in the literature.

Effect of ϕ_{org} in Hybrid Eluents. Figure 2 shows the variation of retention of zwitterionic (amino acids, peptides) and nonionic compounds (substituted benzenes) with the volume fraction of 2-propanol added to micellar eluents. The eluent strength increases with increasing organic modifier concentration which results in a decrease in retention. The linear fit of $\ln k'$ vs volume fraction of 2-propanol (Figure 2b) gives a fairly high correlation ($r^2 = 0.90-0.99$) even though the experiments were performed in water-rich eluents (3-10% propanol). Note that for conventional hydro-organic mobile phases at low concentrations of organic solvents (<10%), $\ln k'$ vs ϕ_{org} plot is usually not linear and sometimes not even quadratic (17). Some corresponding selectivities for amino acids/peptides and the group selectivity for the aromatic compounds are shown in parts a and b of Figure 2, respectively. As shown, the selectivity for a group of peptides and amino acids systematically increases with increasing propanol concentration (i.e. increasing eluent strength). A similar behavior is observed for some of the substituted benzenes while for others functional group selectivity decreases with increasing solvent strength. Figure 3 shows how the slope of τ vs ϕ_{org} changes as a function of micelle-water binding constant K_{mw} for substituted benzenes. This plot suggests that the largest positive changes of selectivity as a function of ϕ_{org} (i.e. selectivity enhancement) are observed for more hydrophilic or less retained compounds (as compared to benzene) while for compounds that are more hydrophobic (or longer retained) than benzene selectivity actually decreases with increasing solvent strength. It is important to note that such a conclusion could not be made for other groups of compounds such as peptides or phenols (18).

The reason can be sought in the three competing equilibria which influence selectivity in MLC as well as the capability of micelles to compartmentalize compounds. The selectivity enhancement was observed for a wide range of ionic and nonionic compounds with various functional groups and for both anionic and cationic surfactants. The addition of an organic solvent would change certain micellar properties (such as critical micelle concentration, aggregation number, etc.) which influence the retention behavior of ionic compounds. However, the observed changes in retention and selectivity in hybrid systems are too large to be explained in terms of changes in micellar properties. This is especially true for nonionic and hydrophobic compounds.

From eq 2, it can be seen that the chromatographic selectivity is dependent upon the partitioning of compounds into stationary phase and micelles. Addition of organic modifier would change the microenvironment of both alkyl bonded stationary phase and micelles due to intercalation of organic solvent. The exact behavior of chromatographic selectivity as a function of fraction of an organic solvent would then depend on how α_{mw} and α_{sw} would change with the type and concentration of organic solvent. A study is under way to examine this effect.

Micelles are microscopically heterogeneous media which provide various microenvironment polarities for various compounds in a given mobile phase composition. They can localize (or compartmentalize) solutes (or organic additives in the mobile phase) in a microenvironment that is different from bulk solvent (19). This can have a direct influence on retention behavior of compounds in MLC which can be distinctly different from that of hydro-organic eluents in RPLC. Retention represents free energy of transfer of a solute or a functional group from mobile phase to stationary phase and is highly sensitive to the microenvironment polarities in the two phases. Consequently, it is not surprising that "peculiar" behavior might be observed as different solutes experience different polarities in their immediate vicinities in a given mobile/stationary phases composition (13, 14). This can be seen in Figure 4a as carbonyl-group selectivity, $\alpha(-CO)$, changes with the hydrophobicity (or carbon number in the side chain) of two homologous pairs for a micellar eluent while it is independent of solute type for a hydro-organic eluent. This can be attributed to the fact that the more hydrophobic pairs are located in a more hydrophobic environment of micelles and therefore experience a smaller change in their microenvironment polarities upon being transferred from mobile to stationary phase. As a result the $-CO$ group selectivity between the more hydrophobic alkyl benzene/alkyl phenone pair is less than the more polar pairs (smaller n_c) and actually approaches unity. It was shown in a previous paper that for compounds with large water-micelle partition coefficients (e.g. hydrophobic compounds) the overall selectivity value is small and its variation with micelle concentration is limited (14). This is also the case for compounds with comparable K_{mw} values (eq 3). Separation can be improved in such cases by introducing another variable (e.g. an organic solvent) in optimization strategies. This is shown in Figure 4b where $\alpha(-CO)$ increases with ϕ_{PROH} for alkyl benzene/alkyl phenone pairs with different carbon numbers. Note that $\alpha(-CO)$ selectivity decreases with an increase in micelle concentration (Figure 4c). Similarly, as will be shown elsewhere, separation of a mixture of phenols can be improved by a simultaneous increase of micelle concentration and organic solvent concentrations (18).

In addition to the competing equilibria, another phenomenon is the compartmentalization effect by micelles which can have a dramatic influence on the solvent strength parameter, S , and therefore on selectivity. The linear relationship between $\ln k'$ and ϕ_{ORG} is valid for both conventional hydro-organic eluents (over a limited ϕ_{ORG} range) as well as for hybrid eluents, i.e.

$$\log k' = -S\phi_{ORG} + \log k'_0 \quad (4)$$

where S is the solvent strength parameter (using S_{hyb} notation for hybrid eluents) the intercept $\log k'_0$ is the capacity factor in a purely aqueous mobile phase (in hydro-organic systems) or at a given micelle concentration ($k'_{0, [M]}$ for hybrid systems). From eq 4, one can derive the relationship between selectivity and ϕ as

$$\ln(\alpha_2) - \ln(\alpha_1) = -(S_b - S_a)(\phi_2 - \phi_1) \quad (5)$$

where α_1 and α_2 are selectivity of compounds a and b (i.e.

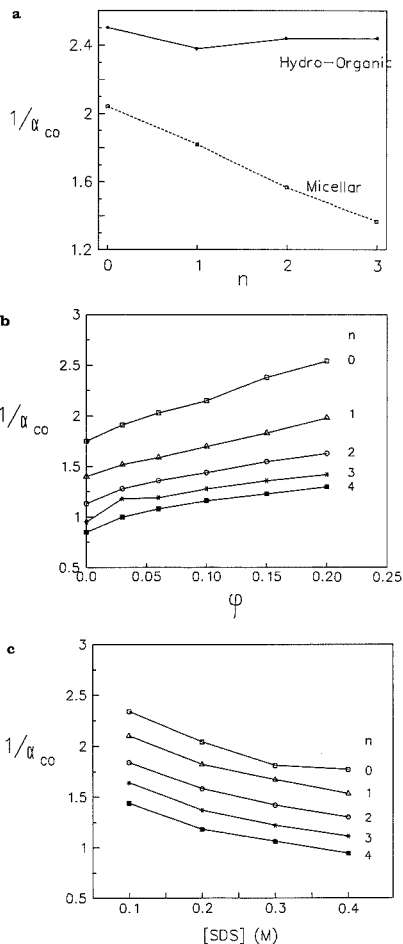


Figure 4. Carbonyl group selectivity (α_{CO}), defined as the ratio of the capacity factors of $C_6H_5CO(CH_2)_nCH_3$ and $C_6H_5(CH_2)_nCH_3$, in MLC: (a) a comparison between carbonyl group selectivity in hydro-organic and micellar LC as a function of the number of carbons in the chain, n ; (b) the inverse of α_{CO} as a function of the fraction of 2-propanol, ϕ , in 0.1 M $C_{16}TAB$ for varying carbon chain lengths; (c) the inverse of α_{CO} as a function of the concentration of SDS in 3% 2-propanol for varying carbon-chain lengths. The inverse of group selectivity $1/\alpha_{CO}$ is plotted (instead of α_{CO}) since selectivity > 1 by definition. Data were taken from ref 13 and 14.

k'_b/k'_a) at two organic modifier concentrations in hydro-organic or hybrid eluents ϕ_1 and ϕ_2 where $\phi_2 > \phi_1$. For conventional RPLC with hydro-organic eluents, Schoenmakers et al. have shown that S values are linearly related to $\ln k'_w$ for a large group of compounds (17), i.e.

$$S = p + q \ln k'_w \quad (6)$$

where p and q are empirical constants. As a result, in hydro-organic eluents S_b is larger than S_a since $k'_b > k'_a$ ($\alpha = k'_b/k'_a$ by definition > 1). In other words, for a group of compounds where eq 6 is applicable, eq 5 predicts a systematic decrease in selectivity as a result of an increase in volume fraction of organic modifier (i.e. increase in elution strength).

In the presence of micelles, the relative S values for different compounds would depend on their interactions with micelles;

i.e. S_b may no longer be larger than S_a in hybrid system even though $k'_b > k'_a$. As a result, the variation of selectivity (increase or decrease) with an increase in volume fraction of organic modifier would depend upon S_{hyb} values.

Snyder and co-workers have shown that changes in band spacing as a result of an increase in organic modifier concentration can be observed for samples having components that differ in molecular weight or functionality (20, 21). Simultaneous enhancement in selectivity and elution strength using binary hydro-organic eluents is not possible for samples that contain solutes with equal (or close) S values (slope of eq 4) or when there is a strong correlation between S values and the corresponding retention (eq 6) (20). Elution order reversal is quite common in conventional hydro-organic RPLC; however, to the best of our knowledge there has not been any report to indicate a monotonic increase in selectivity with an increase in elution strength in hydro-organic systems for a wide range of compounds. In fact, it has been shown recently that although maximum selectivity can be observed at intermediate solvent strength values in certain ternary or quaternary hydro-organic mixtures and for selected compounds, the general trend is higher selectivity at lower eluent strengths (22). As will be shown elsewhere, in hybrid systems, where an increase in elution strength can often coincide with an enhancement of selectivity, a simultaneous optimization of parameters influencing selectivity and solvent strength is required, i.e. a separate optimization of elution strength and selectivity is inefficient (18). In hydro-organic systems, it is common practice to first adjust the elution strength, then optimize the selectivity at a constant solvent strength (23).

The generality of the simultaneous selectivity enhancement with elution strength in hybrid systems indicates that the possible cause(s) is (are) not the same as the typical solvent selectivity effect in hydro-organic mobile phases, as the latter is only observed for a limited group of compounds which selectively interacts with a given solvent.

Since S values reflect the extent of solvation of solutes by organic solvents, the localization of solutes and/or organic solvents in micelles can greatly influence the sensitivity of retention to changes in the concentration of organic solvent. In other words, the S_{hyb} values depend upon the extent of partitioning (or localization) of both solutes and the organic solvent in micelles. In Figure 5a the S values for 11 aromatic compounds in a hybrid system of water-methanol-CTAB micelles are compared with the S values for water-methanol eluents reported by Schoenmakers et al. (17). In a conventional hydro-organic system S varies greatly with the solute molecular weight and functional groups (17, 21). Therefore anthracene has an S value of 12.60 (the largest), benzyl alcohol is ranked ninth ($S = 5.05$) and phenol has the smallest value of 3.13. As a result, the retention of anthracene in conventional hydro-organic RPLC is more sensitive to variations in the concentration of organic solvent than benzyl alcohol or phenol, etc. In the presence of CTAB micelles, however, the corresponding S_{hyb} (MEOH) values and the ranking are quite different and, in fact, can be quite the opposite of that of conventional hydro-organic eluents, e.g. 0.474 for anthracene (ranked tenth, one to the smallest), 1.53 for benzyl alcohol (the largest), and 1.31 for phenol (ranked fourth). Naphthalene and anthracene have the smallest S_{hyb} values (as compared to more polar-substituted benzenes) and therefore are far less affected by the addition of organic solvents. This is due to the fact that these compounds strongly interact with micelles and are less accessible to a polar solvent such as methanol (which does not interact strongly with micelles). In other words, methanol is too polar to compete with the micelles for the interaction with hydrophobic compounds. Hydrophobicity of compounds and organic solvent are im-

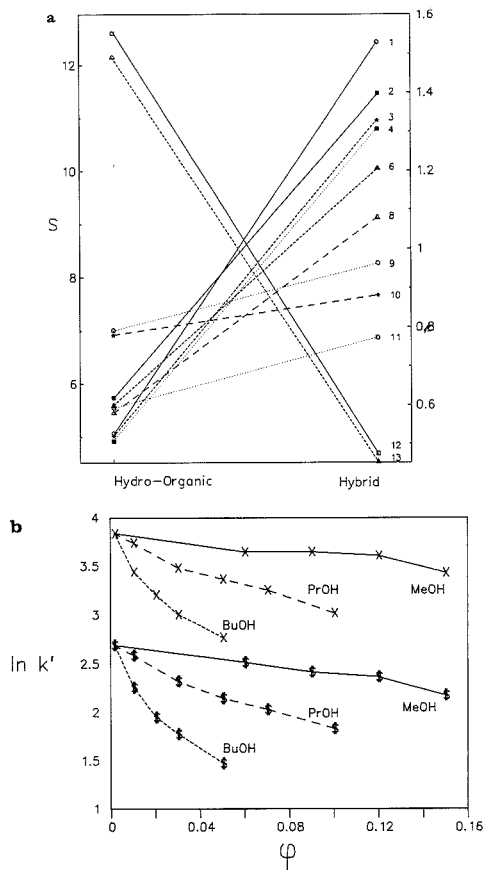


Figure 5. Influence of the concentration and type of organic modifier on the retention behavior in MLC: (a) a comparison between the slopes (absolute value) of $\ln k'$ vs the fraction of methanol in hydro-organic eluents reported in the literature (23) and the slopes observed in hybrid eluents of water-methanol-0.04 M C_{14} TAB micelles, listed in Table I, the numbers refer to Table I; (b) retention data ($\ln k'$) of propiophenone (x) and benzyl alcohol (\$), as a function of the volume fraction ϕ of methanol (MeOH), 2-propanol (PrOH), and butanol (BuOH) in the hybrid eluents of water-alcohol-0.04 M C_{14} TAB micelles.

portant factors in controlling their interaction with the micelles; however, the specific interaction with the ionic head group of micelles (especially with cationic micelles) cannot be overlooked. For example, naphthalene and anthracene are very hydrophobic and the π electrons of their aromatic rings can strongly interact with the cationic head group of CTAB (19). This means that the relationship between S_{hyb} and a solutes' structural properties cannot be easily recognized; e.g. one cannot conclude that S_{hyb} is inversely related to hydrophobicity of solute. Most of the more polar organic compounds are located in the Stern layer of micelles, which is more accessible to methanol, and therefore have a larger S_{hyb} value. Nevertheless their overall values are still much smaller than those of a hydro-organic system. These observations further confirm our previous results that the overall S values of alkyl homologous series and their range of variation in the presence of micelles (S_{hyb}) are strongly limited as compared to those in hydro-organic eluents (13).

Table I. The Slope S (Absolute Value) Observed for 14 Alkyl Benzenes, Applying Linear Regression to the Retention Data, $\ln k'$, vs the Fraction of Different Organic Modifiers in the Hybrid Eluents of Water–Alcohol–0.04 M C_{14} TAB Micelles^a

no.	component	S		
		MeOH	PrOH	BuOH
1	benzyl alcohol	1.53	3.74	10.22
2	acetophenone	1.40	3.46	8.94
3	benzaldehyde	1.33	3.58	8.89
4	phenol	1.31	4.34	12.50
5	acetanilide	1.22	3.80	9.15
6	benzonitrile	1.21	3.42	8.74
7	propiofenone	1.14	3.47	7.27
8	nitrobenzene	1.08	3.14	8.50
9	chlorobenzene	0.96	2.25	6.18
10	anisole	0.88	2.80	9.08
11	benzene	0.74	2.09	5.57
12	anthracene	0.47	2.65	8.32
13	naphthalene	0.45	2.48	6.84
14	butyrophenone	0.45	3.34	8.85

^aMethanol (MeOH), 2-propanol (PrOH), and butanol (BuOH).

In Table I, the S_{hyb} values for 15 aromatic compounds are listed for three organic modifiers, methanol (MeOH), 2-propanol (PrOH), and butanol (BuOH), in the presence of cationic CTAB micelles. As shown the overall S_{hyb} values can be ranked as $S_{\text{BUOH}} > S_{\text{PROH}} > S_{\text{MeOH}}$, which is similar to conventional hydro-organic systems as BuOH is the strongest solvent and the MeOH is the weakest (Figure 5b). The larger S_{hyb} for BuOH and PrOH indicate that these solvents interact more with micelles and consequently can solvate more effectively and/or that they can better compete with micelles for interaction with solutes. Note however, that the overall S_{hyb} for the set of compounds is still smaller than the one in the absence of micelles, as S_{hyb} for BuOH is even smaller than S values for MeOH in conventional hydro-organic eluents. Another important point which again indicates the impact of micelles is the fact that the ranking of S_{hyb} for different solutes is different for MeOH, PrOH, and BuOH. The compounds in Table I are ranked according to S (MeOH) values. In conventional hydro-organic systems, one anticipates observing the same ranking of S values for different solutes, because these three solvents belong to the same selectivity group. In the presence of micelles, however, this may not be the case since these solvents interact differently with micelles and therefore their own microenvironment in micelles would be different. One might conclude that the selectivity of different organic solvents in the presence of micelles might change. If so, this would extend the list of organic solvents for LC separations. Further investigations on the selectivity effect of different organic solvents are underway.

Practical Implications. Improving resolution and reducing separation time are the two important goals in many optimization strategies (23). Simultaneous selectivity enhancement with elution strength could lead to better separations in a shorter time period. This is shown in Figures 6 and 7. The chromatogram shown in Figure 7a illustrates the separation of a mixture of 13 peptides and amino acids by using an anionic micellar eluent (0.10 M SDS) at pH 2.50. Obviously, the separation is poor and the analysis time is long (95 min). The situation improves dramatically upon the addition of 2-propanol to the micellar eluent as shown in Figure 6b. Note the frequent elution reversals as well as dramatic selectivity enhancement between peaks 3, 4, and 5; 9 and 10; or 11, 12, and 13 as a result of adding propanol. On the other hand the resolution between peaks 1 and 2 or 8 and 9 deteriorates. The overall resolution of the chromatogram, however, has improved and the analysis time is much shorter (50 min).

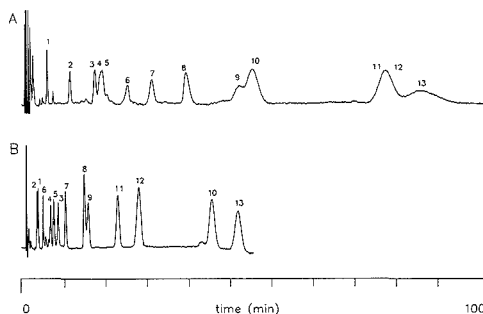


Figure 6. Chromatograms of a mixture of 13 peptides and amino acids: column, 2 × 12.5 cm LichroCART C18, 4.6 mm i.d., 5 μm particle size, thermostated at 40 °C. The flow was 1.5 mL/min (dead volume 1.4 mL). Components: (1) AY, (2) Y, (3) DF, (4) LY, (5) GLY, (6) M, (7) W, (8) R, (9) LW, (10) KF, (11) GLF, (12) FF, (13) RF. (a) Mobile phase: 0.1 M sodium dodecyl sulfate (SDS), 20 mM phosphate buffer, pH = 2.5. (b) Mobile phase: as in part a with 15% 2-propanol.

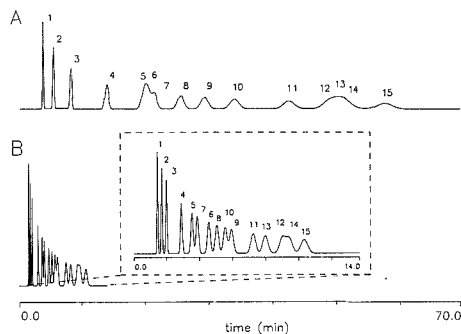


Figure 7. Chromatograms of a mixture of 15 phenols. The chromatograms were simulated on the basis of retention data collected on a 12.5-cm LichroCart C18 column, 4.6 mm i.d., 5 μm particle size, thermostated at 40 °C, assuming 2500 plates and equal concentrations of all components. Components: (1) 4-benzamidephenol, (2) 4-hydroxybenzyl alcohol, (3) 4-hydroxyphenylmethyl alcohol, (4) 4-hydroxybenzylcyanide, (5) 4-hydroxyacetophenone, (6) phenol, (7) 4-hydroxybenzaldehyde, (8) 4-fluorophenol, (9) 4-methylphenol, (10) 4-hydroxypropiofenone, (11) 4-nitrophenol, (12) 4-isopropylphenol, (13) 4-hydroxybenzophenone, (14) 4-hydroxydiphenylmethane, and (15) 4-*tert*-butylphenol. (a) Mobile phase, 0.04 M myristyltrimethylammonium bromide (CTAB), 0.1 M phosphate buffer, pH = 7. (b) Mobile phase: 0.12 M CTAB, 10% 2-propanol, 0.1 M phosphate buffer, pH = 7.

Note that the chromatogram in Figure 6b is obtained under nonoptimum conditions. The low efficiency for early eluting peaks shows that the extracolumn band broadening is severe. There exist large gaps between the later eluting peaks, which can be improved by adjusting the mobile phase composition. However, no attempt was made to further optimize the chromatographic system, as the chromatogram shown in Figure 6 adequately serves the purpose of this paper. By applying one of the currently recognized optimization strategies, one can optimize the conditions to obtain the optimal chromatogram (as defined by the goal of the separation) as described elsewhere (18, 24). As a result of propanol addition, both the chromatographic selectivity and efficiency increased which led to higher resolution. Figure 7 illustrates a similar behavior for a mixture of 15 phenols with a cationic micellar mobile phase. These chromatograms were simulated based on the retention behavior of phenols in hybrid systems. Again in Figure 7a the analysis time is very long and the resolution between several peaks (e.g. 5, 6, and 7 or coelution of 12, 13,

and 14) is poor. The chromatogram can be improved drastically by simultaneously increasing the micelle concentration and addition of propanol. The analysis time is reduced from about 60 to 13 min while most of the overlapped peaks (except peaks 12 and 14) are well resolved. Note that the number of theoretical plates was assumed to be only 20 000 plate/m in the simulations (Figure 7) to account for the possible low efficiency of micellar systems. The situation illustrated in Figure 7 is an example of the general elution problem; however, the solution in Figure 7b is obtained through an isocratic separation and not gradient elution. Again, further improvement of the separation can be achieved by fine tuning the experimental conditions, as will be reported elsewhere (18).

CONCLUSION

The possible simultaneous enhancement of selectivity and elution strength provides an additional reason for examining addition of a small percentage of an organic solvent in micellar eluents. Micellar eluents are generally weak and suffer from poor efficiency. Although the solvent strength can adequately be increased in certain cases by increasing micelle concentration, it has been shown that the chromatographic efficiency in MLC deteriorates at higher micelle concentrations. Addition of an organic solvent to micellar eluent adjusts the eluent strength, improves the chromatographic efficiency, and in many cases can lead to an enhancement of separation selectivity. All these will have a favorable effect on resolution and analysis time. It is important to note that in certain cases selectivity enhancement might not lead to an improvement in resolution if the retention (k' term in the fundamental resolution equation) would fall below the optimum k' range as a result of an increase in elution strength (23). This situation can be even worse if the elution strength is increased through an increase in micelle concentration even though selectivity enhancement is achieved through adjusting micelle concentration. In this case, a decrease in efficiency combined with a decrease in k' (as a result of increasing eluent strength) might actually lead to a decrease in resolution even though peak selectivity is actually increased. Finally, it should be emphasized once again that addition of organic solvent to micellar eluents would not create a system closer to conventional hydro-organic RPLC. The chromatographic capabilities of hybrid eluents of water-organic solvent-micelles are largely

unknown and should be further explored.

LITERATURE CITED

- (1) Armstrong, D. W. *Sep. Purif. Methods* **1985**, *14*, 213.
- (2) Dorsey, J. G. *Adv. Chromatogr.* **1987**, *27*, 167.
- (3) Hinze, W. L. In *Ordered Media in Chemical Separation*; Hinze, W. L., Armstrong, D. W., Eds.; ACS Symposium Series 342; American Chemical Society: Washington, DC, 1987.
- (4) Khaledi, M. G. *BioChromatography* **1988**, *3*, 20.
- (5) Khaledi, M. G. *TRAC, Trends Anal. Chem.* **1988**, *7*, 293.
- (6) Cline Love, L. J.; Habarta, J. G.; Dorsey, J. G. *Anal. Chem.* **1984**, *56*, 1132A.
- (7) Yarmchuk, P.; Weinberger, R.; Hirsch, R. F.; Cline Love, L. J. *Anal. Chem.* **1982**, *54*, 2233.
- (8) Armstrong, D. W.; Stine, G. Y. *Anal. Chem.* **1983**, *55*, 2317.
- (9) Dorsey, J. G.; DeEchegaray, M. T.; Landy, J. S. *Anal. Chem.* **1983**, *55*, 924.
- (10) Yarmchuk, P.; Weinberger, R.; Hirsch, R. F.; Cline Love, L. J. *J. Chromatogr.* **1984**, *283*, 47.
- (11) Armstrong, D. W.; Ward, T. J.; Berthod, A. *Anal. Chem.* **1986**, *58*, 579.
- (12) Borgerding, M. F.; Williams, R. L.; Hinze, W. L.; Quina, F. H. *J. Liq. Chromatogr.* **1989**, *12*, 1367.
- (13) Khaledi, M. G.; Peuler, E.; Ngeh-Ngwainbi, J. *Anal. Chem.* **1987**, *59*, 2738.
- (14) Khaledi, M. G. *Anal. Chem.* **1988**, *60*, 876.
- (15) Rodgers, A. H.; Strasters, J. K.; Khaledi, M. G., unpublished work.
- (16) Riley, C. M.; Tomlinson, E.; Jefferies, T. M. *J. Chromatogr.* **1979**, *185*, 198.
- (17) Schoenmakers, P. J.; Billiet, H. A. H.; de Galan, L. J. *Chromatogr.* **1979**, *185*, 179.
- (18) Strasters, J. K.; Breyer, E. D.; Rodgers, A. H.; Khaledi, M. G., submitted for publication in *J. Chromatogr.*
- (19) Fendler, J. H.; Fendler, E. J. *Catalysis in Micellar and Macromolecular Systems*; Academic Press: New York, 1975.
- (20) Quarry, M. A.; Grobe, R. L.; Snyder, L. R.; Dolan, J. W.; Rigney, M. P. *J. Chromatogr.* **1987**, *384*, 163.
- (21) Snyder, L. R.; Quarry, M. A.; Glajch, J. L. *Chromatographia* **1987**, *24*, 33.
- (22) Coenegracht, P. M. J.; Metting, H. J.; Smilde, A. K.; Coenegracht-Lammers, P. J. M. *Chromatographia* **1989**, *27*, 135.
- (23) Schoenmakers, P. J. *Optimization of Chromatographic Selectivity*; Journal of Chromatography Library, Vol. 35; Elsevier: Amsterdam, 1986.
- (24) Drouen, A. C. J. H.; Billiet, H. A. H.; Schoenmakers, P. J.; de Galan, L. *Chromatographia* **1982**, *16*, 48.

RECEIVED for review June 22, 1989. Accepted October 19, 1989. The authors gratefully acknowledge a research grant from the National Institutes of Health (GM 38738). Acknowledgment is also made to the donors of the Petroleum Research Fund, administered by the American Chemical Society. This work was presented in part at the Eastern Analytical Symposium, Oct 1988, New York.

Analytical and Micropreparative Ultrahigh Resolution of Oligonucleotides by Polyacrylamide Gel High-Performance Capillary Electrophoresis

A. Guttman, A. S. Cohen, D. N. Heiger, and B. L. Karger*

Barnett Institute and Department of Chemistry, Northeastern University, Boston, Massachusetts 02115

In continuation of previous work, the separations of polydeoxyoligonucleotides on polyacrylamide gel capillary columns are presented. The use of gel compositions with relatively low monomer content permits columns of very high plate numbers to be obtained. With a 160-mer, plate counts of 30×10^6 per meter are shown. Columns with high precision in relative migration time from run to run, day to day, and batch to batch are presented. Collection of purified fractions from high-resolution electropherograms is also shown to be feasible using field programming techniques. To accomplish this, separation is allowed to occur under high field for resolution and speed, followed by collection under low field where the velocity of the band is purposely decreased in order to widen the time-based width of the band.

INTRODUCTION

At present, there is a great deal of interest in the separation and characterization of polydeoxyoligonucleotides. The problem is a challenging one since the polydeoxyoligonucleotides may differ only slightly from one another, for example in base number or in sequence of bases. Great strides are being made in electrophoresis for various molecular weight regions, including chromosomal DNA separations (1). At the low molecular weight range, e.g. up to ca. 500 bases, there is a need for improved separation, both in terms of speed and resolving power, particularly for minute sample sizes. Rapid and significant resolving power would result in important potential advances for molecular biology including, among other areas, DNA sequencing (2) and purification of DNA probes (3).

Conventionally, polydeoxyoligonucleotide separations have been best achieved by gel electrophoresis, using flat bed or slab gels, which can be very time consuming (4). In addition, the isolation of individual fragments is inconsistent and fraught with problems.

An improved version of electrophoresis is currently being developed in the form of high-performance capillary electrophoresis (HPCE) (5-8). This instrumental approach to electrophoresis can be characterized as a rapid, high-resolution analytical technique and an effective tool in the isolation of purified materials. We have previously demonstrated the high resolution of gel-filled capillaries for the separation of low molecular weight polydeoxyoligonucleotides (9).

This paper is a continuation of the study of gel-filled capillaries for high-resolution separation of polydeoxyoligonucleotides. We first briefly present results on columns with several gel compositions. Columns of high precision in relative solute migration time have been developed. Using low monomer gel compositions and columns greater than 50 cm in effective length, we demonstrate the capability of such capillary gel columns to generate very large numbers of theo-

retical plates, roughly 30 million plates per meter. Finally, we illustrate a new micropreparative approach to collection of isolated fragments using electric field programming. These results indicate the significant power of capillary gel columns for the separation and analysis of polydeoxyoligonucleotides.

EXPERIMENTAL SECTION

Apparatus. Polyacrylamide gel HPCE was performed in fused-silica tubing (Polymicro Technologies, Phoenix, AZ), 75- μ m i.d., 375- μ m o.d., with several different column lengths. For detection purposes, a 2-mm length of polyimide coating was carefully burned off at a distance of 150-200 mm from one end of the column. A 60-kV high-voltage direct current power supply (Model PS/MK 60, Glassman, Whitehouse Station, NJ) was used to generate the potential across the capillary gel column. A UV detector (Model V4, ISCO, Lincoln, NE), modified as previously described (10), was employed at a wavelength of 260 nm, with a capillary slit of 0.1 mm \times 0.1 mm. Cooling was achieved with a fan. Each end of the capillary was connected to a separate 3-mL vial filled with buffer (for analytical runs). For collection, the low-voltage end (cathode) was placed in a microfuge vial filled with an appropriate amount of water ($\sim 3 \mu$ L) (9, 11). Platinum wire electrodes were inserted into the two vials for connection to the electrical circuit. The electropherograms were acquired and stored on an IBM PC/AT computer via an analog to digital (A/D) interface (Model 762 SB, Nelson Analytical, Cupertino, CA).

Materials. Samples of polydeoxyadenylic acids were purchased from Pharmacia (Piscataway, NJ). The polydeoxythymidylic acids, 20-160-mers, were chemically synthesized by ligation of the 3'-3' ends, yielding 5'-phosphate groups at the two ends of the combined polymers. Individual polydeoxythymidylic acids, differing by 20 polydeoxyoligonucleotides each (i.e. 20-mer, 40-mer, ... 160-mer), were slab gel purified and subsequently combined to give a 20-160-mer mixture. The mixture was the kind gift of Drs. Bischoffer and Field of Genentech, South San Francisco, CA. All other reagents were of electrophoresis research grade (Schwartz/Mann Biotech, Cambridge, MA). All buffer solutions were filtered through a nylon GC filter unit of 0.2- μ m pore size (Schleicher & Schuell, Keene, NH). The buffer solutions were carefully vacuum degassed before use. Samples were kept frozen at -20°C , and the buffers were stored at 4°C before use. Samples were heated at 65°C for 5 min and were then injected at room temperature (9).

Procedures. Polymerization of polyacrylamide was accomplished within the capillary column by passing carefully degassed polymerizing solution slowly into the capillary (9). For stabilization, the gel was chemically bound to the silica wall by using a standard bifunctional agent, (methylacryloxypropyl)trimethoxysilane (12). Gel columns of 3-6% T and 5% C (13) were used in a buffer of 0.1 M Tris, 0.25 M boric acid, pH 7.6 and 7 M urea. The samples were electrophoretically injected into the column by dipping the cathodic end of the capillary into an aqueous solution of the sample and typically applying a field of 3 kV for 5 s for an analytical injection. In the case of the polydeoxyadenylic acids (p(dA)₄₀₋₆₀), the concentration of injection sample was in the range of 20-40 μ g/mL.

RESULTS AND DISCUSSION

High-Resolution Separations. We have previously shown the high resolving power of capillary polyacrylamide gel electrophoresis in the separation of polydeoxyoligonucleotides

* Author to whom correspondence and reprint requests should be addressed.

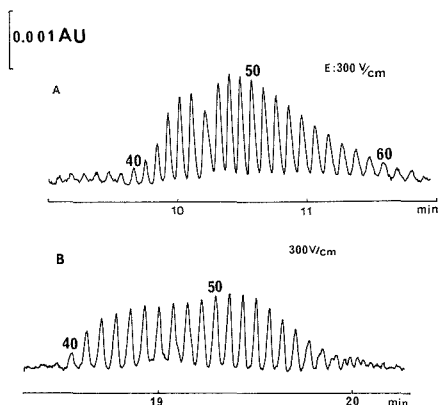


Figure 1. HPCE separation of polydeoxyadenylic acid mixture, $p(dA)_{40-60}$, as a function of gel composition and effective column length (see text): (A) capillary, 350×0.075 mm i.d. (effective length, 150 mm); buffer, 0.1 M Tris/0.25 M borate/7 M urea, pH 7.6; polyacrylamide gel, 6% T and 5% C; applied field, 300 V/cm, 10.8 μ A. (B) capillary, 750×0.075 mm i.d. (effective length, 550 mm); polyacrylamide gel, 3% T and 5%; applied field, 300 V/cm, 17.7 μ A; all other conditions were the same as in A. Figure 1A is reprinted from *Nature* (Vol. 339, pp 641, 642). Copyright 1989 Macmillan Magazines Limited.

using a sample mixture of polydeoxyadenylic acids from 40 to 60 bases long ($p(dA)_{40-60}$) (9). In the above cited paper, we used a column of 7.5% T, 3.3% C gel composition.

In this work, we first briefly examined separation with several gel compositions. Figure 1A shows the separation of the $p(dA)_{40-60}$ sample at 300 V/cm, using a 6% T, 5% C gel composition with an effective column length l of 15 cm. According to slab gel reports (14), this gel composition should produce pore dimensions similar to those from 7.5% T, 3.3% C gel composition. The average plate count for the above capillary column was 2.6×10^5 for each peak, and the average resolution for any pair of solutes was 1.13.

We next turned to design gel columns of increased pore size for the separation of larger molecular weight single-strand polydeoxyoligonucleotides. This was accomplished by reducing the monomer content in the gel composition. Figure 1B shows the separation of the same $p(dA)_{40-60}$ mixture at 300 V/cm, using a 3% T, 5% C gel column. To compensate for the expected lower resolving power of the larger pore size column for the short polydeoxyoligonucleotides, the effective column length was increased from 15 to 55 cm (5, 15). Good separation was again obtained, but at the expense of longer time. The 3% T, 5% C column was an efficient column with an H value of $0.31 \mu\text{m}$ ($N = 1.8 \times 10^6$) vs an H value of $0.57 \mu\text{m}$ for the 6% T, 5% C column. The higher efficiency on the wider pore size column may be a result of a decreased restricted migration through the gel matrix. However, the resolution on the 3% T, 5% C column (1.25) was only slightly greater than on the 6% T, 5% C column (1.13), undoubtedly due to the greater size selectivity on the smaller pore, higher percentage T column.

The 3% T, 5% C column would nevertheless appear advantageous from the point of view of allowing separation of a broader molecular weight range of polydeoxyoligonucleotides. For small polydeoxyoligonucleotides, the poorer selectivity on the lower percentage T column can be compensated by larger values of N . On the other hand, on the 6% T, 5% C column, larger polydeoxyoligonucleotides, e.g. ~ 150 -mer, yielded broad bands, presumably due to restricted migration through the gel matrix. This was not the case for

the 3% T, 5% C gel, and separations of very high performance were observed for solutes in this base number range (see later).

In Figure 1B the various $p(dA)$'s have been identified on the basis of the use of purified single-stranded $p(dA)$ species from 10 to 20 bases in length and the linear behavior of migration time vs base number for the $p(dA)$'s, $r^2 = 0.9995$. Careful studies of migration reproducibility were conducted on the 3% T, 5% C column of Figure 1B. With the 50-mer serving as the basis of study, it was found that the run-to-run reproducibility was 0.9% relative standard deviation RSD ($n = 5$), and the day-to-day reproducibility was 3.2% RSD ($n = 3$). We also examined the column-to-column (batch-to-batch with respect to polymerizing solution) migration time reproducibility where the columns were made by two different workers and found 4.8% RSD ($n = 11$).

The lower reproducibility from day to day and column to column was believed to arise in part from column temperature variations. Since a fan was used for cooling, ambient temperature variations could cause overall column temperature changes. Mobility, and thus migration time, are particularly sensitive to temperature changes, i.e. $\sim 2\%/^{\circ}\text{C}$ (16), due to the sensitivity of liquid viscosity with T. The precision of absolute migration could be improved by fixing the set temperature of the capillary column by using, for example, a solid-state (Peltier) cooling system (17).

To demonstrate that temperature variation was a likely cause of the 3–5% RSD observed, we measured the migration of the 40-mer relative to that of the 50-mer. As in chromatography, we found that relative migration dramatically improved precision. Thus, in terms of relative migration with the same data, the precision from run to run was now 0.07% RSD ($n = 5$), from day to day (same column) 0.1% RSD ($n = 3$), and from column to column 0.7% RSD ($n = 11$). Given the similarity in migration behavior of the polydeoxyoligonucleotides, the use of a specific polydeoxyoligonucleotide as an internal standard can prove useful. From the results, it appears that the columns are highly reproducible. In addition, we were able to use the columns well in excess of 150 injections.

We approximated the amount of sample injected in Figure 1B (i.e. injection at 3 kV for 5 s) by first calibrating an open-tube capillary detector ($\lambda = 260$ nm) with known concentrations of the sample. A linear plot was observed with $r^2 = 0.993$. The average concentration of an individual band was next determined from the average peak height of the band in the electropherogram of Figure 1B. The volume of that given band was then measured (~ 8 nL) by using the time-based peak width and the migration velocity of the species. The total amount (on average) of each peak was calculated to be 600 pg or 12 ng total of $p(dA)_{40-60}$ injected (600 pg \times 20 solutes = 12 ng).

As noted above, a longer column was used with the 3% T, 5% C gel column to generate a greater number of theoretical plates. The ability of such columns to maintain high resolution over a wide molecular range can be seen in Figures 2 and 3. Figure 2 shows the separation of a mixture of polydeoxythymidylic acids, $p(dT)_{20-160}$, each major species differing by 20 bases with $l = 80$ cm and $E = 200$ V/cm, 8.2 μ A. Figure 3 shows the same separation on a column of $l = 50$ cm, with $E = 300$ V/cm, 12 μ A. For this polydeoxythymidylic acid sample, the slab gel purified species reveal additional peaks by HPCE which migrate slightly faster than the main peak. A plot of migration time t (i.e. μs^{-1}) vs base number is again linear for the $p(dT)_{20-160}$ major components, $r^2 = 0.995$. On the basis of this calibration plot, each impurity peak is associated with a progressively $n - 1$ decreased number of bases, i.e. 159, 158, etc. For absolute identification it would be necessary to collect each peak and conduct further structure analysis.

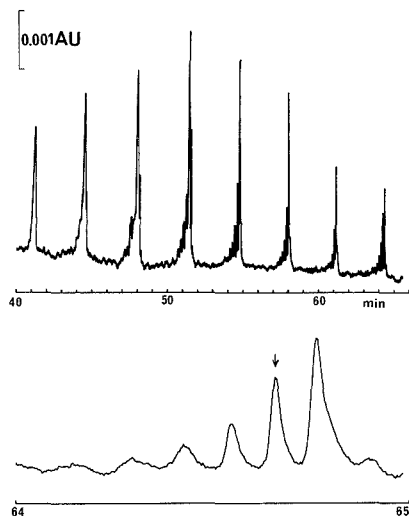


Figure 2. HPCE separation of polydeoxythymidylic acid mixture, p-(dT)₂₀₋₁₆₀; capillary dimensions, 1000 × 0.075 mm i.d. (effective length, 800 mm); applied field, 200 V/cm, 8.2 μA. All other conditions were the same as in Figure 1A.

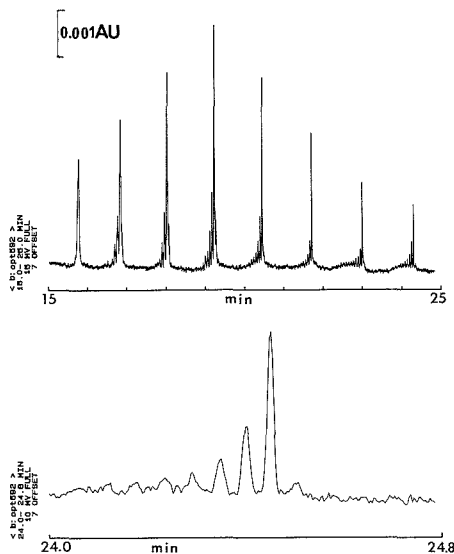


Figure 3. HPCE separation of the test mixture of Figure 2. Conditions were the same as in Figure 2 except for the following: capillary dimensions, 700 × 0.075 mm i.d. (effective length, 500 mm); applied field, 300 V/cm, 13 μA. All other conditions were the same as in Figure 1A.

The ultrahigh resolving power can be readily seen, particularly in Figures 2 and 3 for the time-expanded separation of the 160-mer. The presumed 159-mer in Figure 2 (see arrow) is calculated to contain 12×10^6 plates at 200 V/cm. (Appropriate equations were used to take account of the slight asymmetry of the band (18).) In Figure 3, the 160-mer is calculated to contain 15×10^6 plates for 50 cm or 30×10^6 plates per meter. This latter plate count with an H value of $0.03 \mu\text{m}$ is roughly 10-fold greater than previously reported

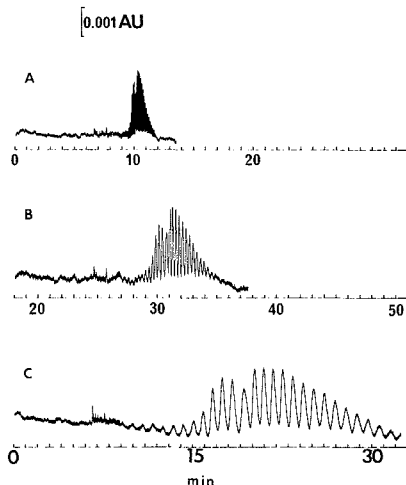


Figure 4. Field programming in the HPCE separation of polydeoxyadenylic acid mixture, p(dA)₄₀₋₆₀; capillary dimensions, 300 × 0.075 mm i.d. (effective length, 150 mm). Applied voltages were as follows: (A) 300 V/cm, 17.7 μA; (B) 100 V/cm, 5.6 μA; (C) 300 V/cm, 17.7 μA, 0–10 min and 30 V/cm, 1.9 μA, 10–30 min. All other conditions were the same as in Figure 1A.

for open-tube capillary electrophoresis of $(1-2) \times 10^6$, e.g. ref 19 or Figure 1B. For both Figures 2 and 3 there is a reduction in plate count as the faster migrating, shorter polydeoxyoligonucleotide species are measured. For example, on the $l = 50$ cm column, the 120-mer is calculated to contain 6×10^6 plates, whereas the 80-mer has 2×10^6 plates. Based on increased peak asymmetry with the faster migrating species, sample concentration overloading (20) may in part play a role in this decrease in plate count.

The results in Figures 1–3 demonstrate that the gel columns represent an excellent approach for resolution of complex polydeoxyoligonucleotide mixtures. They thus possess a real potential for use in DNA sequencing using sensitive labeling and detection techniques (2). In addition, they can be used for rapid assessment of purity of synthesized polydeoxyoligonucleotides (9). We next turn to the use of these high-resolution columns for micropurification.

Field Programming and Micropreparative Collection.

HPCE not only is an analytical tool but also can be used for micropreparative separations. Collection of substances as they migrate out of the capillary has already been demonstrated (9, 11, 21). In the case of gel columns, purified fractions can be obtained by maintaining a constant field and positioning the capillary in a microfuge vial filled with several microliters of water and/or diluted buffer. The combination of this approach with high resolution and rapid separation, where the peak widths may be only a few seconds wide, is difficult for reproducible collection. It is possible, however, to simplify collection while maintaining high-resolution separations by electric field programming.

Since the velocity of the solute can be manipulated by varying the electric field, field programming can simplify the collection process. The strategy is to separate at high field where speed and resolution (in general) are improved and then to collect at low field where the band would broaden in time units with little loss in resolution.

Figure 4 illustrates the principle of this approach. In parts A and B, separation of p(dA)₄₀₋₆₀ is achieved in a 6% T, 5% C gel column using 300 and 100 V/cm, respectively. The average time-based peak width in Figure 4A is 6 s and in

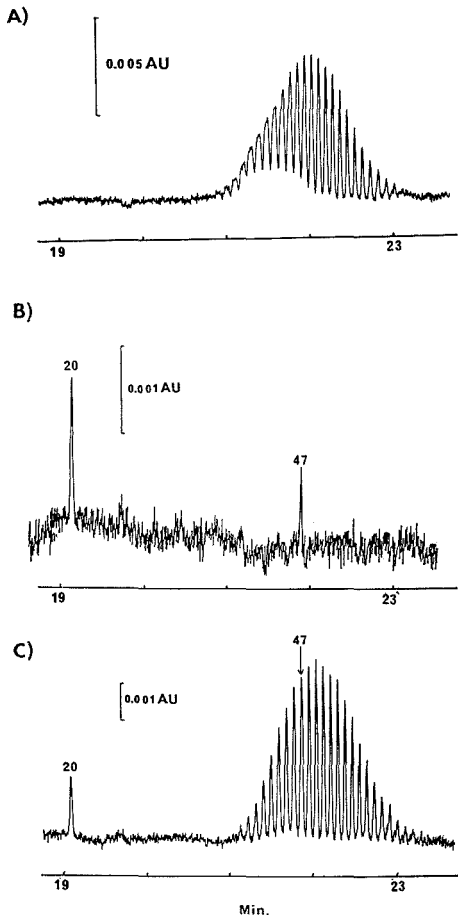


Figure 5. (A) Micropreparative separation of the polydeoxyadenylic acid test mixture, $p(dA)_{40-60}$, (B) analytical run of the isolated $p(dA)_{47}$ spiked with $p(dA)_{20}$, and (C) analytical run of $p(dA)_{40-60}$ spiked with $p(dA)_{20}$. Capillary dimensions were 800×0.075 mm i.d. (effective length, 600 mm). The buffer and the gel were the same as in Figure 1B. The micropreparative and the analytical injections were made electrophoretically at 9 kV for 10 s (A) and 6 kV for 1 s (B and C), respectively. In A the applied field was 300 V/cm for the run and was decreased to 30 V/cm for the collection, over 60 s. In B and C the applied field was held constant at 300 V/cm.

Figure 4B, 18 s. Such narrow widths could create some difficulty in collection, particularly in manual operation.

In Figure 4C, the separation is conducted at 300 V/cm until 1 min prior to the appearance of the first peak in the detector. The field is then decreased to 30 V/cm and detection achieved. Bands of roughly 55-s peak widths are observed with close to base line separation. Note that separation in Figure 4C is comparable to that run continuously at 100 V/cm (Figure 4B).

We can apply the principles of field programming illustrated in Figure 4C to collection, as shown in Figure 5. In Figure 5A, the $p(dA)_{40-60}$ mixture is microseparatively separated on a 3% T, 5% C gel column, effective length 55 cm, using a sample size roughly 6-fold higher than typical for the analytical runs. We attempted to collect a single species from the overloaded sample by using field programming. In this exper-

iment, the sample traveled through the detector, as shown in Figure 5A, and the field was maintained at 300 V/cm until just before the species reached the end of the column. The field was then cut off, and the capillary column and electrode placed in a microfuge tube with 1.5 μ L of water. The field was then applied at 30 V/cm and collection conducted for 60 s. The calculated peak width was 45 s, based on the time width through the detector and the applied field of 30 V/cm. The extra collection time was used in order to be certain to collect the peak, given the manual nature of the experiment.

The collected fraction was reinjected with an internal standard, $p(dA)_{20}$, and the resulting electropherogram is shown in Figure 5B. It can be seen that an individual peak has been successfully collected. The collected peak is assumed to be $p(dA)_{47}$, based on the agreement of the relative migration of the 47-mer to that of the 20-mer in Figure 5B and Figure 5C, the latter of which is for $p(dA)_{40-60}$ and $p(dA)_{20}$ electrophoresed together. The difference in the relative migration times is less than 0.2% in B (0.874) and C (0.8725). It may also be noted that the differences in relative migration of $p(dA)_{46}$ or $p(dA)_{48}$ vs $p(dA)_{20}$ were 1.0%. The identity of $p(dA)_{47}$ in Figure 5C is again based on the linear calibration of migration time of standard $p(dA)$'s vs base number.

Computer control of the collection procedure would improve this field programming approach. The mobility of the species and its peak width at the high field could be directly determined during the run as detection takes place on-column. Knowledge of the distance from the detector to the end of the column would then permit calculation of the point at which the field would be reduced. Also, the actual time-based peak width during collection could be obtained from the measured peak width at the detector and the applied field at collection. It is also to be noted that the sample migrates through the detector to the end of the column under a high field. Since, at a given field, resolution is proportional to (migration distance)^{1/2}, an improved resolution over that observed in the detector will result. This improvement will obviously depend on the relative distance traveled from the detection point to the end of the column. It is also important that the temperature in the postdetector section of the column be the same as in the predetector section (17). Since, as already noted, mobility changes by 2% / °C (16), a temperature difference in the postdetector section would decrease the accuracy of the time the band is predicted to reach the end of the column.

Because of the simplicity of the approach and the ease of automation, field programming should become a useful procedure for collection. It should be possible to conduct collection in a precise manner, permitting heart cutting even of high-resolution complex mixtures. Field programming can also find value in detection where the time for detection influences overall sensitivity, e.g. radioactive detection (22).

ACKNOWLEDGMENT

The technical assistance of A. Arai is acknowledged. The authors also thank Dr. Norbert Bischoffer and Dr. Matthew Field of Genentech for providing the chemically synthesized deoxypolythymidylic acid mixture.

LITERATURE CITED

- (1) Cantor, C. R.; Smith, C. L.; Mathew, M. K. *Ann. Rev. Biophys. Chem.* **1988**, *17*, 287-304.
- (2) Smith, L. M.; Sanders, J. Z.; Kaiser, R. J.; Hughes, P.; Dodd, C.; Connel, C. R.; Heiner, C.; Kent, S. B. H.; Hood, L. E. *Nature* **1986**, *321*, 674-679.
- (3) *Current Protocols in Molecular Biology*; Ansabel, F. M., et al., Eds.; John Wiley and Sons: New York, 1989; 2.12.1-2.12.5.
- (4) Rickwood, D.; James, B. D., Eds. *Gel Electrophoresis of Nucleic Acids: A Practical Approach*; IRC Press: Washington, DC, 1983.
- (5) Karger, B. L.; Cohen, A. S.; Guttman, A. J. *Chromatogr., Biomed. Appl.* **1989**, *492*, 585-614.
- (6) Jorgenson, J. W.; Lukacs, K. D. *Science* **1983**, *222*, 266-272.
- (7) Gordon, M. J.; Huang, X.; Pentoney, S. L., Jr.; Zare, R. N. *Science* **1988**, *242*, 224-228.

- (8) Ewing, A. G.; Wallingford, R. A.; Olefirowicz, T. M. *Anal. Chem.* **1989**, *61*, 292A-303A.
- (9) Cohen, A. S.; Najarian, D. R.; Paulus, A.; Guttman, A.; Smith, J. A.; Karger, B. L. *Proc. Natl. Acad. Sci. USA* **1988**, *85*, 9660-9663.
- (10) Guttman, A.; Paulus, A.; Cohen, A. S.; Grinberg, N.; Karger, B. L. *J. Chromatogr.* **1988**, *448*, 41-53.
- (11) *Electrophoresis '88—Proceedings of the 6th Meeting of the International Electrophoresis Society*; Schaefer-Nielsen, C., Ed.; VCH Publishers: New York, 1988; pp 151-159.
- (12) Cohen, A. S.; Karger, B. L. *J. Chromatogr.* **1987**, *397*, 409-417.
- (13) Hjerten, S.; *Arch. Biochem. Biophys. Suppl.* **1962**, *1*, 147-151.
- (14) Stellwagen, N. *Advances in Electrophoresis*; Chrambach A., Dunn, M. J., Radola, B. J., Eds.; VCH Publishers: New York, 1987; Vol. 1, pp 179-228.
- (15) Terabe, S.; Yashima, T.; Tanaka, N.; Araki, M. *Anal. Chem.* **1988**, *60*, 1673-1677.
- (16) Wieme, R. J. *Chromatography: A Laboratory Handbook of Chromatography and Electrophoresis Methods*, 3rd ed.; Heftmann, E., Ed.; Van Nostrand: New York, 1975; pp 228-281.
- (17) Nelson, R. J.; Cohen, A. S.; Paulus, A.; Guttman, A.; Karger, B. L. *J. Chromatogr.* **1989**, *480*, 111-127.
- (18) Foley, J. P.; Dorsey, J. G. *Anal. Chem.* **1983**, *55*, 730-737.
- (19) Lauer, H. H.; Manigill, D. M. *Anal. Chem.* **1986**, *58*, 166-170.
- (20) Mikkers, F. E. P.; Everaerts, F. M.; Verheggen, Th. P. E. M. *J. Chromatogr.* **1979**, *169*, 1-10.
- (21) Rose, D. J., Jr.; Jorgenson, J. W. *J. Chromatogr.* **1988**, *327*, 23-34.
- (22) Pentoney, S. L., Jr.; Zare, R. N.; Quint, J. F. *Anal. Chem.* **1989**, *61*, 1642-1647.

RECEIVED for review July 3, 1989. Accepted October 19, 1989. The authors gratefully acknowledge Beckman Instruments for support of this work. This is Barnett Institute Contribution No. 382.

Sample Introduction Techniques for the Determination of Osmium Isotope Ratios by Inductively Coupled Plasma Mass Spectrometry

D. Conrad Gregoire

Geological Survey of Canada, 601 Booth Street, Ottawa, Ontario, Canada K1A 0E8

Reported are the relative merits of three sample introduction techniques for the determination of osmium isotope ratios by inductively coupled plasma mass spectrometry (ICP-MS). These are electrothermal vaporization (ETV), osmium tetroxide vapor generation (VG), and conventional solution nebulization (SN). When Te was used as a matrix modifier, electrothermal vaporization was 3 orders of magnitude more sensitive (in terms of signal intensity) for osmium determinations than were either solution nebulization or osmium tetroxide vapor generation. The sensitivity of SN was increased by a factor of 30 by nebulizing Os as the dissolved tetroxide rather than in its reduced form. Osmium isotope ratios were determined with a precision of 0.2% relative standard deviation (RSD) by using solution nebulization, 0.3% by using vapor generation, and 0.5% by using electrothermal vaporization.

In recent years, important new applications in the geosciences for osmium isotope data have emerged. Because ^{187}Re decays to ^{187}Os with a relatively long half-life of approximately 40 billion years, this isotope pair is useful as a geochronometer (1). For certain occurrences such as ultramafic intrusions, Re/Os dating is the only means available to the geologist for dating these rocks. Osmium isotope ratios have been used to calculate the accretion rate of extraterrestrial particles (2) and used as an indicator of crustal versus cosmic origin of platinum group metals in layers of sedimentary strata high in iridium content (3), especially those found at the Cretaceous-Tertiary boundary (4) and other so-called mass extinction boundaries.

Although the abundance of Os in the earth's crust is less than 1 part per billion (ppb), concentrations several orders of magnitude higher can be found in extraterrestrial and certain mantle-derived materials. Accurate and sensitive methods have been reported for the determination of Os at low levels, such as accelerator mass spectrometry (5), resonance

ionization mass spectrometry (6, 7), and ion sputtering mass spectrometry (8, 9). The principal disadvantages of these techniques are the low sample throughput available and the somewhat higher cost of the analytical instrumentation required.

Inductively coupled plasma mass spectrometry (ICP-MS) is a relatively new analytical technique that has been applied to the determination of Os isotopes. The high temperature of the argon plasma coupled with atmospheric pressure sampling of the ionized sample by a quadrupole mass spectrometer makes it possible to quickly analyze solutions containing Os at the parts-per-billion concentration level. An added advantage of ICP-MS over other techniques is the ability to interchange different modes of sample introduction, which can result in dramatic increases in analytical sensitivity as will be shown below.

Osmium isotope ratios of iron meteorites and iridosmines were determined by Masuda et al. (10) by conventional solution nebulization ICP-MS using a concentric glass nebulizer, while Lichte et al. (11) determined the osmium isotope composition of a shale by using a glass frit nebulizer to increase the efficiency of sample transport to the plasma. An increase in integrated signal intensity of 100 times over that obtained with solution nebulization was reported by Russ et al. (12) when osmium was distilled as the tetroxide vapor and transported directly into the argon plasma. Comparable results were obtained by Dickinson et al. (13) using a similar osmium vapor generation technique. For the major osmium isotopes, a precision of 0.3% (13) and an accuracy of 0.1-0.2% were achieved when ICP-MS results were compared to those obtained by secondary ion mass spectrometry. However, relatively large absolute quantities of Os and hence large sample sizes would be required to accurately determine the ratio of ^{187}Os to any other isotope because ^{187}Os generally accounts for less than 2% of the total quantity of Os present.

Electrothermal vaporization techniques (ETV) were first coupled to ICP-MS by Park et al. (14, 15) and later applied to the determination of some platinum group elements by

ICP-MS by Gregoire (16). Among the advantages of ETV techniques demonstrated by these authors are increased sensitivity, accurate measurement of isotope ratios, microliter sample volumes, and the optional use of matrix modification (16).

In this paper, a comparison is made of the accuracy, precision, and sensitivity with which Os isotope ratios can be determined by each of three sample introduction techniques: solution nebulization, tetraoxide vapor generation, and electrothermal vaporization.

EXPERIMENTAL SECTION

Instrumentation. The ICP mass spectrometer used for this study was a Perkin-Elmer/Sciex Elan Model 250. An extended quartz torch was used throughout. For solution nebulization work, a Meinhard C3 concentric glass nebulizer was used and a sample uptake rate of 0.8 mL/min was controlled with a Gilson Minipuls 2 peristaltic pump.

The osmium tetraoxide vapor generation apparatus was a batch type unit similar in construction to the apparatus used by Dickin et al. (13). The 250-mL reaction vessel was wrapped with heater tape and insulated with a layer of glass wool. Above the reaction vessel was mounted a condenser to remove excess water vapor from the carrier gas stream. Argon, used as the sparging/carrier gas, was introduced from the bottom of the reaction vessel at a flow rate of 1.0 L/min. A 0.5-m, 5-mm-i.d. length of Tygon or Pyrex glass tubing was used to transport the argon gas from the condenser to the torch.

The electrothermal vaporization device, constructed in our laboratories, has been described elsewhere (14, 15). The device consisted of a resistively heated strip of metal or a graphite platform measuring 11 × 4 mm. Sample material vaporized on the graphite surface was transported to the plasma by a stream of argon directed tangentially relative to the metal supports on which the graphite parts were mounted. A quartz cover, resembling an inverted thistle tube, formed an envelope above the vaporization surface and was designed to minimize condensation of sample material on the surface of the cover and to maximize the transport of analyte to the plasma. Sample vapor leaving the ETV unit was transported to the plasma via a length (0.5 m) of 5-mm-i.d. Tygon or Pyrex glass tubing.

Four types of graphite were used as the vaporization substrate for ETV work: crystalline graphite, pyrolytically coated crystalline graphite, solid anisotropic pyrolytic graphite, and glassy carbon. Graphite stock was obtained from Ultra Carbon (Bay City, MI) and machined in our laboratories. Preformed glassy carbon platforms (11 × 4 × 1 mm) were obtained from Ringsdorf (Bonn, FRG) and used without further machining. Tantalum metal (A. D. Mackay, Darien, CT) strips were cut from foil sheets (99.95% purity) 0.05 mm in thickness. A 3-mm-diameter steel ball bearing was used to impress a small concave depression in the center of the metal strip in order to contain the sample solution during the drying step.

A specially designed double-pass spray chamber (to be described elsewhere) was used. This device allowed for switching from one sample introduction technique to another without the usual plasma shutdown. Ion lens settings and plasma conditions were optimized by using the steady-state signal produced by solution nebulization. This avoided the more cumbersome and lengthy procedures that would have been required had a transient signal such as that produced by using the ETV been used for optimization of instrument parameters.

Reagents and Sample Preparation. All reagents used were of analytical reagent grade, and distilled deionized water was used throughout. Matrix modifier solutions were made by dissolving salts in distilled water, with the exception of Ni and Te, which were in solution as chlorides in 2 M HCl. Specpure (Aesar/Johnson Matthey, Inc.) 1000 ppm Os as OsCl₃ in 5% HCl was used as the Os test solution for this study.

Iridosmine samples, obtained from the Systematic Reference Series, National Mineral Collection of Canada, were fused in glassy carbon crucibles heated by a Meeker burner. Fifty milligrams of iridosmine (natural Ir/Os alloy) was mixed with 0.3 g of sodium peroxide and fused for a period of 5 min at red heat. The cooled melt was dissolved in 10 mL of distilled water and later acidified

Table I. Instrument Operating Parameters

Mass Spectrometer Settings	
B lens	+2.4 V
E1 lens	-16.4 V
P lens	-14.2 V
S2 lens	-10.7 V
sampler	Ni, 1.14-mm orifice
skimmer	Ni, 0.89-mm orifice
Plasma Conditions (Solution Nebulization)	
rf power	1.0 kW
reflected power	<5 W
auxiliary flow rate	2.2 L/min
nebulizer flow rate	1.0 L/min
plasma flow rate	12.5 L/min
sampling depth ^a	15 mm
Plasma Conditions (Electrothermal Vaporization/OsO ₄ Vapor Generation)	
rf power	0.9 kW
reflected power	5 W
auxiliary flow rate	2.0 L/min
carrier gas flow rate	1.0 L/min
plasma flow rate	12.5 L/min
sampling depth	15 mm
Electrothermal Vaporizer Conditions	
sample/matrix modifier vol	2–5 μL
heating cycle	
dry	10-s ramp to 100 °C 20-s hold at 100 °C
char	10-s ramp to 300 °C 5-s hold at 300 °C
high temperature	5-s hold at 2700 °C

^aDistance in millimeters from the tip of the mass spectrometer sampling cone to the downstream turn of the load coil.

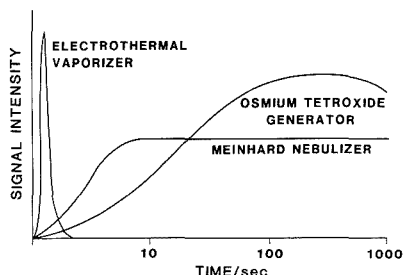


Figure 1. Comparison of time-dependent Os ion count rate for different sample introduction techniques.

with HCl and stored in brown glass containers.

Signal Measurement. The experimental conditions used for the ICP-MS instrument and each of the three sample introduction techniques are given in Table I. All measurements were made using a spectral resolution of 0.6 μm at 10% peak height. The analyte signals resulting from the application of each sample introduction technique required different signal measurement parameters. Solution nebulization produced an essentially steady-state signal and afforded the greatest flexibility for signal measurement. The osmium tetraoxide generator produced a long transient lasting approximately 15 min, and the ETV gave signals lasting on the order of 1 or 2 s. The relative duration and shape of signal pulses from each device are graphically illustrated in Figure 1.

For solution nebulization work, one measurement per isotope was made during each measurement sequence. Data were collected for a period of 0.4 s (dwell time) for each isotope before moving on to the next isotope. Intensities used for the calculation of ratios were obtained by using the mean of 10 measurement sequences as described above. For vapor generation sample introduction, the signal intensity for each of the seven isotopes of Os was calculated as for solution nebulization, with the exception that the dwell time was reduced to 0.2 s. Calculation of isotope

ratios was done as above with data obtained by averaging 10 intensity values taken from the relatively flat portion of the analyte signal curve (Figure 1) where steady-state conditions were most nearly approximated.

The fast transient produced by ETV required rapid monitoring of the analyte signal intensity. Compromise conditions limited the measurement cycle to four isotopes per firing. Monitoring of more than four isotopes resulted in distorted analyte signal pulses and inaccurate data. Data was acquired as above by sequentially measuring the intensity for each isotope, using a dwell time of 5 ms. The measurement cycle was continued until the signal pulse had decayed to the base line. Intensity data for each isotope were obtained by calculating the mean of five intensity readings at the peak of each signal pulse. Isotope ratios were calculated by using the average value obtained for five firings. ^{188}Os was monitored during each ETV measurement cycle and was used as an internal reference to avoid problems associated with differences in the heating cycle when isotope intensities obtained during different firings are compared.

The concentration of Os in the test solution used for each experiment was adjusted to give a maximum signal intensity of 150 000 counts/s for the most abundant Os isotope being determined. Intensity data exceeding this value and given in some of the tables were arithmetically scaled up to provide a comparison of results on a basis of unit analyte mass. No correction was made for dead time in the counting system because of the low count rates being measured. Dead time corrections were not necessary, provided count rates were kept below 200 000 counts/s. This was experimentally verified by measuring the ratio of ^{192}Os to ^{187}Os (25.3) as a function of ^{192}Os count rate. The isotope ratio did not change significantly within the precision of the measurement (0.2%) up to a count rate of 200 000. All isotope ratios for mineral samples (Table VI) were obtained at count rates of the order of 50 000 or less for the most abundant isotope for any isotope pair being determined.

Experimental Procedure. Determinations by solution nebulization were done in the conventional manner as described above. Solutions to be analyzed by using the Os tetroxide generator were first pipetted (10 μL to 1 mL) into the reaction vessel, followed by the addition of 5 mL of cold oxidizing reagent solution. After the vessel was flushed for 30 s with argon, the voltage to the heater tape was increased until a steady-state temperature of 140 $^{\circ}\text{C}$ was achieved. Heating of the reaction vessel to this temperature took approximately 3 min. Once the heating cycle was initiated, the argon carrier gas was directed to the plasma by means of a stopcock located downstream from the water condenser. The signal measurement sequence was also begun at that time. At the end of each run, the stopcock was closed, diverting the argon sparging gas to a vent while spent sample solution was drained from the reaction vessel. The condenser and reaction vessel were rinsed with 50 mL of distilled water prior to the next measurement sequence.

The procedure employed for ETV determinations was described previously (16). Microliter volumes of sample solution and matrix modifier solution were pipetted onto the surface of the vaporization substrate material (platform). The quartz cover was replaced and the heating cycle begun. Between firings, a high-temperature burn at 2700 $^{\circ}\text{C}$ for 10 s was used to remove any unvolatilized material remaining on the surface of the platform. A stopcock system was used to vent the ETV system during the drying and charring heating steps and for directing the carrier gas to the plasma during the high-temperature volatilization step. A trigger pulse from the ETV power supply initiated the ICP-MS signal measurement sequence during the high-temperature step.

Adjustment of ion lens settings was done in the solution nebulization (SN) mode with aqueous standards. Because of the possibility that different plasma conditions were required (cf. Table I) for optimum performance when a dry aerosol is used as opposed to one containing water (SN), a new approach to plasma parameter selection was devised. For both the vapor generation (VG) and ETV studies, plasma conditions such as vertical and horizontal torch positioning and selection of sampling depth and gas flow rates were rapidly optimized in the following manner. A small droplet (3 μL) of Hg metal, used as an indicator element, was placed in a small container located in the argon carrier gas stream. Argon gas flowing past the Hg droplet swept enough Hg

Table II. Effect of Oxidizing Agent on Os (100 ng) Ion Count Rate for OsO_4 Vapor Generation

oxidizing agent	max ^{192}Os count rate, counts/s
periodic acid (10%)	57 400
sulfuric acid/ H_2O_2 (1:1 (v/v))	204 000
perchloric acid (70%)	200 000

vapor to the plasma to give a strong steady-state signal. Instrument parameters could then be varied much as they would be when SN was being used. Instrument optimization could be completed within 5 min, avoiding the time-consuming procedure of performing repeated ETV firings or an entire osmium tetroxide generator run.

PRELIMINARY STUDIES

OsO_4 Vapor Generation. The volatility (bp 130 $^{\circ}\text{C}$) of osmium tetroxide has long been used for the separation of Os from dissolved rock and mineral samples. Classical distillation procedures relied principally on perchloric acid both to dissolve the sample matrix and to volatilize the Os (and Ru). Adaptation of this procedure for batch sparging of OsO_4 into an ICP mass spectrometer involved the study of several experimental parameters, the most important of which were the carrier gas flow rate, the oxidation reaction temperature, and the selection of oxidizing agent.

A carrier gas flow rate of 1.0 L/min was selected to match the flow rate used for SN and ETV work. Within 10% of the selected flow rate, equivalent count rates for an Os solution of a given concentration (for all three sample introduction techniques) could be achieved by adjusting other ICP-MS experimental parameters such as the sampling depth and the radio frequency (rf) power.

The reaction temperature for the conversion of Os to its tetroxide was important since the kinetics of this oxidation are relatively slow (cf. Figure 1). Bazan (17) found that a temperature range of 135–145 $^{\circ}\text{C}$ for this reaction gave optimum results for the batch sparging of osmium tetroxide into an optical emission spectrometer. A temperature of 140 $^{\circ}\text{C}$ was selected for this work because it was found that this temperature struck a balance between sufficiently rapid reaction kinetics and the unwanted volatilization of oxidizing agent and water to the argon plasma. High acid vapor content of the carrier gas caused the premature corrosion of sampler and skimmer orifices.

Various oxidizing agents have been utilized for distilling Os, including 70% perchloric acid (11), 10% periodic acid (12, 13, 17), hydrogen peroxide (13), and aqua regia (6, 10). For ICP-MS work, both hydrogen peroxide and aqua regia were unsuitable because the former quickly decomposed and use of the latter resulted in very corrosive gases reaching the plasma. Table II compares the maximum ^{192}Os count rate obtained for 100 ng of Os (as chloride) when oxidized by three different reagents. Ten percent periodic acid resulted in a maximum count rate of 57 400 counts/s, which was slightly greater than that obtained by Russ et al. (12) who used the same reagent under similar experimental conditions. Both perchloric acid and a 1:1 mixture of concentrated sulfuric acid and 30% hydrogen peroxide gave essentially equivalent results of 200 000 counts/s, which is a factor of 4 times greater than that obtained with 10% periodic acid solution. Although hydrogen peroxide was found to be unsuitable (13) because of its thermal instability, in combination with concentrated sulfuric acid the relatively stable H_2SO_5 is formed. The thermal stability of this reagent was demonstrated when it was used for the oxidation of a second aliquot of Os solution after being heated at 140 $^{\circ}\text{C}$ for a period of 10 min. This mixture was chosen for all subsequent measurements because of the high boiling point of sulfuric acid (338 $^{\circ}\text{C}$ at 98%)

Table III. Effect of ETV Platform Substrate Material on Os (0.25 ng) Ion Count Rate

substrate material	¹⁹² Os count rate, counts/s
crystalline graphite	79 100
pyrolytic graphite coated graphite	89 400
solid anisotropic pyrolytic graphite	88 000
glassy carbon	82 500
tantalum metal	27 700

compared to that of perchloric acid (200 °C) and because the carrier argon gas reaching the plasma contained only OsO₄, water, and liberated oxygen.

Electrothermal Vaporization. A feature of the electrothermal vaporization technique is the microliter quantity of sample solution required for a determination. The higher preconcentration ratios possible and the higher analyte transport efficiency (14) of ETV couple to give lower detection limits than are obtainable by SN. However, refractory elements are often not completely vaporized from a graphite surface or may even form refractory carbides with graphite or high-boiling alloys when metal vaporization surfaces are used (18).

In atomic absorption studies platinum group elements have been reported (19) to vaporize from a graphite surface by first undergoing carbon reduction followed by thermal vaporization of the metal. Osmium is one of the most refractory of elements with a boiling point in excess of 5000 °C and thus may be very difficult to efficiently volatilize by ETV. For this reason, there are several important ETV experimental parameters worthy of study that could affect the efficiency of the vaporization process. These are the vaporization substrate and the selection of an appropriate matrix modifier.

It has been shown in atomic absorption studies (20) that for the vaporization of refractory metals from a graphite surface, the higher the vaporization temperature, the higher the analytical sensitivity. The vaporization temperature used is limited by the sublimation temperature of graphite and the effects of thermal shock on the graphite platforms. For this work, the highest practical temperature was found to be 2700 °C. For metal vaporization surfaces, the vaporization temperature was limited by the melting point of the metal.

The chemical reactivity or activity of the vaporization surface is known (21) to be an important factor in determining the vaporization rate of the analyte, particularly for those elements thought to form refractory carbides or undergo carbon reduction prior to volatilization. Five vaporization surfaces were studied for the vaporization of Os by ETV: graphite, graphite coated with pyrolytic graphite, solid anisotropic pyrolytic graphite, glassy carbon, and tantalum metal. These materials were used to study the effect of progressively decreasing the reactivity of ETV substrate material on the efficiency of Os volatilization. Table III shows the ¹⁹²Os count rates (at the peak of the analyte signal) obtained for 0.25 ng of Os vaporized at 2700 °C from each of the five materials studied. Surprisingly, the four types of graphite used gave little variation in the ¹⁹²Os ion count rate. This result may indicate that the vaporization of Os did not involve reduction by carbon as previously thought but perhaps the vaporization of osmium chloride or some other compound. Thermal decomposition of the chloride likely occurred near the hot graphite surface where the gas-phase temperature was relatively high or was postponed until the gas reached the plasma. In marked contrast, the Ta surface performed poorly compared to carbon surfaces. This may be attributed to the formation of a refractory alloy or solid solution of Os with Ta or some other refractory compound. Other metals with high

Table IV. Effect of Matrix Modifier on Os (0.25 ng) Ion Count Rate by Electrothermal Vaporization

matrix modifier (2 μg)	max ¹⁹² Os count rate, counts/s
—	36 450
sodium chloride	36 800
thiourea	50 100
8-hydroxyquinoline	63 400
nickel	176 900
selenium	183 700
tellurium	653 000

Table V. Comparison of Sensitivity and Precision for the Determination of Osmium Stable Isotopes by Different Sample Introduction Techniques

sample intro technique	¹⁹² Os count rate ^a per ng of Os	precision, ^b % ¹⁹² Os/ ¹⁸⁸ Os
solution nebulization		
OsCl ₃ in solution	900	0.2
OsO ₄ in solution	28 200	0.2
OsO ₄ vapor generation	2 050	0.3
electrothermal vaporization	2 600 000	0.5

^a Mean of 10 measurements. ^b 2σ.

melting points such as W, Re, or Ir could not be used for this work either because of spectral overlaps of stable isotopes of these elements (W, Re) with Os or because of the near proximity (1 u) of a major substrate metal isotope (Ir) with an Os isotope. Even at temperatures below incandescence, large quantities of substrate metal vapor reached the plasma and made measurements of nearby Os isotopes impossible.

Matrix modification is used to alter the vaporization characteristics of the matrix, the analyte, or the vaporization surface. In a recent paper (16) sensitivity was increased by as much as a factor of 10 when Ni was used as a matrix modifier for the determination of platinum group elements by ETV-ICP-MS. Many matrix modification schemes have been reported in the atomic absorption literature. The use of matrix modification in ETV-ICP-MS work is potentially more widely applicable than in atomic absorption work because only vaporization need be enhanced. The added requirement in atomic absorption that atomization take place in addition to vaporization is absent since the argon plasma serves to decompose, atomize, and ionize the analyte.

Table IV summarizes the results obtained for a number of potential matrix modifiers. Individual matrix modifiers were selected to include candidates from the major groups of matrix modifiers, such as those forming chlorides and sulfides and those forming compounds or complexes with Os. Small enhancements in analyte signal were realized when NaCl, thiourea, or 8-hydroxyquinoline were used; however, a 5-fold enhancement in the ¹⁹²Os ion count rate resulted when nickel or selenium was used. An enhancement of nearly 20-fold was obtained when Te was used as a matrix modifier. The mechanism for this enhancement is unclear, but Os does form selenides and tellurides and it is possible that compound formation may result in a more volatile form of Os. The analyte signal pulse obtained when Te was used as matrix modifier was very sharp and lasted only 1.5 s. A sharp analyte signal pulse such as this indicated the virtually total volatilization of analyte from the surface of the graphite platform.

RESULTS AND DISCUSSION

Table V compares the sensitivity and precision obtained for the determination of Os isotopes by using three sample introduction techniques. Solution nebulization was divided into two separate "techniques", one for the nebulization of

Table VI. Comparison of Osmium Isotope Ratios of Iridosmines Determined by Using Different Sample Introduction Techniques

samp intro techn ^a	isotope ratio				
	¹⁹² Os/ ¹⁸⁸ Os	¹⁹⁰ Os/ ¹⁸⁸ Os	¹⁸⁸ Os/ ¹⁸⁸ Os	¹⁸⁷ Os/ ¹⁸⁸ Os	¹⁸⁶ Os/ ¹⁸⁸ Os
	Osmium Standard: Johnson Matthey				
SN	3.089 ± 0.004 ^b	1.994 ± 0.002	1.214 ± 0.004	0.124 ± 0.001	0.120 ± 0.001
VG	3.087 ± 0.003	2.002 ± 0.005	1.210 ± 0.006	0.122 ± 0.002	0.120 ± 0.002
ETV	3.085 ± 0.005	1.989 ± 0.008	1.208 ± 0.010	0.123 ± 0.002	0.122 ± 0.003
	Iridosmine: Ural Mountains, Catalog No. 019604				
SN	3.087 ± 0.002	1.998 ± 0.002	1.226 ± 0.002	0.122 ± 0.001	0.120 ± 0.001
VG	3.088 ± 0.004	1.984 ± 0.004	1.224 ± 0.005	0.120 ± 0.002	0.122 ± 0.001
ETV	3.090 ± 0.006	1.983 ± 0.005	1.199 ± 0.005	0.119 ± 0.002	0.124 ± 0.002
	Iridosmine: California, Catalog No. 019605				
SN	3.089 ± 0.002	1.989 ± 0.002	1.218 ± 0.003	0.123 ± 0.001	0.120 ± 0.001
VG	3.088 ± 0.004	1.986 ± 0.008	1.216 ± 0.005	0.119 ± 0.005	0.123 ± 0.002
ETV	3.087 ± 0.010	1.985 ± 0.006	1.228 ± 0.008	0.121 ± 0.003	0.126 ± 0.003
	Rutheniridosmine: Papua, New Guinea, Catalog No. 012161				
SN	3.085 ± 0.003	1.987 ± 0.003	1.228 ± 0.002	0.124 ± 0.001	0.119 ± 0.001
VG	3.081 ± 0.001	1.993 ± 0.003	1.225 ± 0.005	0.124 ± 0.002	0.121 ± 0.001
ETV	3.091 ± 0.007	1.997 ± 0.009	1.214 ± 0.010	0.123 ± 0.002	0.120 ± 0.002
	Iridosmine: Russian SFSR, Catalog No. 061847				
SN	3.087 ± 0.003	1.989 ± 0.004	1.221 ± 0.003	0.123 ± 0.001	0.120 ± 0.001
VG	3.086 ± 0.005	1.996 ± 0.002	1.214 ± 0.002	0.122 ± 0.003	0.120 ± 0.002
ETV	3.086 ± 0.004	1.983 ± 0.005	1.222 ± 0.006	0.122 ± 0.003	0.123 ± 0.003
Nier ^c	3.087	1.988	1.216	0.124	0.120

^a Key: SN, solution nebulization; VG, osmium tetroxide generation; ETV, electrothermal vaporization. ^b 1 σ , four determinations. ^c Reference 23.

osmium chloride in solution and the other for the nebulization of osmium tetroxide in solution. Osmium tetroxide solutions were prepared by the prior distillation of Os with perchloric acid and collection of OsO₄ vapor in water. Solution nebulization of either reduced or oxidized osmium gave the best measurement precision of 0.2% for the ¹⁹²Os/¹⁸⁸Os isotope ratio. There are at least two factors limiting the precision of isotope ratio measurements by ICP-MS: counting statistics, which are proportional to the inverse of the square root of the total number of counts, and uncertainty caused by noise related to the performance of the nebulizer, the plasma, and instrument instability. The combined effect of these factors has resulted in a practical limit of approximately 0.1% in the precision of isotope ratio measurements by ICP-MS.

The nebulization of Os as the tetroxide dissolved in water increased the sensitivity by a factor of 30. This increase in sensitivity resulted from the efficient volatilization and separation of OsO₄ from the sample solution during the nebulization process. When Os was present as the volatile tetroxide, the very fine droplets formed at the nebulizer, the residence time of these droplets in the spray chamber and the flow of argon to the torch combined to greatly increase the extraction and transport efficiency of Os from solution to the argon plasma. A longer time was required to reach a steady-state signal when OsO₄ solution rather than osmium chloride solution was nebulized. It took approximately 2 min before a steady-state was reached, which was probably the time required for the dead volume in the spray chamber/drain assembly to become saturated with OsO₄ vapor. A significant memory or carryover effect between samples was eliminated by the nebulization of 2 mL of a solution containing 500 ppm Sn as stannous chloride. The nebulization of solutions containing Os and perchloric acid or periodic acid was also investigated. The in situ generation of OsO₄ resulted only in a small increase in sensitivity (20%) owing to the slow kinetics of the oxidation reaction at room temperature. A more serious consequence of this approach was the accelerated corrosion of the sampler and skimmer orifices when solutions of high acid (5%) content such as these were nebulized.

Batch sparging of OsO₄ using the VG gave a maximum count rate about 2 times greater than was obtained for SN of reduced Os and 14 times less than that realized when OsO₄ solution was introduced into the plasma by SN. The precision of the measurement was degraded to 0.3% largely because of the plasma noise introduced by argon bubbling through the sample solution in the reaction vessel and the transient nature of the analyte signal.

Electrothermal vaporization of Os (with Te as matrix modifier) proved to be by far the most sensitive sample introduction technique in terms of maximum signal intensity with an equivalent ¹⁹²Os count rate per nanogram of 2.6 million counts/s. The high sensitivity obtained is somewhat counterbalanced by the poorer precision for the measurement of isotope ratios. A precision of only 0.5% was obtained because of the fast transient signal produced by ETV. An analyte signal pulse lasting only 1.5 s was difficult to measure with precision. Use of improved signal integration techniques would likely result in a better precision for ETV measurements.

In Table VI are compared data for Os isotope ratios for an Os reference solution and four natural osmium alloy samples. Osmium isotope ratios were determined by ICP-MS coupled with three sample introduction techniques. In each case, the direct analysis of fusion melt solutions was done by simple dilution with no prior separation procedures. Correction for mass discrimination was accomplished by a regression treatment (10) using isotopic abundances compiled by De Bièvre et al. (22). For example, the Os isotope ratios determined by all three sample introduction techniques agreed with one another within experimental error. The ¹⁸⁷Os content of all of the samples was invariant and not radiogenically enriched, which in each case indicates a mantle source for the host material. The values obtained compare well with literature values (23) given in the last row of Table VI and are generally accurate to within 0.2% or better for the major isotopes.

In summary, it is clear that the concentration of Os in the sample, the method of sample dissolution/preconcentration, the composition of the sample solution, the sample volume

available, and the measurement precision required will dictate which sample introduction technique is most practical for use. For samples high in Os content (>100 ppb), SN offers the best precision and an analysis time of several minutes with no equipment modifications necessary. However, several milliliters of sample solution was required for each determination.

For samples low in Os (1-100 ppb), ETV offers the greatest sensitivity, the lowest sample consumption (microliters), and an analysis time of several minutes for each sample. Compared to that of the other sample introduction techniques, the precision obtained by ETV is less although adequate for most applications. When sample solutions contained excessive quantities of Re or other interfering elements, it was possible to determine Os isotope ratios by ETV using selective volatilization techniques. Separation of Os from associated interfering elements was accomplished by using a low-temperature (140 °C) in situ selective volatilization of Os from the platform. This was done by using perchloric acid (5 μ L) as a matrix modifier. The low-temperature volatilization of Os resulted in reduced sensitivity ($\times 15$) compared to than obtained with ETV using Te, but was still 2 orders of magnitude more sensitive than SN.

ACKNOWLEDGMENT

The author is grateful to K. N. De Silva for his helpful comments during the course of the work and for critically reviewing the manuscript.

Registry No. ^{192}Os , 15062-08-5; ^{190}Os , 14274-79-4; ^{188}Os , 15761-06-5; ^{187}Os , 15766-52-6; ^{186}Os , 13982-09-7; ^{185}Os , 14274-81-8; iridosmine, 12198-39-9; rutheniridosmine, 75635-39-1; OsO_4 , 20816-12-0.

LITERATURE CITED

- (1) Hirt, B.; Tilton, G. R.; Herr, W.; Hoffmeister, W. *Earth Science and Meteorites*; Geiss, J., Goldberg, E. Eds.; North Holland: Amsterdam, 1963; pp 273-280.
- (2) Esser, B. K.; Turekian, K. K. *Geochim. Cosmochim. Acta* **1988**, *52*, 1383.
- (3) Turekian, K. K. *Geol. Soc. Am. Spec. Pap.* **1982**, *190*, 243.
- (4) Luck, J. M.; Turekian, K. K. *Science* **1983**, *222*, 613.
- (5) Fehn, U.; Teng, F.; Elmore, D.; Kubik, P. W. *Nature* **1986**, *323*, 707.
- (6) Walker, R. J.; Fassett, J. D. *Anal. Chem.* **1986**, *58*, 2923.
- (7) Walker, R. J. *Anal. Chem.* **1988**, *60*, 1231.
- (8) Luck, J.-M.; Birck, J.-L.; Alegre, C.-J. *Nature* **1980**, *283*, 257.
- (9) Luck, J.-M.; Alegre, C.-J. *Nature* **1983**, *302*, 130.
- (10) Masuda, A.; Hirata, T.; Shimizu, H. *Geochem. J.* **1986**, *20*, 233.
- (11) Lichte, F. E.; Wilson, S. M.; Brooks, R. R.; Reeves, D.; Holsbecher, J.; Ryan, D. E. *Nature* **1986**, *322*, 816.
- (12) Russ, G. P., III; Bazan, J. M.; Date, A. R. *Anal. Chem.* **1987**, *59*, 984.
- (13) Dickin, A. P.; McNutt, R. H.; McAndrew, J. J. *J. Anal. At. Spectrom.* **1988**, *3*, 337.
- (14) Park, C. J.; Van Loon, J. C.; Arrowsmith, P.; French, J. B. *Can. J. Spectrosc.* **1987**, *32*, 29.
- (15) Park, C. J.; Van Loon, J. C.; Arrowsmith, P.; French, J. B. *Anal. Chem.* **1987**, *59*, 2191.
- (16) Gregoire, D. C. *J. Anal. At. Spectrom.* **1988**, *3*, 309.
- (17) Bazan, J. M. *Anal. Chem.* **1987**, *59*, 1066.
- (18) Gregoire, D. C.; Chakrabarti, C. L. *Spectrochim. Acta* **1982**, *37B*, 611.
- (19) Rowston, W. B.; Ottaway, J. M. *Analyst* **1979**, *104*, 645.
- (20) Gregoire, D. C.; Chakrabarti, C. L.; Bertels, P. C. *Anal. Chem.* **1978**, *50*, 1730.
- (21) L'vov, B. V.; Nikolaev, V. G.; Novichikhin, A. V.; Polzik, L. K. *Spectrochim. Acta* **1988**, *43B*, 1141.
- (22) De Bievre, P.; Gallet, M.; Holden, N. E.; Barnes, I. L. *J. Phys. Chem. Ref. Data* **1984**, *12*, 809.
- (23) Nier, A. O. *Phys. Rev.* **1937**, *52*, 885.

RECEIVED for review March 13, 1989. Accepted October 2, 1989. Geological Survey of Canada Publication No. 10589.

Effect of Wet Decomposition Methods on the Determination of Cobalt, Copper, Selenium, and Zinc in Biological Samples Using Electrophoresis

J. Y. Yang and M. H. Yang*

Institute of Nuclear Science, National Tsing Hua University, Hsinchu, Taiwan, Republic of China

S. M. Lin

School of Technology for Medical Sciences, Kaohsiung Medical College, Kaohsiung, Taiwan, Republic of China

A method combining radiotracer techniques with paper electrophoresis to investigate the optimal decomposition conditions for cobalt, copper, selenium, and zinc in rat liver samples is described. After oral and intraperitoneal administration of the respective nuclides of ^{60}Co , ^{64}Cu , ^{75}Se , and ^{65}Zn solutions, the livers of the tested rats are removed and decomposed with a nitric and sulfuric acid mixture. The completeness of decomposition is investigated by measuring the respective radionuclide-containing species in the decomposed samples by electrophoretic analysis. The results indicate that the Co- and Se-containing liver samples are more easily decomposed than those containing Cu and Zn under the specific conditions. The same decomposition effects are observed for ingested radioisotopes as for intraperitoneally injected ones. The possible connection of decomposition with the analytical error is discussed.

INTRODUCTION

The interest in trace metals as elements essential to normal biological development or as potential sources of danger to

health has resulted in many reports dealing with methods for their determination in biological materials. Instrumental methods like atomic absorption spectrometry (AAS), inductively coupled plasma atomic emission spectrometry (ICP-AES), and sometimes voltammetric methods are commonly employed for the determination of trace elements in the samples. The samples in most cases are required to be in an aqueous solution, and this usually requires the destruction of the organic material. The completeness of destruction of sample matrix is of vital importance for achieving analytical accuracy, especially in cases when chemical separation (like solvent extraction with $\text{APDC}/\text{CHCl}_3$) is performed prior to the actual determination of the analyte.

Decomposition of the sample is one of the most important steps in trace analytical techniques in which voltammetry and atomic spectroscopy are employed as the measurement methods (1-3). However, to what extent the matrix is destroyed by a specific decomposition method has been so far seldom quantitatively evaluated. Conventionally, when clear and colorless solutions are obtained, or when total recovery of some elements is obtained, it has been tacitly assumed that

oxidation of the organic matter has been completed for practical purposes. However, such assumptions are not necessarily reliable in all cases. More conclusive and direct information as to the presence and identities of any residual matter retained by the acid solution is certainly desirable, especially if such matter might interfere in any subsequent measurements. To investigate the wet oxidation efficiency of a HNO_3 and HClO_4 mixture for various organic substances, Martinie et al. used proton magnetic resonance spectrometry, ultraviolet spectrometry, and carbon microanalysis to identify the residual matter (4). Their results show that compounds with *N*-methyl, *S*-methyl, *C*-methyl, and pyridyl moieties are most resistant toward wet oxidation, and addition of certain ions such as V(V), Ce(III), and Co(II) can exert catalytic influences on certain wet oxidations. A somewhat parallel study to determine the inorganic compositions of nitric and perchloric acid wet-oxidized residues after evaporation to dryness was also reported (5). From an analytical point of view, it is important to find out the distribution of species that contain the trace elements of interest and, if possible, the identities of the species in the decomposed sample. The quantitative information about the species distribution can be a useful guide for further improving the decomposition process in order to achieve accurate analysis by the chosen analytical technique.

In the previous study we developed a method combining radiotracer techniques with paper electrophoresis to investigate the effectiveness of the decomposition process of ^{65}Zn -labeled liver samples (6). The results revealed that aside from the $^{65}\text{Zn(II)}$, there also appears on the electrophoretic histogram one ^{65}Zn -containing organic species under certain specific decomposition conditions. On the basis of this study, it was assumed that the appearance of only one peak corresponding to the $^{65}\text{Zn(II)}$ ion in the electrophoretic histogram may imply total destruction of the sample matrix in the decomposition process, while the additional appearance of ^{65}Zn -containing species other than $^{65}\text{Zn(II)}$ ion may therefore indicate incomplete destruction of the sample. This assumption is, however, not conclusively proven because some other species in the decomposed sample might also migrate equally as Zn(II) in paper electrophoresis.

In this study the work was extended to investigate the behavior of trace elements other than zinc in rat liver by two different wet decomposition processes (reflux and pressure digestion) with a HNO_3 - H_2SO_4 mixture. The effectiveness of decomposition under these specific conditions is revealed from the electrophoretic histograms. It can be expected that complete decomposition is achieved if there appears on the histogram only one peak corresponding to the specific ions of the elements $^{60}\text{Co(II)}$, $^{64}\text{Cu(II)}$, $^{65}\text{Zn(II)}$, and $^{75}\text{Se(VI)}$. The appearance of additional peaks in the histogram may thus indicate the presence of undecomposed biological species. The existence of any organically bonded species other than the specific ions in the decomposed sample solutions might decrease the recovery of that specific element in the separation step and thus result in analytical error.

EXPERIMENTAL SECTION

Labeling with Radioactive Isotopes. The radioisotopes of ^{60}Co , ^{64}Cu , ^{75}Se , and ^{65}Zn were obtained by irradiating spectroscopically pure metals or compounds in the Taiwan Research Reactor at a flux of $5 \times 10^{13} \text{ n cm}^{-2} \text{ s}^{-1}$ for 14 days. The specific activities after 2-day cooling were estimated to be about $5 \mu\text{Ci}/\mu\text{g}$ of Co for ^{60}Co , $3 \mu\text{Ci}/\mu\text{g}$ of Cu for ^{64}Cu , $0.7 \mu\text{Ci}/\mu\text{g}$ of Se for ^{75}Se , and $0.5 \mu\text{Ci}/\mu\text{g}$ of Zn for ^{65}Zn . The irradiated metals or compounds were dissolved in concentrated HNO_3 , and the mixture was evaporated to dryness. Water was added and the resultant solution finally adjusted with NaOH to pH 2-3.

About 0.1 mL of each solution containing approximately 10-50 μg of the respective element of interest was intraperitoneally

injected in one group of the tested rats. The other group of rats was given the radioisotopes (not including ^{64}Cu) orally by mixing with the foodstuff for 10 consecutive days. After 1 day (for ^{64}Cu , half-life 12.74 h) or 7 days (for other nuclides), the rats were sacrificed, and the liver samples were dissected for wet oxidation decomposition.

Decomposition Procedures. The radioisotopically labeled liver samples (each about 0.5 g) were digested with various wet oxidation methods with a mixture of concentrated HNO_3 and H_2SO_4 solution. A Sjöstrand type of wet oxidation reflux apparatus was used (7), and the digestion performed followed basically the procedure established in our previous work (6). The sample was put into the digestion flask (150 mL), and a mixture of 5 mL of HNO_3 and 2 mL of H_2SO_4 was added to start the digestion. In the initial stage reflux was continued with the condensate returning to the flask for about 15 min. Then the tap on the condensate reservoir was closed, and water and HNO_3 were collected in the condensate reservoir. When a slight darkening of the digest occurred, small amounts of condensate were allowed to drain into the flask to continue the oxidation and remove the darkening. The operation was continued until darkening no longer occurred and the white fume of sulfur trioxide was observed. The whole process described above constitutes the one-cycle digestion. Repeating the process two or three times constitutes the so-called two-cycle and three-cycle digesting processes.

The digestion method based on the use of a pressure bomb (Berghof product) was conducted by heating the sample together with 3 mL of HNO_3 and 1 mL of H_2SO_4 at 130°C for 3 h (8). A common digestion method (9) was also tested for the decomposition of the ^{60}Co -labeled sample. The sample together with 6 mL of HNO_3 and 2 mL of H_2SO_4 was put in a beaker covered with a watch glass. The beaker was then heated on a hot plate at 130 - 150°C for 30 min.

After decomposition, the sample solution was adjusted with NaOH solution to about pH 6.5 for electrophoretic analysis.

Electrophoretic Analytical Procedure. Paper electrophoresis was conducted with a CAMAAG high-voltage electrophoretic apparatus as in our previous report (6). About 50- μL aliquots of sample solutions were spotted on $2 \times 48 \text{ cm}$ strips of Whatman 3-mm filter paper that had been previously wetted in acetate buffer (pH 6.5, 0.25 M NaOAc-0.25 M HOAc). A potential of 1000 V was applied for 30 min. The distributions of radioisotopes in the paper strips cut into numbered 1-cm pieces were then measured with a well-type NaI(Tl) scintillation counter.

Solvent Extraction Procedure. Parts of decomposed sample solutions were subjected to solvent extraction for separating Zn(II), Cu(II), and Co(II) ions using APDC/ CHCl_3 as extractant with a pH between 2 and 3. For separation of free selenium, which is supposed to be in the Se(VI) form, from the decomposed sample matrix by solvent extraction, prior reduction of Se(VI) to Se(IV) is necessary. The reduction was made by adding 25 mL of 6 M HCl to the digested sample solution and heating to 95°C for 1 h (10). After reduction, the solution was diluted to 50 mL with water and finally extracted with ammonium 1-pyrrolidinecarbothioate/methyl isopropyl ketone (APDC/MIBK) (50:50) at pH 1.5-2.5 to separate Se(IV) (11).

RESULTS AND DISCUSSION

Wet digestion of biological materials with various acid mixture has been extensively discussed in the literature. Of the methods available, digestion with the acids in an open air system such as a beaker, flask, or test tube is often used for routine analytical purposes (12-14). More elaborate techniques based on the use of reflux digestion (like Sjöstrand apparatus (7)), pressure bomb digestion (8), microwave digestion (15), and combustion (like Trace-O-Mat apparatus (16)) have become more important in trace analysis for the purposes of achieving more effective decomposition of sample, preventing volatility of some specific elements, or reducing the blank introduction. In this study the effectiveness of decomposition of biological samples by the reflux digestion and pressure digestion methods was studied by investigating the distribution of element-containing species of the decom-

posed samples by paper electrophoresis.

The wet oxidation digestion methods with the Sjöstrand reflux apparatus and pressure bomb were chosen because the former is simple, inexpensive, and available to nearly any analytical laboratory, and the latter is especially advantageous for ultratrace analysis, particularly in the analysis of volatile elements. Various acid mixtures like $\text{HNO}_3\text{-H}_2\text{SO}_4$ and $\text{HNO}_3\text{-HClO}_4$ are frequently used for digestion of biological matter. However, HClO_4 is not included in this study simply due to its corrosive effect on the filter paper used in the subsequent electrophoretic analysis.

To begin this study, the paper electrophoretic behaviors of the respective ions of Zn(II), Co(II), Cu(II), and Se(VI), the probable forms expected to be present in the digested sample solution, are first investigated by the procedures as described in our previous work (6). The electrophoretic histograms of the respective elements, indicate that the peaks corresponding to Zn(II), Co(II), and Cu(II) in the acetate buffer of pH 6.5 appeared on the negative side about 6–8 cm from the zero point, and that of Se(VI), which is known to be an oxyanion, appeared on the positive side about 7.5 cm from the zero point under this specific analytical condition. For a biological sample, if it is not completely digested, there should also be present other species containing the element of interest aside from the ionic forms described above. The separation of the totally decomposed species, typically as free ionic forms in the digested sample, can be basically achieved by the proper choice of electrophoretic conditions. However, the question to be clarified is whether the species identified as an undecomposed fraction appearing on the electrophoretic histogram is really an incompletely decomposed species or a species resulting from recombination of once-free ions with the organic residues in the subsequent treatment of decomposed sample solution. To verify this, an experimental design was made by mixing the respective ions of $^{65}\text{Zn(II)}$, $^{60}\text{Co(II)}$, $^{64}\text{Cu(II)}$, and $^{75}\text{Se(VI)}$ with the decomposed liver sample solution containing no radioactive tracer and then subjecting the mixture to electrophoretic analysis. The results so obtained indicated that, aside from the peaks corresponding to the respective ions of $^{65}\text{Zn(II)}$, $^{60}\text{Co(II)}$, $^{64}\text{Cu(II)}$, and $^{75}\text{Se(VI)}$, there appear no other perceivable peaks in the histograms. This excludes the possibility of formation of radioactively labeled species due to isotope-exchange reaction and consequently may imply that any radioactively labeled species other than the ionic form appearing on the histogram should result directly from the undecomposed biological material.

On the basis of the preliminary results obtained, the use of electrophoretic analysis to study the optimal decomposition conditions of ^{65}Zn -, ^{60}Co -, ^{64}Cu -, and ^{75}Se -labeled biological samples was considered feasible. In the following sections the results for the respective elements are described.

Zinc. The decomposition effect on zinc in rat liver treated with ^{65}Zn intraperitoneally has been reported in our previous work (6). It is of interest to further investigate if any difference in the decomposition effect between the liver samples from rats treated orally with ^{65}Zn and those treated intraperitoneally can be observed.

Figure 1 shows the electrophoretic histograms of the liver samples from rats treated orally with ^{65}Zn when the samples subjected to different decomposition processes. As seen from the figure, the peak appears on the negative side about 7 cm from the zero point, corresponding to the $^{65}\text{Zn(II)}$ species, while the peak appearing at about 1 cm from the zero point on the same side as Zn(II), corresponding to a slightly positively charged species, can be assumed to be an incompletely dissociated Zn-containing species. From a and b in the same figure, it is seen that the sample subjected to pressure digestion, as well as one-cycle reflux digestion with a

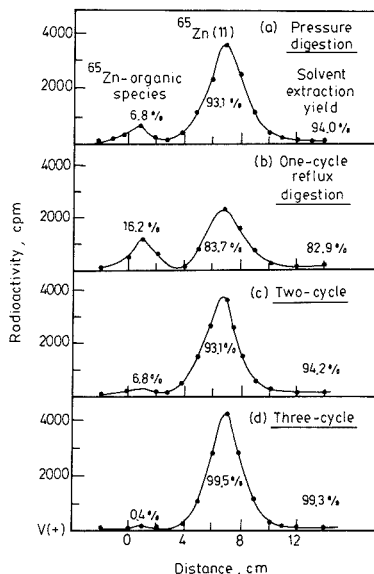


Figure 1. Electrophoretic histograms of liver samples from rats treated orally with ^{65}Zn , obtained after subsection of the samples to various digestion processes.

$\text{HNO}_3\text{-H}_2\text{SO}_4$ mixture, cannot be completely decomposed. However, the pressure digestion, even at conditions of 130°C for 3 h, can result in a more effective decomposition than that achieved by the one-cycle reflux digestion with the Sjöstrand apparatus—the incomplete decomposed fraction of the former being 6.8% and the latter being 16.2%. Figure 1b-d shows the results of the liver samples subjected to varying extents of reflux digestion. It is seen that the percent yields of ^{65}Zn -containing organic species decrease with increasing the digestion cycle, being 16.2%, 6.8%, and 0.4%, corresponding respectively to one, two, and three-cycles of the digestion process. It was also interesting to find that the percentage of ^{65}Zn extracted into the organic phase very closely agreed with the fraction of $^{65}\text{Zn(II)}$ shown in the histograms of Figure 1, and that remaining in the aqueous phase was found equivalent to the fraction of ^{65}Zn organic species. The percentage of extraction for these three samples with different extents of decomposition is also shown in the same figure for ease of comparison. If solvent extraction is performed prior to the actual determination of zinc in the sample subjected only to one-cycle digestion, an error of about 16% might be expected due to the apparently low recovery from this incompletely decomposed sample.

By comparison of the electrophoretic histograms of the liver samples from rats treated orally with ^{65}Zn (Figure 1) with those of the intraperitoneal ones shown in our previous work (6), any significant difference in decomposition efficiency between them under the same digestion conditions is unobserved. We can therefore conclude that the decomposition effects are the same for the ingested ^{65}Zn sample as for the intraperitoneally injected one.

Cobalt. Cobalt is essential as an integral component of vitamin B_{12} . In humans, the cobalt found in the liver to a great extent might be in the form of vitamin B_{12} (17). The decomposition efficiencies for the liver sample obtained by various digestion processes are shown in Figure 2, which indicates that complete digestion of a ^{60}Co -labeled liver sample can be effectively achieved. The yield of $^{60}\text{Co(II)}$ in the de-

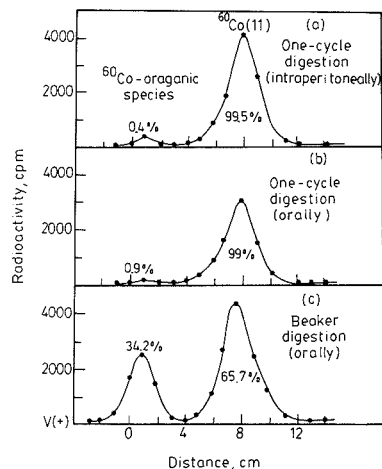


Figure 2. Electrophoretic histograms of liver samples from rats treated both orally and intraperitoneally with ^{60}Co , obtained after subjection of the samples to various digestion processes.

composed sample solution is $\geq 99\%$ even after one cycle of digestion in the liver samples from rats treated both orally and intraperitoneally.

In view of the relatively easy decomposition of the ^{60}Co -labeled liver sample, it is of interest to see if the sample also can be effectively decomposed by boiling with $\text{HNO}_3\text{-H}_2\text{SO}_4$ in a beaker on a heating plate. Figure 2 shows the results obtained under the experimental conditions by heating 0.5 g of sample with 6 mL of HNO_3 plus 2 mL of H_2SO_4 in a beaker at $130\text{--}150^\circ\text{C}$ for about 30 min. It is seen that a yield of only 65.7% of free Co(II) ions can be obtained under this decomposition process, indicating that the common beaker digestion process with the $\text{HNO}_3\text{-H}_2\text{SO}_4$ mixture cannot easily achieve complete decomposition of biological samples as commonly believed. The digestion efficiency can be, however, increased to about 85% by prolonging the heating to 2 h with three additions of 3 mL of HNO_3 during the digestion process. It was also found that the recovery of $^{60}\text{Co(II)}$ can be further increased to about 98% by raising the digestion temperature after 2 h of heating to a level where a fume of sulfur trioxide is observed for 10 min.

Copper. The rat can only be treated with ^{64}Cu intraperitoneally because of the short half-life of ^{64}Cu (12.74 h). The decomposition efficiency for ^{64}Cu -labeled liver samples was investigated by reflux digestion with a $\text{HNO}_3\text{-H}_2\text{SO}_4$ mixture. The yields of free $^{64}\text{Cu(II)}$ ions estimated from the electrophoretic histograms are 93.4%, 99.4%, and 99.8%, corresponding respectively to one-, two-, and three-cycle digestions. These results are found also in coincidence with that obtained by solvent extraction with APDC/CHCl_3 . By comparison of the results between zinc and copper for the one-cycle digestion process, it is seen that copper in rat liver is somewhat easier to release than zinc (7% vs 16%).

Selenium. Increasing concern about the significance and toxicity of selenium has led to the recent development of numerous analytical methods for its determination in various biological materials. The published data for selenium in plasma or serum as compiled by Versieck, varying from 0.042 to $0.19\ \mu\text{g/mL}$, are relatively consistent, compared with the published levels for several other elements (18).

The controversy about the inconsistent results for selenium determination in various biological samples can be basically attributed to incomplete conversion of native forms of sele-

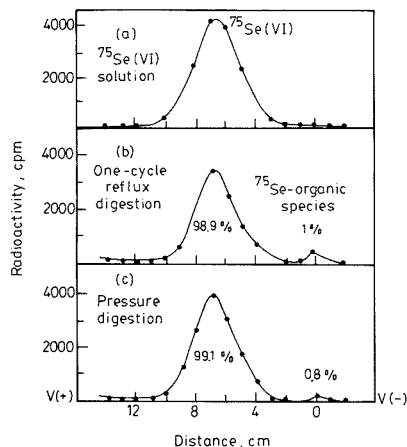


Figure 3. Electrophoretic histograms of various ^{75}Se -containing samples: (a) $^{75}\text{Se(VI)}$ ion; (b) reflux digested liver sample; (c) pressure digested liver sample.

nium such as selenomethionine to selenite-selenate (14), loss of selenium during the digestion process (19), and the state or form of selenium that is not detectable by the analytical technique employed (3). Various extensive studies have revealed that by using oxidative mixtures such as $\text{HClO}_4\text{-HNO}_3$ (10), $\text{H}_2\text{SO}_4\text{-HNO}_3$ (3), $\text{HNO}_3\text{-HClO}_4\text{-H}_2\text{SO}_4$ (20), and $\text{Mg}(\text{NO}_3)_2\text{-HNO}_3\text{-HCl}$ (20) one can achieve quantitative conversion of natural selenium compounds in various samples such as urine, blood, flour, and body tissues into selenate. No loss of selenium by volatilization, provided proper measures are taken to prevent charring during the digestion process, was reported (14, 21). The selenium in the digested sample solution can be finally completely converted from Se(VI) to Se(IV) by boiling the sample in about 6 N HCl (10), which can subsequently be determined by hydride AAS or cathodic stripping voltammetry. The loss of selenium caused by volatilization can be basically controlled by preventing the occurrence of charring during the digestion process (14). Adeloju et al. reported that a digestion procedure using a HNO_3 and H_2SO_4 mixture showed adequate decomposition of the organic matrix and hence permitted accurate determination of the element by cathodic stripping voltammetry in various biological samples (3).

Although the most common digestion method for biological materials utilizes the high oxidation potential of hot concentrated HClO_4 , the present study used a HNO_3 and H_2SO_4 mixture as the digestion solution to investigate the behavior of selenium in liver samples toward the digestion process. The tested rats were orally given $^{75}\text{Se(VI)}$ for 7 consecutive days to incorporate this element into the liver during normal metabolic functioning. The livers removed were digested with both pressurized and refluxing digestion methods. Figure 3 shows the histograms of the samples subjected to pressure and one-cycle reflux digestion. It is seen that in both procedures there appears a predominant peak on the positive side about 7 cm from the zero point and a small peak standing near the zero point. The negatively charged species is presumably a selenate ion resulting from the decomposition of the liver sample in the highly oxidative digestion solutions, while the neutral species standing on the zero point is the undecomposed matrix species. To prove the fraction contains Se(VI) , the digested sample solution was subsequently heated in 6 M HCl . After reduction, the Se(IV) extractable by APDC/MIBK was found very closely equivalent to the ^{75}Se fraction that appeared

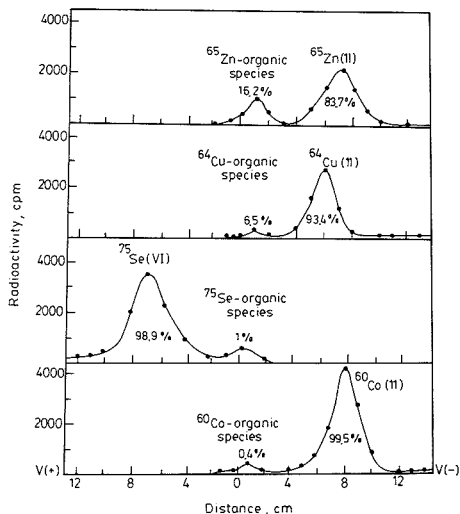


Figure 4. Comparison of decomposition efficiency of one-cycle reflux digestion of ^{60}Co -, ^{64}Cu -, ^{75}Se -, and ^{65}Zn -labeled liver samples.

on the positive side of the histograms.

From the results it is clear that selenium can be almost completely released from the biological matrix into ionic form as selenate after one-cycle or pressure digestion processes. It seems that selenium in biological matrices is not so difficult to digest as previously regarded (14). The reported inconsistency for Se determination most likely may be due not to decomposition efficiency but to the inadequacy of the analytical techniques employed for the determination of selenium (3). Even if the trace metals have been completely released from the biological matrix, there may still remain various types and amounts of organic residue in the digested sample solution. Unlike techniques such as AAS and ICP-AES, which rely on atomization of the element from solution and are not so prone to organic interferences, stripping voltammetry is more susceptible to the interferences (22). The organic residue can foul up the electrode by blockage or interference mechanisms of the adsorption type, and analytical error may thus result from this electroanalytical technique.

The method combining radiotracer techniques with electrophoresis provides a unique possibility to study the relative effectiveness of the decomposition process of biological sam-

ples. Figure 4 summarizes the yields of the one-cycle reflux digestion process for cobalt, copper, selenium, and zinc in liver samples. The results show that the recovery yields for cobalt, copper, selenium, and zinc are 99.5%, 93.4%, 98.9%, and 83.7%, respectively, indicating Co- and Se-containing liver samples are more easily decomposed than those containing Cu and Zn under the specific conditions. Among the liver samples tested, the samples containing zinc are the most difficult to digest by wet oxidation; basically, three-cycle digestion is needed to ensure complete release of zinc from the biological matrix.

ACKNOWLEDGMENT

The authors thank Prof. C. M. Wai of the University of Idaho for a critical reading of the manuscript.

LITERATURE CITED

- (1) Kotz, L.; Henze, G.; Kaiser, G.; Pahlke, S.; Veber, M.; Tölg, G. *Talanta* **1979**, *26*, 681.
- (2) Hasse, S.; Schramel, P. *Mikrochim. Acta* **1983**, *111*, 449.
- (3) Adeloju, S. B.; Bond, A. M.; Briggs, M. H. *Anal. Chem.* **1984**, *56*, 2397.
- (4) Martinie, G. D.; Schilt, A. A. *Anal. Chem.* **1976**, *48*, 70.
- (5) Mansell, R. E.; Tessner, R. P.; Hunerforder, E. J. *Anal. Chim. Acta* **1970**, *51*, 323.
- (6) Yang, J. Y.; Yang, M. H.; Lin, S. M. *Anal. Chem.* **1985**, *57*, 472.
- (7) Mercury Analysis Working Party of BITC (Belgium). *Anal. Chim. Acta* **1976**, *84*, 231.
- (8) Koltz, L.; Kaiser, G.; Tschopel, P.; Tölg, G. Z. *Anal. Chem.* **1972**, *260*, 207.
- (9) Koch, O. G.; Koch-Dedic, G. A. *Handbuch der Spurenanalyse*; Springer-Verlag: Berlin, 1974; Vol. 1.
- (10) Janghorbani, M.; Ting, Bill T. G.; Nahapetian, A.; Young, V. R. *Anal. Chem.* **1982**, *54*, 1188.
- (11) Subramanian, K.; Meranger, J. C. *Anal. Chim. Acta* **1981**, *124*, 131.
- (12) Analytical Methods Committee. *Analyst (London)* **1979**, *104*, 778.
- (13) Van Loon, J. C. *Selected Methods of Trace Metal Analysis: Biological and Environmental Samples*; John Wiley & Sons: New York, 1985.
- (14) Verlinden, M. *Talanta* **1982**, *29*, 875.
- (15) Kingston, H. M.; Jassie, L. B. *Introduction to Microwave Samples Preparation*; American Chemical Society: Washington, DC, 1988.
- (16) Knapp, G.; Raptis, S. E.; Kaiser, G.; Tölg, G.; Schramel, P.; Schreiber, B. *Fresenius' Z. Anal. Chem.* **1981**, *308*, 97.
- (17) Friberg, L.; Nordberg, G. F.; Vouk, V. B. *Handbook on the Toxicology of Metals*; Elsevier/North-Holland Biomedical Press: Amsterdam, 1979.
- (18) Versiek, J.; Cornelis, R. *Anal. Chim. Acta* **1980**, *116*, 217.
- (19) Robberecht, H. J.; Grieken, R. E.; Van Den Bosch, P. A.; Heelstra, H.; Vanden Bergh, D. *Talanta* **1982**, *29*, 1025.
- (20) Hansson, N. D.; Pettersson, J.; Olin, A. *Talanta* **1987**, *34*, 829.
- (21) Michie, N. D.; Dixon, E. J.; Burton, N. G. *J. Assoc. Off. Anal. Chemists* **1978**, *61*, 48.
- (22) Adeloju, S. B.; Bond, A. M.; Noble, M. L. *Anal. Chim. Acta* **1984**, *161*, 303.

RECEIVED for review January 27, 1989. Revised manuscript received October 17, 1989. Accepted October 17, 1989. This work was supported by a grant from the National Science Council of the Republic of China, to which the authors express their thanks.

Electrodeposition of Palladium, Iridium, Ruthenium, and Platinum in Poly(4-vinylpyridine) Films for Electrocatalysis

Kent M. Kost¹ and Duane E. Bartak*

Department of Chemistry, University of North Dakota, Grand Forks, North Dakota 58202

Beth Kazee and Theodore Kuwana

University of Kansas, Center for Bioanalytical Research, 2095 Constant Avenue, Lawrence, Kansas 66046

The electrodeposition of palladium, iridium, ruthenium, and platinum in poly(4-vinylpyridine) films on glassy carbon (gc) electrodes is described. Excellent stability of the polymer-modified electrode system was obtained by cross-linking the polymer directly on the surface of the gc electrode via a "solid-phase" cross-linking reaction. The metal microparticles were electrodeposited from acidic solutions containing the respective metal complex. SEM photomicrographs of these modified electrodes revealed the general morphology of the polymer film, metal particle size, and distribution of the particles. In particular, the SEM photomicrographs showed that the metal microparticles are nucleated at the electrode surface and growth occurs up through the polymer at the sites of nucleation. The size of the microparticles varied according to the deposition technique utilized for reduction, as well as the type of metal complex from which microparticles were formed. The metal microparticle/PVP/gc electrodes were also evaluated for their catalytic activity with regard to hydrogen evolution from acidic solutions. The mechanical and chemical stabilities of the cross-linked films containing metal particles were examined. The polymer-film electrodes containing metal microparticles showed good long-term stability in acidic media.

INTRODUCTION

The electrodeposition of metal microparticles into polymer-modified electrodes has recently gained considerable interest for potential application in the area of electrocatalysis. Platinum and palladium have attracted the most attention due to their excellent catalytic activity with regard the electrolysis of water. Wrighton and co-workers have reported on the use of Pt and Pd dispersed viologen-based polymers to improve hydrogen evolution of p-type semiconductors (1, 2). Kao and Kuwana electrodeposited Pt into poly(vinylacetic acid) on glassy carbon electrodes and reported high catalytic activity with regard to the electrochemical generation of hydrogen and reduction of oxygen (3). Itaya and co-workers described the electrodeposition of Pt into Nafion films on glassy carbon and evaluated the catalytic efficiency for hydrogen evolution based on active Pt surface area measurements (4). We have previously reported on the electrodeposition of Pt into poly(4-vinylpyridine) (PVP) films which had been electrochemically polymerized or cross-linked via a free-radical mechanism (5). More recently, our laboratory described the deposition of Pt into a conducting polymer, polyaniline, and evaluated the catalytic efficiency of the electrode system with regard to hydrogen evolution and methanol oxidation (6). Other metals which have been electrodeposited in polymer modified electrodes include work

by Wrighton who demonstrated that Rh or Pd could be deposited in a cobaltocenium redox polymer (7) and Kuwana who deposited Pd, Ni, Ag, and Cd in a poly(vinylacetic acid) polymer on glassy carbon (8). Due to the continuing interest in the dispersion of metal microparticles in polymer films for electrocatalysis, other metal complexes were examined including palladium, iridium, and ruthenium for their ability to form microparticles in polymers upon electrochemical reduction and the resultant catalytic efficiency of the metal particles with regard to hydrogen evolution.

Poly(4-vinylpyridine) (PVP) in its protonated form has been shown to be an effective matrix for the incorporation of a variety of anionic metal complexes (9). Stabilization of this polymer has been previously accomplished by cross-linking the polymer through a radical initiator procedure (5, 10). Lindholm and Sharp have reported a method by which the PVP polymer can be cross-linked by a nucleophilic reaction (11). The procedure involves the use of an alkyl halide to react with the pyridine residues in a "solid-phase" cross-linking process which resulted in stable films. The use of the alkyl halide cross-linking agent provides an improved means of controlling the degree of polymer film cross-linking relative to free-radical processes.

The objective of the present study is to prepare arrays of metal microparticles (palladium, iridium, platinum, and ruthenium) in cross-linked PVP polymer films and evaluate the electrodes for their catalytic activity in acidic media. In addition, the particles formed upon electrodeposition in the polymer/gc electrode will be evaluated via SEM analysis in order to determine the mechanism of metal particle formation.

EXPERIMENTAL SECTION

Chemicals. Linear poly(4-vinylpyridine) with a molecular weight of approximately 73 000 was obtained from Polysciences, Inc., and was used as received. 1,6-Dibromohexane, potassium hexachloroplatinate, sodium tetrachloropalladate, sodium hexachloroiridate, and ruthenium nitrosyl nitrate were purchased from Aldrich Chemical Co. and used as received. Water was distilled and subsequently passed through a Millipore Q water purification system prior to use. Aqueous solutions were prepared daily with Millipore Q water. Glassware was cleaned in a 2-propanol/KOH bath followed by 1 M H₂SO₄/1 M HNO₃ solution and thoroughly rinsed in Millipore Q water prior to use. All solutions that were used for electrochemical measurements were purged with prepurified nitrogen.

Electrodes, Electrochemical Cells, and Instrumentation. The electrochemical cell used in this work has been previously described (12). A silver/silver chloride (saturated KCl) electrode was used as the reference and all potentials are reported with respect to this reference. The working electrodes (approximately 1.5 cm²) were cut from glassy carbon (gc) plates (GC-20 and GC-30 grade, Tokai). The geometric area of the carbon which was exposed to the solution via a Kalrez (Du Pont) gasket was 0.385 cm². The gc electrodes were hand-polished successively with 600 grit, 1.0-, 0.3-, and 0.05- μ m alumina slurries with copious rinsing of Millipore Q water and ultrasonicated between subsequent

¹Present address: Boehringer Mannheim, Indianapolis, IN 46250.

polishing stages. The auxiliary electrode was a Pt wire which was isolated by a glass frit. All electrochemical measurements were performed with either a PAR Model 273 or an IBM EC 225 potentiostat. Data were acquired with a HP 7035 B X-Y recorder.

The polymer/metal microparticle films were examined by a Hitachi Model S-570 scanning electron microscope (SEM). This SEM is equipped with an extra secondary electron (SE) detector located above the objective lens, which produces a pure SE image in which there is no contribution from the back-scattered electrons (BSE). Therefore, photographs taken using this SE detector contain only topographic information. On the other hand, BSE emission is strongly dependent on the atomic number of the emitter and, since BSE's have much higher energies, they have greater escape depths than SE's. Thus, BSE images were used to obtain compositional and subsurface information and to produce a high level of contrast between the polymer and microparticles. All specimens were examined without any coatings or other preparation. In all SEM photomicrographs, the numbers at the bottom are, from right to left, photo sequence number, acceleration voltage, magnification, and value of dotted scale bar. Qualitative elemental analyses were carried out with a Princeton Gamma-Tech System 4 energy-dispersive X-ray spectrometer (EDS).

Preparation of Cross-Linked PVP Films on Glassy Carbon Electrodes. Cross-linked PVP films were prepared by spin-coating 35 μ L of a mixture of linear PVP (1% in methanol) and the cross-linking agent (alkyl halide) onto the surface of the polished gc electrode. The ratio of 1,6-dibromohexane:PVP, which was found to produce optimum results, was 8 mol % of the dibromohexane relative to the linear polymer. The electrode was then heated to approximately 110 $^{\circ}$ C for 16 h to effect the solid-phase cross-linking reaction.

Deposition of Metal Microparticles in the PVP Films. Acidic solutions containing the metal complexes were placed in contact with the polymer film for approximately 3 h prior to deposition to allow incorporation of the respective species. The conditions for depositing each complex as metal microparticles in the PVP films are described below.

(a) **Palladium.** Single-potential-step chronoamperometry (SPCA) and double-potential-step chronoamperometry (DPCA) techniques were performed on 5 mM tetrachloropalladate solutions in 0.5 M sulfuric acid solution. SPCA conditions utilized an initial potential of 0.800 V (30 s) followed by a reductive step to 0.150 V. DPCA utilized a triple potential program including an initial potential of 0.800 V (30 s), reductive step to -0.200 V (0.4 s), and back to 0.200 V. The time at the final potential varied to allow for the desired amount of palladium to be electrodeposited which was quantified by coulometric measurements. The amount of palladium deposited was calculated by assuming that the reduction from Pd(II) to Pd(0) occurred with 100% current efficiency. This amount will be reported with respect to the cross-sectional area of the carbon substrate.

(b) **Platinum.** Two potentiostatic techniques were used including SPCA and DPCA with 5 mM solutions of the sodium hexachloroplatinate in 0.5 M sulfuric acid. SPCA utilized an initial potential of 0.600 V (60 s) followed by a deposition step at -0.185 V. DPCA depositions were accomplished by an initial potential of 0.800 V (30 s) followed by a reduction potential at -0.400 V (0.4 s) and back to 0.100 V. The amount of charge passed was used to determine the loading level of Pt in the polymer and has been previously described (5).

(c) **Iridium.** Microparticles were deposited into the PVP matrix via controlled-potential exhaustive reduction on a solution of Na_2IrCl_6 in H_2SO_4 . The deposition potential utilized was -0.600 V for 3 h under an argon purge. Due to the fact that the four-electron reduction of Ir(IV) to iridium metal occurs in the potential region of considerable hydrogen evolution, coulometric measurements could not be utilized to quantitate the amount of electrodeposited metal. Therefore, exhaustive reductions were performed on dilute solutions of IrCl_6^{2-} using known concentrations and volumes to obtain metal loading levels.

(d) **Ruthenium.** Depositions were accomplished by controlled-potential exhaustive electrolysis at a potential of -0.400 V using a solution of $\text{Ru}(\text{NO})(\text{NO}_3)_3$ in H_2SO_4 , in which the amount of Ru was known from concentration and volume measurements. Bubbling argon was used to aid in mass transfer for

the electrolysis, which typically was run on a solution volume of 2 mL for 3 h. Again, the loading levels of metal microparticles were calculated under the assumption that all of the available Ru in solution was electrodeposited.

Evaluation of the Metal Microparticle/PVP Films for Electroanalysis. The catalytic activity of the metal microparticle/PVP films was evaluated by the generation of hydrogen from a 0.5 M sulfuric acid solution. Slow scan linear sweep voltammetry (2 mV/s) was utilized to obtain current density measurements over a typical potential range of 0.20 to -0.15 V vs SHE. The logarithm of the cathodic current for hydrogen evolution was plotted vs the potential (Tafel plot) for an overpotential range of 0.0 to -0.15 V vs SHE. Active surface area measurements were obtained by cycling between 0.20 and 0.05 V vs SHE with integration of the charge passed during the hydrogen desorption processes. The electrodes were examined by scanning electron microscopy (SEM) and X-ray fluorescence (EDS) before and after the catalytic measurements were made.

RESULTS AND DISCUSSION

Characterization of Cross-Linked PVP Films on Glassy Carbon. Poly(4-vinylpyridine) (PVP) has been utilized as a film for a number of electrochemical applications with respect to its ability to incorporate electroactive species (5, 11, 13). The film swells upon protonation in acid media, which allows facile loading of the polymer with an anionic electroactive species. Lindholm and Sharp have recently reported a method by which the PVP polymer can be cross-linked directly on the surface of the electrode (11). The advantage of this particular method is the ease of reproducing stable films and the ability to control the degree of cross-linking throughout the film. Although cross-linking increases the stability of the polymer, the attachment of the polymer to the gc electrode is also important for a stable system.

In the present study, glassy carbon electrodes were pretreated to improve the interaction between the polymer film and the gc surface. Several researchers have noted that anodic pretreatment of glassy carbon electrodes introduces oxygen functionalities on the surface (14-17). Engstrom has reported that electrochemical pretreatment increased the amount of oxygen on the carbon electrode by a factor of 2.5 (14). It is believed that the oxygen functionalities include hydroxyl, carbonyl, and carboxyl groups. After these surface functionalities have been introduced on the electrode surface, an electroreduction step is carried out which could reduce these groups to their anionic forms. Surface reduction of carboxyl and hydroxyl groups should result in carboxylate and oxide formation, respectively, with concomitant hydrogen evolution. Surface reduction of the carbonyl group could result in the formation of a relatively stable ketyl radical anion. The result in either case will be the formation of a functionalized carbon surface with anionic oxygenated groups. These oxygen groups have the potential to interact with the alkyl halide during the cross-linking reaction or to interact with the polymer in a manner so as to improve the adhesion between the film and substrate. Figure 1 illustrates a SEM of an electrode that was pretreated, spin-coated with PVP and 1,6-dibromohexane from methanol, and subsequently heated. The magnifications of the upper and lower photographs are 2.40k and 1.20k, respectively. The amount of cross-linking in this polymer should be slightly less than 8%, assuming complete reaction of the alkyl halide with the polymer and the electrode surface. It appears quite similar to that of the linear polymer (5), which is not surprising considering the low extent of cross-linking. It has the same reticulated structure as the linear polymer and the cavities are approximately 2-20 μ m in diameter. A portion of the polymer has been scraped away which shows that the cavities are not holes in the polymer but areas in which the polymer is thinner. A major difference between films that were cross-linked under these conditions and the linear form of PVP is the stability in 1.0 M acid media. The



Figure 1. SEM photomicrograph of a spin-coated poly(4-vinylpyridine) film that has been cross-linked using 1,6-dibromohexane. The magnification is 2.4k (upper) and 1.2k (lower), respectively. The film has been mechanically removed from the glassy carbon surface on the left half of the photograph.

linear PVP films showed excessive peeling from the electrode surface after only an hour in 0.5 M sulfuric acid, while those which were cross-linked (vide supra) showed extended stability for (>36) hours under the same conditions. The thickness of these films was estimated at 0.2–1 μm as measured by cross-sectional SEM measurements.

Electrochemical Deposition of Metal Microparticles into Cross-Linked PVP. A high ratio of surface area to the loading level of metal is desirable when attempting to fabricate metal microparticle/polymer modified electrodes for electrocatalysis. Conditions such as deposition technique, reduction potential, and the form of the metal complex, all play a major role in determining size of the electrodeposited particles. Several metal microparticle/polymer modified electrodes have been developed and successfully employed as catalysts and are herein described.

The reduction of hexachloroplatinate ion to Pt metal microparticles was accomplished by two different potential step techniques including single- and double-potential step chronoamperometry. Integration of the charge during the deposition was used to obtain the loading levels of microparticles. Figure 2 illustrates an SEM photomicrograph of Pt microparticles ($18 \mu\text{g}/\text{cm}^2$) formed upon electrodeposition. The area depicted is typical of the entire electrode with a fairly uniform distribution of Pt. The back-scattered (BSE) (upper segment) reveal that the particles have a generally consistent size on the order of 10–100 nm. The secondary electron (SE) photo shows that the particles are apparently deposited at different depths as indicated by the lighter and darker areas of the image. It is interesting to note that particles are also present in the ridges of the reticulated structure of the polymer, which indicates that growth can occur through the thicker areas of the polymer if sufficient time is given during the deposition process. It should be noted that very few particles were observed by SEM at relatively short deposition times or very

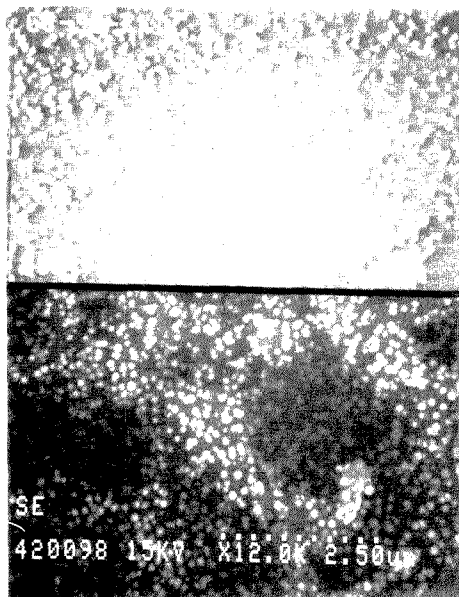


Figure 2. SEM photomicrograph of Pt microparticles deposited in cross-linked poly(4-vinylpyridine). The loading level of Pt is $18 \mu\text{g}/\text{cm}^2$ deposited by single-potential-step chronoamperometry. The magnification is 12k and the distance between two dots on the lower right is 0.25 μm .

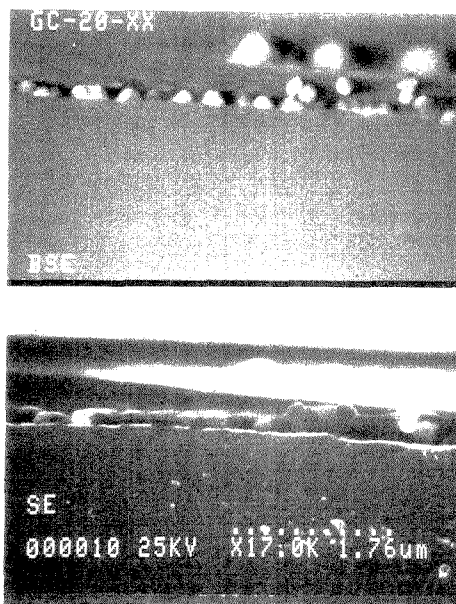


Figure 3. SEM cross-sectional view of Pt microparticles ($<5 \mu\text{g}/\text{cm}^2$) deposited in cross-linked PVP/gc electrode. The magnification is 17k and the distance between two dots on the lower right of the photo is 0.176 μm .

low loading levels ($<5 \mu\text{g}/\text{cm}^2$) even though the EDS data showed a very strong Pt signal. To further explore this phenomenon, cross-sectional SEM analysis was performed on

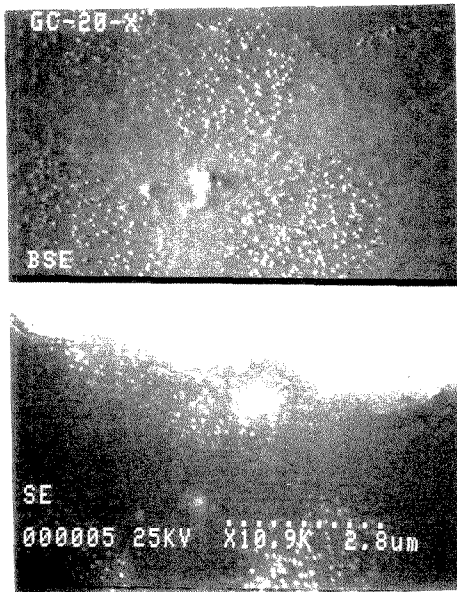


Figure 4. SEM photomicrograph of iridium microparticles electrodeposited in cross-linked PVP. The loading level is approximately $20 \mu\text{g}/\text{cm}^2$ which was deposited by controlled-potential exhaustive electrolysis. A scratch was made on the upper right for contrast purposes. The magnification is 10.9k and the distance between two dots on the lower right portion of the photo is $0.28 \mu\text{m}$.

electrodes with low loading levels of platinum. Figure 3 illustrates such an electrode, which was cleaned in order to expose the polymer/carbon interface. The film was relatively thin in this area of the photomicrograph ($<0.5 \mu\text{m}$) which should allow the anionic chloroplatinate to penetrate the film. It is apparent that the platinum undergoes nucleation at the polymer/gc interface followed by growth of the metal particle through the polymer. Some of the particles appear "suspended" when viewing the BSE photo; however, these particles could have been making initial contact with the carbon and were subsequently disrupted when the gc electrode was cleaned. The particles were identified as platinum from EDS data. Thus, metal deposition in these polymers appears to produce an ensemble of microelectrodes which are in the form of "pillars", which can be observed on the "surface" of the polymer by the SEM technique at longer deposition times or higher loading levels.

Iridium particles were also formed upon reduction of the hexachloroiridate complex using controlled-potential bulk electrolysis on a solution of known concentration. The deposition potential of the iridium complex occurs in the region of hydrogen evolution (i.e., -0.6 V) making coulometric measurements difficult. Thus the reported loading levels are based on the assumption that all of the iridium complex in solution is reduced to iridium metal. The exhaustive electrolysis mode of deposition seemed initially unattractive because the long nucleation/growth times required for reduction could result in the agglomeration of metal into clusters. Figure 4 clearly shows that this is not the case as a uniform dispersion of iridium microparticles with an apparent size of 20–40 nm is very evident. The loading level of iridium in this particular electrode is $20 \mu\text{g}/\text{cm}^2$. The upper portion of the photomicrograph has been carefully peeled away to determine if the nucleation/growth mechanism is followed. Close scrutiny of

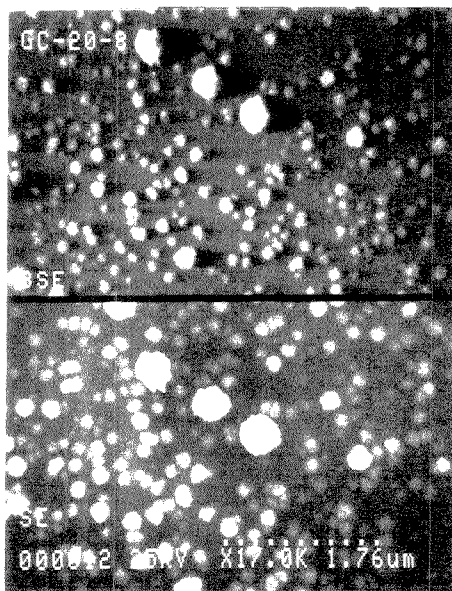


Figure 5. SEM photomicrograph of palladium microparticles electrodeposited into a cross-linked PVP polymer film. The deposition was accomplished by single-potential-step chronoamperometry. The magnification is 17k and the distance between two dots on the lower right represents $0.176 \mu\text{m}$.

the upper area in the SE photo shows that there are particles at the polymer/gc interface. The BSE picture illustrates that there is a uniform dispersion of particles and that they seem to be "growing" up through the film. Those that appear to be in focus are located in areas where the polymer is slightly thinner, which would allow them to reach the top portion of the film at a faster rate. Further examination of both the BSE and SE photomicrographs (Figure 4) reveals that the metal particles are barely discernible in the areas of the film which are thicker (i.e., ridges in the reticulated structure). This observation is consistent with nucleation at the carbon/polymer interface followed by growth through the polymer film to the polymer/solution interface because of the additional time required for the metal particle to grow through a thicker region (i.e., ridge) than a thinner region of the film.

At lower loading levels ($<10 \mu\text{g}/\text{cm}^2$) or short metal deposition times, particles were not evident even though the EDS data showed a strong iridium signal. These electrodes were also active with regard to hydrogen evolution. These data indicate that the particles formed are extremely small or that many of the microparticles are located at the gc electrode surface and growth to the top portion of the polymer has not yet occurred. Thus it appears that metal nucleation occurs initially at the carbon-polymer interface and growth of the metal particle occurs through the polymer film in the form of "pillars" of metal.

Palladium microparticles were formed by potential-step reduction of sodium tetrachloropalladate. Figure 5 is an SEM photomicrograph of Pd microparticles ($8 \mu\text{g}/\text{cm}^2$) deposited by SPCA at 0.15 V. The deposition appears quite uniform throughout the polymer electrode although there is a large variation in the apparent particle size (20–200 nm). In order to determine if particle size variation was the result of increased loading levels of metal microparticles, electrodes with lower loading levels ($<3 \mu\text{g}/\text{cm}^2$) were fabricated under

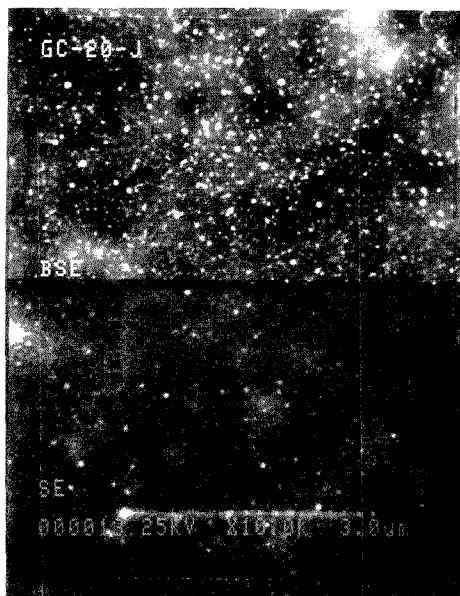


Figure 6. SEM photomicrograph of ruthenium microparticle/cross-linked PVP/gc electrode. The ruthenium loading level of this electrode is $24 \mu\text{g}/\text{cm}^2$ which was deposited by exhaustive electrolysis. The distance between two dots on the lower right corner is $0.3 \mu\text{m}$ and the magnification is 10k .

identical conditions. The results indicated that the sizes of the microparticles were roughly the same. This observation indicates that there may be preferential sites for nucleation and subsequent growth. Of particular interest was the SE photomicrograph obtained on the electrodes with the low loading levels. Very few particles were located in the upper portion of the polymer. The majority appeared to be near the carbon surface and lower regions of the polymer film. Increasing the loading levels resulted in a larger number of particles visible at or near the top of the polymer film. This further supports the idea that the particles are first nucleated at the gc/polymer interface and growth proceeds in an upward movement to the top of the polymer resulting in an array of metal deposition sites. It should be pointed out that there may be other smaller particles which were beyond the resolution of the microscope. However, EDS measurements confirmed the identity of all observable particles as palladium.

The deposition of ruthenium as microparticles in the cross-linked PVP films was accomplished by controlled-potential exhaustive electrolysis in a manner similar to that for iridium. Since concomitant hydrogen evolution occurred during metal deposition, quantitative metal loading levels were obtained by bulk electrolysis of a known concentration. Again the assumption was made that all of the ruthenium in the nitrosyl nitrate complex was reduced to metal microparticles. Figure 6 illustrates an SEM photomicrograph of a Ru microparticle/cross-linked PVP film electrode (magnification 9.9k). The dispersion is fairly uniform with particles located at different depths as evidenced by the lighter and darker images in the SE photo. The BSE photomicrograph shows an apparent particle size of $20\text{--}100 \text{ nm}$.

The results described above suggest that there is a three-dimensional dispersion of metal microparticles in these polymer films. The data indicate that formation of the metal microparticles occurs by nucleation at the gc surface and

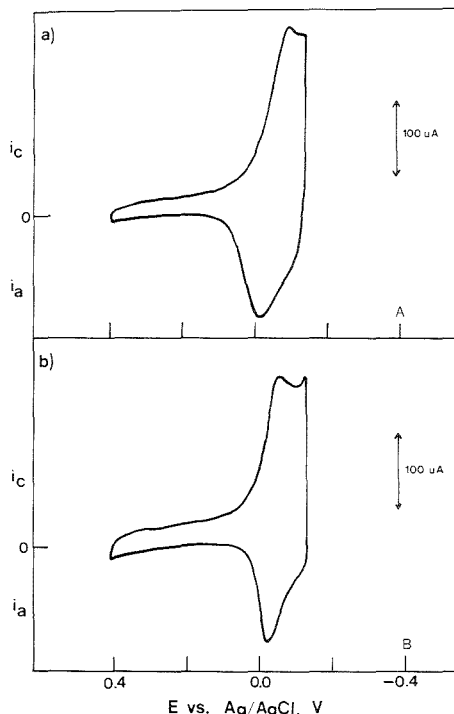


Figure 7. Cyclic voltammograms at 50 mV/s of hydrogen adsorption-desorption waves in $0.5 \text{ M H}_2\text{SO}_4$ solution on $10 \mu\text{g}$ of palladium/ cm^2 of carbon substrate: (a) Pd electrodeposited in a cross-linked PVP film on glassy carbon, (b) Pd electrodeposited directly on glassy carbon.

subsequent growth up through the polymer film. It appears that this nucleation/growth mechanism is typical of metal microparticles electrodeposited in ionomeric type polymers. This is not surprising considering the nonconducting nature of these films. The microparticles, which are formed by initial nucleation at the polymer/gc interface, provide sites for further charge transfer resulting in continued growth of the metal particle through the polymer films.

Catalytic Activity of the Metal Microparticle/Polymer Modified Electrodes. The catalytic activity of the metal microparticle/polymer modified electrodes was evaluated for hydrogen evolution by slow scan (2 mV/s) linear sweep voltammetry in $0.5 \text{ M H}_2\text{SO}_4$. The exchange current density based on the geometric area was found to be dependent on the loading level of metal in the polymer film. The current densities were obtained at both low and high overpotentials for hydrogen evolution. It is difficult to compare the respective metals because of variations in the apparent "active" surface area at similar loading levels. The hydrogen adsorption waves were ill-defined for iridium and ruthenium deposited in the PVP films making it impossible to quantitate the surface area of "active" metal contained in the polymer modified electrode. It should be pointed out that the iridium and ruthenium systems exhibit the characteristic microparticle formation, so it is probable there is a relatively high surface area.

A well-defined hydrogen adsorption wave was obtained when the palladium/PVP/gc electrodes were evaluated for hydrogen evolution behavior in $0.5 \text{ M H}_2\text{SO}_4$. Figure 7 illustrates the cyclic voltammetric behavior for a palladium/PVP/gc electrode vs palladium deposited on polished glassy

Table I. Hydrogen Evolution Data on Palladium/PVP Film Electrodes^a

electrode	Pd loading level, ^b μg/cm ²	active surface area, ^c cm ²	exchange current density, ^d mA/cm ²
GC-30-XIII	3	4.7	0.28
GC-20-tt	6	5.5	0.31
GC-20-K	10	6.5	0.38
GC-20-KK	12	7.0	0.41
GC-30-XIV	14	8.0	0.43
GC-20-T	19	8.8	0.53
GC-20-XL	22	9.1	0.60
glassy carbon ^e	10	4.9	0.31

^aThe activity was determined by linear scan voltammetry at 2 mV/s in a 0.5 M H₂SO₄ solution with bubbling nitrogen. ^bAll Pd loading levels were calculated assuming 100% efficiency for the reduction of Pd(II) to Pd(0). ^cThe active metal area was determined by integration of current for the hydrogen desorption wave on metal polymer film, which had a geometrical area of 0.385 cm². ^dExchange current densities were based upon the geometric area of the carbon substrate. ^eDeposition of palladium was carried out on a polished glassy carbon electrode without polymer.

carbon. In both cases, 10 μg of palladium was electrodeposited in the polymer or directly on the glassy carbon surface. Integration of the current of the Pd/PVP/gc and Pd/gc results in values of 1143 and 1034 μC/cm², respectively, for the two electrodes. Since a monolayer charge of H atoms on a smooth Pd surface corresponds to 210 mC/cm², the active areas of these electrodes are approximately 5.4 and 4.9 cm². Since the geometric area of the exposed carbon/film surface is 0.385 cm², the "roughness factors" for the Pd/PVP/gc and Pd/gc electrodes are 14.1 and 12.8. The slight increase in active area for the Pd deposited in the polymer is probably due to better dispersion. However, in addition, to improved dispersion of the metal, the polymer offers better mechanical stability for the metal particles (vide infra).

The palladium/PVP/gc electrodes were evaluated for their hydrogen evolution activity in 0.5 M sulfuric acid solution. The slopes of the Tafel plots were typically 60 mV/decade change in current density at overpotentials less than 70 mV. Table I summarizes the exchange current densities for hydrogen evolution on these electrodes as a function of Pd loading level in the PVP. The exchange current density, which is based on the active surface area of these electrodes is independent of the metal loading level and has a value of approximately 0.06 mA/cm². This is consistent with the SEM results which show that the particles size is independent of the loading level of Pd (vide supra).

Platinum which was deposited in PVP also produced hydrogen adsorption waves. However, a single broad adsorption wave is obtained instead of the usual two adsorption waves (i.e., strong adsorption and weak adsorption) which are obtained on bulk Pt or Pt, which has been deposited on glassy carbon. The presence of the polymer apparently affects the adsorption of hydrogen on the Pt particles to the extent that there are not the two distinct forms of adsorbed hydrogen as is normally observed on a pure Pt surface. Rather a continuum of energetic adsorbed-hydrogen forms are present when the metal is in the polymer matrix with the result that a broad adsorption wave is observed. Integration of the current for this wave indicates a large active area for the Pt deposited in PVP. For example, 20 μg/cm² of Pt was deposited in a PVP film and directly on a polished glassy carbon surface, respectively. Integration of the current under the adsorption waves in each case reveals an active area of 6.2 and 15.24 cm², respectively, on glassy carbon vs. PVP/gc, both of which have a geometrical area of 0.385 cm². Thus the "roughness factors"

Table II. Summary of Hydrogen Evolution Activities of Metal/PVP Film Electrodes^a

electrode	loading level, ^b μg/cm ² , metal	exchange current density, ^c mA/cm ²	current density, ^d mA/cm ² (η = 85 mV)
GC-30-XIX	26, Pt	1.4	44.0
GC-30-VII	10, Pt	0.8	29.5
GC-30-II	25, Ir	0.7	18.0
GC-30-XV	10, Ir	0.3	4.5
GC-20-K	29, Pd	0.6	4.0
GC-20-K	10, Pd	0.4	2.4
GC-20-J	24, Ru	0.7	28.8
GC-20-G	10, Ru	0.4	6.0

^aThe activity was determined by linear scan voltammetry at 2 mV/s in 0.5 M H₂SO₄ solution with bubbling nitrogen. ^bThe metal loading levels were calculated based upon 100% current efficiency for the reduction of the metal complex to the metal or with the assumption that all of the metal complex in solution was reduced (exhaustive electrolysis). ^cThe exchange current densities were based upon the geometric area of the carbon substrate. ^dThe current density, which was based on the geometric area of the substrate was determined at an overpotential of 85 mV.

for the Pt deposited directly on glassy carbon and for the Pt deposited in a PVP film on glassy carbon are 16 and 40, respectively, with a loading level of 20 μg/cm². In addition to a higher active surface area, the Pt/PVP film is considerably more robust and can be ultrasonicated for considerable lengths of time (e.g., 15 min) and not lose any Pt particles. Hydrogen evolution data were obtained on a series of Pt/PVP/gc electrodes and Tafel plots were made from the data. The slopes of the Tafel plots were approximately 30 mV/decade change in the current density at overpotentials less than 90 mV. The exchange current densities based upon the geometrical area of the film were dependent on the loading level with values of 0.8–1.4 mA/cm² for loading levels of 10–26 μg of Pt/cm² (Table II).

Deposition of iridium into the cross-linked PVP films produced metal-containing films, which were active for the electrogeneration of hydrogen. Hydrogen evolution data were obtained on a series of Ir/PVP/gc electrodes in 0.5 M₂SO₄ and Tafel plots were made on the data. At low overpotentials (less than 40 mV), the slopes of the Tafel plots were linear (35 mV/decade change in current density). Exchange current densities based on the gc geometric area were found to be dependent on the loading level with values of 0.2–0.8 mA/cm² for loading levels of 5–25 μg/cm². The slopes of the Tafel plots were nonlinear at overpotentials above 40 mV so that considerably lower current densities were obtained at an overpotential of 85 mV for the Ir/PVP/gc electrodes relative to that for Pt/PVP/gc electrodes (Table II).

Ruthenium/PVP/gc electrodes were evaluated for their activity for hydrogen evolution in the same manner as Pd, Pt, and Ir deposited in PVP. Ru, which is deposited in PVP, behaves similarly to the Pt group metals and shows an increase in exchange current density with loading level with typical values in the range of 0.2–0.7 mA/cm² for metal amounts of less than 25 μg/cm². The slopes of the Tafel plots were approximately 40 mV/decade change in current density with a metal loading level range of 15–25 μg/cm². Fleischmann and co-workers have previously reported on the electrodeposition of Ru on vitreous carbon and the subsequent hydrogen evolution on Ru/carbon electrodes (18, 19). They found that 20 nm was the critical size of the Ru particles for hydrogen evolution during the deposition process. In addition, they obtained Tafel slopes which varied from 90 to 60 mV/decade of current density as a function of the density of the Ru deposits. Although they did not report exchange current

densities, the intercepts of the Tafel plots indicate exchange current densities which are less than 0.1 mA/cm² based upon area measurements from the SEM data. The difference in Tafel slopes between Ru/PVP/gc and Ru/carbon may reflect a change in the mechanism for hydrogen evolution on metal in the polymer. More importantly, the Ru/PVP/gc electrodes were able to maintain relatively high current density for hydrogen evolution at overpotentials of 85 mV (Table II).

SUMMARY

Previous work by our laboratory has indicated that platinum can be electrodeposited as microparticles (i.e., diameters less than 0.1 μm) in poly(4-vinylpyridine) films (5). The current study indicates that palladium, iridium, and ruthenium in addition to platinum, all of which exhibit electrocatalytic behavior for the evolution of hydrogen, can be deposited as microparticles in cross-linked poly(4-vinylpyridine) films. More importantly, the deposition of these metals in these polymer films occurs initially by nucleation at the carbon substrate and subsequent growth of the metal particles through the polymer at these sites of nucleation. The diameter of the resultant metal particles which have grown through the polymer film appears to be less than 0.1 μm as observed by SEM. The resultant metal/polymer electrodes are mechanically robust in that they can be ultrasonicated without loss of metal. In addition, these metal/polymer electrodes can tolerate 1.0 M acidic solutions without polymer degradation or loss of metal. Thus it appears that an ensemble of metal microelectrodes can be formed in a polymer matrix in a manner that may have analytical applications.

LITERATURE CITED

- (1) Dominey, R. N.; Lewis, N. S.; Bruce, J. A.; Bookbinder, D. C.; Wrighton, M. S. *J. Am. Chem. Soc.* **1982**, *104*, 476.
- (2) Bruce, J. A.; Murahashi, T.; Wrighton, M. S. *J. Phys. Chem.* **1982**, *86*, 1552.
- (3) Kao, W. H.; Kuwana, T. *J. Am. Chem. Soc.* **1984**, *106*, 473.
- (4) Itaya, K.; Takahashi, J.; Uchida, I. *J. Electroanal. Chem.* **1986**, *208*, 373.
- (5) Bartak, D. E.; Kazee, B.; Shimazu, K.; Kuwana, T. *Anal. Chem.* **1986**, *58*, 2756.
- (6) Kost, K. M.; Kazee, B.; Kuwana, T.; Bartak, D. E. *Anal. Chem.* **1988**, *60*, 2379.
- (7) Stalder, C. J.; Chao, S.; Wrighton, M. S. *J. Am. Chem. Soc.* **1984**, *106*, 3673.
- (8) Weisshaar, D. E.; Kuwana, T. *J. Electroanal. Chem.* **1984**, *163*, 395.
- (9) Shigehara, K.; Oyama, N.; Anson, F. C. *J. Am. Chem. Soc.* **1981**, *103*, 2552.
- (10) Eushang, W. C.; Shupack, S. I.; Blubaugh, E. A.; Durst, R. A. *Prepr. Am. Chem. Soc., Div. Polym. Mater. Sci. Eng.* **1985**, *53*, 123.
- (11) Lindholm, B.; Sharp, M. J. *J. Electroanal. Chem.* **1986**, *98*, 37.
- (12) Hu, I. F.; Karweik, D. J.; Kuwana, T. *J. Electroanal. Chem.* **1986**, *188*, 59.
- (13) Oyama, N.; Anson, F. C. *J. Am. Chem. Soc.* **1979**, *101*, 739.
- (14) Engstrom, R. C.; Strasser, V. A. *Anal. Chem.* **1984**, *56*, 136.
- (15) Lausevic, Z.; Jenkins, G. M. *Carbon* **1986**, *24*, 651.
- (16) Nagaoka, T.; Yoshino, T. *Anal. Chem.* **1986**, *58*, 1037.
- (17) Engstrom, R. C. *Anal. Chem.* **1982**, *54*, 2310.
- (18) Fleischmann, M.; Koryta, J.; Thirsk, L. *Trans. Faraday Soc.* **1967**, *63*, 1261.
- (19) Fleischmann, M.; Grenness, M. *Trans. Faraday Soc.* **1972**, *68*, 2305.

RECEIVED for review June 22, 1989. Accepted October 23, 1989. This work was partially supported by the National Science Foundation through an EPSCoR Grant. Purchase of the scanning electron microscope and the energy dispersive X-ray spectrometer with funds from the National Science Foundation is gratefully acknowledged.

Laser-Excited Atomic Fluorescence in a Pulsed Hollow-Cathode Glow Discharge

Mark Glick,¹ Benjamin W. Smith,² and James D. Winefordner*

Department of Chemistry, University of Florida, Gainesville, Florida 32611

A pulsed glow discharge with low background noise is evaluated as an atom reservoir for laser-induced atomic fluorescence spectroscopy. Aqueous solutions are dried in graphite electrodes that are used as disposable hollow cathodes. Atomic vapor is produced in a flowing-gas glow discharge with a water-cooled cathode holder. A dye laser triggers a switching circuit that pulses the glow discharge, and fluorescence measurements are made 100 μs after the discharge is extinguished. The atomic population is large during this dark period, while the background emission is negligible. Linear calibration curves are obtained by nonresonance fluorescence for two elements, Pb and Ir. The detection limits for Pb are 100 pg/mL and 500 fg, and for Ir are 6 ng/mL and 20 pg. The experimental detection limit for Pb is compared to the intrinsic detection limit.

INTRODUCTION

Glow discharges are used extensively as emission sources in atomic absorption and atomic emission spectroscopy. They

have also been used, in a few cases, for the production of atomic vapors for atomic fluorescence spectroscopy (1-5). Glow discharges offer advantages for fluorescence spectroscopy compared to atmospheric atom reservoirs. The low-pressure inert gas atmosphere reduces pressure broadening of the absorption lines and minimizes compound formation and eliminates quenching of the fluorescence radiation. Excellent results have been obtained by using these atom reservoirs for atomic fluorescence measurements.

Direct atomization of solid, metallic samples is the easiest sampling method with glow discharges. Metal samples can function as planar cathodes without sample preparation. Powdered, conducting samples can be packed into a cathode. Solutions can also be analyzed by atomic fluorescence by sputtering the dried residue from planar cathodes (4).

If the glow discharge is pulsed, background emission can be completely eliminated within a few microseconds, but significant atomic vapor can remain for several milliseconds (2, 4). When a laser is used to excite the atoms during this dark period, low background noise fluorescence measurements can be made.

Previous work has shown the possibility of detecting extremely small numbers of atoms in a low-pressure, inert-atmosphere cell, such as a hollow-cathode lamp (6). A glow discharge source should be an excellent atom cell for approaching the intrinsic detection capability of laser-induced,

* Author to whom correspondence should be addressed.

¹ Present address: Department of Chemistry, Indiana University, Bloomington, IN 47405.

² Present address: CCR, Joint Research Centre, Environment Institute, 21020 Ispra (Va), Italy.

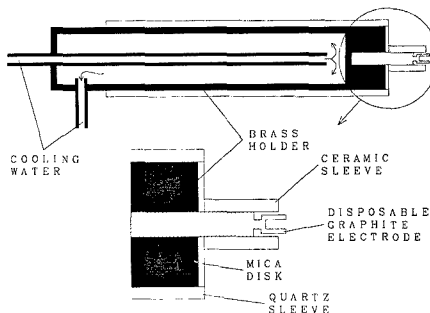


Figure 1. Water-cooled cathode and disposable graphite electrode. The entire assembly is electrically shielded, except the tip of the hollow electrode. Electrical connection is made on the water inlet tubing.

direct-line fluorescence measurements (7). With efficient optical collection and low background noise, detection limits in a glow discharge should be extremely low.

In this work, a pulsed glow discharge with a cathode holder that accepts hollow graphite electrodes was used for the production of atomic vapors for atomic fluorescence measurements. Solutions containing lead and iridium were deposited and dried on the electrodes, and laser-induced, non-resonance fluorescence of the sputtered atoms was measured. The intrinsic detection limit for lead is calculated by using known experimental and fundamental parameters. This intrinsic limit is compared to the experimental detection limit. Advantages of a low-pressure, inert-atmosphere system were realized, as demonstrated by the absolute number density of atoms detected per probing, but the sputtering rate of the discharge elevated the detection limit of the sample.

EXPERIMENTAL SECTION

Glow Discharge Atom Cell. The glow discharge cell was made from commercially available vacuum parts and a machined, brass cathode holder. The discharge chamber was constructed from a six-way, 2.25 in. flange, vacuum cross (Huntington Labs). One port was used for mounting to X-Y translation and vertical translation stages, and one port was used for atmospheric venting. The other ports were used for the cathode holder, the vacuum pump, argon fill gas and a manometer, and a quartz window.

The chamber was electrically grounded and functioned as the anode of the discharge. No other type of anode was necessary to maintain a stable discharge in the hollow cathode. A schematic diagram of the cathode holder is shown in Figure 1. The cathode holder was made from a hollowed rod of brass, with inlet and outlet tubes for cooling water. A quartz sleeve was fitted over the brass cathode holder to insulate the cathode from the grounded chamber. The negative lead of the power supply (Model 803-330, -1.2 kV, Hipotronics, Inc., Brewster, NY) was attached to one of the cooling water tubes. Exposed metal was covered with Teflon and electrical tape to guard against electrical shock. At the end of the brass holder a 0.625-cm hole was drilled to slip-fit the hollow graphite electrodes (4001 HPND, Spectrographic Services, Sussex, NJ). To leave only the graphite cup exposed, ceramic sleeves were made to fit over the electrodes. A mica disk was also used to cover the end of the brass holder and limit sputtering to the electrode. The cathode holder was vacuum-sealed with an O-ring fitting.

Vacuum System. A rotary vacuum pump was adequate for maintaining the vacuum in the flowing mode. Argon was continuously bled into the chamber to hold the pressure at the desired value (0.4–0.7 Torr). The intensity of the laser-excited fluorescence was not greatly affected by the pressure. The pressure was monitored on the same side of the chamber as the Ar inlet.

Laser. The excitation source was a tunable dye laser (Coumarin 540 A, 2×10^{-3} M), pumped by an XeCl excimer laser (LPX 100, Lambda Physik) and frequency doubled with a KDP crystal. This system was chosen for its high radiant power and repetition rate. The laser pulse width was 17 ns. The laser pulse energy

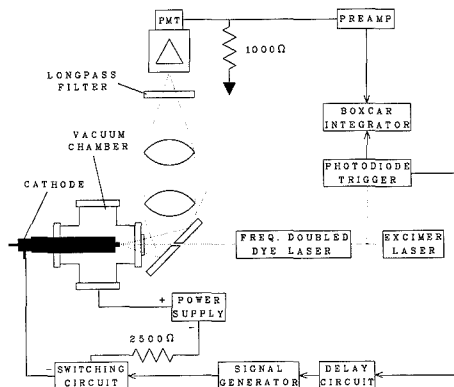


Figure 2. Schematic diagram of the experimental setup.

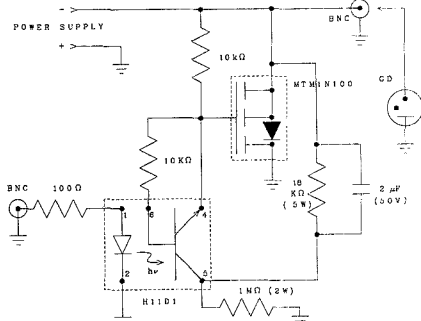


Figure 3. Schematic diagram of the glow discharge pulsing circuit.

was greater than $1 \mu\text{J}$ at the excitation wavelengths of Pb and Ir. The dye laser was tuned to the desired transition by optimizing the fluorescence signal with a concentrated solution of the analyte deposited on an electrode.

Measuring System. A schematic diagram of the experimental setup is shown in Figure 2. The laser beam was directed into the hollow graphite electrode by passing the beam through a mirror pierced with a 4-mm hole. The laser beam completely illuminated the hollow electrode. The fluorescence radiation was collected by the mirror, and a 1:1 image was focused on the slit of the spectrometer. A long-pass filter (WG360 or LG350, Corion) was used to eliminate scattered excitation radiation. An iris diaphragm was used to stop down the solid angle of fluorescence to match the acceptance solid angle ($f/8.6$) of the 0.3-m monochromator (82020, Thermo Jarrell Ash). The monochromator entrance and exit slits were large (1–2 mm), because emission was near zero for the pulsed discharge. The photomultiplier (PMT) (R955, Hamamatsu) signal was terminated with a 1-k Ω resistor, amplified with a wideband amplifier (4163, Evans Associates), and processed with a gated integrator and boxcar averager (SR250, Stanford Research Systems). The effective instrumental bandwidth for all measurements was 1 Hz.

The extent of saturation of the lead transition was determined by attenuating the laser with neutral-density filters and measuring the fluorescence signals. Pulse energy was monitored with a calibrated detector (J3-05DW, Molectron). The dye laser was tuned to 283.3 and 285.0 nm for lead and iridium, and the fluorescence was measured at 405.5 nm for lead and at 357.4 nm for iridium.

Laser pulses were timed to coincide with the dark period of the glow discharge. A switching circuit was designed to pulse the discharge by shunting the power across the glow discharge. A schematic diagram of the switching circuit is shown in Figure 3. Pulses at the input BNC triggered the switching circuit, the

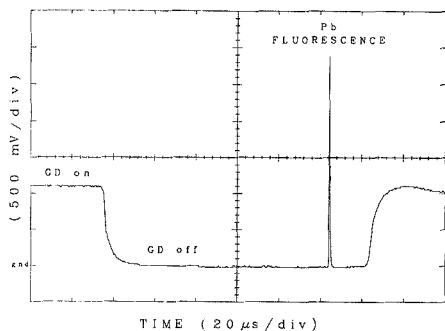


Figure 4. Typical emission/fluorescence scan for Pb.

off-time of the discharge being determined by the width of the pulse. The discharge emission fell to essentially zero within 20 μ s and could be quickly ignited again by switching the power back through the discharge.

To pulse the discharge, a photodiode pickoff from the laser beam triggered a delay circuit (a Wavetek pulse generator), which triggered a second pulse generator just before the next laser pulse. This second pulse generator triggered the switching circuit and was timed so that the discharge would be dark for 100 μ s before the next laser pulse. The boxcar integrator gate, triggered by the photodiode pickoff, was centered within the fluorescence peak.

Procedure. The volume of the hollow electrode cup was approximately 50 μ L—the sample volume used for most measurements. Sample volumes above 50 μ L were deposited and dried in several steps. Solutions were deposited in the hollow graphite electrodes and dried under an infrared lamp for several minutes. An electrode was then slipped into the water-cooled brass holder, and a ceramic sleeve was fitted over the electrode. The ceramic sleeves were cleaned in hot ultrapure nitric acid. To light the discharge, a high-voltage switch was used to throw the glow discharge cell into the circuit. A 2.5-k Ω (20 W) resistor was used in series with the discharge to limit the current. Operating conditions were 400–700 V and 13–47 mA at the power supply. The maximum fluorescence intensity signal was obtained at 500 V (29 mA), and all measurements were made at this setting.

Reproducible results were obtained without complicated flushing and evacuation procedures. The chamber was pumped down and held to below 0.2 Torr for 1 min. Argon was added to bring the chamber up to operating pressure and allowed to flow for 1 min before initiating the discharge. The entire process, from sampling to initiation of discharge, required less than 10 min. As soon as the high voltage was turned on, the discharge ignited inside the hollow cathode. Fluorescence measurements were made during the maximum signal production, which occurred immediately upon initiation of the discharge.

RESULTS AND DISCUSSION

To compare the experimental detection limit in a glow discharge with the calculated intrinsic detection limit, lead was chosen as a model analyte. The lead atom can be approximated as a three-level atomic system in which the direct-line fluorescence transition terminates on a metastable level. When the upper level is saturated with the laser, the calculation of the intrinsic detection limit becomes possible.

Figure 4 shows a typical emission/fluorescence scan, in this case for lead. The emission of the glow discharge completely disappeared within approximately 20 μ s. The laser pulse arrived 100 μ s after the glow discharge voltage had been switched off, and the lead fluorescence appeared during the darkest period of the cycle. Beyond 100 μ s, the atom density began to decrease with no further reduction of the emission, but even at 1 ms there was measurable fluorescence.

A measurement of the true blank signal for lead could not be obtained, because clean graphite electrodes generated a signal for lead. Blank measurements were made by tuning

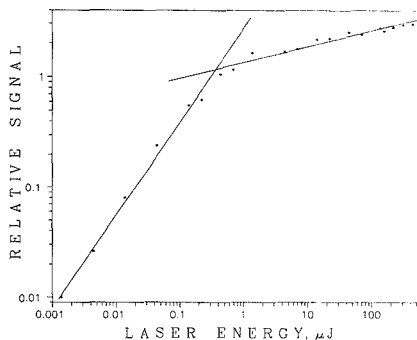


Figure 5. Saturation curve for Pb.

Table I. Definitions and Values for Parameters in Eq 1–4 for Pb

param	definition	value
k	confidence factor	3
R_p	number of laser probings	6000
η_b	saturation parameter	0.75
A_{um}	spontaneous transition probability, s ⁻¹	9×10^7
T	laser pulse width, s	1.7×10^{-8}
Ω_F	solid angle of collection, sr	1.1×10^{-2}
η_t	optical transmission efficiency	0.5
η_{PMT}	quantum efficiency of PMT	0.2
G	gain of PMT	10^7
e	charge of electron, C	1.6×10^{-19}
R_L	PMT load resistance, Ω	10^3
Δt	pulse width at load resistor, s	2.8×10^{-7}
T_s	lifetime of sputtered atoms, s	10^{-3}

the laser off the lead wavelength, which did not change the characteristics of the background fluorescence caused by scattered laser radiation. Contamination by iridium in the graphite electrodes was not a problem, and blank measurements could be made at the iridium wavelength.

Figure 5 shows a plot of lead fluorescence intensity versus laser pulse energy. The nonlinearity at pulse energies greater than 0.1 μ J clearly demonstrates the existence of optical saturation. All measurements were made with at least 1- μ J laser pulses, which ensured saturation but did not needlessly increase scattered radiation. The existence of optical saturation simplified the estimation of absolute number density of lead in the probe volume.

Alkemade has derived the statistical expression for calculating the detection limit defined by the fluctuations inherent in a signal, or the intrinsic detection limit, which is the minimum number of atoms detectable in the probe volume (8):

$$(N_p)_m = \frac{k^2}{\epsilon_d R_p} \quad (1)$$

where k is the statistical confidence factor, R_p is the number of repeated probings, and ϵ_d is the detection efficiency, or number of photons detected per atom per laser pulse. Only when $\epsilon_d = 1$ can the technique be defined as a single-atom detection method. For lead, it can be expressed as

$$\epsilon_d = [1 - \exp(-\eta_s A_{um} T)] (\Omega_F / 4\pi) \eta_t \eta_{PMT} \quad (2)$$

where the parameters are defined in Table I. Using the values listed in Table I for the experimental and fundamental parameters in eq 2, one obtains $\epsilon_d = 5.8 \times 10^{-5}$ for this system. The solid angle of collection was limited by the acceptance solid angle of the monochromator and could be increased by using a nondispersive system. The intrinsic detection limit

Table II. Limiting Noises and Corresponding Detection Limits for Pb

sources of noise	rms noise, μV	LOD, atoms
Extrinsic		
glow discharge bkgd fl + emission + rf + PMT + boxcar	100	900
glow discharge bkgd fl + emission + rf + PMT + boxcar	33	300
bkgd fl + rf + PMT + boxcar	31	280
emission + rf + PMT + boxcar	8.5	80
rf + PMT + boxcar	6.9	60
PMT + boxcar	5.6	50
boxcar	1.2	10
Intrinsic		
fluctuations inherent in the signal		25

is restricted by this value for ϵ_d .

The voltage pulse at the PMT load resistor per atom per laser pulse, ΔV , can be estimated from ϵ_d , the number of photoelectrons at the cathode per atom per laser pulse:

$$\Delta V = \epsilon_d Ge(R_L/\Delta t) \quad (3)$$

where the parameters are defined in Table I. When the values listed in Table I are incorporated in eq 3, $\Delta V = 0.33 \mu\text{V}/(\text{pulse-atom})$.

The extrinsic limiting noises were measured by using an instrumental bandwidth of 1 Hz and were obtained by a data acquisition system. An estimate of the noise was made by calculating the standard deviation of the data acquired over 1 min, taken as an approximation of the root mean square (rms) noise.

Table II lists the magnitudes of these extrinsic noises and the corresponding detection limits (3σ) obtained by using eq 3. Pulsing the glow discharge reduced the noise by a factor of about 3, shown by the first two entries. The detection limit for the secondary entry, 300 atoms in the probe volume, compares favorably with the value obtained in a conventional hollow-cathode lamp that was not pulsed (6).

The major noise contribution originated from broad-band, background fluorescence due to scatter of laser radiation. Since the laser was tuned off the lead transition for the measurement of noises, the background fluorescence was not due to lead in the electrode. Scattered laser radiation was undetectable, because of the large Stokes shift and the long-pass filter which blocked the radiation. Noise from residual emission was also not due to lead, but due to broad-band, glow discharge emission within the bandwidth of the monochromator. The difference between the noise values measured with the glow discharge on and off is probably not significant. No emission could be detected 100 μs after switching off the discharge.

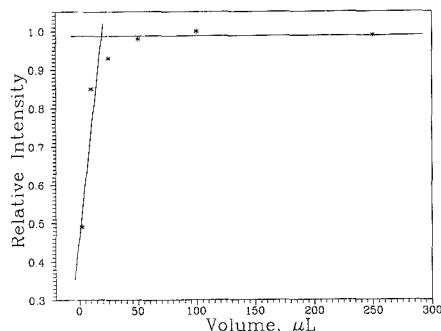
The contributions of radio frequency (rf) noise and PMT dark current noise are shown in the last three entries. The contribution due to rf interference was measured by alternately triggering the switching circuit (while the discharge was off) with the laser and with a pulse generator. The difference between these two values is the contribution of the rf interference. The contributions of the PMT and of the boxcar integrator and accompanying electronics were determined by disconnecting the boxcar from the PMT and shorting its input.

The detection limit of 300 atoms of lead within the probing of the laser beam represents the detection limit determined by extrinsic noises by using calculated values of probing efficiency and collection efficiency (overall detection efficiency, ϵ_d). The last value in Table II represents the intrinsic detection limit for lead calculated from eq 1. This detection limit of

Table III. Limits of Detection for Pb and Ir

element	λ_{exc} , nm	λ_{em} , nm	LOD, ^a ppb	LOD, ^b pg
Pb	283.3	405.8	0.1	0.5
Ir	285.0	357.4	6	20

^a Calculated by using 50- μL samples. ^b Calculated by using 2- μL samples.

**Figure 6. Relative fluorescence intensity vs sample volume.**

25 atoms uses the same detection efficiency and $R_p = 100$. More useful analytically, however, are detection limits that refer to the sample and not to the probe volume.

The detection limits for lead and iridium, determined in the conventional manner, are listed in Table III. The detection limit for lead of 500 fg is larger than both the extrinsic and intrinsic limits in Table II, indicating the deposited sample was either not atomized completely or not probed efficiently, temporally or spatially. The atomization rate was expected to be poor compared to that with an electrothermal atomizer. The fluorescence signals for lead and iridium, although at maxima just after ignition, lasted for many minutes. To better compare the intrinsic detection limit to experimentally obtained detection limits, the atomization and probing efficiencies should be considered.

We define an expression for the intrinsic detection limit rate in the sample that includes in eq 4 the residence time of the produced atoms (T_s), atomization efficiency (ϵ_a), temporal probing efficiency (ϵ_t), and spatial probing efficiency (ϵ_s):

$$(\dot{N}_a)_m = \frac{k^2}{\epsilon_d R_p T_s \epsilon_a \epsilon_t \epsilon_s} \quad (4)$$

where the other parameters are defined in Table I. Estimating $T_s = 1$ ms, which is reasonable since fluorescence signals could be measured up to 1 ms after the discharge had been extinguished, and using $\epsilon_a = \epsilon_t = \epsilon_s = 1$, one obtains $(\dot{N}_a)_m = 1.6 \times 10^6$ atoms/s. This represents the intrinsic, minimum detectable rate of atomization of the sample, below which no signal above the noise will be measured. With an instrumental time constant of 1 s, the intrinsic detection limit in the sample for this system was 1.6×10^6 atoms, or 0.5 fg. This is only 3 orders of magnitude below the experimentally obtained value of 500 fg shown in Table III. The difference between the two detection limits is likely a result of spatial and temporal probing inefficiencies and incomplete atomization, which reduce the efficiencies ϵ_a , ϵ_t , ϵ_s to values less than unity (7).

Figure 6 shows the relationship between sample volume and fluorescence signal intensity when the same sample solution is used. When samples were 50 μL and larger, the intensity of fluorescence was at a maximum. Below 50 μL the signal intensity decreased, but not proportionally to the decrease in volume. A decrease in the sample volume by a factor of

25 (50 to 2 μ L) was accompanied by a signal intensity decrease by a factor of 2. Although the detection limit calculated with 2 μ L and expressed as a concentration *increased* by a factor of 2, the absolute detection limit *decreased* by a factor of 25. This indicated that the concentration detection limit could be sacrificed for better absolute detection limits. The detection limits listed in Table III were determined by using different sample amounts, 50 and 2 μ L, with the smaller volume yielding the better absolute detection limit.

In order to improve the detection limits and to approach the intrinsic detection limit even closer, the experimental system must be improved in several ways. Although the background noise was low, since measurements were made during the dark period of the discharge, laser-induced white fluorescence must be reduced. The design of the optical setup, with the laser beam striking the face of the cathode and the fluorescence being collected along the same axis, hindered the rejection of background fluorescence photons. The solid angle of collection can be increased by using a nondispersive system in which the solid angle is not limited by the monochromator. However, eventually the diameter of the graphite electrode cup will limit the solid angle. The number of probeings, R_p , and the temporal probing efficiency can be increased by using a laser with a higher repetition rate, (e.g. a copper-vapor pumped dye laser).

The important factors in improving the detection limit of the sample appear to be the atomization rate, the temporal probing efficiency, and the spatial probing efficiency. Only by probing efficiently and by rapidly atomizing all of the atoms in the probing time can one obtain sample detection limits that approach the intrinsic detection limit. The results for lead and iridium in a pulsed, hollow-cathode glow discharge demonstrate that even with rather poor detection efficiency (ϵ_d), excellent detection limits are possible.

LITERATURE CITED

- (1) Gough, D. S.; Hannaford, P.; Walsh, A. *Spectrochim. Acta* **1973**, *28B*, 197-210.
- (2) Gough, D. S.; Meldrum, J. R. *Anal. Chem.* **1980**, *52*, 642-646.
- (3) van Dijk, C.; Smith, B. W.; Winefordner, J. D. *Spectrochim. Acta* **1982**, *37B*, 759-768.
- (4) Smith, B. W.; Omenetto, N.; Winefordner, J. D. *Spectrochim. Acta* **1984**, *39B*, 1389-1393.
- (5) Patel, E. M.; Smith, B.; Winefordner, J. D. *Spectrochim. Acta* **1985**, *40B*, 1195-1204.
- (6) Smith, B. W.; Womack, J. B.; Omenetto, N.; Winefordner, J. D. *Appl. Spectrosc.* **1989**, *43*, 873-876.
- (7) Omenetto, N.; Smith, B. W.; Winefordner, J. D. *Spectrochim. Acta*, in press.
- (8) Alkemade, C. Th. J. In *Analytical Application of Lasers*; Piepmeier, E. H., Ed.; Wiley Interscience: New York, 1988; Chapter 4.

RECEIVED for review August 14, 1989. Accepted October 20, 1989. This research was supported by NIH-GM38434-02.

Automated Instrumentation for Comprehensive Two-Dimensional High-Performance Liquid Chromatography of Proteins

Michelle M. Bushey and James W. Jorgenson*

Department of Chemistry, University of North Carolina, Chapel Hill, North Carolina 27599-3290

A comprehensive two-dimensional (2-D) liquid chromatographic separation system is presented. The system uses a microbore cation exchange column, operated under gradient conditions, as the first dimension separation. Effluent from this first column alternately fills one of two loops on a computer-controlled eight-port valve. A second pump then forces loop material onto a second column, a size exclusion column. UV detection is used, and the system is applied to the separation of protein standards and serum proteins. The 2-D system has a higher resolving power and peak capacity than either of the two columns used alone. The entire first column effluent is analyzed on the second column in virtually the same time it takes to complete the first column separation, without the use of stopped flow methods. The entire system is automated and operated under computer control. Three-dimensional (3-D) data representation provides a means of viewing peak profiles in either separation dimension and contour mapping of the 3-D data provides a more reliable means of peak identification from run to run than that provided by single-column elution times.

INTRODUCTION

Complex samples require analytical methods of extremely high resolving power in order to provide reliable analysis of

the sample components. Analyses are frequently carried out in more than one analytical dimension in order to provide the necessary resolution. The coupling of chromatography to mass spectrometry, particularly gas chromatography-mass spectrometry (GC-MS), is an example of a very powerful two-dimensional tool for the analysis of complex samples. Gas chromatography achieves partial separation of complex samples into less complicated mixtures which the mass spectrometer can more easily handle, and the MS finishes resolving peaks that the GC was unable to fully separate. Other examples of multidimensional analytical methods include MS-MS techniques, and LC combined with various spectral detection schemes or voltammetric electrochemical detection. Such techniques are generally powerful and can provide a wealth of information on complex samples. As powerful as these combined techniques are, however, they do not actually provide an enhancement of purification of the sample. To achieve actual high-resolution separation, not only in an analytical sense but in a physical sense, requires the combination of separation methods. This distinction is important if one wishes to obtain, for any reason, highly purified components from complex mixtures.

It has been shown that samples often require more than one separation dimension to reduce peak overlap (1, 2). Two-dimensional electrophoretic techniques, usually utilizing isoelectric focusing followed by gel sieving electrophoresis,

provide the highest resolving power available for the separation of complex protein containing samples (3, 4). Indeed, these techniques are capable of resolving several thousand compounds. Two-dimensional (2-D) electrophoresis is, however, time-consuming and labor intensive. Thin-layer chromatography (TLC) is another example of a 2-D separation where the sample is first developed along one side of the thin layer plate, and then the plate is rotated 90° and a further development occurs in a different solvent system perpendicular to the first separation. But again, this type of separation is time-consuming and labor intensive, and it has the added disadvantage that since the same stationary phase is used in both developments, the two separations are not very orthogonal to each other. Both of these techniques also have the disadvantage that the detection methods used are often time-consuming themselves, and quantification is poor at best.

Other approaches to the analysis of very complex samples are coupled column techniques and two-dimensional column chromatography. Although these methods do not have nearly the same peak capacities as 2-D electrophoresis, they nevertheless are very powerful separation techniques for the analysis of complex samples. While methods such as 2-D electrophoresis and TLC are 2-D in space, coupled column techniques are 2-D in time. Giddings (5, 6) and Guiochon et al. (7) have examined various aspects of multidimensional column chromatography including the improved resolution and increased peak capacity over single-column methods.

Most approaches to coupled-column and 2-D LC techniques involve some sort of fraction collection from the first chromatographic column followed by a reinjection of the collected material onto a second column. In off-line techniques, the fractions are collected in vials and reinjected on the second column at a later time. In on-line techniques, a switching valve is used to do one of the following: trap first column effluent containing the region of interest for reinjection directly onto the second column (heart cutting) or to direct flow from the first column directly onto the head of the second column during a specific time frame. Majors (8) has reviewed many of these techniques. All of these approaches have the limitation of only subjecting a portion of the sample to full two-dimensional analysis, and none permits a comprehensive two-dimensional separation of the entire sample.

To obtain a comprehensive 2-D separation of the entire sample, the following ideal conditions should be addressed: each separation mechanism should be chosen so as to minimize the amount of cross-information in the two systems, that is, the two separation mechanisms should be as different from each other as possible, or as orthogonal as possible; in addition to being orthogonal to the first column, the second column separation should not degrade the first column separation; it should also be possible to obtain peak profiles in both dimensions. Other aspects that are desirable would be a reasonably short analysis time, automation of the entire system, flexible operating conditions, and, finally, effective representation of the two-dimensional data.

Comprehensive 2-D LC provides several advantages over single-dimension LC. Separating power is greatly increased over single-dimension LC. For fully orthogonal methods, assuming no additional broadening is introduced, peak capacity becomes the product of peak capacity in each dimension. Resolution is equal to the square root of the sum of the squares of the resolution for each dimension (6). 2-D separation is more reliable for peak identification from run to run than single-dimension chromatography because two independent elution times are obtained for each peak.

Most coupled-column approaches to date have not been comprehensive two-dimensional separations according to our criteria. Johnson et al. (9) used an on-line heart cutting

technique in the analysis of malathion-treated vegetable matter, but they only analyzed a few fractions from the first column effluent in the second dimension. Fürst et al. (10) coupled a size exclusion (SEC) column on-line to an ion exchange (IEC) column run, which was operated under gradient conditions. This approach was applied to the separation of uremic middle molecules (molecular weights from 350 to 2000). Their analysis time was 48 h and involved only eight fractions from the first column, with each fraction necessitating an analysis time of 6 h on the second column. Huber et al. (11) used an on-line approach but did not analyze the entire first run effluent. Their approach was used in the analysis of herbicides in cereals and only the desired fraction was transferred to the second column; the second column flow rate was stopped until the first column run was completed. Takahashi et al. (12) collected fractions from a cation exchange column for injection onto a reverse-phase column in the analysis of human IgD immunoglobulin tryptic peptides. They approximated a 3-D representation of the data by stacking individual second column runs, but the system was not automated and the analysis time was exceptionally long. Second column separations took 60 min each and 20 fractions were analyzed in the second dimension. In addition to the obvious inconvenience, one of the problems with long analysis times like those listed here is that sensitive biological samples may change their character during such a time frame. Guiochon et al. (13) described a single theoretical column capable of a two-dimensional separation; other references (14-17) are examples of other approaches to 2-D LC and coupled-column techniques.

The closest approach, to our knowledge, to what we introduce here as comprehensive 2-D LC was work done by Erni and Frei (18). They analyzed a complex plant extract with a SEC column as the first dimension and a reversed-phase column as the second dimension. The two columns were connected with an eight-port valve as in our system. But their approach does differ from ours in several ways. First, they sampled the first column only seven times over a 10-h run. Such a low sampling rate essentially precludes 3-D data presentation. Each fraction volume was approximately 1.5 mL. Such a large injection volume necessitated a preconcentration step (peak compression), obtained through use of gradient methods, at the head of the second column.

In contrast, we introduce a system here that uses a cation exchange column under gradient conditions as the first column, coupled through an eight-port, computer-controlled switching valve to a size exclusion column. These two types of separations provide very complementary information and are orthogonal methods. In addition, the entire first column effluent is analyzed on the second column making this approach superior in "survey" applications where the substance of interest is not known. Analyzing the entire first column effluent eliminates the need for prior knowledge of peak elution times, which is necessary in heart cutting techniques and diverted flow methods. Because the entire first column effluent is reanalyzed on the second column without the use of stopped flow methods, we have termed this technique comprehensive 2-D LC to distinguish it from other 2-D LC approaches.

EXPERIMENTAL SECTION

Instrumentation. The heart of the system is the eight-port valve like that used by Erni and Frei (18). The two valve configurations are shown in Figure 1. In the first position, effluent from the first column (C1) is pumped through loop 2 (L2), while the second pump (P2) forces a buffer through loop (L1) onto the second column (C2). When switched to the second position, the contents of L2 are pumped onto the second column by the second pump, and effluent from the first column replaces the buffer in L1. When the first column flow rate, valve loop size, valve

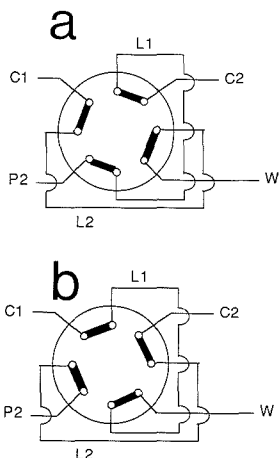


Figure 1. Two configurations of an eight-port, computer-controlled valve. C1 and C2 are columns 1 and 2, respectively, L1 and L2 are loops 1 and 2, respectively, P2 is pump 2, and W is waste.

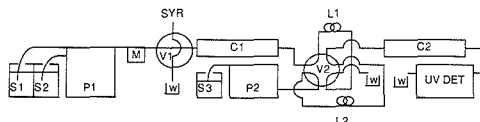


Figure 2. Schematic of 2-D LC instrumental setup. S1, S2, and S3 are buffers A, B, and C; P1, Brownlee microgradient syringe pump; M, 52- μ L mixer; V1, Rheodyne 0.5- μ L injection valve; SYR, injection syringe; C1, cation exchange column; V2, eight-port computer-controlled valve; L1 and L2, 30- μ L loops; P2, Waters Associates Model 6000A piston pump; C2, size exclusion column; UV DET, UV detector operated at 215 nm; W, waste.

switching time, and second column flow rate are properly chosen, none of the first column effluent is wasted, and the entire first column effluent is separated on the second column. The entire 2-D chromatogram is completed in nearly the same time period that it takes to run the first column alone. For example, with a 5 μ L/min flow rate on the first column and 30- μ L loops, if the valve is switched every 6 min, all of the effluent from the first column will be analyzed on the second column since it will take 6 min for the first column to fill one loop. With an adjustment of the flow rate on the second column so that one chromatogram is completed in 6 min, the contents on one loop can be analyzed before the contents of the next loop are injected.

All instrumentation used in this study is commercially available. Figure 2 is a schematic diagram of the instrumental setup. P1 is a Brownlee microgradient syringe pump (Santa Clara, CA). The pump was fitted with a Brownlee 52- μ L mixer column labeled M in Figure 2. V1 is a manually operated Rheodyne 7520 injection valve with a 0.5- μ L internal loop and was purchased from Rheodyne, Inc. (Cotati, CA). SYR is a 10- μ L Hamilton syringe fitted with a 2 in., 22-gauge needle purchased from Alltech Associates (Waukegan, IL). C1 is an Aquapore CX-300 cation exchange column, 250 mm \times 1.0 mm, purchased from Applied Biosystems (Foster, City, CA). V2 is an eight-port electrically actuated valve with $1/16$ in. fittings and a standard port diameter of 0.016 in. Valve material is Nitronic 60. The valve and its fittings were purchased from Valco Instruments Co., Inc. (Houston, TX). L1 and L2 are 30- μ L 316 series stainless steel loops also purchased from Valco Instruments. P2 is a Waters Associates (Milford, MA) Model 6000A piston pump. C2 is a Zorbax BioSeries GF-250 gel filtration column 250 mm \times 9.4 mm. This column was purchased from E. I. du Pont de Nemours and Co. (Wilmington, DE). The detector is a Jasco (Easton, MD) UV1DEC-100II detector operated at 215 nm. All connecting tubing is 0.007 in. i.d., and $1/16$ in. fittings are used. All fittings

and tubing other than those specific to V2 were purchased from Alltech Associates.

Instrument Control. An IBM/PC/XT purchased from IBM (Boca Raton, FL), was fitted with a LabMaster multifunction input/output interface board, which was purchased from Scientific Solutions (Solon, OH). The computer was used to record data and control the valve switching of V2 shown in Figures 1 and 2. The interface board was used as follows: a 16-bit analog-to-digital converter (ADC) was used to acquire data from the Jasco detector output; a programmable parallel port (Intel 8255) was used for control of the valve position; a programmable timer (Advanced MicroSystem 9513) was used for timed data acquisition and time valve movements. The data acquisition rates were 0.5 and 1 point per second depending upon the run conditions.

Hardware and LC instrumentation were controlled by software written in Microsoft Advanced Basic and assembly language; both of which were written in-house. The BASIC portion of the program allowed for user-entered parameters such as frequency of injections on the second column, number of injections on the second column, and data acquisition rate. The number of second column injections and frequency of those injections determine the total system analysis time. The assembly language portion of the program then acquires data at the specified rate and controls timed switching of the eight-port injection valve. At the completion of data acquisition, BASIC programs process the data and convert it to compatible form for use with the plotting software (Golden Graphics Software, Golden, CO). Several options are available for data processing. With Golden Graphics Software, (a) the data can be presented as a three-dimensional plot, viewed from any angle or height, where the x axis represents retention time on the second column, the y axis represents the retention time on the first column, and the z axis is detector response, (b) Golden Graphics Software also allows for contour maps of the three-dimensional data. Entire chromatograms or portions of a chromatogram can be represented in either of these two forms. In-house-written software allows for the following types of data presentation: (a) a second column "slice" of the 3-D plot can be displayed, the equivalent of displaying an individual injection of the second column as the conventional second column chromatogram; (b) this "slice" can be expanded up to the entire injection range by summing individual data points to display the resultant reconstructed second column chromatogram for a portion of, or for the entire, original sample; (c) a first column "slice" of the 3-D plot can be displayed; (d) by varying the width of this "slice" the total reconstructed first column chromatogram can be displayed, or a first column chromatogram for a particular molecular weight range can be displayed.

Chromatographic Conditions. First column gradient conditions were as follows for the first separation of protein standards: a 5 μ L/min flow rate was used and the flow was held isocratic from 0 to 20 min in buffer A, a gradient from 0% to 100% buffer B was started at 20 min and completed at 260 min, the flow was again held isocratic in buffer B until the end of the analysis time. A second protein separation was performed as follows: a 10 μ L/min flow rate was used with the flow held isocratic from 0 to 10 min in buffer A, a gradient from 0% buffer B to 100% buffer B was started at 10 min and completed at 130 min, the flow was again held isocratic in buffer B until the end of the analysis time. Buffer A was 0.2 M NaH_2PO_4 , pH 5. Buffer B was 0.2 M $\text{NaH}_2\text{PO}_4/0.25$ M Na_2SO_4 , pH 5. First column conditions for the separation of serum samples were as follows: a 10 μ L/min flow rate was used with a gradient begun at 10 min at 0% buffer B and completed at 130 min at 100% buffer B, the flow was held isocratic in buffer B until the end of the analysis time. Buffer A was 0.1 M NaH_2PO_4 , pH 5, and buffer B was 0.1 M $\text{NaH}_2\text{PO}_4/0.25$ M Na_2SO_4 , pH 5. Second column conditions for all separations were as follows: a 2.1 mL/min flow rate was used, isocratic in buffer C. Buffer C was 0.2 M NaH_2PO_4 , pH 7.

Samples and Reagents. Buffers were adjusted to the proper pH with NaOH. Deionized water was further purified with a Barnstead Nanopure System (Boston, MA). All buffer solutions were filtered with 0.22- μ m pore size MAGNA Nylon 66 membrane filters from Micron Separations, purchased from Fisher Scientific.

All samples were dissolved in buffer A and were filtered through acrodisc 0.45- μ m filters purchased from Gelman Sciences (Ann Arbor, MI) prior to injection. The following were purchased from

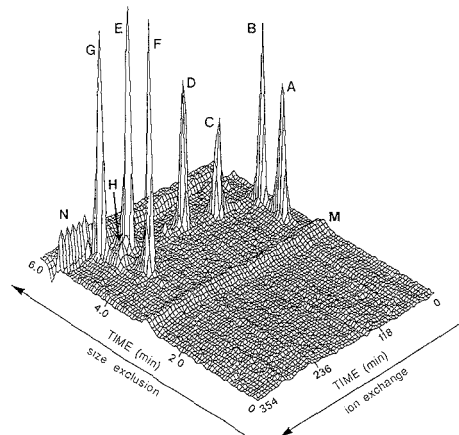


Figure 3. 2-D chromatogram of protein sample: peak A, glucose oxidase; B, ovalbumin; C, β -lactoglobulin A; D, trypsinogen; E, α -chymotrypsinogen A; F, conalbumin; G, ribonuclease A; H, hemoglobin; M, exclusion volume "pressure" ridge; N, inclusion volume "salt" ridge. Ovalbumin and α -chymotrypsinogen A at 0.2%, other proteins at 0.3% (w/v). C1 conditions: 5 μ L/min, 0% to 100% buffer B from 20 to 260 min; buffer A, 0.2 M NaH_2PO_4 , pH 5; buffer B, 0.2 M $\text{NaH}_2\text{PO}_4/0.25$ M Na_2SO_4 , pH 5. Valve actuated every 6 min; detection at 215 nm, data collection rate 0.5 point/s; plot shows every other point collected for injection 1 through 60. Each line perpendicular to the IEC time axis represents one injection on the SEC column.

Sigma (St. Louis, MO): rabbit muscle L-lactic dehydrogenase, bovine pancreatic trypsinogen, bovine pancreatic α -chymotrypsinogen A, chicken egg albumin, bovine blood hemoglobin, bovine milk β -lactoglobulin A, chicken egg white conalbumin, bovine pancreatic ribonuclease A, *Aspergillus niger* glucose oxidase, human serum (lyophilized powder), and horse serum (lyophilized powder). Protein samples were 0.3% (w/v) in each protein with the exception of ovalbumin and α -chymotrypsinogen A, both of which were present at 0.2% (w/v) due to their strong detector responses at 215 nm. Human serum was reconstituted in 1 mL of buffer A and filtered similarly to the protein sample (1 mL was the original volume according to Sigma). Horse serum was reconstituted to 2 mL in buffer A and filtered similarly to the protein sample (2 mL was the original volume according to Sigma).

RESULTS

Figure 3 shows the three-dimensional representation of the comprehensive two-dimensional LC/LC chromatogram of the protein standards sample. The flow rate of 2.1 mL/min through column 2 results in a 6-min SEC chromatogram. Using 30- μ L loops on V2 and a 5 μ L/min flow rate through column 1, one injection on the second column was made every 6 min, the full run time of the SEC column. Separations occurring in the second column (SEC) are shown along the time scale of 0 to 6 min. Separations occurring in the first column (IEC) are shown along the time scale of 0 to 354 min. The large base-line disturbances seen at the end of each size exclusion chromatogram (labeled N in Figure 3) are due to the refractive index change caused by buffer salts from the IEC column. An advantage to using SEC in the second dimension is that all small ions and buffer components that normally appear as base-line disturbances are moved to the end of the chromatogram and are easily ignored in data analysis. This is also true of gradient components in the first column that normally produce a gradual base-line drift in one-dimensional chromatography. The base-line drift due to the increased amounts of Cl^- ion in the first dimension gradient is evident as the magnitude of the base-line disturbance (occurring slightly before 6 min) increases in the later chro-

matograms. When a column run under gradient conditions is followed by SEC, components causing base-line drift are moved to the SEC inclusion volume. The result is an extremely flat "baseplane" as can be seen in all of the presented chromatograms. No smoothing of data was necessary. The small peak evident in each SEC at the exclusion limit of the column (occurring at approximately 3 min), is an injection artifact caused by flow and pressure disturbances due to the switching of V2. In the 3-D plot this peak appears as a ridge (M) in the "baseplane". Because this peak is extremely reproducible from injection to injection, it would be a simple matter to use a base-line subtraction method, similar to that used in LC voltammetry systems (19), to remove it from the chromatogram. However, since the injection ridge is well resolved from the peaks of interest, base-line subtraction was deemed unnecessary in this case. Another feature worth noting in Figure 3 is that due to the nature of SEC, nearly half of the display area of the SEC chromatograms is unused. It is a simple procedure to use the computer software to ignore the uninteresting portions of the chromatogram by not plotting them. This flat portion of data however, is from an analytical point of view, wasted time. With V2 activated every 3 min instead of every 6 min, and the flow rate on the first column increased to 10 μ L/min (with a corresponding change in gradient conditions as described in the Experimental Section), the IEC column will fill one loop every 3 min. The flow rate on the SEC column is left unchanged. The result is that the "useful" portion of one second column chromatogram is overlapped onto the "nonuseful" portion of the following second column chromatogram. This makes better use of the full three-dimensional display region and cuts the analysis time in half.

Figure 4a was obtained under the conditions described above. The flow rate and gradient on the IEC column were changed so that one injection was made every 3 min on the SEC column. The SEC column run time remained at 6 min. The peak-containing region is therefore spread out over twice the display area from that in Figure 3, and the total analysis time is decreased by roughly a factor of 2. The total analysis time, which is equal to the IEC axis time plus the SEC axis time, dropped from approximately 360 to 150 min. An additional protein, L-lactic dehydrogenase, was included in the sample mixture shown Figure 4a. This is the last protein to elute from the IEC column, but it is poorly behaved on the SEC column and elutes in an abnormally low molecular weight range and with a broadened peak shape.

Figure 4b is the same 2-D chromatogram as that shown in Figure 4a but with the low molecular weight "salt" region removed, demonstrating how a cleaner view can be provided via software. Figure 5 is a contour map of Figure 4b. The peak for hemoglobin best shows the improved separation power of multidimensional systems over single-column separations. If size exclusion were the sole separation mechanism used, hemoglobin would coelute with β -lactoglobulin A. If the ion exchange column alone were used to separate the mixture, hemoglobin would coelute with ribonuclease A under these gradient conditions. However, in the two-dimensional system, hemoglobin is completely resolved from both of these proteins. The contour map also allows for easy peak identification from run to run and is more reliable than single-dimension peak times, as stated earlier, since two independent elution times are obtained for each protein as opposed to one for 1-D chromatography.

Our in-house-written software allows for several options in terms of data representation. Individual SEC runs can be displayed. The seventh SEC run from Figure 4b is displayed in Figure 6a; the first peak is glucose oxidase and the second peak is ovalbumin. Figure 6b is equivalent to the size ex-

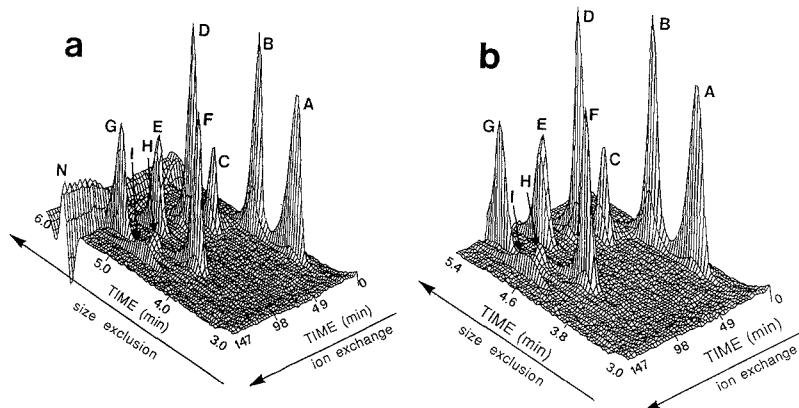


Figure 4. (a) 2-D chromatogram of second protein sample. Conditions were similar to those given in Figure 3 with the following exceptions: C1, 10 $\mu\text{L}/\text{min}$ flow rate; 0% to 100% buffer B from 10 to 130 min; valve actuated every 3 min; data collection rate 1 point/s; plot shows every other point collected. Peaks identified same as Figure 3 where L-lactate dehydrogenase, has been added at 0.3% (w/v). Each line perpendicular to the IEC axis represents an injection on the SEC column. (b) Edited view of Figure 4a without "salt" region.

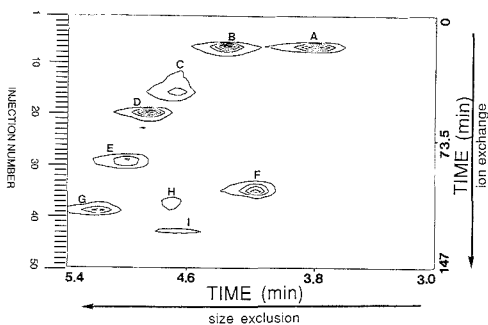


Figure 5. Contour map of Figure 4b. Peaks identified are as in Figure 4.

clusion chromatogram that would be obtained if no IEC had been used. The size exclusion column is clearly insufficient to separate this protein mixture. The letters identifying peaks are therefore only approximate in terms of position. This plot was obtained by expanding the SEC "slice" in Figure 6a to include all second column injections by adding each corresponding data point to the data point in the next SEC chromatogram. A third plot can be constructed which, if the SEC dimension is viewed as a "poor man's mass spectrometer", is the analog of a total ion current chromatogram. The result is the reconstructed IEC chromatogram shown in Figure 6c which would be obtained had no SEC been used in the analysis. This type of data treatment is done by summing IEC "slices" over the entire SEC data range. Each summed second column injection then becomes one point on the ion exchange chromatogram. Because only a relatively small number of points are obtained (equal to the number of injections on the second column), the resulting chromatogram is somewhat undersampled. While this result is inferior to what a first column chromatogram would look like had a detector been placed before V2, it eliminates the need for a detector before the eight-port valve. This helps to reduce extracolumn volume in the system. The reconstructed chromatograms in parts b and c of Figure 6 point out the improved separating power of a two-dimensional approach to complex samples. Figure 6d is similar to Figure 6c, but the IEC "slice" was summed only for peaks eluting from ap-

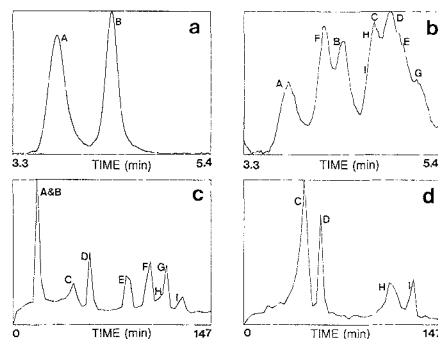


Figure 6. (a) Seventh injection on second column obtained from Figure 4b: peak A, glucose oxidase; peak B, ovalbumin. (b) Reconstructed second column chromatogram obtained by expanding SEC "slice" to include all injections. (c) Reconstructed first column chromatogram obtained by expanding IEC "slice" to include the entire molecular weight range. (d) Reconstructed ion exchange chromatogram obtained by summing data points in the molecular weight range occurring between 4.67 and 4.83 min (280–290 s). All peaks are identified by letters as in Figure 4b.

proximately 4.67 to 4.83 min (280–290 s) on the SEC column. The result is a reconstructed IEC chromatogram of proteins with molecular weights roughly between 30 000 and 40 000.

In Figure 6b, the peak capacity of the SEC column is visually estimated to be 7. In Figure 6c, the peak capacity of the IEC separation is visually estimated to be 18. Assuming these two separation mechanisms are orthogonal to each other, that results in a peak capacity of 126 for this 2-D system. The IEC separation could possibly be improved by use of a different pH or different gradient conditions, and a longer elution time could also be acceptable; nevertheless, in the mode used, the 2-D LC system provides greater resolution and peak capacity than either dimension alone.

Figure 7a is a 3-D representation of a 2-D chromatogram of a human serum sample. This plot stops just before the appearance of the salt peak in the second dimension. Figure 7b is a 3-D representation of a 2-D chromatogram of a horse serum sample, again the plot stops just before the salt peak region. Although neither serum sample is fully separated, the 2-D technique does strongly hint at the complexity of the

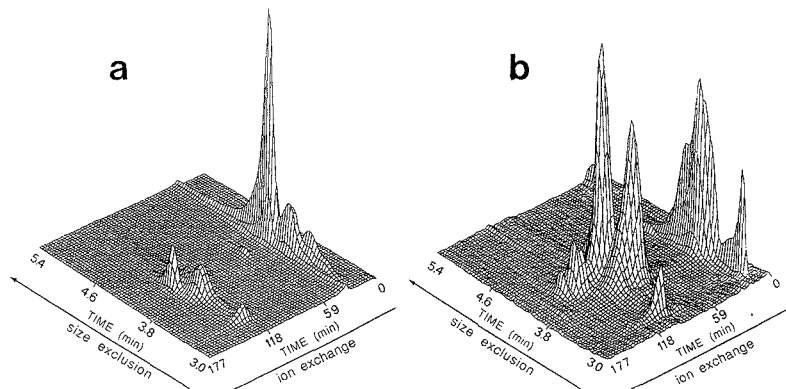


Figure 7. (a) 2-D chromatogram of reconstituted human serum. Same conditions were used as in Figure 4 with the following exceptions: buffer A, 0.1 M NaH_2PO_4 , pH 5; buffer B, 0.1 M $\text{NaH}_2\text{PO}_4/0.25$ M Na_2SO_4 , pH 5. Each line perpendicular to the IEC axis represents one injection on the SEC column. (b) 2-D chromatogram of reconstituted horse serum. Same conditions were used as in Figure 7a.

samples. Neither chromatographic column alone could provide the separation power obtained when 2-D operation is used.

DISCUSSION

The IEC column used in our system is a microbore column. The small column diameter and gradient conditions help to ensure a minimum of dilution and peak broadening. These conditions and a small loop size eliminate the need for a preconcentration step on the head of the second column. Using the microbore column for the first-dimension separation provides flow rates compatible with sample volumes for the SEC column, which is a semipreparative column. This arrangement of a highly efficient separation followed by a less efficient separation is the opposite of what is usually attempted in other multidimensional approaches. Our ordering of the columns is essential to allowing the entire first column effluent to be analyzed on the SEC in a reasonable time frame. There is no need with our system for stopped flow methods or on-column or off-column concentration steps. The first column in our system is run under slow conditions and the second column is run quickly. The result is that the effluent from the first column is sampled by the second column frequently, resulting in a large number of injections on the second column. A high sampling rate means that peak profiles can be obtained for both separation dimensions and not just for the second dimension. Ideally, the first column effluent should be sampled at least several times across each peak width by the second column. This will help to decrease the possibility of spurious peak broadening by the second column.

Both our approach and previous approaches have the potential to suffer from a detection problem, although for different reasons. In previous approaches, a large original sample is broken down into smaller and smaller components during each separation. As the analyzed sample components are further fractionated, the chromatography becomes more and more analytical in nature. The problem is especially noticeable in heart cutting techniques where only a portion of the original constituent reaches the final detector. Detecting these fractionated components is often facilitated by reconcentration steps between separations. In our system, the entire sample will reach the final detector but only after passage through two columns. A larger column is needed as the second dimension to be able to handle the increased sample volume eluting from the first column. The larger the dilution in each column, the more difficult is detection. Some form of peak

compression between the first and second dimension would eliminate the need for a semipreparative column for the second-dimension separation. Such compression might be achieved by adsorbing effluent fractions from the first column in a small cartridge, followed by desorption in a few microliters of solvent into the second column. This would help to decrease the total dilution, and detection limits would improve. Peak compression, however, may be difficult to implement in many cases, and we found for our particular application that peak compression was not necessary.

While other researchers using a similar pair of columns to ours place the SEC column before the IEC column or reversed-phase column, reversing that order and placing the gradient run, cation exchange column as the first dimension, followed by a size exclusion column has several advantages. First, there is no need to run a gradient in the second dimension; thus, starting conditions do not have to be regenerated before the start of the next injection. The result of this is that the second column can be run quickly so the first column is sampled frequently, and stopped flow methods do not have to be used on the first column or, alternatively, no first column effluent is lost during the regeneration time. The lack of a second column gradient also eliminates problems associated with being able to produce rapid, reproducible gradients for the second column. Second, there is a definite beginning and end to size exclusion chromatography analysis times. This helps to ensure that peaks will not overlap from one run to another in the second dimension. Third, all low molecular weight compounds are eluted in the inclusion volume of the second column as stated previously.

Other combinations of columns would also be interesting to investigate. A reverse-phase column, for instance, followed by a SEC column would have similar advantages to those presented in this work. An IEC column followed by a reverse-phase column, or vice versa, might be particularly useful for analysis of peptides from a tryptic digest of a protein. An advantage of this system is that it is modular and flow rates, loop sizes, and columns can be interchanged to fit the needs of the particular analysis. It is also easy to imagine a software system, connected to the appropriate instrumentation, which would allow the user to mark off specific peak areas on a contour map. In the following 2-D analysis, software would then drive a fraction collector to collect the eluting peak. This possible future system would be particularly useful in a system separating tryptic digest fragments. The fact that the entire sample moves through both columns would be a distinct ad-

vantage in such an application.

We have shown that it is possible to obtain two-dimensional separations of protein samples chromatographically. Furthermore, these separations are attainable in an automated system using commercially available equipment, and the analysis time is virtually no longer than that of the first column separation. The method allows for the analysis of the total first column effluent on the second column without significant loss of first column resolution. Frequent sampling of the first column effluent provides peak profiles in both column dimensions. 3-D data representation provides for easy peak identification from run to run and is more reliable than single-column elution times. Most importantly, 2-D separation provides for higher resolution of complex samples and larger peak capacities than single-column chromatography. As pointed out by Giddings (5), the thrust of 1-D chromatographic research is to improve the individual separations, but the thrust of 2-D research will be to improve the combination of separation methods.

ACKNOWLEDGMENT

J.W.J. wishes to thank J. C. Giddings for an insightful discussion on multidimensional separations. We wish to thank Jeff Nystrom for some preliminary work in this area.

LITERATURE CITED

- (1) Davis, Joe M.; Giddings, J. C. *Anal. Chem.* **1985**, *57*, 2168-2177.
- (2) Davis, Joe M.; Giddings, J. C. *Anal. Chem.* **1985**, *57*, 2178-2182.

- (3) O'Farrell, P. H. *J. Biol. Chem.* **1975**, *250*, 4007-4021.
- (4) Anderson, N. G.; Anderson, N. C. *Anal. Biochem.* **1978**, *85*, 331-340.
- (5) Giddings, J. C. *Anal. Chem.* **1984**, *56*, 1258A-1270A.
- (6) Giddings, J. C. *HRC CC, J. High Resolut. Chromatogr. Chromatogr. Commun.* **1987**, *10*, 319-323.
- (7) Guiochon, G.; Beaver, L. A.; Gonnord, M. F.; Siouffi, A. M.; Zakaria, M. *J. Chromatogr.* **1988**, *255*, 415-437.
- (8) Majors, Ronald E. *J. Chromatogr. Sci.* **1980**, *18*, 571-579.
- (9) Johnson, E. L.; Gloor, R.; Majors, R. E. *J. Chromatogr.* **1978**, *149*, 571-585.
- (10) Fürst, Peter; Zimmerman, L.; Oulès, Raymond; Yahiel, Veronique; Johnson, Christina; Bergström, Johas *Anal. Chem.* **1982**, *122*, 394-403.
- (11) Huber, J. F. K.; Fogy, I.; Fiorese, C. *Chromatographia* **1980**, *13*, 408-412.
- (12) Takahashi, Nobuhiro; Takahashi, Yoko; Putnam, Frank W. *J. Chromatogr.* **1983**, *266*, 511-522.
- (13) Guiochon, G.; Gonnord, M. F.; Zakaria, M.; Beaver, L. A.; Siouffi, A. M. *Chromatographia* **1983**, *17*, 121-124.
- (14) Davis, Gregory C.; Kissinger, Peter T. *Anal. Chem.* **1979**, *51*, 1960-1965.
- (15) Lai, S. T.; Nishina, M. M.; Sangermano, L. *HRC CC, J. High Resolut. Chromatogr. Chromatogr. Commun.* **1984**, *7*, 336-337.
- (16) Bhikhabhai, R.; Lindblom, H.; Källman, I.; Fägerstam, L. *Am. Lab.* **1979**, May, 76-81.
- (17) Dunn, Michael H. *LC-GC* **1989**, *7*, 138-140.
- (18) Erni, F.; Frei, R. W. *J. Chromatogr.* **1978**, *149*, 561-569.
- (19) White, Jackie G.; St. Claire III, Robert L.; Jorgenson, James W. *Anal. Chem.* **1986**, *58*, 293-298.

RECEIVED for review August 17, 1989. Accepted October 19, 1989. Support for this work was provided by the Hewlett-Packard Corporation and American Cyanamid.

Near-Infrared Diffuse Reflectance Analysis of Athabasca Oil Sand

Robert C. Shaw

Research Department, Syncrude Canada Ltd., Edmonton, Alberta, Canada T6C 4G3

Byron Kratochvil*

Department of Chemistry, University of Alberta, Edmonton, Alberta, Canada T6G 2G2

The application of near-infrared diffuse reflectance analysis for the determination of bitumen content in samples of Athabasca oil sand is described. Quantitative analysis is performed using calibrations based on linear correlation between spectral features at selected wavelengths and compositional data for a series of known samples. The anhydrous bitumen content of oil sand within a length of core was obtained from spectra recorded at 1-cm sampling intervals. Analyses by a micro Soxhlet extraction procedure provided reference assay data for correlating sample composition and spectral response. The training set included representative samples of oil sand, indurated clay, coal, and interbedded regions. A model based on the first derivative of absorbance spectra provided the best relationship between spectral features and hydrocarbon concentration over a wide range of oil sand grades. This model was used to predict the bitumen content of samples along the entire length of the test core section, thus providing a high-resolution profile of grade variability as a function of depth.

Near-infrared diffuse reflectance (NIR-DR) spectroscopy has become widely accepted for the quantitative measurement of organic species, mineral constituents, and moisture in a variety of solid substrates (1-4). The technique is rapid, is

nondestructive, and in many instances requires little or no sample preparation. Recent advances in instrumentation and software permit simultaneous multicomponent determinations to be performed on a single sample. Comprehensive reviews are available (5, 6).

The wavelength region of interest for NIR-DR work is typically 1000-2500 nm. Bitumen absorption in this region is relatively weak. As a consequence, instrumentation requirements are stringent. High signal to noise ratios require special consideration to factors such as source stability, optical design, sample positioning, and detector sensitivity. Unfortunately, structural information that can be deduced from spectra obtained in the mid-infrared region is often obscured in the near-infrared due to the multiplicity and overlap of higher frequency overtone bands. Further, specular reflection and the effects of particle size, sample packing, and surface irregularities can have a substantial impact on both the overall intensity of reflected radiation and the contrast between base-line and absorbance peaks.

To alleviate these apparent shortcomings, quantitative near-IR analysis is performed using a calibration curve developed by correlating detector response at a number of selected wavelengths to known compositions for a series of standard samples (training set). Multivariate regression techniques and sophisticated algorithms that correct for base-line anomalies, extract and reconstruct component

spectra from complex mixtures, and optimize the number of wavelength readings required for a robust and unbiased estimate for the concentration of each constituent in the sample serve to enhance the versatility of the method (7-13).

In connection with a sampling study of the heterogeneity of the Athabasca oil sand deposit, a need arose to perform a large number of measurements for bitumen content on relatively small portions of material. Methods currently in use for quantitative analysis require large samples and are slow and expensive (14). Accordingly, we investigated the use of near-infrared diffuse reflectance spectroscopy to provide compositional information on small quantities of oil sand.

EXPERIMENTAL SECTION

Samples. Samples were obtained from the Athabasca oil sand deposit in a region operated by Syncrude Canada Ltd. (15). The oil sand used in preliminary studies was freshly mined, stored in sealed containers, and ground with a mortar and pestle just prior to analysis. Samples used for subsequent work were obtained from a core supplied by Syncrude Canada Ltd., representing a typical vertical transect of the Athabasca deposit. This core, originally drilled in 1985, was approximately 120 m in length and encased in a plastic tube having an inside diameter of approximately 6.4 cm and wall thickness of 0.1 cm. As the result of earlier processing, the core had been cut in half longitudinally and a small V-notch sample removed from along the center line. The slabbing operation provides a uniformly textured flat surface for diffuse reflectance measurements. Grades within the ore zone of the core ranged from approximately 1 to 15% by weight bitumen on an anhydrous basis.

A small section of this core, just over 4 m in length, was selected for detailed NIR-DR analysis. The section was chosen to represent what appeared to be typical of grade variations seen over the entire length of core. The core sample, stored under ambient conditions since it was first analyzed, was almost completely dehydrated.

Instrumentation. Preliminary studies were conducted with a Nicolet 7199 Fourier transform infrared (FT-IR) spectrophotometer equipped with a diffuse reflectance attachment. Sample spectra were recorded in absorbance mode ratioed against powdered KBr.

The extensive data base required for detailed inspection of core necessitated use of a spectrophotometer having more rapid data acquisition and processing capabilities. This was provided by a Quantum 1200 near-infrared analyzer (LT Industries, Inc.). Spectra were recorded over the range 1200-2400 nm in reflectance mode. Data were transformed as $\log(1/R)$ to provide the corresponding absorbance spectra. The high-speed optics permitted spectra to be obtained at the rate of 5 scans/s with a spectral resolution of 1 nm. A Compaq Deskpro 286 computer ran the software driving the data acquisition, mathematical processing, modeling, and graphing functions for the analyzer.

The instrument was positioned on end such that the incident radiation could be directed downward onto the surface of the sample. A sampling table, consisting of a core holder, registration guide, and bridge assembly for mounting the spectrophotometer, was constructed to permit core to be rastered beneath the viewing port at 1-cm intervals. The viewing port itself was masked to provide a square sample window measuring 1 cm on a side. A schematic of the sampling table is provided in Figure 1.

Detector response was found to be extremely sensitive to sample elevation. Care was taken to ensure consistent positioning of the sample surface normal to the incident light and at a standard distance from the mask. Spectra generated by averaging the signal over 50 scans limited noise to approximately 0.5% relative. This was considered adequate for all subsequent work. Carbon black was used as reference material.

Digitized sample spectra were obtained for oil sand at 1-cm intervals along the length of the test core section and stored on hard disk in the computer. To establish a model relating the spectral features of these samples to oil sand composition, a reference library of spectra for known samples was assembled. With the spectra of samples in the core on file, it became a matter of analyzing a selected number to provide the requisite assay information. This training set was then used to generate correlations between spectra characteristics and sample composition.

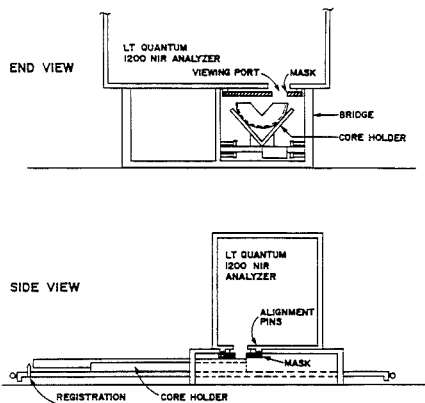


Figure 1. Schematic illustration of the sampling table constructed for core analysis.

Micro Soxhlet Extraction Procedure. A total of 48 samples were selected to represent the broad compositional range of material contained within the test section of core. Samples, each weighing on the order of 1-2 g, were removed from the core by using a scalpel, and their position along the core was labeled so that each could be matched with a corresponding NIR-DR spectrum.

The training set samples were ground in a mortar and pestle. A subsample of the homogenized material was then extracted in a micro Soxhlet assembly by using a 10 x 50 mm cellulose thimble and 10 mL of toluene. Extraction was complete in 10 min. The solvent extract was quantitatively transferred to a tared evaporating dish, allowed to dry overnight at room temperature, and then weighed to obtain the bitumen value. Previous experiments had shown that traces of toluene remaining in the bitumen (as measured by IR upon dissolving the residue in trichloroethylene) can be considered negligible. The tared thimble was dried at 120 °C for 1.5 h and reweighed to obtain the solids content.

Results of replicate determinations on a variety of oil sand samples in which both the thimbles and evaporating dishes were dried in a forced draft oven for 24 h at 120 °C showed consistently low mass closures (the ratio of the sum of the measured bitumen and solids mass to the original sample mass), indicating that measures for the bitumen and/or solids content of the sample are underestimates of the true composition. Sources of error investigated included loss of bitumen light ends upon drying the solvent extract at elevated temperatures, loss of hygroscopic water from thimbles and oil sand samples, and incomplete retention of fine particles in the thimble. The first two sources of bias would lead to low recoveries. The latter problem, if present, would not be detected by examining mass closure data. Solids lost through the thimble would ultimately be measured as bitumen. The toluene used for extraction contained no measurable residue upon evaporation.

A comparison of bitumen weights obtained from sample extracts evaporated under ambient conditions and then dried in an oven for 16 h at 120 °C indicated an average weight loss upon heating on the order of 0.01-0.02 g for bitumen residues weighing approximately 0.2 g. Blank thimble extractions were also done to see whether adsorbed water could affect assay results. Weight losses on the order of 0.01 g were seen upon drying thimbles for 1.5 h at 120 °C. To minimize the effects of these systematic errors, sample thimbles must be dried prior to analysis and extract solutions evaporated to dryness at room temperature.

The precision of the analyses (means based on eight measurements, assay results expressed in weight percent) for low-grade oil sand was as follows: bitumen, 6.05 ± 0.22; solids, 93.56 ± 0.25; mass closure, 0.9962 ± 0.0006. Corresponding results for medium-grade oil sand were as follows: bitumen, 8.54 ± 0.26; solids, 90.69 ± 0.23; mass closure, 0.9923 ± 0.0009. Results for high-grade oil sand were as follows: 16.74 ± 0.19; solids, 82.78 ± 0.18; mass

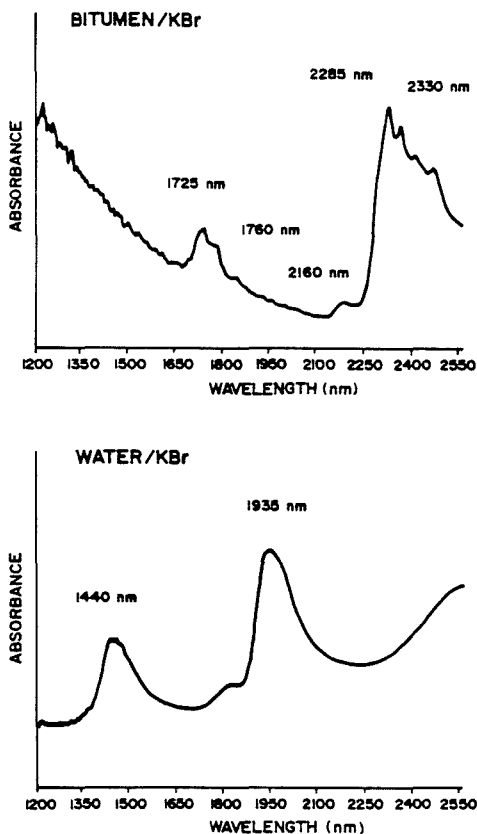


Figure 2. Near-IR diffuse reflectance spectra for bitumen and water dispersed in KBr.

closure, 0.9952 ± 0.0005 . Uncertainties are 1 standard deviation. It should be noted that differences among these replicate sample analyses probably reflect sampling variability more than actual analytical variability.

RESULTS AND DISCUSSION

Preliminary Studies with the Nicolet 7199 Spectrophotometer. Spectra obtained for bitumen, water, quartz, and a variety of clays normally present in oil sand are shown in Figures 2 and 3. The bitumen spectrum shows two distinctive sets of doublets, one with major peaks at 2285 and 2330 nm and the other with peaks at 1725 and 1760 nm. These absorbances, along with the much weaker bands at 2400 and 2460 nm, can be ascribed to overtones and combinations of the fundamental vibration frequencies within constituent methyl and methylene groups. Although the absorbance peak at 2160 nm may signify the presence of aromatic hydrocarbon species, it could also be attributed to contamination by clay, most probably kaolinite.

The diffuse reflectance spectrum for water indicates two strong absorbance peaks at 1440 and 1935 nm. These bands, representing combinations of fundamental vibrations associated with free water molecules, are also seen in the spectra for illite, kaolinite, and montmorillonite. These three spectra also show a major band in the region around 2200 nm, which is diagnostic of aluminum-bearing clays.

Differences in the spectral patterns for the various clays are significant. In the spectrum of kaolinite, for example,

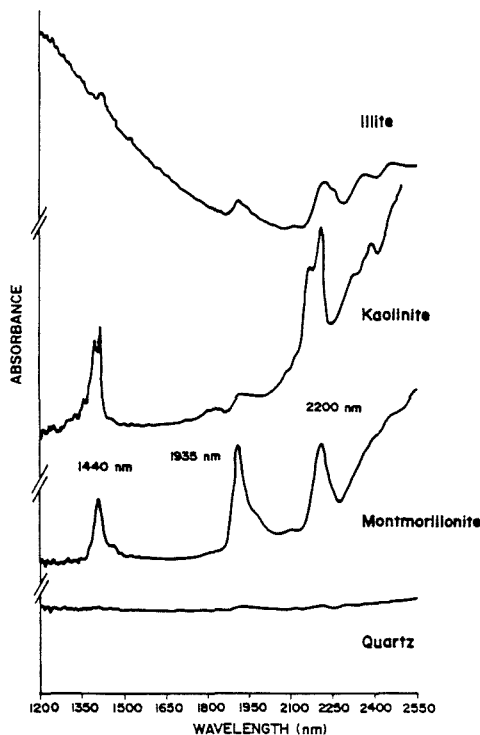


Figure 3. Near-IR diffuse reflectance spectra for various clay minerals and quartz.

peaks centered at 1440 and 2200 nm are resolved as doublets. Only single peaks at these wavelengths are observed for illite and montmorillonite. The splitting of the 1440-nm absorbance band may indicate differences in coupling between the vibrational frequencies of free hygroscopic water and those associated with water of hydration. In contrast with the spectrum for montmorillonite, the free water absorbance at 1935 nm for kaolinite and illite is relatively weak. Further, illite exhibits a progressive increase in absorbance (diminishing reflectance) toward shorter wavelengths in a manner similar to that of bitumen, whereas the opposite trend is evident in the spectra for other types of clay.

The near-infrared diffuse reflectance spectra for fresh and dehydrated high-grade oil sand (approximately 13% bitumen content) in Figure 4 show many of the significant features of the individual component spectra. The free water absorbance band at 1935 nm is absent in the spectrum for the dehydrated sample. Overall reflectivity is affected by the water content of the material. Moisture in fresh oil sand contributes to an increase in absorbance readings at all wavelengths, presumably due to internal reflections within thin films of water. To eliminate uncertainties in absorbance measurements, subsequent spectra were obtained by using aged oil sand samples dried by exposure to the atmosphere. Samples were ground to a fine powder with a mortar and pestle and placed in the sample cup without compaction.

Figure 5 presents spectra obtained for rich-, medium-, and low-grade oil sands. The reduction in the peak heights of the major bitumen absorbance bands (relative to an imposed base line) with decreasing oil saturation is evident.

Differences in the spectra patterns between ores of marine and estuarine origin can be seen in the near-IR diffuse re-

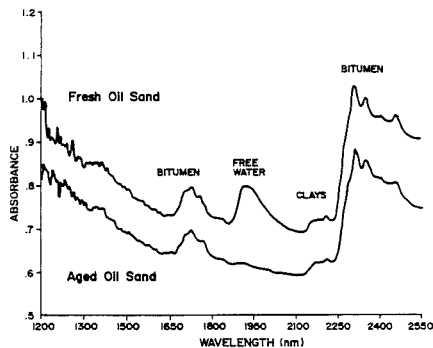


Figure 4. Comparison of near-IR diffuse reflectance spectra for fresh and aged samples of oil sand.

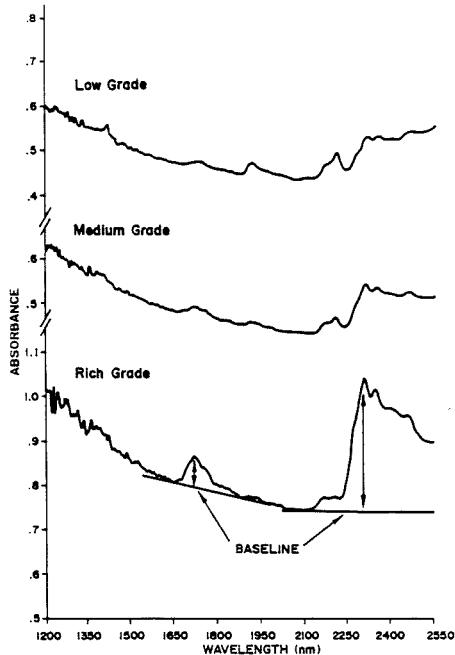


Figure 5. Comparison of near-IR diffuse reflectance spectra for oil sands of varying bitumen content.

flectance spectra presented in Figure 6. Although the two test portions studied here are of similar composition (approximately 13% bitumen content), the total amount of light reflected from the marine sample is markedly less than that from the estuarine material. Further, the spectrum for the marine ore tends to have a shallower slope at short wavelengths, leading to less pronounced curvature in the spectrum toward the higher wavelength region. The ratio of the absolute absorbance at 1200 nm to that of the bitumen peak at 2285 nm is near unity for the estuarine ore and somewhat greater for the marine ore. These traits may be useful to distinguish between oil sands from differing depositional environments.

The reproducibility of diffuse reflectance measurements is affected by the nature of the sample surface presented for analysis. Replicate spectra recorded for a sample of oil sand under various conditions of surface preparation are shown in

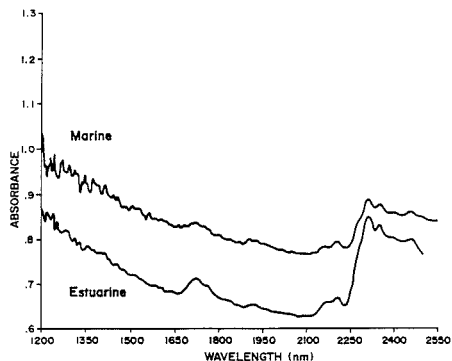


Figure 6. Comparison of near-IR diffuse reflectance spectra for oil sands of marine and estuarine origin. Both contain approximately 13% bitumen.

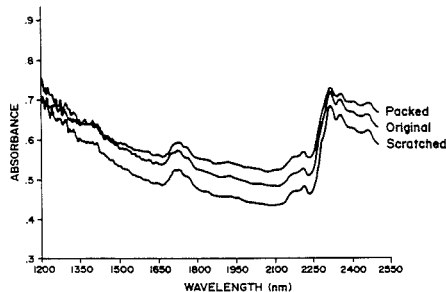


Figure 7. Effect of surface preparation procedure on the diffuse reflectance spectra of an oil sand sample.

Figure 7. The original surface is that obtained by placing the powdered material into the sample cup without compaction. The surface was leveled by screeding the sample with a straight-edge blade. The spectrum for the sample generated after tamping the material into the sample cup with a spatula shows a general decrease in absolute reflectance over much of the wavelength range. At first glance, this would not constitute a serious problem since quantitative analysis is concerned with the relative absorbance from a base line that is drawn with respect to the shape and positioning of the curve. Closer inspection of the spectrum, however, reveals that the peak height of the absorbance band at 2285 nm is diminished in relation to that of the original, uncompacted sample surface. This would lead to an underestimation of bitumen content if a calibration curve had been developed by using the initial sample handling procedure. Roughening of the packed sample by scratching the surface with a pin appears to restore the integrity of the spectrum, albeit with a higher overall reflectivity. Results indicate that methods used to prepare samples for diffuse reflectance analysis must be consistent from sample to sample.

Relationships between the bitumen content and absorbance for peaks centered at 1725 and 2285 nm for a variety of oil sand samples are shown in Figure 8. Differences in the slope of the calibration curves for oil sands of marine and estuarine origin are clearly evident. A significant inverse relationship was also found to exist between absorbance measurements for clays in the region of 2200 nm and bitumen concentration for samples of estuarine ore. The correlation between measured bitumen assay and that predicted from a linear combination of spectral readings from all three wavelengths for this type of oil sand is illustrated in Figure 9.

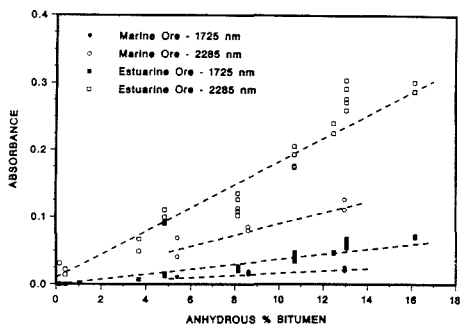


Figure 8. Correlation between predicted versus measured bitumen content and relative absorbance at 1725 and 2285 nm for oil sand samples of marine and estuarine origin. Replicate absorbance readings obtained for each sample provide an indication of the uncertainty of the measurement.

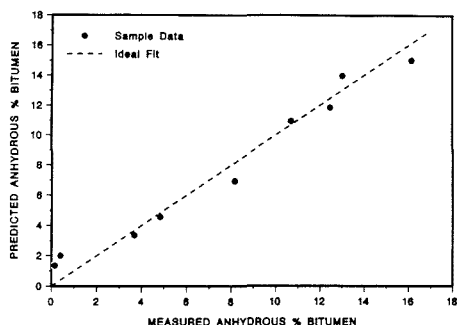


Figure 9. Comparison of predicted versus measured bitumen content for estuarine ore samples based on linear regression of absorbance measurements at 1725, 2200, and 2285 nm.

Results generated by using the Nicolet FT-IR indicated that the bitumen content of oil sand samples can be determined from near-infrared absorbance measurements. Combining the basic technique with more sophisticated data handling and multivariable statistical analysis procedures for correlating spectral response and bitumen assay can greatly enhance the utility of the method. The remainder of this report deals with the analysis of oil sand in a core using a microprocessor-based instrument specifically designed for NIR-DR analysis.

Reproducibility of Sample Spectra Obtained with the Quantum 1200 Near-IR Analyzer. A total of 10 replicate analyses were performed on samples of core (oil sand, clay, and interbedded material) and carbon black to evaluate the precision of absorbance measurements. The core and background samples were removed from the sample table and repositioned between scans. The mean, minimum, and maximum absorbance spectra for each of the core samples are presented in Figure 10. Features characteristic of the hydrocarbon and mineral components of the samples are clearly evident in the spectra. It is also apparent that differences in the overall reflectivity of a sample can be used to distinguish oil sand and clay. The spectra of the interbedded sample (a stratified mixture of oil sand and clay) reveal the traits of both parent materials.

Curvature in plots of standard deviation versus wavelength (not shown) indicates that the precision of absorbance values for a given sample is not constant. The magnitude of the uncertainty varies with wavelength and tends to be inversely related to absorbance.

To provide a common basis for comparing the variability among spectra for each type of core sample, spectra were

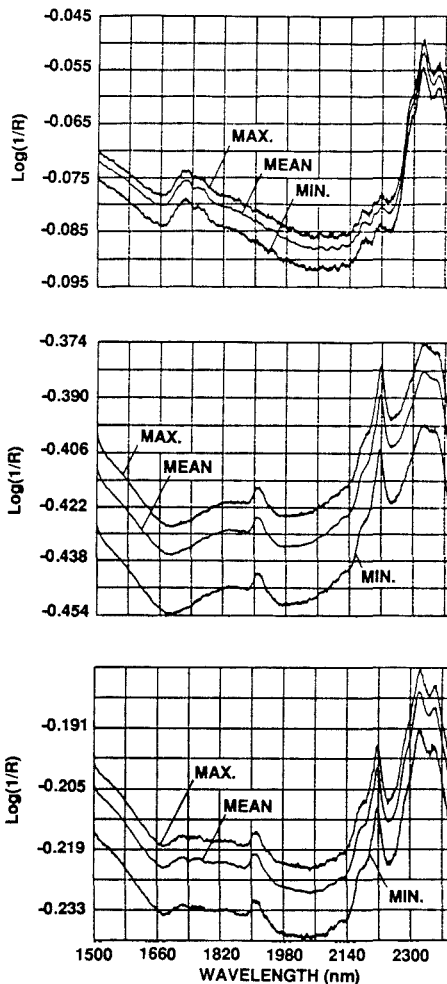


Figure 10. Reproducibility of diffuse reflectance spectra for samples of oil sand (top), clay (middle), and interbedded material (bottom). Results are based on 10 replicate analyses (background is carbon black).

characterized in terms of an average absorbance and standard deviation calculated over the wavelength range 1500–2400 nm based on data points taken at 50-nm intervals. Results were -0.0780 ± 0.0019 , -0.2161 ± 0.0047 , and -0.4203 ± 0.0077 for oil sand, interbedded material, and clay, respectively. The uncertainty among replicate sample spectra is on the order of 2% relative.

The variability among spectra for a particular sample may arise from uncertainties associated with the background correction or inconsistencies in positioning the sample surface (spatial displacement, either lateral or vertical). Given an independent estimate for the standard deviation among replicate absorbance spectra of the reference material, it is possible to determine the relative contribution of each source of error to the total based on the additivity of variances. Replicate absorbance spectra obtained for carbon black (background = 1.0) indicated that the standard deviation is reasonably constant over the wavelength range 1500–2400 nm,

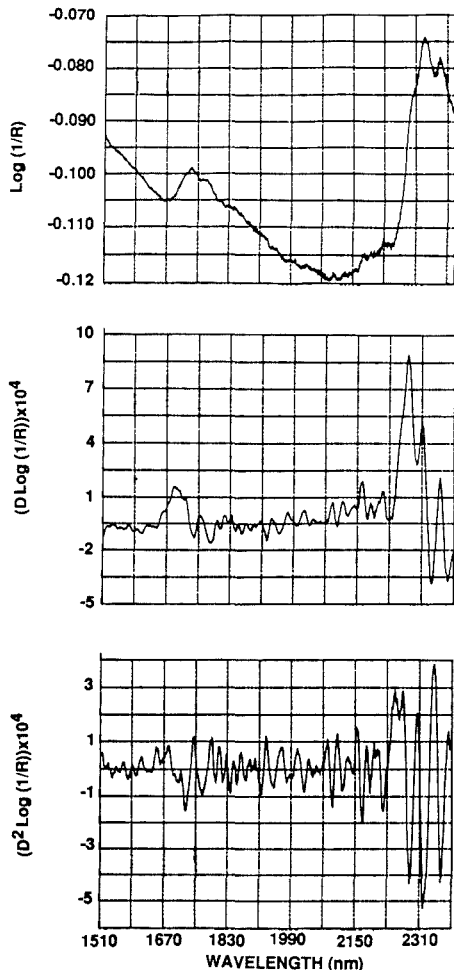


Figure 11. Near-IR diffuse reflectance spectra for a sample of oil sand in the training set illustrating log (1/R) (top), first derivative (middle), and second derivative (bottom) transformations.

averaging 0.00045 absorbance unit (obtained in the same manner as previously discussed for the core samples). Since this value is small in comparison to the standard deviations calculated for the background-corrected spectra of core samples, it appears that uncertainties due to sample positioning are the dominant source of error.

Training Set and Data Modeling. Typical spectra obtained for an oil sand sample included in the training set are illustrated in Figure 11. The first- and second-derivative spectra were generated from log (1/R) transformed data.

Correlation coefficients between compositional data and spectral features as a function of wavelength for samples in the training set are shown in Figure 12. A direct relation between absolute absorbance and bitumen content is observed over virtually all wavelengths in the range 1500–2400 nm. From these results, it appears that a model relating sample bitumen content and absorbance can be based directly on the intensity of light reflected from the sample surface at any given wavelength. Unlike the preliminary correlations established

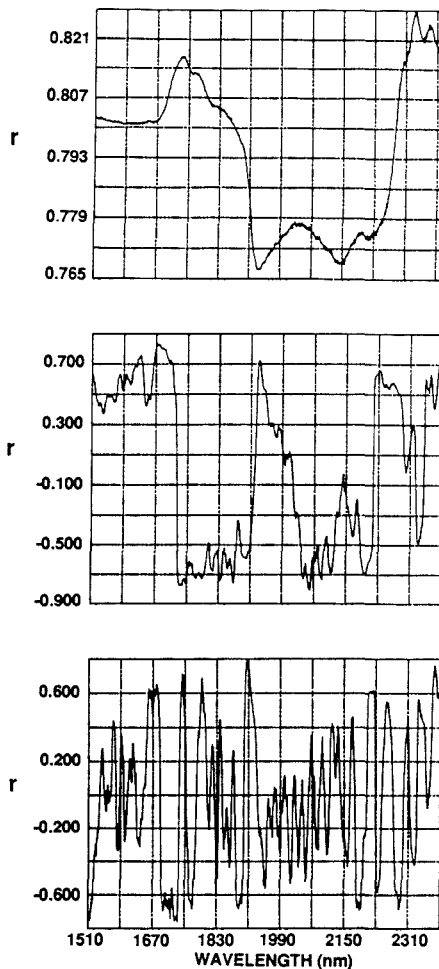


Figure 12. Correlation coefficients for the relationships between compositional data and spectral features as a function of wavelength for samples in the training set based on log (1/R) (top), first derivative (middle), and second derivative (bottom) data.

during studies with the Nicolet FT-IR, in this work we are not looking at the peak height of absorbance bands from some imposed base line.

Correlations using the first or second derivative of the absorbance spectrum are considerably more discriminating than those based on absolute reflectivity. By virtue of the mathematical processing, differences in the base-line intensities of the reflected light are normalized. Derivative spectra are thus more descriptive of the actual absorbance peaks. In these instances there is a wide range of variation in the correlation coefficient as a function of wavelength. Models based on derivative spectra are therefore likely to provide a more robust relationship between spectral features and sample composition.

Stepwise linear regression was used to model the data from the training set in the form

$$Y = C_0 + C_1(W_1) + C_2(W_2) + \dots + C_n(W_n)$$

where Y is the percent bitumen content and W_1, W_2 through

Table I. Regression Statistics for Training Set Models Based on First Derivative of log (1/R) Data

wavelength	model coeff	std error	t value
1984.0	0.7494E+05	0.4727E+04	0.1585E+02
2234.0	0.1403E+05	0.1503E+04	0.9337E+01
1799.0	-0.5040E+05	0.5618E+04	0.8972E+01
2020.0	-0.3181E+05	0.6433E+04	0.4945E+01
intercept	0.1454E+02		
multiple corr coeff (r)		0.9728	
F-test		136.6	
SEC, % bitumen		1.28	
SEP, % bitumen		1.62	
wavelength	model coeff	std error	t value
1690.0	0.6326E+05	0.7213E+04	0.8770E+01
2210.0	-0.1082E+05	0.1962E+04	0.5516E+01
2280.0	-0.1177E+05	0.2346E+04	0.5016E+01
intercept	0.1458E+02		
multiple corr coeff (r)		0.9220	
F-test		60.5	
SEC, % bitumen		2.10	
SEP, % bitumen		2.46	

W_n represent the magnitude of a spectral feature (absolute absorbance or derivative value) at wavelengths for which there is correspondence with sample composition. The coefficients C_0 , C_1 , C_2 through C_n are the associated weighting factors.

To reduce the problem to a manageable level, it was assumed that the magnitude of a spectral feature at a wavelength for which there exists a high correlation between response and sample assay serves to explain most of the variability in the data. This simple model is given by the expression

$$Y = C_0 + C_1(W_1)$$

Any lack of fit is caused by second-order effects, which can be modeled by using additional wavelengths. The selection and addition of subsequent terms are based on their ability to reduce residual error (determined by means of an F -test) and are directly related to an improvement in the multiple correlation coefficient.

A preliminary evaluation of composite models derived by using the spectra (obtained in absorbance, first-derivative, and second-derivative modes) and assay information for all samples in the training set indicated that a model based on first-derivative data would provide the best calibration for sample bitumen content. In all cases, the primary relationship between sample composition and spectral feature was determined for each of 10 starting wavelengths. These wavelengths corresponded to the 10 positions of highest correlation between sample assay and spectral response. This initial set having been established, up to four additional terms were added to reduce the sum of residual errors. The best wavelengths selected for modeling the first-derivative spectra were 1984, 2234, 1799, and 2020 nm.

Armed with the knowledge of the preferred wavelengths for calibration, we developed a regression model using the first-derivative spectra and assay results for 36 samples selected at random from the training set. The remaining sample data in the training set would be used to validate the model in terms of its predictive capability.

The standard error of calibration (SEC) and standard error of prediction (SEP) are statistics commonly used to evaluate the performance of regression models (16-18). These are defined as

$$SEC = \left[\frac{1}{n-p-1} \sum_{i=1}^n (y_i - \hat{y}_i)^2 \right]^{1/2}$$

$$SEP = \left[\frac{1}{m} \sum_{i=1}^m (y_i - \hat{y}_i)^2 \right]^{1/2}$$

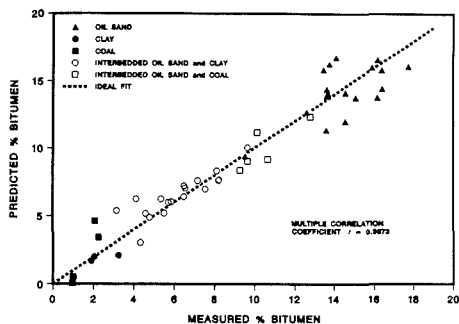


Figure 13. Comparison of predicted versus measured bitumen content for core samples in the training set using the best fit model based on the first derivative of log (1/R) spectral data.

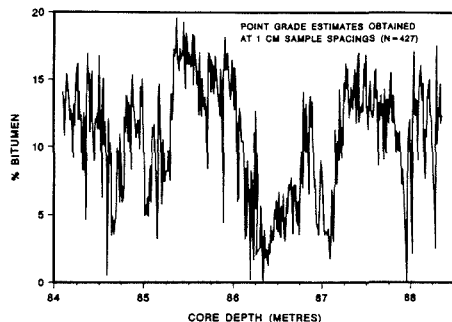


Figure 14. Variation in bitumen content as a function of depth for a 4-m test section of core. Point grade estimates were derived from NIR-DR spectral measurements at 1-cm sample spacings.

where n is the number of calibration samples, p is the number of parameters in the regression equation, m is the number of samples in the validation set, y_i is the measured assay of the i th sample, and \hat{y}_i is the corresponding predicted value from the algorithm.

Regression statistics for the model are presented in Table I. The SEP is comparable to the SEC, providing evidence that the model is reasonable and does not overfit the data. Results are compared to those from a second model developed by using the same grouping of samples from the training set but based on first-derivative values at 1690, 2210, and 2280 nm. These wavelengths represent the points of steepest slope for bitumen and clay absorbances at 1725, 2200, and 2285 nm. Although these three wavelengths have chemical significance, the performance of this model is clearly inferior to that of the former.

When all 48 samples in the training set were merged to enhance the predictive power of the model, the resulting SEC was 1.32% bitumen (multiple correlation coefficient $r = 0.9673$). Inclusion of the validation samples results in only minor perturbations to the model coefficients and the standard error of the estimate. A plot of the predicted grades versus measured bitumen concentration for the training set samples is shown in Figure 13.

The model was used to establish the bitumen content of all samples analyzed by NIR-DR in the test section of core. The resulting grade profile is shown in Figure 14. A high degree of variability is observed not only on a scale of meters, but also at the centimeter level. This variability is significant and has implication with respect to the design of sampling plans for assessing bitumen content in sections of core.

In summary, NIR-DR analysis appears to be a useful tool for estimating the amount of bitumen in oil sand. Through the use of training sets, multiple wavelength calibration, and mathematical processing of spectra, good correlations can be obtained between NIR-DR measurements and micro Soxhlet extraction results.

ACKNOWLEDGMENT

Special thanks are extended to the staff of the Department of Chemistry Machine Shop, University of Alberta, for the design and construction of the core sampling table.

LITERATURE CITED

- (1) Wetzel, D. L. *Anal. Chem.* **1983**, *55*, 1165A-1175A.
- (2) Fysh, S. A.; Swinkels, D. A. J.; Fredericks, P. M. *Appl. Spectrosc.* **1985**, *39*, 354-357.
- (3) Fredericks, P. M.; Tattersall, A.; Donaldson, R. *Appl. Spectrosc.* **1987**, *41*, 1039-1042.
- (4) Crowley, J. K.; Vergo, N. *Clays Clay Miner.* **1988**, *36*, 310-316.
- (5) McDonald, R. S. *Anal. Chem.* **1986**, *58*, 1906-1925.
- (6) Stark, E.; Luchter, K.; Margoshes, M. *Appl. Spectrosc. Rev.* **1986**, *22*, 335-399.
- (7) Honigs, D. E.; Hietje, G. M.; Hirschfeld, T. *Appl. Spectrosc.* **1984**, *38*, 317-322.
- (8) McClure, W. F.; Hamid, A.; Giesbrecht, F. G.; Weeks, W. W. *Appl. Spectrosc.* **1984**, *38*, 322-329.
- (9) Hruschka, W. R.; Norris, K. H. *Appl. Spectrosc.* **1982**, *36*, 261-265.
- (10) Beebe, K. R.; Kowalski, B. R. *Anal. Chem.* **1987**, *59*, 1007A-1017A.
- (11) Montalvo, J. G.; Faught, S. E.; Buco, S. M. *Am. Lab.* **1986**, *18*, 37-55.
- (12) Mark, H. *Anal. Chem.* **1986**, *58*, 2814-2819.
- (13) Honigs, D. E.; Hietje, G. M.; Hirschfeld, T. *Appl. Spectrosc.* **1984**, *38*, 844-847.
- (14) Bulmer, J. T.; Starr, J. *Synchrude Analytical Methods for Oil Sand and Bitumen Processing*; Alberta Oil Sands Technology and Research Authority: Edmonton, AB, Canada, 1979.
- (15) O'Donnell, N. D.; Ostrowski, T. B. *Applied Mining Geology: Ore Reserve Estimation*; Society of Mining Engineers, Inc.: Littleton, CO, 1986; pp 123-135.
- (16) Puchwein, G. *Anal. Chem.* **1988**, *60*, 569-573.
- (17) Cowe, I. A.; Koester, S.; Paul, C.; McNichol, J. W.; Cuthbertson, D. C. *Chromom. Intell. Lab. Syst.* **1988**, *3*, 233-242.
- (18) Wentzell, P. D.; Wade, A. P.; Crouch, S. R. *Anal. Chem.* **1988**, *60*, 905-911.

RECEIVED for review October 26, 1989. Accepted November 6, 1989. The authors are grateful to Syncrude Canada Ltd. for providing facilities and financial support of this project.

Normalized Measure of Overlap between Non-Gaussian Chromatographic Peaks

Eric V. Dose and Georges Guiochon*

Department of Chemistry, University of Tennessee, Knoxville, Tennessee 37996, and Analytical Chemistry Division, Oak Ridge National Laboratory, Oak Ridge, Tennessee 37831

A measure of overlap Ω between two chromatographic peak shapes is defined for the general case. Properties of invariance to chromatographic time and concentration scales, commutativity with respect to peak identity, and scaling of Ω to the range [0, 1] are demonstrated. Analytical expressions for Ω between Gaussian, Lorentzian, rectangular, right-triangular, and isosceles-triangular peak shapes are derived and discussed. The measure Ω appears to be a natural measure of the power of a preparative-chromatographic method to enrich two components of a solution much as the resolution R_s measures the power of an analytical method to resolve two peak shapes for analyte quantitation.

The theory of chromatography has been applied for over 40 years to improving separations of solution components (1, 2) and to the dependence of degree of separation on column efficiency and selectivity (2-4). Most measures of the degree of separation have been limited to peaks of Gaussian (1, 2, 5) or similar shapes (6-9). Non-Gaussian peak shapes obtained in chromatographic systems with nonlinear isotherms or slow retention kinetics sometimes result from unavoidable system conditions such as slow protein diffusion, low stationary-phase capacity, or stationary-phase inhomogeneity. In preparative chromatography, non-Gaussian peak shapes often result from deliberate attempts to overload the column, which may compress the component bands into small eluted volumes, displace other components in order to maximize local competition for sites and thus minimize band overlap, and separate more component material in a single pass. This last practice is designed to increase refined-component production rate with less than a proportional loss of purity.

Several measures of separation have been proposed in the literature. Two survey articles (9, 10) compare several quality criteria, although one (10) applies them only to peaks of Gaussian shape. A very early measure, one incorporated in some more complex expressions of later workers, is the fractional overlap at equal impurity (1). When fractions are divided at the time where the impurity percentages are equal, fractional overlap is defined as the amount of component A eluting after the cut between early-eluting component A and later-eluting component B, or of B in the fraction containing A. Since the time dividing the fractions is unambiguous, the fractional overlap is uniquely defined. However, it does not account in any way for the distribution over time of the impurity component in a fraction, and so it gives no indication of how much improvement in fraction yield or purity would be possible if fractions were taken differently. The fraction-dividing time which gives equal impurity for the two fractions is also difficult to determine for many non-Gaussian peaks. In fact, where the sample has very different amounts of two closely eluted components, as is common in preparative chromatography, all fractions of the minor component may be less pure than the least pure fraction of the major component. In this case, the fraction-dividing time defined in the above manner does not exist.

Later measures (1, 11) built on the fractional overlap suffer the same limitations. Massart (11) applies the concept of the informing power of a signal (12) to the amount of resolution between two peaks in a chromatogram. The method requires that the time axis be divided into best fractions and that the level of impurity in each fraction be taken as the fractional overlap between the main component and the other components. The informing power is inversely related to the product of all the fractional overlaps in the chromatogram. The

analogy to entropy of mixing implied by this definition of informing power is very attractive. Measures founded more directly on entropy of mixing have been presented (13, 14). Unfortunately, as pointed out by Stewart (14), the mechanics of selecting the "best" fraction times removes the uniqueness from all such measures, although it may be agreed upon to use only an arbitrary cut time such as that defined by the fractional overlap. The insensitivity to the impurities' time-distribution within a given fraction greatly weakens the analogy to mixing entropy.

Giddings (2) defined a separation function F for Gaussian peaks which can be related to column length and elution time more directly than can resolution R_s . The same article gives the relation between F and an overlap integral between Gaussian peak shapes in much the same manner as the present article develops such an integral in the general case. However, simplified expressions of that overlap integral expression for non-Gaussian peak shapes have not been derived; we have found that there are difficulties in deriving analytical solutions for some of the integrals involved.

In recent work, Schoenmakers relies on the relative overlap RO_i between two peaks (15), an expression which includes an overlap quantity similar in some ways to that of Glueckauf (1). Since the value of RO_i is normalized to the area of only one of the two peaks, the two peaks' values of RO_i differ in the general case. In other work Schoenmakers offers first-order corrections to R_s for the effects of a very large interfering peak (16). The peak separations of Kaiser (17) and related measures (7, 8) are very useful to describe the degree of separation for Gaussian peak shapes, but their usefulness is not easily extended to peaks with radically non-Gaussian shapes. The linear algebraic methods of Corry et al. (18) are designed to measure the efficiency of a single sorting process. Though chromatography may be described as a sorting process which recurs on passage of component profiles past each theoretical plate in a column, it does not follow that one must apply Corry's methods recursively to each theoretical plate. One may instead apply the methods to the final chromatogram by substituting periods of elution time for receiving bins in a sorting process. An advantage of this method is that penalty functions for component mixing in the collected fractions may be defined to be functions of the other components' concentrations. For such penalty functions, the inefficiency number (18) is a measure of the amount of mixing between eluted components. The resulting measure depends on just how the time axis is divided into receiving bins. As the number of bins increases, this dependence decreases rapidly, until at the limit of very narrow bins (time divisions) there is no such dependence since the sorting is in this case continuous along the time axis. It would be interesting to develop such a measure at the limit of infinitesimally small bins.

In analytical chromatography most peak shapes are sufficiently close to Gaussian that one can express the degree of separation by using a measure designed for Gaussian or near-Gaussian peak shapes. In contrast, it appears that whenever preparative chromatography is performed under economically advantageous instrument conditions, component bands will be of radically non-Gaussian shape (19, 20), that is, the shapes will be so different from Gaussian that natural Gaussian measures such as variance σ^2 , resolution R_s , and even retention time are applied at one's peril.

A general measure of the degree of separation is needed that can be applied to arbitrary peak shapes and that retains the desirable properties of R_s for Gaussian peak shapes. Such properties include the following: invariance, such that the measure is independent of vertical and horizontal scale; commutativity (symmetry), or the uniqueness of the measure such that neither peak need be labeled *first* or *second*; con-

tinuity, such that the measure and its derivatives have no discontinuities with respect to relative location or widths of the peaks; and monotonicity, such that the measure ranks the degree of separation for similar chromatograms in the same order as would a skilled chromatographer. Though the monotonicity property is by far the most difficult for a measure to achieve, it appears to us that it is the most important, as it justifies the very use of the measure. In this work the authors propose for the degree of separation a general measure Ω , related to the quantum mechanical overlap integral, which possesses the above properties and which can be applied to any peak shapes whatsoever.

THEORY

The widely used measure of chromatographic peak separation

$$R_s \equiv \frac{\delta}{(W_A + W_B)/2} \quad (1)$$

where $\delta = |t_A - t_B|$, t_A and t_B are the peak retention times and W_A and W_B are the base-line widths of peaks A and B, respectively, is, strictly speaking, only defined for peaks of Gaussian shape, as

$$C_A = e^{-(t-t_A)^2/2\sigma_A^2} \quad (2)$$

where C_A is the concentration of component A at time t and where σ_A^2 is the horizontal (time) variance of the concentration peak. The base-line width W is taken to be 4σ in the Gaussian case. Equation 1 is commonly applied to slightly asymmetric but otherwise well-shaped peaks seen in analytical chromatography. However, when chromatographic peaks A and B deviate farther from Gaussian shape, as is observed or even sought in preparative chromatography, eq 1 becomes unsuitable as a measure of the degree of separation. Any general measure of resolution or of overlap between peaks of general shape must account for more peak shape information than can be conveyed by t and W . The most generally applicable expression of overlap must use information about the relative position and the entire shapes of the two peaks.

A class of measures of overlap between peaks A and B may be defined as

$${}^n\Omega \equiv \frac{\left[\int_{-\infty}^{\infty} [C_A C_B]^{n/2} dt \right]^n}{\left[\int_{-\infty}^{\infty} C_A^n dt \int_{-\infty}^{\infty} C_B^n dt \right]^{n/2}} \text{ for } n = 1, 2, \dots \quad (3)$$

Of this class, the case $n = 2$ is the simplest in algebraic terms and in application, and in this work ${}^2\Omega$ will be noted simply as Ω , so that

$$\Omega \equiv \frac{\left[\int_{-\infty}^{\infty} C_A C_B dt \right]^2}{\int_{-\infty}^{\infty} C_A^2 dt \int_{-\infty}^{\infty} C_B^2 dt} \quad (4)$$

This expression for overlap is analogous to quantum mechanical overlap between two one-dimensional wavefunctions and shares with them and with the definition of the resolution measure R_s (eq 1) several highly desirable properties of invariance: invariance of Ω with linear scaling, reversal, or translation of the horizontal axis (time); invariance of Ω with linear scaling or inversion of the intensity (concentration); and commutativity with respect to peak identity. The intensity scaling invariance is particularly useful since it allows the substitution for intensity of any measure which is proportional to concentration. For example, two components A and B may be detected at different UV wavelengths or even on different types of linear detectors. These proportional signals could be used directly as C_A and C_B functions in eq 4.

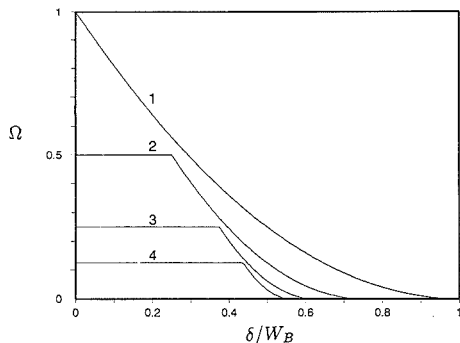


Figure 1. Overlap Ω as a function of separation between rectangular peaks of height 1. Widths W are full rectangle base widths. Key: curve 1, $W_A = W_B$; curve 2, $W_A = 0.5W_B$; curve 3, $W_A = 0.25W_B$; curve 4, $W_A = 0.125W_B$. For negative δ , $\Omega(\delta) = \Omega(-\delta)$.

Using the entire peak shape lends Ω several other desirable properties not shared with R_s . Though R_s is a continuous function, its first derivative with respect to δ is always discontinuous at $t_A = t_B$. In contrast, the degree of continuity of Ω is at least as high as that of C_A and C_B . As examples, where C_A and C_B are Gaussian or Lorentzian, Ω is continuous in all derivatives with respect to δ , but when C_A and C_B describe congruent right triangles, Ω is continuous (unlike C_A and C_B), although in this case $\partial\Omega/\partial\delta$ does have one discontinuity. Furthermore, Ω is defined even when it is not obvious what time should be chosen as the peak retention time.

Normalization of the overlap integral (numerator of eq 4) is accomplished by dividing by each of two integrals (denominator of eq 4), and several of the invariance properties result from this normalization. The most direct result of normalization is that Ω must lie in the range between 0 (no overlap between peaks) to 1 (coincident, congruent peaks) for all nonnegative functions C_A and C_B . (Though negative concentrations are not possible, there may be signals C_A and C_B , e.g. system peaks, which have negative values and for which calculation of Ω may be useful.) The property that Ω never exceeds 1 results directly from Schwarz's inequality (21), which can be written for the present case as

$$\left[\int C_A C_B dt \right]^2 \leq \left[\int C_A^2 dt \right] \left[\int C_B^2 dt \right] \quad (5)$$

Thus $\Omega = 1$ if and only if the two peak shapes C_A and C_B are congruent, that is if $C_B(t) = kC_A(t - \delta)$, for some k and δ , as well as coincident, that is when placed such that $\delta = 0$.

There can exist no δ at which the value of Ω reaches 1 if the peaks are incongruent or if noise is present. If the peaks are incongruent, then Ω must always be less than 1, although there can exist only one δ where Ω reaches a maximum with respect to δ if C_A and C_B each have only one extremum at finite time, as expected for most chromatographic peaks. The meaning of coincidence is clear if both C_A and C_B describe time-symmetric peak shapes. However, if either peak shape is asymmetric, there is no clearly best way to define the peaks' retention times (e.g., as the time of maximum concentration, time equivalent to the peaks' first moments, etc.). When this is ambiguity exists, coincidence may also be defined in any number of ways.

The condition of coincidence may be defined generally and unambiguously as the relative position of two peaks that yields the maximum value, Ω_{\max} . While this definition has the virtues of uniqueness and of compatibility with the expected meaning of coincidence for symmetric peaks, the actual value of δ at which Ω is a maximum is not easy to discover analytically if

the peaks shapes are different and if at least one is asymmetric. If Ω_{\max} is much less than 1, for example if the peaks are of very different shape or width, one may use Ω divided by Ω_{\max} , that is, the renormalized overlap measure

$$\Omega^* = \Omega / \Omega_{\max} \quad (6)$$

By definition, this measure always equals 1 at coincidence. For unimodal peak shapes, Ω^* equals 1 at only one value of δ .

Random noise in either or both peak shapes decreases the expected value of Ω . This decrease agrees with the intuitive notion that congruence between two peak shapes decreases as the signals become lost in noise. The effect of noise on Ω may be examined by adding to C_A and C_B a homoscedastic normal noise component N_A and N_B , of mean zero and variances $\sigma^2_{C_A}$ and $\sigma^2_{C_B}$, respectively. Substitution into eq 4 yields

$$\Omega = \frac{\left[\int_{-\infty}^{\infty} (C_A + N_A)(C_B + N_B) dt \right]^2}{\int_{-\infty}^{\infty} (C_A + N_A)^2 dt \int_{-\infty}^{\infty} (C_B + N_B)^2 dt} = \frac{\left[\int_{-\infty}^{\infty} C_A C_B dt \right]^2}{\left[\int_{-\infty}^{\infty} C_A^2 dt + \mathcal{T} \sigma^2_{C_A} \right] \left[\int_{-\infty}^{\infty} C_B^2 dt + \mathcal{T} \sigma^2_{C_B} \right]} \quad (7)$$

where \mathcal{T} is the width of the integration domain and where N_A and N_B are uncorrelated. Since \mathcal{T} , C_A^2 , C_B^2 , $\sigma^2_{C_A}$, and $\sigma^2_{C_B}$ are all positive, the presence of normal noise in either peak shape increases the denominator, decreases Ω , and thus prevents Ω from reaching 1 under any conditions. If the noise is truly homoscedastic, i.e. if the expectation values of $\sigma^2_{C_A}$ and $\sigma^2_{C_B}$ are independent of t ; if either $\sigma^2_{C_A}$ or $\sigma^2_{C_B}$ is nonzero; and if \mathcal{T} is infinitely wide, as is convenient for analytical expressions of smooth peak shapes such as Gaussian and Lorentzian, then the denominator of eq 7 increases without bounds, and Ω is zero, since the infinite noise contribution $\mathcal{T} \sigma^2$ overwhelms the finite normalization integral $\int C^2 dt$. This catastrophic integral divergence is not expected to be a problem in practice since numerical evaluation of Ω is performed over finite domain widths \mathcal{T} and not over the infinitely wide domain of eq 3 and similar equations. However, the degree to which noise depresses of the computed value of Ω depends on the integration range chosen, removing the property of uniqueness for peak shapes without absolute peak widths. We are examining the effect of noise on the computed values of Ω .

A consequence of eq 4 is that as the width of one of the peaks decreases, the dependence of Ω on δ increasingly resembles the square of the shape of the other peak. For example, in Figure 1, the dependence of Ω on δ in curve 4 ($W_A = W_B/8$) markedly resembles a rectangle of width W_B (Ω is symmetric about $\delta = 0$ in this case), and in Figure 2, curve 4 ($W_A = W_B/8$) resembles a right triangle of bandwidth W_B . Because this property results directly from the form of eq 4 at the limit of one peak becoming a delta function, the property holds for any shape of C_A and C_B as either $W_A \rightarrow 0$ or $W_B \rightarrow 0$. This is demonstrated by considering the limit of Ω at a given δ between one peak A of general shape and a rectangular peak B of area 1 and whose width W_B decreases to zero. The result is

$$\lim_{W_B \rightarrow 0} \Omega(\delta) = \frac{\int_{\delta - W_B/2}^{\delta + W_B/2} (C_A W_B^{-1}) dt \int_{-\infty}^{\infty} C_A^2 dt}{\int_{-\infty}^{\infty} C_A^2 dt \int_{-W_B/2}^{W_B/2} W_B^{-2} dt} = \frac{W_B}{\int_{-\infty}^{\infty} C_A^2 dt} [C_A(\delta)]^2 \quad (8)$$

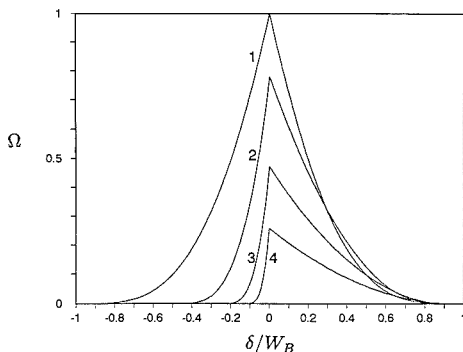


Figure 2. Overlap Ω as a function of separation between right-triangular shaped peaks of height 1. Widths W are full triangle base widths. Key: curve 1, $W_A = W_B$; curve 2, $W_A = 0.5W_B$; curve 3, $W_A = 0.25W_B$; curve 4, $W_A = 0.125W_B$.

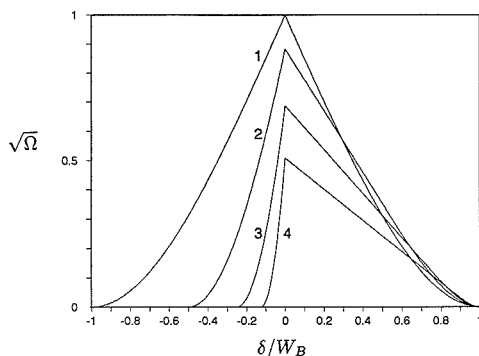


Figure 3. Square-root of Ω (linearized overlap, see text) as a function of separation between right-triangular shaped peaks of height 1. Widths W are full triangle base widths. Key: curve 1, $W_A = W_B$; curve 2, $W_A = 0.5W_B$; curve 3, $W_A = 0.25W_B$; curve 4, $W_A = 0.125W_B$.

In the expression on the far right side of eq 8 only the $[C_A(\delta)]^2$ term depends on δ .

Figure 3 displays $\Omega^{1/2}$ as a function of δ for two right triangle peaks in the same manner as Figure 2 depicts Ω . For many peak shapes, $\Omega^{1/2}$ will vary more linearly with δ than will Ω , especially where the peaks are of very different widths or where the peaks may be approximated by linear segments.

The measure Ω may be thought of as the degree of proximity of two peaks in abstract peak space. The dimensions of this space would include retention time and various descriptors of peak shape. The question arises of whether some function $d(\Omega)$ which depends only on Ω , say $-\log_{10}(\Omega)$, may not only reflect the distance between two peaks in abstract peak space but might also be a formal *metric* (22) of that space. Such a function would satisfy these criteria for any three peaks A, B, and C

$$d_{AB} = d_{BA} \quad (9a)$$

$$d_{AC} \leq d_{AB} + d_{BC} \quad (9b)$$

$$d_{AA} = 0 \quad (9c)$$

$$d_{AB} = 0 \text{ implies } A = B \quad (9d)$$

Conditions 9a and 9c clearly may be met, and condition 9d may be met if the peaks are scaled to equal area. However, it is hypothesized here that no $d(\Omega)$ can be a metric because there will be for each definition of $d(\Omega)$ at least one case which

fails to satisfy the triangle inequality 9b. For example, in the case of broad peak B between narrow peaks A and C, we expect that there will always exist some shape of B such that the distance measure d_{AC} is very large compared to d_{AB} and d_{BC} , violating condition 9b.

A measure of overlap may be more useful than R_s for measuring the effectiveness of preparative separations since overlap corresponds to the level of mixing of two components in the product fractions and not necessarily to the distance between the peak centers or maximum concentrations. The utility of nonclassical modes of separation is accounted for by overlap measures in ways that classical measures of separation cannot do. For example, two Gaussian peaks which have very different widths but which are centered at the same time may be said to be well separated chemically, even though R_s is zero, because product fractions may be collected which are highly enriched in each component. The measure Ω_{\max} decreases as the difference in peak widths increases, corresponding to the observed improvement in chemical enrichment, unlike R_s and other similar measures which are always zero at coincidence regardless of the peak widths and resulting potential degree of separation.

RESULTS AND DISCUSSION

Closed analytical expressions for Ω can be derived for a very wide range of peak shapes with both continuous and discontinuous first derivatives. The derivatives are particularly simple when the two peak shapes are equivalent. Closed expressions for Ω can be found in many cases where the peak shapes are different, though closed forms are difficult or impossible to obtain when one peak shape has continuous derivatives and the other's are discontinuous. For example, Ω is easily written for either two Gaussian peaks or two triangular peaks, but not for the overlap between a Gaussian and a triangular peak.

It is not necessary for these derivations to include the absolute times t on which the peaks are centered but only their relative position since eq 4 is invariant to horizontal translation. Likewise, any concentration measure proportional to C_A and C_B may be chosen due to the concentration-scaling invariance of eq 4. Derivation of closed forms is greatly eased by thoughtful selection of horizontal and vertical scales.

Expressions for Gaussian Peak Shapes. For Gaussian peak shapes

$$C_A = e^{-t^2/2\sigma_A^2} \quad (10)$$

$$C_B = e^{-(t-\delta)^2/2\sigma_B^2}$$

substitution into eq 4 and integration over all t yields

$$\Omega = \frac{2\sigma_A\sigma_B}{\sigma_A^2 + \sigma_B^2} e^{-\delta^2/2(\sigma_A^2 + \sigma_B^2)} \quad (11)$$

The dependence of Ω on δ for two Gaussian peaks can be seen to have Gaussian form itself. This property holds for overlap between Gaussian peaks of all widths and separations. Special cases of eq 11 are instructive as examples of the general behavior of Ω . In the limits of large $|\delta|$

$$\lim_{\delta \rightarrow +\infty} \Omega = 0$$

$$\lim_{\delta \rightarrow -\infty} \Omega = 0 \quad (12)$$

and at coincidence ($\delta = 0$)

$$\Omega_{\max} = \frac{2\sigma_A\sigma_B}{\sigma_A^2 + \sigma_B^2} \quad (13)$$

which equals 1 only if $\sigma_A = \sigma_B$, that is, only if the peaks are congruent as well as coincident. The general expression for

Ω for congruent Gaussian peaks is

$$\Omega = e^{-\delta^2/4\sigma^2} \quad (14)$$

which clearly may equal 1 only when $\delta = 0$. For congruent Gaussian peaks, Ω is related to the resolution R_s as

$$\Omega = e^{-4R_s^2} \quad (15)$$

The exponent of the general expression for overlap Ω between Gaussian peaks (eq 11) is closely related to the separation factor F of Giddings (2)

$$F = \frac{\delta^2}{8(\sigma_A^2 + \sigma_B^2)} \quad (16)$$

so that for Gaussian peak shapes

$$\Omega = \frac{2\sigma_A\sigma_B}{\sigma_A^2 + \sigma_B^2} e^{-4F} \quad (17)$$

This relation suggests that $-\log \Omega$ will behave much as does F for Gaussian peak shapes. For example, since F is proportional to column length L in the absence of detector dispersion, etc. (2), then for Gaussian peak shapes and k constant

$$-\log \Omega = kL \quad (18)$$

Expressions for Non-Gaussian Peak Shapes. Closed expressions for Ω may be derived for Lorentzian peak shapes, which may be written

$$C_A = \left[1 + \left(\frac{t}{W_A} \right)^2 \right]^{-1} \quad (19)$$

$$C_B = \left[1 + \left(\frac{t - \delta}{W_B} \right)^2 \right]^{-1}$$

where W_A and W_B are the characteristic widths of peaks A and B. Substitution into eq 4 yields

$$\Omega = \frac{4W_A W_B (W_A + W_B)^2}{[(W_A + W_B)^2 + \delta^2]^2} \quad (20)$$

The dependence of Ω on δ for two Lorentzian peaks is itself the square of a Lorentzian. At large $|\delta|$, Ω tends toward zero, and at coincidence

$$\Omega_{\max} = \frac{4W_A W_B}{(W_A + W_B)^2} \quad (21)$$

which equals 1 only if the peaks are congruent.

When either peak shape for which an expression for Ω is being derived has a discontinuous derivative, the integration domains of eq 4 must be segmented into regions where the derivatives are continuous, and the sum for each integral in the numerator and denominator of eq 4 must be used. For example, the integral in the numerator of eq 4 may be written as the sum of N integrals

$$\sum_{i=1}^N \int_{T_{i-1}}^{T_i} C_{A,i}(t) C_{B,i}(t) dt \quad (22)$$

where concentrations $C_{A,i}$ and $C_{B,i}$ need be continuous only over the time segment i , ($t = T_{i-1}$ to T_i) and where $T_0 = -\infty$ and $T_N = +\infty$. If the two peak shapes are both incongruent and nonsmooth, there are probably several topologically distinct configurations of the two peaks, each of which may require several segments of integration domain. Closed expressions for Ω describing the overlap between asymmetric triangles and other more complex peak shapes can in general be derived, albeit with much tedium. For example, there are seven topologically distinct ways to draw two triangles on a

line, of which six include overlap between the peaks. Five of these six ways require multiple integrals in the numerator of eq 4.

Derivations of Ω for three simple nonsmooth peak shapes will be given here. First, rectangular shape is an approximation to (1) chromatographic peak shapes of an unmodified loop or swept-volume injection pulse or, (2) in a very rough sense, to the peak shape resulting from a chromatographic system whose sorption isotherm has an inflection point (often referred to as an S-shaped isotherm) (23). If rectangular peaks A and B have base widths W_A and W_B , $W_A \leq W_B$, and centers separated by δ , then by substitution into eq 4

$$\Omega = \begin{cases} 0 & \text{A and B not overlapping} \\ \frac{(W_A + W_B - 2\delta)^2}{4W_A W_B} & \text{for A and B partially overlapping} \\ \frac{W_A}{W_B} & \text{for A wholly within B} \end{cases} \quad (23)$$

Equation 23 is a typical form of Ω between two nonsmooth shapes in that it is given as a series of expressions each valid over a certain set of conditions.

In Figure 1 are given the dependences of Ω on the separation δ between the centers of two rectangularly shaped peaks A and B. Since the shape of each Ω vs δ curve is symmetric about 0, only the curves over $\delta > 0$ are given. When W_A and W_B are equal (curve 1), Ω decreases quadratically and monotonically with increasing separation, reaching 0 where the peak edges just touch at $\delta = W_A = W_B$. When $W_A < W_B$ (curves 2, 3, and 4), $\Omega = W_A/W_B$ for $\delta \leq |W_B - W_A|/2$, and for $\delta > |W_B - W_A|/2$, the edge of peak A emerges from peak B. Ω then decreases until $\Omega = 0$ for $\delta \geq (W_A + W_B)/2$, where the peaks do not overlap at all, and $\Omega = 0$.

The right triangle is a plausible approximation to single-component peak shapes in nonlinear chromatography, especially for systems whose sorption isotherms are moderately curved but which do not have an inflection point in the concentration range of interest (referred to as Langmuir-type or anti-Langmuir-type isotherms) (19, 23, 24). The right triangle is also the asymptotic peak shape at long elution times for ideal chromatographic systems whose sorption isotherm is curved at the origin. For two right triangles A and B whose base widths are W_A and W_B and whose right angles are both separated by δ and on the low- t side of the triangles (early-eluting fronts)

$$\Omega = \begin{cases} 0 & \text{for A and B nor overlapping} \\ \frac{(W_B - \delta)^4 (3W_A - W_B + \delta)^2}{4W_A^3 W_B^3} & \text{for A and B partially overlapping, } t_A > t_B \\ \frac{W_A (3W_B - W_A - 3\delta)^2}{4W_B^3} & \text{for wholly within B} \end{cases} \quad (24)$$

In Figure 2 these functions are plotted for four values of W_A/W_B . Where $W_B = W_A$ (curve 1) the plot of Ω vs δ is symmetric about $\delta = 0$ since the two peaks are congruent. Where $W_B \gg W_A$ (curve 4) the plot resembles the square of the shape of the wider peak B. This resemblance is confirmed by Figure 3 in which the plot of $\Omega^{1/2}$ vs δ increasingly resembles a right triangle of width W_B as W_A goes to zero.

Isosceles-triangular peak shapes, which are the simplest line-segment approximations to chromatographic peak shapes (25) resulting from nearly linear isotherms, require 11 integration domains to derive Ω expressions for the five possible ways in which two such peaks can overlap. For peaks A and B having half base widths w_A and w_B , $w_B > w_A$, peak centers

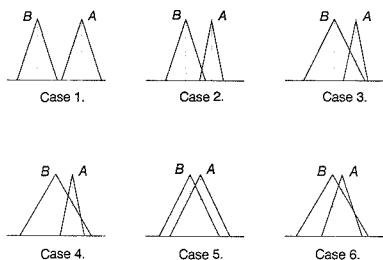


Figure 4. Schematic diagrams of all six possible relative configurations of two isosceles-triangle-shaped peaks. Cases correspond, in order, to the six cases of eq 20.

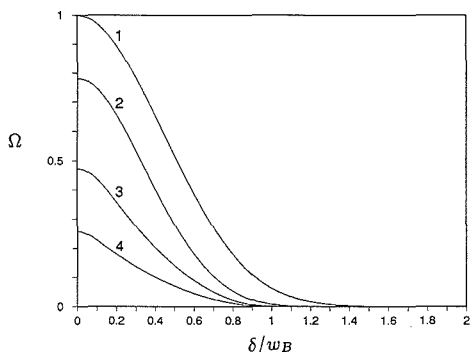


Figure 5. Overlap Ω as a function of separation between isosceles-triangle-shaped peaks of height 1. Widths w are triangle half base widths. Key: curve 1, $w_A = w_B$; curve 2, $w_A = 0.5w_B$; curve 3, $w_A = 0.25w_B$; curve 4, $w_A = 0.125w_B$. For negative δ , $\Omega(\delta) = \Omega(-\delta)$.

separated by δ , $t_A \geq t_B$, and $\delta \geq 0$, the six cases in eq 25 can be used. The six cases in eq 25 are displayed graphically,

$$\Omega = \begin{cases} 0 & \text{for A and B not overlapping;} \\ \frac{(w_A + w_B - \delta)^6}{16w_A^3w_B^3} & \text{for } w_B < \delta < w_A + w_B; \\ \frac{9w_A(w_B - \delta)^2}{4w_B^3} & \text{for } w_A < \delta < w_B - w_A; \\ \frac{[(w_B - \delta)^3 + (w_A - \delta)^3 + 3w_Aw_B(2\delta - w_A - w_B) - \delta^3]^2}{16w_A^3w_B^3} & \text{for } w_B - w_A < \delta < w_A; \\ \frac{(3w_A^2w_B - w_A^3 - 3\delta^2w_A + \delta^3)^2}{4w_A^3w_B^3} & \text{for } \delta < w_B - w_A, \delta < w_A. \end{cases} \quad (25)$$

in order, as cases 1–6 in Figure 4.

The unexpectedly high sixth-order dependence of Ω on δ where Ω is near zero causes Ω to be small but nonzero over a broad range of separations δ . For example, where $w_A = w_B$, Ω in Figure 5 is essentially indistinguishable from zero at all separations greater than 1.4 times the peak half-width w_A , even though $\Omega > 0$ up to $2w_A$. This asymptotic behavior occurs because, unlike in the right triangle or rectangular cases, C_A and C_B in the region of overlap are both approaching zero as the separation increases.

General Properties of the Overlap Measure Ω . That $\Omega = 1$ for congruent, coincident peaks and that Ω is invariant to vertical scaling is readily established by substituting $C_B = kC_A$, k constant, into eq 4. It is similarly established that $\Omega = 0$ where the peaks are orthogonal, that is where $\int C_A C_B dt$

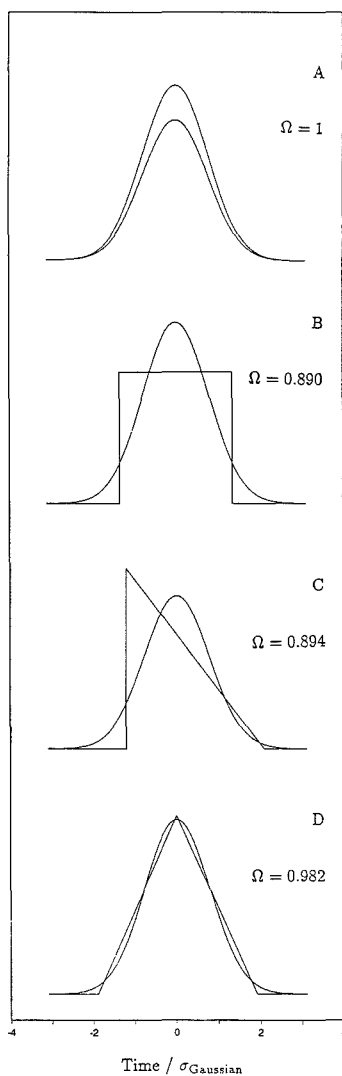


Figure 6. Overlap Ω between Gaussian peak and other peak shape. Both peaks of height 1 and variance $\sigma_1^2 = 1$. Key: A, Gaussian; B, rectangle; C, right triangle; D, isosceles triangle.

$= 0$ over all t . For all other relationships between two real functions of t , C_A and C_B , Ω must lie between 0 and 1. Further, since t does not appear in the integrands but only as the variable of integration in eq 4, and since it appears to the same total degree in the numerator and denominator of eq 4, Ω is invariant to linear transformations of the horizontal (time) axis.

The most important property of the measure Ω is its monotonicity, the correspondence of variations in Ω with variations in the degree of separation of two components. Figures 1, 2, and 5 give examples of the sensitivity of Ω to the peak separation along the time axis. Figure 6 gives examples of the sensitivity of Ω to peaks' shapes. In each case a Gaussian peak is positioned over another peak with exactly the same first moment (mean time) and second central movement

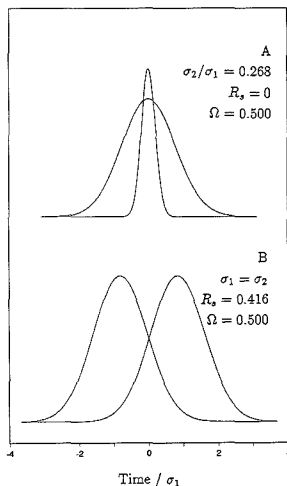


Figure 7. Two Gaussian pairs with overlap $\Omega = 0.500$: A, coincident, incongruent peaks separated by 1.665σ .

(variance). The Gaussian peaks in case A are thus coincident and congruent, and $\Omega = 1$. The rectangular and right triangular peaks each overlap strongly with the Gaussian peak, but Ω falls significantly short of 1, while the isosceles triangular and Gaussian peaks are very nearly congruent (25) and thus Ω very close to but not quite equal to 1. The right triangular peak, placed in Figure 6 at $\delta = -1.56$ in order to give the same first moment (mean time) as the Gaussian peak, may be moved slightly to $\delta = -1.69$ in order to maximize Ω at 0.895. Any movement of the symmetric peaks along the time axis decreases Ω . Thus Ω ranks the similarity of the peak shapes to a coincident Gaussian shape as Gaussian \succ isosceles \succ rectangular \sim right triangular, in agreement with expectations.

Because analytical separations depend on temporal separation of the peak centers to allow measurement of the peak areas or heights, the usual data used to determine component concentrations, measures such as resolution R_s , are quite satisfactory. However, preparative chromatography requires a more general measure of the degree of separation, one which can account for different modes of component purification. For example, it is possible in preparative chromatography to construct multiple sequential stages of partial separation to effect an adequate final separation, an option not generally available to analytical chromatographic separations. Thus in designing a preparative chromatographic separation one is ultimately concerned with enrichment, i.e., with partial resolution or reduction of peak overlap of two or more components of a mixture, where in analytical chromatography one must be concerned with a component's nearly complete resolution from other components for the purposes of accurate quantitation.

Figure 7 illustrates how Ω measures enrichment afforded by preparative chromatography. The R_s value of 0.416 (case B) indicates modest resolution, and although individual peak height estimates would be very rough, numerical deconvolution of the peak shapes would not be hopeless. The two congruent peaks in case B are partially resolved in the usual manner, and $\Omega = 0.500$. The same value Ω is obtained in case A where two coincident Gaussian peaks have different widths. This enrichment in case A of component 1 at $|t| \geq 0.7\sigma_1$ and of component 2 at $|t| \leq 0.7\sigma_1$ may, depending on the cost of the separation process, the value of the products, and purity requirements, be just as valuable as the more conventional

Table I. Overlap and Column Length^a

L^b	Ω	$p\Omega^c$	$p\Omega/L$
5	0.214 07	0.669	0.134
10	0.038 85	1.411	0.141
15	0.009 99	2.001	0.133
20	0.002 23	2.651	0.133
25	0.000 33	3.481	0.139

^aChromatograms simulated using the semiideal model of chromatography under the following conditions. Competitive Langmuir isotherm parameters: Component 1, $A = 20$, $B = 2.07 \text{ M}^{-1}$; component 2, $A = 25$, $B = 2.5875 \text{ M}^{-1}$. Flow rate, $4.986 \text{ mL min}^{-1}$; column diameter, 0.46 cm . Amount injected (in 0.01 mL): component 1, $100.4 \mu\text{mol}$; component 2, $301.1 \mu\text{mol}$. Plate height, $50 \mu\text{m}$. ^bColumn length in cm. ^c $-\log_{10}(\Omega)$.

separation in case B. Although case A would probably be useless for analytical chromatography, reflected in the resolution measure R_s of zero, the component enrichment available for preparative chromatography is rather effective, and this is reflected in the decrease of the overlap Ω value of 0.500 from a value of 1 at injection. These examples suggest that each measure is appropriate to the intended mode of chromatography.

Of course, the cases in Figure 7 represent special cases for Gaussian peaks, and both overlap-decreasing, enrichment-enhancing mechanisms demonstrated in the two cases, peak separation and differential peak broadening, may work together in real preparative separations. However, the two mechanisms do not develop at the same rate during elution. Resolution (case B) increases with time, and where σ_2/σ_1 is constant, then for k constant

$$-\log \Omega = kt \quad (26)$$

For example, if case B of Figure 7 occurs at time t , then at time $2t$, $\Omega = 0.250$, and so on. However, σ_2/σ_1 and thus the first term on the right side of eq 11 rapidly settle to a constant value after injection. Thus the decrease in Ω due to simple difference in peak width occurs rapidly after injection and very little thereafter while the decrease in Ω due to separation of the concentration profiles in the column, described by the second term on the right side of eq 10, continues to develop. In addition, competitive isotherms tend to cause component bands to displace each other from the boundary between them, and Ω will reflect this important mode of separation where R_s generally will not. Equation 13, which states that Ω decreases exponentially with column length for Gaussian concentration profiles, may also be approximately true for non-Gaussian peak shapes developing from preparative separations. In Table I is given an example of this behavior for a separation of two components whose sorption partition behavior is described by a competitive Langmuir isotherm (20). These results are simulated by using the semiideal model of chromatography and using the conditions given in Table I (20). Our initial investigations indicate that Ω decreases monotonically with column length L (see Figures 8 and 9 for examples), and in fact that $p\Omega$ ($-\log_{10}(\Omega)$, analogous to pH) values are roughly proportional to L over the range of L given in Table I. We are investigating the generality of eq 18 through simulations employing the ideal and semiideal models of chromatography.

We have performed initial simulation experiments into the relationship of preparative-chromatographic yields and production rates to computed values of Ω . Chromatograms were simulated by using the semiideal model under various conditions (changes in column lengths, flow rates, loading factors, etc.), and Ω was computed for each using eq 4 over the time domain where C_A or C_B are nonzero. For the cases studied to date it appears that for 95% and 99% purity requirements,

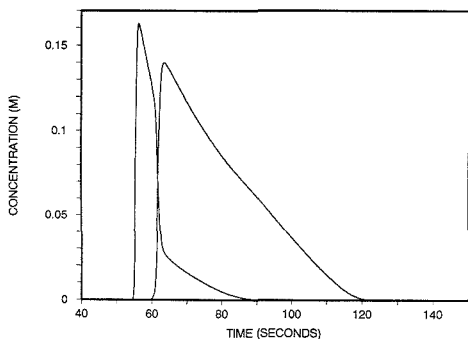


Figure 8. Chromatogram simulated using the semiideal model of chromatography under the following conditions. Competitive Langmuir isotherm parameters: component 1, $A = 20$, $B = 2.07 \text{ M}^{-1}$; component 2, $A = 25$, $B = 2.5875 \text{ M}^{-1}$. Flow rate, $4.986 \text{ mL min}^{-1}$; column length, 10 cm; column diameter, 0.46 cm. Amount injected (in 0.01 mL): component 1, $100.4 \mu\text{mol}$; component 2, $301.1 \mu\text{mol}$. Plate height, $50 \mu\text{m}$.

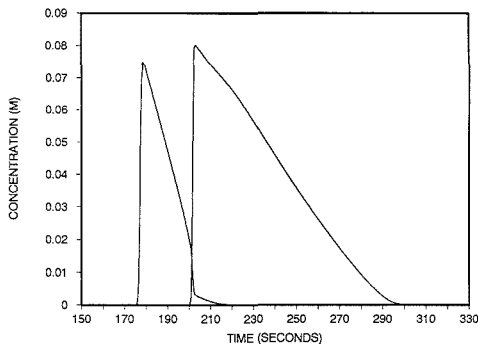


Figure 9. Chromatogram simulated using the semiideal model of chromatography under the same conditions as Figure 8 except column length of 25 cm.

the production rates are maximal under conditions giving Ω values of 0.02–0.05. An exception exists when purification of the later-eluted component to 99% is required, a very difficult case, where Ω at maximal production rate is 0.002–0.005. We will report on the generality of these relationships in a later publication.

In Table II is given an example of the effect of chromatogram noise on the computed value of Ω . In the cases where noise is 1% of the chromatograms' peak concentration, a reasonable upper limit for the typically high concentrations employed in preparative chromatography, the relative error is small where Ω is large but appears to increase rapidly with decreasing Ω . The relative imprecision depends similarly on Ω . The form of eq 7 and the data in Table II suggest that for the high signal-to-noise ratios expected in preparative chromatograms, absolute values of Ω will be well determined for all values of Ω and that relative errors in Ω may be large for small values of Ω . Such errors will only be important in preparative chromatography when very high purities are needed. In a subsequent publication we will report on results

Table II. Effect of Chromatogram Noise on Computed Value of Ω^a

L^b	Ω (no noise)	$\hat{\Omega}$ (1% noise) ^c	$\sigma_{\hat{\Omega}}$ (1% noise) ^d	$\sigma_{\hat{\Omega}}/\hat{\Omega}$ (in %)
5	0.214 07	0.213 56	0.002 40	1.13
10	0.038 85	0.038 66	0.000 52	1.34
15	0.009 99	0.010 12	0.000 56	5.57
20	0.002 23	0.002 15	0.000 20	9.37
25	0.000 33	0.000 41	0.000 10	25.23

^aChromatograms simulated using the semiideal model of chromatography under conditions given in Table I. To each simulated chromatogram is added Gaussian noise of standard deviation equal to 1% of chromatogram peak concentration. ^bColumn length in cm. ^cAverage of five simulated, noise-modulated chromatograms. ^dStandard deviation of five simulated, noise-modulated chromatograms.

from experiments designed to clarify the extent to which noise perturbs measured values of Ω .

The measure of resolution R_s is popular with analytical chromatographers because it gauges what they want to know—how well resolved are the regularly shaped, symmetric peaks encountered in their analyses. The overlap measure Ω possesses many properties which suggest that it is a natural measure of preparative chromatographic enrichment power much as R_s is a natural measure of analytical separation power.

LITERATURE CITED

- (1) Glueckauf, E. *Trans. Faraday Soc.* **1955**, *51*, 34–44.
- (2) Giddings, J. C. *Anal. Chem.* **1960**, *32*, 1707–1711.
- (3) Purnell, J. H. *J. Chem. Soc.* **1960**, 1268–1274.
- (4) Knox, J. H. *J. Chromatogr. Sci.* **1977**, *15*, 352–364.
- (5) Said, A. S. *J. Gas Chromatogr.* **1964**, 60–71.
- (6) Morgan, S. L.; Deming, S. N. *J. Chromatogr.* **1975**, *112*, 267–285.
- (7) Wegschneider, W.; Lankmayr, E. P.; Budna, K. W. *Chromatographia* **1982**, *15*, 498–504.
- (8) El Fallah, M. Z.; Martin, M. *Analisis* **1988**, *16*, 241–248.
- (9) Strasters, J. K.; Bartha, A.; Billiet, H. A. H.; deGalan, L. J. *Liq. Chromatogr.* **1988**, *11*, 1827–1854.
- (10) Debets, H. J. G.; Bajema, B. L.; Doornbos, D. A. *Anal. Chim. Acta* **1983**, *151*, 131–141.
- (11) Massart, D. L.; Smits, R. *Anal. Chem.* **1974**, *46*, 283–286.
- (12) Kaiser, H. *Anal. Chem.* **1970**, *42*, 24A–39A.
- (13) DeClerk, K.; Cloete, C. E. *Sep. Sci. Technol.* **1971**, *6*, 627–635.
- (14) Stewart, G. H. *Sep. Sci. Technol.* **1978**, *13*, 201–213.
- (15) Schoenmakers, P. J.; Strasters, J. K.; Bartha, A. *J. Chromatogr.* **1988**, *458*, 355–370.
- (16) Schoenmakers, P. J.; Naish, P. J.; Hunt, R. J. *Chromatogr.* **1987**, *24*, 579–587.
- (17) Kaiser, R. E. *Gas Chromatographie*; Geest & Portig: Leipzig, 1960; p 33.
- (18) Corry, W. D.; Seaman, G. V. F.; Szafron, D. A. *Sep. Sci. Technol.* **1983**, *17*, 1469–1483.
- (19) Knox, J. H.; Pyper, M. J. *Chromatogr.* **1986**, *363*, 1–30.
- (20) Ghodbane, S.; Guiochon, G. *J. Phys. Chem.* **1988**, *92*, 3682–3686.
- (21) Abramowitz, M.; Stegun, L. A. *Handbook of Mathematical Functions, Applied Mathematics Series 55*; National Bureau of Standards: Washington, DC, 1964; p 11.
- (22) Edwards, R. E. *Functional Analysis, Theory and Applications*, Holt, Rinehart, and Winston: New York, 1965; p 24.
- (23) Guiochon, G.; Golshan-Shirazi, S.; Jaulmes, A. *Anal. Chem.* **1988**, *60*, 1856–1866.
- (24) Guiochon, G.; Golshan-Shirazi, S. *J. Phys. Chem.*, in press.
- (25) Hamilton, P. B.; Bogue, D. C.; Anderson, R. A. *Anal. Chem.* **1960**, *32*, 1782–1792.

RECEIVED for review August 22, 1989. Accepted October 24, 1989. This work has been supported in part by Grant DE-FG05-86ER13487 from the U.S. Department of Energy, Office of Energy Research, and by the cooperative agreement between the University of Tennessee and Oak Ridge National Laboratory. We also acknowledge the University of Tennessee Computing Center's support of the computational effort.

Gas Sensor and Permeation Apparatus for the Determination of Chlorinated Hydrocarbons in Water

Joseph R. Stetter* and Zhuang Cao

Department of Chemistry, Illinois Institute of Technology, Chicago, Illinois 60616

A solid-state gas sensor with a selective response to chlorinated hydrocarbons has been combined with a simple silicone rubber permeation apparatus. The apparatus has been tested in a way that simulates the on-line analysis of chlorinated hydrocarbons in a liquid process stream. The system can provide information on whether or not the sampled stream contains chlorinated hydrocarbons as well as quantitation of the chlorinated hydrocarbon in the sample. No sensor response was observed for 1000 ppm hexane or phenol while concentrations of a few parts per million of chlorobenzene were easily detected. The permeation apparatus offers a new and convenient method to analyze the contents of an aqueous sample but allows use of a gas sensor. Since many more types of gas sensors are convenient and available than are liquid sensors, this approach may be more generally useful if other gas sensors are interfaced to the liquid sampling system by means of semipermeable membrane technology.

INTRODUCTION

Chemical sensing techniques with continuous real-time analysis have attracted intense interest in the last decade (1). The on-line determination of specific chlorinated hydrocarbons in wastewater is an important analytical problem. Water often contains more than a single pollutant and the most frequently applied methods for analysis include separation methods, especially gas chromatography. The Federal Environmental Protection Agency (EPA) approved method of collection and analysis of volatile organic priority pollutants involves obtaining a grab water sample from an effluent stream, transporting the sample to a laboratory, and analyzing the sample by a procedure called the purge and trap technique which includes analysis by GC/MS (2). While GC/MS methods are extremely versatile, sensitive, and selective, they are not real-time (continuous) or inexpensive. On-line process monitoring or screening methods that could be applied in the field would benefit from a low-cost alternative for the determination of chlorinated hydrocarbons.

There have been significant advances in the field of membrane technology. Helligth and Taylor (3) have described a method for on-line aqueous based reversed-phase high-performance liquid chromatography/Fourier transform infrared spectrometry. This method involved the detection of the organics in an aqueous/organic segmented stream through a flow cell which is constructed by using multiple layers of Teflon membranes. Blanchard and Hardy (2) introduced a separation method based on the permeation of volatile organic compounds through a silicone polycarbonate membrane from an aqueous sample matrix into an inert gas stream. A portion of this stream was then injected into a capillary gas chromatograph. Recently, Melcher (4) developed a silicone membrane/flow injection system for the determination of trace organic compounds in aqueous samples. Organic compounds in the injected sample permeate a tubular silicone-rubber membrane and are collected in a gaseous extractant external to the flowing liquid. The extractant containing the permeated compounds flows through a detector producing a peak response. No examples of the use of permeation mem-

branes with simple chemical sensors have been reported.

In contrast to the above methods, our efforts have centered upon the development of an interface that employs a tubular silicone-rubber membrane to extract volatile chlorinated hydrocarbon compounds from a water matrix for subsequent presentation to a gas sensor. The purpose of this paper is to illustrate that the use of a rugged permeation membrane in combination with a low cost, small, selective gas sensor can provide a tool for on-line and near real-time, selective analysis of chlorinated hydrocarbons in an aqueous sample matrix.

EXPERIMENTAL SECTION

Sensor. The specific sensor for chlorinated hydrocarbon vapors used in this work consists of an inner (negative) and an outer (positive) electrode separated by a rare-earth-doped ionic semiconductor as shown in Figure 1. Typical materials of construction include mixtures of lanthanum oxide and lanthanum fluoride (5). The outer electrode serves as a heater as well as a sensor terminal. The temperature of the sensor element is maintained at approximately 500 °C. A dc potential of about 4 V across the electrodes is maintained and the resistance is measured using Ohm's law and the voltage drop across a known resistor (see Figure 1). In the absence of a chlorinated hydrocarbon vapor, a high resistance is observed and the conduction between the terminals is very small. But in the presence of a chlorinated hydrocarbon vapor, the resistance decreases significantly and this increases the current flow between the terminals. The magnitude of the sensor background current at constant dc bias voltage is very sensitive to the presence of chlorinated organic vapors in the atmosphere surrounding the sensor since these gases alter the resistance of the semiconductor surface. This resistance or impedance change in the presence of chlorinated organic vapor is the analytical "signal" from this sensor, i.e., the impedance is a function of the concentration of the chlorinated vapor present. The sensor is relatively insensitive to many hydrocarbon contaminants found in industrial situations. The enhanced reactivity toward compounds with high electron affinity makes the sensor selective to chlorinated organic vapors even in the presence of hydrocarbons.

Electronic Apparatus. An in-house electronic circuit was built for the control of the sensor heater voltage and for the detection of the analytical signal. A separate battery is used to apply a fixed voltage to the sensor at pin 1 (Figure 1) and this battery is in series with a fixed resistor. To measure the current through the sensor, the voltage drop across the fixed (1 k Ω) resistor is measured. Once the current is known, the impedance of the sensor is calculated by dividing the bias voltage by the current. The conductance of the sensor is the inverse of the impedance.

Permeation Apparatus. Since the chlorinated hydrocarbon sensor is a gas sensor, it is necessary to convert the aqueous sample containing the analyte into a vapor sample suitable for analysis by the gas sensor. After several permeable membranes and several geometries were tried, a permeation apparatus as illustrated in Figure 2 was assembled for our initial evaluation of the sensor. The permeable tubing is Silastic Medical-Grade Tubing (0.012 in. i.d. \times 0.025 in. o.d.) manufactured by Dow Corning. Silicone materials preferentially allow organic compounds to permeate while rejecting water and other highly polar molecules. Many strands of permeable tubing are used to increase the total transport of analyte at low concentrations and increase the total flow rate of vapor to the sensor at low applied pressures. Since chlorobenzene is almost insoluble in water, the water was stirred during analysis to provide mixing and homogeneous contact of the solution with the silicone tubing. Both "wrist-action shaker"

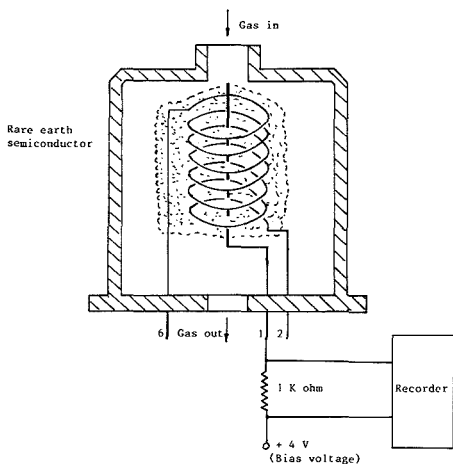


Figure 1. Chlorinated organic vapor sensor.

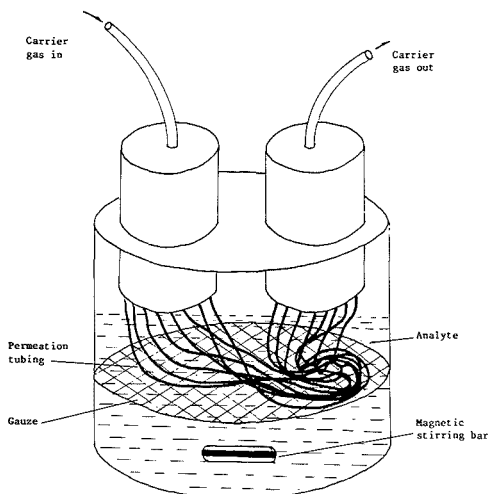


Figure 2. Permeation apparatus used to expose aqueous samples to permeable tubing.

and "bar-stirrer" methods were attempted but the best mixing was accomplished with a simple magnetic stirrer. The gauze (see Figure 2) separates the permeable tubing and magnetic stirrer to prevent the stirring bar from inflicting damage to the tubing.

Procedure. Figure 3 presents a block diagram of the experimental apparatus for measurement of the concentration of a chlorinated hydrocarbons in a water. The carrier gas (typically air) is pushed through the tubing with a small air pump and then directed to the sensor. When the permeable tubing is submerged in the water, organic compounds permeate through the silicone wall and are picked up in the carrier gas while polar liquids (and especially water vapor) are preferentially rejected. The gas sensor can detect the chlorinated organic vapors and the sample flow is maintained constant during analysis. The output of the sensor is continuously monitored and is a function of the concentration of chlorinated hydrocarbon in the vapor phase or in the water.

RESULTS AND DISCUSSION

Sensor Characterization. It has long been known that adsorption of a foreign species on a semiconductor surface will provide surface states (6) and that the electrical properties of semiconductor oxide catalysts change when adsorption or reactions occur on their surfaces (7).

Consider the nature of the semiconductor material. If the conductance of the sensor can be interpreted as resulting from a single surface state, then

$$\sigma = \sigma_0 [a/a_0] \exp[-(E_c - E_s)/kT] \quad (1)$$

where σ is the conductance, $[a/a_0]$ is the ratio of occupied to unoccupied states, E_c is the energy of the conduction band, and E_s is the energy of the surface state (8).

At constant temperature the conductance of the sensor bead changes with the partial pressure of the reacting gas due to a change in the ratio of the densities of states. This pressure dependence of conductance often takes the form

$$\sigma/\sigma_0 = kP^m \quad (2)$$

for chemisorption on a transition-metal-oxide system (6, 9, 10). This is consistent with the effect produced by a modified Langmuir adsorption isotherm equation (11) for a condensable vapor (such as the volatile chlorinated hydrocarbons used in this study) chemisorbing on the sensor surface. We can now express eq 1 as

$$\sigma = \sigma_0 b P^m \exp[-(E_c - E_s)/kT] \quad (3)$$

At constant temperature eq 3 can be interpreted as

$$\ln \sigma = \ln k' + m \ln P \quad (4)$$

Equation 3 may also be interpreted at constant P^m as

$$\ln \sigma = \ln k'' - (E_c - E_s)/kT \quad (5)$$

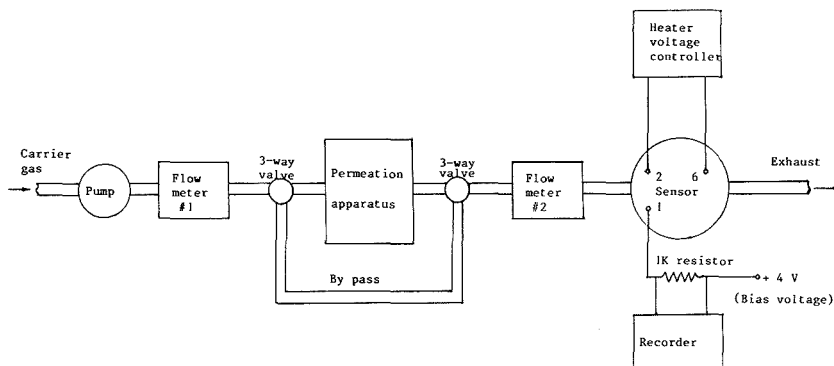


Figure 3. Experimental apparatus for selective analysis of aqueous chlorinated hydrocarbons using a gas sensor.

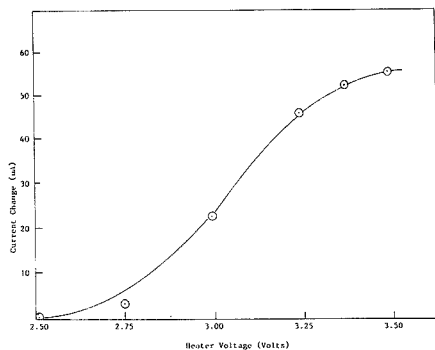


Figure 4. Sensor signal to 1000 ppm chlorobenzene in air (140 cm³/min) at different heater voltages (i.e. operating temperature).

Table I. Relationship between Sensor Signal and Flow Rate^a

flow rate, cm ³ /min	conductance (σ), Ω^{-1}	log cond ln σ
110	1.48×10^{-6}	-11.12
150	1.15×10^{-6}	-11.37
175	9.63×10^{-6}	-11.55
200	8.12×10^{-6}	-11.72
310	3.76×10^{-6}	-12.49
360	2.96×10^{-6}	-12.73
516	1.16×10^{-6}	-13.67

^aRegression of flow rate and log yield: constant, -10.4566, R^2 , 0.9980; slope, -0.0063.

This type of model for the gas sensor response has been used to describe the response of p-type cobalt oxide to carbon monoxide (12) and can be used to explain the response of n-type semiconductors to various gases (13, 14).

The sensitivity of the chlorinated hydrocarbon sensor is highly dependent upon the heater voltage which controls the temperature of the sensor. The sensor signals at the different heater voltages at constant concentration of 1000 ppm chlorobenzene in air are given in Figure 4. The sensitivity increases as the heater voltage increases (i.e., as the temperature of the sensor is increased) but after a voltage of 3.365 V, the signal amplitude increases slowly. In order to prolong the lifetime of chlorinated hydrocarbon sensor and to maximize the sensitivity, a heater voltage of 3.365 V was used.

At high gas sample flow rate, the sensor signal decreases with the increasing flow rate. Since more heat is lost from the bead as the flow rate increases, the temperature of bead is inversely proportional to the carrier gas flow rate. This is consistent with eq 5, which predicts that the conductance of the bead should increase with a decrease in flow rate. Table I shows the relationship between sensor signal and flow rate. These data support the interpretation that simple dilution of the sample in the air carrier gas causes the loss in sensor signal at higher flow rates. The least-squares regression result (correlation coefficient, 0.998) supports eq 5 and our hypothesis. Considering both the analyte transport efficiency and sensor signal decrease with flow rate, an optimum flow rate of about 170 cm³/min was chosen for this particular sensor system geometry.

Table II illustrates the concentration dependence of the chlorinated hydrocarbon sensor response and these data support the conductance theory described by eq 4 above. The five gas concentrations (6.25, 12.5, 25, 50, and 100 ppm) of chlorobenzene in air were detected by the sensor at constant heater temperature and constant flow rate with an amplifier of gain about 10. The linear relationship of the log conduc-

Table II. Sensor Response to Chlorobenzene in Air at Different Concentrations

conc P, ppm	cond σ , Ω^{-1}	log conc (ln P)	log cond (ln σ) ^b
6.25	1.325×10^{-6}	1.833	-13.534
6.25	1.350×10^{-6}	1.833	-13.515
12.50	2.200×10^{-6}	2.526	-13.027
12.50	2.250×10^{-6}	2.526	-13.005
25.00	4.100×10^{-6}	3.219	-12.405
25.00	4.125×10^{-6}	3.219	-12.398
50.00	8.500×10^{-6}	3.912	-11.675
50.00	8.625×10^{-6}	3.912	-11.660
100.00	1.502×10^{-5}	4.605	-11.106
100.00	1.496×10^{-5}	4.605	-11.110

^a $\sigma = (5.3854 \times 10^{-7}) + (1.4727 \times 10^{-7})P$; correlation coefficient, 0.9955. ^b $\ln \sigma = -15.2148 + 0.8920 \ln P$; correlation coefficient, 0.9966.

Table III. Sensor Responses to Chlorobenzene in Water at Different Concentrations

conc P, ppm	cond σ , Ω^{-1}	log conc ln P	log cond ln σ
500	8.325×10^{-7}	6.21	-14.00
1000	1.288×10^{-6}	6.91	-13.56
2000	2.088×10^{-6}	7.60	-13.08
5000	3.125×10^{-6}	8.52	-12.68
10000	3.700×10^{-6}	9.21	-12.51
50000	4.825×10^{-6}	10.82	-12.24

^a $\ln \sigma = -16.1562 + 0.3829 \ln P$; correlation coefficient, 0.9565.

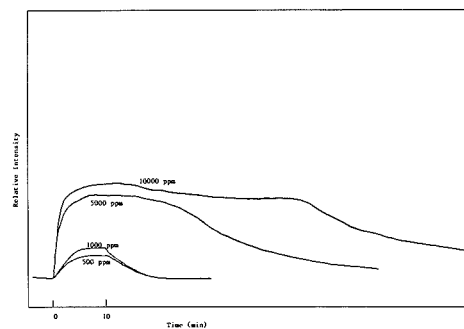


Figure 5. Responses of gas sensor to the air flow from the permeation apparatus during 10-min exposures of the permeation apparatus to aqueous chlorobenzene samples.

tance and log partial pressure (i.e. the gas concentration) of chlorobenzene vapor is consistent with the results predicted by our model of sensor response at concentrations below about 500 ppm.

A series of different concentrations of chlorobenzene in water were prepared. The signals produced when the silicone tubing is immersed in the aqueous samples are shown in Figure 5. The high concentration requires more time to completely purge from the system than the low concentration. The reason for this can be explained because a longer time is required for cleaning the contamination from the silicone tubing after saturation with the analyte. The signal magnitude at high concentrations (500–50000 ppm) of chlorobenzene in water (Table III) is clearly not linear. However, the response is linear at low concentrations and low concentrations are of greater interest here (see Figure 6). The linear regression line for chlorobenzene in Figure 6 has a correlation coefficient of 0.9993 confirming linear response. The nonlinear results above about 500 ppm may be attributed to the low solubility of chlorobenzene in water. Studies have confirmed the ability

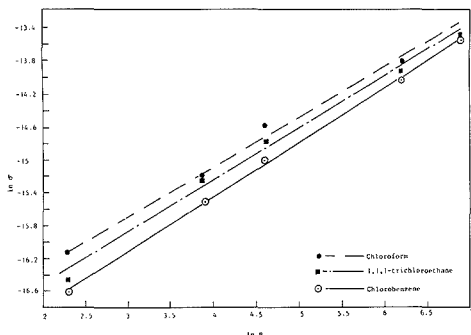


Figure 6. Responses of sensor to chlorobenzene, 1,1,1-trichloroethane, and chloroform at several concentrations in aqueous samples.

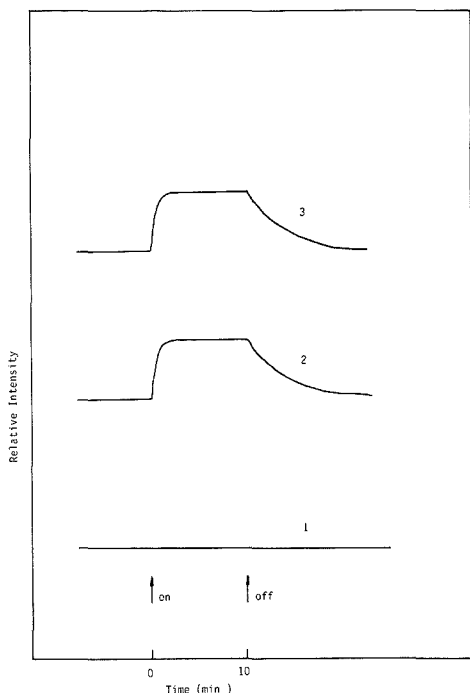


Figure 7. Response characteristics for the sensor to (1) 100 ppm aqueous phenol, (2) 100 ppm chlorobenzene in water, and (3) 100 ppm chlorobenzene in 100 ppm aqueous phenol.

to use silicone membranes beyond the solubility point (15), but a precise model of this behavior has not yet been published.

Three different chlorinated hydrocarbons, chlorobenzene, 1,1,1-trichloroethane, and chloroform, in water were (individually) analyzed by using the sensor-permeation system. The responses at different aqueous concentrations (10–500

ppm) were recorded by using an amplifier with a gain of 220 to boost the signal. There is a clear relationship between the response for all three chlorinated compounds and the concentration. This response was more clearly linear for the less volatile compound. With the same apparatus, no response could be detected for 1000 ppm of either hexane and phenol in the water. Figure 7 shows response characteristics for the sensor to (1) 100 ppm aqueous phenol, (2) 100 ppm chlorobenzene in water, and (3) 100 ppm chlorobenzene in 100 ppm aqueous phenol. It illustrates that the apparatus can be used for monitoring chlorinated hydrocarbons in water even in the presence of phenol.

CONCLUSIONS

There are several major conclusions from this study. Using a semipermeable membrane allows the application of relatively inexpensive gas sensors to the analysis of liquid samples. The use of inexpensive gas sensors offers an opportunity to design relatively low cost, small, and rugged equipment with the potential for continuous on-line analysis of aqueous streams. The simple silicone permeation tube is rugged, resistant to many chemicals, and easily inserted into the water stream and can provide the analyte to the gas sensor in a form suitable for quantitative analysis. The selectivity of gas sensors can be exploited by using the approach described herein.

There is a linear relation between the sensor response and the sample concentration for chlorinated hydrocarbons at low concentrations. The fact that the system operates with dilute samples under constant conditions simplifies stability problems associated with the use of semiconductor sensors.

Future work will be focused upon understanding the sensor mechanism so that sensors with greater sensitivity can be fabricated. In addition, optimum geometry for the permeation system will be investigated to allow the design of practical field sampling systems for continuous analysis of chlorinated hydrocarbons in water with more rapid response time.

ACKNOWLEDGMENT

We wish to acknowledge the inciteful comments of Robert Bredeweg on this work, especially for suggesting the silicone membrane technology for the permeator.

LITERATURE CITED

- (1) Callis, J. B.; Illman, D. L.; Kowalski, B. R. *Anal. Chem.* **1987**, *59*, 624A–637A.
- (2) Blanchard, R. D.; Hardy, J. K. *Anal. Chem.* **1986**, *58*, 1529–1532.
- (3) Hellegeth, J. W.; Taylor, L. T. *Anal. Chem.* **1987**, *59*, 295–300.
- (4) Meicher, R. G. *Anal. Chim. Acta* **1988**, *214*, 299–313.
- (5) Loh, Jack C.; Lu, Chih-shun Solid State Sensor, US Patent 3,751,968, 1973.
- (6) Bardeen, J. *Phys. Rev.* **1947**, *71*, 717.
- (7) Weller, S. W.; Voltz, S. E. *Adv. Catal.* **1957**, *9*, 215–222.
- (8) Morrison, S. R. *Surf. Sci.* **1974**, *45*, 20.
- (9) Barry, T. I.; Stone, F. S. *Proc. R. Soc. London, A* **1960**, *355*, 124.
- (10) Logothetis, E. M.; Park, K.; Meitzler, A. H.; Laud, K. R. *Appl. Phys. Lett.* **1975**, *26*, 209.
- (11) Thomas, J. M.; Thomas, W. J. *Introduction to the Principles of Heterogeneous Catalysis*; Academic Press: New York, 1967; p 44.
- (12) Stetter, J. R. *J. Colloid Interface Sci.* **1978**, *65*, 432–443.
- (13) Heiland, G. *Sens. Actuators* **1982**, *2*, 343–361.
- (14) Sleyama, T.; Kato, A.; Fujishiro, K.; Nagatani, M. *Anal. Chem.* **1962**, *34*, 1502–1503.
- (15) Coyne, B.; et al. Determining Organic Compounds Using a Membrane, US Patent 4,715,217, 1987.

RECEIVED for review July 31, 1989. Accepted November 7, 1989. The support of the Dow Chemical Co. is gratefully acknowledged.

On-Line Fluorescence Lifetime Detection for Chromatographic Peak Resolution

W. Tyler Cobb and Linda B. McGown*

Department of Chemistry, P. M. Gross Chemical Laboratory, Duke University, Durham, North Carolina 27706

Frequency-domain fluorescence lifetime measurements, made on-the-fly during high-performance liquid chromatography, were used to resolve overlapping chromatographic peaks of polycyclic aromatic hydrocarbons. Two-component heterogeneity analysis of the multifrequency lifetime data provided fractional intensity contributions for the individual components, which were multiplied by the total fluorescence intensity to yield the peaks of each component. Excellent results were obtained when the fluorescence lifetimes of the components were fixed in the heterogeneity analysis to values obtained from the on-the-fly lifetime chromatograms. Positive errors in the peak intensities were observed when the lifetimes were allowed to float in the heterogeneity analysis; the source of the error has not yet been identified but may be due to systematic bias in the heterogeneity analysis software.

INTRODUCTION

Recent studies have explored fluorescence lifetime detection on-the-fly in high-performance liquid chromatography (HPLC), using both time-domain (1-5) and frequency-domain (6, 7) techniques. Analytical applications have included lifetime determinations for peak identification (5-7) and time-delay measurements for improvement of signal-to-noise ratios (1-3). Time-domain techniques have not yet been described for the resolution of overlapping chromatographic peaks. Preliminary studies of peak resolution in the frequency-domain, using on-the-fly measurements of phase shift and demodulation, have been described for a three-frequency instrument (7).

In this paper, we describe the first use of on-the-fly lifetime determinations with a multifrequency fluorometer for chromatographic peak resolution in HPLC. Heterogeneity analysis of the multifrequency data with a nonlinear least-squares fit provides the fluorescence lifetimes and fractional intensity contributions of each of the overlapping components, at 1-s intervals along the chromatographic peak. Alternatively, the lifetimes can be fixed to values found from the lifetime chromatograms for the individual components in nonoverlapping peak regions, leaving only the fractional intensities to be calculated. In either case, the peaks of the individual components are reconstructed by multiplying the fractional intensity by the steady-state intensity at each point. Two mixtures of polycyclic aromatic hydrocarbon (PAH) compounds were studied: a 6-component mixture and an 11-component mixture. The chromatographic conditions were intentionally adjusted to give poor chromatographic resolution, in order to test the heterogeneity analysis resolution for a model system of PAHs with extensive peak overlap.

THEORY

The theory of phase-modulation fluorescence lifetime determinations and heterogeneity analysis has been described elsewhere (8). Briefly, the sample is excited with intensity modulated light, resulting in a similarly modulated fluorescence signal that is phase-shifted and demodulated as a function of the fluorescence lifetime of the emitting species.

The lifetime τ can be calculated from both the phase-shift and the demodulation, to give lifetimes τ_p and τ_m , respectively. For a homogeneous system of a single lifetime component, $\tau_p = \tau_m$. If the signal is heterogeneous, i.e., due to more than one ground-state component, then $\tau_m > \tau_p$. Determinations of τ_p and τ_m at multiple modulation frequencies can be used to resolve the heterogeneous signals, yielding the lifetime and fractional intensity contribution of each component.

Chromatographic peak resolution is accomplished by performing heterogeneity analysis at discrete points along the chromatogram. At each point, the fractional intensity of each component is calculated by heterogeneity analysis and multiplied by the total intensity at that point to find the intensity of the component. The peak of the component is constructed from the calculated intensities of the component along the chromatogram.

EXPERIMENTAL SECTION

The PAHs (99%, Analabs) and solvents (HPLC grade, Burdick and Jackson) were used as received for solution preparation. Solvents used as mobile phases were further purified by vacuum filtration. Micromolar solutions of individual PAHs were prepared in acetonitrile, and PAH mixtures were prepared directly from these solutions.

Reversed-phase chromatography was performed with a dual-pump HPLC system (Waters) with a 10×0.3 cm glass cartridge column assembly, including Vydac 201P packing and a C-18 guard column, and fixed UV absorption detection at 254 nm. The PAHs were injected manually and eluted isocratically with a flow rate of 0.3 mL/min. The 6-component mixture was eluted with a 100% acetonitrile mobile phase; an 87% solution of acetonitrile in water was used for elution of the 11-component mixture.

The eluted PAHs passed from the absorbance detector into the 4800S phase-modulation spectrofluorometer (SLM Instruments, Inc.), for on-the-fly, simultaneous detection of fluorescence intensity and lifetime. The instrumental configuration for these studies includes a 450-W xenon arc lamp, excitation monochromator, electrooptic modulator compartment, a 20- μ L black quartz, "low-fluorescence" flow cell (Hellma) in a thermostated sample chamber, emission filters, PMT detectors, and an IBM PC-AT for data acquisition and analysis.

Lifetime calculations and heterogeneity analysis were performed with software provided with the instrument. A reference fluorophore, 9-anthracenecarbonitrile (9AC, $\tau = 11.31$ ns in acetonitrile), was used to calibrate the phase and modulation of the excitation, as has been previously described (7). The instrument heterogeneity analysis software provides a nonlinear least-squares (NLLS) fit to multifrequency data.

The fluorescence lifetimes of the PAH compounds used in the two mixtures are shown in Table I. The lifetimes were determined on-line, under the same conditions that were used for the heterogeneity analysis experiments. For both mixtures, phase and modulation data were collected on-line, at 1-s intervals, at five modulation frequencies: 4, 10, 15, 25, and 35 MHz for the 6-component mixture, and 5, 10, 15, 25, and 40 MHz for the 11-component mixture. The 6-component mixture was excited at 360 nm, and emission was observed through a combination of a 399-nm longpass filter and a 600-nm shortpass filter. For the 11-component mixture, excitation was at 330 nm, and emission was observed through a combination of a 345-nm longpass filter and a 600-nm shortpass filter. Under these wavelength conditions,

Table I. Abbreviations, Peak Numbers and Fluorescence Lifetimes of the PAH Compounds

PAH	abbrevia- tion	peak no. ^a		τ , ns
		6-comp	11-comp	
anthracene			1	4.0
fluoranthene		1	2	30.5
benz[a]anthracene	BaA		3	15.8
chrysene			4	12.9
benzo[e]pyrene	BeP		5	16.9
benzo[b]fluoranthene	BbF	2	6	27.3
benzo[k]fluoranthene	BkF	3	7	7.8
benzo[a]pyrene	BaP	4	8	14.9
dibenzo[a,h]anthracene	DBA		9	13.9
benzo[ghi]perylene	BgP	5	10	20.3
indeno(1,2,3-cd)pyrene	IP	6	11	6.9

^a Peak numbers for 6-component and 11-component mixtures. In order of elution, corresponding to numbers in Figures.

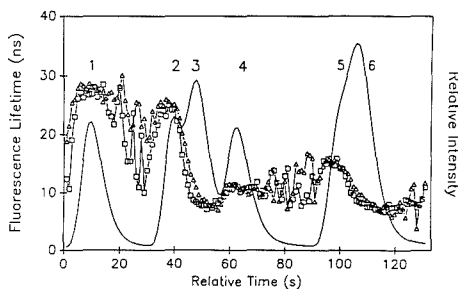


Figure 1. Fluorescence lifetime chromatogram of the 6-component mixture at 10 MHz. Solid line is steady-state (dc) intensity, squares are τ_p , and triangles are τ_m . Peak numbers correspond to PAHs as numbered in Table I.

background from scattered light and Raman scattering are negligible.

RESULTS AND DISCUSSION

6-Component Mixture. Figure 1 shows the fluorescence lifetime chromatogram for the 6-component mixture at 10 MHz. In regions where only one fluorescent component is present, $\tau_p = \tau_m = \text{constant}$ (where the constant is the lifetime of the component), as expected. For regions where the chromatographic peaks overlap, $\tau_m > \tau_p$ and the lifetimes change continuously across the region of overlap, reflecting the changing fractional intensity contributions of the two different components. For example, the extensively overlapping BgP and IP peaks show the homogeneous BgP lifetime of 20.3 ns at the beginning of the peaks, followed by the heterogeneous lifetime region in which $\tau_m > \tau_p$ and the lifetimes are decreasing, converging on the shorter lifetime of 6.9 ns for IP in the homogeneous IP region at the end of the peaks. In this case, as well as in the overlapping peaks of BbF and BkF, and BkF and BaP, the lifetime chromatogram is able to indicate (1) the presence of more than one component ($\tau_m > \tau_p$) and (2) the lifetimes of both components in the overlapping peaks.

It is important that the chromatogram in Figure 1 also shows fluorescence intensity, which is simply the dc, or unmodulated component, of the emission signal. It is an advantage of the frequency domain approach that the phase, modulation, and steady-state intensity information is all obtained simultaneously, on-the-fly, from the same emission signal.

The NLLS heterogeneity analysis of the five-frequency data set was performed point-by-point for the 6-component mixture. The fractional intensity contributions calculated by

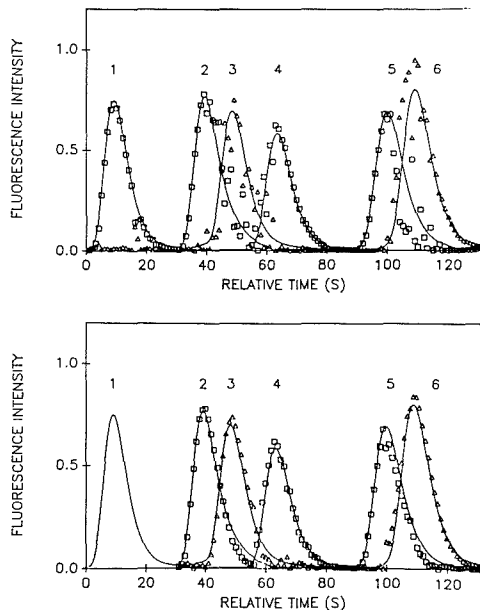


Figure 2. Heterogeneity analysis results for the 6-component mixture. Solid lines are peaks for the same amount of each PAH as in the mixture, injected separately (i.e., the "true values"). Squares and triangles represent the peaks calculated from the two-component fits. (a) Lifetimes of the two components allowed to float. (b) Lifetimes fixed to values found from Figure 1.

NLLS were multiplied by the dc intensity at each point, in order to obtain the resolved peaks of the individual components.

The peaks resolved by NLLS for each component in the mixture were compared with peaks obtained for identical amounts of each component, injected separately. The comparison is shown in Figure 2a for the five-frequency data set. The heterogeneity analysis was also performed on various four- and three-frequency subsets of the five-frequency data set. Results for four-frequency data sets were very similar to those for the five-frequency set, whereas the results showed significant degradation when only three frequencies were used.

As shown in Figure 2a, the NLLS results for a two-component fit are excellent for the chromatographically resolved fluoranthene, as well as for the peripheral, homogeneous regions of the five partially resolved PAHs. In the heterogeneous, overlapping regions, results are fairly good for BbF, BaP, and BgP, including good estimates of peak height. Results for BkF and IP are poor; in both cases, peak heights are overestimated. Of course, the performance of the heterogeneity analysis is not bad, considering the almost complete overlap of BgP and IP and the overlap of BkF on both sides of its peak (Figure 1).

In order to improve the resolution of peaks in the mixtures, we fixed the lifetimes of the components in the heterogeneity analysis to the values found from the lifetime chromatograms. As shown in Figure 1, there is a region at the periphery of each peak where the lifetime information is essentially homogeneous. Excellent results were obtained when the lifetimes were fixed, as shown in Figure 2b.

11-Component Mixture. Our first observation for the 11-component mixture was the presence of a small but significant background signal that had not been observed for the 6-component mixture. The background was eventually

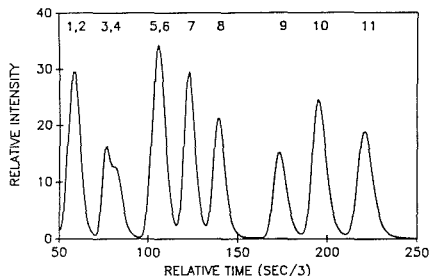


Figure 3. Steady-state (dc) chromatogram of the 11-component mixture at 10 MHz. Numbers above peaks refer to PAHs as numbered in Table 1.

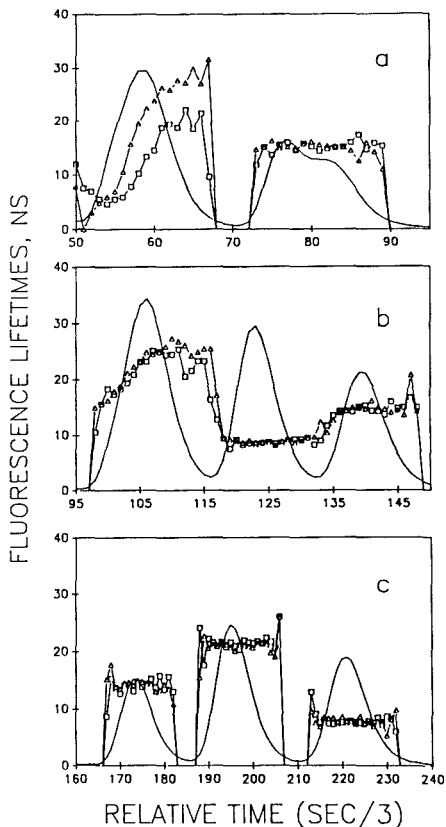


Figure 4. Fluorescence lifetime chromatogram of the 11-component mixture at 10 MHz, with an expanded time axis relative to Figure 3: (a) peaks 1 through 4, expanded time axis; (b) peaks 5 through 8, expanded time axis; (c) peaks 9 through 11, expanded time axis. Legend as in Figure 1.

identified as emission from the flow cell when excited at 330 nm, which is required for simultaneous excitation of the 11 PAHs. The background is not excited at the 360-nm wavelength used for the 6-component mixture, which is why the background did not appear in the earlier studies.

The background emission is a broad peak from 400 to 600 nm, with a maximum around 530 nm. The excitation spec-

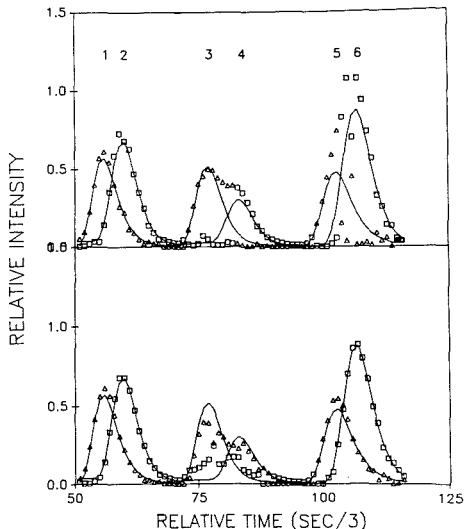


Figure 5. Heterogeneity analysis results for components 1 through 6 in the 11-component mixture: (a) lifetimes of the two components allowed to float; (b) lifetimes fixed to values found from Figure 4.

trum has an undetermined maximum below 290 nm in the UV and decreases to zero near and above 350 nm. Similar spectra are obtained for the flow cell containing acetonitrile, water, methanol, or air.

For fluorescence intensity detection, the flow cell emission can be "zeroed out" using PMT voltage offsets. Unfortunately, when lifetime measurements are made, the background signal can still contribute to the observed phase and modulation, even though its dc contribution is offset to zero. We attempted to determine the lifetime of the flow cell luminescence but were unable to detect an ac (modulated) signal in the 1–250 MHz range of the instrument. The complete demodulation at these frequencies, along with the large Stoke's shift of the emission, is indicative of phosphorescence (consistent with the "low-fluorescence" designation by the manufacturer), but this could not be verified within the frequency range of our instrument.

Fortunately, the complete demodulation of the flow cell background means that it will not interfere with the PAH lifetime determinations, since it will appear as a constant, unmodulated dc contribution. It is therefore valid to use the PMT offset to eliminate the background signal, and this was done for the chromatograms of the 11-component mixture.

The steady-state (dc) fluorescence intensity chromatogram of the mixture is shown in Figure 3. Under these chromatographic conditions, extensive (almost complete) overlap is observed between peaks 1 and 2 (anthracene and fluoranthene) and peaks 5 and 6 (BeP and BbF). Peaks 3 and 4 (BaA and chrysene) are also highly overlapping. The remaining components, corresponding to peaks 7 through 11, are well-resolved.

The lifetime chromatogram for the mixture at 10 MHz is shown in Figure 4, in which the time scale is expanded to emphasize the regions of peak overlap and lifetime heterogeneity. Figure 4 clearly illustrates the ability of frequency-domain measurements to provide accurate lifetimes and to indicate regions of heterogeneity. Only in one case, that of the overlapping peaks 3 and 4 (Figure 4b), are the results misleading. The region clearly contains two peaks, yet the lifetimes appear homogeneous. This is due to the very similar

lifetimes of the two components (16 ns for BaA and 13 ns for chrysene), which are not discernibly different at 10 MHz.

Heterogeneity analysis was performed on the five-frequency data set. The NLLS-resolved peaks and the peaks obtained for the corresponding, individually injected components, are shown in Figure 5 for the partially resolved peaks 1 through 6. Results are shown for NLLS both with floating lifetimes (Figure 5a) and with the lifetimes fixed (Figure 5b). In both cases, results are good for peaks 1 and 2, which have the greatest lifetime difference. Results are systematically high for peaks 5 and 6 with floating lifetimes and are greatly improved when lifetimes are fixed. Peaks 3 and 4, with the very similar lifetimes, are unresolved when lifetimes are allowed to float; some improvement is observed when the lifetimes are fixed.

CONCLUSIONS

This work has demonstrated the resolution of chromatographic peaks by heterogeneity analysis of multifrequency fluorescence lifetime data, collected on-the-fly for HPLC-eluted PAH compounds. Excellent results were obtained when lifetimes were fixed in the heterogeneity analysis to values obtained directly from the lifetime chromatograms. Positive

errors were generally observed when the lifetimes were allowed to float in the heterogeneity analysis. The source of the positive error is not yet known; however, we have observed similar errors for batch heterogeneity analyses of these components. We are currently investigating the possibility of systematic bias in the system software for NLLS heterogeneity analysis.

LITERATURE CITED

- (1) Richardson, J.; Larson, K.; Haugen, G.; Johnson, D.; Clarkson, J. *Anal. Chim. Acta* **1980**, *116*, 407.
- (2) Imasaka, T.; Ishibashi, K.; Ishibashi, N. *Anal. Chim. Acta* **1982**, *142*, 1.
- (3) Furuta, N.; Otusuki, A. *Anal. Chem.* **1983**, *55*, 2407.
- (4) Desilets, D.; Kissinger, P.; Lytle, F. *Anal. Chem.* **1987**, *59*, 1830.
- (5) Kawabata, Y.; Sauda, K.; Imasaka, T.; Ishibashi, N. *Anal. Chim. Acta* **1988**, *208*, 255.
- (6) Cobb, W. T.; McGown, L. B. *Appl. Spectrosc.* **1987**, *41*, 1275.
- (7) Cobb, W. T.; McGown, L. B. *Appl. Spectrosc.* **1989**, *43*, 1363.
- (8) Lakowicz, J. R. *Principles of Fluorescence Spectroscopy*; Plenum Press: New York, 1983.

RECEIVED for review September 1, 1989. Accepted November 6, 1989. This work was supported by the U.S. Environmental Protection Agency (Grant R81-2887-01-0).

The Physical Sense of Simulation Models of Liquid Chromatography: Propagation through a Grid or Solution of the Mass Balance Equation?

Martin Czok and Georges Guiochon*

Department of Chemistry, University of Tennessee, Knoxville, Tennessee 37996-1600, and Division of Analytical Chemistry, Oak Ridge National Laboratory, Oak Ridge, Tennessee 37831-6120

Two distinctly different approaches have been used to simulate the movement of bands through a chromatographic column. One example of the first approach is the Craig distribution model, which replaces the continuous column with a specific number of discrete equilibration processes. Thus it introduces the concept of (theoretical) plates into chromatography, but is not able to explain satisfactorily their significance. The second approach is based on the mass balance equation which can be integrated numerically over time and space to give the elution profile. This calculation can be performed by using finite difference methods to extrapolate from the concentration value at a given time and position in the column to the next value. In this paper we discuss the physical meaning of the numerical integration process followed by the finite difference methods. We show that both approaches are equivalent and that the band broadening produced by the different methods, due to "numerical diffusion", can be explained similarly. Since this effect is sufficiently well-known now, we can introduce a variable amount of additional diffusion and thereby control the overall dispersion.

INTRODUCTION

In analytical chromatography the migration of sample zones through the column is described by simple relationships. The peaks are nearly symmetrical, their retention times are directly proportional to the column length, and so the band variances,

the retention times, and the bandwidths are independent of the composition of the sample. Therefore it is relatively easy to calculate the performance of the chromatographic system under various experimental conditions and to choose the optimum ones for the experiment.

This remains true only as long as the sample load is low compared to the saturation capacity of the column. For preparative separations, large volumes of very concentrated solutions are injected in order to produce as much purified material as possible in a given time. Consequently, the column is highly overloaded and the peak profiles become unsymmetrical and depend strongly on the amount of material injected. Most noticeably, the migration velocity of the band front changes with the sample size.

A better understanding of these phenomena is needed to develop practical optimization procedures for the applications of preparative chromatography. Several simple equations have been proposed that predict the nonlinear behavior of the band of a pure compound in overloaded chromatography (1-5). As far as a generalization of these equations to the case of mixtures of two or more components is possible (6-9), they can be used to find the optimum conditions for a preparative separation (6, 7, 10, 11). Because of the strong mutual interactions that take place between two solutes and the severe deformation of their bands, however, an accurate description of the complete elution profile is necessary to achieve a correct optimization (8-11).

For this purpose computer programs have been developed that imitate the migration of the bands down the column (2, 6, 12-19). The simulated chromatograms obtained under

different chromatographic conditions can then be compared. A simplex optimization approach can be used in simple cases (20). The accuracy of these predictions may depend on the way the elution profiles are generated. Due to the approximations made in the numerical calculations, we have to expect certain errors (19, 21). In some cases these errors can be compensated in part, but for a complete control of them, we need to know how they form and propagate.

In this paper we compare three finite difference methods and explain the calculation procedures followed from two different points of view. The previously published derivation (17) was based on theoretical results regarding the solution of systems of partial differential equations (14). Since it is difficult for an analytical chemist to visualize this type of formalism, we present first a physical model of the calculation process, in which the sample mass is transferred stepwise through a grid of cells. In one special case this approach coincides with the model of chromatography introduced by Craig (22-25). Using the analogy to a binomial distribution, we can also find expressions that relate the band broadening due to the mode of propagation to the grid spacing. A comparison of the rate and plate models has been given recently for linear chromatography by Karol who showed the convergence of both approaches (26).

I. CHROMATOGRAPHIC TERMS

In chromatography, we may assume that the column has only one dimension and that the movement of the mobile phase takes place only along the column axis. An individual sample molecule can move at only one of two possible velocities. Part of the time, the molecule is dissolved in the eluent and is transported at the mobile phase velocity, u , while for the remaining time, it interacts with the stationary phase and does not move at all. Thus, its retention time, t_R , is the sum of the time that the eluent itself needs to pass through the column (hold-up time, t_0) and the extra time that the sample molecule stays in the stationary phase (net retention time). The capacity factor commonly used in linear chromatography, k' , is the ratio of these two times. For reasons that will be clarified later, and in view of extending the concept to nonlinear chromatography, we will use the symbol κ for this ratio. The fraction of time a molecule spends in the mobile phase is then equal to $1/(\kappa + 1)$. The linear velocity of the sample molecule, u_R (i.e., the ratio of the column length to the overall retention time), is the average of the two velocities, u and zero. Thus, $u_R = u/(\kappa + 1)$, with $t_R = L/u_R = (1 + \kappa)t_0$. We see later in this section how to extend this concept, which is classical in linear chromatography, to nonlinear chromatography.

If we consider a large number of molecules instead of one, the fraction of molecules that are in the mobile phase at any time is equal to the fraction of time spent there, on the average, by one molecule. Thus, κ is the mass distribution coefficient (25), the ratio between the amounts of compound in the stationary and the mobile phases, at a given time. Since we assume instantaneous equilibration (which is always nearly achieved in practice), we have very frequent interchanges between retained and free molecules. Thus, we can consider the movement of the molecules as continuous and the velocity of a group of molecules at concentration C is u_R (microaveraged velocity).

In linear chromatography the retained amount of a compound is strictly proportional to its concentration in the mobile phase and the fraction of molecules adsorbed is constant. Consequently, the mass distribution coefficient, $\kappa_0 = k'$, is constant, and so is the average velocity of the molecules of an injected band, $u_{R,0}$. When the adsorption isotherm is not linear, however, this fraction depends on the local concentration and varies over the entire peak profile. This means

that molecules in different parts of the peak move at different velocities and, consequently, the peak shape must change during its migration. Therefore the local values of u_R and κ are both functions of the local concentration through the adsorption isotherm. It must be remembered, however, that the velocity u_R is the velocity at which those molecules propagate which are at time t and position z of the column in a slice of mobile phase where the concentration is C . Concentrations decrease during the elution of a band, so a short time later the same molecules will be found at lower concentration; their velocity has changed (usually decreased) and the slice that holds them is thicker.

The examples in this paper were calculated with either linear or Langmuir isotherm expressions. The Langmuir equilibrium isotherm relates the concentration of solute in the stationary phase, q , to its concentration in the mobile phase, C , as follows:

$$q = \frac{aC}{1 + bC} \quad \text{or} \quad \frac{q}{C} = \frac{a}{1 + bC}$$

For low sample concentrations, the ratio between q and C approaches a constant value, the Nernst distribution coefficient, $K = a$. Since we define κ as the mass distribution ratio, the dependence of κ on the concentration is given by the analogous relation (the limit at low concentrations being $k' = \kappa_0$)

$$\kappa = \frac{\kappa_0}{1 + bC} \quad (1)$$

However, other isotherm types can be employed as well. Especially, for a multicomponent mixture there is competition for the adsorption sites between the different components of the sample mixture, and an appropriate competitive isotherm must be used. Then, the κ value for one compound depends on the concentrations of all the other solutes. In all of these cases, the expression (1) has to be replaced by the corresponding one that gives κ as the mass distribution ratio between the two phases. Throughout this paper, the symbol κ stands for any such expression.

The local average linear velocity of the solute molecules, $u_R = u/(\kappa + 1)$, is calculated with this κ value, and therefore depends also on the local concentrations for a multicomponent system. It should not be mistaken for the velocity u_z , associated to a certain concentration of solute on a continuous diffuse profile, which is used in other publications (1, 4, 21, 27) and is based on the derivative of the adsorption isotherm ($u_z = u/[1 + (dq/dC)]$). The velocity u_z describes quantitatively how the position of the point where the concentration is equal to C on the continuous part of the profile at time t is related to the position of the point of the same concentration at time $t + dt$. It is very convenient to use u_z to describe the change in the profile during the band migration (27), but it is not the velocity of propagation of the molecules in the slice of a band where the concentration is C . On the contrary, u_R is this propagation velocity.

We compare now two procedures for accounting quantitatively for the elution profile of a pulse of a pure compound. The same method could be used for a multicomponent mixture or for other types of chromatographic experiments (e.g., frontal analysis, system peaks, displacement). The details are more complex but the principles remain the same.

II. PROPAGATION THROUGH A GRID

Since it is not feasible to monitor the movement of each individual molecule with an infinitely high time resolution, the column is divided into slices of width Δz and time is given in multiples of Δt . (The appropriate choice of this space and time increment size will be discussed later.) Thus, we have discretized time and space and defined a grid, as shown in

Table I. Development of the Chromatograms of Figure 3 ($k' = 5$): Injection Pulse 10 Concentration Units in 0.1 s

Method I: Symmetrical in Time ($C_{z,t-1}$, $C_{z,t}$) $\Delta z = 500 \mu\text{m}$, $\Delta t = 4.0 \text{ s}$, $P = 2.0$					
time					
l	0.25	-	-	-	-
e	0.125	0.125	-	-	-
n	0.0625	0.1250	0.0625	-	-
g	0.03125	0.09375	0.09375	0.03125	-
t	0.01563	0.06250	0.09375	0.06250	0.01563
h

Method II: Symmetrical in Space ($C_{z-1,t}$, $C_{z,t}$) $\Delta z = 1000 \mu\text{m}$, $\Delta t = 2.0 \text{ s}$, $P = 0.5$					
time					
l	0.25	0.125	0.0625	0.03125	0.01563
e	-	0.125	0.1250	0.09375	0.06250
n	-	-	0.0625	0.09375	0.09375
g	-	-	-	0.03125	0.06250
t	-	-	-	-	0.01563
h	-	-	-	-	-

Method III: Symmetrical Toward Diagonal ($C_{z-1,t-1}$, $C_{z-1,t}$) $\Delta z = 250 \mu\text{m}$, $\Delta t = 1.0 \text{ s}$, $P = 1.0$					
time					
l	0.5	0.25	0.125	0.0625	0.03125
e	0.25	0.25	0.1875	0.1250	0.07813
n	0.125	0.1875	0.1875	0.15625	0.11719
g	0.0625	0.1250	0.15625	0.15625	0.13672
t	0.03125	0.07813	0.11719	0.13672	0.13672
h

Craig Model: As Method II, $u = \Delta z / \Delta t$ $\Delta z = 600 \mu\text{m}$, $\Delta t = 0.4 \text{ s}$, $P = 0.167$					
time					
l	0.41667	0.34722	0.28935	0.24113	0.20094
e	-	0.06944	0.11574	0.14468	0.16075
n	-	-	0.01157	0.02894	0.04282
g	-	-	-	0.00193	0.00643
t	-	-	-	-	0.00032
h	-	-	-	-	-

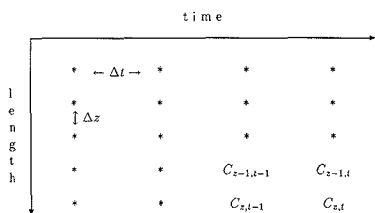
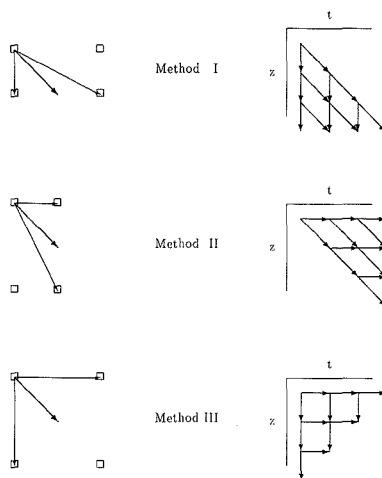
**Figure 1.** Grid of concentration values over elution time and column length.

Figure 1 and Table I. Now, we want to calculate $C_{z,t}$, which denotes the concentration in the z th slice of the column after the t th time interval. The solute concentration in the mobile phase, averaged over Δz and Δt , has to be calculated for every segment of the column, after each time interval. In linear chromatography the mobile phase concentration $C_{z,t}$ is strictly proportional to the total amount of sample in this cell and the change of concentrations in the mobile phase therefore is equivalent to the displacement of mass in both phases.

The vertical columns of the grid represent the concentration profiles along the chromatographic column at a given time; the horizontal rows show how the concentration changes over

**Figure 2.** Three different methods for propagation through a grid.

time at one point in the column. Thus, the first row ($z = 0$) is entered as the injection profile and the last row ($z = L$) is the elution profile at the end of the column, the simulated chromatogram.

When a zone of the sample moves through the column, the corresponding concentrations are transferred through the grid from the head of the column to the outlet and from the time of injection to the time of elution. In the simplest case, the amount in the first cell would be displaced by exactly one length increment for every time interval. Then the sample would be handed down along the diagonal of the grid and the new concentration $C_{z,t}$ would be identical with the concentration $C_{z-1,t-1}$ that at the previous time had been at the preceding position. At any given grid spacing this is possible only for one specific peak velocity, $u_R = \Delta z / \Delta t$, i.e. for one retention. For all other κ values, however, the sample band has to move through the grid at different angles and the two neighboring points in the grid, $C_{z-1,t}$ and $C_{z,t-1}$, will also contribute to the new concentration.

Each κ value corresponds to a vector in the grid that gives the direction in which the sample migrates. In the general case, this direction does not point from the center of one cell to the center of another one. The mass should rather be moved to some point between two grid locations. This means that it is not possible to transfer simply the full content of one cell to the next. In order to propagate correctly the content of one cell, the mass is split up in two parts and shared between two neighboring cells, in the proper ratio, so the center of mass still moves to the target location.

This can be done in many different ways, the most important and practical of which are combinations of the three simple ways shown in Figure 2 as methods I, II, and III. The target vector is the same in all three cases, but it is replaced by three different combinations of grid vectors. The grid spacing also has to be adjusted so that the target vector points in the space between the grid vectors (see below).

In method I the contents of each cell (z,t) are propagated from the row z (current position in the column) to the row $z + 1$ (next position). In order to produce the correct average time delay corresponding to the proper retention, one part is transferred with a retention of one full Δt to the time $t + 1$, and the remainder needs no time at all. Thus the amount from cell (z,t) is distributed between the cells ($z+1,t$) and ($z+1,t+1$). The fraction that is moved in time by one time

interval is equal to $1/P$, which is determined by the κ value. P is the normalized peak velocity or Courant number (21)

$$P = \frac{u}{\kappa + 1} \frac{\Delta t}{\Delta z}$$

Since the target displacement (see Figure 2) is produced as a combination of the two grid vectors, the new center of mass can only lie between the points $(z+1,t)$ and $(z+1,t+1)$. There is no contribution toward more distant cells. Therefore the range of κ values that can be produced by this propagation scheme is limited. On the low side ($P = \infty$), infinitely fast transport through the column is theoretically possible, even though this does not correspond to any practical situation. The upper limit, on the other hand, is given by the diagonal of the grid. At a given mobile phase velocity and grid spacing, the highest κ value accessible is given by $P = 1$, hence

$$\kappa_{\max} + 1 = u(\Delta t / \Delta z)$$

This limit is identical with the one calculated from the "Courant-Friedrich-Lewy condition" (14, 28), which is derived from the theory of partial differential equations. Here it follows from obvious considerations. Thus, method I is mathematically sound and very convenient (see later). However, since it requires that part of the cell content is frozen in time, it has no physical meaning or equivalent.

With method II, propagation is carried out from column t to column $t + 1$. After one time interval, part of the mass from (z,t) has traveled to the next cell downstream $(z+1,t+1)$, whereas the remainder stays at the old position $(z,t+1)$. This scheme can be duplicated experimentally. In fact, one special case of method II turns out to be identical with the Craig distribution mechanism (see following section). Method II is the natural complement of method I: here it is the lowest possible κ value that is determined by the diagonal of the grid, while infinitely slow propagation is possible ($\kappa = \infty$) as the other extreme. The fraction of molecules that move ahead to the next position in the column is equal to P .

In method III, finally, the target displacement is produced with the help of the two orthogonal grid vectors and mass is transferred from the cell (z,t) into the cells $(z,t+1)$ and $(z+1,t)$. Mass is split up perpendicular to the diagonal of the grid. The distribution ratio is $1/(1+P)$ to $P/(1+P)$. With this method there is no limit to the range of κ values that are accessible to simulation: both infinitely fast and slow propagations can be generated, i.e., propagation parallel to either of the axes of the grid. Again, since it is not possible to freeze time in practice, method III cannot be duplicated experimentally.

In all three cases, mass from one cell is distributed between two following cells, which are, respectively, one step down the column, one step in time, or both. Thus we can calculate the concentrations at all the points in the grid, from the injection profile, at the upper left corner, to the elution band profile on the lower right. At the same time, each new cell concentration value is made up of two contributions, coming from two preceding cells. This leads to the following equations which are used to transfer mass from one point of the grid down to the next, until finally the completed last row gives the chromatogram:

method I

$$C_{z,t} = \left(1 - \frac{1}{P}\right) C_{z-1,t} + \frac{1}{P} C_{z-1,t-1}$$

method II

$$C_{z,t} = (1 - P) C_{z,t-1} + P C_{z-1,t-1}$$

method III

$$C_{z,t} = \frac{1}{1+P} C_{z,t-1} + \frac{P}{1+P} C_{z-1,t} \quad (2)$$

Chart I

method	α	β	γ	limit
I	-	$1 - (1/P)$	$1/P$	$P \geq 1$
II	$1 - P$	-	P	$P \leq 1$
III	$1/(1+P)$	$P/(1+P)$	-	-

These three basic propagation methods can be considered as special cases of a general propagation procedure described by the following equation:

$$C_{z,t} = \alpha C_{z,t-1} + \beta C_{z-1,t} + \gamma C_{z-1,t-1} \quad (3)$$

The three numerical coefficients α , β , and γ determine the contributions of the three previous cells to the composition of a new cell content. These coefficients have to obey two basic relationships: their sum must be unity, in order to conserve mass, and the ratio of position-dependent over time-dependent contributions is equal to the normalized propagation velocity, P , in order to transfer mass in the proper direction

$$\alpha + \beta + \gamma = 1 \quad \frac{\beta + \gamma}{\alpha + \gamma} = P = \frac{u}{\kappa + 1} \frac{\Delta t}{\Delta z} \quad (4)$$

Chart I summarizes the values of the parameters for the three methods.

A Particular Case: The Craig Model. An early model that was used to explain the continuous chromatographic process is the Craig model (22-25). It replaces a column with a great number of identical separation flasks connected in series. Each flask or tube contains certain volumes of two immiscible fluids with different densities that serve as stationary and mobile phases, respectively. The sample mixture is introduced into the first tube and both phases are equilibrated. Then the mobile phase of each tube is transferred to the next tube, taking along its part of the solute. The mobile phase in the last flask is collected, while fresh mobile phase is introduced into the first flask. Each flask is equilibrated and the process repeated as long as necessary. Consecutive cycles transport the solute downstream, where its concentration can be monitored in the "effluent" from the last tube.

When this model is applied to chromatography, the time per cycle is called the time interval Δt and the volume of one tube corresponds to the volume of one column segment of width Δz . This means that the mobile phase moves by exactly one Δz for every time unit Δt , or

$$u = \Delta z / \Delta t$$

A retained solute travels more slowly, since at equilibrium only the fraction $1/(\kappa + 1)$ of its amount is present in the mobile phase and transferred to the next stage. Since the normalized mobile phase velocity $u(\Delta t / \Delta z)$ is equal to unity, the quantity P in this case is equal to $1/(\kappa + 1)$.

Thus, the situation is identical with a special case of method II, with a given ratio of grid spacings. When for method II a minimum κ value of zero is chosen (i.e. an unretained peak can be propagated through the grid along its diagonal), this method coincides with the Craig model.

III. BINOMIAL DISTRIBUTION IN A GRID

In the previous section, we have pointed out that, in order to propagate the band of a retained compound at the proper velocity, we must split up the contents of each cell between two cells of the next column or row, so that the center of mass is moved correctly. This means that every step leads to some dispersion. The distribution ratio is governed by the local κ value. When the isotherm is linear, the distribution process

Table II. Evaluation of the Chromatograms of Figure 3 and Table I^a

	retention time, s	peak variance, s ²	HETP, μm	skew factor
method I (Δz = 500 μm, Δt = 4.0 s)	400.0 600.0	1066.7 1199.9	1000 500	0.04 0.00
method II (Δz = 1000 μm, Δt = 2.0 s)	400.0 600.0	266.7 1200.0	250 500	0.20 0.17
method III (Δz = 250 μm, Δt = 1.0 s)	400.0 600.0	666.7 1200.0	625 500	0.09 0.09
Craig model (Δz = 600 μm, Δt = 0.4 s)	400.0 600.0	480.0 1200.0	450 500	0.13 0.13

^aConditions: column length $L = 15$ cm, dead time $t_m = 100$ s, linear velocity $u = 0.15$ cm/s, $k' = 3$ and 5 . Retention times, variances, and skew factors were calculated from the weighted sums $\sum_i C_{L,t} t^n$ according to the method of moments (25).

continues with a constant ratio through the entire grid. In nonlinear chromatography, however, this ratio varies with the current concentration.

This can be seen most clearly in the Craig model, with a compound for which $\kappa = 1$. For every time interval, the solvent is transferred by one length increment. Only half of the solute is transported with the mobile solvent, since the remainder stays in the stationary phase. In the next cycle, both halves are split up into two parts each, one being carried on and the other kept behind. This produces a concentration profile of $1/4$ to $2/4$ to $1/4$ which is the beginning of a symmetrical binomial distribution (22–24). If the κ value is not equal to one, or if a different grid spacing is used, the profile will not be perfectly symmetrical at first. After a sufficient number of distribution steps, however, all three methods will produce a nearly Gaussian distribution curve (23, 24).

On the right-hand side of Figure 2, the first few steps are indicated by arrows, and Table I gives examples for the numbers generated. Like the natural behavior represented by the Einstein equation (25), method II produces a distribution that is symmetrical along the column. With method I the projection onto the time axis is symmetrical, and with method III it is symmetrical toward the diagonal of the grid. This can also be seen from the results in Table I. For the three methods, the grid spacing was chosen so that the concentrations are split up into equal parts. With the Craig model this would have been possible only for a κ value of 1, since the solvent has to move by exactly one Δz per Δt .

When the peaks of the simulated chromatogram are evaluated (Table II), the skew factor for method II corresponds very well to the value expected when a symmetrical peak is eluted (29), whereas that for method I is unnaturally small.

The band broadening produced by the migration through the grid can be calculated by using a relationship previously derived for the variance of an unsymmetrical binomial distribution (30)

$$\sigma_g^2 = rp(1-p) \quad (5)$$

In eq 5, the variance is given in the corresponding units of the grid, r is the number of distribution steps, and p and $1-p$ are the fractions in which the contents of one cell are split up. For method I the variance σ_g^2 is produced parallel to the time axis and is therefore equal to $\sigma_z^2/\Delta t^2$. The number of segments of the column is $L/\Delta z$, and the corresponding value for p is found in eq 2. Similar reasoning leads to the expressions for the other two methods

method I (symmetrical in time)

$$\sigma_t^2 = \Delta t^2 \sigma_g^2 \quad r = L/\Delta z \quad p = 1/P$$

method II (symmetrical in space)

$$\sigma_z^2 = \Delta z^2 \sigma_g^2 \quad r = t_r/\Delta t \quad p = P$$

method III (symmetrical with respect to the diagonal)

$$\sigma_z^2 = \left(\Delta z \sigma_g + \Delta t \sigma_g \frac{u}{\kappa + 1} \right)^2 \\ = \Delta z^2 \sigma_g^2 (1 + P)^2$$

$$r = \frac{L}{\Delta z} + \frac{t_r}{\Delta t} \\ = \frac{L}{\Delta z} \left(1 + \frac{1}{P} \right)$$

$$p = \frac{P}{1 + P} \\ = \frac{1}{1 + (1/P)}$$

The expressions for method III are more complicated since the contributions of both coordinates have to be included. The number of distribution steps is equal to the sum of the numbers of space and time intervals. Likewise, both the projections of the standard deviation σ_g on the time and length axes are added and then the time contribution σ_t is converted to the equivalent standard deviation in length units.

Once we have found the appropriate parameters for eq 5, we can calculate the height equivalent to a theoretical plate, $H = \sigma_z^2/L$ or $H = L(\sigma_t^2/t_r^2)$. For the three methods considered, band broadening consists of the same two terms, varying only in the sign

method I

$$H = -\Delta z + \frac{u}{\kappa + 1} \Delta t$$

method II

$$H = +\Delta z - \frac{u}{\kappa + 1} \Delta t$$

method III

$$H = +\Delta z + \frac{u}{\kappa + 1} \Delta t \quad (6)$$

These equations show that the dispersion produced by the accumulation in the individual band propagation steps depends on the step sizes Δz and Δt and on the angle under which the sample migrates through the grid, as determined by its κ value. For the first two methods H becomes zero when the concentration travels along the diagonal of the grid. For κ values beyond this limit the concentration profiles would start oscillating wildly and the corresponding HETP values would appear negative, which is physically meaningless.

Now it is possible to choose the appropriate grid spacing that will produce the desired amount of band broadening. This was done in the examples discussed in Figure 3 and Table II. The chromatograms were calculated for a binary mixture (linear isotherms) by using the methods I to III and the Craig method. The κ_0 or k' values are 3 and 5, respectively. In all cases, the second peak has an HETP value of 500 μm. The profiles calculated for this peak by the four methods coincide on all four chromatograms. For the first peak, with $k' = 3$, the values of the HETP were between 250 and 1000 μm, depending on the method used.

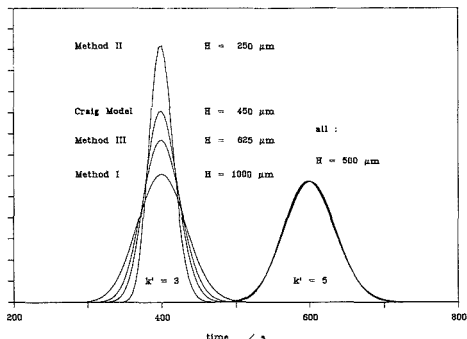


Figure 3. Chromatogram of two compounds ($k'_0 = 3$ and $k'_0 = 5$) calculated according to four different methods (linear isotherms). Column length $L = 15$ cm, dead time $t_m = 100$ s. Grid spacing: method I, $\Delta z = 500 \mu\text{m}$, $\Delta t = 4.0$ s; method II, $\Delta z = 1000 \mu\text{m}$, $\Delta t = 2.0$ s; method III, $\Delta z = 250 \mu\text{m}$, $\Delta t = 1.0$ s; Craig model, $\Delta z = 600 \mu\text{m}$, $\Delta t = 0.4$ s.

Equation 6 indicates also that we can obtain the same value of H with many different pairs of values of Δz and Δt . For each method there is one choice of the normalized propagation velocity, P , that leads to an exactly symmetrical distribution process (see Table I and second peak in Figure 3). For method I this corresponds to a value of 2 of the Courant number, P , equal to the one already recommended in the literature (17, 21). This choice has the further advantage that the resulting plate height is equal to the grid spacing, Δz , or, conversely, that the length increment is equal to the theoretical plate height. However, other combinations can be employed equally well, as long as P is kept greater than one.

For the other two methods the symmetrical case does not seem to have any particular significance. The corresponding values for P are 0.5 and 1, respectively, and the theoretical plate heights are 0.5 or 2 times as long as the grid spacing along the column length. Only at high retention does the plate height for both methods II and III approach Δz .

This is also true for the Craig model, which is a special case of method II. Originally, the Craig machine had served to introduce the concept of theoretical plates into chromatography. As in distillation, each stage represents one equilibration step, and each such step improves the quality of the separation. Therefore the height of one stage can be taken as a measure of the efficiency of the column. However, this works only for continuous processes. When, for the simulation of chromatograms, time is also digitalized, we must expect that additional sources of dispersion arise (e.g., see the discussion of binomial and Poisson type distributions in ref 24). Only with infinitely small time increments or at infinitely high retention can we restore in the Craig model the equivalence between Δz and the height of a theoretical plate.

IV. SOLUTION OF THE MASS BALANCE EQUATION

In the preceding two sections we have explained a procedure by which a solute is moved stepwise down the column, until the simulated chromatogram is generated and we have discussed the properties of this procedure. A different approach to solve the same problem is based on the use of the partial differential equation which states the mass balance of a compound in a liquid chromatography column (17, 31)

$$u \frac{\partial C}{\partial z} + \frac{\partial C}{\partial t} + F \frac{\partial Q}{\partial t} = D \frac{\partial^2 C}{\partial z^2} \quad (7a)$$

where Q is the concentration of the compound in the sta-

tionary phase and F is the phase ratio (assumed to be equal to unity in the previous sections). Assuming a semi-equilibrium model, $Q \approx q$, where q is the concentration in the stationary phase in equilibrium with the concentration C in the mobile phase, as given by the isotherm. This equation is often written under an equivalent form, where we define k' as equal to $F(dq/dC)$ in nonlinear chromatography

$$u \frac{\partial C}{\partial z} + (k' + 1) \frac{\partial C}{\partial t} = D \frac{\partial^2 C}{\partial z^2} \quad (7b)$$

This definition of k' is a classical extension of the k' concept (14, 17, 18) but should probably be avoided because of potential confusions. To eliminate these problems, we have used in the previous sections the symbol κ for the mass distribution ratio. In linear chromatography, κ and k' are equal and can be used interchangeably. We continue with κ in the present section.

The net flux of solute into a volume element of the column results in its accumulation in the mobile and stationary phases. The factor $k' + 1$ relates the mobile phase concentration to the total amount in both phases. According to Fick's second law, all concentration gradients are eroded by diffusion (right-hand side of the equation). When diffusion can be neglected, this part is set to zero. Equation 7a becomes

$$u \frac{\partial C}{\partial z} + (\kappa + 1) \frac{\partial C}{\partial t} \approx 0 \quad (8)$$

In the simple case of a linear isotherm (29, 32), eq 8 can be solved in closed form. When the adsorption isotherm is nonlinear, and if diffusion has to be taken into account, however, no analytical solution of eq 7 is available. A numerical solution must be calculated by iterative integration over time and space. For this purpose the finite difference method has been used (14, 17, 21). In this section we discuss the case of "linear, ideal chromatography", in which we assume the isotherm to be linear, the two phases to be always in equilibrium, and that there is no band broadening of kinetic origin. The extension to nonlinear chromatography and the effect of axial dispersion are treated in the next two sections. We use eq 7b and 8 only in the case of linear chromatography. In nonlinear chromatography, eq 7a is used.

There are two different ways to replace each of the two differential quotients in eq 8 by finite difference quotients, if we use the three previous points in the grid (Figure 1), located at positions $(z-1, t)$, $(z, t-1)$, and $(z-1, t-1)$. Since two positions in the column are used, the change in concentration over time can be given for both locations. Likewise, for the concentration gradient both times can be used

$$\begin{aligned} \text{(a)} \quad \frac{\partial C}{\partial z} &= \frac{C_{z,t} - C_{z-1,t}}{\Delta z} & \text{(c)} \quad \frac{\partial C}{\partial t} &= \frac{C_{z,t} - C_{z,t-1}}{\Delta t} \\ \text{(b)} \quad \frac{\partial C}{\partial z} &= \frac{C_{z,t-1} - C_{z-1,t-1}}{\Delta z} & \text{(d)} \quad \frac{\partial C}{\partial t} &= \frac{C_{z-1,t} - C_{z-1,t-1}}{\Delta t} \end{aligned}$$

This allows four different combinations that can be inserted into the differential equation (8). The equation is then rearranged to isolate the new concentration $C_{z,t}$ and express it in terms of the previously known concentrations. This procedure gives three equations which are identical with the three eq 2, that result from the "propagation through a grid" approach

method I with (a) and (d)

$$C_{z,t} = \left(1 - \frac{1}{P}\right) C_{z-1,t} + \frac{1}{P} C_{z-1,t-1}$$

method II with (b) and (c)

$$C_{z,t} = (1 - P) C_{z,t-1} + P C_{z-1,t-1}$$

method III with (a) and (c)

$$C_{z,t} = \frac{1}{1+P}C_{z,t-1} + \frac{P}{1+P}C_{z-1,t}$$

The fourth equation, combination of (b) and (d), is useless, since neither term contains $C_{z,t}$.

Other computational schemes, using other combinations of values of the concentration calculated for other positions on the grid (e.g., at $(z-2,t)$ or $(z,t-2)$), can be used if needed, but their consideration is not justified for the solution of the present problem.

Depending on the method chosen, it may be easier to carry out the successive calculations of $C_{z,t}$ over time for every position or over the length of the column for every time.

The two approaches—propagation through a grid and solution of the mass balance equation—are therefore equivalent and can be used interchangeably to explain the band migration and to account for the results predicted by the theory of nonlinear chromatography. In the following sections we extend this comparison to the band broadening resulting from computational errors.

V. ADAPTATION TO NONLINEAR CHROMATOGRAPHY

As long as a linear adsorption isotherm is used, the mass distribution ratio κ for one compound stays the same for all points in the column and at all times. This greatly simplifies the equations for band propagation used in the preceding sections. For nonlinear chromatography, however, we must carry out the whole derivation again, using a concentration-dependent distribution ratio. Thus, κ has now become implicitly a function of time and position. For the overloaded elution of a pure compound, κ depends on the local concentration, as shown in eq 1 for a Langmuir isotherm. When the elution of a multicomponent mixture is simulated, a suitable competitive isotherm has to be chosen (6, 8, 9, 18, 33). Then, the local value of κ depends on the concentrations of all the compounds involved in the separation. Any adsorption isotherm can be used, as long as κ is given as the ratio of the amounts of the solute in the stationary and the mobile phase of one cell.

There are two different ways to derive the proper finite difference equation for the numerical calculation of solutions of eq 7a, either by extending the finite difference equations written in the previous section or by writing directly the finite difference equations equivalent to eq 7a (with $D \approx 0$, as in the ideal model).

In order to write directly the finite difference equation equivalent to eq 7a, we must include one of the following two differences for the derivative of the stationary phase concentration:

$$(c) \quad \frac{\partial q}{\partial t} = \frac{q_{z,t} - q_{z,t-1}}{\Delta t}$$

$$(d) \quad \frac{\partial q}{\partial t} = \frac{q_{z-1,t} - q_{z-1,t-1}}{\Delta t}$$

In order to be consistent, the same locations must be used to calculate the two concentration differentials. Then, we obtain the following difference equations:

method I with (a) and (d)

$$u \frac{C_{z,t} - C_{z-1,t}}{\Delta z} + \frac{C_{z-1,t} - C_{z-1,t-1}}{\Delta t} + F \frac{q_{z-1,t} - q_{z-1,t-1}}{\Delta t} = 0$$

method II with (b) and (c)

$$u \frac{C_{z,t-1} - C_{z-1,t-1}}{\Delta z} + \frac{C_{z,t} - C_{z,t-1}}{\Delta t} + F \frac{q_{z,t} - q_{z,t-1}}{\Delta t} = 0$$

method III with (a) and (c)

$$u \frac{C_{z,t} - C_{z-1,t}}{\Delta z} + \frac{C_{z,t} - C_{z,t-1}}{\Delta t} + F \frac{q_{z,t} - q_{z,t-1}}{\Delta t} = 0$$

Alternatively, and using the proper local κ values, the finite difference equation equivalent to the mass balance equation (8) can be written in one of the three following forms, depending on the combination of differences used:

method I with (a) and (d)

$$u \frac{C_{z,t} - C_{z-1,t}}{\Delta z} + \frac{(\kappa_{z-1,t} + 1)C_{z-1,t} - (\kappa_{z-1,t-1} + 1)C_{z-1,t-1}}{\Delta t} = 0$$

method II with (b) and (c)

$$u \frac{C_{z,t-1} - C_{z-1,t-1}}{\Delta z} + \frac{(\kappa_{z,t} + 1)C_{z,t} - (\kappa_{z,t-1} + 1)C_{z,t-1}}{\Delta t} = 0$$

method III with (a) and (c)

$$u \frac{C_{z,t} - C_{z-1,t}}{\Delta z} + \frac{(\kappa_{z,t} + 1)C_{z,t} - (\kappa_{z,t-1} + 1)C_{z,t-1}}{\Delta t} = 0$$

The two series of equations are obviously identical, because of the definition of $\kappa = q/C$.

Clearly, the equation for method I is the easiest to solve, since it contains only one variable, the solute concentration in the mobile phase $C_{z,t}$, that refers to the new cell. For method II, by contrast, only the total amount per unit volume, $C(\kappa + 1)$, is explicitly given. As $\kappa_{z,t}$ depends on $C_{z,t}$, the new mobile phase concentration has to be calculated iteratively. The same applies to method III. Instead of being able to use the simple eqs 2, we have to derive $C_{z,t}$ from the following equations:

method I with (a) and (d)

$$C_{z,t} = C_{z-1,t} - \frac{\Delta z}{u \Delta t} [(\kappa_{z-1,t} + 1)C_{z-1,t} - (\kappa_{z-1,t-1} + 1)C_{z-1,t-1}]$$

method II with (b) and (c)

$$C_{z,t} = \frac{(\kappa_{z,t-1} + 1)C_{z,t-1} - \frac{u \Delta t}{\Delta z}(C_{z,t-1} - C_{z-1,t-1})}{\kappa_{z,t} + 1}$$

method III with (a) and (c)

$$C_{z,t} = \frac{C_{z-1,t} + \frac{\Delta z}{u \Delta t}(\kappa_{z,t-1} + 1)C_{z,t-1}}{1 + \frac{\Delta z}{u \Delta t}(\kappa_{z,t} + 1)}$$

Method I has been used extensively and quite successfully in most of our previous work with Golshan-Shirazi, Lin, and Ghodbane (4, 8-11, 14, 17-21, 27), with a Courant number equal to 2. Method II is the backward finite difference (explicit form). We have used it with a Courant number of 0.5 and found it less attractive than method I at high column efficiencies (most of our simulation work assumes column efficiency to be between 2000 and 10 000 theoretical plates), mainly because of the excessive computer time required. Method III is the forward finite difference method (implicit form) used by Lin et al. (34).

Conservation of Mass. With method I every concentration is split up into two parts that together with one contribution each from the two neighboring cells make up the new concentration values at the new position. So all the mass in one row of the grid is transferred to the next row. The summation over all concentration values in one row gives the same result for all rows—over time, every point in the column will

see the same amount of solute pass in the mobile phase.

$$\sum_t C_{z,t} \Delta t = \text{area under the chromatogram}$$

This seems to be different with method II. Here it is the total amount, given in concentration units, that is passed on from two cells at the previous time. When we sum up the quantity $C(\kappa + 1)$ over any column of the grid, we again have conservation of mass: at all times the total amount in both phases together is constant. Summation over the mobile phase concentrations alone, however, will reflect only what is currently in the mobile phase. With an isotherm of the Langmuir type, the amount of solute in the eluent will be very high following the injection, and it will slowly decrease toward the fractional typical of linear conditions, as the sample is diluted.

$$\sum_z C_{z,t}(\kappa_{z,t} + 1) \frac{\Delta z}{u} = \text{area under the chromatogram}$$

Though the distribution processes are different, both relationships are found to be true for all three methods.

VI. ERROR IN THE SOLUTION OF THE MASS BALANCE EQUATION

In a previous section we have explained the origin and discussed the amount of band broadening generated by the three propagation methods used for the simulation of the band migration through a chromatographic column. Expressions have been derived above for the height equivalent to a theoretical plate which results from the "numerical diffusion" introduced by the need to split up the amount of one cell between the next two cells at each step of the propagation through the digitized space (eqs 6). It is also possible to derive these expressions from the algorithm of numerical integration of eq 8 by finite differences.

When the differential quotients of the mass balance equation are replaced by finite difference quotients, a linear approximation is made, and the higher order terms are neglected. Thus, we can expect the numerical solution of eq 8 to deviate from the true solution of the ideal model (which assumes that there is no diffusion and that equilibrium is always achieved between phases). This error leads to some additional band broadening and smoothing. The effect appears very similar to the one due to axial dispersion but is caused by "numerical diffusion". To calculate the error made, we may use the Taylor expansions of the four concentrations involved in the finite difference quotients and truncate them after the quadratic terms

$$C_{z,t} = \text{reference}$$

$$C_{z,t-1} = C_{z,t} - \Delta t \frac{\partial C}{\partial t} + \frac{\Delta t^2}{2} \frac{\partial^2 C}{\partial t^2} - \dots$$

$$C_{z-1,t} = C_{z,t} - \Delta z \frac{\partial C}{\partial z} + \frac{\Delta z^2}{2} \frac{\partial^2 C}{\partial z^2} - \dots$$

$$C_{z-1,t-1} = Z_{z,t} - \Delta t \frac{\partial C}{\partial t} - \Delta z \frac{\partial C}{\partial z} + \frac{\Delta t^2}{2} \frac{\partial^2 C}{\partial t^2} + \frac{\Delta z^2}{2} \frac{\partial^2 C}{\partial z^2} + \Delta t \Delta z \frac{\partial^2 C}{\partial t \partial z} - \dots$$

When these expressions are inserted into the general solution of the propagation model, eq 3, we obtain an expression relating the reference concentration, $C_{z,t}$, and the first and second derivative terms. Thus, on the right-hand side of the new equation there are three terms with the reference concentration, four terms containing the first derivatives with respect to time and space, and five second derivative terms, all multiplied by combinations of the factors α , β , and γ . Use of the two basic relationships 4 between these three coefficients permits considerable simplification.

The concentration terms cancel out. The four terms containing the first derivatives combine to give the mass balance without the diffusion term (eq 8). Therefore, the sum of the remaining five second derivative terms must correspond to the diffusion term of the complete mass balance equation (7a). The time dependence can be transformed into a pure position dependence according to (ref 19, eqs 42 and 43)

$$\frac{\partial^2 C}{\partial t \partial z} = -\frac{u}{k' + 1} \frac{\partial^2 C}{\partial z^2} \quad \frac{\partial^2 C}{\partial t^2} = \frac{u^2}{(k' + 1)^2} \frac{\partial^2 C}{\partial z^2}$$

Using these relationships, which are valid for the ideal model, permits the determination of the coefficient of the derivative $\partial^2 C / \partial z^2$. This coefficient can be identified with the apparent diffusion coefficient D_a . Since $H = 2D_a/u$, we obtain the general equation relating the plate height, the grid spacing, and the way in which the concentration in the new cell depends on the concentrations in the three preceding cells

$$H = \Delta z \left(P \frac{1 + \beta}{1 - \beta} - 1 \right)$$

This equation is identical with the three relations (6) derived from considerations on the binomial distribution. The same result is also obtained when we introduce the three-term Taylor expansions in the mass balance equation (8) (21).

In the above derivation the series expansions were truncated after the quadratic terms. This means that we included only part of the error in the expression for band broadening. Still, the result is identical with the one obtained from the binomial distribution. The remaining error in both derivations is easily explained for the binomial distribution: by dividing length and time in intervals, we have replaced the smooth curve by a step function. For a great number of steps the deviation from a smooth Gaussian curve is quite small and is comparable in magnitude to round-off errors.

VII. CONTROL OF NUMERICAL DIFFUSION

The previous discussion shows that band broadening due to the propagation process depends both on grid increments, Δz and Δt , and on the current κ value. We must choose the proper increment values for the peak of lowest efficiency produced and then add diffusion, if needed, to correct for insufficient band broadening.

Choice of Δt and Δz . In the examples of Figure 3 and Table II, the choice of Δz and Δt was based on the characteristics of the second peak ($\kappa_0 = 5$). Under linear conditions, a symmetrical binomial distribution was produced for this peak with the HETP given. For method I these values are those recommended in the literature (17, 21). The efficiency of the first peak cannot be controlled independently, however. Depending on the method used, the first peak is either much too narrow or too broad for the result of the simulation to look realistic (see Figure 3).

When the equilibrium isotherm is not linear, the local κ value of even a pure compound changes over time, during the passage of the band. Furthermore the extent of this change is different for the three methods and also depends on the grid increments. In Figure 4, we show the profiles calculated by the three different methods, using the same values of the increments, Δz and Δt , as in Figure 3, corresponding to a plate height of 500 μm for $\kappa_0 = 5$ (second peak), i.e., a column efficiency of 300 theoretical plates. A Langmuir isotherm was used and the sample amount injected was equal to 10% of the column saturation capacity. Results of the same procedure are shown in Figure 5 for a 5000 theoretical plate column ($H = 30 \mu\text{m}$).

At the extreme tail of the peak in Figure 4, the concentration is low enough to allow migration of the molecules at the velocity corresponding to $\kappa_0 = 5$, and the profiles calculated

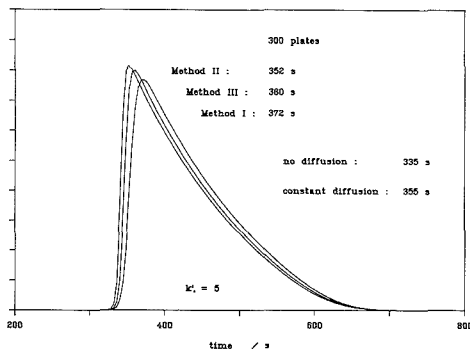


Figure 4. Overloaded chromatogram of one compound ($k'_0 = 5$) calculated according to three different methods (Langmuir isotherm at a load of 10% of the column capacity (4)). Grid spacing: method I, $\Delta z = 500 \mu\text{m}$, $\Delta t = 4.0 \text{ s}$; method II, $\Delta z = 600 \mu\text{m}$, $\Delta t = 0.4 \text{ s}$; method III, $\Delta z = 250 \mu\text{m}$, $\Delta t = 1.0 \text{ s}$; (Craig model, $\Delta z = 600 \mu\text{m}$, $\Delta t = 0.4 \text{ s}$).

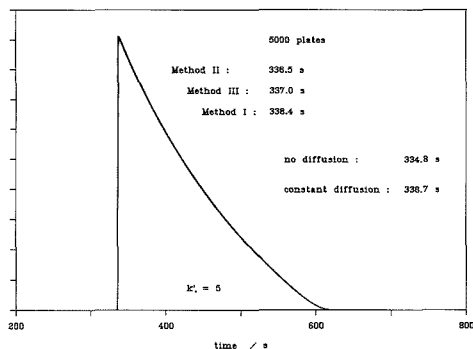


Figure 5. Same as Figure 4, but higher efficiency: 5000 plates. Grid spacing: method I, $\Delta z = 30 \mu\text{m}$, $\Delta t = 0.240 \text{ s}$; method II, $\Delta z = 36 \mu\text{m}$, $\Delta t = 0.024 \text{ s}$; method III, $\Delta z = 15 \mu\text{m}$, $\Delta t = 0.060 \text{ s}$.

by all three methods coincide. The position of the three fronts and band maxima, however, differs to a significant extent. From the analytical solution of the mass balance equation for the ideal case (4), we know that without diffusion we would get a vertical front at 335 s, followed by a tail that extends to the retention time of linear chromatography. With axial dispersion, the concentration in the peak maximum decays faster than in the ideal model and the band front slows down earlier. When numerical diffusion is kept constant for every distribution step, as shown later, the peak maximum is eluted at 355 s for the 300-plate column (Figure 4). The results given by the three simple methods, which introduce uncontrolled diffusion, scatter around this later value (Figure 4). With method II, for which band broadening decreases with decreasing κ , the peak maximum is narrower than it should be and, therefore, it is eluted earlier, since the velocity increases with increasing concentration. For the other two methods, the effective band broadening at low values of κ is higher than the HETP value chosen and the retention times are higher, too.

It should be emphasized, however, that the marked differences between the results obtained (see Figure 4) are magnified by the low value of the column efficiency simulated. For the 5000 theoretical plate column, the differences between the retention times predicted by the ideal model (335 s) and by the three simple numerical methods discussed (336.5–338 s) is hardly significant. The profiles can barely be distin-

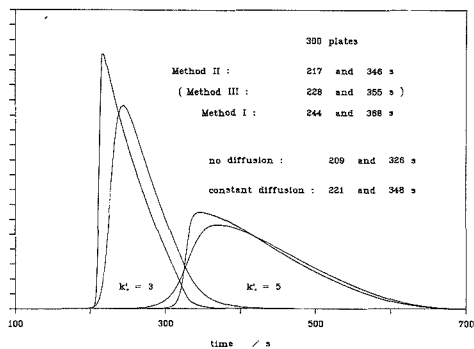


Figure 6. Overloaded chromatogram of a two-component mixture (ratio 1:1, $k'_0 = 3$ and 5) calculated according to three different methods (competitive Langmuir isotherm at a cumulative load of 10% of the column capacity). Grid spacing is the same as that given in Figure 4.

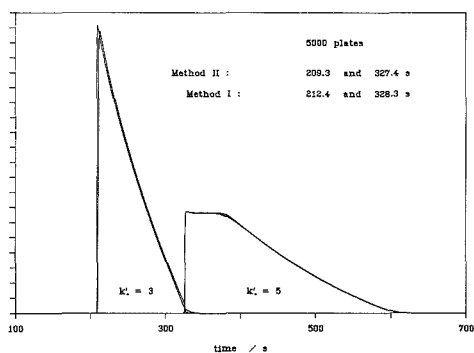


Figure 7. Same as Figure 6, but higher efficiency: 5000 plates. Grid spacing is the same as that given in Figure 5.

guished (see Figure 5). Thus, either one of the three methods discussed here can be used conveniently to simulate the chromatograms obtained with a conventional packed column in preparative liquid chromatography, where the nominal efficiency almost always exceeds a few thousand plates. For columns with a lesser efficiency, a diffusion correction becomes necessary. Alternatively, it may be more appropriate to treat the simulation problem with a kinetic model when the mass transfer kinetics becomes so slow that the column efficiency is of the order of a few hundred plates or fewer (34).

Figures 6 and 7 show the chromatograms calculated for the same 1:1 binary mixture on a 300 and a 5000 theoretical plate column. Competitive binary Langmuir isotherms have been used (18). For the sake of clarity, only the profiles predicted by methods I and II have been shown in these figures. Again, the results are very similar for the 5000-plate column (Figure 7), but quite different for the 300-plate column (Figure 6). In the latter case, method II predicts a much steeper profile than method I but gives nearly the exact retention time. In spite of the high sample load, this result does not seem to be quite in agreement with the low column efficiency. Certainly, at least for the low-efficiency columns, a diffusion correction is necessary.

Finally, Figures 8 to 11 show the results of calculations made for two binary mixtures of different compositions, 1:5 and 5:1, respectively, using the same competitive binary Langmuir isotherms as for Figures 6 and 7, and columns having 300 and 5000 theoretical plates, respectively. The differences are quite

Chart II

	I	II	III
$\Delta z = H_t$	$\frac{1}{\kappa_{\max}}$	1	1/2
$\Delta t = \frac{H_t}{u}$	$\frac{\kappa_{\max} + 1}{\kappa_{\max}}$	1	1/2
$\frac{L}{\Delta z} \frac{t_r}{\Delta t} = \frac{L^2(k' + 1)}{H_t^2}$	$\frac{\kappa_{\max}^2}{\kappa_{\max} + 1}$	1	4

significant for the 300-plate column (Figures 8 and 10). On the contrary, the differences are marginal for the 1:5 mixture (Figure 9) and the first component of the 5:1 mixture (Figure 11) both on the 5000-plate column. In the latter case, the Craig model predicts a very steep front for the band of the second component, in marked disagreement with method I (8, 18, 20).

If we want overall band broadening to be independent of κ , we have to keep the numerical diffusion, H_n , smaller than the target plate height, H_t , even for the broadest possible peak. Then we apply an appropriate amount of additional diffusion to all peaks that are too narrow. With methods I and III the highest value of H_n is found for $\kappa = 0$, and we have to find a pair of Δz and Δt values that will give the desired band broadening for this unretained peak. The efficiency of all other peaks can be adjusted later. In method II, including the Craig model, the highest band broadening will occur at very high retention and the grid spacing is chosen with respect to $\kappa = \infty$.

Another constraint is the limit in the κ range due to the band propagation mechanism in methods I and II ($P \geq 1$ and $P \leq 1$, respectively; see definition of P). Of course, all κ values considered must satisfy the proper inequality. In linear chromatography this condition is easy to meet, but in overloaded elution the local values of κ depend on the respective concentrations. With Langmuir isotherms, for example, the program will encounter κ values between κ_0 at infinite dilution, in the tail of the peak, and almost zero at high concentration, right after injection. With method I this is not a problem, since this method can handle all low κ values. Method III does not have any limit at all. For method II, however, Δz and Δt have to be chosen to permit the handling of $\kappa = 0$. In this case the general method II degenerates to the special case of the Craig model.

Finally, computation time should be kept as short as possible. If we want to monitor the band migration through a column of length L from its injection until the peak maximum is eluted, we have to calculate concentration values for $L/\Delta z$ column segments at $t_R/\Delta t$ times. This is the number of points in the complete grid. Therefore, we will try to use the largest increment values possible. In the following, these criteria are applied to the three methods:

method I

$$H_n = -\Delta z + \frac{u}{\kappa + 1} \Delta t$$

broadest peak (at $\kappa = 0$): $H_t = H_n^0 = -\Delta z + u \Delta t$

$$\text{upper limit (at } \kappa_{\max}\text{): } \Delta z = \frac{u}{\kappa_{\max} + 1} \Delta t$$

$$\Rightarrow \Delta z = \frac{1}{\kappa_{\max}} H_t \quad \Delta t = \frac{\kappa_{\max} + 1}{\kappa_{\max}} \frac{H_t}{u}$$

method II

$$H_n = +\Delta z - \frac{u}{\kappa + 1} \Delta t$$

broadest peak (at $\kappa = \infty$): $H_t = H_n^\infty = \Delta z$

lower limit (at $\kappa_{\min} = 0$): $\Delta t = \Delta z/u$

$$\Rightarrow \Delta z = H_t \quad \Delta t = H_t/u$$

method III

$$H_n = +\Delta z + \frac{u}{\kappa + 1} \Delta t$$

broadest peak (at $\kappa = 0$): $H_t = H_n^0 = \Delta z + u \Delta t$

fastest computation: maximize $\Delta z \Delta t$

$$\Rightarrow \Delta z = \frac{1}{2} H_t \quad \Delta t = \frac{1}{2} \frac{H_t}{u}$$

Chart II compares the preferred choices of Δz and Δt for the three methods.

The last line of this table gives an estimate of the computing time needed with each of the three methods. It is proportional to the number of grid points for which the concentration values are calculated. The result shows that with limited diffusion the Craig model will be the most efficient, whereas the other two are roughly equal at κ_0 values around 5.

Additional Diffusion. The choice of Δz and Δt made above assures that the numerical diffusion H_n caused by band propagation will always be lower than the target value H_t . In order to simulate the band broadening effect properly, we must now introduce a variable amount of additional diffusion depending on the local κ values. Fick's second law

$$\frac{\partial C}{\partial t} = D \frac{\partial^2 C}{\partial z^2}$$

or its difference version

$$\frac{C_{z,t+1} - C_{z,t}}{\Delta t} = D \frac{C_{z+1,t} - 2C_{z,t} + C_{z-1,t}}{\Delta z^2}$$

states that for each band propagation step the concentration $C_{z,t}$ must be redistributed over the three positions $z - 1$, z , and $z + 1$. The apparent diffusion coefficient, D , corresponds to a resulting HETP value

$$D = \frac{uH}{2(\kappa + 1)}$$

Since part of the target HETP is already supplied by the propagation mechanism (eq 8), we must supply the rest by additional diffusion. The appropriate amount of additional band broadening, H_x , is given by

$$H_x = H_t + H_x$$

$$H_x = H_t - \left(\pm \Delta z \pm \frac{u}{\kappa + 1} \Delta t \right)$$

With our choice of Δz and Δt , this leads to the following values for the coefficients of this extra diffusion, D_x , at the local κ value (D_x is given as the fraction of mass that is transferred to each one of the neighboring cells):

method I

$$D_x \frac{\Delta t}{\Delta z^2} = \frac{1}{2(\kappa + 1)^2} \kappa (\kappa_{\max} + 1)^2$$

method II

$$D_x \frac{\Delta t}{\Delta z^2} = \frac{1}{2(\kappa + 1)^2}$$

method III

$$D_x \frac{\Delta t}{\Delta z^2} = \frac{1}{2(\kappa + 1)^2} \kappa$$

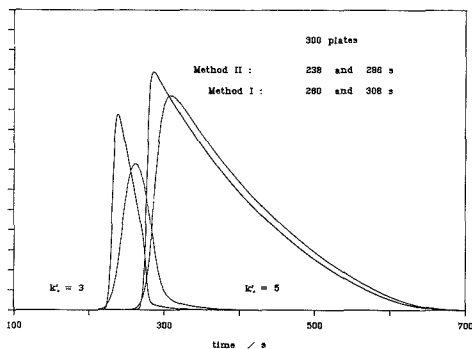


Figure 8. Same as Figure 6, 300 plates, ratio 1:5.

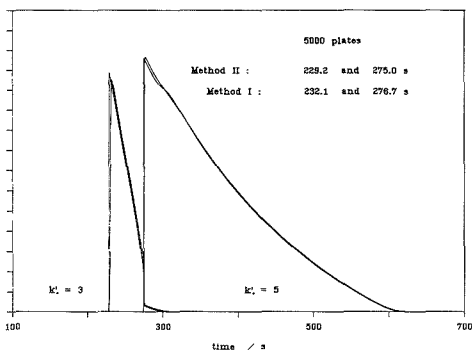


Figure 9. Same as Figure 8, 5000 plates, ratio 1:5.

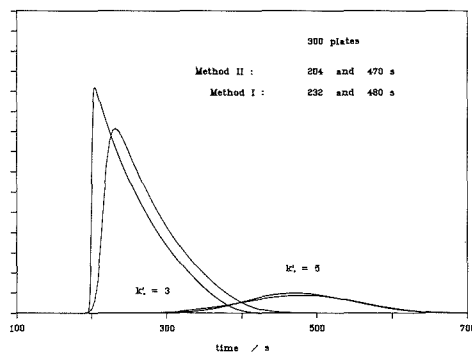


Figure 10. Same as Figure 6, 300 plates, ratio 5:1.

With these values of the additional diffusion coefficients, we can now adjust the dispersion after every propagation step. This leads, for example, to the chromatograms shown in Figures 12 and 13. The difference between the results obtained with the three methods has been reduced to the effect of small round-off errors. This shows that, properly corrected as explained, the three methods can be used interchangeably.

When the amount of additional diffusion needed after one step of propagation is very high, however, a single diffusion step would transfer more mass from position z to the neighboring positions than was present in the cell. The resulting negative concentration values would lead to uncontrollable oscillations of the concentration profile. In this case each diffusion process is split up into several consecutive steps with

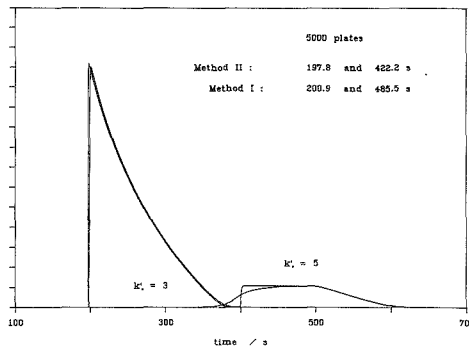
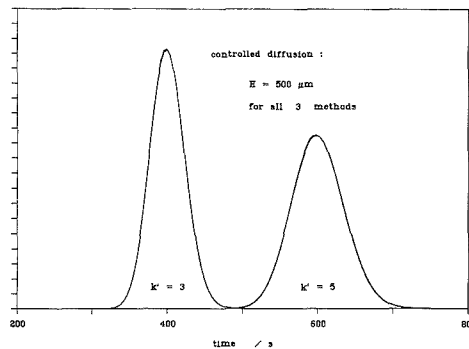
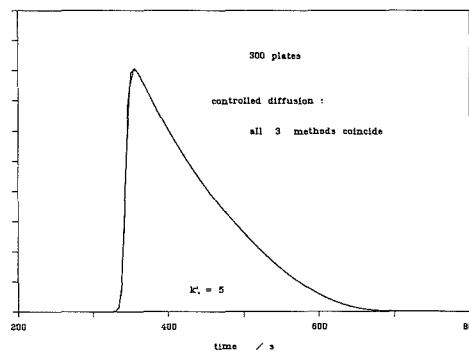


Figure 11. Same as Figure 10, 5000 plates, ratio 5:1.

Figure 12. Same as Figure 3, four different methods with diffusion control (300 plates). Grid spacing: method I, $\Delta z = 100 \mu\text{m}$, $\Delta t = 0.40 \text{ s}$; method II, $\Delta z = 500 \mu\text{m}$, $\Delta t = 0.33 \text{ s}$; method III, $\Delta z = 250 \mu\text{m}$, $\Delta t = 0.17 \text{ s}$ (Craig model, $\Delta z = 500 \mu\text{m}$, $\Delta t = 0.33 \text{ s}$).Figure 13. Same as Figure 4, three different methods with diffusion control (300 plates). Grid spacing: method I, $\Delta z = 100 \mu\text{m}$, $\Delta t = 0.40 \text{ s}$; method II, $\Delta z = 500 \mu\text{m}$, $\Delta t = 0.33 \text{ s}$; method III, $\Delta z = 250 \mu\text{m}$, $\Delta t = 0.17 \text{ s}$ (Craig model, $\Delta z = 500 \mu\text{m}$, $\Delta t = 0.33 \text{ s}$).

correspondingly smaller D_x . The maximum amount of diffusion allowed for one step is reached when $1/2 C_{z,i}$ is transferred to each of the neighboring cells. This is the case when:

$$D_x \frac{\Delta t}{\Delta z^2} = \frac{1}{2}$$

With the values chosen for Δz and Δt , however, we find the following worst cases:

method I (at $\kappa = 1$)

$$D_x \frac{\Delta t}{\Delta z^2} = \frac{1}{8}(\kappa_{\max} + 1)^2$$

method II (at $\kappa = 0$)

$$D_x \frac{\Delta t}{\Delta z^2} = \frac{1}{2}$$

method III (at $\kappa = 1$)

$$D_x \frac{\Delta t}{\Delta z^2} = \frac{1}{8}$$

This means that with methods II and III the diffusion coefficients will always be acceptable. With method I, on the other hand, one propagation step will have to be followed by several diffusion steps in practically all cases, making this method by far the slowest.

VIII. CONCLUSION

We have discussed three calculation procedures that can be used to simulate band propagation and band broadening in nonlinear chromatography. To explain their properties, two different approaches have been used. When the amount of "numerical diffusion" due to each propagation step is known, it is possible to control this effect by introducing an additional diffusion step. Since this requires iterative calculations, computation time is increased significantly.

Method I is the easiest and fastest to use as long as the efficiency of the column is large enough that its effect on the bandwidth and the band profile can be neglected. However, it does not correctly reflect the diffusion process found in nature (Einstein equation), as it produces symmetrical peaks over time instead of space. On the other hand, for a highly efficient column and with a significant degree of concentration overload, results which are in good agreement with those of the other methods can be obtained in a much shorter time.

As soon as diffusion has to be controlled, however, method I proves to be the slowest, since band broadening for $\kappa = 0$ has to be kept lower than the target value, which allows a very small amount of numerical diffusion, and diffusion has to be added in several installments. In this case the Craig model, as the special case of method II, is preferable. Another advantage of the Craig method is the fact that it presents no upper limit for high retention values. This is important for the simulation of gradient elution, where initial retention may

be very high, especially in the case of polymers.

The third method was included in this paper for the sake of comparison and completeness. It offers no advantages versus the Craig model but takes longer to calculate. It is not useful in the general case, but its special properties may be important under some particular circumstances.

LITERATURE CITED

- (1) Knox, J. H.; Pyper, H. *J. Chromatogr.* **1986**, *363*, 1.
- (2) Eble, J. E.; Grob, R. L.; Antle, P. E.; Snyder, L. R. *J. Chromatogr.* **1987**, *384*, 25.
- (3) Eble, J. E.; Grob, R. L.; Antle, P. E.; Snyder, L. R. *J. Chromatogr.* **1987**, *384*, 46.
- (4) Golshan-Shirazi, S.; Guiochon, G. *Anal. Chem.* **1988**, *60*, 2364.
- (5) Golshan-Shirazi, S.; Guiochon, G. *J. Phys. Chem.*, in press.
- (6) Eble, J. E.; Grob, R. L.; Snyder, L. R. *J. Chromatogr.* **1987**, *405*, 1.
- (7) Eble, J. E.; Grob, R. L.; Antle, P. E.; Cox, G. B.; Snyder, L. R. *J. Chromatogr.* **1987**, *405*, 31.
- (8) Golshan-Shirazi, S.; Guiochon, G. *J. Phys. Chem.* **1989**, *93*, 4143.
- (9) Golshan-Shirazi, S.; Guiochon, G. *J. Chromatogr.* **1989**, *484*, 125.
- (10) Golshan-Shirazi, S.; Guiochon, G. *Anal. Chem.* **1989**, *61*, 1276.
- (11) Golshan-Shirazi, S.; Guiochon, G. *Anal. Chem.* **1989**, *61*, 1368.
- (12) Stranahan, J. J.; Deming, S. N. *Anal. Chem.* **1982**, *54*, 1540.
- (13) Poppe, H.; Kraak, J. C. *J. Chromatogr.* **1983**, *255*, 395.
- (14) Rouchon, P.; Schonauer, M.; Valentin, P.; Guiochon, G. *Sep. Sci.* **1987**, *22*, 1793.
- (15) Eble, J. E.; Grob, R. L.; Antle, P. E.; Snyder, L. R. *J. Chromatogr.* **1987**, *405*, 51.
- (16) Snyder, L. R.; Cox, G. B.; Antle, P. E. *J. Chromatogr.* **1988**, *444*, 303.
- (17) Guiochon, G.; Golshan-Shirazi, S.; Jaulmes, A. *Anal. Chem.* **1988**, *60*, 1856.
- (18) Guiochon, G.; Ghodbane, S. *J. Phys. Chem.* **1988**, *92*, 3682.
- (19) Lin, B.; Ma, Z.; Guiochon, G. *J. Chromatogr.* **1989**, *484*, 83.
- (20) Ghodbane, S.; Guiochon, G. *Chromatographia* **1988**, *26*, 53.
- (21) Lin, B.; Guiochon, G. *Sep. Sci. Technol.* **1989**, *24*, 31.
- (22) Craig, L. C. *J. Biol. Chem.* **1944**, *155*, 519.
- (23) Martin, A. J. P.; Synge, R. L. M. *Biochem. J.* **1941**, *35*, 1358.
- (24) Keulemans, A. I. M. *Gas Chromatography*; Verver, C. G., Ed.; Reinhold: New York, 1957; pp 106-113.
- (25) Karger, B. L.; Snyder, L. R.; Horváth, Cs. *An Introduction to Separation Science*, 2nd ed.; Wiley-Interscience: New York, 1979.
- (26) Karol, P. *Anal. Chem.* **1989**, *61*, 1937.
- (27) Lin, B.; Golshan-Shirazi, S.; Ma, Z.; Guiochon, G. *Anal. Chem.* **1988**, *60*, 2647.
- (28) Courant, R.; Friedrichs, K. O.; Lewy, H. *Math. Ann.* **1928**, *100*, 32.
- (29) Kucera, E. *J. Chromatogr.* **1965**, *65*, 237.
- (30) Klinkenberg, A.; Sjenitzer, F. *Chem. Eng. Sci.* **1956**, *5*, 258.
- (31) Glueckauf, E. *J. Chem. Soc.* **1949**, 3280.
- (32) Wilson, J. N. *J. Am. Chem. Soc.* **1940**, *62*, 1583.
- (33) Frenz, J.; Horváth, Cs. *AIChE J.* **1985**, *31*, 400.
- (34) Lin, B.; Golshan-Shirazi, S.; Guiochon, G. *J. Phys. Chem.* **1989**, *93*, 3343.

Received for review August 1, 1989. Accepted October 24, 1989. This work was supported in part by Grant CHE-8901382 of the National Science Foundation and by the cooperative agreement between the University of Tennessee and the Oak Ridge National Laboratory.

Bayesian versus Fourier Spectral Analysis of Ion Cyclotron Resonance Time-Domain Signals

Joseph E. Meier and Alan G. Marshall*¹

Department of Chemistry, The Ohio State University, 120 West 18th Avenue, Columbus, Ohio 43210

The frequency-domain spectrum obtained by Fourier transformation (FT) of a time-domain signal is accurate only for a continuous noiseless time-domain signal of infinite duration. For discrete noisy truncated time-domain signals, non-FT (e.g., Bayesian analysis) methods may provide more accurate spectral estimates of time-domain signal frequencies, relaxation time(s), and relative abundances. In this paper, we show that Bayesian analysis of simulated and experimental ion cyclotron resonance (ICR) time-domain noisy signals can produce a spectrum with mass accuracy improved by a factor of 10 or more over that obtained from a magnitude-mode discrete fast Fourier transform (FFT) spectrum. Moreover, Bayesian analysis offers the useful advantage that it automatically estimates the *precision* of its iteratively determined spectral parameters. The main disadvantage of Bayesian analysis is its lengthy computation time compared to that of FFT (hours vs seconds on the same hardware for ~4K time-domain data points); the Bayesian computation time increases rapidly with the number of spectral peaks and (less rapidly) with the number of time-domain data points. Bayesian analysis should thus prove useful for those FT/ICR applications involving relatively few data points and/or requiring high mass accuracy.

INTRODUCTION

Fourier Transform Spectral Analysis. In Fourier transform spectroscopy (1), a (discrete) spectrum is produced by (discrete) Fourier transformation (usually with a fast algorithm (2)) of a digitized time-domain response to an excitation whose duration is short compared to the relaxation time of the time-domain signal. Among several methods for obtaining a frequency-domain discrete spectrum from a time-domain discrete signal, the fast Fourier transform (FFT) (2, 3) has the very great advantage that it can produce a spectrum of the entire Nyquist-limited bandwidth *simultaneously and rapidly* (~1 s for complex FFT of ~32K data, for a typical micro- or minicomputer array processor).

Unfortunately, the FT spectrum represents the "true" spectrum for the system only for a *noiseless, continuous* time-domain signal of *infinite* duration. For example, truncation of a time-domain signal after a *finite* acquisition period broadens the FT spectral peaks and introduces auxiliary "wiggles" ("Gibbs oscillations") in the peak shape (1). Moreover, if a *continuous* time-domain signal is "undersampled" (i.e., digitized at a frequency less than twice the highest ("Nyquist") frequency in the spectrum), then the apparent frequencies of the FT spectral peaks may be shifted ("aliased", "folded-over") from their true spectral frequencies (4). Finally, the presence of random noise in the time-domain signal "corrupts" our knowledge (and the corresponding FT spectral representation) of that signal.

A tacit assumption of the FT approach is that the time-domain and FT frequency-domain representations of a noisy signal are deterministically related, i.e., that the FT spectrum uniquely represents the most we can know about the time-domain signal. However, when noise is present, an infinite number of frequency-domain discrete spectra could equally well represent the time-domain signal, in the sense that the inverse FT of each such spectrum agrees to within the same root-mean-square deviation with the experimental discrete noisy signal. The problem then becomes, what is the "best" spectrum that can be inferred from a noisy time-domain discrete signal?

As discussed in detail elsewhere (1, 5), the answer depends on the definition of "best" and on the number of "constraints" (if any) that limit the functional form of the time-domain signal. For example, the "maximum entropy method" (6) (not to be confused with the "Burg maximum entropy method" (7), which is equivalent to autoregression) produces a maximally smooth probability distribution ("spectrum") whose inverse FT yields a time-domain signal that agrees to within a specified root-mean-square deviation from the actual time-domain discrete noisy signal. Other methods with different constraints and/or different criteria of "best" are variously known as "linear prediction", "autoregression", "all-poles", "poles and zeroes", etc. (1, 5).

Bayesian Analysis. In particular, the "Bayesian" spectral estimation method (8) allows for the introduction of "prior" information about the signal, before attempting to estimate a discrete spectrum. For example, the time-domain signal may be assumed to consist of a sum of exponentially damped sinusoids of different frequencies, amplitudes, phases, and exponential damping constants. In this paper, we describe and apply Bayesian spectral analysis (8) to ion cyclotron resonance mass spectrometry (ICR/MS) time-domain data. We present simulated and experimental examples of Bayesian and FFT spectra of the same time-domain ICR data. Depending on the number of time-domain data points, the number of signal frequencies present, acquisition period, and signal-to-noise ratio, Bayesian spectral analysis may provide more accurate spectral parameter estimates (e.g., superior mass resolution and/or mass accuracy) than those based on least-squares fits to a discrete FFT magnitude-mode spectrum of the same time-domain discrete data.

THEORY

Bayesian Spectral Analysis. Bayesian spectral analysis is the application of Bayes' theorem (8-10) for iterative determination of the most probable spectral estimate for a given time-domain data set, according to any available prior information and assumed functional forms for the signal and noise.

$$P(H/D,I) = \frac{P(H/I) P(D/H,I)}{P(D/I)} \quad (\text{Bayes' theorem}) \quad (1)$$

The terms are defined as follows:

$P(H/D,I)$ is the probability distribution (known as posterior probability, which is a discrete spectrum of the probability

* Author to whom correspondence should be addressed.

¹ Also a member of the Department of Biochemistry.

that there is a signal at each of the discrete spectral frequencies) of the hypothesis (H) (e.g., that the data can be represented as a sum of exponentially damped sinusoids plus noise), conditional on the data (D) and on any prior information (I) (e.g., initial values or probable range of values of one or more particular signal parameters, such as oscillation frequencies, damping constants, or amplitudes).

$P(H/I)$ is the "prior" probability of the hypothesis (i.e., an initial spectral estimate that forms the starting point of the analysis), conditional on the prior information (I).

$P(D/H,I)$ is the "direct" probability distribution for each time-domain data point, conditional on the hypothesis and prior information.

$P(D/I)$ is the "prior" probability distribution of the data, conditional on prior information: i.e., a point-by-point measure of what the time-domain data would be for the given initial "prior" information. In practice, $P(D/I)$ is typically absorbed into a normalization constant and does not affect the estimates for a given signal model (8).

Equation 1 is simply a general abstract property of conditional probabilities, whose consequences are readily understood from a specific signal model (see below). It is fair to note that the definition of the terms and choice of the most appropriate prior distribution in eq 1 are sometimes disputed (10).

Recent experience with the Bayesian family of spectral estimators suggests that it offers a relatively "robust" (i.e., generally applicable, with well-defined range of validity) method for estimating signal frequencies (9, 10). A strength of the Bayesian method is that its accuracy can be tested with a series of increasingly complex signal models (8-10). A hypothesis, H, for which $P(D/H,I)$ is large is more likely to be true than an H for which $P(D/H,I)$ is small (9). Thus, one criterion ("maximum-likelihood method") for evaluating a given hypothesis (signal model) is simply to maximize iteratively (by varying the signal and noise parameters) $P(D/H,I)$: i.e., to find the signal and noise parameters that would generate a *time-domain* response that most closely matches the experimental data (8).

In Bayesian analysis, on the other hand, we seek the posterior probability (most probable *spectrum*) of our time-domain data, conditional (see eq 1) on both $P(D/H,I)$ and $P(H/I)$. The first step is to introduce a hypothesis: i.e., a proposed functional form for the signal and noise, and at least some initial values for the signal parameters. We begin with a simple model (undamped single sinusoid) and then elaborate it (damped multiple sinusoids) to show how the model affects the accuracy of the Bayesian spectral estimate. In Bayesian analysis, phase is treated as a "nuisance" parameter (see below), which is estimated and then eliminated from the subsequent estimation of, for example, signal frequencies.

General Model. As demonstrated by Bretthorst (8), the method of developing a posterior probability distribution (estimated spectrum) from a given model will be illustrated first from a general model and then from a series of increasingly complex specific models. In general, the time-domain response may be represented as the sum of signal, $f(t_i)$, and noise, $e(t_i)$, as shown in eq 2.

$$s(t_i) = f(t_i) + e(t_i) \quad (2a)$$

in which

$$f(t_i) = \sum_{j=1}^m B_j G_j(t_i, \text{model parameters}) \quad (2b)$$

Here $s(t_i)$ is the i th discrete time-domain data point, $e(t_i)$ is Gaussian-distributed random noise with zero mean and standard deviation, σ ; B_j is the amplitude with which model function (e.g., a sinusoid) G_j enters; and the summation is over the number, m , of model functions (e.g., sinusoids) and G_j is

a function of the model parameters (in our case, frequency, time-domain exponential decay rate constant, and amplitude). The "direct" probability distribution, $P(D/H,I)$, can then be shown to take the form (8)

$$P(D/H,I) \propto \sigma^{-N} \exp(-NQ/(2\sigma^2)) \quad (3a)$$

in which

$$Q = \bar{s}^2 - \frac{2}{N} \sum_{j=1}^m \sum_{i=1}^N B_j s(t_i) G_j(t_i) + \frac{1}{N} \sum_{j=1}^m \sum_{k=1}^m \mathbf{g}_{jk} B_j B_k \quad (3b)$$

$$N \text{ is the number of time-domain data points} \quad (3c)$$

$$\sigma \text{ is the standard deviation of the noise} \quad (3d)$$

$$\bar{s}^2 = \left(\sum_{i=1}^N [s(t_i)]^2 \right) / N = \text{mean-square data} \quad (3e)$$

$$\text{and} \quad \mathbf{g}_{jk} = \sum_{i=1}^N G_j(t_i) G_k(t_i) \quad (3f)$$

If the model functions, $G_j(t_i)$, are orthogonal (as for undamped sinusoids), then the matrix, \mathbf{g}_{jk} , is diagonal (8). More generally, a set of $G_j(t_i)$ functions (whether initially orthogonal or not) can be transformed into an orthogonal set of functions, $H_j(t_i)$ (8):

$$H_j(t_i) = \frac{1}{\lambda_j^{1/2}} \sum_{k=1}^m b_{jk} G_k(t_i) \quad (4)$$

in which b_{kj} is the j th component of the k th normalized eigenvector of \mathbf{g}_{jk} , such that

$$\sum_{k=1}^m \mathbf{g}_{jk} b_{ik} = \lambda_i b_{ik} \quad (5)$$

and λ_i is the i th eigenvalue of \mathbf{g}_{jk} . We can now write a new model equation in terms of our orthogonal functions:

$$f(t_i) = \sum_{k=1}^m A_k H_k(t_i, \text{model parameters}) \quad (6)$$

in which the nonorthogonal function amplitudes, B_k , are linearly related to the orthogonal function amplitudes, A_k , by

$$B_k = \sum_{j=1}^m \frac{A_j b_{jk}}{\lambda_j^{1/2}} \quad (7a)$$

and

$$A_k = (\lambda_k)^{1/2} \sum_{j=1}^m B_j b_{kj} \quad (7b)$$

The orthonormal model can then be substituted into $P(D/H,I)$ and, after simplification of the quadratic term, can be used to generate a general equation for the posterior probability. At this stage, it is convenient to further simplify the result by integrating over the "nuisance" parameters (amplitude (A) and noise standard deviation (σ)) to obtain a posterior probability that is a function only of frequency (8). Thus, if we are initially interested in estimating only the signal frequencies, then we can significantly reduce the size of the parameter search array by eliminating our need to determine A and σ . In fact, removal of the "nuisance" parameters by integration is one of the advantages of Bayesian analysis. (Once the signal frequencies have been determined, then the "nuisance" parameters may be estimated at those frequencies.) For the general model, the posterior probability distribution may then be derived as (8)

$$P(\text{model parameters}/D,I) \propto \left(1 - \frac{m\bar{h}^2}{N\bar{s}^2} \right)^{(m-N)/2} \quad (8a)$$

in which

$$\bar{h}^2 = \frac{1}{m} \sum_{j=1}^m h_j^2 \quad (8b)$$

$$\text{and } h_j = \sum_{i=1}^N s_i H_j(t_i) \quad 1 \leq j \leq m \quad (8c)$$

A posterior probability function can be calculated for almost any model with the above general equations. By integrating out the "nuisance" parameters, we make no prior assumptions about the signal component amplitudes or the level of noise that is present.

Undamped Single-Sinusoid Model. We are now in a position to develop the posterior probability distribution for specific signal models. A particularly simple model is that the data is assumed to consist of a single undamped ("stationary") sinusoid plus noise:

$$f(t_i) = B_1 \cos(\omega t_i) + B_2 \sin(\omega t_i) \quad (9)$$

In this model, $m = 2$ (i.e., a single frequency must be represented by two sinusoids to account for the phase of the time-domain signal), and the data points are equally spaced in time. The matrix, \mathbf{g}_{jk} , becomes

$$\mathbf{g}_{jk} = \begin{pmatrix} \sum_{t=-T}^T \cos^2 \omega t & \sum_{t=-T}^T \cos \omega t \sin \omega t \\ \sum_{t=-T}^T \cos \omega t \sin \omega t & \sum_{t=-T}^T \sin^2 \omega t \end{pmatrix} \quad (10)$$

in which the data acquisition period extends from $-T$ to T . Solving for the posterior probability gives (8)

$$P(\omega/D, I) \propto \left(1 - \frac{[R(\omega)]^2/C + [I(\omega)]^2/S}{N\bar{s}^2} \right)^{(2N-1)/2} \quad (11)$$

in which $R(\omega)$ and $I(\omega)$ are the real and imaginary parts of the discrete Fourier transform and

$$C = \frac{N}{2} + \frac{\sin(N\omega)}{2 \sin(\omega)} \quad (12a)$$

$$S = \frac{N}{2} - \frac{\sin(N\omega)}{2 \sin(\omega)} \quad (12b)$$

For a single undamped sinusoid, it turns out that the FFT is an accurate spectral estimator in the limit that N is large, so that the normalization constants C and S reduce to $N/2$. For small N and/or low frequency, on the other hand, it is clear that C and S can deviate significantly from $N/2$: e.g., $C \rightarrow N$ and $S \rightarrow 0$ as $\omega \rightarrow 0$. Finally, this model is obviously inappropriate in the presence of time-domain damping and/or for signals containing two or more natural frequencies.

Damped Single-Sinusoid Model. An improved model allows for exponential decay of the time-domain signal:

$$f(t_i) = (B_1 \cos(\omega t_i) + B_2 \sin(\omega t_i))e^{-t_i/\tau} \quad (13)$$

Even if the true time-domain decay is not exponential, eq 13 still leads to a more accurate spectral estimate than eq 9 (8).

An even better model is that the time-domain data consists of a sum of many exponentially damped sinusoids:

$$f(t_i) = \sum_{j=1}^m [(B_{1j} \cos \omega_j t_i + B_{2j} \sin \omega_j t_i) e^{-t_i/\tau_j}] \quad (14)$$

in which m is the number of distinct signal frequencies present. The damped multiple-sinusoid signal model is the most complex model considered here; it also contains the largest parameter array space that must be searched to locate a maximum for the posterior probability. The parameter array size is $N(2m + 1)$, where N is the number of time-domain points. Nevertheless, the gain in accuracy from the multi-

sinusoid model may compensate for its increased computation time, provided that the number of spectral peaks is not too large. A description of the Bayesian spectral analysis algorithm is provided as an appendix.

Precision of Bayesian and FT Analyses. In this section, we compare the precision of Bayesian and FT analyses for determination of the frequency of a noisy time-domain single-frequency signal, in the above-noted limits that N is large (see eq 12) and time-domain damping is not included in the Bayesian signal model. The precision, $p(\nu)$, in determination of signal frequency, ν , is defined as the "natural" spectral line width, $\Delta\nu$ (namely, $(1/\pi\tau)$ or $(3^{1/2}/\pi\tau)$ for Lorentzian absorption- or magnitude-mode), in which τ is the time-domain exponential damping constant, divided by the standard deviation, $\sigma(\nu)$, of the frequency estimate. It is perhaps easier to state (equivalently) that the *imprecision* (namely, $1/p(\nu)$) is the absolute imprecision, $\sigma(\nu)$, scaled (i.e., divided) by the spectral "natural" line width, $\Delta\nu$; in other words, we seek a measure of precision that is independent of the *absolute* natural line width, $\Delta\nu$ (11).

$$p(\nu) = \frac{\Delta\nu}{\sigma(\nu)} \quad (15)$$

For the Bayesian method $\sigma(\nu)$ may be determined by approximating eq 11 by a Gaussian distribution and then taking $\sigma(\nu)$ as the standard deviation for that Gaussian distribution (8):

$$\sigma(\nu)_{\text{Bayes}} = \frac{1.1\sigma}{B_1 T N^{1/2}} \text{ Hz} \quad (16)$$

in which B_1 is the *time-domain* signal amplitude (for the model of eq 9), σ is the standard deviation of the *time-domain* noise (see eq 2), and $T = N\Delta t$ is the time-domain acquisition period, in which N is the number of time-domain data points and Δt is the "dwell time" (seconds) between sampled time-domain data points. The precision of the Bayesian estimate may then be written

$$p(\nu)_{\text{Bayes}} = \frac{B_1 T (3N)^{1/2}}{1.1\sigma\pi\tau} \quad (17)$$

The precision obtainable by a least-squares fit to a magnitude-mode FFT Lorentzian spectrum can be shown to be (11)

$$p(\nu) = (\pi/4)^{1/2} (\text{SNR}) (T\Delta\nu)^{1/2} \quad (18a)$$

in which (12, 13)

$$\text{SNR} = \frac{B_1 \tau [1 - \exp(-T/\tau)]}{\sigma(2N)^{1/2}} \quad (18b)$$

SNR is the magnitude-mode *frequency-domain* peak-height-to-noise ratio, and $T\Delta\nu$ [= (points/hertz)·(hertz/line width)] is the number of frequency-domain data points per (magnitude-mode) spectral line width. The implications of eqs 17 and 18 will be explored in the Results and Discussion section.

EXPERIMENTAL SECTION

Simulated Time-Domain Data. The Bayesian spectral analysis programs were first tested on simulated noisy damped discrete time-domain sinusoids. Each N -point time-domain signal consisted of a sum of cosines of known frequencies and amplitudes, exponentially damped with a common damping constant. The arithmetic mean value of this data set was then subtracted from each data point to give a signal with zero mean. An N -point data set of Gaussian-distributed random noise with zero mean and unit standard deviation was then scaled (to give the desired initial time-domain signal magnitude-to-noise ratio) and added to the discrete signal. The reported signal-to-noise ratio is the ratio of

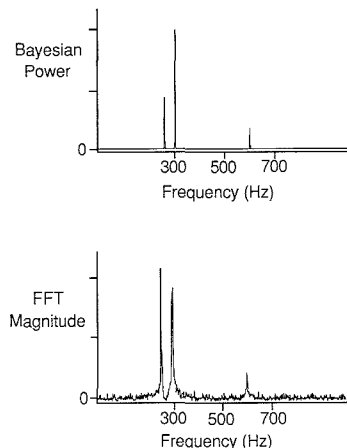


Figure 1. Power spectrum (top) plotted from a Gaussian approximation to the amplitudes and frequencies and their standard deviations determined by Bayesian analysis from a damped multiple-sinusoid model, for a simulated time-domain signal consisting of a sum of three sinusoids with different frequencies (257, 300, and 600 Hz, with relative amplitudes of 1:2:0.5), and a common exponential decay time-constant (110 ms), with Gaussian-distributed random noise added to give a time-domain initial signal-to-noise ratio of ~ 100 . A total of 1024 time-domain data points were generated over a time span on 0.512 s (i.e., Nyquist bandwidth of 1000 Hz). The FFT magnitude-mode spectrum (bottom) was computed from the same data.

the square root of the mean signal power to the mean noise power, namely, B_1/σ . Bayesian estimates for signal frequencies, damping constants, and relative magnitudes may then be compared to the "true" input values for the original noiseless damped sinusoids.

Experimental ICR Time-Domain Data. Experimental data were collected on a Nicolet FTMS-2000 FT/ICR instrument operating at 3.0 T. Of the two experimental data sets, one was produced from an electron-ionized (70 eV) mixture of nitrogen and carbon monoxide, and the second from electron-ionized (70 eV) xenon. The N_2^+ and CO^+ signal was processed in heterodyne mode with the reference frequency set at 1.786 MHz (i.e., somewhat above the highest ICR frequency of interest) and a Nyquist bandwidth of 237 kHz. The Xe^+ signal was digitized directly at 1.0 MHz (Nyquist bandwidth of 500 kHz).

All experimental data sets were subjected to both Bayesian and conventional FFT analysis. For the experimental data sets the FFT was done on raw (16K data points) and once zero-filled (to 32K) time-domain discrete data sets. With or without zero-filling, each time-domain data set was then subjected to FFT followed by a magnitude computation to yield a magnitude-mode spectrum. Finally, a 32K zero-filled data set multiplied by a Gaussian weight function ("window") was FFT-processed to provide for comparison of Bayesian and apodized FFT spectra. (The Gaussian window improves resolution at the base of each FFT spectral peak, but at a significant loss in signal-to-noise ratio.)

RESULTS AND DISCUSSION

Bayesian Analysis of Simulated Noisy Time-Domain Damped Sinusoids. Figure 1 shows the Bayesian power spectrum and the FFT magnitude-mode spectrum computed from a simulated sum of three noisy time-domain damped (with the same exponential decay time constant) sinusoids. Table I lists the true values of all of the test parameters, along with the values determined from Bayesian analysis based on a damped multiple-sinusoid model, along with the frequency estimates obtained by a three-point "exact" interpolation of an FFT magnitude-mode spectrum to a Lorentzian magnitude-mode peak shape (14, 15). The Bayesian-estimated frequencies are very close to the true values, with maximum error of only 0.0203%. In this case, the Bayesian estimates

Table I. Signal Sinusoidal Frequencies, Exponential Damping Time Constants (τ), and Relative Abundances (A_i/A_j) of Sinusoidal Components Resulting from Bayesian Analysis of a 1024-point Time-Domain Simulated Data Set^a

parameter	true value	Bayesian est	% error	FFT est	% error
freq, Hz	257.00	256.95	0.0203	256.67	0.1284
	300.00	300.01	0.0043	300.01	0.0043
	600.00	599.99	0.0023	600.13	0.0217
τ , ms	110.00	104.6	4.9		
	110.00	112.9	2.6		
	110.00	95.2	13.4		
A_1/A_2	0.500	0.433	13.4		
A_1/A_3	2.000	2.47	23.4		
peak height/noise	100.0	126.4			

^aTrue signal and noise parameters are shown in the "true value" column. Also included for comparison are the frequency estimates obtained from a three-point "exact" interpolation from a 512-point FFT magnitude-mode spectrum. The listed error is the deviation of the Bayesian (or FFT) estimate from the true value of each parameter. The peak-height-to-noise ratio for the Bayesian power spectrum (Figure 1, top) appears somewhat higher than that of the original time-domain noisy signal, because noise has largely been removed from the Bayesian spectrum before display (see text).

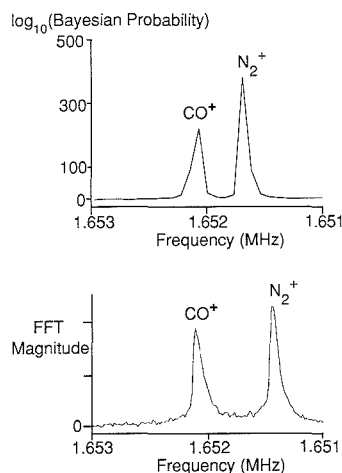


Figure 2. Bayesian (top) and FFT magnitude-mode (bottom) spectra of an experimental time-domain ICR signal arising from N_2^+ and CO^+ . The Bayesian spectrum was computed at 2048 discrete frequencies from the first 4096 time-domain data. The FFT spectrum (16K points) was computed from the full 16K time-domain ICR data zero-filled to 32K. The ordinate of the Bayesian spectrum represents the base-10 logarithm of the posterior probability computed from eq 8, based on an undamped single-sinusoid time-domain signal model.

are more accurate than those based on the FFT magnitude-mode spectrum for the same number of time-domain data points. In our and other (8) experience with simulated and experimental time-domain noisy damped multiple sinusoids, Bayesian analysis gives highest precision in estimating signal frequencies, intermediate precision for time-domain exponential damping time constants, and lowest precision for relative abundances of the component time-domain oscillators (see below).

Undamped Single-Sinusoid Model Applied to Experimental ICR Time-Domain Data. Figure 2 compares Bayesian (undamped single-sinusoid model) and Fourier transform frequency-domain representations of the same

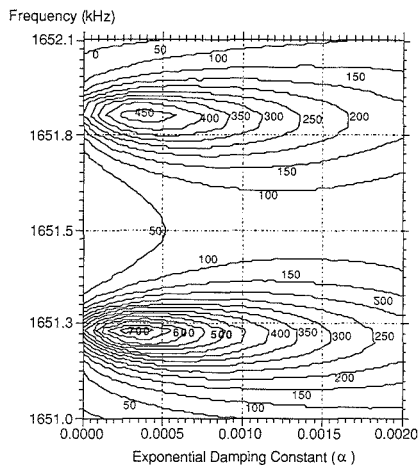


Figure 3. Plot of contours of constant posterior probability (log scale) as a function of time-domain signal frequency (ν) and reciprocal exponential damping time-constant, $\alpha = (\Delta t/\tau)$, with τ scaled in multiples of dwell period, Δt , for a Bayesian-analyzed 4096-point time-domain ICR N_2^+ and CO^+ data set, based on a damped single-sinusoid signal model. Computation time for a 50×50 grid of ν_0 and τ values was 2.5 h. From the graph, N_2^+ and CO^+ are estimated to have similar exponential damping time-constants of ~ 5.2 ms.

time-domain ion cyclotron resonance signal (heterodyne mode) from CO^+ and N_2^+ . The vertical scales of the two spectra are not directly comparable: The FT spectrum is displayed in magnitude mode, whereas the Bayesian spectrum is reported as the base-10 logarithm of the posterior probability distribution. Base-line "noise" is present in the Bayesian spectrum, but is visible only by vertical scale expansion. The *peak-height-to-noise ratio* of the Bayesian spectrum is higher than that for the FT spectrum, because the Bayesian algorithm recognizes that noise is present and assigns a very low posterior probability to signal frequencies not highly supported by the time-domain data. Thus, noise is largely excluded from the Bayesian spectral *base line*, but is manifested as the *width* (i.e., standard deviation in signal frequency) of the Bayesian spectral peak. The Bayesian spectral *line width* in this example is essentially the same as that for FT data reduction, because the Bayesian undamped sinusoid model does not admit damping of the time-domain signal. The main point is that the Bayesian method based on an undamped single-sinusoid model can provide good initial estimates of the *number* and *magnitude* of the distinct oscillation frequencies present in the discrete time-domain noisy signal, for use as input values for subsequent more accurate spectral estimates (see below).

Damped Single-Sinusoid Model Applied to Experimental ICR Time-Domain Data. Figure 3 shows the result of Bayesian analysis (damped single-sinusoid model), displayed as a plot of contours of constant posterior probability (log scale), for the same CO^+ and N_2^+ time-domain data analyzed in Figure 2. This Bayesian analysis spans a 50×50 grid of equally spaced increments in frequency (1.651–1.652 MHz) and exponential decay reciprocal time constant, $1/\tau$ (0–1000 s^{-1} in equally spaced increments; i.e., $1 \text{ ms} \leq \tau \leq \infty$). Even for such a small parameter array, the computation and plotting required 2.5 h! Figure 3 clearly shows two frequency-domain peaks with comparable time-domain exponential decay rate constants ($\sim 194 \text{ s}^{-1}$), corresponding to exponential damping time constants of ~ 5.2 ms. These estimates (note that the peak frequencies are shifted from the initial estimates

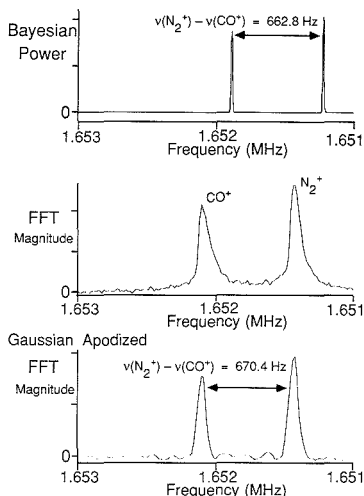


Figure 4. Power spectrum (top) plotted (as in Figure 1) from a Gaussian approximation to the amplitudes and frequencies and their standard deviations, and computed (3 h) by Bayesian analysis from a damped multiple-sinusoid signal model, based on the first 4096 time-domain ICR signal data for N_2^+ and CO^+ . The FFT magnitude-mode spectra obtained from the full 16K time-domain data zero-filled to 32K without (middle) or with (bottom) Gaussian apodization (windowing) are shown for comparison.

based on the *undamped* single-sinusoid model of Figure 2) were then used as starting points for the final Bayesian analysis based on an undamped multiple-sinusoid model.

Damped Multiple-Sinusoid Model Applied to Experimental ICR Time-Domain Data. Figure 4 (top) shows the power spectrum resulting from the Bayesian analysis of the same CO^+ and N_2^+ data set as in Figures 2 and 3, but this time based on a damped multiple-sinusoid model for the time-domain signal. The actual output from this Bayesian analysis (3-h computation time) consists of the values of ω_0 and τ that maximize the posterior probability distribution, along with the amplitudes, B_1 and B_2 , of the cosine and sine components of each oscillatory signal component and the standard deviations for each of the above parameters. Thus, an advantage of the Bayesian approach is that it naturally provides a measure of the *precision* of its estimated spectral parameters (8).

It is important to understand the nature of the Bayesian spectral display: The topmost spectrum in Figure 4 (or in Figure 1) is a plot of the power spectral amplitude, $B_1^2 + B_2^2$, for each estimated signal frequency, ν , displayed as a Gaussian distribution with standard deviation $\sigma(\nu)$. Thus, the width of the Bayesian spectral peak represents a measure of precision in estimate of ν , whereas the width of the corresponding unapodized (Figure 4, middle) *FT magnitude-mode* spectrum is a measure of the time-domain exponential damping rate constant, $1/\tau$. In the Bayesian analysis, $1/\tau$ (not shown) is determined as an *independent* parameter. Thus, the Bayesian spectral line width (Figure 4, top) generally appears narrower than that for either unapodized (Figure 4, middle) or apodized (Figure 4, bottom) *FT magnitude-mode* spectra and in this case yields more precise estimates for the signal frequencies, ν . (The Bayesian spectral line width is approximately the same as that in the FFT spectrum when, as in Figure 2, the Bayesian time-domain signal model does not include exponential damping.)

Theoretical Frequency Precision of Bayesian vs FFT Analysis. Figure 5 shows a plot of the base-10 logarithm of

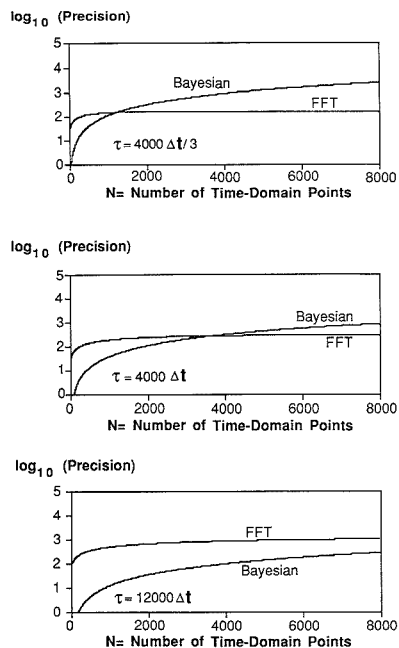


Figure 5. Logarithm (base 10) of the signal frequency precision (eqs 17 and 18) vs number of time-domain data points, based on either Bayesian or Fourier analysis of the same simulated time-domain signals. In the three plots, time-domain initial signal-to-noise ratio is 10.0; and the time-domain damping constant $\tau = 4000\Delta t/3$, $4000\Delta t$, or $12000\Delta t$ s, for a sampling rate of $(1/\Delta t)$ points/s. The Bayesian analysis is based on an undamped single-sinusoid time-domain signal model, and the FFT analysis is based on nonlinear least-squares best fit to an FFT magnitude-mode spectrum (see text).

the precision, $p(\nu)$ (Bayesian or FFT, computed from eqs 17 and 18), as a function of N (number of time-domain data points) for a time-domain signal-to-noise ratio of 10 and $\tau = 4000\Delta t/3$, $4000\Delta t$, and $12000\Delta t$ (i.e., $T = 3\tau$, $T = \tau$, and $T = \tau/3$). (The three plots in Figure 5 are thus the same graph, plotted at three different horizontal scales.) Since the Bayesian (undamped single-sinusoid model) and FFT magnitude-mode spectral line widths [$\Delta\nu = 3^{1/2}/(\pi\tau)$ Hz, in the limit that $T \gg \tau$] are comparable (see Figure 2), we have introduced an additional (compared to ref 9) factor of $3^{1/2}$ into eq 17 to facilitate comparison between Bayesian and FFT precision. For signals that are significantly damped ($T \geq \tau$) during the time-domain acquisition period, the Bayesian precision surpasses the FFT precision (by up to 2 orders of magnitude) for a sufficiently large value of N . We should not be too surprised that the Bayesian precision can be superior to that based on an FFT spectrum, since the Bayesian algorithm "knows" the form of the time-domain signal (and that noise is present), whereas the FFT algorithm does not. Unfortunately, since Bayesian computation time increases with increasing N (4–6 h for 4096 time-domain data points on a Nicolet 1280 minicomputer), it is at present impractical to exploit the full available precision of Bayesian analysis for large time-domain data sets ($\geq 32K$).

The enhanced precision of Bayesian analysis (vs that of FFT) for large N follows directly from eqs 17 and 18. Since $T = N\Delta t$, Bayesian precision effectively increases as $N^{3/2}$, (for the single nondamped frequency model of eq 17) whereas precision based on nonlinear least-squares fit to a magni-

tude-mode FFT spectrum increases only as N for small N ($T \ll \tau$) and is independent of N for large N (i.e., $T \gg \tau$). Thus, for a sufficiently large number of data points, N , Bayesian frequency precision will always be higher than FFT frequency precision, provided that the experimental time-domain signal is well-approximated by a sum of damped sinusoids of different frequencies.

The relative precision of FFT analysis (vs Bayesian) improves as τ/T increases (lowermost graph in Figure 5), because a longer time-domain damping constant produces a narrower (and higher-magnitude) FFT spectral peak. Basically, Bayesian analysis produces independent estimates for ν and τ , whereas the precision in determination of ν from FFT analysis depends on the spectral "natural" line width, which is in turn proportional to $1/\tau$. Thus, the FFT precision in determination of ν decreases as τ decreases, because the FFT spectral line width increases, and the frequency-domain peak-height-to-noise ratio decreases.

Finally, it is worth noting that the signal-to-noise ratio, B_1/σ , in eq 17 for Bayesian precision is defined for a time-domain noisy signal, whereas the signal-to-noise ratio, SNR, in eq 18 for the FFT precision is defined from the frequency-domain magnitude-mode spectral peak-height-to-noise ratio. As discussed in more detail elsewhere (13), the frequency-domain FFT peak height, $(B_1/2)\tau[1 - \exp(-T/\tau)]$, is obtained (12) by integrating the time-domain signal over the acquisition period, T , and the frequency-domain noise (13) is simply $(N\sigma/2)^{1/2}$; the ratio of these two factors leads to eq 18b.

Experimental Frequency Precision of Bayesian vs FFT Analysis. Figure 4 shows the absolute ICR frequency difference (Bayesian vs unapodized and apodized FFT spectra) between CO^+ and N_2^+ , compared to the difference, 663.4 Hz, computed from the sum of the nuclidic masses (16) minus the mass of one electron (16) at a magnetic field value of 3.016 T—the magnetic field strength need only be approximately correct for this ICR frequency difference estimate. The ICR frequency difference computed from the apodized FT magnitude-mode spectrum (by parabolic fit to the three largest-magnitude data points in each peak) was 670.4 Hz, compared to an ICR frequency difference of 662.8 Hz from Bayesian analysis. In this case, the ICR mass difference from Bayesian analysis is indeed more accurate (-0.000010 u) than that produced by parabolic fit to the FT magnitude-mode spectrum ($+0.00012$ u). Although a three-point fit of each peak to a magnitude-mode Lorentzian (12, 13, 17) improves the estimate of the FT magnitude-mode spectral peak frequency difference (665.0 Hz, corresponding to a mass difference error of $+0.000027$ u), the Bayesian estimate is still the best, even though the Bayesian estimate was based on only one-fourth as many time-domain data points as the FFT estimates.

Relative Abundances from Bayesian Analysis. Bayesian analysis of a time-domain ICR noisy signal also yields estimates for the relative abundances of ions of different mass-to-charge ratio. Figure 6 shows the results of Bayesian analysis on the first 2048 time-domain ICR positive ion signal data from an electron-ionized Xe sample. The computation time was long (6 h) because of the relatively large number of determined ICR frequencies (6) and number of time-domain data points, requiring a computational data array of $2048 \times ((6 \times 2) + 1)$ words. It is worth noting that the magnitude-mode Fourier transform spectrum (based on the full 16K time-domain data, zero-filled to 32K before FFT) reveals a seventh low-magnitude peak (~ 362 kHz, arising from $^{128}\text{Xe}^+$); the Bayesian analysis program slowed down significantly when asked to search for that peak. If more time-domain data points had been included in the Bayesian analysis, then the correspondingly more accurate spectral estimate would probably have identified the low-magnitude signal. Faster

Table II. Ion Cyclotron Resonance Frequencies and Relative Abundances for Six Xe⁺ Isotopes^a

isotope	comptd	$\nu_{132\text{Xe}} - \nu$ l, Hz			relative abundance		
		discrete FFT		Bayesian	true	discrete FFT	Bayesian
		parabolic inter	Lorentzian inter				
¹²⁹ Xe	8170	8162 (+0.0024 u)	8174 (+0.0012 u)	8169 (-0.0003 u)	98.14	98.9 (+0.77%)	99.8 (+1.66%)
¹³⁰ Xe	5408	5327 (-0.024 u)	5344 (-0.019 u)	5384 (-0.0072 u)	15.24	24.5 (+60.8%)	20.9 (+37.3%)
¹³¹ Xe	2680	2678 (-0.0006 u)	2681 (+0.0003 u)	2682 (+0.0006 u)	78.81	82.4 (+4.56%)	87.9 (+11.5%)
¹³² Xe	0	0	0	0	100.00	100.0	100.0
¹³⁴ Xe	5248	5308 (+0.018 u)	5307 (+0.018 u)	5293 (+0.013 u)	38.66	38.1 (-1.4%)	42.7 (+10.5%)
¹³⁶ Xe	10342	10390 (+0.0143 u)	10380 (+0.011 u)	10368 (+0.008 u)	33.09	36.0 (+8.8%)	39.6 (+19.6%)

^a Each ICR frequency (or magnitude) is reported as the difference in frequency (or ratio of magnitude) with respect to that of the most abundant isotope, ¹³²Xe. ICR reference frequencies were computed as for Figure 4 (i.e., computed from known isotope mass minus the electron mass (13) and converted to ICR frequency based on an assumed magnetic field strength of 3.016 T). Relative spectral peak magnitudes are compared to known relative abundances of the xenon isotopes (13). Bayesian and FFT procedures were as for Table I.

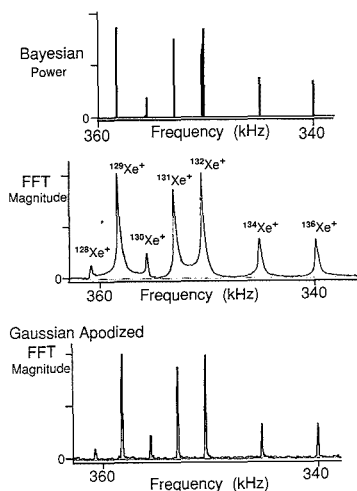


Figure 6. Bayesian power spectrum (top) computed and displayed as for Figure 4, from the first 2048 data points of a time-domain ICR signal produced by seven Xe⁺ isotopes. Because of the relatively large number of peaks, computation time was ~6 h (or ~4.5 h with closer initial estimates for the ICR frequencies). As in Figure 4, the FFT magnitude-mode spectra obtained from the full 16K time-domain data zero-filled to 32K without (middle) or with (bottom) Gaussian apodization are shown for comparison.

Bayesian algorithms for handling such larger data sets are under development (8).

Table II compares the accuracy of the FFT and Bayesian spectral estimates for the ICR frequencies and relative abundances of the isotopes of Xe⁺. On the average, the Bayesian frequency estimates were more accurate by a factor of ~3 than the FFT frequency estimates based on parabolic three-point interpolation (and more accurate by a factor of ~2 than FFT frequency estimates based on three-point interpolation to a Lorentzian line shape (12, 13)), even though the FFT spectra were computed from 8 times as many time-domain data points. The isotopic relative abundance estimates for both Bayesian and FFT methods were about equally accurate: The values from FFT analysis were markedly better than those from Bayesian analysis, except for the much larger FFT error for the low-abundance ¹³⁰Xe⁺ isotope.

CONCLUSION

These theoretical and experimental results demonstrate that Bayesian analysis is capable of providing higher mass accuracy than that obtained from a discrete FFT of the same time-domain noisy exponentially damped multiple-sinusoid signal.

Moreover, the Bayesian method inherently provides a measure of its own precision. In this approach, we apply the Bayesian method to successively more complex signal models, until the estimated parameter precision fails to improve further (8, 10). In Bayesian analysis, any spectral feature that cannot be fitted to the signal model is assigned to the noise, thereby decreasing the precision with which the spectral parameters may be determined. Because computation time increases with increasing signal model complexity, the computation time for a given model can be reduced by using the parameters estimated from a simpler model as initial estimates for the more complex model. In the present Bayesian analysis examples, the signal model was sufficiently general (i.e., unlimited width in the probability distribution for each signal parameter) and the number of distinct signal frequencies sufficiently small that the Bayesian method did not introduce any false spectral peaks. The Bayesian method includes various other spectral estimation methods (e.g., linear prediction, least squares, MEM, FFT) as special cases. Thus, the artifacts and inaccuracies of all such methods are to some extent commonly shared. However, the advantages of Bayesian analysis are its generality and its inherent ability to estimate the precision (rather than just the values) of the signal parameters.

The principal disadvantage of Bayesian analysis compared to FFT data reduction is the relatively long computation period (hours vs seconds for the same data analyzed with the same hardware). As the number of distinct signal frequencies (spectral peaks) increases, Bayesian analysis requires increasingly long computation time and/or increasingly accurate initial estimates for the spectral parameters of interest. (The accuracy of the initially estimated parameters determines the time required to locate the maximum in the posterior probability distribution.) Computation time also increases (but less rapidly) with increasing number of time-domain data points. In practice, a compromise must be made between precision and computation time.

From the above considerations, Bayesian analysis will be preferred over FFT data reduction in cases for which (a) high signal frequency accuracy (e.g., high mass accuracy in FT/ICR (18, 19)) is required; (b) the number of time-domain data points is small ($\leq 2K$ or so, as in gas chromatograph/FT/ICR experiments (20)); (c) the time-domain signal is truncated after less than about one exponential damping time constant, leading to Gibbs oscillations in the FFT spectrum; and/or (d) two or more signal oscillation frequencies are closely spaced (i.e., by less than the spacing between two adjacent frequency-domain data points) (1, 8).

ACKNOWLEDGMENT

The authors thank L. Bretthorst, Washington University, St. Louis, MO, for sharing his computer algorithm from which the present Bayesian analysis of ICR time-domain data was adapted. The authors also thank Zhenmin Liang for his

assistance in acquisition of experimental ICR time-domain data used to test the Bayesian analysis programs.

APPENDIX

Bayesian Spectral Analysis Algorithm. The application of Bayesian spectral analysis to experimental time-domain data is straightforward, but tedious. First, the simple undamped single-sinusoid model is used to obtain an estimate of the number and frequencies of the time-domain signal sinusoids. Equation 8 can be used to calculate a posterior probability distribution, by calculating $P(\omega/D, I)$ at discrete frequencies equally spaced throughout the spectral bandwidth of interest. At each discrete spectral frequency, the matrix $\{g_{jk}\}$ is evaluated and its eigenvalues and eigenvectors are determined. From those eigenvalues and eigenvectors, P (model parameters/ D, I) may then be calculated. For spectral peaks with high signal-to-noise ratio (say, $\geq 10:1$), an FFT magnitude-mode spectrum may be used to provide initial estimates for the signal frequencies, provided that those frequencies are well separated (i.e., by more than one FFT discrete spectral frequency spacing, $1/T$ Hz, in which T is the time-domain acquisition period in seconds). Next, a damped single-sinusoid model may be used to obtain an estimate of the time-domain damping constant, τ , by varying not only signal sinusoid frequency, ω , but also the signal exponential damping constant value, τ . The two-dimensional output distribution, $P(\{\omega, \tau\}/D, I)$, is best visualized as a plot of contours of constant posterior probability. Lastly, a refined spectral estimate is computed from the damped multisinusoid model. The frequency and damping constant estimates found above are used as initial guesses, and the $N \times (2m + 1)$ parameter space is searched to find those ω_j values that maximize the right-hand side of eq 8. The parameter search is time-consuming because the eigenvalues and eigenvectors of the matrix g_{jk} must be recomputed for each point of the (ω, τ) parameter grid. Thus, accurate initial estimates for signal frequencies and damping constant can significantly reduce the time required to compute the posterior probability distribution.

The computer code that calculates the posterior probability distribution for each of the above models consists first of a subroutine, Prob, that calculates the (base-10) logarithm of the posterior probability according to eq 8. The input for the subroutine requires N (the number of time-domain data points), m (the number of sinusoid frequencies in the signal), and the matrix g_{jk} , as well as a subroutine for calculating the eigenvectors and eigenvalues of g_{jk} . For the undamped single-sinusoid and damped single-sinusoid models, only a main

"driving" program, which sets up g_{jk} and calls Prob, to compute the posterior probability distribution for each of the scanned ω and τ values is needed. For the damped multiple-sinusoid model, two programs are required: a first driver that computes g_{jk} and calls the Prob subroutine to determine the value of the posterior distribution at a particular search point (i.e., for particular ω and τ) and a second program that searches the ω and τ parameter array to find those values that maximize the posterior probability. A general search routine (8) was chosen to accommodate the sharply peaked maximum in the posterior probability distribution. Finally the calculated sinusoid frequencies are used as described above to calculate estimates for the signal amplitudes and errors (and thus the signal-to-noise ratio(s)).

LITERATURE CITED

- (1) Marshall, A. G.; Verdun, F. R. *Fourier Transforms in NMR, Optical, and Mass Spectrometry: A User's Handbook*; Elsevier: Amsterdam, 1989.
- (2) Nussbaumer, H. J. *Fast Fourier Transform and Convolution Algorithms*, 2nd ed.; Springer-Verlag: Berlin, 1982.
- (3) Cooley, J. W.; Tukey, J. W. *Math. Comput.* **1965**, *19*, 297-301.
- (4) Wang, M.; Marshall, A. G. *Anal. Chem.* **1988**, *60*, 341-344.
- (5) Kay, S. M. *Modern Spectral Estimation*; Prentice-Hall: Englewood Cliffs, NJ, 1988.
- (6) Gull, S. F.; Skilling, J. *IEE Proc.* **1984**, *131*, 646-659.
- (7) Ulrych, T. J.; Bishop, T. N. *Rev. Geophys. Space Phys.* **1975**, *13*, 183-200.
- (8) Bretthorst, G. L. *Bayesian Spectrum Analysis and Parameter Estimation. In Lecture Notes in Statistics*; Springer-Verlag: New York, 1988, Vol. 48.
- (9) Berger, J. D. *Statistical Decision Theory and Bayesian Analysis. In Springer Series in Statistics*, 2nd ed.; Springer-Verlag: New York, 1988.
- (10) Bax, G. E.; Tiao, G. C. *Bayesian Inference in Statistical Analysis*; Addison-Wesley Publishing Co.: Reading, MA, 1973.
- (11) Chen, L.; Cottrell, C. E.; Marshall, A. G. *Chemom. Intell. Lab. Systems* **1986**, *1*, 51-58.
- (12) Marshall, A. G. *Anal. Chem.* **1979**, *51*, 1710-1714.
- (13) Liang, Z. Ph.D. Thesis, The Ohio State University, Columbus, OH, 1990.
- (14) Giancaspro, C.; Comisarow, M. B. *Appl. Spectrosc.* **1983**, *37*, 153-165.
- (15) Verdun, F. R.; Giancaspro, C.; Marshall, A. G. *Appl. Spectrosc.* **1988**, *42*, 715-721.
- (16) *CRC Handbook of Chemistry and Physics*, 62nd ed.; CRC Press, Inc.: Boca Raton, FL, 1981.
- (17) Keefe, C. D.; Comisarow, M. B. *Appl. Spectrosc.* **1989**, *43*, 605-607.
- (18) Marshall, A. G. *Acc. Chem. Res.* **1985**, *18*, 316-322.
- (19) Bamberg, M.; Allemann, M.; Wanczek, K.-P. *Proceedings of the 35th American Society for Mass Spectrometry Conference on Mass Spectrometry and Allied Topics*; Denver CO, May, 1987; pp 1116-1117.
- (20) Ledford, E. B., Jr.; White, R. L.; Ghaderi, S.; Wilkins, C. L.; Gross, M. L. *Anal. Chem.* **1980**, *52*, 2450.

RECEIVED for review July 7, 1989. Accepted October 27, 1989. This work was supported by N. I. H. GM-31683 and The Ohio State University.

Resonance Ionization Mass Spectrometry of Sputtered Osmium and Rhenium Atoms

Joel D. Blum,*¹ M. J. Pellin, W. F. Calaway, C. E. Young, and D. M. Gruen

Materials Science, Chemistry, and Chemical Technology Divisions, Argonne National Laboratory, Argonne, Illinois 60439

I. D. Hutcheon and G. J. Wasserburg

Lunatic Asylum of the Charles Arms Laboratory, Division of Geological and Planetary Sciences, California Institute of Technology, Pasadena, California 91125

The mass spectrometric analysis of Os and Re was investigated by use of a pulsed primary Ar⁺ ion beam to provide sputtered atoms for resonance ionization mass spectrometry. A useful yield of 10⁻² and a detection limit of 8 ppb were demonstrated for Os concentration measurement. In situ measurements of Os concentration are obtainable by this method at the sub-part-per-million level in conducting and semiconducting materials with a full width at half maximum beam diameter of ~70 μm. An ionization scheme for Os that utilizes three resonant energy levels (including an autoionizing energy level) was investigated and found to have superior sensitivity and selectivity compared to nonresonant and one and two energy level resonant ionization schemes. An elemental selectivity for Os over Re of ≥10³ was demonstrated. It was found that detuning the ionizing laser from the autoionizing energy level to an arbitrary region in the ionization continuum resulted in a 5-fold decrease in signal intensity and a 10-fold decrease in elemental selectivity.

INTRODUCTION

The mass spectrometric analysis of small quantities of Os and Re is an important analytical goal in geochemistry with two main applications: (1) the in situ measurement of Os and Re concentrations at very low levels in geologic materials and in phases synthesized in laboratory experiments; (2) the measurement of Os isotope ratios both in situ and on small samples of Os chemically separated from geologic materials. In both instances the number of Os and Re atoms available for measurement is quite low. Therefore, it is of interest to develop a mass spectrometric measurement technique with a high ratio of ions detected to atoms present in the ion source (useful yield). The technique must also be able to discriminate against molecular interferences in the case of concentration measurements and discriminate between ¹⁸⁷Os and ¹⁸⁷Re atoms in the case of Os isotope ratio measurements.

At Argonne National Laboratory we have developed a resonance ionization mass spectrometer for ultrasensitive surface analysis of semiconductors with monolayer depth resolution. Surface analysis by resonance ionization of sputtered atoms (SARISA) has a high useful yield (≥10⁻²) and a demonstrated sensitivity at the parts-per-billion (ppb) level for Fe concentration measurements in a Si matrix (1-3). It employs a pulsed primary ion beam to create a cloud of sputtered neutrals that efficiently fill the ionizing volume of

pulsed lasers and an energy and angular refocusing time-of-flight mass spectrometer to maximize photoion detection. SARISA appears to be well suited for in situ determinations of Os and Re concentrations.

A major obstacle that must be addressed in order to demonstrate the utility of resonance ionization of sputtered atoms for Os and Re analyses is the identification of suitable ionization schemes for these elements. To this end, we have investigated a series of multiphoton ionization schemes for Os and Re with the goal of maximizing the Os photoion yield and minimizing the isobaric interference between Os and Re at mass 187. In this study we have evaluated the useful yield, detection limit, and selectivity of SARISA for the measurement of Os concentrations. This information is also important in evaluating the potential of the SARISA photoion source as a prototype of an elementally selective and highly efficient ion source for an isotope ratio mass spectrometer.

EXPERIMENTAL SECTION

Apparatus. The experiments were performed by use of the SARISA apparatus, described in detail by Pellin et al. (2). The instrument consists of three main subunits: a pulsed primary ion source, three pulsed tunable lasers, and an energy and angular refocusing time-of-flight mass spectrometer (Figure 1).

A mass analyzed 5 keV Ar⁺ sputtering beam with a current of 2.0 μA and a full width at half maximum (fwhm) diameter of ~70 μm is produced by a Colutron ion gun. During analyses, the primary ion beam is chopped into pulses of 200 ns width by electrostatic deflection and is synchronized with the lasers operating at a 40-Hz repetition rate. The Ar⁺ ion pulses strike the target in a chamber pumped to the low 10⁻⁹ Torr pressure range. The sputtering rate in the pulsed mode is ~10 min per monolayer of target. Sputtered species fill a volume above the target during and after the arrival of the primary ion pulse. During sputtering, the target is held at a 1.5-kV potential; incoming Ar⁺ ions are decelerated to 3.5 keV and positive secondary ions produced by sputtering are accelerated to 1.5 keV. The secondary ions are not transmitted through the mass spectrometer which is designed to accept ions with 1.0 ± 0.1 keV energy.

Three hundred nanoseconds after the end of each ion pulse a XeCl excimer laser is fired producing a ~10-ns, 250-mJ UV pulse with a bandwidth of 0.3 to 0.5 nm centered about 307.9 nm. The excimer output is split into three beams which either are used to pump tunable dye lasers (loaded with Rhodamine, Coumarin, or DCM dye) or, for some experiments, are focused directly into the ionization region. When necessary, the visible fundamental dye laser output is frequency doubled in a nonlinear crystal to produce UV pulses. The laser beams are spatially and temporally overlapped in a volume that extends from about 0.5 to 1.5 mm above the target surface and has a diameter of ~1 mm. Photoionization of sputtered neutrals occurs within this volume and the photoions are accelerated away from the target and into the mass spectrometer. The target potential is lowered at the beginning of each laser shot, so that ions produced by photoionization are transmitted through the mass spectrometer, and is then

* Author to whom correspondence should be addressed.

¹ Present address: Division of Geological and Planetary Science, California Institute of Technology, Pasadena, CA 91125.

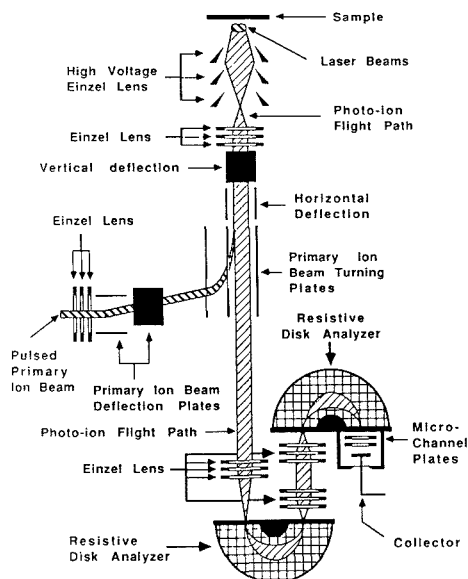


Figure 1. Schematic diagram of the SARISA experimental apparatus from Pellin et al. (2).

switched back to 1.5 kV before the arrival of the next primary ion pulse to again suppress the detection of sputtered secondary ions.

The photoion beam is focussed and shaped in the time-of-flight mass spectrometer by a series of einzel lenses, deflection plates, and two hemispherical energy analyzers, after which it strikes a chevron-type microchannel plate electron multiplier (Figure 1). The resulting electron pulse is measured by a transient charge digitizer at high signal levels or by a pulse-counting system at lower signal levels. The maximum ion transmission of the mass spectrometer is $\sim 70\%$ (3).

Samples. Four samples of metallic solid solutions were used as targets in this study. Two samples were synthesized from pure metals (4) and two samples are from meteorites. Synthetic sample 1 contains 95.2% Ni, 2.5% Os, and 2.3% Re. Synthetic sample 2 contains 99.8% Ni, 0.1% Os, and 0.1% Re. The meteorites are the Negrillos and Coahuila type ILAB hexahedrite iron meteorites, which are essentially comprised of a homogeneous mixture of 94.2% Fe, 5.4% Ni, and 0.4% Co with many other metals including Os, Re, Ir, Pt, and Au as parts-per-million level trace impurities. Radiochemical neutron activation analyses by Pernicka and Wasson (5) indicate that the Negrillos meteorite contains 25 ppm Os and 1.4 ppm Re ($\pm 12\%$) and that the Coahuila meteorite contains 3.4 ppm Os and 0.4 ppm Re ($\pm 12\%$). All concentrations are given in atomic proportions.

Ionization Schemes. Osmium was ionized by five different schemes to evaluate their relative sensitivities and selectivities. Rhenium was ionized by only the two simplest schemes. The ionization schemes all originate from the ground electronic state and can be grouped into five general types designated A through E (Figure 2). We report wavelengths as nanometers in air and energy levels as inverse centimeters in vacuum. Scheme A is nonresonant and requires the simultaneous absorption of two (in the case of Re) or three (in the case of Os) photons from the broad-band 307.9-nm excimer laser to reach the ionization continuum. Scheme B uses one ~ 240 - or ~ 300 -nm UV photon from a dye laser (λ_1) to raise Os or Re atoms to a resonant energy level (E_1) and one 307.9-nm excimer photon to ionize the atoms. Scheme C uses one ~ 240 - or ~ 300 -nm UV photon from a dye laser (λ_1) to raise atoms to a resonant energy level (E_1) and one additional photon (when ~ 240 -nm photons are used) or two additional photons (when ~ 300 -nm photons are used) of the same

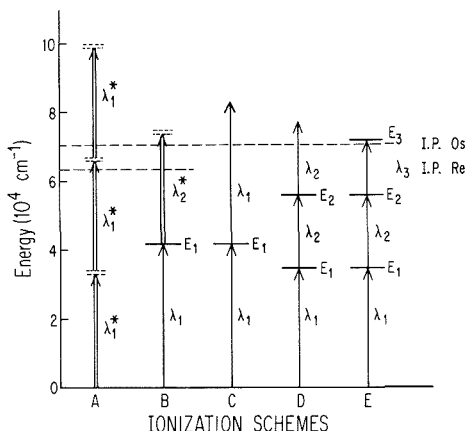


Figure 2. Generalized ionization schemes evaluated for Os (A-E) and Re (A-B). Asterisks denote broad-band excimer radiation.

Table I. Resonant Energy Levels Evaluated in this Study^a

ionization scheme	energy level, cm ⁻¹		
	E ₁	E ₂	E ₃
B _{Re}	41 557		
	41 313		
B _{Os}	41 876		
	41 726		
	41 232		
	41 225		
	40 362		
	34 365		
C	b		
D	41 726	58 175	
	41 232	56 729	
	40 362	56 222	
	34 365	55 402	
	34 365	55 402	71 032

^aE₁ and E₂ levels are from ref 18. ^bSame as B_{Os}.

energy to ionize them. Scheme D uses one ~ 240 - or ~ 300 -nm UV photon (λ_1) from a dye laser to raise atoms to a first resonant energy level (E_1), one ~ 480 - or ~ 600 -nm visible photon (λ_2) from a second dye laser to raise atoms to a second resonant energy level (E_2), and a second visible photon (λ_2) from the second dye laser to produce photoions. In schemes A through D atoms are raised to an arbitrary energy above the ionization continuum by the ionizing photon. Scheme E is the same as scheme D except that the ionizing photon (λ_3) is generated from a dye laser tuned to reach an autoionizing resonant energy level (E_3) above the ionization potential (IP). The specific energy levels evaluated for each scheme are given in Table I.

Scheme E was found to be most favorable for Os ionization (following criteria discussed below) and will therefore be described in more detail (Figure 3). UV photons from the first dye laser are tuned to 290.906 nm to populate the E_1 level [$E_1 = 34\,365$ cm⁻¹; angular momentum quantum number (J) = 5] from the ground state ($J = 4$). Visible photons at 475.216 nm then pump atoms from E_1 to the E_2 level ($E_2 = 55\,402$ cm⁻¹; $J = 5$). Finally, the third dye laser is tuned to pump atoms from E_2 over the IP ($\geq 69\,000$ cm⁻¹) to the most favorable autoionizing E_3 energy level ($E_3 = 71\,032$ cm⁻¹) that could be accessed by scanning the third dye laser across the 635- to 665-nm region.

The energy needed per pulse to saturate each of the three levels was investigated by monitoring the Os⁺ signal in the mass spectrometer while sequentially placing a series of partially transmitting filters into each of the laser beams separately. The important parameter for saturation is the energy density, which can be controlled by the size, shape, and position of the laser

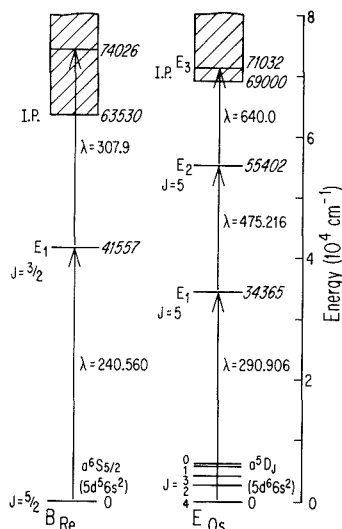


Figure 3. Specific ionization schemes used for Re and Os analyses.

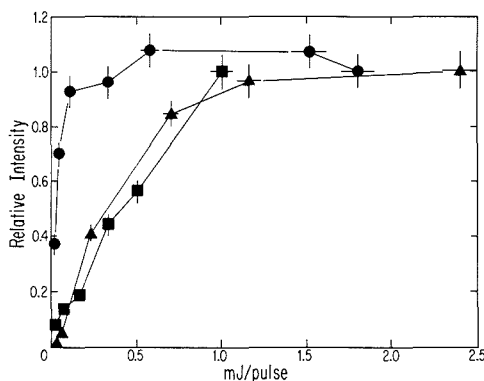


Figure 4. Relative Os signal intensity as a function of laser energy per pulse for ionization scheme E as each of the three laser beams was attenuated separately, while the other two beams were held at full energy. Error bars are included where estimated uncertainty exceeds symbol size. Saturation was not reached for λ_1 at a maximum energy of ~ 1 mJ/pulse (squares) but was reached for λ_2 at ~ 0.5 mJ/pulse (circles) and λ_3 at ~ 1.5 mJ/pulse (triangles).

beams as well as by the amount of incoming energy. By tightly focusing the laser beams, we were able to saturate each of the three energy levels, but in this configuration only a small portion of the cloud of sputtered atoms was ionized. Under normal operating conditions, we defocused the lasers to a diameter of ~ 1 mm in order to access a large portion of the cloud of sputtered atoms. With two of the three laser beams kept at full energy and one beam attenuated, E_1 was found not to be completely saturated with a maximum energy of ~ 1 mJ/pulse for λ_1 , E_2 was saturated at an energy of ~ 0.5 mJ/pulse for λ_2 , and E_3 was saturated at an energy of ~ 1.5 mJ/pulse for λ_3 (Figure 4). Subsequent experiments were run with an energy of ~ 1 mJ/pulse, ~ 2 mJ/pulse, and ~ 4 mJ/pulse at λ_1 , λ_2 , and λ_3 , respectively.

Rhenium atoms were ionized by schemes A and B only (Figure 2). In scheme B (Figure 3), UV photons at 240.560 nm populated the E_1 level ($E_1 = 41\,557\text{ cm}^{-1}$; $J = 3/2$) from the ground state ($J = 5/2$). The broad-band 307.9-nm excimer photons then raised the atoms from the excited energy level to the IP ($\geq 63\,530\text{ cm}^{-1}$).

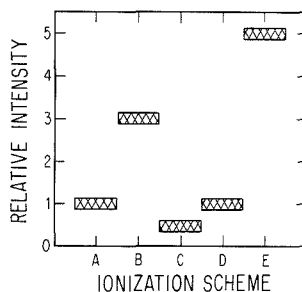


Figure 5. Relative signal intensities for Os ionization schemes.

RESULTS AND DISCUSSION

Sensitivity and Selectivity of Ionization Schemes.

Synthetic sample 1 was used to investigate the relative sensitivity and selectivity of the ionization schemes for Os. We will use the Os^+ signal intensity for nonresonant ionization by scheme A as a reference value and discuss the Os^+ signal levels for the resonant schemes relative to this value (Figure 5). Ionization by scheme B was ~ 3 times more efficient than scheme A, showing the enhancement of ionization probability from the addition of a resonant step to the broad-band 307.9-nm laser beam. The ionization energy in scheme A significantly overshoots the IP, whereas the ionization energy in scheme B places the atom only slightly above the IP (Figure 2). The increased ionization of scheme B over A suggests that the broad-band laser in scheme B overlaps an autoionizing resonance or that the ionization cross section in the continuum decreases at energies much higher than the IP.

Ionization by scheme C was $\sim 50\%$ less efficient than by scheme A. This probably arises because the ~ 1 mJ/pulse UV dye laser does not have enough energy to saturate the ionization process. In scheme D the addition of a second resonance level allows the ionization step to be pumped by the visible dye laser fundamentals which have higher energy (~ 2 mJ/pulse) than the frequency doubled UV pulses. The increase in energy more nearly saturates the ionization step and results in a $\sim 50\%$ higher efficiency than by scheme C (about the same efficiency as scheme A). Scheme E is identical with scheme D except that the visible ionizing photons are tuned to match an autoionizing energy level, producing a signal enhancement of a factor of ~ 5 over scheme D and suggesting that the ionization step is only saturated at the autoionizing resonance. Similar ionization enhancements have been observed for Gd (6) and U (7) when dye lasers were tuned to match autoionizing energy levels.

The in situ measurement of the isotopic composition of Os in samples that also contain Re would require that the ^{187}Re peak (62.6% abundance isotope) be suppressed to eliminate isobaric interference with the ^{187}Os peak ($\sim 1.6\%$ abundance isotope). As a measure of the selectivity of each Os^+ ionization scheme, we measured the $^{192}\text{Os}^+/^{185}\text{Re}^+$ ratio without correction for instrumental fractionation (to an accuracy of $\sim 10\%$) for each scheme and normalized it to the true ratio of these stable isotopes in the synthetic sample calculated from the Os and Re concentrations and natural isotopic abundances. Since there was some variability in the $^{192}\text{Os}^+/^{185}\text{Re}^+$ ratio for different energy levels following a given ionization scheme, we have plotted in Figure 6 the $^{192}\text{Os}^+/^{185}\text{Re}^+$ ratio for the energy levels with the maximum selectivity for each scheme. Nonresonant ionization by 307.9-nm photons (scheme A) was slightly more efficient for Re than for Os and showed a $\sim 30\%$ Re enhancement. The addition of an Os resonant step to the excimer photons (scheme B) enhanced Os ionization by as much as 3-fold. For resonance ionization using narrow band

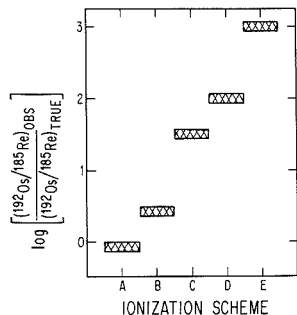


Figure 6. Relative selectivity for Os over Re measured as the log of the ratio of the observed to the true $^{192}\text{Os}^+ / ^{185}\text{Re}^+$ ratio for the Os ionization schemes.

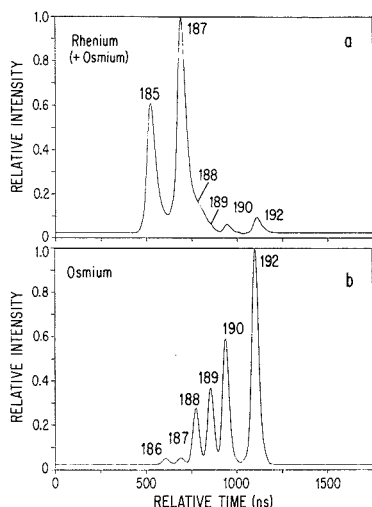


Figure 7. (a) Re spectrum (scheme B) taken at low mass resolution (~ 250) and (b) Os spectrum (scheme E) taken at higher mass resolution (~ 400) in the same synthetic sample (2.3% Re; 2.5% Os). Labels indicate the masses of the Re (185 and 187) and Os (186 to 190 and 192) isotope peaks. Note that scheme B for Re has low selectivity and scheme E for Os has high selectivity.

dye lasers only, Os was enhanced relative to Re by as much as 33 for single resonance (scheme C), 10^2 for double resonance (scheme D), and $\geq 10^3$ for triple resonance (scheme E). A signal intensity versus time-of-flight spectrum is shown in Figure 7a for resonance ionization of Re (mass 185 and 187) using ionization scheme B. The low selectivity of scheme B for Re is illustrated by the presence of nonresonantly ionized Os which is visible at masses 188 to 192. A similar spectrum is shown in Figure 7b for resonance ionization of Os from the same sample by ionization scheme E. The extremely high selectivity of scheme E for Os is illustrated by the complete absence of Re at mass 185 and 187. An Os selectivity similar to that of scheme E was reported for thermal vaporization RIMS using a two-photon single resonance scheme similar to scheme C, except that the transition originated from the $\sim 8\%$ populated thermally excited a^5D_3 state (Figure 3) rather than the ground state (8).

Os Concentration Measurement. Synthetic sample 2 and the two iron meteorite specimens were used to investigate the ability to measure Os concentrations quantitatively. Time-

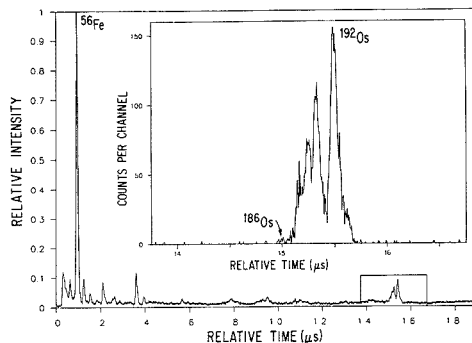


Figure 8. A time-of-flight spectrum collected with charge digitization for an Os analysis of the Negrillos iron meteorite using ionization scheme E. The peaks at 0–10 μs are due to nonresonant ionization of the major constituents in the sample (Fe, Ni, Co, and their oxides) and the peaks beginning at $\sim 15 \mu\text{s}$ are due to resonant ionization of the 25 ppm Os. Inset shows counts per 5-ns channels across the Os peaks for a 125-s pulse-counting experiment in which only $1/5$ of a monolayer of material was removed from a 100- μm spot.

Table II. Pulse Counting Data for 125-s Os Analyses of Samples

sample	Os conc, ppm	Os ⁺ counts	counts per ppm
synth 2	1000	346 000	346
Negrillos	25	6 480	259
Coahuila	3.4	1 120	329
mean			311 ± 53 ($2\sigma_m$)

of-flight spectra were collected for 125 s (5000 laser shots) with a fwhm mass resolution at mass 187 ($M/\Delta M$) of ~ 250 , which adequately resolved the peaks for the purpose of concentration measurement. Mass resolution can be increased to ~ 400 using an aperture positioned in the photoion path, but only at the cost of a loss in signal intensity by a factor of ~ 10 .

A time-of-flight spectrum of the Negrillos meteorite collected with charge digitization is shown as an example in Figure 8. The peaks at 0 to 10 μs are due to nonresonant ionization of the major constituents in the sample (Fe, Ni, Co, and their oxides), and the peaks beginning at $\sim 15 \mu\text{s}$ are due to resonant ionization of the 25 ppm Os. Because of the low concentration of Os a pulse counting system was also used to measure the Os peaks. The ion signal is recorded by dividing arrival times into 5-ns channels. The Os mass spectrum is shown as an inset in Figure 8 in which counts per 5-ns channels for a 125-s analysis are plotted. The small peak at 15 μs is ^{186}Os which is present at 0.40 ppm.

A background of 16 counts per 125 s across masses 186 to 192 was determined by detuning the UV laser 12 cm^{-1} from the center of the E₁ resonance level and repeating the experiment. The absence of interferences resonant with the UV laser frequency was verified by measuring a background of 18 counts per 125 s across these masses on stainless steel (Fe, Ni, Cr alloy) with the lasers tuned for Os analysis. This background intensity is assumed to represent the instrumental background for a sample containing no Os and was subtracted from the total counts measured for each sample to determine the net Os⁺ counts.

The Os⁺ counts summed over the major isotopes (masses 186 to 192) are given in Table II for three samples which have Os concentrations known to $\pm 12\%$ (5). The data demonstrate that for Os concentrations between ~ 3 and 1000 ppm the measured Os⁺ intensity is linearly proportional to the Os concentration in each sample. The ratio of Os⁺ intensity to

Os concentration (relative ion yield) is constant to within $\sim 20\%$ for all three samples and the data define a linear calibration curve whose slope, $311 \pm 53 (2\sigma_m)$ Os⁺ counts per ppm Os, can be used to determine Os concentrations in samples of similar bulk composition.

The mean relative ion yield and background count rate were used to calculate the minimum detection limit for Os in metallic Ni-Fe phases. Following the treatment of Ziebold (9) we calculate from Poisson statistics that the detection limit for Os at the 95% confidence level is 41 ppb for a 125-s analysis and 7.7 ppb for a 3600-s analysis. We note that a 3600-s analysis would consume only ca. six monolayers of the sample.

Variations in the relative ion yield due to matrix effects should depend primarily on the sputtering rate of the sample as long as the dominant sputtered species are neutral atoms. Therefore, sputtering rates must be determined for each target material analyzed. Considerable data exist for pure elements which indicate variations of up to a factor of ~ 3 (10). Sputtering rates of most multielement matrix materials are unknown and will have to be measured. If large populations of ions or molecules are produced during sputtering, the population of sputtered neutral atoms available for photoionization will be diminished and will cause shifts in the relative ion yield.

Useful Yield. The useful yield is defined as the ratio of ions detected to atoms present in the ion source. The useful yield is determined from the ratio of Os⁺ ions detected per laser shot to the number of Os atoms sputtered from the sample per primary ion pulse. The mean relative Os⁺ ion yield corresponds to 0.062 count per ppm per laser shot. The amount of target material sputtered per primary ion pulse can be estimated from the sputter yield of pure Fe and Os under bombardment by 3.5-keV Ar⁺ ions, which for both Fe and Os is 2.5 atoms per Ar⁺ ion (10). With a primary ion current of $\sim 2.0 \mu\text{A}$ and a pulse width of 0.20 μs , 2.5×10^6 ions strike the target per pulse and, therefore, approximately 6.3×10^6 Fe atoms are sputtered per pulse. Assuming that trace levels of Os are sputtered at the same rate as the Fe matrix, 6.3 Os atoms will be sputtered during each pulse per ppm of Os in the sample. Dividing the mean Os⁺ counts per laser shot by the number of sputtered Os atoms per primary ion pulse gives a useful yield of 10^{-2} . The Os mass spectrum for the 25 ppm Os sample shown in Figure 8 was collected during 5000 primary ion pulses (125 s) by sputtering 7.8×10^5 Os atoms ($1/5$ of a monolayer in a 100- μm spot) and detecting 6.5×10^3 Os⁺ ions.

The useful yield of the experiment described here appears to be considerably higher than that reported for other mass spectrometric techniques for Os analysis. However, in making such a comparison one must consider that the typical operating conditions (for instance, the mass resolution and the required sample preparation) of the various techniques differ markedly. The useful yield for resonance ionization mass spectrometry of chemically separated Os vaporized from a thermally pulsed filament has been reported at 10^{-7} (8) and the useful yield of inductively coupled plasma mass spectrometry of chemically separated Os has been reported at 10^{-5} to 10^{-6} (11). We have determined the useful yield for Os analysis by secondary ion mass spectrometry to be $\sim 10^{-4}$ using the Caltech Cameca IMS 3-F ionprobe with a O⁻ primary ion beam and a metallic Os target. Osmium analyses have also previously been made by thermal ionization of oxide species (12, 13), secondary ion mass spectrometry (14, 15), accelerator mass spectrometry (16), and laser ablation mass spectrometry (17), but useful yields have been reported.

Applications. In situ Os and Re concentrations can now be measured at the sub-part-per-million level in conducting

and semiconducting materials with a fwhm beam diameter of $\sim 70 \mu\text{m}$ using SARISA. The linear dependence of the Os⁺ signal on Os concentration allows the use of synthetic and well-characterized natural standards for quantitative analysis. Minor changes in the experimental configuration should allow analyses of most high IP elements including all of the Pt-group elements. These measurements may be applied to geochemical studies related to chemical fractionation and diffusion in metallic and sulfide phases in meteorites and terrestrial rocks and ore deposits as well as in phases synthesized in laboratory experiments.

The SARISA apparatus used in this study uses a low-resolution mass spectrometer (see mass spectra in Figures 7 and 8) and is therefore not appropriate for Os isotope ratio measurement. However, the high useful yield and selectivity for Os demonstrated here suggest that the SARISA photoion source may be superior to thermal vaporization as the ion source for Os isotope ratio measurements by resonance ionization. An important issue that remains to be resolved is whether the pulsed photoion source described here can be coupled with a mass spectrometer with sufficient mass resolution and abundance sensitivity for the measurement of Os isotopic ratios with $\leq 1\%$ precision. If this can be accomplished, it will be possible to measure the isotopic composition of Os using much smaller sample sizes than needed for thermal vaporization resonance ionization. If measurements can be precisely calibrated by using standards, in situ isotopic analyses may eventually be possible.

ACKNOWLEDGMENT

We thank three anonymous reviewers, J. Whitten for technical assistance, J. Wasson for providing meteorite specimens, J. Blake for comments, and E. Stolper and G. Rossman for the use of furnaces.

Registry No. Os, 7440-04-2; Rh, 7440-15-5.

LITERATURE CITED

- Pellin, M. J.; Young, C. E.; Calaway, W. F.; Burnett, J. W.; Jorgensen, B.; Schweitzer, E. L.; Gruen, D. M. *Nucl. Instrum. Method* **1987**, *B18*, 446-451.
- Pellin, M. J.; Young, C. E.; Gruen, D. M. *Scanning Microsc.* **1988**, *2*, 1353-1364.
- Pellin, M. J.; Husinsky, W.; Calaway, W. F.; Burnett, J. W.; Schweitzer, E. L.; Young, C. E.; Jorgensen, B.; Gruen, D. M. *J. Vac. Sci. Technol.* **1987**, *B5*, 1477-1481.
- Blum, J. D.; Wasserburg, G. J.; Hutcheon, I. D.; Beckett, J. R.; Stolper, E. M. *Geochim. Cosmochim. Acta* **1989**, *53*, 483-489.
- Pernicka, E.; Wasson, J. T. *Geochim. Cosmochim. Acta* **1987**, *51*, 1717-1726.
- Rimke, H.; Peuser, P.; Sattelberger, P.; Trautmann, N.; Herrmann, G.; Ruster, W.; Ames, F.; Kluge, H. J.; Otten, E. W. In *Resonance Ionization Spectroscopy*; Hurst, G. S., Morgan, C. G., Eds.; Institute of Physics Conference Series No. 84; Institute of Physics: Bristol, 1987; pp 235-238.
- Janes, G. S.; Irving, I.; Pike, C. T.; Levy, R. H.; Levin, L. *IEEE J. Quantum Electron.* **1976**, *QE-12*, 111-120.
- Walker, R. J.; Fassett, J. D.; Travis, J. C. In *Resonance Ionization Spectroscopy*; Lucatorto, T. B., Parks, J. E., Eds.; Institute of Physics Conference Series No. 94; Institute of Physics: Bristol, 1989; pp 337-342.
- Ziebold, T. O. *Anal. Chem.* **1967**, *39*, 858-861.
- Matsunami, N.; Yamamura, Y.; Itikawa, Y.; Itoh, N.; Kazumata, Y.; Miyagawa, S.; Morita, K.; Shimizu, R.; Tawara, H. *Energy Dependence of the Yields of Ion-Induced Sputtering of Monatomic Solids*; Institute of Plasma Physics: Nagoya, Japan, 1983.
- Russ, G. P.; Bazan, J. M. *Anal. Chem.* **1987**, *59*, 984-989.
- Hirt, B.; Tilton, G.; Herr, W.; Hoffmeister, W. In *Earth Science and Meteoritics*; Geiss, J., Goldberg, E., Eds.; North Holland: Amsterdam, 1963; pp 273-280.
- Herr, W.; Wolffe, R.; Eberhardt, P.; Kopp, E. In *Radioactive Dating and Methods of Low-Level Counting*; IAEA: Vienna, 1967; pp 499-508.
- Luck, J. M.; Allegre, C. J. *Nature* **1983**, *302*, 130-132.
- Luck, J. M.; Allegre, C. J. *EOS* **1986**, *67*, 393.
- Teng, R. T. D.; Fehn, U.; Elmore, D.; Hemmick, T. K.; Kubik, P. W.; Gove, H. E. *Nuclear Instrum. Methods, Phys. Res.* **1987**, *B29*, 281-285.
- Simons, D. S. *Int. J. Mass Spectrom. Ion Processes* **1983**, *55*, 15-30.
- Meggers, W. F.; Corliss, C. H.; Scribner, B. F. *Tables of NBS Spectral Line Intensities Part 1*, 2nd ed. U.S. Department of Commerce, Na-

tional Bureau of Standards Monograph 145; U.S. Government Printing Office: Washington, DC, 1975.

RECEIVED for review May 9, 1989. Accepted October 24, 1989. This study was performed as part of a doctoral dissertation by the senior author at the California Institute of Technology

(Caltech). Work was supported by the U.S. Department of Energy through BES-Material Sciences Contract W-31-109-ENG-38 to Argonne National Laboratory and BES-Engineering and Geosciences Grant DE-FG03-88ER13851 to Caltech. Caltech Division of Geological and Planetary Sciences Contribution Number 4759 (675).

CORRESPONDENCE

Reversing Enantioselectivity in Capillary Gas Chromatography with Polar and Nonpolar Cyclodextrin Derivative Phases

Sir: In the 1980s a wide variety of chiral stationary phases (CSPs) were developed for the liquid chromatographic (LC) separation of enantiomers while relatively little was done in gas chromatography (GC). Some of these CSPs were based on naturally occurring chiral molecules such as protein (1-3), cellulose, and so on, while others were based on synthetic molecules (4, 5). One of the advantages of the synthetic approach in developing CSPs was that either enantiomeric modification could be used, thereby reversing retention order. This was useful for a number of reasons. For example, when determining optical purities in which one enantiomer is in excess, it is preferable to have the less concentrated isomer elute first. This is because the enantiomer in excess frequently produces a large, tailing peak. Often, the tailing can overlap with a smaller, late eluting peak. In addition, enantiomeric reversals can be useful in confirming separations and in mechanistic studies. Reversing enantioselectivity by using opposite configuration amino acid derivatives as GC stationary phases or different analyte derivatives was noted previously as well (6, 7). In this work, we report several new chiral GC stationary phases that consist of hydrophilic and hydrophobic derivatives of cyclodextrin. In addition to separating enantiomers that cannot be resolved by LC, many of these CSPs are interesting in that they show opposite enantioselectivity.

Much of the early work on the use of native cyclodextrins as GC stationary phases was done by Smolkova-Keulemansova and co-workers (8-10) and Sybilska and associates (11). Because of their highly crystalline nature, native cyclodextrins (CD's) sometimes were difficult to use as stationary phases and generally were inefficient. However, this work demonstrated that CD's were highly selective, formed inclusion complexes with vaporized solutes and were worthy of continued study. Recently, König and co-workers produced lipophilic alkyl and alkyl-acyl derivatives of cyclodextrins that were liquids (12, 13). When coated on glass capillaries, a number of enantioselective GC separations were accomplished. Also, Schurig et al. have dissolved native and permethylated cyclodextrins in various GC stationary-phase liquids thereby obtaining viable CSP's (14). In an earlier work, we discussed requirements for obtaining liquid cyclodextrin derivatives as well as the use of nonpolar dialkyl α -, β -, and γ -CD stationary phases on fused silica capillaries (15).

Early kinetic work on cyclodextrin-catalyzed hydrolysis of racemic oxazolones indicated that α -CD and β -CD may have different enantioselectivities (16). However, these have never been confirmed or utilized in separations. Also, to our knowledge, there has never been a report showing that different derivatives of the same cyclodextrin show the opposite

enantioselectivity. In this communication, we show that the polar permethyl-*O*-((*S*)-2-hydroxypropyl)-CD often has the opposite enantioselectivity of the nonpolar alkyl derivatives. In a few cases, analogous α -, β -, and γ -cyclodextrin derivatives show opposite enantioselectivities. Consequently, it is no longer required that opposite molecular antipodes be "in hand" in order to have a generally useful chromatographic method in which enantioselectivities can be reversed. This approach is particularly useful for CSPs which utilize naturally occurring molecules that exist in a single enantiomeric form.

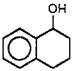
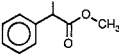
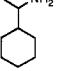
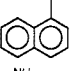
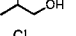
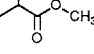
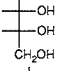
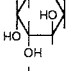
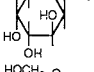
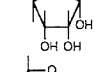
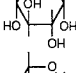
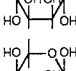
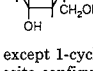
EXPERIMENTAL SECTION

Fused silica capillary tubing (0.25 mm i.d.) was obtained from Alltech. (2,6-Di-*O*-alkyl) cyclodextrins were made as previously reported (17). The heptakis(2,6-di-*O*-pentyl)cyclodextrins were made by reacting excess 1-bromopentane with 3.0 g of the desired cyclodextrin in 30 mL of dimethyl sulfoxide (DMSO) at 50 °C for 2 h. The product was isolated by precipitation with water. The waxy precipitate was washed and dissolved in chloroform (CHCl₃). The CHCl₃ solution was washed with water and the CHCl₃ was evaporated to leave the product, which was subsequently vacuum dried. This material then can be trifluoroacetylated by dissolving it in tetrahydrofuran (THF) with an excess of trifluoroacetic anhydride (TFA). The mixture is boiled for 2 h, then poured over ice to precipitate the product. The precipitate was washed with cold water and dissolved in CHCl₃. The CHCl₃ solution was extracted 3 times with 5% aqueous NaHCO₃ and 3 times with water. The CHCl₃ layer was dried with anhydrous Na₂SO₄ and evaporated. This viscous liquid was dried under vacuum overnight.

Permethyl derivatives of *O*-((*S*)-2-hydroxypropyl)cyclodextrin mixtures were made in two steps. First, the respective cyclodextrin was dissolved in aqueous NaOH (5% (w/w)) and the solution cooled in ice bath; then (*S*)-propylene oxide was slowly added while stirring. After about 6 h in an ice bath the reaction was allowed to proceed for a day at room temperature, neutralized, and dialyzed briefly in order to remove the contaminating salts. The re-formed solution was filtered and the product obtained by freeze-drying. Permethylation was achieved by a reaction with methyl iodide after the dissolution of cyclodextrin derivative in a solution of NaH in DMSO (18, 19). Additional data on the make-up and properties of this compound are to be published subsequently. The capillaries were coated via the static method as previously reported (20).

Amines and alcohols were derivatized with TFA or acetic anhydride. In each case, approximately 1.0 mg of the racemic analyte was dissolved in 0.5 mL of methylene chloride and 200 μ L of the desired anhydride added. After reaction, dry N₂ was bubbled through the solution to remove excess reagent. Sugars were trifluoroacetylated by the above procedure except that THF was used as the solvent. Also, because this reaction was somewhat

Table I. GC Enantioselectivity Retention Data for Permethyl-(*S*)-hydroxypropyl (PMHP) Derivatized Cyclodextrin and Dipentyl-Derivatized Cyclodextrin

racemic compound ^a	structure ^b	α	elution order	stationary phase ^c	temp, °C
1,2,3,4-tetrahydro-1-naphthol		1.03	<i>S,R</i>	PMHP- α -CD	100
		1.03	<i>R,S</i>	dipentyl- α -CD	100
mandelic acid methyl ester		1.04	<i>S,R</i>	PMHP- α -CD	120
		1.01	<i>R,S</i>	dipentyl- β -CD	100
1-cyclohexylethylamine		1.05	<i>S,R</i>	PMHP- β -CD	100
		1.03	<i>R,S</i>	dipentyl- α -CD	45
1-(1-naphthyl)ethylamine		1.03	<i>S,R</i>	PMHP- α -CD	150
		1.09	<i>R,S</i>	dipentyl- β -CD	150
2-amino-1-propanol		1.05	<i>S,R</i>	PMHP- β -CD	120
		1.16	<i>R,S</i>	DPTFA- β -CD ^d	110
2-chloropropionic acid methyl ester		1.13	<i>S,R</i>	PMHP- β -CD	50
		2.14	<i>R,S</i>	DPTFA- β -CD ^d	60
erythrose		1.03	L,D	PMHP- β -CD	80
		1.07	D,L	dipentyl- β -CD	80
arabinose		1.04	D,L	PMHP- β -CD	90
		1.20	L,D	dipentyl- β -CD	70
1- <i>O</i> -methyl- β -D,L-arabinopyranoside		1.10	D,L	PMHP- β -CD	90
		1.10	L,D	dipentyl- β -CD	90
ribose		1.08	D,L	PMHP- β -CD	100
		1.07	L,D	dipentyl- β -CD	80
xylose		1.05	L,D	PMHP- β -CD	80
		1.05	D,L	dipentyl- β -CD	70
lyxose		1.05	D,L	PMHP- β -CD	80
		1.05	L,D	dipentyl- β -CD	80
sorbiose		1.12	L,D	PMHP- β -CD	90
		1.04	D,L	dipentyl- β -CD	100

^aAll compounds are trifluoroacetyl derivatives except 1-cyclohexylethylamine which was the acetyl derivative. ^bSugars are shown in the D-configuration, the L-enantiomers have the opposite configuration at all stereogenic centers. ^cAll columns are 10 m long except for that dipentyl- β -CD column used to resolve mandelic acid methyl ester (which was 30 m). ^dThis stationary phase consists of trifluoroacetylated heptakis(2,6-di-*O*-pentyl)- β -cyclodextrin.

slower and the TFA was volatile, three additional aliquots of TFA were added at 7-min intervals.

Both Hewlett-Packard (5710A) and Varian (3700) gas chromatographs were used for all separations. Split injection and flame ionization detection were utilized. The injection port temperature was 200 °C and N₂ was used as the carrier gas.

RESULTS AND DISCUSSION

Permethyl derivatives of *O*-((*S*)-2-hydroxypropyl)cyclodextrin mixtures (PMHP-CD) are liquids at room temperature and can be used to coat undecivated fused silica capillaries. They are nonvolatile and appear to be thermally stable at

temperatures up to 300 °C in the absence of oxygen. Also, these cyclodextrin derivatives have an affinity for water and seem to be much more polar than previously described alkyl-derivatized cyclodextrins (12, 13). Many racemic solutes can be resolved on both PMHP-CD and alkyl-CD stationary phases. Most of these compounds (for which standards are available) have their enantiomeric elution order reversed on the two stationary phases. This is true for a variety of structural types of molecules including alcohols, amines, carboxylic acid esters, and sugars (Table I). Enantiomeric reversals also can occur between PMHP-CD stationary phases

Table II. GC Enantioselective Separation Data for Analogous Derivatives of α -, β -, and γ -Cyclodextrin

compound	separation factor, α	elution order	stationary phase	column length, m	temp, °C
1,2,3,4-tetrahydro-1-naphthol	1.03	<i>S,R</i>	PMHP- α -CD	10	100
	1.07	<i>R,S</i>	PMHP- β -CD	20	120
1-(1-naphthyl)ethylamine	1.06	<i>S,R</i>	dipentyl- β -CD	10	150
	1.09	<i>R,S</i>	dipentyl- γ -CD	10	150
limonene oxide ^a	1.06, 1.20	+, -, -, +	PMHP- α -CD	10	90
	1.02, 1.03	-, +, -, +	PMHP- β -CD	20	100

^aThis compound has two pairs of enantiomers. The reversal occurs only for the first pair of isomers.

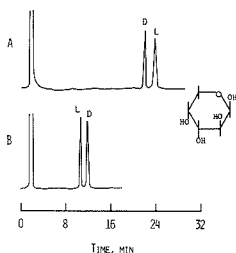


Figure 1. Separation of D,L-arabinose on (A) a 10 M permethyl-*O*-(*S*)-2-hydroxypropyl- β -cyclodextrin column (PMHP- β -CD) and (B) a 10 M dipentyl- β -cyclodextrin column (DP- β -CD). Both separations were done at 80 °C with N₂ carrier gas. Note that the elution order of the *D*- and *L*-enantiomers is reversed on these CSPs. The structure shown is of β -L-arabinose.

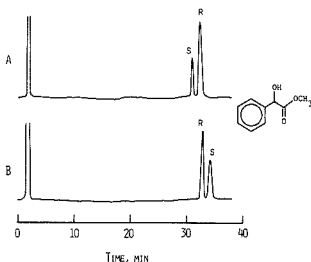


Figure 2. Enantiomeric separation of mandelic acid methyl ester on (A) a 10 M permethyl-*O*-(*S*)-2-hydroxypropyl- α -cyclodextrin column (PMHP- α -CD) and (B) a 10 M dipentyl- β -cyclodextrin column (DP- β -CD). Both separations were done at 120 °C with N₂ carrier gas. Note that the elution order of the *R*- and *S*-enantiomers is reversed on these CSPs. This mixture was made so that the concentration of the *R*-enantiomer was 50% more than the *S*-enantiomer.

and trifluoroacetylated DP-CD stationary phase. See, for example, the data on 2-amino-1-propanol (Table I). Figures 1 and 2 show the chromatographically observed reversal in retention for D,L-arabinose and the methyl ester of mandelic acid.

Although it appeared to be less common, enantioselective reversals also can occur among like-derivatized α -, β -, and γ -cyclodextrins. Examples of this phenomenon are given in Table II. Peak reversals have been observed between α - and β -CD and between β - and γ -CD, but not between α - and γ -CD. Because the cyclodextrins are "size-selective", this is not surprising (21–23).

According to the Gibbs–Helmholtz equation, it may be possible (in certain cases) to obtain a temperature-dependent inversion of the enantiomeric elution order. Indeed, there have been examples of this reported in the recent literature (24, 25). Retention versus temperature studies were done for many of the enantiomers separated in this work. A typical example for (*R,S*)-1-(1-naphthyl)ethylamine is shown in Figure 3. In

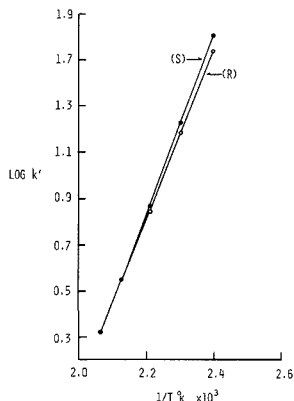


Figure 3. Plots of the log of the capacity factors (k') of (*R*)- and (*S*)-1-(1-naphthyl)ethylamine versus the reciprocal of the absolute temperature (K). No discontinuities or temperature-induced inversion of enantiomers was observed.

no case was a temperature-dependent inversion of the elution order observed for these solutes on these derivatized cyclodextrin stationary phases. As temperature is increased, the separation factor (α) decreases. Eventually a temperature is reached at which the enantiomers coelute. Further increases in temperature causes the retention of the coeluting isomers to decrease until they elute at the dead volume of the column. Currently, it is not known if this behavior is typical of all cyclodextrin-based GC stationary phases or if it is unique to the solutes and CD derivatives used in this study.

In addition to being of great practical importance, this work raises several questions as to the nature of chiral recognition in these cyclodextrin derivatives. The definite size selectivity effects between the hydrophobic alkyl derivatives of α -, β -, and γ -CD seem to indicate that an inclusion complex is formed at these elevated temperatures. However, comparable size selectivities are not observed for the more polar PMHP-cyclodextrins (15). The role played by the different substituents on the CD is most intriguing and difficult to explain. Undoubtedly there are a combination of factors (including polarity, steric bulk, orientation, degree of substitution, direct interactions, etc.) that affect chiral recognition. Currently, we are attempting to evaluate these by gas-phase calorimetry, computer modeling, and energy minimization studies.

ACKNOWLEDGMENT

The preparative help of Drs. C. T. Rao and Yan Xia is gratefully acknowledged.

LITERATURE CITED

- Hermansson, J. J. *Chromatogr.* **1983**, *269*, 71–80.
- Allenmark, S.; Bomgren, B.; Boren, H. J. *Chromatogr.* **1983**, *269*, 63–68.
- Lindner, K. R.; Mannschrek, A. J. *Chromatogr.* **1980**, *193*, 308–310.
- Pirkle, W. H.; House, D. W.; Fin, J. M. J. *Chromatogr.* **1980**, *103*, 143–158.

- (5) Pirkle, W. H.; Pochapsky, T. C. *J. Am. Chem. Soc.* **1986**, *108*, 5627-28.
 (6) Feibusch, B.; Gil-Av, E.; Tamari, T. *Perkin Trans. 2* **1972**, 1197-1203.
 (7) Lochmüller, C. H.; Souter, R. W. *J. Chromatogr.* **1975**, *88*, 41-54.
 (8) Smolkova-Keulemansova, E. *J. Chromatogr.* **1982**, *251*, 17-34.
 (9) Smolkova-Keulemansova, E.; Kralova, H.; Krysl, S.; Fell, L. *J. Chromatogr.* **1982**, *241*, 3-8.
 (10) Smolkova-Keulemansova, E.; Fell, L.; Krysl, S. *J. Inclusion Phenom.* **1985**, *3*, 183-196.
 (11) Koscielski, T.; Sybiliska, D.; Jurczak, J. *J. Chromatogr.* **1983**, *280*, 131-134.
 (12) König, W. A.; Lutz, S.; Mischnick-Lubbecke, P.; Brassat, B.; Wenz, G. *J. Chromatogr.* **1988**, *447*, 193-197.
 (13) König, W. A.; Lutz, S.; Wenz, G.; von der Bey, E. *HRC CC, J. High Resolut. Chromatogr. Chromatogr. Commun.* **1988**, *11*, 506.
 (14) Schurig, V.; Nowolny, H.-P. *J. Chromatogr.* **1988**, *441*, 155-163.
 (15) Armstrong, D. W. *Pittsburgh Conference Abstract Book*; **1989**, 001.
 (16) Daffe, V.; Fastré, J. *J. Am. Chem. Soc.* **1980**, *102*, 3601-3607.
 (17) Croft, A. P.; Bartsch, R. A. *Tetrahedron* **1983**, *39*, 1417-1474.
 (18) Pitha, J.; Pitha, J. *J. Pharm. Sci.* **1985**, *74*, 987-990.
 (19) Pitha, J.; Rao, C. T.; Lindberg, B.; Seffers, P., submitted for publication in *Carbohydr. Res.*
 (20) Bouche, J.; Verzele, M. *J. Gas Chromatogr.* **1968**, *6*, 501-505.
 (21) Hinze, W. L. *Sep. Purif. Methods* **1981**, *10*, 159-237.
 (22) Armstrong, D. W.; DeMond, W. *J. Chromatogr. Sci.* **1984**, *22*, 411-415.
 (23) Armstrong, D. W.; Ward, T. J.; Armstrong, R. D.; Beesley, T. E. *Science* **1986**, *232*, 1132-1134.
 (24) Watabe, K.; Charles, R.; Gil-Av, E. *Angew. Chem.* **1989**, *101*, 195-197.
 (25) Schurig, V.; Ossig, A.; Link, R. *Angew. Chem.* **1989**, *101*, 197-200.

Daniel W. Armstrong*
Weiyong Li

Department of Chemistry
University of Missouri—Rolla
Rolla, Missouri 65401

Josef Pitha

National Institutes of Health
NIA/GRC
Baltimore, Maryland 21224

RECEIVED for review July 13, 1989. Accepted October 30, 1989.
Support of this work by the Department of Energy, Office of Basic Sciences (DE FG02 88ER13819) is gratefully acknowledged.

Effect of a Difference of the Column Saturation Capacities for the Two Components of a Mixture on the Relative Intensities of the Displacement and Tag-Along Effects in Nonlinear Chromatography

Sir: The displacement and tag-along effects have been predicted by computations based on the use of the semiideal model of nonlinear chromatography (1). They are often observed in preparative applications of liquid chromatography, when the column is overloaded, and have been reported in many recent contributions (2-4). These effects are due to the fact that the velocity associated to a certain concentration of one of the components (5) depends also on the concentration of the other components locally present (6). The intensity of the displacement and the tag-along effects controls the shape of the profiles of the individual component bands of a mixture when these bands are not completely resolved. It is important to note that the displacement effect also controls the profile of an elution band after it has been separated from the bands of the compounds eluted after it. The profile of this band may never recover from the consequences of its interaction with the later eluted bands (6, 7). It is therefore important to understand what are the parameters which determine the intensity of these two effects and their relative intensity.

The intensities of the displacement and of the tag-along effects depend essentially on the sample size, the composition of the feed and the parameters of the competitive equilibrium isotherm of the components involved. Most work carried out so far has been mainly concerned with the relative composition of the feed (1-4). The analytical solution of the ideal model has been derived in the case of a binary mixture, when the two components have competitive Langmuir equilibrium isotherms (6). This solution shows that the factor which controls the intensities of the displacement and the tag-along effects is not the mere relative composition of the feed or ratio of the concentrations of the two components ($C_{0,2}/C_{0,1}$) but is rather the ratio of the individual loading factors for the two components ($L_{f,1}/L_{f,2} = q_{s,1}C_{0,2}/q_{s,2}C_{0,1}$), where $L_{f,1}$ and $L_{f,2}$ are the individual loading factors of the two components, $q_{s,1}$ and $q_{s,2}$ their column saturation capacities, and $C_{0,1}$ and $C_{0,2}$ their concentrations in the feed). The loading factor of the column for a given compound is the ratio of the actual amount injected

with the sample to the column saturation capacity for this compound ($L_{f,i} = N_i/(1 - \epsilon)SLq_{s,i}$, where N_i is the amount injected, in moles, $q_{s,i}$ is the column packing saturation capacity in mol/mL, ϵ is the column packing porosity, and S and L are the column cross-section area and length, in cm^2 and cm, respectively).

INTENSITY OF THE DISPLACEMENT EFFECT

The intensity of the displacement effect can be measured by the ratio of the concentrations of the first eluted component in the front ($C_{1,A'}$) and the rear ($C_{1,M}$) sides of the second shock. If the second component does not displace the first one, there is no rear shock for the first component band. If the second component displaces strongly the first one, there will be an important rear shock for the first band. The ratio of the concentrations of the first component on both sides of the shock is given by eq 54 of ref 6

$$\frac{C_{1,A'}}{C_{1,M}} = 1 + \frac{b_2}{\alpha b_1 r_1} \quad (1)$$

In eq 1, b_1 and b_2 are the second coefficients of the binary Langmuir isotherms of the two components and $\alpha = a_2/a_1$, the ratio of their first coefficients, is also the analytical relative retention. r_1 in eq 1 is the root of eq 22 of ref 6, which is in almost all cases nearly identical with $C_{0,1}/C_{0,2}$. The competitive Langmuir isotherms are written

$$q_i = \frac{a_i C_i}{1 + b_1 C_1 + b_2 C_2} \quad (2)$$

where $i = 1, 2$. With a Langmuir isotherm, the column saturation capacity, $q_{s,i}$, is equal to the ratio a_i/b_i . Introducing into eq 1 the value of $r_1 \approx C_{0,1}/C_{0,2}$ and the relationships between the coefficients of the competitive Langmuir isotherm, α , and the column saturation capacities, we obtain

$$\frac{C_{1,A'}}{C_{1,M}} = 1 + \frac{q_{s,1}C_{0,2}}{q_{s,2}C_{0,1}} = 1 + \frac{L_{f,2}}{L_{f,1}} \quad (3)$$

Since the intensity of the displacement effect is measured by the amplitude ratio of the concentrations of the first component on both sides of the rear concentration shock of the first component band, it will depend essentially on the ratio of the individual loading factors for the two components. If the loading factor for the second component is small or negligible with respect to the loading factor of the first component, the displacement effect will be small or insignificant. On the other hand, if the loading factor of the second component is larger than that of the first component, the displacement effect will be important. Since the theory discussed here is an application of the ideal model, it is not surprising to see that a significant displacement effect can be observed at low loading factors for both components if the ratio of the loading factor of the second component to that of the first one is large. With the ideal model, the asymptotic band profile at low sample sizes is a rectangular triangle (8).

We see from eq 3 that if the two components of a binary mixture have the same column saturation capacity, the intensity of the displacement effect is controlled by the relative composition of the feed. However, if the column saturation capacities are different for both components, the ratio of these two capacities will modify the effect of the relative composition of the feed. If the column saturation capacity of the first component is lower than that of the second one (i.e., in this case the two single component isotherms diverge rapidly, the one with the stronger slope at the origin having the higher asymptote), the ratio of the loading factors ($L_{t,2}/L_{t,1}$) will be smaller than the ratio of the component concentrations in the feed and the intensity of the displacement effect will appear to be reduced.

Conversely, if the column saturation capacity of the first component is larger than that of the second one, the ratio of the loading factors will be higher than the ratio of their concentrations in the feed. The displacement effect will be more intense than anticipated on the basis of the feed composition. In this latter case, the single compound isotherms of the pure components are expected to intersect. There is nothing particular in this fact, as the two isotherms are not really drawn in the same q_1, C_1 plane. These isotherms are plots of the amounts of one component sorbed in the stationary phase at equilibrium versus its concentration in the mobile phase. The two plots are merely superimposed on the same graph, leaving the intersection point with no more physical meaning than a mirage. The properties of the competitive Langmuir isotherms in such a case have been discussed (9). It should be pointed out, however, that the competitive Langmuir isotherm model rarely accounts better than fairly for the actual competitive isotherms when the column saturation capacity of the first component is lower than or close to that of the second component. It tends to do quite poorly when the column saturation capacity of the first component is larger than that of the second one.

INTENSITY OF THE TAG-ALONG EFFECT

The intensity of the tag-along effect is measured by the length of the concentration plateau of the second component left behind by the first component. This plateau results from the fact that the velocity associated to a certain concentration of the second component is a decreasing function of the local concentration of the first component (because of the competition for access to retention sites). The limit of this velocity for a zero concentration of the first component is larger than the velocity associated to the same concentration of the pure second component (6). This creates a discontinuity in the concentration dependence of the velocity associated to a certain concentration of the second component, hence the origin of the concentration plateau on the rear part of the second component band profile.

The length of the concentration plateau of the second component is given by eq 49 of ref 6

$$\Delta t = \frac{\gamma(\gamma - 1)}{\alpha^2} (t_{R,0,2} - t_0) \quad (4)$$

where t_0 is the dead time, $t_{R,0,2}$ is the limit retention time of the second component at very low sample size ($t_{R,0,2} = (1 + Fa_2)t_0$), and γ is a function of the isotherm coefficients ($\gamma = (\alpha b_1 r_1 + b_2)/(b_1 r_1 + b_2)$). In the simplifying assumption that r_1 is practically equal to the concentration ratio, $C_{0,1}/C_{0,2}$, eq 4 becomes

$$\Delta t = \frac{q_{s,2}C_{0,1} \left(1 + \frac{q_{s,2}C_{0,1}}{q_{s,1}C_{0,2}} \right)}{q_{s,1}C_{0,2} \left(\alpha + \frac{q_{s,2}C_{0,1}}{q_{s,1}C_{0,2}} \right)^2} \alpha^{-1} (t_{R,0,2} - t_0) \quad (5)$$

or

$$\Delta t = \frac{L_{t,1}}{L_{t,2}} \frac{1 + \frac{L_{t,1}}{L_{t,2}}}{\left(\alpha + \frac{L_{t,1}}{L_{t,2}} \right)^2} \alpha^{-1} (t_{R,0,2} - t_0) \quad (6)$$

which is equivalent to

$$\Delta t = \frac{1 + \frac{L_{t,2}}{L_{t,1}}}{\left(1 + \alpha \frac{L_{t,2}}{L_{t,1}} \right)^2} (k'_{0,2} - k'_{0,1}) t_0 \quad (7)$$

Equation 7 shows first that the intensity of the tag-along effect depends essentially on the ratio of the loading factors and is proportional to the difference between the limit column capacity factors at very low sample size. When the loading factor for the first component is much smaller than the loading factor for the second component, the intensity of the tag-along effect is low and proportional to the ratio $L_{t,1}/L_{t,2}$ (eq 6). We have seen that, under these conditions, the displacement effect is intense.

On the contrary, when the loading factor for the second component is much smaller than the loading factor for the first one, the ratio $L_{t,2}/L_{t,1}$ in eq 7 is small, the intensity of the tag-along effect is high, and it is essentially given by the difference ($k'_{0,2} - k'_{0,1}$). In the intermediate cases, the intensity of the tag-along effect is given by eq 7. For a given feed composition and sample size, an increase in the column saturation capacity of the second component results in a decrease of the ratio of the loading factors, hence an increase of the intensity of the tag-along effect.

As a conclusion, a variation in the loading factor ratio and, accordingly, a variation in the ratio of column saturation capacities at constant feed composition and sample size have opposite influences on the displacement and the tag-along effects. This is illustrated by the three chromatograms in Figure 1, showing the individual band profiles of the components of a binary mixture with a 1:3 relative composition of the feed and a constant sample size. The column saturation capacity for the second component is successively lower than (Figure 1a), equal to (Figure 1b), and higher (Figure 1c) than the column saturation capacity for the first component. Obviously, the intensity of the displacement effect decreases and the intensity of the tag-along effect increases with decreasing ratio of the loading factors ($L_{t,2}/L_{t,1}$) at constant feed composition and sample size, from Figure 1a to Figure 1c.

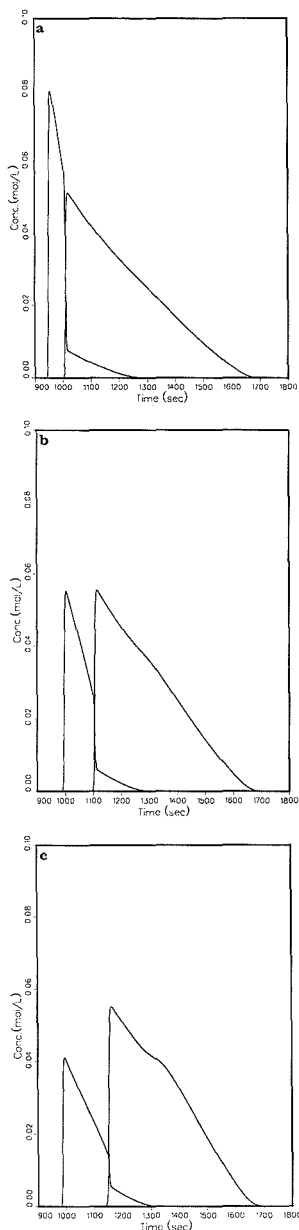


Figure 1. Individual elution band profiles for a binary mixture: calculated chromatograms for a 25 cm long column; column efficiency, 5000 theoretical plates; phase ratio, $F = 0.25$; mobile phase linear velocity, 0.125 cm/s; relative retention, $\alpha = 1.20$; $K_{0,1} = 6.0$; relative feed composition, 1:3; sample size, 0.083 mmol of the first component and 0.249 mmol of the second component; (a) $q_{s,1} = 10$, $q_{s,2} = 5$; $L_{1,1} = 1\%$, $L_{1,2} = 6\%$, $L_{1,2}/L_{1,1} = 6.0$; (b) $q_{s,1} = 7.5$, $q_{s,2} = 7.5$, $L_{1,1} = 1.33\%$, $L_{1,2} = 4\%$, $L_{1,2}/L_{1,1} = 3.0$; (c) $q_{s,1} = 5$, $q_{s,2} = 10$, $L_{1,1} = 2\%$, $L_{1,2} = 3\%$, $L_{1,2}/L_{1,1} = 1.5$.

While the relative intensity of the displacement and/or tag-along effects depends on the loading factor ratio, the degree of band overlay depends on the absolute value of the

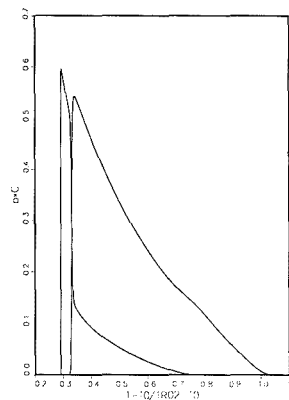


Figure 2. Dimensionless plots of the individual elution band profiles for a binary mixture, plots of b_1C_1 and b_2C_2 versus $(t - t_0)/(t_{R,0,2} - t_0)$ for both components. Conditions as in Figure 1, except that in all three cases $L_{1,1} = 5\%$ and the feed composition is adjusted so that $L_{1,2}/L_{1,1} = 3.0$. The figure shows the elution profiles obtained for the two compounds under the following three sets of conditions: condition 1, $q_{s,1} = 5$, $q_{s,2} = 10$; relative composition of feed, 1:6; condition 2, $q_{s,1} = 7.5$, $q_{s,2} = 7.5$, relative composition of feed, 1:3; condition 3, $q_{s,1} = 10$, $q_{s,2} = 5$, relative composition of feed, 2:3. For both components, the three elution profiles cannot be distinguished.

loading factors. According to eq 40 of ref 6, the retention time of the front shock of the second component is given by

$$t_{f,2} = t_p + t_0 + (t_{R,0,2} - t_0) \times \frac{1 + \frac{q_{s,2}C_{0,1}}{q_{s,1}C_{0,2}} \left(1 - \left[\left(1 + \frac{q_{s,2}C_{0,1}}{\alpha q_{s,1}C_{0,2}} \right) L_{f,2} \right]^{1/2} \right)^2}{1 + \frac{q_{s,2}C_{0,1}}{\alpha q_{s,1}C_{0,2}}} \quad (8)$$

At constant value of the loading factor for the second component, $L_{f,2}$, when the ratio of the column saturation capacities, $q_{s,2}/q_{s,1}$, decreases, the retention time of the second component increases and the degree of band overlapping decreases. A similar result can be derived from eq 70 of ref. 6, which states that exact separation between the two bands (ideal "touching bands") is achieved for a sample size equal to

$$L_{f,2,T} = \frac{\left(\frac{\alpha - 1}{\alpha} \right)^2}{1 + \frac{q_{s,2}C_{0,1}}{\alpha q_{s,1}C_{0,2}}} \quad (9)$$

According to eq 9, when the ratio $q_{s,2}/q_{s,1}$ decreases (either $q_{s,2}$ decreases or $q_{s,1}$ increases, or both), $L_{f,2,T}$ increases and we observe a better separation at constant loading factor. On the other hand, however, at constant sample size the loading factor is inversely proportional to the column saturation capacity.

The ratios of the column saturation capacities are 0.5, 1, and 2 for parts a, b, and c of Figure 1, respectively. According to the previous discussion and if the loading factor for the second component remained constant, the separation should become worse from Figure 1a to Figure 1b and to Figure 1c. However, since the sample size is kept constant and the column saturation capacity for the second component is increased from Figure 1a (5 mmol/mL) to Figure 1b (7.5 mmol/mL) and Figure 1c (10 mmol/mL), the loading factor for the second component decreases from Figure 1a to Figure 1c and the actual separation improves in the same order.

DIMENSIONLESS PLOT OF A TWO-COMPONENT BAND SYSTEM

In a previous publication, we have shown that dimensionless profiles can be obtained for the solutions of the ideal model of chromatography for a single component. At constant column efficiency, the elution bands observed for different sample sizes and different compounds can be scaled by plotting a dimensionless concentration, bC , versus a dimensionless time, $(t - t_0)/(t_{R,0} - t_0)$. The scaling factor in this case is the loading factor.

A similar result can be obtained for the elution bands of the components of a binary mixture, but some restricting conditions must be satisfied. The column efficiency must remain constant. In addition, the loading factors of both components and their limit relative retention, α , must also remain constant, which is a serious limitation to the interest of that kind of reduced plots. Figure 2 shows that, when the conditions just stated are met, identical reduced plots are obtained for the elution bands of the components of a binary mixture when the column saturation capacity and the feed composition are varied while keeping constant the two loading factors.

LITERATURE CITED

- (1) Guiochon, G.; Ghodbane, S. *J. Phys. Chem.* **1988**, *92*, 3682.
- (2) Perry, J., Communication, 13th International Symposium on Preparative Chromatography, Washington, DC, May 1989.

- (3) Newburger, J.; Guiochon, G., Communication, 11th International Symposium on Preparative Chromatography, Washington, DC, May 1989.
- (4) Cox, G. B.; Eble, S.; Snyder, L. R., Communication, 13th International Symposium on Column Liquid Chromatography, Stockholm, Sweden, June 1989.
- (5) Lin, B.; Golshan-Shirazi, S.; Ma, Z.; Guiochon, G. *Anal. Chem.* **1988**, *60*, 2647.
- (6) Golshan-Shirazi, S.; Guiochon, G. *J. Phys. Chem.* **1989**, *93*, 4143.
- (7) Golshan-Shirazi, S.; Guiochon, G. *J. Chromatogr.*, in press.
- (8) Golshan-Shirazi, S.; Guiochon, G. *J. Phys. Chem.*, in press.
- (9) Huang, J. X.; Guiochon, G. *J. Colloid Interface Sci.* **1989**, *128*, 577.

¹ Author to whom correspondence should be addressed, at the University of Tennessee.

Sadroddin Golshan-Shirazi
Georges Guiochon*,¹

Department of Chemistry
University of Tennessee
Knoxville, Tennessee 37996-1600
and Division of Analytical Chemistry
Building 4500-S, M.S. 120
Oak Ridge National Laboratory
Oak Ridge, Tennessee 37831-6120

RECEIVED for review August 22, 1989. Accepted October 26, 1989. This work has been supported in part by Grant CHE-8901382 of the National Science Foundation and by the cooperative agreement between the University of Tennessee and the Oak Ridge National Laboratory.

TECHNICAL NOTES

Anion-Exchange Separation of Carbohydrates with Pulsed Amperometric Detection Using a pH-Selective Reference Electrode

William R. LaCourse,* David A. Mead, Jr.,¹ and Dennis C. Johnson

Department of Chemistry, Iowa State University, Ames, Iowa 50011

INTRODUCTION

The activity of noble metal electrodes (i.e., Au and Pt) is observed to decrease for the anodic, amperometric detection of virtually all electroactive, aliphatic, compounds at constant (dc) applied potentials. This loss of activity is commonly attributed to "fouling" of electrode surfaces by adsorbed organic reactants and/or reaction products, as well as the formation of surface oxides at large, positive, values of applied potential (1, 2). Pulsed amperometric detection (PAD) is based on multistep potential waveforms, applied at a frequency of ca. 1 Hz, which incorporate amperometric detection with alternated anodic and cathodic polarizations to clean and reactivate the electrode surface. In the detection of the $-CH_2OH$ functionalities of alcohols and carbohydrates, adsorbed carbonaceous species (e.g., free radicals) are oxidatively desorbed by an electrocatalytic process simultaneously with the anodic formation of surface oxide following a positive potential step applied after the brief detection period. The inherent activity of the "clean" electrode surface is then regenerated by a subsequent negative potential step which causes the cathodic dissolution of the oxide film prior to the next detection step in the waveform. This on-line, intermittent, pulsed cleaning and reactivation of the electrode is sufficient to maintain a uniform and reproducible electrode activity.

¹ Present address: Commonwealth Edison, Maywood, IL 60153.

A disadvantage of PAD is observed for detection processes which occur at potential values for which surface oxide is formed simultaneously with the desired detection process. The result is a large base-line signal in liquid chromatographic applications of PAD. Furthermore, the base line is commonly observed to drift because of the gradual increase in the true electrode area caused by surface reconstruction under the repeated conditions of the oxide on/off cycles in the PAD waveform. Also, the base-line signal is very sensitive to changes in solution pH because of the inherent pH dependency of the oxide formation reaction.

Integrated pulsed amperometric detection (IPAD), previously known as potential sweep-pulsed coulometric detection (PS-PCD) (3), was developed to minimize the base line found for PAD in detection processes occurring with simultaneous oxide formation. IPAD incorporates a rapid, cyclic potential sweep within the detection period of the multistep waveform. The cyclic sweep, which commences in a positive direction from a potential value at which the electrode is virtually free of oxide, proceeds through the potential region of the desired anodic response for the analyte and then returns to a potential at which all oxide formed during the positive scan is cathodically dissolved. The electrode current is integrated during the cyclic sweep and, accordingly, the anodic charge accumulated for oxide formation on the positive scan is compensated automatically by the cathodic charge for subsequent dissolution of the oxide on the negative scan (3). Hence, IPAD

has a smaller base-line signal than that associated with PAD for the same detection reaction. Furthermore, a substantially lower base-line drift is expected as a result of small variations in the pH and composition of the mobile phase or as a result of the increase in true electrode surface area. Nevertheless, the strategy in IPAD is not sufficient for total elimination of base-line change for large variations in pH and the substitution of a pH-sensitive electrode for the conventional pH-independent SCE reference has been suggested to give further improvement to base-line characteristics in pH-gradient chromatography (4, 5).

Significant advances in the chromatographic separations of simple and complex carbohydrates have resulted from development of new, highly efficient, anion-exchange stationary phases (6-8). These polymer-based materials are robust and tolerant of the alkaline mobile phases desired for optimum sensitivity in the various forms of pulsed electrochemical detection. Anion-exchange liquid chromatography with PAD (LC-PAD) has been applied for the determination of sugar alcohols, monosaccharides, and oligosaccharides (6-9). Typically, mobile phases contain sodium hydroxide or barium hydroxide. Carbohydrates are weak acids with pK_a values in the range of ca. 12-14 (8, 10). Under alkaline conditions, carbohydrates are readily separated in highly efficient anion-exchange columns and the order of increasing k' correlates with decreasing values of pK_a (8). The conclusion that retention is the result of an anion-exchange mechanism is supported by the observation that k' is decreased by addition of an inert anion (e.g., acetate) to the mobile phase (8). Amines (11) and amino sugars (12-16), and several sulfur compounds (17), also have been separated on anion-exchange columns in LC-PAD. The great advantage of PAD in these separations of aliphatic compounds is that direct detection can be achieved with high sensitivity without the need for preinjection or postcolumn derivatizations.

The use of acetate-gradient elution has been described for complex mixtures of carbohydrates (15, 16). We anticipate also that there can be advantage from the use of pH-gradient elution. IPAD has been applied to the determination of amino acids in protein hydrolyzates (18) using a ternary gradient with postcolumn addition of alkaline buffer.

The base-line signal in LC-PAD for carbohydrate separations based on pH-gradient elution can shift in an anodic direction as a function of increasing pH. This shift occurs because the optimum potential for detection of carbohydrates at Au electrodes in alkaline solutions coincides with a value for onset of anodic formation of surface oxide. This onset potential shifts to more negative values with increasing pH by an amount ca. -60 mV pH^{-1} , and the resulting base-line signal shifts in the anodic direction with increased pH as a result of the increased rate of oxide formation. Manual or electronically programmed adjustment of the detection potential during development of the pH gradient is impractical because of the difficulty of predicting the exact pH of the mobile phase in the detector cell. The use of postcolumn addition of a concentrated buffer solution to stabilize the effluent pH is useful; however, the practice causes peak dilution, requires additional hardware, and tends to increase systematic noise.

Here, we describe the use of a glass-membrane, pH-sensitive reference electrode for pH-gradient elution in LC using PAD and IPAD. The selection of a reference electrode in voltammetric and amperometric analyses is traditionally based upon the desire to maintain a constant reference potential that is independent of changes in solution composition. If a pH-sensitive electrode, having pH response approximately equivalent to that of the oxide formation process, is substituted for a conventional pH-independent reference electrode

(e.g., SCE), the voltammetric wave for the oxide formation process should appear to be independent of solution pH. The use of glass-membrane reference electrodes has been described for potentiometric (19) and chelometric analyses (20). A zirconium oxide pH sensor was used as a reference for monitoring corrosion and redox potentials (21). No application was found in the literature for a pH-sensitive reference in voltammetric analysis.

EXPERIMENTAL SECTION

Reagents. All solutions were prepared from reagent grade chemicals. Carbohydrate solutions were prepared immediately prior to use to minimize degradation. Triply distilled water was further purified in a Barnstead NANOpure II system, followed by filtration (0.22 μm). All mobile phases were filtered before use with 0.45- μm Nylon-66 filters (Rainin Corp., Woburn, MA) and a solvent filtration kit (Rainin).

Apparatus and Procedures. Voltammetric data were obtained at a Au rotated disk electrode (RDE) (Pine Instrument Co., Grove City, PA). An electrically grounded "Faraday cage" constructed from copper screen was placed around the cell to minimize pickup of electrical noise for all experiments involving use of the glass, pH electrode.

Liquid chromatographic work employed a gradient chromatography system (Dionex Corp., Sunnyvale, CA). Separations were performed with an HPLC-AS6A anion-exchange analytical column with an AG-6 guard column (Dionex). Isocratic chromatography was performed with a mobile phase of 50 mM NaOH. The gradient program consisted of starting at 2 mM NaOH, ramping linearly to 200 mM NaOH at 15.0 min, and holding at 200 mM NaOH for the duration of the chromatographic run (30 min). All flow rates were 0.5 mL min^{-1} . All injection volumes were 50 μL .

Postcolumn addition of 0.2 M KNO_3 was accomplished with a constant pressure pump (Dionex) at 40 psi which was connected after the analytical column by a tee-connector. A woven Teflon mixing coil was placed after the tee-connector to enhance the rate of mixing of the electrolyte and eluent streams. With the postcolumn addition of electrolyte at 0.5 mL min^{-1} , the PAD cell experienced an isocratic condition of 25 mM NaOH/0.1 M KNO_3 and a gradient solution profile of 1 mM NaOH/0.1 M KNO_3 to 100 mM NaOH/0.1 M KNO_3 .

PAD was performed with the Model PAD-2 electrochemical detector (Dionex). IPAD was performed by software-generated waveforms from a modified Computer Aided Electroanalysis System (Cypress Systems, Lawrence, KS). The Cypress Systems potentiostat was interfaced via a 12-bit analog to digital converter with an IBM-AT compatible personal computer (Everex Systems, Inc., Fremont, CA) connected to a Model 7440A Colorpro plotter (Hewlett-Packard, San Diego, CA).

The thin-layer electrochemical cell (Dionex) was modified to incorporate a Universal pH electrode (Fisher Scientific Co., Springfield, NJ) or a miniature SCE as the reference. The working electrode and counter electrode materials were Au and stainless steel, respectively.

RESULTS AND DISCUSSION

Voltammetry. Current-potential ($I-E$) curves are shown in Figure 1 obtained at the Au RDE in 1 mM NaOH/0.1 M KNO_3 with (—) and without (---) the presence of 0.5 mM glucose. Anodic waves are observed during the positive scan in the residual $I-E$ curve (---) which correspond to the formation of surface oxide at $E > \text{ca. } +0.20 \text{ V}$ (wave A) and O_2 evolution at $E > \text{ca. } +0.8 \text{ V}$ (wave B), respectively. The surface oxide is cathodically dissolved on the negative scan to produce a peak at ca. $+0.05 \text{ V}$ (wave C). Reduction of residual, dissolved O_2 occurs for $E < \text{ca. } -0.15 \text{ V}$ (wave D) during the positive and negative scan.

In the $I-E$ curve obtained for the presence of glucose (—), the anodic signal for $E > \text{ca. } -0.5 \text{ V}$ (wave E) corresponds to oxidation of the aldehyde functionality. The anodic signal for oxidation of alcohol groups of glucose is observed on the positive scan in the region -0.15 to $+0.45 \text{ V}$ (wave F). The anodic response for glucose on the positive scan is sharply

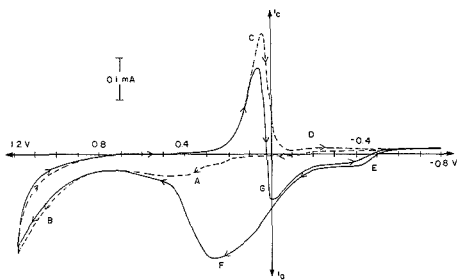
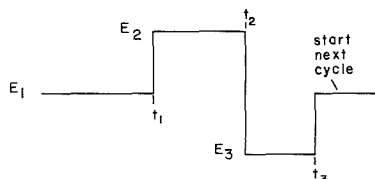


Figure 1. Voltammetric response ($I-E$) for glucose at a gold RDE using a SCE reference: conditions, 1 mM NaOH/0.1 M KNO_3 , deaerated, 1000 rev min^{-1} rotation speed, 150 mV s^{-1} scan rate; solution: (---) supporting electrolyte, (—) 0.5 mM glucose.

Table I. Waveform for Pulsed Amperometric Detection (PAD)



potential, mV vs SCE	time, ms	potential, mV vs PHE	time, ms
E_1 , +200	t_1 , 420	E_1 , +450	t_1 , 420
E_2 , +800	t_2 , 120	E_2 , +1050	t_2 , 120
E_3 , -600	t_3 , 240	E_3 , -350	t_3 , 240

inhibited by the surface oxide formed at $E > \text{ca. } +0.45$ V. During the subsequent negative scan, the cathodic dissolution of the surface oxide (wave C) regenerates an active electrode and oxidation of the glucose is reestablished at ca. +0.10 V (wave G). The voltammetric response of glucose in the region ca. -0.20 to +0.45 V is qualitatively typical of that for all alcohols, polyalcohols, and carbohydrates tested for Au electrodes in this medium.

The waveforms used in PAD and IPAD for the detection of carbohydrates are derived from the $I-E$ response shown in Figure 1. Hence, the value for the detection potential (E_1) in the triple-step waveform of PAD described in Table I is chosen at +0.20 V to give the maximum sensitivity for carbohydrates. The amperometric response at $E_1 = +0.20$ V is composed primarily of anodic current from glucose oxidation with a small contribution from surface oxide formation. Carbonaceous species (e.g. free radicals) which are adsorbed during the detection process and which gradually "foul" the electrode surface, leading ultimately to total loss of electrode activity, are oxidatively desorbed from the electrode surface quite efficiently by stepping the potential to $E_2 = +0.80$ V. The surface oxide film formed at E_2 is cathodically removed by the subsequent step to $E_3 = -0.6$ V. The triple-step PAD waveform described in Table I is applied at a frequency of ca. 1 Hz.

The waveform for application of IPAD for carbohydrates (see Table II) consists of a triangular potential sweep applied during the detection period with continuous integration of the electrode current during the triangular sweep. It is important to choose values for the potentials E_1 and E_3 (see Table II) that are more negative than those required for complete reduction of surface oxide and the values $E_1 = E_3 = -0.20$ V are

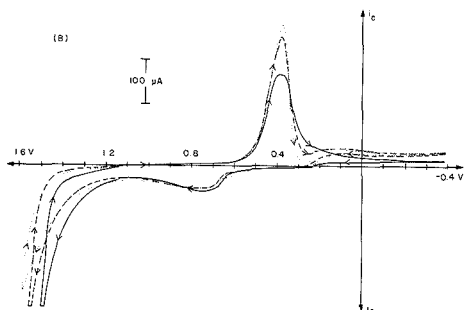
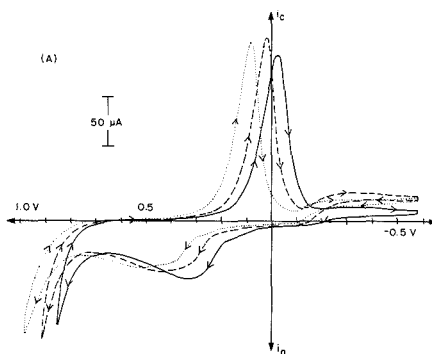


Figure 2. Voltammetric response ($I-E$) of supporting electrolyte at a gold RDE for SCE (A) and glass pH (B) reference electrodes: (···) 1 mM NaOH/0.1 M KNO_3 , (---) 10 mM NaOH/0.1 M KNO_3 , (—) 100 mM NaOH/0.1 M KNO_3 , deaerated; 1000 rev min^{-1} rotation speed, 150 mV s^{-1} scan rate.

appropriate for the conditions of Figure 1. The upper value for the cyclic scan was chosen to be $E_2 = +0.60$ V on the basis of Figure 1.

The value $E_1 = +0.20$ V chosen above for PAD corresponds to the optimum sensitivity for a mobile phase consisting of 1 mM NaOH/0.1 M KNO_3 . However, the potential for onset of oxide formation at Au electrodes shifts to more negative values with increases in pH at a rate of ca. -60 mV pH^{-1} , as is illustrated by the residual $I-E$ curves shown in Figure 2A. These curves were obtained with the Au rotating disk electrode (RDE) using a SCE reference in solutions of 1 mM NaOH/0.1 M KNO_3 at pH = ca. 11 (···), 10 mM/0.1 M KNO_3 at pH = ca. 12 (---), and 100 mM NaOH/0.1 M KNO_3 at pH = ca. 13 (—). The KNO_3 was added to ensure a high ionic strength. The negative shift of the onset potential for oxide formation is obvious with increases in NaOH concentration. Hence, it is apparent that the optimum value of E_1 chosen for carbohydrate detection in 1 mM NaOH would result in a large change in base line for LC-PAD under a gradient from 1 to 100 mM NaOH. A less optimal detection potential (e.g., -0.10 V $\leq E_1 < +0.20$ V) may be chosen to reduce the effect of the base-line change, albeit at the expense of decreased sensitivity.

A glass-membrane, pH-sensitive electrode was substituted for the SCE reference in the electrolysis cell and the residual response obtained again for the Au RDE in the solutions used in Figure 2A. The resulting $I-E$ curves are shown in Figure 2B. Because the pH sensitivity of the glass-membrane electrode (-59 mV pH^{-1} at 25 °C) is virtually the same as for the onset of oxide formation (-60 mV pH^{-1}), the apparent potential for onset of the wave for oxide formation is nearly independent of pH.

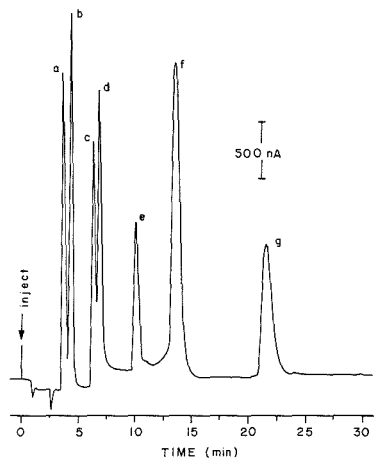


Figure 3. Anion-exchange separation of carbohydrates under isocratic elution with pulsed amperometric detection using a SCE reference electrode: sugars (ppm), (a) sorbitol (13), (b) fucose (15), (c) glucose (25), (d) fructose (44), (e) sucrose (25), (f) turanose (50), (g) maltose (25).

It is especially noteworthy that the potential value for onset of anodic oxide formation obtained by using the pH reference (Figure 2B) is significantly different from those values observed for the SCE reference (Figure 2A). Furthermore, the value in Figure 2B cannot be predicted from Figure 2A unless the so-called "asymmetry potential (E_0)" is determined for the pH electrode. As a consequence for LC with PAD or IPAD, the optimum potential values to be applied in the waveforms when the pH reference is used should be based on I - E data obtained by using the pH reference electrode. Alternately, the potential values could be estimated after the value of E_0

Table II. Waveform for Integrated Pulsed Amperometric Detection (IPAD)

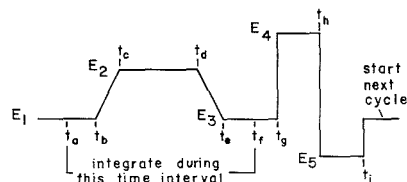


Figure 4. Anion-exchange separation of carbohydrates under gradient elution with pulsed amperometric detection using a SCE (A) and a glass pH (B) reference electrode. Sugars (ppm) are the same as in Figure 3.

potential, mV vs SCE	time, ms	potential, mV vs pH/E	time, ms
E_1 , -200	t_a , 220	E_1 , +50	t_a , 220
	t_b , 15	E_2 , +600	t_b , 15
	t_c , 180	E_3 , -200	t_c , 180
	t_d , 10	E_4 , +800	t_d , 10
	t_e , 180	E_5 , -600	t_e , 180
	t_f , 15		t_f , 15
	t_g , 20		t_g , 20
	t_h , 120		t_h , 120
	t_i , 240		t_i , 240

for the pH electrode is determined by potentiometric measurement vs the SCE reference in a standard buffer solution. For this paper, the applied potentials (i.e., E_1 , E_2 , and E_3) used with the SCE reference were increased uniformly to produce an equivalent response for sorbitol when using the pH reference. The same increases were applied to the values in the IPAD waveform when using the pH reference.

Liquid Chromatography-Pulsed Amperometric Detection. Figure 3 shows the anion-exchange separation of a carbohydrate mixture using PAD (SCE reference) under isocratic conditions. A moderately satisfactory separation was achieved in less than 25 min with only two pairs of partially unresolved peaks. The efficiency of separation for early eluting peaks can be improved by the use of gradient elution chromatography. Results for the separation of the same mixture

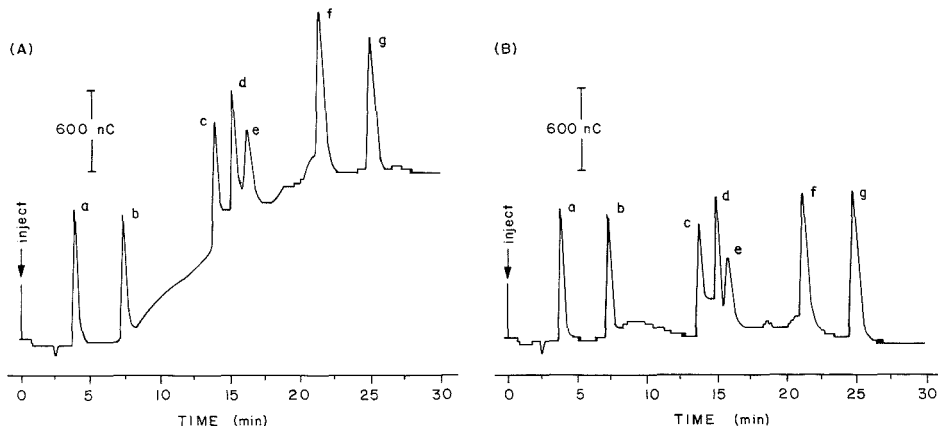


Figure 5. Anion-exchange separation of carbohydrates under gradient elution with integrated pulsed amperometric detection using a SCE (A) and a glass, pH (B) reference electrode. Sugars (ppm) are the same as Figure 3.

of carbohydrates using a linearly increasing NaOH concentration gradient are shown for PAD in Figure 4A with the SCE reference and in Figure 4B for the pH reference. The increase in C_{NaOH} from 1 to 100 mM is considered typical of pH-gradient separations of carbohydrates on high efficiency anion-exchange columns. Since the value of E_1 for the PAD waveform was chosen to correspond to the maximum sensitivity for glucose in 1 mM NaOH/0.1 M KNO_3 , the base line obtained by using the SCE reference (Figure 4A) increased severely in the anodic direction. The chromatogram obtained for the identical C_{NaOH} gradient after substitution of the pH electrode for the SCE reference is shown in Figure 4B. It is clearly apparent the base-line shift obtained by using the pH-sensitive reference is substantially less than for the SCE reference.

The small, remaining base-line shift observed in Figure 4B for use of the pH-sensitive reference is tentatively concluded to be the result of perturbations of the pH within the diffusion layer at the electrode surface as a consequence of faradaic processes occurring within the PAD waveform, as demonstrated by Larew and Johnson (22). The anodic formation of oxide at E_1 and E_2 produces H^+ , $\text{Au} + \text{H}_2\text{O} \rightarrow \text{AuO} + 2\text{H}^+ + 2\text{e}^-$, and the cathodic dissolution of the oxide at E_3 produces OH^- , $\text{AuO} + \text{H}_2 + 2\text{e}^- \rightarrow \text{Au} + 2\text{OH}^-$. If the flux of buffer from the bulk solution to the electrode is small, i.e., a low buffer capacity in the bulk solution, the pH in the diffusion layer at the working electrode surface in the LC detector can be substantially different than the value detected by the pH reference electrode located at a position slightly downstream from the working electrode. Therefore, it is to be expected that use of the pH reference electrode in place of the SCE cannot totally eliminate base-line shift for low values of C_{NaOH} in the gradient elution process. Possible contribution to the base-line shift originating from Na^+ error in the pH electrode was concluded to be insignificant, based on manufacturer claims.

IPAD was applied for the NaOH-gradient separation and the results are shown in Figure 5A for the SCE reference and Figure 5B for the pH reference electrodes, respectively. As illustrated by Figure 5A, IPAD was sensitive to large changes in pH when using the SCE reference. This occurred because the values $E_1 = E_3 = -0.20$ V in the waveform (Table II) were optimized for complete oxide reduction in 1 mM NaOH/0.1 M KNO_3 . As the NaOH concentration was increased, cathodic dissolution of the oxide was incomplete (see Figure 2A). In comparison, the base-line shift was substantially decreased

for LC-IPAD when the pH reference was used. In that case, the values $E_1 = E_3 = +0.05$ V corresponded to complete dissolution of the oxide and, because of the effect of the pH reference, the oxide reduction peak did not shift with changes in solution pH. A comparison of the results in Figures 4 and 5 demonstrates that the switch from the SCE to the pH reference electrode resulted in a ca. 90% decrease in the base-line drift for LC-PAD (from 1500 to 150 nA) and a 100% decrease from LC-IPAD (from 1200 to 0 nC).

ACKNOWLEDGMENT

The contributions of Larry A. Larew and helpful comments of Roy Rocklin are gratefully appreciated.

LITERATURE CITED

- Breiter, M. W. *Electrochim. Acta* **1963**, *8*, 973.
- Gilman, S. In *Electroanalytical Chemistry*; Bard, A. J., Ed.; Marcel Dekker: New York and Basel, 1967; Vol. 2, p 111.
- Neuburger, G. G.; Johnson, D. C. *Anal. Chem.* **1988**, *60*, 2288.
- Mead, D. A.; Larew, L. A.; Johnson, D. C. In *Advances in Ion Chromatography*; Jandik, P., Cassidy, R. M., Eds.; Century International, Inc.: Franklin, MA, Vol. 1, p 13.
- Weich, L. E.; LaCourse, W. R.; Mead, D. A., Jr.; Johnson, D. C.; Hu, T. *Anal. Chem.* **1989**, *61*, 555.
- Rocklin, R. D.; Pohl, C. A. *J. Liq. Chromatogr.* **1983**, *6*, 1577.
- Edwards, W. T.; Pohl, C. A.; Rubin, R. *Tappi J.* **1987**, *70*, 203.
- Olechno, J. D.; Carter, S. R.; Edwards, W. T.; Gillen, J. G. *Am. Biotechnol. Lab.* **1987**, *5*, 38.
- Johnson, D. C. *Nature* **1986**, *321*, 451.
- Rendleman, J. A. *Adv. Chem.* **1973**, No. 117, 51.
- Polta, J. A.; Johnson, D. C. *J. Liq. Chromatogr.* **1983**, *6*, 1727.
- Polta, J. A.; Johnson, D. C.; Merkel, K. E. *J. Chromatogr.* **1985**, *324*, 407.
- Hardy, M. R.; Townsend, R. R.; Lee, Y. C. *Anal. Biochem.* **1988**, *170*, 54.
- Hardy, M. R.; Townsend, R. R. *Proc. Natl. Acad. Sci.* **1988**, *85*, 3289.
- Townsend, R. R.; Hardy, M. R.; Hindsgeul, O.; Lee, Y. C. *Anal. Biochem.* **1988**, *174*, 459.
- Townsend, R. R.; Hardy, M. R.; Olechno, J. D.; Carter, S. R. *Nature* **1988**, *335*, 379.
- Polta, T. Z.; Johnson, D. C. *Chromatogr. Forum* **1986**, *1*, 37.
- Weich, L. E.; LaCourse, W. R.; Mead, D. A., Jr.; Johnson, D. C. *Anal. Chem.* **1989**, *61*, 555.
- Yin, X.; Liu, Y. *Fenzi Haxue* **1984**, *12*, 937.
- Copello, M. A.; De Dorfman, E. A. *Ann. Soc. Client. Argent.* **1966**, *182*, 3.
- Neldrach, L. W. *J. Electrochem. Soc.* **1982**, *129*, 1445.
- Larew, D. C.; Johnson, D. C. *Electroanal. Chem.* **1989**, *264*, 131.

RECEIVED for review June 20, 1989. Accepted October 26, 1989. The majority of this research was supported by a grant from Dionex Corp., Sunnyvale, CA. The National Science Foundation contributed a portion of the funding for purchase of the Cypress Systems instrument through Contract CHE-8312032.

THE AMERICAN CHEMICAL SOCIETY PRESENTS . . .

25 Unique Sources of Archival-Quality Chemistry Research and News

ACCOUNTS OF CHEMICAL RESEARCH

Editor, Fred W. McLafferty
Cornell University
12 issues a year. ISSN 0001-4842
Member \$24 Nonmember \$127

ANALYTICAL CHEMISTRY

Editor, George H. Morrison
Cornell University
24 issues a year. ISSN 0003-2700
Member \$29 Nonmember \$59

BIOCHEMISTRY

Editor, Hans Neurath
University of Washington
*51 issues a year. ISSN 0006-2960
Member \$85 Nonmember \$690

BIOCONJUGATE CHEMISTRY

Editor, Claude F. Meares
University of California, Davis
The unifying medium of conjugation chemistry. BIOCONJUGATE CHEMISTRY will emphasize the joining of two different molecular functions by chemical or biological means.
6 issues a year. ISSN 1043-1802
Member \$29 Nonmember \$249

New in 1990!

BIOTECHNOLOGY PROGRESS

Editor, Jerome S. Schultz
University of Pittsburgh
Jointly published with the American Institute of Chemical Engineers, this established journal offers *new, bimonthly access* to significant research in process development, product development, and equipment/instrumentation design for the biotechnology industry.
6 issues a year. ISSN 8756-7938
Member \$25 Nonmember \$250

New in 1990!

CHEMICAL & ENGINEERING NEWS

Editor, Michael Heylin
51 issues a year. ISSN 0009-2347
Nonmember \$60

CHEMICAL RESEARCH IN TOXICOLOGY

Editor, Laurence J. Marnett
Vanderbilt University
For the latest original findings, in primary research, on the toxicological effects of chemical agents.
6 issues a year. ISSN 0893-228X
Member \$46 Nonmember \$269

CHEMICAL REVIEWS

Editor, Josef Michl
University of Texas, Austin
8 issues a year. ISSN 0009-2665
Member \$26 Nonmember \$225

CHEMISTRY OF MATERIALS

Editor, Leonard V. Interrante
Rensselaer Polytechnic Institute
This new, international journal provides a molecular-level perspective at the interface of chemistry, chemical engineering, and materials science.
6 issues a year. ISSN 0897-4756
Member \$49 Nonmember \$299

CHEMTECH

Editor, Benjamin J. Luberoff
12 issues a year. ISSN 0009-2703
Member \$39 Nonmember (Pers.) \$69
Nonmember (Inst.) \$299

ENERGY & FUELS

Editor, John W. Larsen
Lehigh University
A practitioner's guide to the chemistry of fossil fuels—from formation to methods of utilization.
6 issues a year. ISSN 0887-0624
Member \$48 Nonmember \$294

ENVIRONMENTAL SCIENCE & TECHNOLOGY

Editor, William H. Glaze
University of North Carolina,
Chapel Hill
12 issues a year. ISSN 0013-936X
Member \$36 Nonmember (Pers.) \$67
Nonmember (Inst.) \$276

INDUSTRIAL & ENGINEERING CHEMISTRY RESEARCH

Editor, Donald R. Paul
University of Texas, Austin
12 issues a year. ISSN 0888-5885
Member \$55 Nonmember \$372

INORGANIC CHEMISTRY

Editor, M. Frederick Hawthorne
University of California, Los Angeles
26 issues a year. ISSN 0020-1669
Member \$82 Nonmember \$612

JOURNAL OF AGRICULTURAL AND FOOD CHEMISTRY

Editor, Irvin E. Liener
University of Minnesota
*12 issues a year. ISSN 0021-8361
Member \$25 Nonmember \$204

JOURNAL OF THE AMERICAN CHEMICAL SOCIETY

Editor, Allen J. Bard
University of Texas, Austin
26 issues a year. ISSN 0002-7863
Member \$75 Nonmember \$630

JOURNAL OF CHEMICAL AND ENGINEERING DATA

Editor, Bruno J. Zapolinski
Texas A&M University
4 issues a year. ISSN 0021-9568
Member \$30 Nonmember \$207

JOURNAL OF CHEMICAL INFORMATION AND COMPUTER SCIENCES

Editor, George W.A. Milne, N.I.H.
4 issues a year. ISSN 0095-2338
Member \$18 Nonmember \$108

JOURNAL OF MEDICINAL CHEMISTRY

Editor, Philip S. Portogbesa
University of Minnesota
12 issues a year. ISSN 0022-2623
Member \$42 Nonmember \$329

THE JOURNAL OF ORGANIC CHEMISTRY

Editor, Clayton H. Heathcock
University of California, Berkeley
26 issues a year. ISSN 0022-3263
Member \$56 Nonmember \$428

JOURNAL OF PHYSICAL AND CHEMICAL REFERENCE DATA

Editor, David R. Lide, Jr.
National Institute of Standards &
Technology
*6 issues a year. ISSN 0047-2689
Member \$70 Nonmember \$325

THE JOURNAL OF PHYSICAL CHEMISTRY

Editor, Mostafa A. El-Sayed
University of California, Los Angeles
26 issues a year. ISSN 0022-3654
Member \$70 Nonmember \$670

LANGMUIR

Editor, Arthur W. Adamson
University of Southern California
*12 issues a year. ISSN 0743-7463
Member \$58 Nonmember \$429

MACROMOLECULES

Editor, Field H. Winslow
AT&T Bell Laboratories
*26 issues a year. ISSN 0024-9297
Member \$57 Nonmember \$553

ORGANOMETALLICS

Editor, Dietmar Seyferth
Massachusetts Institute of Technology
12 issues a year. ISSN 0276-7333
Member \$59 Nonmember \$521

For subscription information write:

American Chemical Society
Marketing Communications Dept.
1155 Sixteenth Street, N.W.
Washington, D.C. 20036 U.S.A.

Call toll free 1-800-227-5558.

In Washington, D.C. and outside the U.S.
call 202-872-4363.

Telex: 440159 ACSP UI or 89 2582
ACSPUBS. FAX: 202-872-4615.

For nonmember rates in Japan contact:

Maruzen Co., Ltd.,
3-10 Nihonbashi 2-Chome, Chuo-ku,
Tokyo 103, Japan

*Frequency change in 1990.

Rates are valid through December 31, 1990.

Finally, a real GC/MS for under \$50,000!

HP 5890 Series II GC sets new industry standards with high temperature operation, cool-column injection and pressure programming.

MS ChemStation (DOS series) is 386-based to provide speed and multi-tasking for highest lab productivity.

Sensitive, universal and specific, the HP 5971A MSD produces true EI spectra even from dirty, complex matrices.



Complete quadrupole GC/MS system actually fits on a five-foot lab bench.

Mouse interface simplifies operation.

Now any lab can afford a GC/MS with an HP mass selective detector (MSD). Our new PC-controlled system costs only \$49,770* yet gives you high performance.

There's multitasking for acquiring and analyzing data simultaneously. There's true, classical EI spectra that stand up to challenge. There's Microsoft® Windows software

for ease of use. Plus access to PC word processing, spreadsheets and desktop publishing. And for total automation, you can add an optional autosampler and bar-code reader.

Put the system to work in *any* size laboratory. Even network it to other vendors' data systems. Then enjoy the highest uptime in

the industry because HP is consistently rated number 1 for reliability, service and support. For more, call 1 800 556-1234, Ext. 10218. In CA, 1 800 441-2345, Ext. 10218.

*US list price. Microsoft, MSN, and Windows are registered trademarks of Microsoft Corporation.

 **HEWLETT
PACKARD**